frontiers | Research Topics

Plasma waves in space physics: Carrying on the research legacies of peter gary and richard thorne

Edited by
Joseph E. Borovsky, Charles William Smith, Yuri Y. Shprits, Misa Cowee and Richard Horne

Published in
Frontiers in Astronomy and Space Sciences
Frontiers in Physics

ISSN 1664-8714
ISBN 978-2-83251-874-8
DOI 10.3389/978-2-83251-874-8

About Frontiers

Frontiers is more than just an open access publisher of scholarly articles: it is a pioneering approach to the world of academia, radically improving the way scholarly research is managed. The grand vision of Frontiers is a world where all people have an equal opportunity to seek, share and generate knowledge. Frontiers provides immediate and permanent online open access to all its publications, but this alone is not enough to realize our grand goals.

Frontiers journal series

The Frontiers journal series is a multi-tier and interdisciplinary set of open-access, online journals, promising a paradigm shift from the current review, selection and dissemination processes in academic publishing. All Frontiers journals are driven by researchers for researchers; therefore, they constitute a service to the scholarly community. At the same time, the *Frontiers journal series* operates on a revolutionary invention, the tiered publishing system, initially addressing specific communities of scholars, and gradually climbing up to broader public understanding, thus serving the interests of the lay society, too.

Dedication to quality

Each Frontiers article is a landmark of the highest quality, thanks to genuinely collaborative interactions between authors and review editors, who include some of the world's best academicians. Research must be certified by peers before entering a stream of knowledge that may eventually reach the public - and shape society; therefore, Frontiers only applies the most rigorous and unbiased reviews. Frontiers revolutionizes research publishing by freely delivering the most outstanding research, evaluated with no bias from both the academic and social point of view. By applying the most advanced information technologies, Frontiers is catapulting scholarly publishing into a new generation.

What are Frontiers Research Topics?

Frontiers Research Topics are very popular trademarks of the *Frontiers journals series*: they are collections of at least ten articles, all centered on a particular subject. With their unique mix of varied contributions from Original Research to Review Articles, Frontiers Research Topics unify the most influential researchers, the latest key findings and historical advances in a hot research area.

Find out more on how to host your own Frontiers Research Topic or contribute to one as an author by contacting the Frontiers editorial office: frontiersin.org/about/contact

Plasma waves in space physics: Carrying on the research legacies of peter gary and richard thorne

Topic editors

Joseph E. Borovsky — Space Science Institute, United States
Charles William Smith — University of New Hampshire, United States
Yuri Y. Shprits — GFZ German Research Centre for Geosciences, Germany
Misa Cowee — Los Alamos National Laboratory (DOE), United States
Richard Horne — British Antarctic Survey (BAS), United Kingdom

Citation

Borovsky, J. E., Smith, C. W., Shprits, Y. Y., Cowee, M., Horne, R., eds. (2023). Plasma waves in space physics: Carrying on the research legacies of peter gary and richard thorne. Lausanne: Frontiers Media SA. doi: 10.3389/978-2-83251-874-8

Table of contents

frontiers | Frontiers in Astronomy and Space Sciences

TYPE Editorial
PUBLISHED 22 February 2023
DOI 10.3389/fspas.2023.1149649

OPEN ACCESS

EDITED AND REVIEWED BY
John C. Dorelli,
Goddard Space Flight Center, National Aeronautics and Space Administration, United States

*CORRESPONDENCE
Joseph E. Borovsky,
jborovsky@spacescience.org

SPECIALTY SECTION
This article was submitted to Space Physics, a section of the journal Frontiers in Astronomy and Space Sciences

RECEIVED 22 January 2023
ACCEPTED 03 February 2023
PUBLISHED 22 February 2023

CITATION
Borovsky JE, Cowee MM, Horne RB, Shprits YY and Smith CW (2023), Editorial: Plasma waves in space physics: Carrying on the research legacies of Peter Gary and Richard Thorne.
Front. Astron. Space Sci. 10:1149649.
doi: 10.3389/fspas.2023.1149649

Editorial: Plasma waves in space physics: Carrying on the research legacies of Peter Gary and Richard Thorne

Joseph E. Borovsky[1]*, Misa M. Cowee[2], Richard B. Horne[3], Yuri Y. Shprits[4] and Charles W. Smith[5]

[1]Space Science Institute, Boulder, CO, United States, [2]Los Alamos National Laboratory, Los Alamose, NM, United States, [3]British Antarctic Survey, Cambridge, United Kingdom, [4]Department of Earth and Space Sciences, University of California, Los Angeles, Los Angeles, CA, United States, [5]Space Science Center, University of New Hampshire, Durham, NH, United States

KEYWORDS

plasma waves, plasma instabilities, plasma turbulence, wave-particle interactions, radiation belt, solar wind

Editorial on the Research Topic
Plasma waves in space physics: Carrying on the research legacies of Peter Gary and Richard Thorne

The importance of plasma waves to the evolution of the solar wind and to the evolutions and interactions of the multiple particle populations of the Earth's magnetosphere is overwhelming. Two giants in the field of plasma-wave physics recently passed -- Peter Gary and Richard Thorne (cf. Figure 1). Peter and Richard largely established the complexities of plasma waves, plasma instabilities, wave-particle interactions, and the dissipation of turbulence. They opened the eyes of the space-research community to the impact of plasma waves in the solar wind and in the Earth's magnetosphere. Seminal publications are (Thorne et al., 1973; Thorne, 2010; Thorne et al., 2013; Gary et al., 1984; Gary 1991; Gary and Smith, 2009) and the textbook Gary (1993). They both collaborated widely both nationally and internationally, a key factor that made them world leaders. The Frontiers Research Topic "*Plasma Waves in Space Physics: Carrying On the Research Legacies of Peter Gary and Richard Thorne*" was designed to honor their hard work, their accomplishments, and their leadership and to extend their research legacies into the future.

The goals of the Research Topic were 1) to celebrate the scientific achievements of Richard Thorne, Peter Gary, and the entire space-plasma-physics research community, 2) to showcase state-of-the-art research findings, and 3) to take an assessment (a) of the present state of knowledge and (b) of where the research community goes in the future.

From this Frontiers Research Topic 14 papers on plasma waves, wave-particle interactions, plasma-wave instabilities, and plasma turbulence are contained in this electronic book. Synopses of the 14 papers are as follows, ordered by papers that focus on 1) plasma waves, 2) wave-particle interactions, 3) plasma-wave instabilities, and 4) plasma turbulence.

Hartinger et al. (2022) review the progress made by the "ULF Wave Modeling, Effects, and Applications" GEM focus group. This review article makes the connection of modern UL F wave research to the ULF wave research of Peter Gary and Richard Thorne.

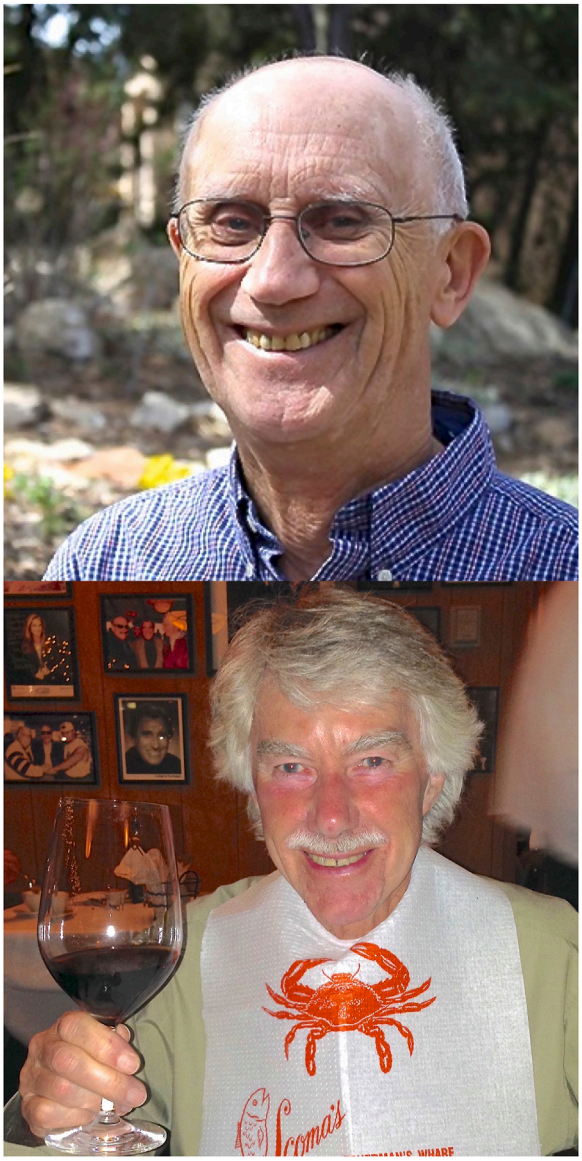

FIGURE 1
Photographs of Peter Gary (top) and Richard Thorne (bottom).

Albert et al. (2022) examine the equations of motion for test particles encountering field-aligned whistler-mode waves. The investigation focuses on which approximations in the equations of motion capture phase trapping and phase bunching as functions of particle pitch angle.

Haas et al. (2022) examine the pitch-angle distribution of ~10 keV electrons in the ring-current region of the Earth's magnetosphere finding that wave-particle interactions are a minor contributor for moderate storms but an important contributor for strong (Kp > 6) storms. They investigate the use of the Kp index as a proxy (predictor) of the flux of electrons in the ring current region of the Earth's magnetosphere.

Lejosne et al. (2022) review different physical processes that lead to the energization of radiation-belt electrons. They specifically compare radial-diffusion acceleration versus chorus-wave energization, pointing out the insightful contributions of Richard Thorne in focusing on whistler-mode-chorus wave-particle interactions. The Lejosne et al. review highlights the existing challenges in discerning the relative importance of the two processes (radial diffusion versus whistler-mode wave-particle energization) for radiation-belt electron acceleration.

Smirnov et al. (2002) extensively examine the evolution of outer-radiation-belt electron pitch-angle distributions during 129 geomagnetic storms, versus the energy range of the electrons and verses dayside/nightside. They find that the pitch-angle distributions of lower-energy electrons show little evolution through a storm but that higher-energy electrons show distinct evolution through the various phases of a storm.

Borovsky (2021) discusses a system-science view of diverse ion and electron populations interacting *via* wave-particle interactions, both in the solar wind and in the Earth's magnetosphere. An important point is that the diverse ions and electrons are co-located because of their confinement by the magnetic field.

Verscharen et al. (2022) review multiple electron plasma-wave instabilities in the solar wind driven by non-equilibrium electron distributions as a function of distance from the sun. The review importantly discusses unsolved questions about electron-driven instabilities in the solar wind.

Zenteno-Quinteros and Moya (2022) examine the whistler-heat-flux instability in the solar wind driven by the high-energy tails of the solar-wind electron distribution functions. They use a "core-strahlo" description of the electron distribution with a skewed kappa distribution of the strahl population.

Winske and Wilson (2002) focus on Peter Gary's contributions to the understanding of electromagnetic ion-beam instabilities driving ULF waves in the Earths foreshock. The discussion focuses on theory, ISEE-spacecraft observations, and subsequent unsolved Research Topic.

Le et al. (2003) examine the resonant right-hand ion-beam instability in the Earth's foreshock driven in the solar-wind plasma by ions reflected from the Earth's bow shock. Using hybrid computer simulations and spacecraft observations they find that plasma-wave modes with a variety of propagation angles are excited.

Birn et al. (2022) examine the statistics of test electrons in MHD simulations of magnetotail dipolarization events to examine expected electron anisotropy distributions which could drive plasma waves *via* micro-instabilities. They confirm that the dynamics of the electrons are chiefly governed by betatron and first-order Fermi acceleration.

Narita et al. (2002) overview the legacy of Peter Gary, who made large contributions to the picture of short-wavelength plasma turbulence. In the kinetic range of turbulence two pathways for energy cascade are discussed, one involving Alfven waves and the other involving magnetosonic waves.

Cui et al. (2022) use particle-in-cell simulations to explore the various roles that the whistler-anisotropy instability play in whistler turbulence. They find that the whistler-anisotropy instability may act as a regulation mechanism for turbulence in the kinetic range *via* wave-particle interactions.

Allanson et al. (2022) use a Markovian approach to examine charged-particle dynamics for electromagnetic waves propagating parallel to or antiparallel to a uniform magnetic field. They derive quasilinear diffusion coefficients are derived using this physically intuitive approach.

Author contributions

All authors listed have made a substantial, direct, and intellectual contribution to the work and approved it for publication.

Funding

JB was supported at the Space Science Institute by the NSF GEM Program *via* grant AGS-2027569 and by the NASA HERMES Interdisciplinary Science Program *via* grant 80NSSC21K1406.

Acknowledgments

The authors of this editorial were honored to be able to oversee this Research Topic focused on the legacy of Peter Gary and Richard Thorne. The authors thank Xochitl Blanco-Cano and Olga Khabarov for their help with editorial duties and the authors thank the many reviewers of these articles Laxman Adhikari, Jay Albert, Anton Artemyev, Fraz Bashir, Xochitl Blanco-Cano, Mourad Djebi, Alexei Dmitriev, Phil Erickson, Stephen Fuselier, Nickolay Ivchenko, Amy Keesee, Kris Klein, Arnaud Masson, Thom Moore, Agnit Mukhopadhyay, Yasuhito Narita, Yoshiharu Omura, Kristoff Paulson, Victor Sergeev, Danny Summers, Xin Tao, Daniel Verscharen, Dan Winske, Peter Yoon, and Qiugang Zong.

Conflict of interest

The authors declare that the research was conducted in the absence of any commercial or financial relationships that could be construed as a potential conflict of interest.

Publisher's note

References

Gary, S. P. (1991). Electromagnetic ion/ion instabilities and their consequences in space plasmas: A review. *Space Sci. Rev.* 56, 373. doi:10.1007/bf00196632

Gary, S. P., Smith, C. W., Lee, M. A., Goldstein, M. L., and Forslund, D. W. (1984). Electromagnetic ion beam instabilities. *Phys. Fluids* 27, 1852. doi:10.1063/1.864797

Gary, S. P., and Smith, C. W. (2009). Short-wavelength turbulence in the solar wind: Linear theory of whistler and kinetic Alfven fluctuations. *J. Geophys. Res.* 114, A12105. doi:10.1029/2009ja014525

Gary, S. P. (1993). *Theory of space plasma instabilities*. Cambridge, UK: Cambridge University Press.

Thorne, R. M., Li, W., Ma, Q., Bortnik, J., Chen, L., Baker, D. N., et al. (2013). Rapid local acceleration of relativistic radiation-belt electrons by magnetospheric chorus. *Nature* 504, 411–414. doi:10.1038/nature12889

Thorne, R. M. (2010). Radiation belt dynamics: The importance of wave-particle interactions. *Geophys. Res. Lett.* 37, L22107. doi:10.1029/2010gl044990

Thorne, R. M., Smith, E. J., Burton, R. K., and Holzer, R. E. (1973). Plasmaspheric hiss. *J. Geophys. Res.* 78, 1581–1596. doi:10.1029/ja078i010p01581

frontiers in Astronomy and Space Sciences

PERSPECTIVE
published: 03 November 2021
doi: 10.3389/fspas.2021.780321

Magnetospheric Plasma Systems Science and Solar Wind Plasma Systems Science: The Plasma-Wave Interactions of Multiple Particle Populations

Joseph E. Borovsky *

Center for Space Plasma Physics, Space Science Institute, Boulder, CO, United States

Building upon the research legacies of Peter Gary and Richard Thorne, this perspective discusses a plasma-system picture wherein multiple ion and electron populations interact with each other *via* multiple types of plasma waves. The two cases discussed are 1) the Earth's magnetosphere with ion and electron populations trapped in the closed flux tubes of the magnetic dipole and 2) the solar wind with ion and electron populations expanding away from the Sun in open magnetic flux tubes. For the magnetosphere, internal convection drives particle populations into stronger magnetic fields, leading to particle anisotropies; for the solar wind the expansion of the plasma away from the Sun results in the particle populations moving into weaker magnetic fields, leading also to particle anisotropies. In both cases, the anisotropies of the diverse ion and electron populations produce kinetic instabilities resulting in the production of diverse types of plasma waves and wave-particle interactions. Following the extensive research of Richard Thorne, web diagrams of plasma-wave interactions are laid out for the multiple ion and electron populations of the magnetosphere and following the extensive research of Peter Gary web diagrams of plasma-wave interactions are laid out for the multiple ion and electron populations of the solar wind. The advantages of a systems-analysis approach to these two plasma systems is discussed.

Keywords: magnetosphere, solar wind, system science, plasma waves, plasma instabilities

OPEN ACCESS

Edited by:
Xochitl Blanco-Cano, National Autonomous University of Mexico, Mexico

Reviewed by:
Alexei V. Dmitriev, Lomonosov Moscow State University, Russia
Arnaud Masson, European Space Astronomy Centre (ESAC), Spain

***Correspondence:**
Joseph E. Borovsky
jborovsky@spacescience.org

Specialty section:
This article was submitted to Space Physics, a section of the journal Frontiers in Astronomy and Space Sciences

Received: *20 September 2021*
Accepted: *19 October 2021*
Published: *03 November 2021*

Citation:
Borovsky JE (2021) Magnetospheric Plasma Systems Science and Solar Wind Plasma Systems Science: The Plasma-Wave Interactions of Multiple Particle Populations. Front. Astron. Space Sci. 8:780321. doi: 10.3389/fspas.2021.780321

INTRODUCTION

The Earth's magnetosphere and the solar wind provide two valuable opportunities to bring systems science into the field of plasma physics. Both the magnetospheric system and the solar-wind system are comprised of multiple electron and ion populations with interactions between the populations occurring largely via plasma waves. Many of the plasma-wave interactions of the magnetosphere were uncovered and quantified by Richard Thorne in over 4 decades of research (e.g. Thorne, 1968; Thorne et al., 2017) and many of the plasma-wave interactions of the solar wind were uncovered and quantified by Peter Gary in over 4 decades of research (e.g. Gary, 1974; Gary et al., 2020). Without theses two visionary researchers, these two coherent plasma-systems pictures could not be created.

Both the magnetosphere and the solar wind exhibit multiple populations of ions and electrons that are co-located (i.e. that reside on the same magnetic-field lines) so that the multiple populations

easily interact with each other. The evolution of magnetized plasmas often leads to anisotropies giving rise to instabilities and wave-particle interactions: for the magnetosphere the particle anisotropies arise from solar-wind-driven magnetospheric internal convection pushing particle populations into the strong magnetic field of the dipolar regions and for the solar wind the particle anisotropies arise from the solar-wind expansion into weaker magnetic fields away from the Sun. For every plasma-wave instability, wave-particle interactions act in two fashions: in driving the waves and in dissipating the waves. In this manner two diverse particle populations can interact with each other.

In this perspective article the plasma system science of the magnetosphere and the plasma system science of the solar wind will be briefly outlined. The magnetosphere is a driven closed system (more or less), with the multiple particle populations trapped in dipolar (or stretched) magnetic flux tubes. The solar wind is an open system with multiple particle populations born in the solar corona and moving outward at different speeds from the Sun in open magnetic flux tubes.

This paper is organized as follows. In *The Magnetospheric System* Section the magnetospheric plasma system is described. In *The Solar-Wind System* Section the solar-wind plasma system is described. *Discussion* Section contains discussions of 1) previous system-science analysis that has been done for the magnetosphere and the solar wind, 1) the availability of data for future studies, and 3) some advantages that systems analysis may provide.

THE MAGNETOSPHERIC SYSTEM

The Earth's magnetosphere is a system of multiple trapped particle populations with free energy added from the solar wind, which drives internal convection. Convection of particle populations into the stronger field of Earth's dipole drives particle anisotropies and free energy for plasma waves. The resulting multiple plasma instabilities gives rise to multiple couplings between the diverse particle populations, resulting in a complex evolution of those diverse particle populations. A thorough review of the Earth's magnetosphere as a system wherein the multiple ion and electron populations interact *via* plasma waves appears in Borovsky and Valdivia (2018).

The key to the interaction of the different particle populations is the fact that they are co-located on the same magnetic field lines. There are three major regions in the Earth's magnetosphere and the three regions contain differing particle populations. The first region is the stretched-field "magnetotail" on the nightside of the Earth. The major particle populations of the magnetotail are the ion plasma sheet, the electron plasma sheet, the cusp-mantle (ions and electrons), and the polar wind (ions and electrons). The second region is the "outer dipole": this region contains the ion plasma sheet (ions), the electron plasma sheet (electrons), substorm-injected ions, substorm-injected electrons, the electron radiation belt, the ion radiation belt, cloak ions, cloak electrons, and polar-wind ions and electrons. The third region is the "inner dipole" closest to the Earth: this region contains the plasmasphere (ions and electrons), the ion plasma sheet, substorm-injected ions, the electron radiation belt, and the ion

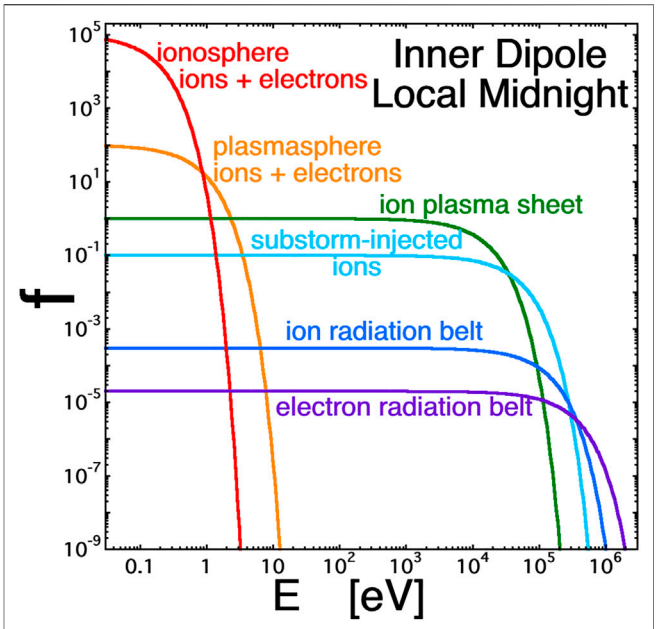

FIGURE 1 | A sketch of the distribution functions of 5 ion populations and 3 electron populations on the same magnetic field line in the inner-dipole region of the nightside magnetosphere.

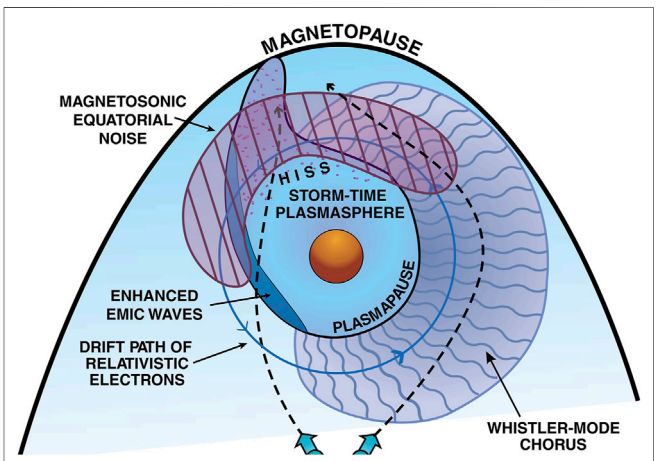

FIGURE 2 | A reproduction of the classic Figure 1 of Thorne (2010) that sketches in the equatorial plane of the Earth's magnetosphere the major types of plasma waves observed in the different regions of the magnetosphere. The viewing is from above the north pole of the Earth: the Sun is at the top of the sketch, dawn is to the right, and dusk is to the left.

radiation belt. The boundary between the inner and outer dipole regions is the plasmapause, which is the outer boundary of the dense, cold plasmasphere.

As an example of the co-location of multiple particle populations, **Figure 1** provides a sketch of the distribution functions of the ions and electrons in the inner dipolar region at local midnight. The plot is a log-log plot, sketching each particle distribution as a Maxwellian, which in general they are not. (The hotter populations often have anisotropies and

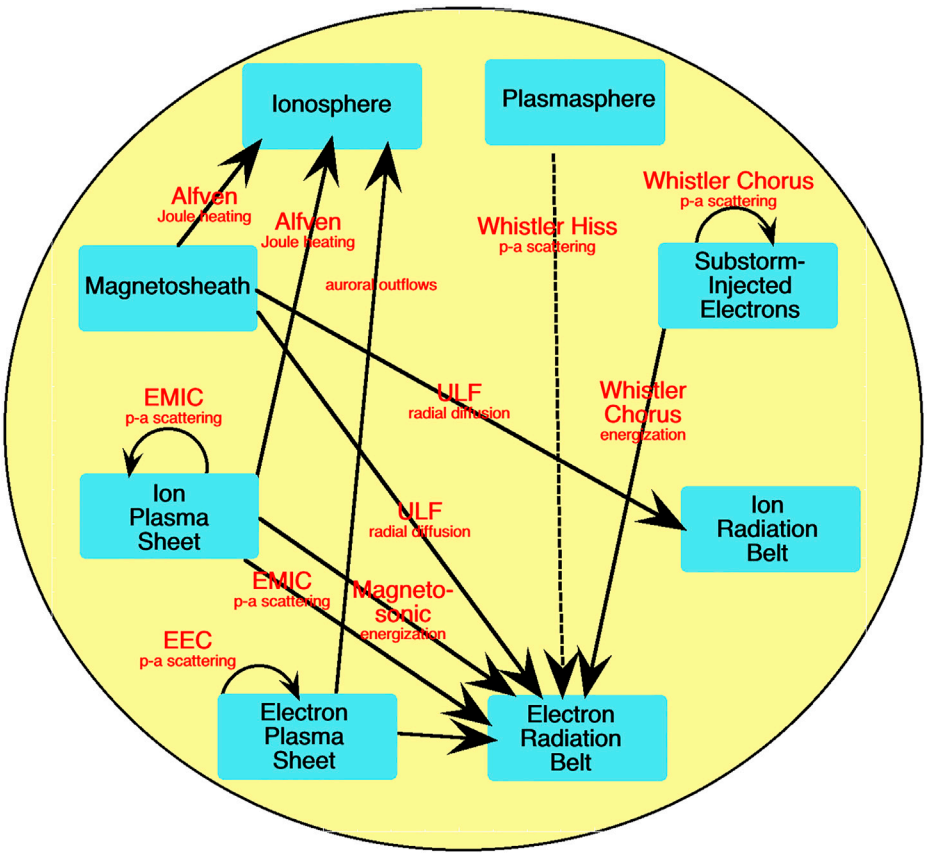

FIGURE 3 | A sketch of the web of plasma-wave interactions between the major ion and electron populations of the Earth's magnetosphere.

biteouts). The populations range in energy from the ionosphere ($T_i \approx T_e \sim 0.1$ eV) and plasmasphere ($T_i \approx T_e \sim 0.5$ eV) to the ion radiation belt (which has a tail of particles in the 1-MeV range of energies) and the electron radiation belt (which has a tail of particles in the 10-MeV range).

The plasma populations of the magnetosphere interact *via* plasma waves. The typical types of plasma waves observed depend on the region of the magnetosphere and the ion and electron populations in that region that can drive the waves. **Figure 2** is a classic sketch from Thorne (2010) that has been reproduced in numerous scientific publications: the sketch depicts the equatorial plane of the Earth's magnetosphere and the major types of plasma waves that impact the electron radiation belt observed in the various regions. The types of plasma waves seen inside the plasmapause (inner dipole) differ from the types seen outside the plasmapause (outer dipole), with drastically different consequences for the particle populations in those two regions. Critical to the evolution of the electron radiation belt, **Figure 2** depicts that whistler-mode chorus waves exist outside of the plasmasphere (outer dipole), whistler-mode hiss waves exist inside of the plasmasphere (inner dipole), and electromagnetic ion-cyclotron (EMIC) waves tend to exist inside the plasmasphere (inner dipole).

In the interactions of co-located particle populations *via* plasma waves in the Earth's magnetosphere, typically a warm (keV) population of particles with medium density is the driver for the waves and typically a very-energetic populations (100's of keV) with a very-low-density is the absorber of the wave energy. And often there is a high-density cold population of ions or electrons that regulates the plasma-wave dispersion relation, determining what waves can be driven and determining the resonance conditions for those waves (cf. Delzanno et al., 2021).

In **Figure 3** a map is displayed of the basic web of interactions between the multiple electron and ion populations of the Earth's magnetosphere and the type of plasma wave that mediates each interaction. (The various plasma waves in **Figure 3** are elaborated upon in Section 6 of Borovsky and Valdivia (2018).). In the map of **Figure 3** the direction of each arrow indicates the transfer of wave action: from the driving population to the receiving population. For the receiving population, the waves can lead to energization and/or to pitch-angle scattering, with pitch-angle scattering often leading to scattering into the atmospheric loss cone where the scattered ions or electrons are lost from the magnetospheric system into the atmosphere. Note in **Figure 3** that a number of "circular" wave interactions are indicated: here one portion of a single population will drive waves that affect another portion of the same population. This often produces

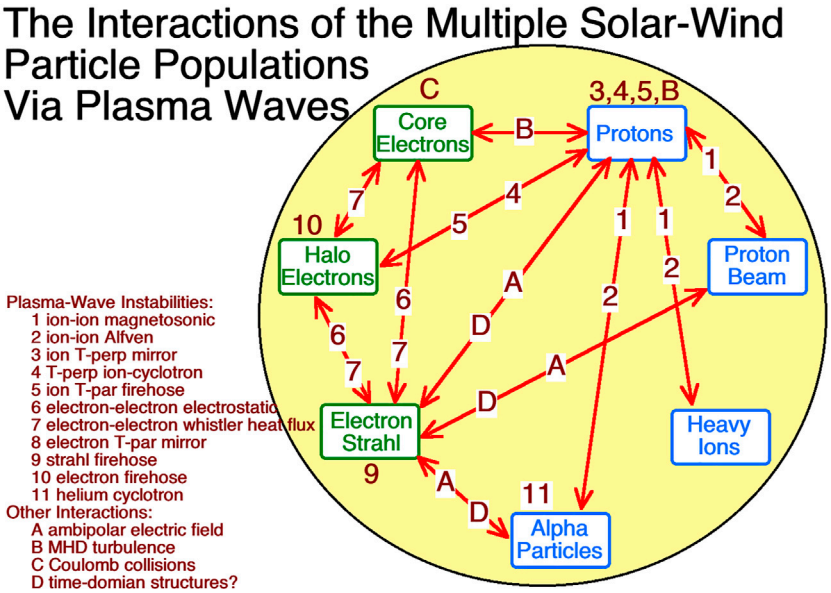

FIGURE 4 | A sketch of the web of plasma-wave interactions between the major ion and electron populations of the solar wind. (This interaction map is an update of Figure 8 of Viall and Borovsky (2020), which was assembled by the author with critical guidance from Peter Gary).

pitch-angle scattering into the atmospheric loss cone, resulting in a loss from the magnetospheric system and perhaps producing aurora in the upper atmosphere.

The complicated system of instability-driven wave-particle interactions that drive the evolution of the multiple ion and electron populations of the Earth's magnetosphere were largely worked out by Richard Thorne. Focused review articles on these various interactions can be found in Thorne and Kennel (1971), Thorne et al., (1973, 1979, 2010, 2013, 2017), Thorne (1974, 2010), Thorne and Summers (1991), and Thorne and Horne (1992, 1994).

One hallmark of a "complex system" is that the system exhibits "emergence", new things "emerge", i.e. the system creates something from nothing. Examples of emergence are given in Borovsky and Valdivia (2018). On example of emergence in the Earths magnetospheric system is the electron radiation belt: here the system takes medium-energy short-lifetime substorm-injected electrons and, via a complex web of interactions, creates a population of high-energy long-lifetime relativistic electrons.

THE SOLAR-WIND SYSTEM

The magnetic structure of the solar-wind plasma resembles a spaghetti of magnetic flux tubes with strong current sheets forming the boundaries between adjacent flux tubes (Michel, 1967; Bruno et al., 2001; Borovsky, 2008; Greco et al., 2008; Pecora et al., 2019). The field of most of the solar wind is "open", with field lines magnetically connecting the Sun to the distant heliosphere. The multiple solar-wind particle populations are born in the solar corona and move outward (at different speeds) along the magnetic field in the open flux tubes. Note, however, that many of the details of the physical processes in the corona that are acting in the birth of the solar wind are not known (cf. Cranmer et al., 2017).

The solar-wind plasma in the inner heliosphere has 7 major particle populations: protons, alpha particles, highly charged heavy ions, an antisunward proton beam, core electrons, halo electrons, and a field-aligned energetic electron strahl. Minor populations can include a sunward streaming proton beam.

As the fast energetic strahl electrons move outward from the Sun they produce an ambipolar electric field that pulls ions outward from the Sun against the Sun's gravity (Jockers, 1970; Lemaire, 2010). This magnetic-field-aligned electrostatic "interplanetary electric field", in part, accelerates the solar wind to high velocities. (A similar process occurs on the sunlit ionosphere of Earth where multi-eV photoelectrons from the atmosphere produce an ambipolar electric field that pulls sub-eV ions out against the Earth's gravity: this is the "polar wind" (Schunk, 2007).) The field-aligned potential drop from the Sun to infinity is on the order of 1 kV, with most of that drop occurring between the Sun and the orbit of Mercury. As the ion and electron populations of the solar wind move outward from the Sun (at different speeds), they interact and evolve. Some of the plasma-wave interactions between the major particle populations are mapped out in **Figure 4**.

Free energy sources for the system evolution are (cf. Borovsky and Gary, 2014; Smith and Vasquez, 2021) 1) electron heat flux, 2) large-amplitude Alfvén waves, 3) the relative drift between alpha particles and protons, and 4) anisotropies driven by the

changing magnetic-field strength. Well beyond 1 AU other sources are interplanetary shocks (Smith et al., 1985) and interstellar pickup ions (Lee, 2018).

It is thought that whistle-mode scattering of the field-aligned strahl electrons gives rise to the quasi-isotropic energetic electron halo population (Gary and Saito, 2007): as evidence, with distance from the Sun the strahl population becomes fractionally less dense and the halo population becomes fractionally more dense (Stverak et al., 2009).

A key source of energy in the solar wind resides in outward propagating Alfvénic fluctuations from the corona. About half of the solar wind at 1 AU is Alfvénic, with strong correlations between the vector changes in the magnetic field and the vector changes in the proton flow velocity. In the Alfvénic solar wind, it is observed that the magnetic structure moves en masse relative to the proton plasma at a speed of about 0.7 v_A (Borovsky, 2020a; Nemecek et al., 2020), where v_A is the measured Alfvén speed. In the reference frame of the magnetic structure, to within measurement error all proton flows $\underline{\mathbf{v}}$ are parallel to the local magnetic-field direction $\underline{\mathbf{B}}$; with $v_\perp = 0$ there is (to within measurement error) no time evolution of the magnetic structure as it moves outward through the inner heliosphere. This is an example of the Chadrasekhar dynamic equilibrium ("CDE") (cf. Fig. 7.1 of Parker (1979)) where a nonlinear tangle (spaghetti) of magnetic field will propagate en masse without evolution provided that the flow is everywhere parallel to the local field. The alpha particles of the solar wind (and perhaps also the heavy ions) reside nearly at rest in the reference frame of the magnetic structure (Nemecek et al., 2020): it is not known why. The outward-propagating Alfvénic structure interacts with the particle populations 1) via parametric instabilities (e.g. Malara et al., 2001; Vasquez and Hollweg, 1996) and 2) *via* an MHD-turbulence cascade where the Alfvén waves transfer energy into electrons and ions via mode conversion (Gary and Smith, 2009; Gary et al., 2020) followed by kinetic (cyclotron or Landau) damping (Leamon et al., 1998; Gary and Borovsky, 2004, 2008).

Because of the relative motion of the alpha particles with respect to the proton population, ion-ion streaming instabilities can couple the two populations (Gary, 1991; Gary et al., 2000a). In particular, the alpha-proton magnetosonic instability acts to heat both populations in a fashion such that the protons and alpha particles both have the same thermal speed (Gary et al., 2000b), which is observed in the solar wind (Feynman, 1975).

As the particle populations move outward from the Sun into weaker magnetic fields, conservation of the particle first adiabatic invariants v^2_{perp}/B decreases the perpendicular temperatures of the populations and leads to anisotropy. For the protons the firehose instability driven by $T_{parallel} > T_{perp}$ acts to return the proton population toward isotropy (Gary et al., 1998, 2001). Similar instabilities act on the alpha-particle anisotropy (Gary et al., 2003) and on the electron anisotropy (Gary and Nishimura, 2003).

Core electrons originate from the low-energy portion of the strahl population (e.g. Boldyrev et al., 2020). The core electrons are locally trapped along the magnetic field (Marsch, 2006): 1) moving toward the Sun the core electrons mirror as the interplanetary magnetic field gets stronger nearer to the Sun and 2) moving away from the Sun the interplanetary electric field pulls them back. The core-electron temperature reflects the local potential of the plasma with respect to infinity (away from the Sun) (Feldman et al., 1975).

Review articles on the diverse types of solar-wind plasma waves and their impact on the solar-wind particle populations can be found in Gary (1991, 1992, 1999), Gary et al. (1975a,b, 1976, 1984, 1994, 1999, 2000a), and Gary and Karimabadi (2006) and in the monograph Gary (1993).

Here we see the system, with the strahl driving the interplanetary potential that drives the solar wind outward. As the populations move through each other at different speeds (all moving outward), they interact *via* plasma waves (cf. Figure FF03).

The magnetic-field structure of the solar wind resembles a spaghetti of magnetic flux tubes separated by current sheets. The diameters of the flux tubes vary, but a typical flux tube at 1 AU has a diameter of about 4×10^5 km, and a spacecraft crosses from one flux tube to the next every 10 or 20 min. From tube to tube there can be differences in the plasma properties: proton specific entropy, ion composition, magnetic-field strength, plasma beta, etc. Important for this system-science picture, the strahl intensity (Borovsky, 2020b) and the electron temperature (Borovsky et al., 2021) can vary from tube to tube with sudden jumps in the values as the current-sheet wall between flux tubes is crossed. The electron-temperature jumps indicate that the interplanetary electric potential differs from flux tube to flux tube. This implies that each flux tube is an independent evolving system, and that as a solar-wind spacecraft crosses from tube to tube it is measuring different realizations of system evolution. This opens the possibility of statistical plasma system science.

DISCUSSION

This section discusses previous system-science analysis that has been done for the magnetosphere and the solar wind, the availability of quality data for future studies, and the advantages that systems analysis may provide.

Plasma Systems Science and Data Availability

Reviews of magnetospheric system-science work can be found in Valdivia et al., [2005, 2013], Vassiliadis (2006), Stepanova and Valdivia, 2016, and Borovsky and Valdivia (2018). Early magnetospheric system science began with two-variable correlation studies between near-Earth solar-wind measurements and measures of the strength of magnetospheric activity (Snyder et al., 1963; Clauer et al., 1981; McPherron et al., 2015): those studies yielded critical information about the processes by which the solar wind drives magnetospheric activity and important information about the multiple reaction times of the magnetospheric system to changes in the solar wind. Later, vector-vector correlation studies (Borovsky and Osmane, 2019) yielded information about multiple modes of reaction of the magnetospheric system to the solar wind. Information-

transfer studies (Wing and Johnson, 2019) have further refined our knowledge about solar-wind driving and in future can be used to examine the causality pathways through the multiple ion and electron populations of the magnetosphere as they undergo the web of interactions (cf. **Figure 3**). Toy mathematical models (Smith et al., 1986; Goertz et al., 1993; Vassiliadis et al., 1993; Klimas et al., 1997; Freeman and Morley 2004; Spencer et al., 2018) have also been constructed and used to gain understandings of the dynamical behaviors of the solar-wind-driven magnetospheric system. In contrast, for the solar-wind plasma system very little system analysis has been performed. Most of the data analytics applied to the solar wind has focused on investigating the nature of the MHD fluctuations in the wind (e.g. Burlaga and Klein, 1986; Marsch and Tu, 1997; Wawrzaszek et al., 2019), not on the particle-population evolution. Here again, information-transfer analysis may be helpful for uncovering and gauging the importance of the various intercouplings of the particle populations with distance from the Sun.

For magnetospheric systems science diverse measurements of the magnetosphere-ionosphere system have been available for over 5 decades, as are measurements of the solar wind at Earth that drives the system. For solar wind system science quality spacecraft data throughout the inner heliosphere from about 15 solar radii to 1 AU (215 solar radii) and beyond are available from multiple spacecraft. For the most part this spacecraft data is centralized and publically available, but with effort more plasma data from the spacecraft of diverse government agencies could be made publically available for scientific purposes.

Advances That Could be Made With a Systems Science Approach

For the Earth's magnetosphere, global simulations codes cannot build in all of the diverse ion and electron populations, all of the kinetic wave processes, and the huge span of important spatial scales. Ring-current-subsystem codes (Jordanova et al., 2001, 2012; Gamayunov et al., 2009) and radiation-belt-subsystem codes (Varotsou et al., 2005; Shprits et al., 2008a,b; Jordanova et al., 2018) resort to using diffusion coefficients or particle lifetimes to represent the action of waves (energization, pitch-angle scattering, and radial diffusion) acting upon the particle populations, typically with diffusion coefficients based on statistical pictures of plasma-wave observations parameterized by magnetospheric-activity levels. Systems analysis examines the behavior of the actual measured system that includes all of these attributes, extracting information about the behavior of the true, fully realized system. This perspective article encourages the development of systems science methodologies specifically for the critical science challenge of understanding the time-evolving solar-wind-driven magnetosphere-ionosphere system, where physics-based simulations are a long way from containing the physics necessary to simulate the coupled system. The situation is similarly difficult for the evolving solar wind: in the near future simulation codes will not be able to capture all of the diverse ion and electron populations and kinetic wave-particle processes that act as the solar wind evolves from the solar corona outward into the heliosphere. System science analysis of the actual system will be needed.

A systems science analysis can yield unique information about the behavior of a system, including the uncovering of hidden or unnoticed modes of behavior. Systems science analysis works even before all of the physics is identified or understood. It can find couplings and feedback loops in the operation of a system. This information has the potential to guide reductionist data analysis, to guide the development of simulation techniques, and to guide the design of new instruments and new measurement techniques. Systems analysis can be used to test the veracity of simulation codes: performing the same systems analysis on simulation data as on the actual system can compare the statistical behavior of the simulations and the actual system.

Systems science tools that may be developed specifically for the multiple interacting plasmas of the magnetospheric system or the solar-wind system may be generalizable to other problems: laboratory plasma experiments, fusion machines, solar physics, and plasma astrophysics. The tools developed for the solar-wind-driven magnetospheric system may also be useful for other driven systems, such as biological organisms and economic systems.

An integration of magnetospheric systems science into the broader research field of "Earth systems science" could enhance the scientific and societal impact of plasma physics (Thorne, 1977, 1980; Tinsley 2000; Georgieva et al., 2005; Rycroft et al., 2012; Sinnhuber et al., 2012; Clilverd et al., 2016; Lam and Tinsley 2016).

DATA AVAILABILITY STATEMENT

The original contributions presented in the study are included in the article/Supplementary Materials, further inquiries can be directed to the corresponding author.

AUTHOR CONTRIBUTIONS

JB initiated this project, performed the analysis, and wrote the manuscript.

FUNDING

This work was supported at the Space Science Institute by the NSF GEM Program via grant AGS-2027569, by the NSF SHINE program *via* grant AGS-1723416, by the NASA Heliophysics LWS program *via* award NNX16AB75G, and by the NASA Heliophysics Guest Investigator Program *via* award NNX17AB71G.

ACKNOWLEDGMENTS

This paper is dedicated to the memory of my friend, collaborator, and mentor Peter Gary and to the memory of my friend and colleague Richard Thorne. The author thanks Gian Luca Delzanno, Mick Denton, Adnane Osmane, and Juan Valdivia for helpful conversations.

REFERENCES

Boldyrev, S., Forest, C., and Egedal, J. (2020). Electron temperature of the solar wind. *Proc. Natl. Acad. Sci. USA* 117, 9232–9240. doi:10.1073/pnas.1917905117

Borovsky, J. E., and Gary, S. P. (2014). How important are the alpha-proton relative drift and the electron heat flux for the proton heating of the solar wind in the inner heliosphere. *J. Geophys. Res. Space Phys.* 119, 5210–5219. doi:10.1002/2014ja019758

Borovsky, J. E., Halekas, J. S., and Whittlesey, P. L. (2021). The electron structure of the solar wind. *Front. Astron. Space Sci.* 8, 69005. doi:10.3389/fspas.2021.690005

Borovsky, J. E. (2020a). On the motion of the heliospheric magnetic structure through the solar wind plasma. *J. Geophys. Res.* 125, e2019JA027377. doi:10.1029/2019ja027377

Borovsky, J. E., and Osmane, A. (2019). Compacting the description of a time-dependent multivariable system and its multivariable driver by reducing the state vectors to aggregate scalars: the Earth's solar-wind-driven magnetosphere. *Nonlin. Process. Geophys.* 26, 429–443. doi:10.5194/npg-26-429-2019

Borovsky, J. E. (2008). The flux-tube texture of the solar wind: Strands of the magnetic carpet at 1 AU. *J. Geophys. Res.* 113, A08110. doi:10.1029/2007ja012684

Borovsky, J. E. (2020b). The magnetic structure of the solar wind: Ionic composition and the electron strahl. *Geophys. Res. Lett.* 47, e2019GL084586. doi:10.1029/2019gl084586

Borovsky, J. E., and Valdivia, J. A. (2018). The Earth's Magnetosphere: A Systems Science Overview and Assessment. *Surv. Geophys.* 39, 817–859. doi:10.1007/s10712-018-9487-x

Bruno, R., Carbone, V., Veltri, P., Pietropaolo, E., and Bavassano, B. (2001). Identifying intermittency events in the solar wind. *Planet. Space Sci.* 49, 1201–1210. doi:10.1016/s0032-0633(01)00061-7

Burlaga, L. F., and Klein, L. W. (1986). Fractal structure of the interplanetary magnetic field. *J. Geophys. Res.* 91, 347–350. doi:10.1029/ja091ia01p00347

Clauer, C. R., McPherron, R. L., Searls, C., and Kivelson, M. G. (1981). Solar wind control of auroral zone geomagnetic activity. *Geophys. Res. Lett.* 8, 915–918. doi:10.1029/gl008i008p00915

Clilverd, M. A., Rodger, C. J., Andersson, M. E., Seppälä, A., and Verronen, P. T. (2016). Linkages between the radiation belts, polar atmosphere and climate: electron precipitation through wave particle interactions. in *Waves, Particles, and Storms in Geospace*, G. Balasis, I. A. Daglis, and I. R. Mann (eds.), pg. 354–376. Oxford University Press, Oxford.doi:10.1093/acprof:oso/9780198705246.003.0015

Cranmer, S. R., Gibson, S. E., and Riley, P. (2017). Origins of the ambient solar wind: Implications for space weather. *Space Sci. Rev.* 212, 1345–1384. doi:10.1007/s11214-017-0416-y

Delzanno, G. L., Borovsky, J. E., Henderson, M. G., Resendiz Lira, P. A., Roytershteyn, V., and Welling, D. T. (2021). The impact of cold electrons and cold ions in magnetospheric physics. *J. Atmos. Solar-Terrestrial Phys.* 220, 105599. doi:10.1016/j.jastp.2021.105599

Feldman, W. C., Asbridge, J. R., Bame, S. J., Montgomery, M. D., and Gary, S. P. (1975). Solar wind electrons. *J. Geophys. Res.* 80, 4181–4196. doi:10.1029/ja080i031p04181

Feynman, J. (1975). On solar wind helium and heavy ion temperatures. *Sol. Phys.* 43, 249–252. doi:10.1007/bf00155156

Freeman, M. P., and Morley, S. K. (2004). A minimal substorm model that explains the observed statistical distribution of times between substorms. *Geophys. Res. Lett.* 31, L12807 1–4. doi:10.1029/2004gl019989

Gamayunov, K. V., Khazanov, G. V., Liemohn, M. W., Fok, M.-C., and Ridley, A. J. (2009). Self-consistent model of magnetospheric electric field, ring current, plasmasphere, and electromagnetic ion cyclotron waves: Initial results. *J. Geophys. Res.* 114, A03221. doi:10.1029/2008ja013597

Gary, S. P., Bandyopadhyay, R., Qudsi, R. A., Matthaeus, W. H., Maruca, B. A., Parashar, T. N., et al. (2020). Particle-in-cell Simulations of Decaying Plasma Turbulence: Linear Instabilities versus Nonlinear Processes in 3D and 2.5D Approximations. *ApJ* 901, 160. doi:10.3847/1538-4357/abb2ac

Gary, S. P., and Borovsky, J. E. (2004). Alfvén-cyclotron fluctuations: Linear Vlasov theory. *J. Geophys. Res.* 109, A06105. doi:10.1029/2004ja010399

Gary, S. P., and Borovsky, J. E. (2008). Damping of long-wavelength kinetic Alfvén fluctuations: Linear theory. *J. Geophys. Res.* 113, A12104. doi:10.1029/2008ja013565

Gary, S. P. (1999). Collisionless dissipation wavenumber: Linear theory. *J. Geophys. Res.* 104, 6759–6762. doi:10.1029/1998ja900161

Gary, S. P. (1991). Electromagnetic ion/ion instabilities and their consequences in space plasmas: A review. *Space Sci. Rev.* 56, 373–415. doi:10.1007/bf00196632

Gary, S. P., Feldman, W. C., Forslund, D. W., and Montgomery, M. D. (1975a). Electron heat flux instabilities in the solar wind. *Geophys. Res. Lett.* 2, 79–82. doi:10.1029/gl002i003p00079

Gary, S. P., Feldman, W. C., Forslund, D. W., and Montgomery, M. D. (1975b). Heat flux instabilities in the solar wind. *J. Geophys. Res.* 80, 4197–4203. doi:10.1029/ja080i031p04197

Gary, S. P., and Karimabadi, H. (2006). Linear theory of electron temperature anisotropy instabilities: Whistler, mirror, and Weibel. *J. Geophys. Res.* 111, A11224. doi:10.1029/2006ja011764

Gary, S. P., Li, H., O'Rourke, S., and Winske, D. (1998). Proton resonant firehose instability: Temperature anisotropy and fluctuating field constraints. *J. Geophys. Res.* 103, 14567–14574. doi:10.1029/98ja01174

Gary, S. P., Montgomery, M. D., Feldman, W. C., and Forslund, D. W. (1976). Proton temperature anisotropy instabilities in the solar wind. *J. Geophys. Res.* 81, 1241–1246. doi:10.1029/ja081i007p01241

Gary, S. P., and Nishimura, K. (2003). Resonant electron firehose instability: Particle-in-cell simulations. *Phys. Plasmas* 10, 3571–3576. doi:10.1063/1.1590982

Gary, S. P., and Saito, S. (2007). Broadening of solar wind strahl pitch-angles by the electron/electron instability: Particle-in-cell simulations. *Geophys. Res. Lett.* 34, L14111. doi:10.1029/2007gl030039

Gary, S. P., Scime, E. E., Phillips, J. L., and Feldman, W. C. (1994). The whistler heat flux instability: Threshold conditions in the solar wind. *J. Geophys. Res.* 99, 23391–23399. doi:10.1029/94ja02067

Gary, S. P., Skoug, R. M., and Daughton, W. (1999). Electron heat flux constraints in the solar wind. *Phys. Plasmas* 6, 2607–2612. doi:10.1063/1.873532

Gary, S. P., Skoug, R. M., Steinberg, J. T., and Smith, C. W. (2001). Proton temperature anisotropy constraint in the solar wind: ACE observations. *Geophys. Res. Lett.* 28, 2759–2762. doi:10.1029/2001gl013165

Gary, S. P., Smith, C. W., Lee, M. A., Goldstein, M. L., and Forslund, D. W. (1984). Electromagnetic ion beam instabilities. *Phys. Fluids* 27, 1852. doi:10.1063/1.864797

Gary, S. P., and Smith, C. W. (2009). Short-wavelength turbulence in the solar wind: Linear theory of whistler and kinetic Alfvén fluctuations. *J. Geophys. Res.* 114, A12105. doi:10.1029/2009ja014525

Gary, S. P. (1974). Solar cosmic-ray acceleration by a plasma instability. *ApJ* 187, 195–196. doi:10.1086/152611

Gary, S. P. (1992). The mirror and ion cyclotron anisotropy instabilities. *J. Geophys. Res.* 97, 8519–8529. doi:10.1029/92ja00299

Gary, S. P. (1993). *Theory of Space Plasma Microinstabilities*. Cambridge: Cambridge University Press.

Gary, S. P., Yin, L., Winske, D., and Ofman, L. (2003). Consequences of proton and alpha anisotropies in the solar wind: Hybrid simulations. *J. Geophys. Res.* 198, 1068. doi:10.1029/2002ja009654

Gary, S. P., Yin, L., Winske, D., and Reisenfeld, D. B. (2000b). Alpha/proton magnetosonic instability in the solar wind. *J. Geophys. Res.* 105, 20989–20996. doi:10.1029/2000ja000049

Gary, S. P., Yin, L., Winske, D., and Reisenfeld, D. B. (2000a). Electromagnetic alpha/proton instabilities in the solar wind. *Geophys. Res. Lett.* 27, 1355–1358. doi:10.1029/2000gl000019

Georgieva, K., Kirov, B., Atanassov, D., and Boneva, A. (2005). Impact of magnetic clouds on the middle atmosphere and geomagnetic disturbances. *J. Atmos. Solar-Terrestrial Phys.* 67, 163–176. doi:10.1016/j.jastp.2004.07.025

Goertz, C. K., Shan, L.-H., and Smith, R. A. (1993). Prediction of geomagnetic activity. *J. Geophys. Res.* 98, 7673–7684. doi:10.1029/92ja01193

Greco, A., Chuychai, P., Matthaeus, W. H., Servidio, S., and Dmitruk, P. (2008). Intermittent MHD structures and classical discontinuities. *Geophys. Res. Lett.* 35, L19111. doi:10.1029/2008gl035454

Jockers, K. (1970). Solar wind models based on exospheric theory. *Astron. Astrophys.* 6, 219.

Jordanova, V. K., Delzanno, G. L., Henderson, M. G., Godinez, H. C., Jeffery, C. A., Lawrence, E. C., et al. (2018). Specification of the near-Earth space environment with SHIELDS. *J. Atmos. Solar-Terrestrial Phys.* 177, 148–159. doi:10.1016/j.jastp.2017.11.006

Jordanova, V. K., Farrugia, C. J., Thorne, R. M., Khazanov, G. V., Reeves, G. D., and Thomsen, M. F. (2001). Modeling ring current proton precipitation by electromagnetic ion cyclotron waves during the May 14-16, 1997, storm. *J. Geophys. Res.* 106, 7–22. doi:10.1029/2000ja002008

Jordanova, V. K., Welling, D. T., Zaharia, S. G., Chen, L., and Thorne, R. M. (2012). Modeling ring current ion and electron dynamics and plasma instabilities during a high-speed stream driven storm. *J. Geophys. Res.* 117, A00L18. doi:10.1029/2011ja017433

Klimas, A. J., Vassiliadis, D., and Baker, D. N. (1997). Data-derived analogues of the magnetospheric dynamics. *J. Geophys. Res.* 102, 26993–27009. doi:10.1029/97ja02414

Lam, M. M., and Tinsley, B. A. (2016). Solar wind-atmospheric electricity-cloud microphysics connections to weather and climate. *J. Atmos. Solar-Terrestrial Phys.* 149, 277–290. doi:10.1016/j.jastp.2015.10.019

Leamon, R. J., Smith, C. W., Ness, N. F., Matthaeus, W. H., and Wong, H. K. (1998). Observational constraints on the dynamics of the interplanetary magnetic field dissipation range. *J. Geophys. Res.* 103, 4775–4787. doi:10.1029/97ja03394

Lee, M. A. (2018). The story of interstellar pickup ions and their excitation of hydromagnetic waves in the solar wind. *ASP Conf. Ser.* 513, 205–214.

Lemaire, J. (2010). Half a century of kinetic solar wind models. *AIP Conf. Proc.* 1216, 8. doi:10.1063/1.3395971

Malara, F., Primavera, L., and Veltri, P. (2001). Nonlinear evolution of the parametric instability: numerical predictions versus observations in the heliosphere. *Nonlin. Process. Geophys.* 8, 159–166. doi:10.5194/npg-8-159-2001

Marsch, E. (2006). Kinetic physics of the solar corona and solar wind. *Living Rev. Solar Phys.* 3, 1. doi:10.12942/lrsp-2006-1

Marsch, E., and Tu, C.-Y. (1997). Intermittency, non-gaussian statistics and fractal scaling of MHD fluctuations in the solar wind. *Nonlin. Process. Geophys.* 4, 101–124. doi:10.5194/npg-4-101-1997

McPherron, R. L., Hsu, T.-S., and Chu, X. (2015). An optimum solar wind coupling function for theALindex. *J. Geophys. Res. Space Phys.* 120, 2494–2515. doi:10.1002/2014ja020619

Michel, F. C. (1967). Model of solar wind structure. *J. Geophys. Res.* 72, 1917–1932. doi:10.1029/jz072i007p01917

Nemecek, Z., Durovcova, T., Safrankova, J., Nemec, F., Matteini, L., StansbyJantizek, D. N., et al. (2020). What is the solar wind frame of reference. *Astrophys. J.* 889, 163.

Parker, E. N. (1979). *Cosmical Magnetic Fields. Sect*, 7.2. Oxford: Clarendon Press.

Pecora, F., Greco, A., Hu, Q., Servidio, S., Chasapis, A. G., and Matthaeus, W. H. (2019). Single-spacecraft identification of flux tubes and current sheets in the solar wind. *ApJ* 881, L11. doi:10.3847/2041-8213/ab32d9

Rycroft, M. J., Nicoll, K. A., Aplin, K. L., and Giles Harrison, R. (2012). Recent advances in global electric circuit coupling between the space environment and the troposphere. *J. Atmos. Solar-Terrestrial Phys.* 90-91, 198–211. doi:10.1016/j.jastp.2012.03.015

Schunk, R. W. (2007). Time-dependent simulations of the global polar wind. *J. Atmos. Solar-Terrestrial Phys.* 69, 2028–2047. doi:10.1016/j.jastp.2007.08.009

Shprits, Y. Y., Elkington, S. R., Meredith, N. P., and Subbotin, D. A. (2008a). Review of modeling of losses and sources of relativistic electrons in the outer radiation belt I: Radial transport. *J. Atmos. Solar-Terrestrial Phys.* 70, 1679–1693. doi:10.1016/j.jastp.2008.06.008

Shprits, Y. Y., Subbotin, D. A., Meredith, N. P., and Elkington, S. R. (2008b). Review of modeling of losses and sources of relativistic electrons in the outer radiation belt II: Local acceleration and loss. *J. Atmos. Solar-Terrestrial Phys.* 70, 1694–1713. doi:10.1016/j.jastp.2008.06.014

Sinnhuber, M., Nieder, H., and Wieters, N. (2012). Energetic particle precipitation and the chemistry of the mesosphere/lower thermosphere. *Surv. Geophys.* 33, 1281–1334. doi:10.1007/s10712-012-9201-3

Smith, C. W., and Vasquez, B. J. (2021). Driving and dissipation of solar-wind turbulence: What is the evidence. *Front. Astron. Space Sci.* 7, 611909. doi:10.3389/fspas.2020.611909

Smith, R. A., Goertz, C. K., and Grossman, W. (1986). Thermal catastrophe in the plasma sheet boundary layer. *Geophys. Res. Lett.* 13, 1380–1383. doi:10.1029/gl013i013p01380

Smith, Z. K., Dryer, M., and Steinolfson, R. S. (1985). A study of the formation, evolution, and decay of shocks in the heliosphere between 0.5 and 30.0 AU. *J. Geophys. Res.* 90, 217–220. doi:10.1029/ja090ia01p00217

Snyder, C. W., Neugebauer, M., and Rao, U. R. (1963). The solar wind velocity and its correlation with cosmic-ray variations and with solar and geomagnetic activity. *J. Geophys. Res.* 68, 6361–6370. doi:10.1029/jz068i024p06361

Spencer, E., Vadepu, S. K., Srinivas, P., Patra, S., and Horton, W. (2018). The dynamics of geomagnetic substorms with the WINDMI model. *Earth Planets Space* 70, 118. doi:10.1186/s40623-018-0882-9

Stepanova, M., and Valdivia, J. A. (2016). Contribution of Latin-American scientists to the study of the magnetosphere of the Earth. A review. *Adv. Space Res.* 58, 1968–1985. doi:10.1016/j.asr.2016.03.023

Stverak, S., Maksimovic, M., Travnicwk, P. M., Marsch, E., Fazakerley, A. N., and Scime, E. E. (2009). *J. Geophys. Res.* 114, A05104.

Thorne, R. M. (1974). A possible cause of dayside relativistic electron precipitation events. *J. Atmos. Terrestrial Phys.* 36, 635–645. doi:10.1016/0021-9169(74)90087-7

Thorne, R. M., Bortnik, J., Li, W., Chen, L. J., Ni, B. B., and Ma, Q. L. (2017). How whistler-mode waves and thermal plasma density control the global distribution of the diffuse aurora and the dynamical evolution of radiation belt electrons. *Geophys. Monog. Ser.* 222, 117–125. doi:10.15142/T38G6X

Thorne, R. M., Church, S. R., and Gorney, D. J. (1979). On the origin of plasmaspheric hiss: The importance of wave propagation and the plasmapause. *J. Geophys. Res.* 84, 5241–5247. doi:10.1029/ja084ia09p05241

Thorne, R. M. (1977). Energetic radiation belt electron precipitation: A natural depletion mechanism for stratospheric ozone. *Science* 195, 287–289. doi:10.1126/science.195.4275.287

Thorne, R. M., and Horne, R. B. (1994). Energy transfer between energetic ring current H+and O+by electromagnetic ion cyclotron waves. *J. Geophys. Res.* 99, 17275–17282. doi:10.1029/94ja01007

Thorne, R. M., and Horne, R. B. (1992). The contribution of ion-cyclotron waves to electron heating and SAR-arc excitation near the storm-time plasmapause. *Geophys. Res. Lett.* 19, 417–420. doi:10.1029/92gl00089

Thorne, R. M., and Kennel, C. F. (1971). Relativistic electron precipitation during magnetic storm main phase. *J. Geophys. Res.* 76, 4446–4453. doi:10.1029/ja076i019p04446

Thorne, R. M., Li, W., Ni, B., Ma, Q., Bortnik, J., Chen, L., et al. (2013). Rapid local acceleration of relativistic radiation-belt electrons by magnetospheric chorus. *Nature* 504, 411–414. doi:10.1038/nature12889

Thorne, R. M., Ni, B., Tao, X., Horne, R. B., and Meredith, N. P. (2010). Scattering by chorus waves as the dominant cause of diffuse auroral precipitation. *Nature* 467, 943–946. doi:10.1038/nature09467

Thorne, R. M. (2010). Radiation belt dynamics: The importance of wave-particle interactions. *Geophys. Res. Lett.* 37, L22107. doi:10.1029/2010gl044990

Thorne, R. M., Smith, E. J., Burton, R. K., and Holzer, R. E. (1973). Plasmaspheric hiss. *J. Geophys. Res.* 78, 1581–1596. doi:10.1029/ja078i010p01581

Thorne, R. M., and Summers, D. (1991). Landau damping in space plasmas. *Phys. Fluids B: Plasma Phys.* 3, 2117–2123. doi:10.1063/1.859624

Thorne, R. M. (1980). The importance of energetic particle precipitation on the chemical composition of the middle atmosphere. *Pageoph* 118, 128–151. doi:10.1007/bf01586448

Thorne, R. M. (1968). Unducted whistler evidence for a secondary peak in the electron energy spectrum near 10 keV. *J. Geophys. Res.* 73, 4895–4904. doi:10.1029/ja073i015p04895

Tinsley, B. A. (2000). Influence of solar wind on the global electric circuit, and inferred effects on cloud microphysics, temperature, and dynamics in the troposphere. *Space Sci. Rev.* 94, 231–258. doi:10.1007/978-94-010-0888-4_22

Valdivia, J. A., Rogan, J., Muñoz, V., Gomberoff, L., Klimas, A., Vassiliadis, D., et al. (2005). The magnetosphere as a complex system. *Adv. Space Res.* 35, 961–971. doi:10.1016/j.asr.2005.03.144

Valdivia, J. A., Rogan, J., Muñoz, V., Toledo, B. A., and Stepanova, M. (2013). The magnetosphere as a complex system. *Adv. Space Res.* 51, 1934–1941. doi:10.1016/j.asr.2012.04.004

Varotsou, A., Boscher, D., Bourdarie, S., Horne, R. B., Glauert, S. A., and Meredith, N. P. (2005). Simulation of the outer radiation belt electrons near geosynchronous orbit including both radial diffusion and resonant interaction with whistler-mode chorus waves. *Geophys. Res. Lett.* 32, L19106. doi:10.1029/2005gl023282

Vasquez, B. J., and Hollweg, J. V. (1996). Formation of arc-shaped Alfvén waves and rotational discontinuities from oblique linearly polarized wave trains. *J. Geophys. Res.* 101, 13527–13540. doi:10.1029/96ja00612

Vassiliadis, D., Sharma, A. S., and Papadopoulos, K. (1993). An empirical model relating the auroral geomagnetic activity to the interplanetary magnetic field. *Geophys. Res. Lett.* 20, 1731–1734. doi:10.1029/93gl01351

Vassiliadis, D. (2006). Systems theory for geospace plasma dynamics. *Rev. Geophys.* 44, RG2002 1–39. doi:10.1029/2004rg000161

Viall, N. M., and Borovsky, J. E. (2020). Nine outstanding questions of solar wind physics. *J. Geophys. Res. Space Phys.* 125, e2018JA026005. doi:10.1029/2018JA026005

Wawrzaszek, A., Echim, M., and Bruno, R. (2019). Multifractal analysis of heliospheric magnetic field fluctuations observed by Ulysses. *ApJ* 876, 153. doi:10.3847/1538-4357/ab1750

Wing, S., and Johnson, J. R. (2019). Applications of information theory in solar and space physics. *Entropy* 21, 140. doi:10.3390/e21020140

Conflict of Interest: The author declares that the research was conducted in the absence of any commercial or financial relationships that could be construed as a potential conflict of interest.

frontiers in Astronomy and Space Sciences

ORIGINAL RESEARCH
published: 14 January 2022
doi: 10.3389/fspas.2021.805699

Weak Turbulence and Quasilinear Diffusion for Relativistic Wave-Particle Interactions Via a Markov Approach

Oliver Allanson[1,2]*, *Thomas Elsden*[3,4], *Clare Watt*[2] *and Thomas Neukirch*[5]

[1]Environmental Mathematics Group & Geophysical and Astrophysical Fluid Dynamics Group, Department of Mathematics, University of Exeter, Exeter, United Kingdom, [2]Department of Mathematics, Physics and Electrical Engineering, Northumbria University, Newcastle upon Tyne, United Kingdom, [3]School of Mathematics and Statistics, University of Glasgow, Glasgow, United Kingdom, [4]Department of Physics and Astronomy, University of Leicester, Leicester, United Kingdom, [5]School of Mathematics and Statistics, University of St Andrews, St Andrews, United Kingdom

We derive weak turbulence and quasilinear models for relativistic charged particle dynamics in pitch-angle and energy space, due to interactions with electromagnetic waves propagating (anti-)parallel to a uniform background magnetic field. We use a Markovian approach that starts from the consideration of single particle motion in a prescribed electromagnetic field. This Markovian approach has a number of benefits, including: 1) the evident self-consistent relationship between a more general weak turbulence theory and the standard resonant diffusion quasilinear theory (as is commonly used in e.g. radiation belt and solar wind modeling); 2) the general nature of the Fokker-Planck equation that can be derived without any prior assumptions regarding its form; 3) the clear dependence of the form of the Fokker-Planck equation and the transport coefficients on given specific timescales. The quasilinear diffusion coefficients that we derive are not new in and of themselves, but this concise derivation and discussion of the weak turbulence and quasilinear theories using the Markovian framework is physically very instructive. The results presented herein form fundamental groundwork for future studies that consider phenomena for which some of the assumptions made in this manuscript may be relaxed.

Keywords: space plasma, plasma waves, wave-particle interactions, relativistic, Markov, quasilinear theory, weak turbulence, radiation belts

OPEN ACCESS

Edited by:
Joseph Eric Borovsky,
Space Science Institute, United States

Reviewed by:
Danny Summers,
Memorial University of Newfoundland, Canada
Jay M. Albert,
Air Force Research Lab, United States

***Correspondence:**
Oliver Allanson
oliverallanson@gmail.com

Specialty section:
This article was submitted to Space Physics, a section of the journal Frontiers in Astronomy and Space Sciences

Received: *30 October 2021*
Accepted: *26 November 2021*
Published: *14 January 2022*

Citation:
Allanson O, Elsden T, Watt C and Neukirch T (2022) Weak Turbulence and Quasilinear Diffusion for Relativistic Wave-Particle Interactions Via a Markov Approach. Front. Astron. Space Sci. 8:805699. doi: 10.3389/fspas.2021.805699

1 INTRODUCTION

Quasilinear diffusion theory forms the basis of much of the modeling and interpretation of particle transport and energization due to interactions with electromagnetic waves; at terrestrial (Horne et al., 2005; Summers, 2005; Thorne, 2010) and planetary (Woodfield et al., 2014; Kollmann et al., 2018) radiation belts; in the solar atmosphere and solar wind (Steinacker and Miller, 1992; Vocks et al., 2005; Vocks, 2012; Verscharen and Chandran, 2013; Jeong et al., 2020); and for the dynamics of cosmic rays (Schlickeiser, 1989; Mertsch, 2020).

The classic derivations of quasilinear theory (Drummond and Pines, 1962; Vedenov et al., 1962; Kennel and Engelmann, 1966; Lerche, 1968; Lyons, 1974; Summers, 2005) not only provide the form of the Fokker-Planck equation to describe the particle dynamics, but also the diffusion coefficients that encode the effect of the resonant wave-particle interactions as a function of the background magnetic field strength, plasma refractive index, and electromagnetic wave spectral properties. It is

also possible to derive the diffusion coefficients due to resonant wave-particle interactions via a different technique, i.e., a Hamiltonian analysis of single particle interactions with given wave modes (e.g., see Albert (2001); Albert (2010)). Furthermore, Lemons (2012) has demonstrated a quite general method to derive both the form of the Fokker-Planck equation itself, as well as the transport coefficients that apply in a particular circumstance.

The method presented by Lemons (2012) (building on work presented in Lemons et al. (2009)) is in principle quite general and could be applied to a wide range of phenomena, but was applied to a particular restricted case in that paper, namely particle pitch-angle dynamics due to interactions with a stationary transverse magnetic field only. Using a Markovian analysis [e.g., see Wang and Uhlenbeck (1945); Reif (2009); Zheng et al. (2019); Allanson et al. (2020)] Lemons (2012) derives a theory to describe both the weak turbulence and quasilinear regimes. Despite the fact that the electromagnetic perturbation considered is a stationary magnetic field only, the equations derived by Lemons (2012) do in fact reproduce the standard form for pitch-angle diffusion by field-aligned propagating electromagnetic waves using the quasilinear theory - for the particular case of pitch-angle diffusion only. This corresponds to the subset of plasma environments in which the plasma frequency is significantly larger than the gyrofrequency ($f_{pe} \gg f_{ce}$, e.g., see **Eq. 8** in Summers and Thorne (2003)).

In this paper, we study relativistic particle dynamics due to interactions with travelling electromagnetic waves, and therefore build upon the work by Lemons (2012) who considered time-invariant magnetic fields. This addition allows us to study both energy and pitch-angle dynamics, and is therefore applicable in regions with any value of f_{pe}/f_{ce}. Some of the most important expressions in this paper may not be new in and of themselves (e.g. the quasilinear theory for field-aligned waves). However, this concise self-consistent derivation and discussion of both the weak turbulence and quasilinear theories by using the Markovian framework is physically very instructive. We emphasize that the methods presented herein do allow in principle for the derivation of not only the transport (drift and diffusion) coefficients, but also the very form of the transport (Fokker-Planck) equation itself, based upon prescribed electromagnetic waves and some sensible physical assumptions.

In **Section 2** we present the derivation of the general Fokker-Planck equation in energy and pitch-angle space, using the Chapman-Kolmogorov equation as a starting point, and we indicate its relationship to the most basic form (i.e., the non-bounce-averaged and two-dimensional form in e.g., Glauert and Horne (2005); Summers (2005)) of the energy and pitch-angle diffusion equation as is employed in radiation belt studies (although typically after a bounce-averaging procedure (Glauert et al., 2014)). In **Section 3** we calculate the exact relativistic equations of motion for particle position, gyrophase, pitch-angle and kinetic energy, due to interactions with field-aligned electromagnetic waves. In **Section 4** we present the main calculations and results of this paper, namely the derivation of the weak turbulence and quasilinear diffusion coefficients. We conclude and discuss future possible directions in **Section 5**, which may include the relaxing of some assumptions as presented in this manuscript.

2 FOKKER-PLANCK EQUATION DERIVED USING MARKOV THEORY

Consider a spatially uniform (or equivalently, a spatially averaged) collisionless particle distribution function, $g_s = g_s(\mathbf{p}, t)$, for particle species s, normalized according to

$$\int g_s(\mathbf{p}, t) d^3p = n_s,$$

where $\int d^3p$ is taken to be the integral over all relativistic momentum space ($-\infty < p_x, p_y, p_z < \infty$), and n_s is the number density (such that $Vn_s = N_s$, with N_s the total number of particles in a spatial volume V). The relativistic momentum is defined as $\mathbf{p} = \gamma m_{0s}\mathbf{v}$, with $\mathbf{v}$ the velocity, $\gamma = (1 - v^2/c^2)^{-1/2}$, m_{0s} the rest mass, and c the speed of light in a vacuum. Under the assumption of a gyrotropic distribution function ($g_s(\mathbf{p}, t) = g_s(p_\parallel, p_\perp, t)$), we can reduce the triple integration to a double integration according to,

$$2\pi \int_{p_\parallel=-\infty}^{p_\parallel=\infty} \int_{p_\perp=0}^{p_\perp=\infty} g_s(p_\parallel, p_\perp, t) p_\perp dp_\perp dp_\parallel = n_s,$$

where $p_\parallel = \mathbf{p} \cdot \mathbf{B}_0/|\mathbf{B}_0|$ and $p_\perp = |\mathbf{p} \times \mathbf{B}_0|/|\mathbf{B}_0|$, for $\mathbf{B}_0$ the local background magnetic field, and we assume that $B_0 = |\mathbf{B}_0| > 0$ without loss of generality. The relativistic momentum and kinetic energy, E, are related by $p^2c^2 = E(E + 2E_{Rs})$ (Glauert and Horne, 2005), for $E_{Rs} = m_{0s}c^2$ the rest-mass energy. To clarify, E is the relativistic kinetic energy only, and not the total relativistic energy. Furthermore, the particle pitch angle, $0 < \alpha < \pi$, is defined by $p_\parallel = |\mathbf{p}| \cos\alpha$ and $p_\perp = |\mathbf{p}| \sin\alpha$. Using these definitions and the Jacobian relation, $dp_\perp dp_\parallel = c^{-2}(E + E_{Rs}) dE d\alpha$, we can rewrite the integrals so that

$$\frac{2\pi}{c^3} \int_{\alpha=0}^{\alpha=\pi} \int_{E=0}^{E=\infty} f_s(E, \alpha, t)(E + E_{Rs}) \sqrt{E(E + 2E_{Rs})} \sin\alpha dE d\alpha = n_s,$$

where we have made the association $g_s(p_\parallel, p_\perp, t) = f_s(E, \alpha, t)$. From hereon in we will dispense with the s subscript for brevity. We will now derive the general form of the equation that evolves f in time, as is consistent with Markovian stochastic particle dynamics in energy and pitch-angle space.

2.1 Fokker-Planck Equation in a General Form

Markovian dynamics are a special example of a stochastic/random process, and are essentially characterized by the requirement that the conditional probability of a given future state (at an immediately successive time $t = t_0 + \Delta t$) only depends on the current state (at $t = t_0$) (Wang and Uhlenbeck, 1945; Zheng et al., 2019). The Markovian stochastic formalism is appropriate to use in this paper since we are seeking a solution of particle motion in a statistical sense (i.e., the evolution of a particle

distribution function), and not a deterministic sense (i.e., the exact dynamics of a very large number of particles).

The Chapman-Kolmogorov equation is the basic equation for Markov theory, and is also sometimes known as the Einstein-Smoluchowski equation, (e.g., see Wang and Uhlenbeck (1945); Einstein (1956); Reif (2009); Zheng et al. (2019)). The Chapman-Kolmogorov equation for f, adapted to be written in energy and pitch-angle space, is

$$f(E,\alpha,t+\Delta t)(E+E_{\mathrm{R}})\sqrt{E(E+2E_{\mathrm{R}})}\sin\alpha = \int_{E'=0}^{\infty}\int_{\alpha'=0}^{\pi}\Psi(E,\alpha;E',\alpha',\Delta t) f(E',\alpha',t)(E'+E_{\mathrm{R}})\sqrt{E'(E'+2E_{\mathrm{R}})}\sin\alpha' dE' d\alpha'.$$

Here, $\Psi(E, \alpha; E', \alpha', \Delta t)$ is the transition probability density that a particle located at (E', α') at time t will reach (E, α) at time $t + \Delta t$. Using a standardized procedure based on so-called "Kramers-Moyal" theory (essentially using Taylor series, and as described in e.g. Wang and Uhlenbeck (1945); Einstein (1956); Walt (1994); Reif (2009); Roederer and Zhang (2013); Lemons (2012); Zheng et al. (2019)), we derive the following Fokker-Planck equation

$$\frac{\partial f}{\partial t} = -\frac{1}{G_1}\frac{\partial}{\partial E}\left(G_1\mathcal{C}_E f\right) - \frac{1}{G_2}\frac{\partial}{\partial\alpha}\left(G_2\mathcal{C}_\alpha f\right) + \frac{1}{G_1}\frac{\partial^2}{\partial E^2}\left(G_1\mathcal{D}_{EE} f\right) + \frac{1}{G_2}\frac{\partial^2}{\partial\alpha^2}\left(G_2\mathcal{D}_{\alpha\alpha} f\right) + \frac{2}{G_1 G_2}\frac{\partial^2}{\partial\alpha\partial E}\left(G_1 G_2\mathcal{D}_{E\alpha} f\right), \tag{1}$$

for $G_1(E) = (E + E_{\mathrm{R}})\sqrt{E(E + 2E_{\mathrm{R}})}$ and $G_2(\alpha) = \sin\alpha$, and the drift and diffusion coefficients defined as

$$\{\mathcal{C}_\alpha, \mathcal{C}_E\} = \left\{\frac{\langle\Delta\alpha\rangle}{\Delta t}, \frac{\langle\Delta E\rangle}{\Delta t}\right\},$$

$$\{\mathcal{D}_{\alpha\alpha}, \mathcal{D}_{E\alpha}, \mathcal{D}_{EE}\} = \left\{\frac{\langle(\Delta\alpha)^2\rangle}{2\Delta t}, \frac{\langle\Delta E\Delta\alpha\rangle}{2\Delta t}, \frac{\langle(\Delta E)^2\rangle}{2\Delta t}\right\},$$

where $\langle\ldots\rangle$ denotes a suitable statistical or ensemble average, and the set notation $\{\ldots\}$ is used only to write the definitions in a compact manner. The denominator in the transport coefficients, $\Delta t = t - t_0$, is a 'suitable' timescale over which to consider the drift/diffusion, and helps to define the increments $\Delta\alpha = \alpha(t_0 + \Delta t) - \alpha(t_0)$, $\Delta E = E(t_0 + \Delta t) - E(t_0)$ (e.g., see Liu et al. (2010); Liu et al. (2012)); Lemons (2012); Allanson et al. (2019); Allanson et al. (2020) for discussions regarding ensemble averages and timescales). Note that here we are using the same formal definitions of transport coefficients as in e.g., Lemons (2012); Glauert et al. (2014), such that $\mathcal{C}_\alpha$, $\mathcal{C}_E$, $\mathcal{D}_{\alpha\alpha}$, $\mathcal{D}_{\alpha E}$, and $\mathcal{D}_{EE}$, have units of s^{-1}, Js^{-1}, s^{-1}, Js^{-1} and $\mathrm{J}^2\mathrm{s}^{-1}$, respectively.

Equation 1 is the Fokker-Planck equation that describes particle transport (diffusion and drift) in relativistic kinetic energy and pitch-angle space, under the assumption of Markovian stochastic dynamics and a uniform background magnetic field. It is currently written in a very general form, and an investigation of the particle dynamics in a given system (i.e., a given set of background and perturbative forces and considered timescales) may reveal the exact form of the diffusion and drift coefficients, their relationship, and thus the exact form of **Eq. 1** itself.

2.2 Fokker-Planck Equation Reduced to a More Familiar Form

Equation 1 can be re-written as

$$\frac{\partial f}{\partial t} = -\frac{1}{G_1}\frac{\partial}{\partial E}\left[f\left(G_1\mathcal{C}_E - \frac{\partial}{\partial E}\left(G_1\mathcal{D}_{EE}\right) - \frac{G_1}{G_2}\frac{\partial}{\partial\alpha}\left(G_2\mathcal{D}_{\alpha E}\right)\right)\right] - \frac{1}{G_2}\frac{\partial}{\partial\alpha}\left[f\left(G_2\mathcal{C}_\alpha - \frac{\partial}{\partial\alpha}\left(G_2\mathcal{D}_{\alpha\alpha}\right) - \frac{G_2}{G_1}\frac{\partial}{\partial E}\left(G_1\mathcal{D}_{\alpha E}\right)\right)\right] + \frac{1}{G_1}\frac{\partial}{\partial E}\left[G_1\left(\mathcal{D}_{EE}\frac{\partial f}{\partial E} + \mathcal{D}_{\alpha E}\frac{\partial f}{\partial\alpha}\right)\right] + \frac{1}{G_2}\frac{\partial}{\partial\alpha}\left[G_2\left(\mathcal{D}_{\alpha\alpha}\frac{\partial f}{\partial\alpha} + \mathcal{D}_{\alpha E}\frac{\partial f}{\partial E}\right)\right].$$

Examination of the particle dynamics in a given system can reveal the relationship between the drift and diffusion coefficients, sometimes known as the "*drift-diffusion relation*" (e.g. see Lemons (2012)). As one specific example, consider that the following drift-diffusion relations could be satisfied,

$$\mathcal{C}_E = \frac{1}{G_1}\frac{\partial}{\partial E}\left(G_1\mathcal{D}_{EE}\right) + \frac{1}{G_2}\frac{\partial}{\partial\alpha}\left(G_2\mathcal{D}_{\alpha E}\right), \tag{2}$$

$$\mathcal{C}_\alpha = \frac{1}{G_2}\frac{\partial}{\partial\alpha}\left(G_2\mathcal{D}_{\alpha\alpha}\right) + \frac{1}{G_1}\frac{\partial}{\partial E}\left(G_1\mathcal{D}_{\alpha E}\right), \tag{3}$$

then **Eq. 1** reduces to the following transport equation for energy and pitch angle diffusion

$$\frac{\partial f}{\partial t} = \frac{1}{\sin\alpha}\frac{\partial}{\partial\alpha}\left[\sin\alpha\left(\mathcal{D}_{\alpha\alpha}\frac{\partial f}{\partial\alpha} + \mathcal{D}_{\alpha E}\frac{\partial f}{\partial E}\right)\right] + \frac{1}{(E+E_{\mathrm{R}})\sqrt{E(E+2E_{\mathrm{R}})}}\frac{\partial}{\partial E}\left[(E+E_{\mathrm{R}})\sqrt{E(E+2E_{\mathrm{R}})}\left(\mathcal{D}_{EE}\frac{\partial f}{\partial E} + \mathcal{D}_{\alpha E}\frac{\partial f}{\partial\alpha}\right)\right]. \tag{4}$$

Equation 4 is exactly consistent with the standard relativistic quasilinear equation as derived via a different approach (see discussion of derivations and regions of applicability in Sections 1 and 5), used to describe energy and pitch-angle dynamics due to wave-particle interactions in the resonant diffusion quasilinear theory (Glauert and Horne, 2005; Summers, 2005) prior to 'bounce-averaging'.

Equation 4 (or some variant thereof that may also include dynamics in real/radial space, and/or a so-called 'bounce-/drift-averaging' procedure) is often known as 'the diffusion equation' in the terrestrial and planetary magnetospheric communities. This reflects the fact that one can only see diffusion coefficents "$\mathcal{D}$" playing a role in the dynamics. The exact form of "the diffusion equation" (e.g., see Kennel and Engelmann (1966); Schulz and Lanzerotti (1974)) is a result of the most typical derivation method employed—essentially a perturbative analysis

of the Vlasov-Maxwell system (see a discussion in **Section 5** of this paper).

However it is important to note that some form of drift processes are in principle playing a role, despite the fact they do not appear in **Eq. 4**. The drift-diffusion relations in **Eqs 2**, **3** demonstrate this fact. **Equations 2**, **3** do not state that the drift coefficients "$\mathcal{C}$" = 0, but rather that "$\mathcal{C}$" takes a restricted set of values such that the only drift to occur is determined by gradients in the diffusion coefficients themselves (e.g., see discussions in Lemons (2012) and Zheng et al. (2019) for the slightly simpler cases of dynamics in pitch-angle space only and a single "action-integral" space only, respectively). These insights are one benefit of using this Markovian approach—and one can conclude that **Eq. 4** describes a particular subset of a more rich set of possible particle dynamics, that are described by **Eq. 1**.

It is therefore of great interest to try and derive Fokker-Planck equations for a given system using the Markovian approach (as opposed to the historically more standard Vlasov-Maxwell approach), to see if we can gain more insights regarding energetic particle dynamics. One important question is to discover when a more standard "diffusion equation" such as **Eq. 4** is appropriate, and when a more rich formalism such as **Eq. 1** is necessary.

3 EXACT EQUATIONS OF MOTION

We consider a right-handed *xyz* co-ordinate system, with a uniform background magnetic field $\mathbf{B}_0 = (B_0, 0, 0)$ defining x as the "parallel'" direction, with "perpendicular" quantities in the yz plane. Particle velocities are defined according to

$$\mathbf{v} = \left(v_x, v_y, v_z\right) = |\mathbf{v}|\left(\cos\alpha,\ \sin\alpha\cos\phi,\ \sin\alpha\sin\phi\right).$$

The magnetic components of a field-aligned electromagnetic spectrum can be expressed as a sum over all considered wave-modes $\mathbf{k}$. We define $\mathbf{k} = \bar{k}|\Omega_0|c^{-1}\hat{\mathbf{x}}$, with $\Omega_0 = qB_0/(m_0\gamma)$ the signed relativistic gyrofrequency in the background field $\mathbf{B}_0$, and $\bar{k}$ a dimensionless variable such that $-\infty < \bar{k} < \infty$. We can define the magnetic wave fields using Fourier transforms over the dimensionless variable $\bar{k}$

$$B_y(x,t) = \frac{1}{2\pi}\int_{-\infty}^{\infty}\tilde{B}_y(\bar{k},x,t)d\bar{k} = \frac{1}{2\pi}\int_{-\infty}^{\infty}\tilde{B}(\bar{k})\cos\psi(\bar{k},x,t)d\bar{k}, \tag{5}$$

$$\begin{aligned} B_z(x,t) &= \frac{1}{2\pi}\int_{-\infty}^{\infty}\tilde{B}_z(\bar{k},x,t)d\bar{k} \\ &= \mp\frac{1}{2\pi}\int_{-\infty}^{\infty}\tilde{B}(\bar{k})\sin\psi(\bar{k},x,t)d\bar{k}. \end{aligned} \tag{6}$$

The $\mp$ sign corresponds to right-/left-handed waves (e.g., field-aligned whistler-mode and electromagnetic ion-cyclotron waves respectively). Note that by using a dimensionless $\bar{k}$, this implies that $\tilde{B}(\bar{k})$ has the same dimensions as B_0, i.e. that of a magnetic field. The phase is defined by $\psi(\bar{k},x,t) = \mathbf{k}\cdot\mathbf{x} - \omega(\bar{k})\Delta t = \bar{k}|\Omega_0|c^{-1}x - \omega(\bar{k})\Delta t$, with $\omega = \omega(\bar{k})$ the dispersion relation of mode $\bar{k}$. For completeness, the Fourier amplitudes of the magnetic and electric perturbations, $\tilde{\mathbf{B}}(\bar{k},x,t)$ and $\tilde{\boldsymbol{\mathcal{E}}}(\bar{k},x,t)$ respectively, associated with a given single wave mode characterized by the wave-vector $\mathbf{k}$, are defined by

$$\begin{aligned} \tilde{\mathbf{B}}(\bar{k},x,t) &= \left(0, \tilde{B}_y(\bar{k},x,t), \tilde{B}_z(\bar{k},x,t)\right) \\ &= \tilde{B}(\bar{k})\left(0,\ \cos\psi(\bar{k},x,t),\ \mp\sin\psi(\bar{k},x,t)\right), \end{aligned} \tag{7}$$

$$\begin{aligned} \tilde{\boldsymbol{\mathcal{E}}}(\bar{k},x,t) &= \left(0, \tilde{\mathcal{E}}_y(\bar{k},x,t), \tilde{\mathcal{E}}_z(\bar{k},x,t)\right) \\ &= v_{\mathrm{ph}}(\bar{k})\left(0, \tilde{B}_z(\bar{k},x,t), -\tilde{B}_y(\bar{k},x,t)\right), \end{aligned} \tag{8}$$

where we have used the assumption that the electromagnetic fields $\propto e^{i(\mathbf{k}\cdot\mathbf{x}-\omega(\bar{k})(t-t_0))}$, such that $\nabla\times\tilde{\boldsymbol{\mathcal{E}}} = i\mathbf{k}\times\tilde{\boldsymbol{\mathcal{E}}}$, $\partial\tilde{\mathbf{B}}/\partial t = -i\omega(\bar{k})\tilde{\mathbf{B}}$, and $v_{\mathrm{ph}}(\bar{k}) = \omega(\bar{k})/|\mathbf{k}|$. The electric components of the wave can then be constructed from **Eqs 5**, **6** by using **Eq. 8**.

Starting from the Lorentz force law ($\mathbf{F} = q(\boldsymbol{\mathcal{E}} + \mathbf{v}\times\mathbf{B})$), we derive the exact relativistic equations of motion for particle position x, gyrophase ϕ, pitch-angle α, and kinetic energy E, due to interactions with a field-aligned right-/left-handed electromagnetic spectrum as defined by **Eqs 5**, **6**. The details of this process are in **Supplementary Appendix A**, and the results are given by **Eqs 9–12** below.

$$\frac{dx}{dt} = |\mathbf{v}|\cos\alpha = v_{\parallel} = c\frac{\sqrt{E(E+2E_{\mathrm{R}})}}{E+E_{\mathrm{R}}}\cos\alpha, \tag{9}$$

$$\frac{dE}{dt} = \mp\frac{\Omega_0}{2\pi}\sqrt{E(E+2E_{\mathrm{R}})}\sin\alpha\int_{-\infty}^{\infty}\frac{1}{\eta(\bar{k})}\epsilon(\bar{k})\sin\zeta(\bar{k},x,t)d\bar{k}, \tag{10}$$

$$\frac{d\alpha}{dt} = \pm\frac{\Omega_0}{2\pi}\int_{-\infty}^{\infty}\left(1 - \frac{1}{\eta(\bar{k})}\frac{E+E_{\mathrm{R}}}{\sqrt{E(E+2E_{\mathrm{R}})}}\cos\alpha\right)\epsilon(\bar{k})\sin\zeta(\bar{k},x,t)d\bar{k}, \tag{11}$$

$$\frac{d\phi}{dt} = \Omega_0\left[-1 + \frac{1}{2\pi}\int_{-\infty}^{\infty}\left(\cot\alpha - \frac{1}{\eta(\bar{k})\sin\alpha}\frac{E+E_{\mathrm{R}}}{\sqrt{E(E+2E_{\mathrm{R}})}}\right)\epsilon(\bar{k})\cos\zeta(\bar{k},x,t)d\bar{k}\right], \tag{12}$$

with $\zeta(\bar{k},x,t) = \psi(\bar{k},x,t) \pm \phi(x,t)$ a combination of wave phase and particle gyrophase; $\epsilon(\bar{k}) = \tilde{B}(\bar{k})/B_0$ a dimensionless/normalised magnitude of magnetic wave field mode $\bar{k}$; and $\eta(\bar{k}) = |\mathbf{k}|c/\omega(\bar{k})$ the refractive index of mode $\bar{k}$. In **Table 1** we list many (but not all) of the important algebraic symbols used in this manuscript.

4 DERIVATION OF THE WEAK TURBULENCE TRANSPORT COEFFICIENTS

4.1 Expansions of the Equations of Motion

The equations of motion **Eqs 9–12** are nonlinear, coupled ordinary differential equations in the variables (x, E, α, ϕ). Therefore we seek solutions via expansion in a small dimensionless parameter, and the form of the equations suggests that $\epsilon(\bar{k})$ is a sensible small parameter to choose. This is an example of a solution in a regime of "weak

TABLE 1 | Many of the important algebraic symbols that are used in this article.

Variable name	Symbol	Notes
Distribution function	$f = f(E, \alpha, t)$	Gyrotropic and spatially averaged
Position	x	$-L/2 < x < L/2$, $L \to \infty$
Relativistic Kinetic Energy	E	Does not include rest mass energy
Rest mass	m_0	
Speed of light in vacuo	c	
Particle charge	q	Includes the sign of charge
Particle rest mass energy	E_R	$E_R = m_0c^2$
Relativistic momentum	$\mathbf{p}$	$\mathbf{p} = \gamma m_0\mathbf{v}$, $\lvert\mathbf{p}\rvert^2c^2 = E(E + 2E_R)$
Velocity	$\mathbf{v}$	
Background magnetic field	$\mathbf{B}_0$	$\mathbf{B}_0 = B_0\hat{\mathbf{x}}$
Parallel and perpendicular	$\parallel$ and $\perp$	$\mathbf{p}_\perp = \mathbf{p} \times \mathbf{B}_0/\lvert\mathbf{B}_0\rvert$, $p_\parallel = \mathbf{p} \cdot \mathbf{B}_0/\lvert\mathbf{B}_0\rvert$
Pitch angle	α	$\mathbf{p}_\perp = \mathbf{p}\sin\alpha$, $\mathbf{p}_\parallel = \mathbf{p}\cos\alpha$
Particle gyrophase	ϕ	
Relativistic gyrofrequency (signed)	Ω_0	$\Omega_0 = qB_0/(m_0\gamma)$
EM perturbations (Fourier transforms)	$\tilde{\mathcal{E}}$ and $\tilde{\mathbf{B}}$	**Equations 5–8**
Wavenumber	$\mathbf{k}$	$\mathbf{k} = k\hat{\mathbf{x}} = \lvert\Omega_0\rvert c^{-1}\bar{k}\hat{\mathbf{x}}$
Wave frequency	ω	$\omega = \omega(\bar{k})$
Refractive index	η	$\eta(\bar{k}) = \lvert\mathbf{k}\rvert c/\omega$
Normalised Fourier amplitude	ϵ	$\epsilon(\bar{k}) = \tilde{B}(\bar{k})/\lvert B_0\rvert$
Elapsed time	Δt	$\Delta t = t - t_0$
Ensemble averages	$\langle \ldots, \rangle$	**Equation 18**
Diffusion coefficients	$\{\mathcal{D}_{\alpha\alpha}, \mathcal{D}_{E\alpha}, \mathcal{D}_{EE}\}$	**Equation 19**
Superscript notation	e.g $x^{(n)}$	variable of order ϵ^n
Subscript notation	e.g. x_0	variable evaluated at $t = t_0$

turbulence" (e.g., see Sagdeev and Galeev (1969)), which in our context will mean to solve the equations of motion up to and including the second order in $\epsilon(\bar{k})$.

In the same way as was done in Lemons (2012), we look for solutions up to and including second order, i.e., of the form

$$x(t) \approx x^{(0)}(t) + x^{(1)}(t) + x^{(2)}(t), \tag{13}$$

$$E(t) \approx E^{(0)}(t) + E^{(1)}(t) + E^{(2)}(t), \tag{14}$$

$$\alpha(t) \approx \alpha^{(0)}(t) + \alpha^{(1)}(t) + \alpha^{(2)}(t), \tag{15}$$

$$\phi(t) \approx \phi^{(0)}(t) + \phi^{(1)}(t) + \phi^{(2)}(t), \tag{16}$$

such that terms with a "(n)" superscript are proportional to ϵ^n. Without loss of generality, we state the following initial conditions: $x(t_0) = x^{(0)}(t_0) = x_0$; $E(t_0) = E^{(0)}(t_0) = E_0$; $\alpha(t_0) = \alpha^{(0)}(t_0) = \alpha_0$; and $\phi(t_0) = \phi^{(0)}(t_0) = \phi_0$. Therefore

$$x^{(1)}(t_0) = x^{(2)}(t_0) = E^{(1)}(t_0) = E^{(2)}(t_0) = \alpha^{(1)}(t_0) = \alpha^{(2)}(t_0) = \phi^{(1)}(t_0) = \phi^{(2)}(t_0) = 0. \tag{17}$$

Inserting **Eqs 13–16** into the equations of motion **Eqs 9–12** leads to zeroth-, first- and second-order equations of motion for $x^{(0)}$, $x^{(1)}$, $x^{(2)}$, $E^{(0)}$, $E^{(1)}$, $E^{(2)}$, $\alpha^{(0)}$, $\alpha^{(1)}$, $\alpha^{(2)}$, $\phi^{(0)}$, $\phi^{(1)}$ and $\phi^{(2)}$. Full details of this expansion process and solution methods are given in **Supplementary Appendix B**.

4.2 Diffusion Coefficients for Weak Turbulence

In this paper we have considered integral sums of Fourier modes (Fourier transforms) for the electromagnetic perturbations. This corresponds to an infinite spatial domain (whereas a finite spatial domain would correspond to a finite sum of discrete Fourier modes). Therefore we conduct a spatial average over $-L/2 < x < L/2$ but formally send $L \to \infty$. The further averaging procedure that we will consider will be over gyrophase, ϕ. In particular we will assume that (to zeroth order) particles are uniformly distributed over position x and phase ϕ, i.e. $x^{(0)}(t)$ and $\phi^{(0)}(t)$ remain uniformly distributed over $[-L/2, L/2]$ and $[0, 2\pi]$ respectively. This "random-phase" approximation (Lemons et al., 2009; Lemons, 2012) is standard in the derivations of quasilinear theory (e.g., assumptions regarding spatial and azimuthal/gyrotropic symmetries of the distribution function in Kennel and Engelmann (1966)). We therefore define the ensemble averaging $\langle \ldots \rangle$ for a generic function A as

$$\langle A \rangle = \lim_{L\to\infty} \frac{1}{L} \int_{-L/2}^{L/2} \left(\frac{1}{2\pi} \int_0^{2\pi} A d\phi_0 \right) dx_0. \tag{18}$$

We use this definition of ensemble averaging to complete the derivation of the weak turbulence diffusion coefficients in **Supplementary Appendices B, C**. Note that the integrals are performed "over the initial conditions" for particle position and gyrophase, x_0 and ϕ_0 respectively. The zeroth-order solutions for $x^{(0)}(t)$ and $\phi^{(0)}(t)$ in **Supplementary Appendix B** demonstrate that particles initially uniformly distributed in x_0 and ϕ_0 will stay uniformly distributed at all later times t, to zeroth-order. Therefore the assumption of random-phase is justified and consistent to zeroth-order. This corresponds philosophically to the "integration over unperturbed (i.e., zeroth-order) orbits, as is commonplace in the aforementioned Vlasov-Maxwell treatments of quasilinear theory (e.g., see Kennel and Engelmann (1966); Verscharen and Chandran (2013).

We note that the expansions defined by **Eqs 14**, **15**, the initial conditions of **Eq. 17**, and the zeroth-order solutions of the equation of motion in **Supplementary Appendix B** lead to the following definitions (up to second-order)

$$\begin{aligned}\Delta\alpha = \alpha(t_0+\Delta t)-\alpha(t_0) &\approx \alpha^{(1)}(t_0+\Delta t)+\alpha^{(2)}(t_0+\Delta t),\\ \Delta E = E(t_0+\Delta t)-E(t_0) &\approx E^{(1)}(t_0+\Delta t)+E^{(2)}(t_0+\Delta t).\end{aligned}$$

Therefore, considering contributions to the diffusion coefficients in energy and pitch-angle up space up to and including second order in $\epsilon(\bar{k})$ leads to

$$\{\mathcal{D}_{\alpha\alpha},\mathcal{D}_{\alpha E},\mathcal{D}_{EE}\}\approx\left\{\frac{\langle\alpha^{(1)^2}\rangle}{2\Delta t},\frac{\langle\alpha^{(1)}E^{(1)}\rangle}{2\Delta t},\frac{\langle E^{(1)^2}\rangle}{2\Delta t}\right\}. \tag{19}$$

The calculations in **Supplementary Appendices B, C** then provide the following weak turbulence expressions

$$\begin{aligned}\mathcal{D}_{\alpha\alpha} = \frac{|\Omega_0|}{4\pi}\frac{c}{|\Omega_0|}\int_{-\infty}^{\infty}\left[\lim_{L\to\infty}\left(\frac{1}{L}\epsilon^2(\bar{k})\right)\right]\left(1-\frac{\omega(\bar{k})}{\mathbf{k}\cdot\mathbf{v}_\parallel^{(0)}}\cos^2\alpha_0\right)^2\\ \times\frac{\left\{1-\cos\left[\left(\left(\omega(\bar{k})-\mathbf{k}\cdot\mathbf{v}_\parallel^{(0)}\right)/\Omega_0\pm1\right)\Delta t\Omega_0\right]\right\}}{\Delta t|\Omega_0|\left(\left(\omega(\bar{k})-\mathbf{k}\cdot\mathbf{v}_\parallel^{(0)}\right)/\Omega_0\pm1\right)^2}d\bar{k}\end{aligned} \tag{20}$$

$$\begin{aligned}\mathcal{D}_{\alpha E} = -\frac{|\Omega_0|}{4\pi}\frac{c}{|\Omega_0|}\sqrt{E_0(E_0+2E_R)}\sin\alpha_0\\ \int_{-\infty}^{\infty}\left[\lim_{L\to\infty}\left(\frac{1}{L}\epsilon^2(\bar{k})\right)\right]\frac{1}{\eta(\bar{k})}\left(1-\frac{\omega(\bar{k})}{\mathbf{k}\cdot\mathbf{v}_\parallel^{(0)}}\cos^2\alpha_0\right)\\ \times\frac{\left\{1-\cos\left[\left(\left(\omega(\bar{k})-\mathbf{k}\cdot\mathbf{v}_\parallel^{(0)}\right)/\Omega_0\pm1\right)\Delta t\Omega_0\right]\right\}}{\Delta t|\Omega_0|\left(\left(\omega(\bar{k})-\mathbf{k}\cdot\mathbf{v}_\parallel^{(0)}\right)/\Omega_0\pm1\right)^2}d\bar{k}\end{aligned} \tag{21}$$

$$\begin{aligned}\mathcal{D}_{EE} = \frac{|\Omega_0|}{4\pi}\frac{c}{|\Omega_0|}(E_0(E_0+2E_R))\sin^2\alpha_0\int_{-\infty}^{\infty}\left[\lim_{L\to\infty}\left(\frac{1}{L}\epsilon^2(\bar{k})\right)\right]\frac{1}{\eta(\bar{k})^2}\\ \times\frac{\left\{1-\cos\left[\left(\left(\omega(\bar{k})-\mathbf{k}\cdot\mathbf{v}_\parallel^{(0)}\right)/\Omega_0\pm1\right)\Delta t\Omega_0\right]\right\}}{\Delta t|\Omega_0|\left(\left(\omega(\bar{k})-\mathbf{k}\cdot\mathbf{v}_\parallel^{(0)}\right)/\Omega_0\pm1\right)^2}d\bar{k}\end{aligned} \tag{22}$$

with

$$\mathbf{v}_\parallel^{(0)} = c\frac{\sqrt{E_0(E_0+2E_R)}}{E_0+E_R}\cos\alpha_0\hat{\mathbf{x}}, \tag{23}$$

the zeroth order approximation solution for the parallel velocity (i.e. the unperturbed solution).

Equations 20–22 show that the weak turbulence diffusion coefficients all involve integrating over a time-dependent factor that we define as A

$$A = \frac{[1-\cos(R\Delta t\Omega_0)]}{R^2\Delta t|\Omega_0|}, \tag{24}$$

with

$$R = \left(\omega(\bar{k})-\mathbf{k}\cdot\mathbf{v}_\parallel^{(0)}\right)/\Omega_0\pm1. \tag{25}$$

The term designated by R determines how close to resonance a given particle is with a given right-/left-handed electromagnetic wave mode (described by $\omega=\omega(\bar{k})$). $R=0$ indicates an exact cyclotron resonance (e.g., see Tsurutani and Lakhina (1997)), and larger values of $|R|$ indicate that a wave and particle are further away from resonance. In **Figure 1** we plot some important features of A.

In **Figure 1A** we show A as a function of $|\Omega_0|\Delta t$, for given fixed values of $|R|=0.05, 0.1, 0.2, 0.5$. There are two important features to note: 1) A and therefore the weak turbulence diffusion coefficients demonstrate a periodic dependence on the elapsed timescale Δt (albeit with the contributions becoming less significant as $|\Omega_0|\Delta t\to\infty$); 2) for smaller values of $|R|$ (i.e., closer to cyclotron resonance), the contribution to the weak turbulence coefficients from this factor A is more significant, at all times.

In **Figure 1B** we show the maximum value of A that is obtained, as a function of the value of $|\Omega_0|\Delta t$, and for given fixed values of $|R|$ from $R=10^{-2}$ to $R=1$ (see colour bar). When $|R|$ indicates that waves and particles are closer to resonance (i.e. $|R|$ is closer to 0), then A maximizes at later times (this can also be seen from **Figure 1A**). One important implication to note is that particles further away from resonance (larger values of $|R|$) contribute most to A at earlier times.

In **Figure 1C** we show A as a function of R, for given fixed values of $|\Omega_0|\Delta t=10, 10^2, 10^3$. This shows that as $|\Omega_0|\Delta t\to\infty$, the weak turbulence diffusion coefficients are essentially determined only *via* particles that are close to or exactly in resonance $|R|\approx0$. Equivalently, for smaller elapsed times $|\Omega_0|\Delta t$, we can state that the contribution to diffusion from non-resonant particles is non-negligible and worthy of consideration.

4.3 Diffusion Coefficients in Resonant Diffusion Quasilinear Theory

The expressions for the diffusion coefficients, "$\mathcal{D}$", defined by **Eqs 20–22** are in principle valid for any Δt that satisfies $\Delta t_C\le\Delta t\ll1/|D|$, for Δt_C a particle de-correlation time (e.g., see Liu et al. (2010); Lemons (2012); Osmane and Lejosne (2021) for discussions of the de-correlation time). The standard interpretation of the quasilinear theory in this context is to understand that $\Delta t_C\gg|\Omega_0|^{-1}$, i.e., that particles decorrelate over many gyroperiods. As we let $\Delta t|\Omega_0|\to\infty$ in our formalism, we see that A tends to zero everywhere away from $R=0$. At $R=0$, the limit as $\Delta t|\Omega_0|\to\infty$ is at first not clear, and so we can use l'Hopital's rule to show that

$$\lim_{\Delta t|\Omega_0|\to\infty}\frac{1-\cos(R\Delta t\Omega_0)}{\Delta t|\Omega_0|R^2}=\lim_{\Delta t|\Omega_0|\to\infty}\left|\frac{\sin(R\Delta t\Omega_0)}{R}\right|=\pi\delta(R),$$

via one definition of the Dirac delta function. This gives

$$\begin{aligned}\mathcal{D}_{\alpha\alpha,QL} = \frac{\Omega_0^2}{W_0}\frac{\pi}{2}\int_{-\infty}^{\infty}\tilde{W}(\bar{k})\left(1-\frac{\omega(\bar{k})}{\mathbf{k}\cdot\mathbf{v}_\parallel^{(0)}}\cos^2\alpha_0\right)^2\\ \delta\left(\omega(\bar{k})-\mathbf{k}\cdot\mathbf{v}_\parallel^{(0)}\pm\Omega_0\right)d\bar{k},\end{aligned} \tag{26}$$

making use of: (i) $\delta(X/\Omega_0)=|\Omega_0|\delta(X)$; (ii) defining $W_0=B_0^2/(2\mu_0)$ as the background magnetic field energy density; (iii) and defining

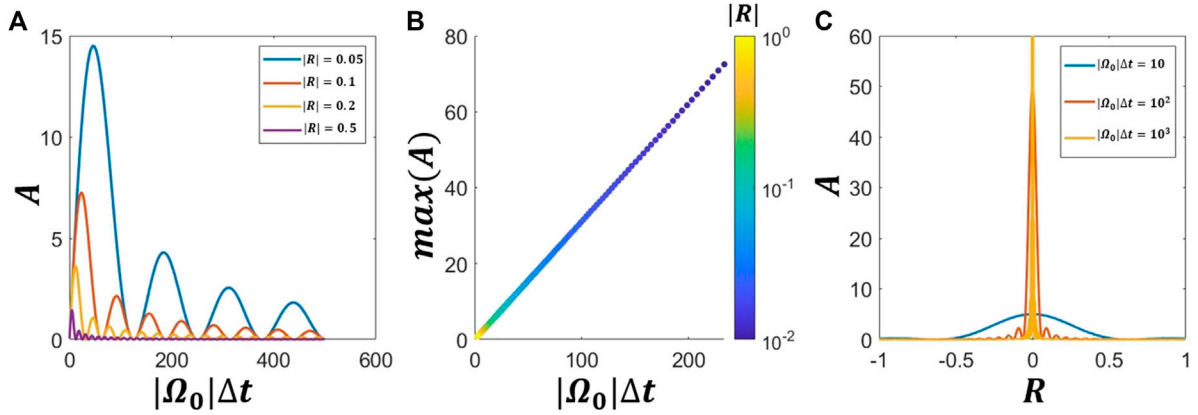

FIGURE 1 | In **(A)** we show A as a function of $|\Omega_0|\Delta t$, for given fixed values of $R = 0.05, 0.1, 0.2, 0.5$. In **(B)** we show the maximum value of A that is obtained, as a function of the value of $|\Omega_0|\Delta t$, and for given fixed values of R from $R = 10^{-2}$ to $R = 1$ (see colour bar). In **(C)** we show A as a function of R, for given fixed values of $|\Omega_0|\Delta t = 10, 10^2, 10^3$.

$$\tilde{W}(\bar{k}) = \frac{1}{2\pi}\frac{c}{|\Omega_0|}\lim_{L\to\infty}\frac{1}{L}\frac{\tilde{B}^2(\bar{k})}{2\mu_0},$$

the magnetic wave energy density associated with mode $\mathbf{k} = |\Omega_0|c^{-1}\bar{k}\hat{\mathbf{x}}$. $\tilde{W}(\bar{k})$ is defined such that the spatially averaged magnetic wave energy density associated with the magnetic wave turbulent spectrum, W_{wave}, is defined as

$$W_{\text{wave}} = \frac{B^2_{\text{wave}}}{2\mu_0} = \int_{-\infty}^{\infty}\tilde{W}(\bar{k})d\bar{k}.$$

Note that the "$\lim_{L\to\infty}1/L$" does not send all results to zero. This spatial average (over an infinite domain) is common in studies of quasilinear theory (e.g., see Kennel and Engelmann (1966); Summers (2005)). In fact, the "$1/L$" factor in the denominator competes with an "L" factor in the numerator due to the fact that the integral over all space (i.e., L) of $B_y^2 + B_z^2 = (B_y + iB_z)(B_y - iB_z)$ yields

$$LB^2_{\text{wave}} = \frac{1}{2\pi}\int_{-\infty}^{\infty}\tilde{B}^2(k)dk = \frac{1}{2\pi}\frac{c}{|\Omega_0|}\int_{-\infty}^{\infty}\tilde{B}^2(\bar{k})d\bar{k}. \tag{27}$$

A discussion of this feature is given in Lyons (1974), for example.

Similarly, we obtain

$$\mathcal{D}_{\alpha E,QL} = -\frac{\Omega_0^2}{W_0}\frac{\pi}{2}\sin\alpha_0\sqrt{E_0(E_0+2E_R)} \times\int_{-\infty}^{\infty}\tilde{W}(\bar{k})\frac{1}{\eta(\bar{k})}\left(1-\frac{\omega(\bar{k})}{\mathbf{k}\cdot\mathbf{v}_{\parallel}^{(0)}}\cos^2\alpha_0\right)\delta\left(\omega(\bar{k})-\mathbf{k}\cdot\mathbf{v}_{\parallel}^{(0)}\pm\Omega_0\right)d\bar{k}, \tag{28}$$

$$\mathcal{D}_{EE,QL} = \frac{\Omega_0^2}{W_0}\frac{\pi}{2}\sin^2\alpha_0(E_0(E_0+2E_R)) \int_{-\infty}^{\infty}\tilde{W}(\bar{k})\frac{1}{\eta^2(\bar{k})}\delta\left(\omega(\bar{k})-\mathbf{k}\cdot\mathbf{v}_{\parallel}^{(0)}\pm\Omega_0\right)d\bar{k}. \tag{29}$$

The definitions of "$\mathcal{D}$" in equations **Eqs 26**, **28**, **29** are consistent with those in the standard relativistic and non-bounce-averaged quasilinear theory, e.g., see Glauert and Horne (2005); Summers (2005).

Therefore, taking $|\Omega_0|\Delta t \to \infty$ has allowed us to obtain the time-independent quasilinear diffusion coefficients in energy and pitch-angle space, from the corresponding time-dependent weak turbulence coefficients. This calculation and process mirrors the same result as presented in Lemons (2012), for the more restricted pitch-angle case.

5 DISCUSSION

5.1 Weak Turbulence Diffusion Coefficients

The first main result of this paper is the derivation of the diffusion coefficients, $\mathcal{D}_{\alpha\alpha}$, $\mathcal{D}_{\alpha E}$ and $\mathcal{D}_{EE}$, under the assumption of "weak turbulence" only–namely that the amplitude of the "k^{th}" mode is much smaller than that of the background uniform field, $\epsilon(\bar{k}) = \tilde{B}(\bar{k})/B_0 \ll 1$. Under this assumption, we spatially average and impose one further condition of "random phase" (i.e., particles uniformly distributed over gyrophase, and also known as gyrotropy), to obtain the weak turbulence diffusion coefficients in **Eqs 20–22**.

The result is a diffusion coefficient, "$\mathcal{D}$", that is not only a function of the plasma refractive index, background magnetic field strength and electromagnetic wave perturbation spectrum, but also a function of elapsed timescale, Δt. The expressions in **Eqs 20–22** are in principle valid for any Δt that satisfies $\Delta t_C \leq \Delta t \ll 1/|D|$, for Δt_C a particle de-correlation time. The details and properties of these weak turbulence diffusion coefficients require further investigation (in particular their dependency on time). However, we note that it is now well established that the considered elapsed timescale can play a crucial role on the nature of particle diffusion in energy and pitch-angle space (e.g., see Watt et al. (2021)). A careful consideration of the elapsed timescale has been shown to be important in the interpretation of the diffusion coefficient and general nature of the charged particle dynamics: for situations with zero wave-growth rate (e.g., see Liu et al. (2010); Liu et al. (2012); Lemons (2012); Allanson et al. (2020)); but also in the context of growing

and saturating wave modes (e.g., see Camporeale and Zimbardo (2015); Allanson et al. (2021))

One particularly interesting observation to make is that when considered over finite timescales, the weak turbulence diffusion coefficients demonstrate the contribution towards particle diffusion of wave modes that are not in exact resonance ($R \neq 0$). Specifically, the terms in the integrand of **Eqs 20–22** admit contributions towards particle diffusion (i.e. for a specific value of energy and pitch angle) from a range of wave modes (i.e., different values of $\bar{k}$), i.e. not only those wave modes that satisfy the cyclotron resonance condition ($R = 0$). This phenomenon is known as resonance broadening—the importance of which has been noted by numerous authors (e.g., see Dupree (1966); Karimabadi and Menyuk (1991); Karimabadi et al. (1992); Cai et al. (2020)).

Furthermore, we note that Lemons (2012) discussed some possible restrictions to the validity of the general methodology that they, and we, present. Namely, that for very small pitch angles the assumption of a very small magnetic field perturbation (as compared to the background magnetic field strength) may not be sufficient to derive meaningful weak turbulence and quasilinear theories. This is essentially due to the appearance of a $\cot\alpha$ factor appearing in the equation for $d\phi/dt$ (**Eq. 3b** in Lemons (2012), and note that they use θ in place of α). Lemons (2012) develop a "small-correlation time" theory to specifically investigate the small pitch angle regime, but explain that it will be difficult to demonstrate the validity of their theory. **Equation 12** in this manuscript demonstrates that there may be a similar regime of interest for the system that we consider. However, these considerations are subtle and are beyond the scope of this study.

It will be interesting to further investigate the properties of the weak turbulence diffusion coefficients: 1) the nature of their dependency on elapsed timescale Δt; 2) and the role of the resonance-broadening effect (and in particular its correspondence to the pre-existing literature). These considerations are left for future work and are beyond the scope of this study.

5.2 Quasilinear Diffusion as a Limit of Weak Turbulence

The second main result of this paper is a new derivation *via* the Markov method of the pitch-angle and energy diffusion coefficients ($\mathcal{D}_{\alpha\alpha,QL}$, $\mathcal{D}_{\alpha E,QL}$ and $\mathcal{D}_{EE,QL}$), that are equivalent to those used in the standard relativistic quasilinear theory, in the resonant diffusion limit (e.g., see Glauert and Horne (2005); Summers (2005)). These results are given in **Eqs 26–29**, and are derived from the weak turbulence diffusion coefficients in **Eqs 20–22** under the assumptions of elapsed times much greater than the gyroperiod, $\Delta t \gg 1/|\Omega_0|$. These results build on the pitch-angle diffusion results similarly derived by Lemons (2012). We have derived these equations in the context of field-aligned waves only. Because the waves are field-aligned, an integral over wave normal angle is avoided, as is the sum over different resonance numbers, which would be required in a treatment of obliquely propagating wave modes (e.g., see Lyons (1974); Glauert and Horne (2005); Albert (2005). It will be interesting in future works to consider non-zero wave normal angles.

5.3 Novel Derivation of the Weak Turbulence and Quasilinear Diffusion Theories

The standard derivations of the quasilinear theory (Drummond and Pines, 1962; Vedenov et al., 1962; Kennel and Engelmann, 1966; Lerche, 1968; Lyons, 1974; Summers, 2005) are founded upon a perturbative analysis of the Vlasov-Maxwell equations (e.g., see Schindler (2007)), and describe the evolution of a gyrophase-averaged (gyrotropic) particle distribution function in an infinite and homogeneous collisionless plasma with a uniform and static background magnetic field, although we do note a comparatively recent example of a derivation by Brizard and Chan (2004) that does include spatial inhomogeneities from the very outset. The standard derivations rely on a number of assumptions: 1) sufficiently small electromagnetic wave power and a correspondingly sufficiently large spectral width (e.g., see Karpman (1974); Tong et al. (2019)); 2) sufficiently small wave growth rates and slowly varying wave spectra, and a correspondingly slowly varying spatially averaged distribution function (e.g., see Kennel and Engelmann (1966); Davidson et al. (1972)); 3) a wave spectrum that satisfies the so-called "Chirikov resonance overlap condition" (e.g., see Zaslavskiĭ and Chirikov (1972); Artemyev et al. (2015)). Quasilinear theory in the limit of resonant diffusion further restricts that wave growth rates actually tend to zero (Kennel and Engelmann, 1966), and this is the version of the quaslinear theory that is commonly used in numerical radiation belt diffusion models (e.g., see Beutier and Boscher (1995); Albert et al. (2009); Su et al. (2010); Subbotin et al. (2010); Glauert et al. (2014)).

The approach presented in this paper to derive the weak turbulence and quasilinear diffusion coefficients has some important benefits. Firstly, our derivations rely on fewer technical assumptions than those mentioned above for the case of the quasilinear theory in the resonant diffusion limit (zero wave growth rate). Ultimately, the main two assumptions are the small wave amplitudes ϵ_k, and the "random-phase" criteria. Secondly, we believe that the theory has a very intuitive and "user-friendly" entry point, namely an expansion of particle trajectories that obey the Lorentz force law, $\mathbf{F} = q(\boldsymbol{\mathcal{E}} + \mathbf{v} \times \mathbf{B})$, under the influence of prescribed electromagnetic waves expressed as Fourier transforms. There may be considerable algebra that follows, but the route through the calculation is quite straightforward to understand and is based on commonly used techniques. Furthermore, the emergent dependence of the transport coefficients on timescale is one example of the insight that can be derived using this approach. We anticipate that this approach can be used to derive transport equations and associated transport coefficients for a wider variety of systems and circumstances, and we leave this for future work, e.g., electromagnetic fields with non-zero wave normal angles.

5.4 Nonlinear Wave-Particle Interactions

Numerous observations have shown the prevalence of high-amplitude electromagnetic whistler-mode and ion-cyclotron waves in the Earth's inner magnetosphere (Cattell et al., 2008; Cully et al., 2008; Breneman et al., 2011; Kellogg et al., 2011; Wilson et al., 2011; Hendry et al., 2019; Tyler et al., 2019; Zhang et al., 2019; Zhang et al., 2021), such as are responsible for local changes in the energy and pitch-angle of radiation belt electrons. These high "nonlinear" wave amplitudes cast some doubt on the applicability of the quasilinear theory in such cases. Furthermore, a number of co-ordinated wave and particle measurements have directly demonstrated the existence of nonlinear wave-particle interactions in the Earth's inner magnetosphere (Agapitov et al., 2015; Foster et al., 2016; Kurita et al., 2018; Mozer et al., 2018; Shumko et al., 2018). Therefore, an improved theoretical understanding and modelling capability of radiation belt dynamics that incorporates the most appropriate elements of the quasilinear and nonlinear theories of wave-particle interactions is an important and outstanding question (e.g., see Omura et al. (2008); Albert et al. (2013); Tao et al. (2012a,b); Omura et al. (2015); Camporeale (2015); Camporeale and Zimbardo (2015); Artemyev et al. (2018); Mourenas et al. (2018); Vainchtein et al. (2018); Zheng et al. (2019); Gan et al. (2020); Allanson et al. (2020); Allanson et al. (2021)).

Theoretical and modeling studies (Albert and Bortnik, 2009; Liu et al., 2012; Zheng et al., 2012; Lee et al., 2018; Artemyev et al., 2018; Vainchtein et al., 2018; Mourenas et al., 2018; Zheng et al., 2019; Gan et al., 2020; Allanson et al. (2020); Allanson et al. (2021)) indicate that an effective incorporation of nonlinear wave-particle interactions into existing modeling paradigms may require the addition of extra, or modified, transport coefficients (or some other addition) to the version of the Fokker-Planck equation that is currently used (e.g., see Schulz and Lanzerotti (1974); Glauert et al. (2014)). There are a number of candidate methods to achieve this (or a similar) goal, and a number of these are summarized in Artemyev et al. (2021). A fully nonlinear model of wave-particle interactions in the radiation belts would necessarily need to include inhomogeneous background magnetic fields and number density, to incorporate: 1) phase decorrelation specifically due the inhomogeneity itself (e.g., see Albert (2010)): 2) nonlinear effects known as phase bunching and phase trapping (e.g., see Omura et al. (2008)). We do not include such spatial inhomogeneities and therefore cannot describe these associated effects. However, we emphasize that the methods in this paper do present a consistent mechanism that allows for the derivation of not only the transport (drift and diffusion) coefficients, but also the very form of the transport (Fokker-Planck) equation itself, based upon prescribed electromagnetic waves and some sensible physical assumptions. In future works, we could derive drift-diffusion relations such as **Eqs 2**, **3** from first principles for other situations, as opposed to a-priori assuming them to hold. This advance is one of the main benefits of using the approach demonstrated in this paper, and it remains to be seen if these methods can be applied to include the inhomogeneous cases.

6 SUMMARY

In this paper we have presented new derivations of relativistic weak turbulence and quasilinear diffusion models. These models describe charged particle dynamics due to interactions with right-/left-handed electromagnetic waves, and specifically for the case of waves that are travelling parallel (and/or anti-parallel) to the direction of the background magnetic field. The approach differs from the most standard methods of derivation, that are based upon the Vlasov-Maxwell set of equations (e.g., see Kennel and Engelmann (1966)). Instead, our approach uses the principles of Markovian dynamics, and is fundamentally based on solutions to the single-particle Lorentz force equation, $\mathbf{F} = q(\boldsymbol{\mathcal{E}} + \mathbf{v} \times \mathbf{B})$. In particular, we expand the relevant equations of motion up to second order in a small parameter, $\epsilon(\bar{k}) = \tilde{B}(\bar{k})/|\mathbf{B}_0|$, (the relative magnitude of magnetic perturbations to the background magnetic field), and then ensemble average the solutions to obtain the diffusion coefficients. The approach used in this paper builds upon the work by Lemons (2012), in which pitch-angle dynamics were considered due to interactions with a static magnetic field profile. The main conclusions and results of this paper are as follows:

- A derivation and discussion of the general Fokker-Planck equation to describe stochastic charged particle dynamics in energy and pitch-angle space, using Markov theory (**Eq. 1**; **Section 2**). This equation includes all possible advective and diffusive dynamics, in principle. The form of the drift and diffusion coefficients are then to be determined on a system-by-system basis. In this paper we solve for the diffusive dynamics only, and leave investigations of the drift coefficients and drift-diffusion relations for future works;
- In sections 3 and 4 we solve the Lorentz force law using expansions in the small parameter $\epsilon(\bar{k})$, and then ensemble average the results to derive the diffusion coefficients for a weak turbulence approximations. The obtained diffusion coefficients $\mathcal{D}_{\alpha\alpha}, \mathcal{D}_{\alpha E}$ and $\mathcal{D}_{EE}$ **Eqs 20–22** are in principle valid for any elapsed time Δt provided $\Delta t_C \leq \Delta t \ll 1/|D|$, for Δt_C the particle de-correlation time. These weak turbulence diffusion coefficients: 1) display an interesting dependency on Δt; 2) and also explicitly incorporate the effects of non-resonant particles, as well as the standard effects of cycolotron-resonant particles;
- The weak turbulence diffusion coefficients recover the standard form as used in the resonant-diffusion limit of relativistic quasilinear theory (e.g., see Glauert and Horne (2005); Summers (2005)), when we consider elapsed timescales much greater than a gyroperiod (i.e., we allow $\Delta t \gg 1/|\Omega_0|$, and formally $|\Omega_0|\Delta t \to \infty$);
- Whilst the form of the quasilinear diffusion coefficients is not new in and of itself, our new derivation has a number of benefits, including: 1) the evident self-consistent relationship between a more general weak turbulence theory and the standard resonant diffusion quasilinear theory (as is commonly used in e.g. radiation belt and solar wind modeling); 2) the general nature of the Fokker-Planck equation that can be derived without any prior assumptions regarding its form; 3) the clear dependence of the form of the Fokker-Planck equation and the transport coefficients on given specific timescales.

DATA AVAILABILITY STATEMENT

The original contributions presented in the study are included in the article/**Supplementary Material**, further inquiries can be directed to the corresponding author.

AUTHOR CONTRIBUTIONS

OA derived the equations and wrote the article. TE reproduced the equations and consulted on the article. CW 1) consulted on the article; 2) discussed key themes with OA on many occasions; 3) and provided **Figure 1**. TN 1) consulted on the article; 2) provided key early input with regards to the ensemble averaging method.

FUNDING

OA acknowledges financial support from the University of Exeter and from the United Kingdom Natural Environment Research Council (NERC) Independent Research Fellowship NE/V013963/1. OA and CW acknowledge financial support from the NERC Highlight Topic Grant NE/P017274/1 (Rad-Sat), and from United Kingdom Science and Technology Facilities Council (STFC) *via* Consolidated Grant ST/W000369/1. TE acknowledges financial support from an Early Career Fellowship, split jointly by the Leverhulme Trust (ECF-2019-155) and the University of Leicester in the first instance (2019-21), but presently the University of Glasgow (2021-). TN acknowledges financial support from the STFC *via* Consolidated Grant ST/S000402/1. The University of Exeter cover the Open Access Publication Fee *via* a UKRI block grant.

SUPPLEMENTARY MATERIAL

The Supplementary Material for this article can be found online at: https://www.frontiersin.org/articles/10.3389/fspas.2021.805699/full#supplementary-material

REFERENCES

Agapitov, O. V., Artemyev, A. V., Mourenas, D., Mozer, F. S., and Krasnoselskikh, V. (2015). Nonlinear Local Parallel Acceleration of Electrons through Landau Trapping by Oblique Whistler Mode Waves in the Outer Radiation belt. *Geophys. Res. Lett.* 42, 10,140–10,149. doi:10.1002/2015GL066887

Albert, J. M., and Bortnik, J. (2009). Nonlinear Interaction of Radiation belt Electrons with Electromagnetic Ion Cyclotron Waves. *Geophys. Res. Lett.* 36, L12110. doi:10.1029/2009GL038904

Albert, J. M. (2001). Comparison of Pitch Angle Diffusion by Turbulent and Monochromatic Whistler Waves. *J. Geophys. Res.* 106, 8477–8482. doi:10.1029/2000JA000304

Albert, J. M. (2010). Diffusion by One Wave and by many Waves. *J. Geophys. Res.* 115, A00F05. doi:10.1029/2009JA014732

Albert, J. M. (2005). Evaluation of Quasi-Linear Diffusion Coefficients for Whistler Mode Waves in a Plasma with Arbitrary Density Ratio. *J. Geophys. Res.* 110, A03218. doi:10.1029/2004JA010844

Albert, J. M., Meredith, N. P., and Horne, R. B. (2009). Three-dimensional Diffusion Simulation of Outer Radiation belt Electrons during the 9 October 1990 Magnetic Storm. *J. Geophys. Res. Space Phys.* 114, A09214. doi:10.1029/2009ja014336

Albert, J. M., Tao, X., and Bortnik, J. (2013). *Aspects of Nonlinear Wave-Particle Interactions*. Editors D Summers, I. R. Mann, D. N. Baker, and M Schulz, 199, 255–264. Washington, DC: American Geophysical Union. doi:10.1029/2012GM001324 https://agupubs.onlinelibrary.wiley.com/doi/book/10.1029/GM199.

Allanson, O., Watt, C. E. J., Allison, H. J., and Ratcliffe, H. (2021). Electron Diffusion and Advection during Nonlinear Interactions with Whistler-Mode Waves. *J. Geophys. Res. Space Phys.* 126, e2020JA028793. doi:10.1029/2020ja028793

Allanson, O., Watt, C. E. J., Ratcliffe, H., Allison, H. J., Meredith, N. P., Bentley, S. N., et al. (2020). Particle-in-cell Experiments Examine Electron Diffusion by Whistler-Mode Waves: 2. Quasi-Linear and Nonlinear Dynamics. *J. Geophys. Res. Space Phys.* 125, e2020JA027949. doi:10.1029/2020JA027949

Allanson, O., Watt, C. E. J., Ratcliffe, H., Meredith, N. P., Allison, H. J., Bentley, S. N., et al. (2019). Particle-in-cell Experiments Examine Electron Diffusion by Whistler-mode Waves: 1. Benchmarking with a Cold Plasma. *J. Geophys. Res. Space Phys.* 124, 8893–8912. doi:10.1029/2019JA027088

Artemyev, A. V., Mourenas, D., Agapitov, O. V., and Krasnoselskikh, V. V. (2015). Relativistic Electron Scattering by Magnetosonic Waves: Effects of Discrete Wave Emission and High Wave Amplitudes. *Phys. Plasmas* 22, 062901. doi:10.1063/1.4922061

Artemyev, A. V., Neishtadt, A. I., Vasiliev, A. A., and Mourenas, D. (2018). Long-term Evolution of Electron Distribution Function Due to Nonlinear Resonant Interaction with Whistler Mode Waves. *J. Plasma Phys.* 84, 905840206. doi:10.1017/S0022377818000260

Artemyev, A. V., Neishtadt, A. I., Vasiliev, A. A., Zhang, X.-J., Mourenas, D., and Vainchtein, D. (2021). Long-term Dynamics Driven by Resonant Wave-Particle Interactions: from Hamiltonian Resonance Theory to Phase Space Mapping. *J. Plasma Phys.* 87, 835870201. doi:10.1017/S0022377821000246

Beutier, T., and Boscher, D. (1995). A Three-Dimensional Analysis of the Electron Radiation belt by the Salammbô Code. *J. Geophys. Res.* 100, 14853–14861. doi:10.1029/94JA03066

Breneman, A., Cattell, C., Wygant, J., Kersten, K., Wilson, L. B., Schreiner, S., et al. (2011). Large-amplitude Transmitter-Associated and Lightning-Associated Whistler Waves in the Earth's Inner Plasmasphere at L < 2. *J. Geophys. Res.* 116, A06310. doi:10.1029/2010JA016288

Brizard, A. J., and Chan, A. A. (2004). Relativistic Quasilinear Diffusion in Axisymmetric Magnetic Geometry for Arbitrary-Frequency Electromagnetic Fluctuations. *Phys. Plasmas* 11, 4220–4229. doi:10.1063/1.1773554

Cai, B., Wu, Y., and Tao, X. (2020). Effects of Nonlinear Resonance Broadening on Interactions between Electrons and Whistler Mode Waves. *Geophys. Res. Lett.* 47, e2020GL087991. doi:10.1029/2020GL087991

Camporeale, E. (2015). Resonant and Nonresonant Whistlers-Particle Interaction in the Radiation Belts. *Geophys. Res. Lett.* 42, 3114–3121. doi:10.1002/2015GL063874

Camporeale, E., and Zimbardo, G. (2015). Wave-particle Interactions with Parallel Whistler Waves: Nonlinear and Time-dependent Effects Revealed by Particle-In-Cell Simulations. *Phys. Plasmas* 22, 092104. doi:10.1063/1.4929853

Cattell, C., Wygant, J. R., Goetz, K., Kersten, K., Kellogg, P. J., von Rosenvinge, T., et al. (2008). Discovery of Very Large Amplitude Whistler-Mode Waves in Earth's Radiation Belts. *Geophys. Res. Lett.* 35, L01105. doi:10.1029/2007GL032009

Cully, C. M., Bonnell, J. W., and Ergun, R. E. (2008). Themis Observations of Long-Lived Regions of Large-Amplitude Whistler Waves in the Inner Magnetosphere. *Geophys. Res. Lett.* 35, L17S16. doi:10.1029/2008GL033643

Davidson, R. C., Hammer, D. A., Haber, I., and Wagner, C. E. (1972). Nonlinear Development of Electromagnetic Instabilities in Anisotropic Plasmas. *Phys. Fluids* 15, 317–333. doi:10.1063/1.1693910

Drummond, W. E., and Pines, D. (1962). Nonlinear Stability of Plasma Oscillations. *Nucl. Fusion Suppl.* 3, 1049–1058.

Dupree, T. H. (1966). A Perturbation Theory for strong Plasma Turbulence. *Phys. Fluids* 9, 1773–1782. doi:10.1063/1.1761932

Einstein, A. (1956). *Investigations on the Theory of the Brownian Movement*. Dover Books on Physics Series. New York, NY: Dover Publications.

Foster, J. C., Erickson, P. J., Baker, D. N., Jaynes, A. N., Mishin, E. V., Fennel, J. F., et al. (2016). Observations of the Impenetrable Barrier, the Plasmapause, and the VLF Bubble during the 17 March 2015 Storm. *J. Geophys. Res. Space Phys.* 121, 5537–5548. doi:10.1002/2016JA022509

Gan, L., Li, W., Ma, Q., Albert, J., Artemyev, A., and Bortnik, J. (2020). Nonlinear Interactions between Radiation belt Electrons and Chorus Waves: Dependence on Wave Amplitude Modulation. *Geophys. Res. Lett.* 47, e2019GL085987. doi:10.1029/2019GL085987

Glauert, S. A., and Horne, R. B. (2005). Calculation of Pitch Angle and Energy Diffusion Coefficients with the PADIE Code. *J. Geophys. Res.* 110, A04206. doi:10.1029/2004JA010851

Glauert, S. A., Horne, R. B., and Meredith, N. P. (2014). Three-dimensional Electron Radiation belt Simulations Using the BAS Radiation Belt Model with New Diffusion Models for Chorus, Plasmaspheric Hiss, and Lightning-generated Whistlers. *J. Geophys. Res. Space Phys.* 119, 268–289. doi:10.1002/2013JA019281

Hendry, A. T., Santolik, O., Kletzing, C. A., Rodger, C. J., Shiokawa, K., and Baishev, D. (2019). Multi-instrument Observation of Nonlinear EMIC-Driven Electron Precipitation at Sub-MeV Energies. *Geophys. Res. Lett.* 46, 7248–7257. doi:10.1029/2019GL082401

Horne, R. B., Thorne, R. M., Shprits, Y. Y., Meredith, N. P., Glauert, S. A., Smith, A. J., et al. (2005). Wave Acceleration of Electrons in the Van Allen Radiation Belts. *Nature* 437, 227–230. doi:10.1038/nature03939

Jeong, S.-Y., Verscharen, D., Wicks, R. T., and Fazakerley, A. N. (2020). A Quasi-Linear Diffusion Model for Resonant Wave-Particle Instability in Homogeneous Plasma. *ApJ* 902, 128. doi:10.3847/1538-4357/abb099

Karimabadi, H., Krauss-Varban, D., and Terasawa, T. (1992). Physics of Pitch Angle Scattering and Velocity Diffusion, 1. Theory. *J. Geophys. Res.* 97, 13853–13864. doi:10.1029/92JA00997

Karimabadi, H., and Menyuk, C. R. (1991). A Fast and Accurate Method of Calculating Particle Diffusion: Application to the Ionosphere. *J. Geophys. Res.* 96, 9669–9687. doi:10.1029/91JA00315

Karpman, V. I. (1974). Nonlinear Effects in the ELF Waves Propagating along the Magnetic Field in the Magnetosphere. *Space Sci. Rev.* 16, 361–388. doi:10.1007/BF00171564

Kellogg, P. J., Cattell, C. A., Goetz, K., Monson, S. J., and Wilson, L. B. (2011). Large Amplitude Whistlers in the Magnetosphere Observed with Wind-Waves. *J. Geophys. Res.* 116, A09224. doi:10.1029/2010JA015919

Kennel, C. F., and Engelmann, F. (1966). Velocity Space Diffusion from Weak Plasma Turbulence in a Magnetic Field. *Phys. Fluids* 9, 2377–2388. doi:10.1063/1.1761629

Kollmann, P., Roussos, E., Paranicas, C., Woodfield, E. E., Mauk, B. H., Clark, G., et al. (2018). Electron Acceleration to Mev Energies at jupiter and Saturn. *J. Geophys. Res. Space Phys.* 123, 9110–9129. doi:10.1029/2018ja025665

Kurita, S., Miyoshi, Y., Kasahara, S., Yokota, S., Kasahara, Y., Matsuda, S., et al. (2018). Deformation of Electron Pitch Angle Distributions Caused by Upper Band Chorus Observed by the Arase Satellite. *Geophys. Res. Lett.* 45, 7996–8004. doi:10.1029/2018GL079104

Lee, S.-Y., Lee, E., Seough, J., Lee, J.-g., Hwang, J., Lee, J.-J., et al. (2018). Simulation and Quasi-Linear Theory of Whistler Anisotropy Instability. *J. Geophys. Res. Space Phys.* 123, 3277–3290. doi:10.1029/2017ja024960

Lemons, D. S., Liu, K., Winske, D., and Gary, S. P. (2009). Stochastic Analysis of Pitch Angle Scattering of Charged Particles by Transverse Magnetic Waves. *Phys. Plasmas* 16, 112306. doi:10.1063/1.3264738

Lemons, D. S. (2012). Pitch Angle Scattering of Relativistic Electrons from Stationary Magnetic Waves: Continuous Markov Process and Quasilinear Theory. *Phys. Plasmas* 19, 012306. doi:10.1063/1.3676156

Lerche, I. (1968). Quasilinear Theory of Resonant Diffusion in a Magneto-Active, Relativistic Plasma. *Phys. Fluids* 11, 1720–1727. doi:10.1063/1.1692186

Liu, K., Lemons, D. S., Winske, D., and Gary, S. P. (2010). Relativistic Electron Scattering by Electromagnetic Ion Cyclotron Fluctuations: Test Particle Simulations. *J. Geophys. Res.* 115, A04204. doi:10.1029/2009JA014807

Liu, K., Winske, D., Gary, S. P., and Reeves, G. D. (2012). Relativistic Electron Scattering by Large Amplitude Electromagnetic Ion Cyclotron Waves: The Role of Phase Bunching and Trapping. *J. Geophys. Res.* 117, A06218. doi:10.1029/2011JA017476

Lyons, L. R. (1974). General Relations for Resonant Particle Diffusion in Pitch Angle and Energy. *J. Plasma Phys.* 12, 45–49. doi:10.1017/S0022377800024910

Mertsch, P. (2020). Test Particle Simulations of Cosmic Rays. *Astrophys Space Sci.* 365, 135. doi:10.1007/s10509-020-03832-3

Mourenas, D., Zhang, X.-J., Artemyev, A. V., Angelopoulos, V., Thorne, R. M., Bortnik, J., et al. (2018). Electron Nonlinear Resonant Interaction with Short and Intense Parallel Chorus Wave Packets. *J. Geophys. Res. Space Phys.* 123, 4979–4999. doi:10.1029/2018JA025417

Mozer, F. S., Agapitov, O. V., Blake, J. B., and Vasko, I. Y. (2018). Simultaneous Observations of Lower Band Chorus Emissions at the Equator and Microburst Precipitating Electrons in the Ionosphere. *Geophys. Res. Lett.* 45, 511–516. doi:10.1002/2017GL076120

Omura, Y., Katoh, Y., and Summers, D. (2008). Theory and Simulation of the Generation of Whistler-Mode Chorus. *J. Geophys. Res.* 113, A04223. doi:10.1029/2007JA012622

Omura, Y., Miyashita, Y., Yoshikawa, M., Summers, D., Hikishima, M., Ebihara, Y., et al. (2015). Formation Process of Relativistic Electron Flux through Interaction with Chorus Emissions in the Earth's Inner Magnetosphere. *J. Geophys. Res. Space Phys.* 120, 9545–9562. doi:10.1002/2015JA021563

Osmane, A., and Lejosne, S. (2021). Radial Diffusion of Planetary Radiation Belts' Particles by Fluctuations with Finite Correlation Time. *ApJ* 912, 142. doi:10.3847/1538-4357/abf04b

Reif, F. (2009). *Fundamentals of Statistical and Thermal Physics*. Long Grove, Illinois: Waveland Press.

Roederer, J., and Zhang, H. (2013). *Dynamics of Magnetically Trapped Particles: Foundations of the Physics of Radiation Belts and Space Plasmas*. Astrophysics and Space Science Library. Springer Berlin Heidelberg.

Sagdeev, R. Z., and Galeev, A. A. (1969). *Nonlinear Plasma Theory* (New York: W.A. Benjamin, Inc.).

Schindler, K. (2007). *Physics of Space Plasma Activity*. Cambridge, United Kingdom: Cambridge University Press.

Schlickeiser, R. (1989). Cosmic-ray Transport and Acceleration. I - Derivation of the Kinetic Equation and Application to Cosmic Rays in Static Cold media. II - Cosmic Rays in Moving Cold media with Application to Diffusive Shock Wave Acceleration. *ApJ* 336, 243. doi:10.1086/167009

Schulz, M., and Lanzerotti, L. (1974). *Particle Diffusion in the Radiation Belts*. Physics and chemistry in space. Berlin-Heidelberg: Springer-Verlag. doi:10.1007/978-3-642-65675-0

Shumko, M., Turner, D. L., O'Brien, T. P., Claudepierre, S. G., Sample, J., Hartley, D. P., et al. (2018). Evidence of Microbursts Observed Near the Equatorial Plane in the Outer Van allen Radiation belt. *Geophys. Res. Lett.* 45, 8044–8053. doi:10.1029/2018GL078451

Steinacker, J., and Miller, J. A. (1992). Stochastic Gyroresonant Electron Acceleration in a Low-Beta Plasma. I - Interaction with Parallel Transverse Cold Plasma Waves. *ApJ* 393, 764. doi:10.1086/171544

Su, Z., Xiao, F., Zheng, H., and Wang, S. (2010). STEERB: A Three-Dimensional Code for Storm-Time Evolution of Electron Radiation belt. *J. Geophys. Res.* 115, A09208. doi:10.1029/2009JA015210

Subbotin, D., Shprits, Y., and Ni, B. (2010). Three-dimensional Verb Radiation belt Simulations Including Mixed Diffusion. *J. Geophys. Res.* 115, A03205. doi:10.1029/2009JA015070

Summers, D. (2005). Quasi-linear Diffusion Coefficients for Field-Aligned Electromagnetic Waves with Applications to the Magnetosphere. *J. Geophys. Res.* 110. doi:10.1029/2005JA011159

Summers, D., and Thorne, R. M. (2003). Relativistic Electron Pitch-Angle Scattering by Electromagnetic Ion Cyclotron Waves during Geomagnetic Storms. *J. Geophys. Res.* 108 (A4), 1143. doi:10.1029/2002JA009489

Tao, X., Bortnik, J., Albert, J. M., and Thorne, R. M. (2012a). Comparison of Bounce-Averaged Quasi-Linear Diffusion Coefficients for Parallel Propagating Whistler Mode Waves with Test Particle Simulations. *J. Geophys. Res.* 117, A10205. doi:10.1029/2012JA017931

Tao, X., Bortnik, J., Thorne, R. M., Albert, J. M., and Li, W. (2012b). Effects of Amplitude Modulation on Nonlinear Interactions between Electrons and Chorus Waves. *Geophys. Res. Lett.*, L0610239. doi:10.1029/2012GL051202

Thorne, R. M. (2010). Radiation belt Dynamics: The Importance of Wave-Particle Interactions. *Geophys. Res. Lett.* 37, L22107. doi:10.1029/2010GL044990

Tong, Y., Vasko, I. Y., Artemyev, A. V., Bale, S. D., and Mozer, F. S. (2019). Statistical study of whistler waves in the solar wind at 1 au. *ApJ* 878, 41. doi:10.3847/1538-4357/ab1f05

Tsurutani, B. T., and Lakhina, G. S. (1997). Some Basic Concepts of Wave-Particle Interactions in Collisionless Plasmas. *Rev. Geophys.* 35, 491–501. doi:10.1029/97RG02200

Tyler, E., Breneman, A., Cattell, C., Wygant, J., Thaller, S., and Malaspina, D. (2019). Statistical Occurrence and Distribution of High-Amplitude Whistler Mode Waves in the Outer Radiation Belt. *Geophys. Res. Lett.* 46, 2328–2336. doi:10.1029/2019GL082292

Vainchtein, D., Zhang, X. J., Artemyev, A. V., Mourenas, D., Angelopoulos, V., and Thorne, R. M. (2018). Evolution of Electron Distribution Driven by Nonlinear Resonances with Intense Field-Aligned Chorus Waves. *J. Geophys. Res. Space Phys.* 123, 8149–8169. doi:10.1029/2018JA025654

Vedenov, A. A., Velikhov, E., and Sagdeev, R. (1962). Quasilinear Theory of Plasma Oscillations. *Nucl. Fusion Suppl.* 2, 465–475.

Verscharen, D., and Chandran, B. D. G. (2013). The Dispersion Relations and Instability Thresholds of Oblique Plasma Modes in the Presence of an Ion Beam. *ApJ* 764, 88. doi:10.1088/0004-637x/764/1/88

Vocks, C. (2012). Kinetic Models for Whistler Wave Scattering of Electrons in the Solar Corona and Wind. *Space Sci. Rev.* 172, 303–314. doi:10.1007/s11214-011-9749-0

Vocks, C., Salem, C., Lin, R. P., and Mann, G. (2005). Electron Halo and Strahl Formation in the Solar Wind by Resonant Interaction with Whistler Waves. *ApJ* 627, 540–549. doi:10.1086/430119

Walt, M. (1994). *Introduction to Geomagnetically Trapped Radiation*. Cambridge Atmospheric and Space Science Series. Cambridge, United Kingdom: Cambridge University Press. doi:10.1017/CBO9780511524981

Wang, M. C., and Uhlenbeck, G. E. (1945). On the Theory of the Brownian Motion II. *Rev. Mod. Phys.* 17, 323–342. doi:10.1103/RevModPhys.17.323

Watt, C. E. J., Allison, H. J., Thompson, R. L., Bentley, S. N., Meredith, N. P., Glauert, S. A., et al. (2021). The Implications of Temporal Variability in Wave-Particle Interactions in Earth's Radiation Belts. *Geophys. Res. Lett.* 48. doi:10.1029/2020GL089962

Wilson, L. B., III, Cattell, C. A., Kellogg, P. J., Wygant, J. R., Goetz, K., Breneman, A., et al. (2011). The Properties of Large Amplitude Whistler Mode Waves in the Magnetosphere: Propagation and Relationship with Geomagnetic Activity. *Geophys. Res. Lett.* 38. doi:10.1029/2011GL048671

Woodfield, E. E., Horne, R. B., Glauert, S. A., Menietti, J. D., and Shprits, Y. Y. (2014). The Origin of Jupiter's Outer Radiation belt. *J. Geophys. Res. Space Phys.* 119, 3490–3502. doi:10.1002/2014JA019891

Zaslavskiĭ, G. M., and Chirikov, B. V. (1972). Stochastic Instability of Non-linear Oscillations. *Sov. Phys. Usp.* 14, 549–568. doi:10.1070/pu1972v014n05abeh004669

Zhang, X.-J., Mourenas, D., Shen, X.-C., Qin, M., Artemyev, A. V., Ma, Q., et al. (2021). Dependence of Relativistic Electron Precipitation in the Ionosphere on Emic Wave Minimum Resonant Energy at the Conjugate Equator. *J. Geophys. Res. Space Phys.* 126. doi:10.1029/2021JA029193

Zhang, X. J., Mourenas, D., Artemyev, A. V., Angelopoulos, V., Bortnik, J., Thorne, R. M., et al. (2019). Nonlinear Electron Interaction with Intense Chorus Waves: Statistics of Occurrence Rates. *Geophys. Res. Lett.* 46, 7182–7190. doi:10.1029/2019GL083833

Zheng, L., Chen, L., and Zhu, H. (2019). Modeling Energetic Electron Nonlinear Wave-Particle Interactions with Electromagnetic Ion Cyclotron Waves. *J. Geophys. Res. Space Phys.* 124, 3436–3453. doi:10.1029/2018JA026156

Zheng, Q., Zheng, Y., Fok, M.-C., and Lui, A. T. Y. (2012). Electron Energy Diffusion and Advection Due to Non-linear Electron-Chorus Wave Interactions. *J. Atmos. Solar-Terrestrial Phys.* 80, 152–160. doi:10.1016/j.jastp.2012.01.011

Conflict of Interest: The authors declare that the research was conducted in the absence of any commercial or financial relationships that could be construed as a potential conflict of interest.

Publisher's Note: All claims expressed in this article are solely those of the authors and do not necessarily represent those of their affiliated organizations, or those of the publisher, the editors, and the reviewers. Any product that may be evaluated in this article, or claim that may be made by its manufacturer, is not guaranteed or endorsed by the publisher.

frontiers in Astronomy and Space Sciences

ORIGINAL RESEARCH
published: 23 March 2022
doi: 10.3389/fspas.2022.836811

Storm-Time Evolution of the Equatorial Electron Pitch Angle Distributions in Earth's Outer Radiation Belt

Artem Smirnov[1,2], Yuri Shprits[1,2,3], Hayley Allison[1], Nikita Aseev[1], Alexander Drozdov[3], Peter Kollmann[4], Dedong Wang[1] and Anthony A. Saikin[3]*

[1]Helmholtz Centre Potsdam - GFZ German Research Centre for Geosciences, Potsdam, Germany, [2]Institute of Physics and Astronomy, University of Potsdam, Potsdam, Germany, [3]Department of Earth, Planetary and Space Sciences, University of California, Los Angeles, Los Angeles, CA, United States, [4]Applied Physics Laboratory, Johns Hopkins University, Laurel, MD, United States

In this study we analyze the storm-time evolution of equatorial electron pitch angle distributions (PADs) in the outer radiation belt region using observations from the Magnetic Electron Ion Spectrometer (MagEIS) instrument aboard the Van Allen Probes in 2012–2019. The PADs are approximated using a sum of the first, third and fifth sine harmonics. Different combinations of the respective coefficients refer to the main PAD shapes within the outer radiation belt, namely the pancake, flat-top, butterfly and cap PADs. We conduct a superposed epoch analysis of 129 geomagnetic storms and analyze the PAD evolution for day and night MLT sectors. PAD shapes exhibit a strong energy-dependent response. At energies of tens of keV, the PADs exhibit little variation throughout geomagnetic storms. Cap PADs are mainly observed at energies <300 keV, and their extent in L shrinks with increasing energy. The cap distributions transform into the pancake PADs around the main phase of the storm on the nightside, and then come back to their original shapes during the recovery phase. At higher energies on the dayside, the PADs are mainly pancake during pre-storm conditions and become more anisotropic during the main phase. The quiet-time butterfly PADs can be observed on the nightside at $L>5.6$. During the main phase, butterfly PADs have stronger 90°-minima and can be observed at lower L-shells (down to $L = 5$), then transitioning into flat-top PADs at $L \sim 4.5 – 5$ and pancake PADs at $L<4.5$. The resulting PAD coefficients for different energies, locations and storm epochs can be used to test the wave models and physics-based radiation belt codes in terms of pitch angle distributions.

Keywords: pitch angle, pitch angle distributions, electrons, radiation belts, magnetosphere, van allen probes

OPEN ACCESS

Edited by:
Olga V. Khabarova, Institute of Terrestrial Magnetism Ionosphere and Radio Wave Propagation (RAS), Russia

Reviewed by:
Nickolay Ivchenko, Royal Institute of Technology, Sweden
Qiugang Zong, Peking University, China

****Correspondence:***
Artem Smirnov
artem.smirnov@gfz-potsdam.de

Specialty section:
This article was submitted to Space Physics, a section of the journal Frontiers in Astronomy and Space Sciences

Received: *15 December 2021*
Accepted: *01 March 2022*
Published: *23 March 2022*

Citation:
Smirnov A, Shprits Y, Allison H, Aseev N, Drozdov A, Kollmann P, Wang D and Saikin AA (2022) Storm-Time Evolution of the Equatorial Electron Pitch Angle Distributions in Earth's Outer Radiation Belt. Front. Astron. Space Sci. 9:836811. doi: 10.3389/fspas.2022.836811

1 INTRODUCTION

The radiation belts of the Earth contain charged energetic particles, mainly electrons and protons, trapped by the geomagnetic field. The energetic electrons are primarily observed in two regions, namely the inner ($L<2.5$) and outer ($3.5 < L<7$) belts, separated by the slot region where fluxes typically drop by several orders of magnitude (e.g., Ganushkina et al., 2011). The radiation belt electrons can be characterized in terms of their flux intensity and angular distributions (e.g., Clark

et al., 2014). These distributions, also named the pitch angle distributions (PADs), play a crucial role in understanding the dynamics of the radiation belts, as specific PAD types can reveal the processes governing the particle transport, source and loss mechanisms, and wave activities (e.g., Horne et al., 2003; Gannon et al., 2007; Ni et al., 2015).

There are several common types of pitch angle distributions in the radiation belt region. The so-called pancake, or normal, PADs have a maximum flux at 90° pitch angle (PA) with a smooth decrease in flux towards the loss cone (e.g., West et al., 1973). The pancake PADs can be formed as a result of the particle PA diffusion, inward radial diffusion, as well as wave-particle interactions (e.g., with hiss and chorus waves in the outer belt (Su et al., 2009; Meredith et al., 2000)), and consititute the most dominant PAD type in the inner magnetosphere on the dayside (Gannon et al., 2007). The PADs where electron flux at 90° is smaller than at intermediate pitch angles (~ 30°–75°) are called the butterfly distributions (West et al., 1973). The butterfly PADs in the outer radiation belt are mainly present at nightside magnetic local times (MLTs) and form due to drift shell splitting (Roederer, 1967; Sibeck et al., 1987), magnetopause shadowing (West et al., 1973) and wave activity (Artemyev et al., 2015; Ni et al., 2020). The flat-top PADs exhibit a relatively constant flux at a wide range of pitch angles around 90°. The flat-top PADs can be a transition phase between the butterfly and pancake PADs, and they also occur due to strong wave-particle interactions with whistler mode waves in regions of low electron densities (Horne et al., 2003). The head-and-shoulders, or cap, distributions resemble pancake PADs for non-equatorially mirroring electrons but have an additional bump in flux around 90° PA; they generally result from resonant interactions with the plasmaspheric hiss waves (Lyons et al., 1972). Wave-particle interactions with ultra low frequency (ULF) waves, particularly in the Pc4-Pc5 range, are known to also affect the electron pitch angle distributions (Zong et al., 2017). For instance, during the drift resonance events electron flux oscillations around 90° are observed faster than at lower PAs, which leads to the formation of the so-called boomerang stripes in the pitch angle distributions (e.g., Hao et al., 2017; Zhao et al., 2020).

Pitch angle distributions can be approximated using different trigonometric functions. The standard formulation used in several previous studies includes fitting PADs to the $\sin^n\alpha$, where α is the particle pitch angle and n is the steepness of the distribution (see e.g., Vampola, 1998; Gannon et al., 2007, etc.). This parametrisation, however, has several limitations. For instance, it fails to capture butterfly distributions which constitute the dominant PAD shape on the nightside at L > 5, as well as cap distributions occurring at lower L-shells (e.g., Zhao et al., 2018; Allison et al. (2018)). To mitigate this limitation, Allison et al. (2018) employed a combination of two terms of the said form, which allowed to resolve the cap distributions. Another formulation used in the radiation belts research includes fitting equatorial PADs with Legendre polynomials which comprise a set of spherical functions (see e.g., Chen et al., 2014; Zhao et al., 2018; Zhao et al., 2021). In particular, Zhao et al. (2018) demonstrated that equatorial PADs in the outer zone can be approximated by the first 3 even terms of the Legendre series expansion, while at L < 3 it was necessary to include higher harmonics due to the larger loss cones and generally steeper PAD shapes. In this study, we use Fourier sine series expansion to approximate equatorial electron PADs (**Eq. 1**). The Fourier expansion has been used for PAD approximation in the planetary magnetospheres (for Saturn's radiation belts Clark et al., 2014) but to our knowledge has not been applied to study electrons in the Earth's radiation belts yet. One of the main advantages of using the Fourier sine series expansion is a possibility to integrate **Equation 1** over the solid angle to derive omnidirectional flux.

Several studies have investigated the morphology of electron pitch angle distributions in the inner magnetosphere, both during quiet and geomagnetically active times. Roederer (1967) analyzed effects of the drift shell splitting on energetic electrons in the model magnetosphere and demonstrated that the drift shell splitting effects could only be observed above L = 5. The spatial structure of 80 keV–2.8 MeV electron PADs was described by West et al. (1973) using Ogo-5 satellite data. The dayside PADs were found to exhibit mainly pancake shape, while the nightside distributions at L > ~ 6 showed butterfly shapes, which were attributed to a combination of the drift shell splitting in presence of a negative flux gradient in L, and magnetopause shadowing. Selesnick and Blake (2002) computed anisotropies of relativistic electron PADs by tracing drift paths of particles for different pitch angles and levels of Kp and found a good agreement with average flux anisotropies calculated from Polar electron data under quiet geomagnetic conditions. Lyons et al. (1972) was one of the first papers that computed the PA-diffusion of electrons at energies 20 keV–2 MeV driven by the resonant interactions with whisler mode waves and showed the existence of the cap pitch angle distributions could be attributed to the resonant interactions with the plasmaspheric hiss waves. Furthermore, it was demonstrated that with increasing energy, the bump in flux at 90° PA, characteristic of the cap PADs, decreased in magnitude as the cyclotron resonance branch extended to higher pitch angles at higher energies. Lyons and Williams (1975a) analyzed the quiet-time structure of electron PADs at energies below 560 keV and observed a generally good agreement in PAD shapes with the theoretical predictions by Lyons et al. (1972). Furthermore, Lyons and Williams (1975b) reported that the storm-time electron PADs were very different from those during quiet times. In particular, the quiet-time cap distributions on the nightside were found to transform into the pancake PADs and then reform to their pre-storm structure several days after the storm. A comprehensive study by Gannon et al. (2007) analyzed electron PADs at energies of hundreds of keV based on data from Medium Electrons A instrument aboard the Combined release and Radiation Effects Satellite (CRRES). They reported that butterfly pitch angle distributions were the most prevalent type on the nightside at high L-shells, whereas on the dayside the pancake PADs constituted the dominant PAD shape.

In recent years, several statistical studies analyzed the storm-time evolution of electron PADs using data from the Van Allen Probes constellation. Ni et al. (2015) used 15 months of the Relativistic Electron Proton Telescope (REPT) data to investigate the variability of PADs of electrons with energies > 2 MeV. By fitting the PADs with a $\sin^n\alpha$ function, the authors tracked the spatiotemporal variability of the sine power n and

found that pancake PADs became more peaked at 90° PA during the storm times compared to the quiet times. The occurrence rate of the butterfly distributions were investigated in Ni et al. (2016), and it was found that at nightside MLTs at high L-shells, up to 80% of PADs can be of butterfly type, which was in good agreement with previous studies by West et al. (1973) and Gannon et al. (2007). Pandya et al. (2020) analyzed the storm-time morphology of PADs of 1.8–6.3 MeV electrons for 27 Coronal Mass Ejection (CME) and 28 Corrotating Interaction Region (CIR) driven storms using the REPT data. The authors reported a strong dependence of PAD shapes on MLT, while the dependence on the storm driver was found to be negligible. Greeley et al. (2021) used REPT data to analyze PAD evolution during enhancements of the ultra relativistic electron fluxes separately for CIR- and CME-driven storms. The study showed that CME-driven storms generally resulted in more anisotropic PADs than CIR-driven storms. Furthermore, it was shown that PADs return to their pre-storm configurations more rapidly during storms driven by CMEs.

The previous studies that used Van Allen Probes data for analyzing the pitch angle distributions have mainly concentrated on relativistic and ultra relativistic energies sampled by the REPT instrument. Observations by the Magnetic Electron Ion Spectrometer (MagEIS) have been used in several recent studies (e.g., Shi et al., 2016; Allison et al., 2018; Zhao et al., 2018) which aimed at creating statistical PAD models but did not investigate PAD evolution for different phases of geomagnetic storms. In this study, we perform, for the first time, a comprehensive statistical analysis of electron PADs sampled by the MagEIS detector at energies 30 keV–1.6 MeV. Furthermore, our study is the first one to use the Van Allen Probe dataset during the mission's entire lifespan in 2012–2019 for PAD analysis. We identify 129 storms in 2012–2019, and examine the morphology of the normalized PAD shapes for day and night MLTs at different energies.

Storm-time evolution of omnidirectional electron fluxes has been analyzed in detail in Turner et al. (2019) for both MagEIS and REPT energies. In this study, we concentrate on the PAD shapes normalized from 0 to 1. It should be noted that in the inner belt, pitch angle distributions appear relatively independent of activity (e.g., Ni et al., 2016) and exhibit very steep shapes due to larger loss cones which require higher harmonics for modeling (Zhao et al., 2018), therefore, in the present study we analyze PADs for L-values from 3 to 6. The paper consists of 5 parts. **Section 2** describes the data set and the methodology employed in this study. In **Section 3**, we analyze the storm-time PAD evolution by means of the superposed epoch analysis of 129 storms during the Van Allen Probes era. The results are discussed in **Section 4**, and the conclusions are drawn in the final section.

2 DATASET AND METHODOLOGY

2.1 Data

The Van Allen Probes mission, originally known as the Radiation Belt Storm Probes (RBSP), operated in 2012–2019 and consisted of two spacecraft, denoted as RBSP-A and RBSP-B, flying in a near-equatorial orbit with an inclination of 10.2° (Mauk et al., 2012). The apogee of the probes was at ~5.8 R_E and perigee at an altitude of ~620 km. The orbital period was equal to 9 h. The full MLT revolution was achieved every ~22 months. The L-shells sampled by Van Allen Probes range from 1.2 to around 6.2 on the nightside and 5.8 on the dayside.

The Magnetic Electron Ion Spectrometer (MagEIS) instruments aboard each of the probes measured electron flux over a broad energy range using one low-energy unit (LOW) for energies 20–240 keV, two medium-energy units (M75 and M35) for observing electron flux at energies 80 keV–1.2 MeV, and a high-energy unit (HIGH) to sample data at energies from 0.8 to 4.8 MeV (Blake et al., 2013). LOW, HIGH and M75 units were mounted at 75° to the spin axis, and the M35 unit was installed at 35° to the spin axis. Such a configuration was selected to provide broader pitch angle coverage for the MagEIS detector. In this study we employ the full data set of the MagEIS pitch angle resolved electron flux (level 3) in 2012–2019 averaged by 5 min with an assumed symmetry with respect to 90° PA. Following Zhao et al. (2018), we remove PADs for which the maximum electron flux value is below 100 $cm^{-2}s^{-1}sr^{-1}keV^{-1}$ as those PADs correspond to background levels of the MagEIS detector and are less indicative of the physics.

In order to analyze pitch angle distributions at the geomagnetic equator, it is necessary to propagate the locally measured electron flux values for each pitch angle to the equatorial plane using an appropriate geomagnetic field model. Since in this study we are concerned with variation of pitch angle shapes with increasing geomagnetic activity, the values are propagated to the magnetic equator using the TS04D storm-time model (Tsyganenko and Sitnov, 2005) with the internal field specified by the International Geomagnetic Reference Field (IGRF) model. The TS04D model requires as inputs the By and Bz components of the interplanetary magnetic field (IMF), solar wind velocity, density and dynamic pressure and the Dst index, as well as special *W* and *G* indices defined in (Tsyganenko and Sitnov, 2005). The values of the solar wind parameters superposed for 129 storms used in this study are shown in the Supporting information (**Supplementary Figure S2**).

2.2 PAD Approximation Using Fourier Sine Series

In this study we approximate equatorial electron PADs using the Fourier sine series expansion of the form:

$$j(\alpha) = A_0 + A_1 \sin\alpha + A_3 \sin 3\alpha + A_5 \sin 5\alpha, \quad (1)$$

where *j* is electron flux as a function of pitch angle α. It should be noted that the even terms ($\sin 2\alpha$ and $\sin 4\alpha$) represent shapes that are asymmetric around 90°, which is inconsistent with the trapped particle populations considered here, and therefore are omitted. In this study, we use the Fourier expansion up to degree 5, as this combination can effectively fit all the PAD types observed in the outer belt (shown in **Figures 1**, **2** and discussed below). We fit the values of electron flux to equatorial pitch angles in linear scale using least-squares and obtain values of the coefficients A_0, A_1, A_3 and A_5. As can be seen from **Equation 1**, the A_0 coefficient shows the value of electron flux in the edge of the loss cone and represents the minimum flux

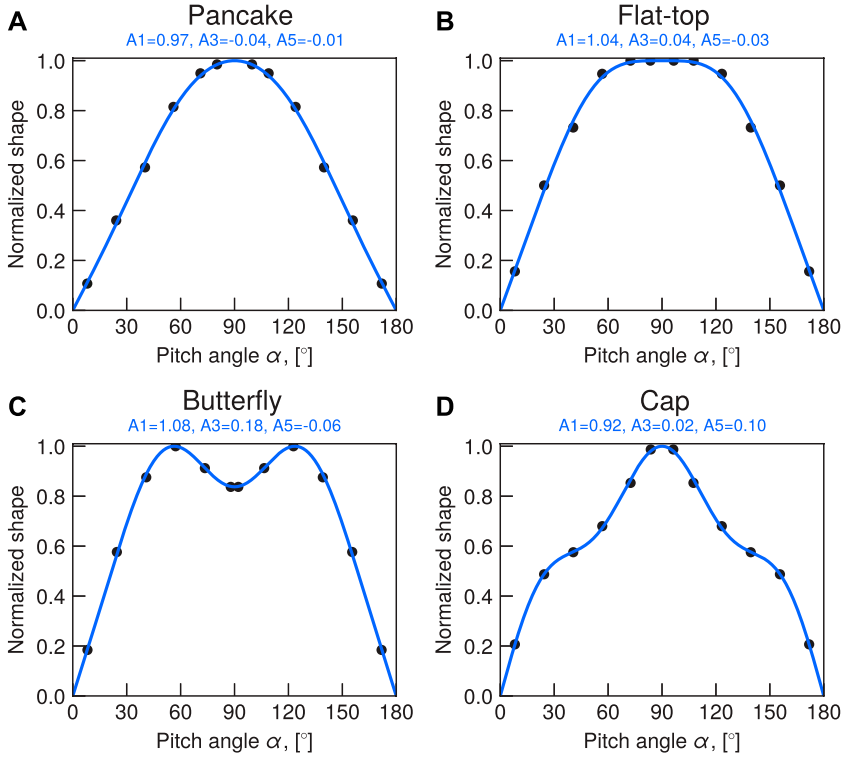

FIGURE 1 | Examples of the fitted pancake **(A)**, flat-top **(B)**, butterfly **(C)** and cap **(D)** equatorial PADs, normalized using equation 2. The dots show normalized MagEIS observations and the solid lines give fitted shapes.

value for a given PAD. Furthermore, we determine maximum value of electron flux, denoted as $j_{\max}$, within each pitch angle distribution. Carbary et al. (2011) proposed a criterion to remove low quality PAD fits, which has been used in several other studies (e.g., Ni et al., 2016). This criterion uses the normalized standard deviation of the difference between the observed and fitted electron flux and is defined as $\sigma_N = \sigma/(j_{\max} - A_0)$. The fits with the corresponding σ_N values ≤ 0.2 represent good quality fits (for details, see Carbary et al., 2011), while entries with $\sigma_N > 0.2$ were deemed as bad fits and excluded from the analysis. Examples of high- and low-quality PAD fits with the corresponding σ_N values are shown in the **Supplementary Figure S1**.

In order to normalize PADs to span from 0 to 1, we apply the following equation to the coefficients A_i, $i = \{1, 3, 5\}$:

$$\tilde{A}_i = \frac{A_i}{j_{\max} - A_0}, \tag{2}$$

where $\tilde{A}_i$ denotes the normalized value of the respective coefficient A_i. It should be noted that the PAD shapes normalized by **Equation 2** do not carry information about the flux levels and only reflect the shape of the distributions. In this study we analyze the storm-time evolution of these normalized pitch angle shapes for day and night MLTs at energies 30 keV–~1.6 MeV. The dependencies observed here are used to create a PAD model in the outer radiation belt, which is presented in Smirnov et al. (2022).

Figure 1 shows examples of the four main types of pitch angle distributions observed in the outer radiation belt region, namely the pancake, flat-top, butterfly and cap PADs, fitted using **Equation 1** and normalized by **Equation 2**. Note that while distinguishing these shapes is useful for discussions, we do not assign these discrete categories to our PADs but keep describing them through the continuous A values. Generally, the pancake PAD shape, shown in **Figure 1A**, resembles the first sine harmonic, and therefore has a large value of the corresponding coefficient A1 and low values of coefficients before the third and fifth terms (A3 and A5, respectively). The A3 coefficient corresponding to the sin (3α) term shows contribution of the butterfly shape. Since sin (3α) exhibits two peaks at 30° and 150° PA with a minimum at 90°, it can be used together with the first sine harmonic to approximate butterfly PADs (an example is given in **Figure 1C**). The flat-top PAD shape (**Figure 1B**) corresponds to high values of A1 with low values of A3, and small negative values of A5. The cap distributions (**Figure 1D**) can be fitted by a combination of the first and fifth sine harmonics. The sin (5α) function has 3 peaks (at 30°, 90° and 150°) with two depletions in between of the

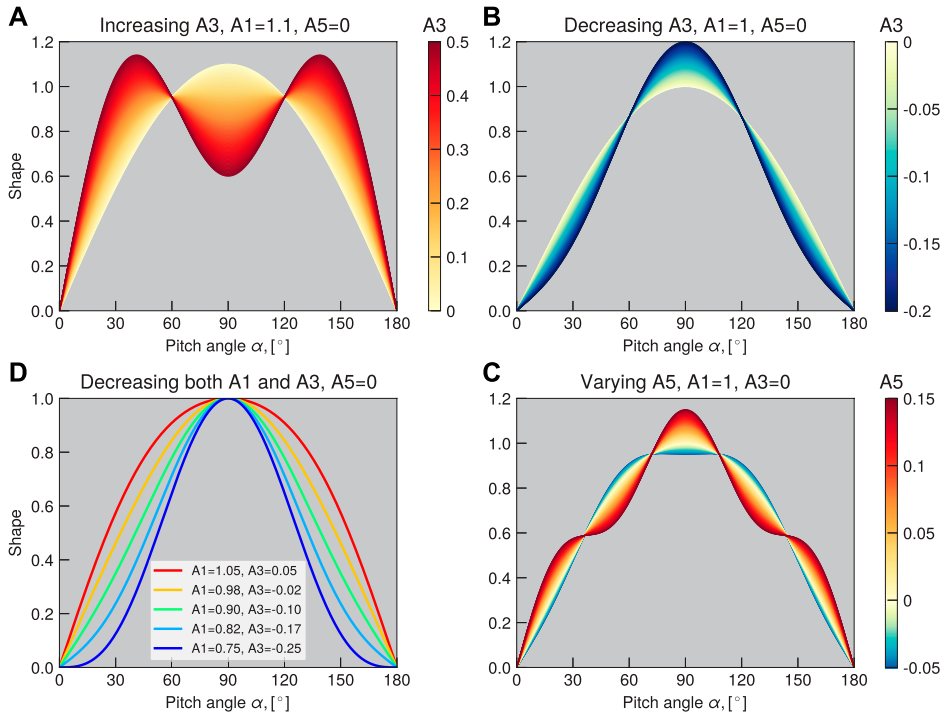

FIGURE 2 | Sketches of PAD shapes resulting from different combination of the A1, A3 and A5 coefficients. **(A)** Increasing the butterfly coefficient A3 under fixed A1 and A5 = 0 leads to stronger 90° minima; **(B)** negative values of A3 (also under fixed A1 and A5 = 0) lead to more anisotropic pancake distributions; **(C)** decreasing both A1 and A3 also creates steeper pancake PADs; **(D)** Negative A5 values result in flat-top PADs, while positive A5 values correspond to cap PAD shapes.

peaks. In combination with the general pancake shape given by $\sin(\alpha)$ it can well fit the head-and-shoulder structure.

In **Figure 2** we show different combinations of the pancake (A1), butterfly (A3) and cap (A5) coefficients, and the resulting PAD shapes. In panel (a), we fix A1 = 1.1 and A5 = 0 and start increasing the A3 magnitude from 0 to 0.5. It can be seen that for A3 = 0 a pancake shape is observed, while under higher A3 values butterfly PADs are created, and the 90° minimum becomes more pronounced. In **Figure 2B**, the A3 coefficient is decreased from 0 to -0.2. As a result, the pancake distribution becomes steeper (i.e., the anisotropy increases). In panel (c) we decrease both A1 and A3 coefficients, which also results in narrower PAD shapes. Such an increase in anisotropy of electron PADs is observed on the dayside during geomagnetic storms, and will be discussed later in **Sections 3** and **4**. In **Figure 2D** we vary the cap coefficient A5 under fixed A1 and A3. When A5 is zero, a perfect pancake distribution is observed. When A5 becomes negative, there is a transition of pancake PADs into the flat-top distributions. When A5 increases and becomes positive, cap distributions are produced. It should be noted that in case of the butterfly distributions, the A3 coefficient can increase to relatively large values (up to 0.7), while only small A5 values (0.05–0.15) are needed to resolve the head-and-shoulders PAD shape. As can be seen from **Figures 1**, **2**, the Fourier approximation fits well all main types (pancake, butterfly and cap) of equatorial pitch angle distributions. Other PAD shapes can also be resolved by this approximation, for instance, the field-aligned distributions (e.g., Clark et al., 2014, see also **Supplementary Figure S5**).

3 SUPERPOSED EPOCH ANALYSIS OF STORM-TIME PAD EVOLUTION

3.1 L and MLT Dependence

In this section, we analyze evolution of the PAD shapes in the outer radiation belt for day and night MLTs during geomagnetic storms in 2012–2019. To select the storm events for this analysis, we follow the methodology of Turner et al. (2019). As a proxy of the magnetic storm strength, we use the SYM-H index. We select events corresponding to the minimum SYM-H of less than -50 nT, while also requiring that there are no storms 2 days before nor after the event in question, to avoid the repeat events. Using this procedure, we find 129 storms throughout the Van Allen Probes era (the list of storms from October 2012 until October 2017 is given in Turner et al. (2019), their table A1, and the additional events in starting from October 2017 and until the end of the Van Allen Probes mission in late 2019 are listed in **Table 1**). **Figure 3A** shows the SYM-H index, solar wind (SW) dynamic pressure (Pdyn) and SW electric field (-v·Bz) superposed for the storms used in this study. Following Turner et al. (2019), we select the

TABLE 1 | Additional list of geomagnetic storms in October 2017—September 2019 used in this study (storms before October 2017 are listed in Turner et al. (2019) (their Table A1).

Number	Date (yyyy/mm/dd)	Time UT of min (SYM-H)
1	2017/10/14	05:35
2	2017/11/08	04:05
3	2017/11/21	06:50
4	2018/02/27	13:00
5	2018/03/10	04:35
6	2018/03/18	21:45
7	2018/04/20	09:30
8	2018/05/06	02:30
9	2018/06/01	07:15
10	2018/08/26	07:10
11	2018/09/11	10:10
12	2018/09/22	07:45
13	2018/10/07	21:50
14	2018/11/05	06:00
15	2019/05/11	03:10
16	2019/05/14	07:50
17	2019/08/05	11:45
18	2019/09/01	06:25
19	2019/09/05	05:20

values of indices, as well as PAD shape coefficients, starting from 84 h before the SYM-H minimum for each storm and up to 84 h after the minimum. The data are binned into 3-h epochs with the zero epoch corresponding to the time of SYM-H minimum. For the spatial binning, 0.2 L was selected as an appropriate step.

In **Figure 3**, the rows (b-e) show the superposed evolution of the PAD shape coefficients A1, A3 and A5 for 58 keV, as well as a higher energy of 735 keV for day (09–15 h) and night (21–03 h) MLTs. In each subplot, the *x*-axis represents the time epochs with respect to min (SYM-H), and the *y*-axis gives the McIlwain L parameter (Lm), calculated using the TS04D storm-time model. The color-coded values of the pancake (A1), butterfly (A3) and cap (A5) coefficients in these coordinates are shown in the left, middle and right columns, respectively. The corresponding standard deviations and number of points in each bin are shown in the Supporting information (**Supplementary Figure S3**). In **Figure 3** we concentrate on two energies, while the energy dependence will be later generalized in **Section 3.2**.

At lower energies on the dayside, shown in **Figure 3B**, the pancake coefficients A1 generally decrease from 0.9 to 0.7 with decreasing L-values. The same can be seen for the A3 coefficients that turn from around zero at L = 6 to negative values of approximately -0.2 at L = 3. When both A1 and A3 coefficients decrease, the pancake distributions become narrower (see **Figure 2C**). At the same time, the cap coefficient shows positive values at L = 3.5- ~ 5.6 and has a maximum at L ~ 4. This indicates that at a broad range of L-values, the cap distributions will be present (see also **Figure 5**), and that they are most pronounced around $L \sim 4$. In **Figure 3**, the row (c) shows the storm-time evolution of the coefficients for night MLTs at the same energy of 58 keV.

Figure 3D shows the evolution of the PAD coefficients for the 735 keV MagEIS energy channel. For this energy, a very strong evolution during the geomagnetic storms can be observed. Based on the row (d), two regions separated by L ~5.2 can be qualitatively defined during pre-storm times. At L < 5.2 the A1 values are around 1.1 which indicates broad pancake shapes. At L > ~5–5.2, the A3 coefficient becomes close to zero and turns negative at higher L values. At the same time, the pancake coefficient A1 decreases, which corresponds to steeper pancake PADs (the cap coefficient at high L-shells remains close to zero). When approaching the storm's main phase, both A1 and A3 decrease which can be observed down to L ~4.5. This indicates that during the main phase of the storm, the pancake distributions at higher L-shells become steeper, which is also demonstrated in **Figure 4D**. The coefficients return to their pre-storm configuration in the slow recovery phase.

In contrast, on the nightside, the butterfly coefficients A3 increase at high L-shells when approaching the storm's main phase. In **Figure 3E**, one can also distinguish two distinct regions separated by L = 5. At L < 5, the A3 coefficient is small with values around zero, while at L higher than 5, the A3 values are much larger, both for quiet and disturbed times. The A3 values during the pre-storm phase reveal the contribution of quiet-time drift shell splitting, whereas those around the maximum of the dynamic pressure indicate a combination of the drift shell splitting and magnetopause shadowing. It can be seen that at L > 5, the values of the pancake coefficient decrease, whereas the butterfly coefficient exhibits a significant increase around the main phase (see also **Supplementary Figure S4**). This means that the resulting PADs will have a stronger minimum around 90° PA. After the drop in dynamic pressure, the A3 values return to their original value range. It is worth mentioning that this recovery is faster than on the dayside. Indeed, already at 12–18 h after the min (SYM-H) the A3 and A1 coefficients are restored to their quiet time range for nightside MLTs, whereas on the dayside it takes 36–48 h to return to the pre-storm configuration. In **Figure 5** one can see that for higher energies, the butterfly coefficient becomes even more pronounced. Interestingly, at L between 3.5 and 5, one observes the steepening of the pancake distributions at nightside MLT during the storm-times, which will be discussed in detail below. It is also worth noting that the standard deviations of the *A* coefficients increase around the main phase of the storm (**Supplementary Figure S3**). This indicates that although our analysis well depicts the average storm-time behavior of electron PADs, geomagnetic storms correspond to a variety of complex processes (e.g., Reeves et al., 2003) that may not be captured without distinguishing other factors, such as the storm driver, the storm strength, etc.

Figure 4 shows the normalized PAD shapes for the four phases of the geomagnetic storms. In the top row, we show the SYM-H index, solar wind dynamic pressure and y-component of the solar wind electric field superposed for 129 storms analyzed in this study. To demonstrate the PAD shapes corresponding to different phases of the storms, we select 4 epochs, the first one at around 54 h before the SYM-H minimum (indicating the pre-storm conditions), the second one coinciding with the maximum of the SW dynamic pressure (3 h before min (SYM-H), indicative of the main phase conditions), the third one at 12 h past the SYM-H

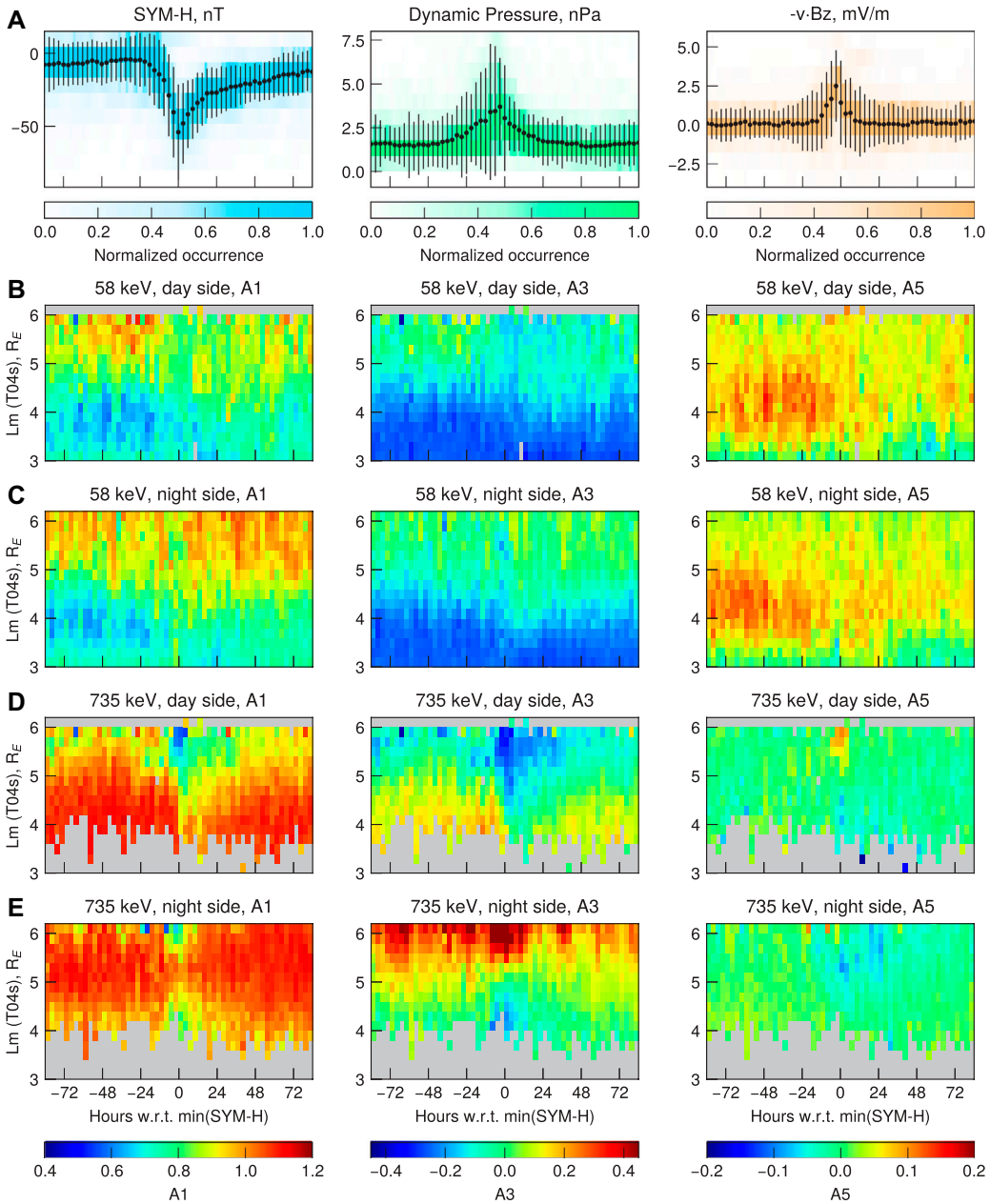

FIGURE 3 | (A) SYM-H index, SW dynamic pressure and electric field superposed for 129 storms in 2012–2019, **(B)** 3-h averaged dayside values of the A1 (pancake), A3 (butterfly) and A5 (cap) coefficients for 58 keV electrons, binned by the epochs (with respect to the SYM-H index minimum) and Lm. The coefficients in the same format for nightside evolution of 58 keV coefficients is shown in row **(C)**. The storm-time evolution of the 735 keV electron PADs for day- and nightside is given in rows **(D)** and **(E)**, respectively.

minimum (referred to as "fast recovery"), and the fourth epoch at 69 h after min (SYM-H) (i.e., in the "slow recovery"). These four epochs are marked on the superposed SYM-H, Pdyn and SW electric field plots. In **Figure 4**, the row (B) shows normalized PAD shapes for the 58 keV MagEIS channel on the dayside. The pitch angle distributions at low L-values (L < 3.5) exhibit pancake shapes, while at L ~ 3.5, the PADs transition into cap shapes (the morphology of cap PADs with respect to energy, L and MLT is described in detail in the following subsection). In the row (C) the PAD shapes are evaluated for 58 keV electrons at nightside MLTs. Generally, they look similar to the dayside shapes, except during the main phase (slice 2) where the nightside PADs exhibit pancake shapes for $L > 5.2$ while on the dayside distinct cap distributions can be observed. These results are in line with previous observations reported by Lyons and Williams (1975a). They showed that at energies of tens to hundreds of

keV there is a loss of head-and-shoulder structure during the main phase of the storm. The cap distributions generally arise due to interactions with the plasmaspheric hiss waves (e.g., Lyons et al., 1972). Due to erosion of the plasmasphere around the main phase, cap distributions transition into the pancake PADs. During the recovery phase, the plasmapause extends to higher L-values, and interactions with plasmaspheric hiss cause the quiet-time cap distributions to re-form.

In **Figure 4** (row D), we show the PAD shapes of the 735 keV electrons on the dayside (09 < MLT < 15). It can be seen that for L > 3.5, the distributions during pre-storm conditions exhibit pancake shapes. During the main phase, as noted above and shown in **Figure 4D**, the pancake distributions become narrower and then gradually recover to their original broader shapes. The magnetosphere is compressed around the main phase of the storm, which is reflected in the peak of the SW dynamic pressure (**Figure 4A**). This compression is more pronounced at dayside MLTs and gives rise to a westward electric current which will move ions and electrons inwards and adiabatically increase their kinetic energy (Walt, 2005). In this case, the third adiabatic invariant breaks down, whereas the first two invariants are conserved. Equatorially mirroring particles experience the highest adiabatic energy change. When comparing 90° particles with other pitch angles after inward transport, the 90° particles originated from the lowest energies where the phase space density was highest, explaining why the PAD is more peaked at 90° than

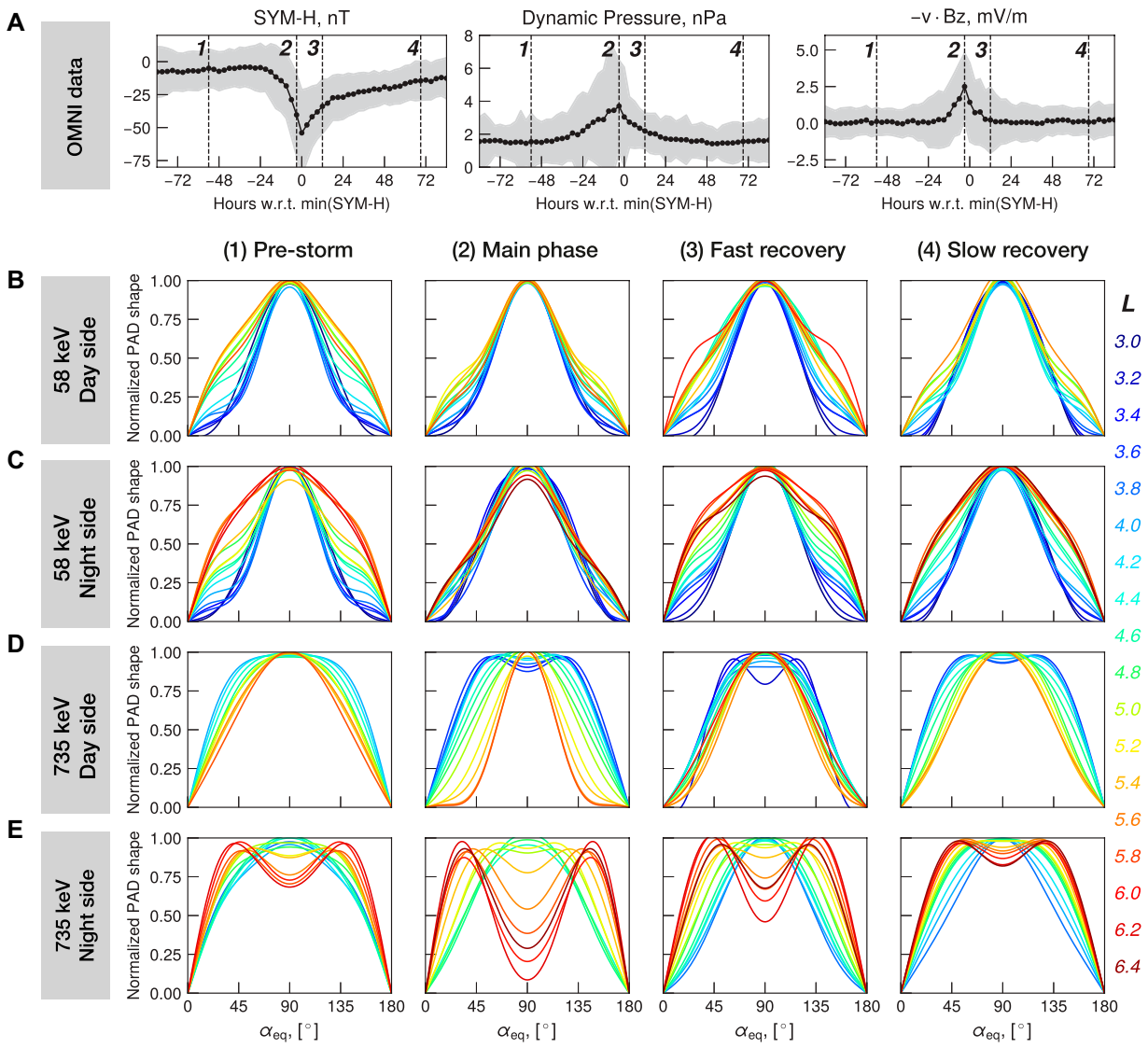

FIGURE 4 | (A) Superposed SYM-H index, SW dynamic pressure and electric field. The dashed lines denote epochs at which the PAD shapes are shown below. **(B)** Normalized PAD shapes of 58 keV electrons for 4 phases of the storm at dayside MLT. The lines are colored by the Lm values shown in a legend below. **(C)** Same as (b) but for the nighttime MLT. **(D)** Normalized PAD shapes for 735 keV electrons at dayside, and **(E)** at nightside.

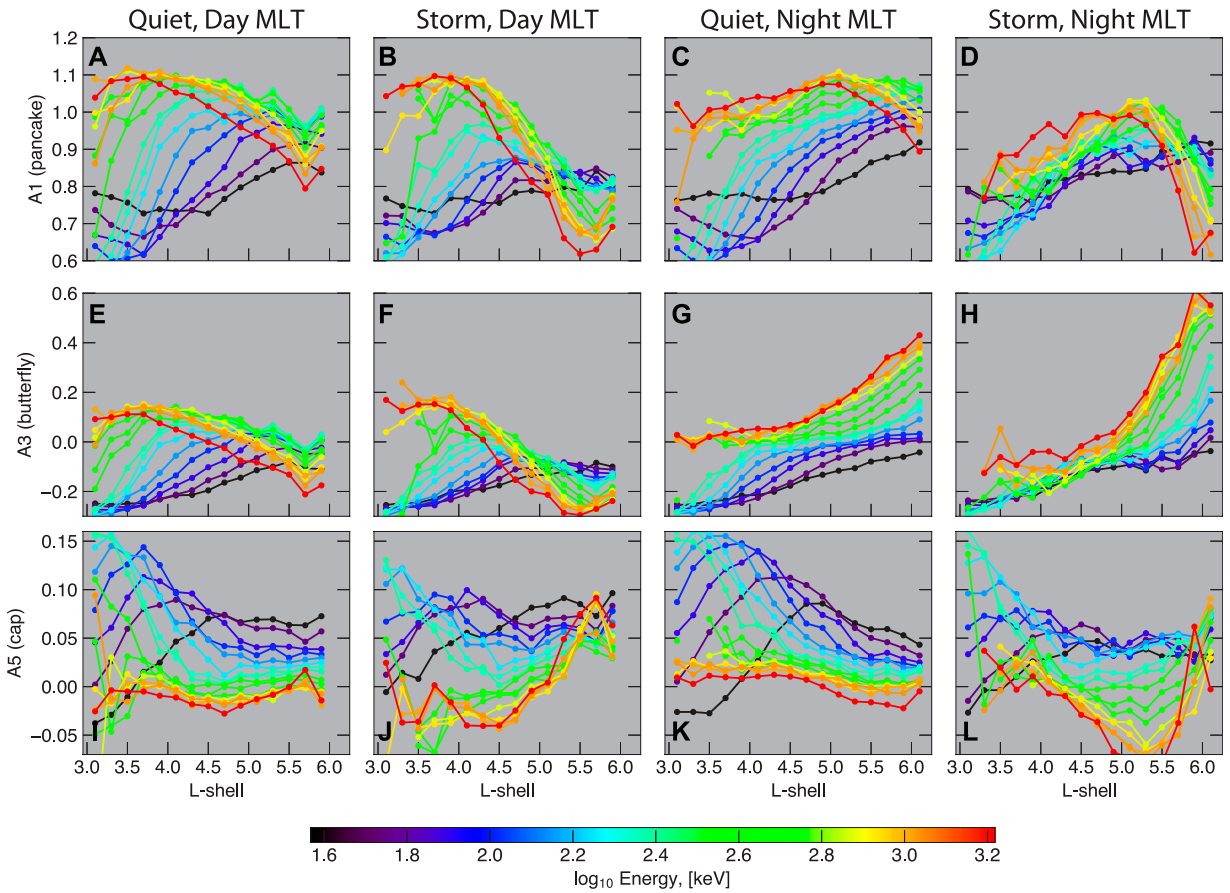

FIGURE 5 | Energy dependence of the PAD shape coefficients for pre-storm and main phase conditions at day and night MLT sectors.

before. As the system goes into the recovery, the pitch angle scattering and radial diffusion smooth out these highly anisotropic pancake distributions into their broader pre-storm shapes (Walt, 2005), which can be seen in slices 3 and 4 in **Figure 4D**. One interesting feature following the main phase is the appearance of the butterfly distributions in the inner zone. This has been previously attributed to the magnetosonic waves (e.g., Ni et al., 2016) and hiss waves (Albert et al., 2016).

The normalized PAD shapes of the 735 keV electrons at nightside MLTs for the 4 storm phases are demonstrated in **Figure 4** (row E). Our statistics cover L from 3 to around 6.4 for nightside MLTs, and for the pre-storm conditions butterfly distributions are observed at L = 5.6–6.4. At L = 5–5.6, we observe the flat-top distribution shapes (as a transition region between butterfly and pancake PADs), and pancake distributions for L < 5. The pre-storm butterflies observed on the nightside at high L-shells are indicative of the quiet-time drift shell splitting effects. Roederer (1967) showed that due to the asymmetry of the geomagnetic field particles starting at the same point but with different pitch angles will end up at different radial distances at the opposite side of the magnetosphere. If electrons start from the same point on the nightside, the near equatorially-mirroring particles would drift further from the Earth on the dayside than particles of lower pitch angles. The PA-dependence of the drift paths leads to the formation of the butterfly distributions. While the drift-shell splitting is not energy dependent, it has been well established that a negative radial gradient in phase space density (PSD) is a necessary component to create the butterfly PADs (Roederer, 1967). At lower energies, the flux gradient is smaller than at high energies (see e.g. **Figure 3** in Turner et al., 2019), and therefore the drift shell splitting has less influence on the PADs. This is consistent with the absence of butterflies at low (58 keV) energies (**Figures 4B,C**). In **Figure 3E**, **Figure 4E** we demonstrate that during the main storm phase, the 90°-minimum in the butterfly distributions becomes stronger at high L on the nightside. In **Figure 3E** this manifests as an increase in the A3 coefficients around the maximum of the dynamic pressure. In **Figure 4E**, slice 2 shows that the butterfly PADs also extend to lower L-values. With increasing dynamic pressure, drift shell splitting intensifies and thus the butterfly distributions can be observed at lower L-shells. At around L = 4.8–5.0, PADs transition into the flat-top/broad pancake and then to steeper pancake distributions at L < 4.5. In **Figure 4E**, PADs at L < 3.6 during the pre-storm phase corresponded to background levels of

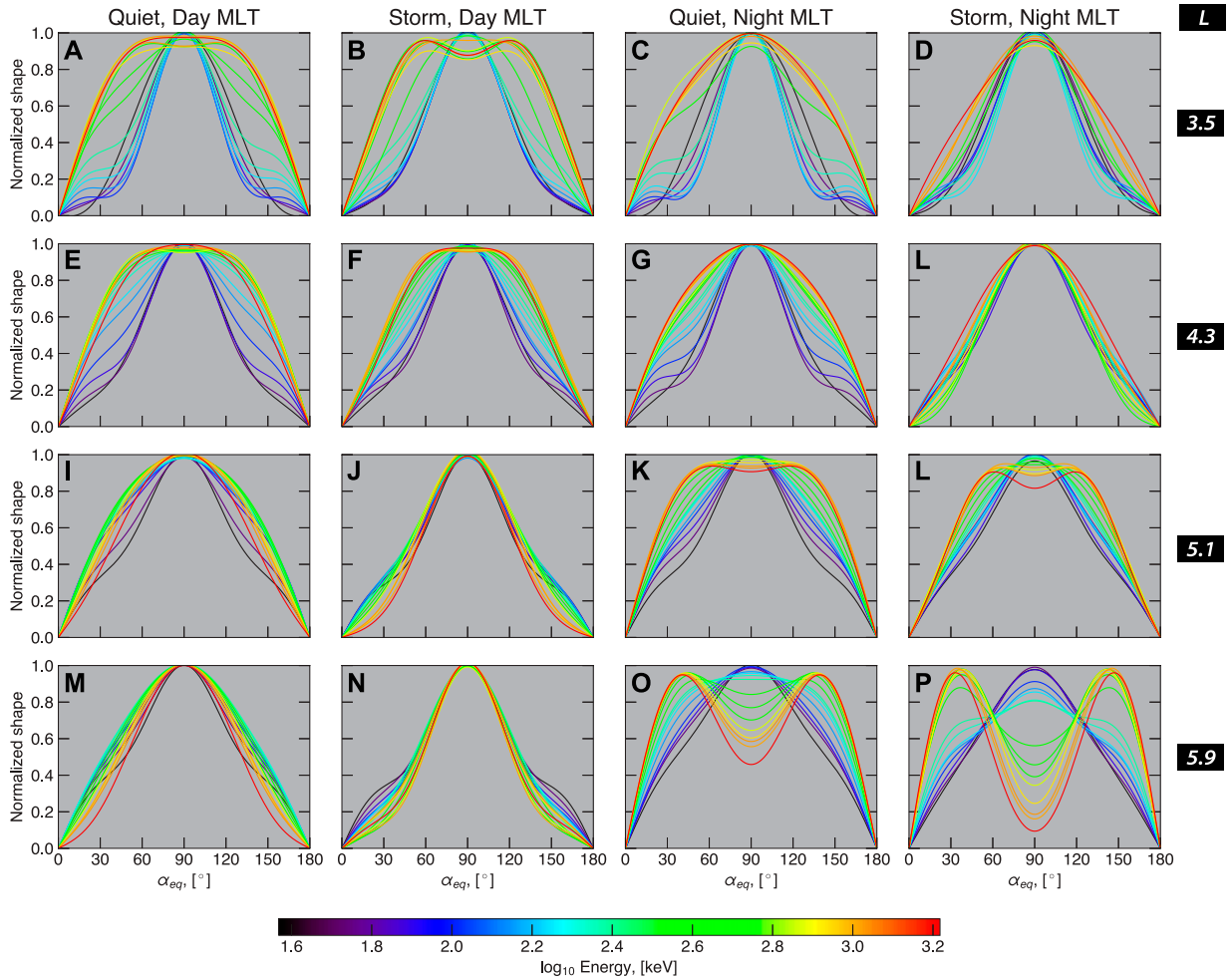

FIGURE 6 | Energy dependence of pitch angle shapes at different L-values for quiet and storm conditions on the day and nightside MLT.

electron flux and were removed, whereas after the main phase the flux values are increased in the slot region (e.g., Reeves et al., 2016), and the pitch angle distributions exhibit pancake shapes.

3.2 Energy Dependence

Figure 5 demonstrates the energy dependence of the PAD shape coefficients for L = 3—6 at day and night MLTs. The resulting PAD shapes plotted as a function of energy under several fixed values of L are shown in **Figure 6**. The values shown here are superposed for 129 storms for the pre-storm and main phase conditions. We first analyze the day-time morphology. It can be seen from **Figure 5** (A and B) that at energies of $< \sim 100$ keV, the pancake coefficient A1 appears similar for storm and quiet conditions. The same can be observed for the butterfly coefficient A3 in panels (E and F). At higher energies at $L < 5$, both A1 and A3 coefficients generally decrease with decreasing energy during quiet times. At the same time, in **Figure 5I**, the cap coefficient is intensified at energies of hundreds of keV and below. It is worth noting that the peak of the cap coefficient across the L-shells is strongly energy-dependent, and moves inward with increasing energy (**Figure 5I**). At higher energies the cap coefficient values are generally around zero (at $L > 3.2$), which is consistent with the theoretical results by Lyons et al. (1972) and is attributed to the fact that with increasing energy, the dominant first-order cyclotron resonance extends to higher PAs (see **Figure 4** in Lyons et al. (1972)) and pitch angle scattering can then affect all equatorial pitch angles.

During the main phase at dayside MLTs, the A1 and A3 coefficients decrease (**Figure 5**, panels B and F), which is especially evident for $L > 4.5$. At energies below 300 keV, the values of the cap coefficient remain at around 0.05 which means that the cap distributions persist at lower energies during the main phase. The cap coefficient decreases at $L < 4.5$ for energies above 300 keV and turns negative, which results in the flattop distributions (**Figure 6F**). At $L > 4.5$, the A1 and A3 coefficients decrease, while the A5 coefficient increases. This increase in the A5 coefficient corresponds to strongly anisotropic pancake PADs

(see also **Figure 4D**, slice 2) during the main phase on the dayside. Furthermore, the degree of this anisotropy increases with energy (see also **Figures 6I,J**).

During the pre-storm phase the butterfly distributions dominate at L > 5.5 on the nightside (also discussed in **Section 3.1**). In **Figure 5D** one can see that at L > 5 the pancake coefficient equals approximately 0.9–1.1, while during the main phase the values drop down to 0.6–0.8 across the MagEIS energy range. At the same time, there is a dramatic increase in the butterfly coefficient A3 at large L-shell on the nightside. For instance, at energies of ~ 300 keV the pre-storm A3 values were around 0.2, while during the main phase they are magnified by a factor of 2. Furthermore, from **Figure 6**(P) it is obvious that the 90° minimum gets stronger with increasing energy. At L of ~5, the A5 coefficient becomes negative, and as shown in **Figure 2** this corresponds to the flat-top PAD shape. At $L < 5.1$, the butterfly coefficients A3 significantly decrease at all energies (**Figure 5H**) and remains small at lower L-shells, where PADs have pancake shapes.

4 DISCUSSION

In this study we employed a Fourier sine series expansion to approximate electron pitch angle distributions. It was shown that a combination of the first, third and fifth sine harmonics can effectively fit all main types of PADs in the outer radiation belt. This approximation has previously been used for analyzing distributions of electrons in planetary magnetospheres, for instance, by Clark et al. (2014). In case of the terrestrial radiation belts, most studies fitted electron PADs to the $\sin^n(\alpha)$ function, where n shows the steepness of the distribution (larger values of n correspond to more anisotropic distributions). This approximation is very easy to use, and the resulting values can be incorporated into the radiation belts simulations (e.g., Shi et al., 2016). However, the $\sin^n(\alpha)$ function can only approximate flat-top, pancake and isotropic distributions but is not capable of fitting butterfly and cap shapes. Butterfly distributions can account for up to 80% of PADs on the nightside, and cap distributions dominate lower energies both for day and night-side MLTs during geomagnetically quiet times. Allison et al. (2018) combined two $\sin^n(\alpha)$ terms with different n values which helped two resolve the cap but not butterfly distributions. Due to the fact that different types of PADs can be linked to specific processes acting within the radiation belts, it is crucial to use an approximation that can fit all of the PAD types. We have shown (**Figures 1**, **2**) that the Fourier series are capable of resolving all main PAD shapes. Furthermore, the expression used here (**Eq. 1**) is easy to integrate over the solid angle and can be used to compute omnidirectional flux values using an analytic expression. We note that the methodology developed in this study can be extended to a range of magnetospheric problems, for instance, to analyzing pitch angle distributions of low-energy electrons and ions.

It is well-known that electrons in the inner radiation belt are stable both in terms of their amplitudes (e.g., Shprits et al., 2013), and pitch angle distributions (e.g., Zhao et al., 2018). Furthermore, electrons at energies over 1 MeV are generally absent in the inner zone (Fennell et al., 2015). Therefore, for analyzing the PAD dynamics during geomagnetic storms we concentrated on the outer radiation belt region. While several studies have already used RBSP data for analyzing the storm-time PAD evolution (e.g., Ni et al., 2015; Ni et al., 2016; Drozdov et al., 2019; Ni et al., 2020; Pandya et al., 2020; Greeley et al., 2021), they focused on relativistic and ultra-relativistic energies sampled by the REPT detector. In the current paper we concentrated on lower energies, from 30 keV to around 1.6 MeV, using observations by the MagEIS detector during the entire lifespan of the Van Allen Probes mission in 2012–2019. Our study has a certain overlap in energies (> 1 MeV) with the previous works by Pandya et al. (2020) and Greeley et al. (2021) and therefore our results can also be compared to those studies. Due to the fact that RBSP orbit was revolving in MLT quite slowly, with a full revolution being completed every 22 months, the statistics for analyzing both MLT and storm driver dependence would be limited, and therefore in the present study we concentrated on the day- and night-time PAD morphology. Furthermore, Pandya et al. (2020) showed that at least for relativistic energies, the dependence of PAD evolution on storm driver was negligible.

It has been shown that the morphology of electron PADs is significantly different during geomagnetically quiet times compared to the active times (Lyons and Williams, 1975b). During periods of low geomagnetic activity, pitch angle distributions at energies below ~300 keV exhibit cap (or, head-and-shoulder) shapes. This configuration results from cyclotron and Landau resonance with hiss waves, and is strongly energy-dependent (Lyons et al., 1972; Lyons and Williams, 1975a). In particular, in **Figures 4**, **5** we demonstrate that the cap coefficient A5 exhibits a peak at L ~ 5 for 37 keV electrons, and then moves inward in L with increasing energy, which is in line previous results of (e.g., Shi et al., 2016) who reported that peak of PAD anisotropy, corresponding to cap PADs, was moving to smaller L-values under increasing energy. The same conclusion was reported by Allison et al. (2018). For each energy, Allison et al. (2018) highlighted regions where the combination of two $\sin^n(\alpha)$ terms was performing better than a single sine term. Those regions corresponded to the cap distributions. It was found that the extent of this region diminished with increasing energy, but was practically independent of Kp levels. In the current study we observed loss of the head-and-shoulders structure during the main phase of the storm at nightside MLTs, which is consistent with previous studies by Lyons and Williams (1975b) and Zhao et al. (2018). Due to the fact with increasing geomagnetic activity the plasmasphere is eroded (e.g., Goldstein et al., 2019), there would be no hiss waves at higher L-shells that could generate cap PADs (see e.g., Lyons and Williams, 1975b). Furthermore, during active times the low-energy particles are injected from the tail (e.g., Reeves et al., 1996). Turner et al. (2015a) demonstrated that injections of electrons with energies below 240 keV can be frequently observed within the geostationary orbit. Furthermore, Motoba et al. (2020) performed a superposed epoch analysis of dispersionless injections using RBSP data and showed that the corresponding pitch angle distributions of tens-of-keV electrons

exhibited pancake shapes. Therefore, the transformation of cap PADs into pancakes during the main phase at low energies on the nightside (**Figures 3C**, **Figure 4C**) is likely due to the combination of the plasmasphere erosion and particle injections from the tail.

At energies $>\sim 150$ keV, pancake distributions are observed on the dayside at $L > 4$ (**Figure 6**). The pancake distributions generally result from the particle pitch angle diffusion (e.g., West et al., 1973). During geomagnetically quiet times, pancake distributions exhibit relatively broad shapes. During active times, we observe narrowing of the pancake PADs. During the main phase, PADs at high L-shells ($L > 5.8$) become strongly anisotropic, but distributions at lower L-shells still have broad shapes. The opposite is observed during the fast recovery phase (approximately 12 h after the SYM-H minimum) - the narrowing moved inwards in L-shell, while at higher L-values the distributions already started to recover to their pre-storm shapes. In the slow recovery phase, the distributions returned to their pre-storm morphology. These results go well with previous findings of Pandya et al. (2020) and Greeley et al. (2021) who also reported narrowing of the pancake PADs during the main phase of the storm. These signatures (narrowing of pancake PADs which progressively moving inward and the subsequent relaxation to pre-storm shapes) are indicative of the inward radial diffusion (Schulz and Lanzerotti, 1974).

On the nightside, the PAD morphology is very different than on the dayside. At energies >200 keV the quiet-time distributions are mainly of pancake type at $L < 5$. For L-shells around 5 and energies of around 200 keV, the pancake distributions transform into flat-top PADs. Then, at higher energies there is an emerging minimum at 90° PA which intensifies with increasing energy (see **Figure 6**). Energy dependence of the butterfly distributions can be explained as follows. During quiet conditions at $L > 5$ the equatorially mirroring particles in the nightside are transported to larger radial distances in the dayside than the lower PA particles, which is known as magnetic drift shell splitting (e.g., Roederer, 1967; Sibeck et al., 1987). This effect, however, depends only on magnetic field and not on particle energy. At the same time, it has been well established that a negative radial gradient in PSD is a necessary component for the drift shell splitting to be effective (Roederer, 1967). Recently, Turner et al. (2019) presented a superposed epoch analysis of omnidirectional electron flux observed by the Van Allen Probes mission. In their **Figure 2** one can see that flux gradient in L at lower energies is relatively flat. On the other hand, at higher energies there is a strong negative flux gradient which enables the drift shell splitting to have the full effect on pitch angle distributions and create butterfly PADs. Therefore, with increasing energy the drift shell splitting effects become more evident due to stronger radial gradients in flux.

During the main phase of the storm, the butterfly distributions on the nightside are intensified (**Figures 4–6**). Such an intensification is most likely due to a combination of the enhanced drift shell splitting and magnetopause shadowing. While the magnetopause is usually located at radial distances of $>10R_E$, it is well-known that during active times the last closed drift shell can move inward down to L ~ 4. Equatorially mirroring electrons travel to larger distances than low-PA electrons and therefore can get lost to the magnetopause, creating the butterfly distributions. The storm-time butterfly distributions are not observed below L = 5 (see **Figures 3–5**). At L around 5, one can observe a transition of the butterfly into flat-top PADs. Horne et al. (2003) proposed two potential explanations for such a transition at higher energies, namely the inward radial diffusion and wave particle interactions. They concluded that the radial diffusion could be an important factor but did not account for energy dependence of flat-top PADs. By considering the cyclotron resonance with whistler mode chorus waves in presence of low plasma densities, Horne et al. (2003) were able to reproduce a realistic energy dependence of the flat-top PADs.

In this study, we analyzed the normalized electron pitch angle distributions measured by the MagEIS detector onboard the Van Allen Probes mission. The storm-time spin-averaged electron flux intensities were previously investigated by Turner et al. (2019), and it was reported that electrons of different energies exhibited a significantly different response to geomagnetic storms (see also Turner et al., 2015b). In our study, the storm-time morphology of the PAD shapes was also found to vary greatly with energy. It is worth noting that the results presented here can be combined with averaged picture of the spin-averaged electron flux evolution from Turner et al. (2019), as both the flux intensities and pitch angle distribution shapes are important for distinguishing between the loss and acceleration processes (e.g., Chen et al., 2005). Furthermore, due to complex mechanisms acting in the outer belt during the storm times, different particle populations can evolve into one another. For instance, electrons with energies up to tens of keV (the so-called seed population) can be injected during the substorm activity and produce waves that can energize the tens to hundreds of keV electrons to higher energies. In order to investigate these processes in detail, it is beneficial to analyze phase space densities under different values of μ and K, which gives an opportunity to see the time lags between the different populations (see, for instance, Boyd et al., 2016). We note, however, that in the current study we did not make any assumptions on the processes acting within the outer belt, and therefore the PAD shapes averaged for different storm epochs and energies obtained in this study already include part of the information on the mechanisms mentioned above and provide a good indication of the averaged storm-time behavior of the 30 keV–1.6 MeV electrons.

5 CONCLUSIONS

Using the full MagEIS data set of pitch angle resolved electron flux at energies 30 keV - ~1.6 MeV in 2012–2019, we analyze equatorial electron PADs at L = 3–6. We use a combination of the first, third and fifth sine harmonics to approximate the pitch angle distributions. The corresponding expression can be

analytically integrated, and the values of coefficients before the three terms relate to the main PAD shapes. We perform a superposed epoch analysis of 129 strong geomagnetic storms during the Van Allen Probes era for day and night MLTs. Our findings are as follows.

1. Cap distributions are mainly present at energies < 300 keV, and their spatial extent in L shrinks with increasing energy. During the main phase on the nightside, cap PADs transform into pancakes at L > 4.5, likely due erosion of the plasmasphere and particle injections from the tail. During the recovery phase, the cap distributions are re-formed at high L-shells.
2. At higher energies on the dayside, the distributions are mainly pancake. They exhibit broad shapes during quiet conditions and become more anisotropic during the main phase of the storm due to the field's compression. The degree of this anisotropy smoothly increases with energy.
3. The butterfly distributions can be observed on the nightside at L > 5.6 during the pre-storm phase. During the main phase, the butterfly PADs can be found at lower L-values (down to L = 5), likely due to the combination of drift shell splitting and magnetopause shadowing. Furthermore, the 90° minimum intensifies with increasing energy. This is consistent with stronger negative radial flux gradients at higher energies, which allow the drift shell splitting to create stronger butterfly PADs.
4. On the nightside, there is a transition region between the butterfly and pancake PADs, populated by the flat-top distributions. During quiet conditions, this transition is located at $L \sim 5.5$ and moves inward to $L \sim 5$ during the main phase of the storm.

The PAD shape coefficients for different L-shells, MLTs and phases of geomagnetic storms obtained in this study can be used for comparisons with the results achieved through the existing wave models when the flux magnitude is taken into consideration, as well as the outputs of the physics-based radiation belt simulations, in terms of PAD shapes. Furthermore, the dependencies reported here can further be used to improve the existing empirical models of the pitch angle distributions in Earth's outer radiation belt.

DATA AVAILABILITY STATEMENT

The original contributions presented in the study are included in the article/**Supplementary Material**, further inquiries can be directed to the corresponding author.

AUTHOR CONTRIBUTIONS

AS and YS conceived the idea of the study. AS performed the analysis with input from YS, HA, NA, AD and PK. AS wrote the manuscript; YS, HA, NA, AD, PK, GR, DW and AAS contributed to structuring and editing the manuscript.

FUNDING

This project has received funding from the European Union's Horizon 2020 research and innovation programme under grant agreement No. 870452 (PAGER). HA was supported by the Alexander von Humboldt foundation.

ACKNOWLEDGMENTS

AS acknowledges support from the International Space Science Institute (ISSI—Bern, Switzerland) through the ISSI team on "Imaging the Invisible: Unveiling the Global Structure of Earth's Dynamic Magnetosphere".

SUPPLEMENTARY MATERIAL

The Supplementary Material for this article can be found online at: https://www.frontiersin.org/articles/10.3389/fspas.2022.836811/full#supplementary-material

REFERENCES

Albert, J. M., Starks, M. J., Horne, R. B., Meredith, N. P., and Glauert, S. A. (2016). Quasi-Linear Simulations of Inner Radiation belt Electron Pitch Angle and Energy Distributions. *Geophys. Res. Lett.* 43, 2381–2388. doi:10.1002/2016gl067938

Allison, H. J., Horne, R. B., Glauert, S. A., and Del Zanna, G. (2018). Determination of the Equatorial Electron Differential Flux from Observations at Low Earth Orbit. *J. Geophys. Res. Space Phys.* 123, 9574–9596. doi:10.1029/2018ja025786

Artemyev, A. V., Agapitov, O. V., Mozer, F. S., and Spence, H. (2015). Butterfly Pitch Angle Distribution of Relativistic Electrons in the Outer Radiation Belt: Evidence of Nonadiabatic Scattering. *J. Geophys. Res. Space Phys.* 120, 4279–4297. doi:10.1002/2014ja020865

Blake, J. B., Carranza, P. A., Claudepierre, S. G., Clemmons, J. H., Crain, W. R., Dotan, Y., et al. (2013). "The Magnetic Electron Ion Spectrometer (MagEIS) Instruments Aboard the Radiation Belt Storm Probes (RBSP) Spacecraft," in *The Van Allen Probes Mission*. Editors N. Fox and J. L. Burch (Boston, MA: Springer), 383–421. doi:10.1007/978-1-4899-7433-4_12

Boyd, A. J., Spence, H. E., Huang, C. L., Reeves, G. D., Baker, D. N., Turner, D. L., et al. (2016). Statistical Properties of the Radiation Belt Seed Population. *J. Geophys. Res. Space Phys.* 121, 7636–7646. doi:10.1002/2016ja022652

Carbary, J., Mitchell, D., Paranicas, C., Roelof, E., Krimigis, S., Krupp, N., et al. (2011). Pitch Angle Distributions of Energetic Electrons at Saturn. *J. Geophys. Res. Space Phys.* 116. doi:10.1029/2010ja015987

Chen, Y., Friedel, R. H. W., Henderson, M. G., Claudepierre, S. G., Morley, S. K., and Spence, H. E. (2014). REPAD: An Empirical Model of Pitch Angle Distributions for Energetic Electrons in the Earth's Outer Radiation belt. *J. Geophys. Res. Space Phys.* 119, 1693–1708. doi:10.1002/2013ja019431

Chen, Y., Friedel, R., Reeves, G., Onsager, T., and Thomsen, M. (2005). Multisatellite Determination of the Relativistic Electron Phase Space Density at Geosynchronous Orbit: Methodology and Results during Geomagnetically Quiet Times. *J. Geophys. Res. Space Phys.* 110. doi:10.1029/2004ja010895

Clark, G., Paranicas, C., Santos-Costa, D., Livi, S., Krupp, N., Mitchell, D. G., et al. (2014). Evolution of Electron Pitch Angle Distributions across Saturn's Middle Magnetospheric Region from MIMI/LEMMS. *Planet. Space Sci.* 104, 18–28. doi:10.1016/j.pss.2014.07.004

Drozdov, A. Y., Aseev, N., Effenberger, F., Turner, D. L., Saikin, A., and Shprits, Y. Y. (2019). Storm Time Depletions of Multi-MeV Radiation Belt Electrons Observed at Different Pitch Angles. *J. Geophys. Res. Space Phys.* 124, 8943–8953. doi:10.1029/2019ja027332

Fennell, J. F., Claudepierre, S. G., Blake, J. B., O'Brien, T. P., Clemmons, J. H., Baker, D. N., et al. (2015). Van Allen Probes Show that the Inner Radiation Zone Contains No MeV Electrons: ECT/MagEIS Data. *Geophys. Res. Lett.* 42, 1283–1289. doi:10.1002/2014gl062874

Gannon, J., Li, X., and Heynderickx, D. (2007). Pitch Angle Distribution Analysis of Radiation belt Electrons Based on Combined Release and Radiation Effects Satellite Medium Electrons A Data. *J. Geophys. Res. Space Phys.* 112. doi:10.1029/2005ja011565

Ganushkina, N. Y., Dandouras, I., Shprits, Y., and Cao, J. (2011). Locations of Boundaries of Outer and Inner Radiation Belts as Observed by Cluster and Double Star. *J. Geophys. Res. Space Phys.* 116. doi:10.1029/2010ja016376

Goldstein, J., Pascuale, S., and Kurth, W. S. (2019). Epoch-Based Model for Stormtime Plasmapause Location. *J. Geophys. Res. Space Phys.* 124, 4462–4491. doi:10.1029/2018ja025996

Greeley, A. D., Kanekal, S. G., Sibeck, D. G., Schiller, Q., and Baker, D. N. (2021). Evolution of Pitch Angle Distributions of Relativistic Electrons during Geomagnetic Storms: Van Allen Probes Observations. *J. Geophys. Res. Space Phys.* 126, e2020JA028335. doi:10.1029/2020ja028335

Hao, Y. X., Zong, Q.-G., Zhou, X.-Z., Rankin, R., Chen, X. R., Liu, Y., et al. (2017). Relativistic Electron Dynamics Produced by Azimuthally Localized Poloidal Mode ULF Waves: Boomerang-Shaped Pitch Angle Evolutions. *Geophys. Res. Lett.* 44, 7618–7627. doi:10.1002/2017gl074006

Horne, R. B., Meredith, N. P., Thorne, R. M., Heynderickx, D., Iles, R. H., and Anderson, R. R. (2003). Evolution of Energetic Electron Pitch Angle Distributions during Storm Time Electron Acceleration to Megaelectronvolt Energies. *J. Geophys. Res. Space Phys.* 108, SMP–11. doi:10.1029/2001ja009165

Lyons, L. R., Thorne, R. M., and Kennel, C. F. (1972). Pitch-Angle Diffusion of Radiation belt Electrons within the Plasmasphere. *J. Geophys. Res.* 77, 3455–3474. doi:10.1029/ja077i019p03455

Lyons, L. R., and Williams, D. J. (1975b). The Quiet Time Structure of Energetic (35-560 keV) Radiation belt Electrons. *J. Geophys. Res.* 80, 943–950. doi:10.1029/JA080i007p00943

Lyons, L. R., and Williams, D. J. (1975a). The Storm and Poststorm Evolution of Energetic (35-560 keV) Radiation belt Electron Distributions. *J. Geophys. Res.* 80, 3985–3994. doi:10.1029/ja080i028p03985

Mauk, B. H., Fox, N. J., Kanekal, S. G., Kessel, R. L., Sibeck, D. G., and Ukhorskiy, A. (2012). "Science Objectives and Rationale for the Radiation Belt Storm Probes Mission," in *The Van Allen Probes Mission*. Editors N. Fox and J. L. Burch (Boston, MA: Springer), 3–27. doi:10.1007/978-1-4899-7433-4_2

Meredith, N. P., Horne, R. B., Johnstone, A. D., and Anderson, R. R. (2000). The Temporal Evolution of Electron Distributions and Associated Wave Activity Following Substorm Injections in the Inner Magnetosphere. *J. Geophys. Res.* 105, 12907–12917. doi:10.1029/2000ja900010

Motoba, T., Ohtani, S., Gkioulidou, M., Mitchell, D. G., Ukhorskiy, A., Takahashi, K., et al. (2020). Pitch Angle Dependence of Electron and Ion Flux Changes during Local Magnetic Dipolarization inside Geosynchronous Orbit. *J. Geophys. Res. Space Phys.* 125, e2019JA027543. doi:10.1029/2019ja027543

Ni, B., Yan, L., Fu, S., Gu, X., Cao, X., Xiang, Z., et al. (2020). Distinct Formation and Evolution Characteristics of Outer Radiation belt Electron Butterfly Pitch Angle Distributions Observed by Van Allen Probes. *Geophys. Res. Lett.* 47, e2019GL086487. doi:10.1029/2019gl086487

Ni, B., Zou, Z., Gu, X., Zhou, C., Thorne, R. M., Bortnik, J., et al. (2015). Variability of the Pitch Angle Distribution of Radiation belt Ultrarelativistic Electrons during and Following Intense Geomagnetic Storms: Van Allen Probes Observations. *J. Geophys. Res. Space Phys.* 120, 4863–4876. doi:10.1002/2015ja021065

Ni, B., Zou, Z., Li, X., Bortnik, J., Xie, L., and Gu, X. (2016). Occurrence Characteristics of Outer Zone Relativistic Electron Butterfly Distribution: A Survey of Van Allen Probes REPT Measurements. *Geophys. Res. Lett.* 43, 5644–5652. doi:10.1002/2016gl069350

Pandya, M., Bhaskara, V., Ebihara, Y., Kanekal, S. G., and Baker, D. N. (2020). Evolution of Pitch Angle-Distributed Megaelectron Volt Electrons during Each Phase of the Geomagnetic Storm. *J. Geophys. Res. Space Phys.* 125, e2019JA027086. doi:10.1029/2019ja027086

Reeves, G. D., Friedel, R. H. W., Larsen, B. A., Skoug, R. M., Funsten, H. O., Claudepierre, S. G., et al. (2016). Energy-dependent Dynamics of keV to MeV Electrons in the Inner Zone, Outer Zone, and Slot Regions. *J. Geophys. Res. Space Phys.* 121, 397–412. doi:10.1002/2015ja021569

Reeves, G., Henderson, M., McLachlan, P., Belian, R., Friedel, R., and Korth, A. (1996). Radial Propagation of Substorm Injections. *Int. Conf. substorms* 389, 579.

Reeves, G., McAdams, K., Friedel, R., and O'Brien, T. (2003). Acceleration and Loss of Relativistic Electrons during Geomagnetic Storms. *Geophys. Res. Lett.* 30. doi:10.1029/2002gl016513

Roederer, J. G. (1967). On the Adiabatic Motion of Energetic Particles in a Model Magnetosphere. *J. Geophys. Res.* 72, 981–992. doi:10.1029/jz072i003p00981

Schulz, M., and Lanzerotti, L. J. (1974). *Particle Diffusion in the Radiation Belts*. New York: Springer-Verlag. doi:10.1007/978-3-642-65675-0

Selesnick, R., and Blake, J. (2002). Relativistic Electron Drift Shell Splitting. *J. Geophys. Res. Space Phys.* 107, SMP–27. doi:10.1029/2001ja009179

Shi, R., Summers, D., Ni, B., Fennell, J. F., Blake, J. B., Spence, H. E., et al. (2016). Survey of Radiation Belt Energetic Electron Pitch Angle Distributions Based on the Van Allen Probes MagEIS Measurements. *J. Geophys. Res. Space Phys.* 121, 1078–1090. doi:10.1002/2015ja021724

Shprits, Y. Y., Subbotin, D., Drozdov, A., Usanova, M. E., Kellerman, A., Orlova, K., et al. (2013). Unusual Stable Trapping of the Ultrarelativistic Electrons in the Van Allen Radiation Belts. *Nat. Phys* 9, 699–703. doi:10.1038/nphys2760

Sibeck, D. G., McEntire, R. W., Lui, A. T. Y., Lopez, R. E., and Krimigis, S. M. (1987). Magnetic Field Drift Shell Splitting: Cause of Unusual Dayside Particle Pitch Angle Distributions during Storms and Substorms. *J. Geophys. Res.* 92, 13485–13497. doi:10.1029/ja092ia12p13485

Smirnov, A., Shprits, Y., Allison, H., Aseev, N., Drozdov, A., Kollmann, P., et al. (2022). An Empirical Model of the Equatorial Electron Pitch Angle Distributions in Earth's Outer Radiation belt. *Space Weather under Rev*.

Su, Z., Zheng, H., and Wang, S. (2009). Evolution of Electron Pitch Angle Distribution Due to Interactions with Whistler Mode Chorus Following Substorm Injections. *J. Geophys. Res. Space Phys.* 114. doi:10.1029/2009ja014269

Tsyganenko, N., and Sitnov, M. (2005). Modeling the Dynamics of the Inner Magnetosphere during strong Geomagnetic Storms. *J. Geophys. Res. Space Phys.* 110. doi:10.1029/2004ja010798

Turner, D. L., Claudepierre, S. G., Fennell, J. F., O'Brien, T. P., Blake, J. B., Lemon, C., et al. (2015a). Energetic Electron Injections Deep into the Inner Magnetosphere Associated with Substorm Activity. *Geophys. Res. Lett.* 42, 2079–2087. doi:10.1002/2015gl063225

Turner, D. L., Kilpua, E., Hietala, H., Claudepierre, S., O'Brien, T., Fennell, J., et al. (2019). The Response of Earth's Electron Radiation Belts to Geomagnetic Storms: Statistics from the Van Allen Probes Era Including Effects from Different Storm Drivers. *J. Geophys. Res. Space Phys.* 124, 1013–1034. doi:10.1029/2018ja026066

Turner, D. L., O'Brien, T. P., Fennell, J. F., Claudepierre, S. G., Blake, J. B., Kilpua, E. K. J., et al. (2015b). The Effects of Geomagnetic Storms on Electrons in Earth's Radiation Belts. *Geophys. Res. Lett.* 42, 9176–9184. doi:10.1002/2015gl064747

Vampola, A. (1998). "Outer Zone Energetic Electron Environment Update," in Conference on the high energy radiation background in space. Workshop record, Snowmass, CO, USA, 22-23 July 1997 (IEEE), 128–136.

Walt, M. (2005). *Introduction to Geomagnetically Trapped Radiation*. Cambridge, UK: Cambridge University Press.

West, H. I., Buck, R. M., and Walton, J. R. (1973). Electron Pitch Angle Distributions throughout the Magnetosphere as Observed on Ogo 5. *J. Geophys. Res.* 78, 1064–1081. doi:10.1029/ja078i007p01064

Zhao, H., Friedel, R., Chen, Y., Baker, D., Li, X., Malaspina, D., et al. (2021). Equatorial Pitch Angle Distributions of 1–50 keV Electrons in Earth's Inner Magnetosphere: an Empirical Model Based on the Van Allen Probes Observations. *J. Geophys. Res. Space Phys.* 126, e2020JA028322. doi:10.1029/2020ja028322

Zhao, H., Friedel, R. H. W., Chen, Y., Reeves, G. D., Baker, D. N., Li, X., et al. (2018). An Empirical Model of Radiation Belt Electron Pitch Angle Distributions Based on Van Allen Probes Measurements. *J. Geophys. Res. Space Phys.* 123, 3493–3511. doi:10.1029/2018ja025277

Zhao, X., Hao, Y., Zong, Q.-G., Zhou, X.-Z., Yue, C., Chen, X., et al. (2020). Origin of Electron Boomerang Stripes: Localized ULF Wave-Particle Interactions. *Geophys. Res. Lett.* 47, e2020GL087960. doi:10.1029/2020gl087960

Zong, Q., Rankin, R., and Zhou, X. (2017). The Interaction of Ultra-low-frequency Pc3-5 Waves with Charged Particles in Earth's Magnetosphere. *Rev. Mod. Plasma Phys.* 1, 1–90. doi:10.1007/s41614-017-0011-4

Conflict of Interest: The authors declare that the research was conducted in the absence of any commercial or financial relationships that could be construed as a potential conflict of interest.

Publisher's Note: All claims expressed in this article are solely those of the authors and do not necessarily represent those of their affiliated organizations, or those of the publisher, the editors and the reviewers. Any product that may be evaluated in this article, or claim that may be made by its manufacturer, is not guaranteed or endorsed by the publisher.

frontiers | Frontiers in Astronomy and Space Sciences

MINI REVIEW
published: 14 April 2022
doi: 10.3389/fspas.2022.867394

ULF Wave Modeling, Effects, and Applications: Accomplishments, Recent Advances, and Future

Michael D. Hartinger[1]†, Kazue Takahashi[2]†, Alexander Y. Drozdov[3]†, Xueling Shi[4,5]†, Maria E. Usanova[6]† and Brian Kress [7]†*

[1]Space Science Institute, Center for Space Plasma Physics, Boulder, CO, United States, [2]The Johns Hopkins University Applied Physics Laboratory, Laurel, MD, United States, [3]Earth, Planetary, and Space Sciences Department, UCLA, Los Angeles, CA, United States, [4]Virginia Tech, Department of Electrical and Computer Engineering, Blacksburg, VA, United States, [5]High Altitude Observatory, National Center for Atmospheric Research, Boulder, CO, United States, [6]Laboratory for Atmospheric and Space Physics, University of Colorado, Boulder, CO, United States, [7]National Oceanic and Atmospheric Administration, National Centers for Environmental Information, Boulder, CO, United States

Ultra Low Frequency (ULF) waves play important roles in magnetosphere-ionosphere coupling, ring current and radiation belt dynamics, and modulation of higher frequency wave modes and energetic particle precipitation. The "ULF wave modeling, effects, and applications" (UMEA) focus group - part of the Geospace Environment Modeling effort from 2016 to 2021 - sought to improve understanding of the physics of ULF waves and their specification in geospace models. Through a series of in person and virtual meetings the UMEA focus group brought modelers and experimentalists together to compare ULF wave outputs in different models, plan observation campaigns focused on ULF waves, discuss recent advances in ULF wave research, and identify unresolved ULF wave science questions. This article summarizes major discussion points and accomplishments in the UMEA focus group over the last 6 years, recent advances and their connection to Richard Thorne and Peter Gary's significant contributions to ULF wave research, and the future of ULF wave research.

Keywords: ULF wave, pulsation, field line resonance, magnetosphere-ionosphere coupling, solar wind-magnetosphere coupling, EMIC wave, radiation belt, radial diffusion

OPEN ACCESS

Edited by:
Charles William Smith, University of New Hampshire, United States

Reviewed by:
Kristoff Paulson, Harvard University, United States

***Correspondence:**
Michael D. Hartinger
mhartinger@spacescience.org

†These authors have contributed equally to this work and share first authorship

Specialty section:
This article was submitted to Space Physics, a section of the journal Frontiers in Astronomy and Space Sciences

Received: *01 February 2022*
Accepted: *28 February 2022*
Published: *14 April 2022*

Citation:
Hartinger MD, Takahashi K, Drozdov AY, Shi X, Usanova ME and Kress B (2022) ULF Wave Modeling, Effects, and Applications: Accomplishments, Recent Advances, and Future. Front. Astron. Space Sci. 9:867394. doi: 10.3389/fspas.2022.867394

1 INTRODUCTION TO ULF WAVES

Ultra Low Frequency (ULF) waves are the lowest frequency plasma waves in the Earth's magnetosphere, with frequencies from 0.001–5 Hz (Jacobs et al., 1964). At the lower end of the ULF band, waves are often well described using a magnetohydrodynamic (MHD) approximation and include eigenmodes with wavelengths comparable to the size of the magnetosphere. Higher frequency ULF waves include electromagnetic ion cyclotron (EMIC) waves, and these are better described with other mathematical approximations (e.g., local linear kinetic theory Gary et al., 1995). ULF waves play important roles in magnetosphere-ionosphere (MI) coupling (e.g., Keiling, 2009), ring current/radiation belt dynamics (e.g., Turner et al., 2012; Kress et al., 2013; Murphy et al., 2015), modulation of VLF waves/precipitation (e.g., Li et al., 2011; Brito et al., 2015; Jaynes et al., 2015), geomagnetically induced currents (GIC) (e.g., Heyns et al., 2021), substorms (e.g., Kepko and Kivelson, 1999; Liang et al., 2009; Keiling and Takahashi, 2011), and other areas relevant to space weather prediction. They are an important component of geospace environment models and thus relevant to the Geospace Environment Modeling (GEM) effort, a community

driven effort supported by the United States National Science Foundation that seeks to improve our understanding of the geospace environment, including solar wind-magnetosphere-ionosphere coupling via ULF waves.

The GEM "ULF wave modeling, effects, and applications" (UMEA) focus group (FG) formed in 2016 and ran through 2021. This focus group was motivated by (1) unprecedented availability of coordinated, multi-point space and ground-based observations (e.g., Hartinger et al., 2013; Takahashi et al., 2013), (2) high quality particle and field measurements of ULF wave-particle interactions (e.g., Claudepierre et al., 2013), (3) new and improved simulations better able to capture the excitation and dynamics of ULF waves (e.g., Claudepierre et al., 2010; Lysak et al., 2015) and (4) an ongoing effort in the GEM community to improve models of ULF waves. UMEA's goal was to bring modelers and experimentalists together to address the following questions: What excites ULF waves? How do ULF waves couple to the plasmasphere, ring current, and radiation belt populations? What is the role of ULF waves in MI coupling? This mini-review describes the recent advances in ULF wave research discussed in the UMEA FG from 2016 to 2021, including improved abilities to simulate ULF waves. It also discusses future directions in ULF wave research needed to improve the specification of ULF waves in models. Finally, it connects current and future work to the many important contributions from Richard Thorne and Peter Gary to ULF wave research, including EMIC waves, ULF modulation of Very Low Frequency (VLF) waves, and radiation belt wave-particle interactions.

2 WHAT EXCITES ULF WAVES?

Recent work is revealing new information about the manner in which upstream pressure disturbances with different spatial scales and orientations couple to magnetospheric ULF waves. Oliveira et al. (2020) showed how interplanetary shocks with different impact angles drive ULF waves with different properties. Multi-satellite investigations have yielded new insights into the large spatial scales over which upstream pressure disturbances can drive EMIC waves (Engebretson et al., 2018). Numerous studies have been conducted examining the role of ion foreshock disturbances (e.g., Wang et al., 2020a) and magnetosheath jets (e.g., Archer et al., 2019) in driving ULF waves with different properties. However, there remain few statistical studies that make one-to-one comparisons between ion foreshock or magnetosheath disturbances and ULF waves, limiting our understanding of the properties of such waves; more studies are needed that make use of multi-satellite/multi-constellation measurements. UMEA discussions also indicate that more modeling work is needed to determine how the spatial scale and speed of the upstream pressure disturbance affects ULF wave properties; most past modeling work has focused on two extremes—disturbances across the entire magnetopause or infinitesimal disturbances over a very small section of the magnetopause—whereas observations indicate a wide range of possible spatial scales and speeds on the magnetopause. Recently developed 3D ULF wave models indicate that the 3D properties of Alfven resonances depend on the external driver properties, and that standing Alfven waves and field line resonances in 3D geometries have unique properties that can differ from 2D model predictions (Elsden and Wright, 2017; Elsden and Wright, 2018). Finally, north-south and east-west asymmetries in upstream pressure disturbances can profoundly impact ULF wave properties in the magnetosphere (e.g., Shen et al., 2018; Wang et al., 2019; Oliveira et al., 2020), and more models and globally distributed observations are needed to understand how these asymmetries ultimately affect global wave properties and in turn predict what types of wave-particle interactions may occur in the inner magnetosphere. Energetic particle measurements are increasingly being used as an additional tool to remote sense wave mode structure and local time variations in wave properties (e.g., Hao et al., 2020; Zhao et al., 2020).

ULF waves can also be excited by mechanisms internal to the magnetosphere, including the magnetotail where plasma bubbles convecting earthward produce Pi2-band oscillations (Wang C. P. et al., 2020), buoyancy waves are excited (Wolf et al., 2018), and the ring current where high-m poloidal waves (Shi et al., 2018b; Zhai et al., 2021) and compressional Pc5 waves (Soto-Chavez et al., 2019) are excited. Significant advances have been made in spacecraft measurements of the wave mode structure, particle resonances with the waves, and unstable ion phase space density. New information on the global extent and azimuthal wave number has become available using HF radar (e.g., Shi et al., 2018a) and GPS TEC techniques (e.g., Watson et al., 2015). On the theoretical side, models have been developed for poloidal wave mode structures incorporating finite ion pressure (Xia et al., 2017), and a gyrokinetic code has been developed to simulate excitation of poloidal waves in a dipole magnetosphere (Yamakawa et al., 2019). Numerical simulations that combine MHD background and kinetic particle effects might be a logical direction in future studies of internally excited ULF waves.

3 HOW DO ULF WAVES COUPLE TO THE PLASMASPHERE?

Cold plasmapheric plasma can affect ULF wave generation and propagation. In relation to wave propagation, there has been an ongoing debate whether the plasmapause can serve as a barrier to ULF waves, controlling the radial extent of ULF wave power propagation, as previously suggested (e.g., Lee et al., 2002; Hartinger et al., 2010). However, a recent study by Sandhu et al. (2021) demonstrated no clear evidence for a sharp reduction in wave power across the plasmapause. Instead, it uncovered trapping of highly enhanced wave power in plasmaspheric plumes during disturbed geomagnetic conditions, giving a deeper insight into the storm-time ULF wave dynamics and contributing to modelling efforts of ULF wave driven radial diffusion during geomagnetically active periods.

In turn, ULF waves can have an effect on cold plasma. Plasmaspheric electrons and ions were found heated and their fluxes modulated by ULF waves. It was suggested that ~1 eV ions can be energized by 10–100 times by ULF wave electric fields

due to betatron acceleration (Yue et al., 2016) and E × B drift (Zhang S. et al., 2019). Zong et al. (2012) presented observations of simultaneous plasmaspheric O+ ion enhancements and ULF waves, suggesting ULF waves can interact with oxygen torus ions. In addition, more recent studies (e.g., Ren et al., 2019, and references therein) reported acceleration of cold plasmaspheric electrons by ULF waves through drift-bounce resonance. Overall, this intermediate energy population (a few eV to hundreds of eV) also known as warm plasma cloak (Chappell et al., 2008) has been actively investigated over the past few years (Borovsky and Valdivia, 2018; Delzanno et al., 2021).

Interactions between cold plasma and EMIC waves were also actively discussed in the UMEA FG, with much of the work motivated by the many significant contributions of Peter Gary and Richard Thorne to EMIC wave research, including the factors controlling their generation (plasma temperature, temperature anisotropy, ion composition), storm time evolution, and effect on a wide range of ion and electron populations (Gary, 1992; Gary et al., 1994, 1995; Thorne and Horne, 1992, 1997). EMIC waves can resonantly interact with multiple particle species, being an important loss process for both ring current ions and radiation belt electrons, as well as a cold plasma heating mechanism. They can couple energy and momentum between magnetospheric plasma in a wide energy range, from a few eV to several MeV. Similarly to ULF waves, there is a two-way relationship between EMIC waves and cold plasma. Plasmaspheric plasma density and ion composition controls EMIC wave growth and propagation, as well as the energy of energetic particles in resonance with EMIC waves (e.g., Usanova et al., 2016; Usanova and Mann, 2016; Blum and Breneman, 2020). Nosé et al. (2020) found a close relationship between EMIC wave occurrence and the structure of the oxygen torus. EMIC waves can heat plasmaspheric ions, as predicted earlier by theory and simulations and confirmed by state-of-the-art MMS satellite measurements (Kitamura et al., 2018; Abid et al., 2021). These new findings point to the importance of cold ion composition measurements for new satellite missions (Lee et al., 2021). Recent studies have also emphasized the role of nonlinear processes in EMIC wave-particle interactions and the potential to include those in global magnetospheric models which will be a next crucial step towards predictive modeling (Usanova, 2021, and references therein).

4 HOW DO ULF WAVES COUPLE TO THE RING CURRENT?

ULF waves also play an important role in the dynamics of higher energy ring current particles. This includes storm time intervals through interaction with ring current ions via drift-bounce resonance. However, the energy transfer between magnetospheric particles and ULF waves through wave-particle interactions has been mostly excluded from models of ring current dynamics. Based on drift-kinetic simulations, Yamakawa et al. (2019) and Yamakawa et al. (2020) showed that high-m Pc3-5 ULF waves can be excited through the drift-bounce resonance by ring current ions associated with the injection from the magnetotail. Oimatsu et al. (2018) showed in a Van Allen Probes case study that energy transfer from the ring current protons to the poloidal Pc4 wave via the drift-bounce resonance contributes up to 85% of the increase in the Dst^* index, where Dst^* is the solar wind pressure-corrected Dst index. Recent studies have shown that ULF waves can interact with relativistic electrons and ring current ions at the same time (e.g., Yang et al., 2010; Ren et al., 2016). Multiple drift and/or drift-bounce resonances can occur with different plasma species or the same species at different energies simultaneously (Rankin et al., 2020). Since ULF waves can interact with various magnetospheric particle populations (sometimes simultaneously), including the plasmaspheric electrons, ring current ions, and radiation belt energetic electrons, it is still a question if and how ULF waves mediate coupling between different particle populations (Zong, 2021). The incorporation of ULF wave-particle interactions into ring current models is therefore an important target for future studies, and improved energy budgets are needed to quantify the impact of these waves on the ring current.

Higher frequency EMIC waves are also related to ring current dynamics. Anisotropic ring current proton distributions with Tperp>Tpara (with respect to the background magnetic field) provide the source of free energy for EMIC instability (Cornwall, 1965; Horne and Thorne, 1993). Energetic He+ and O+ ring current species, abundant in the magnetosphere during geomagnetically active times, can absorb the wave energy and split the EMIC wave spectrum into multiple sub-bands. The wave growth rates and cut-off frequencies of each sub-band are determined by the hot ion temperature anisotropy, ion composition, and cold plasma density (Kozyra et al., 1984). As the EMIC wave instability evolves, the initially unstable proton distribution isotropizes due to pitch-angle scattering and loss of protons into the atmosphere (e.g., Usanova et al., 2010; Søraas et al., 2013; Yahnin et al., 2021). This process is incorporated in global ring current models (Jordanova et al., 2012) which showed its contribution to a gradual recovery of magnetic storms. The relationship between EMIC waves and the ring current is an ongoing and active area of research.

5 HOW DO ULF WAVES COUPLE TO THE RADIATION BELTS?

ULF waves play a major role in the dynamics of higher energy radiation belt particles through radial transport. ULF wave-particle interactions can lead to rapid dropouts (e.g., Turner et al., 2012; Zou et al., 2020; Olifer et al., 2021) as well as significant energization of electrons (e.g., Kanekal et al., 2016; Jaynes et al., 2018). Thorne et al. (2007) discussed how both ULF waves and local wave-particle interaction can contribute to the acceleration of relativistic electrons. ULF waves can accelerate electrons up to relativistic energies (e.g., Elkington et al., 2003), and plasma density depletions can create preferential conditions for local diffusive acceleration of electrons from ~hundreds of keV to several MeV (Thorne et al., 2013; Allison et al., 2021).

While significant progress has been achieved and many derived parameterizations have been applied in the simulations (e.g., Ozeke et al., 2014; Drozdov et al., 2021), the role of ULF waves in the electron dynamics remains an open question. For example, with sparse measurements it is challenging to determine the azimuthal mode number of ULF waves (Barani et al., 2019), which necessitates assumptions in the estimation of radial diffusion coefficients. Other challenges arise from the sparse distribution of ULF wave measurements. One approach to supplement sparse measurements is the use of realistic, validated global MHD simulations (Elkington et al., 2012); this is one motivation for the UMEA objective of improving such simulations. The effect of ULF waves can be included in simulations via radial diffusion parameterizations (Lejosne and Kollmann, 2020).

ULF waves can also modulate higher-frequency, EMIC and VLF wave growth (e.g., Li et al., 2011; Gamayunov and Engebretson, 2021; Shang et al., 2021), transferring energy from large to small scales. Concerning EMIC waves, the pioneering work by Lyons and Thorne (1972) demonstrated that these waves can play a critical role in the dynamics of multi-MeV electrons. They are highly effective in scattering electrons in the vicinity of the loss cone, can produce localized precipitation (e.g., Blum et al., 2015) and lead to the formation of bite-outs in electron pitch-angle distributions (Usanova et al., 2014) and minima in phase space density profiles (Shprits et al., 2017). A few examples of recent advances in EMIC wave research include significantly improved data coverage and statistics (e.g., Allen et al., 2016; Sigsbee et al., 2016, 2020; Wang et al., 2017; Engebretson et al., 2018; Lee et al., 2019; Vines et al., 2019, 2021; Grison et al., 2021; Jun et al., 2021), investigation of the association of the EMIC waves with injections (e.g., Remya et al., 2018; Jun et al., 2019; Kim et al., 2021), improved understanding of EMIC wave generation (e.g., Lee et al., 2021), exploration of the possibility of sub-MeV electron scattering (e.g., Zhang X. J. et al., 2019; Capannolo et al., 2019; Denton et al., 2019) and quantifying their effect in modeling (e.g., Ma et al., 2016; Drozdov et al., 2017; Cervantes et al., 2020; Wang D. et al., 2020; Drozdov et al., 2020).

6 WHAT IS THE ROLE OF ULF WAVES IN MAGNETOSPHERE-IONOSPHERE COUPLING?

ULF waves can carry significant energy to the ionosphere and play important roles in M-I coupling. They can cause modulation and enhancement of several ionospheric parameters (e.g., electron density and ionospheric conductance) and provide ion frictional heating in the ionosphere-thermosphere (I-T) system. When propagating to the ground, ULF waves can couple to geomagnetic/geoelectric field perturbations (e.g., Hartinger et al., 2020) and potentially drive GICs that may damage technological infrastructures (Heyns et al., 2021; Yagova et al., 2021). Recent studies have shown that ULF wave-related precipitation of energetic electrons can affect ionospheric conductivities and modulate Hall and Pedersen conductances by a factor of 7–10 (e.g., Wang et al., 2020d). These large conductivity modulations in turn affect M-I coupling processes and I-T heating rates (Verkhoglyadova et al., 2018). Watson et al. (2015, 2016) reported TEC variations related to Pc4 and Pc5-6 ULF waves, with the Pc5-6 waves showing peak-to-peak amplitudes as large as 7 TECU.

More work is needed in ULF wave models to incorporate more realistic, event-specific conductivity. Though several mechanisms linking ULF waves to TEC perturbations have been proposed by Pilipenko et al. (2014), most work has focused on event studies. Comprehensive statistical studies are thus need to identify the favored conditions and mechanisms for significant TEC perturbations related to ULF waves. While many previous statistical studies used 1-min resolution data to characterize geomagnetic perturbations for GIC hazard analysis, it has been shown by recent studies that higher sampling rate data (<1 min) are needed to capture more transient and shorter-period wave events such as those associated with SSCs (e.g., Trichtchenko, 2021).

7 ULF WAVE MODELING AND THE GEM ULF WAVE MODELING CHALLENGE

ULF waves in the magnetosphere are studied using coupled global magnetospheric models (e.g., Claudepierre et al., 2008; Hartinger et al., 2014; Claudepierre et al., 2016; Komar et al., 2017) and in simplified field geometries to isolate and better understand underlying physics (Xia et al., 2017; Denton, 2018; Elsden and Wright, 2020; Lysak et al., 2020). Examples of simulations of ULF waves in the magnetosphere presented at GEM UMEA sessions include studies of: global magnetospheric ULF wave modes (Claudepierre et al., 2010; Elsden et al., 2016; Elsden and Wright, 2017, 2020; Xia et al., 2017; Lysak et al., 2020), magnetospheric ULF wave propagation (Degeling et al., 2018), growth and propagation of EMIC waves (Denton et al., 2014), magnetopause surface waves (Lin et al., 2017; Archer et al., 2021), and interaction of ULF waves with ring current and radiation belt particle populations (Komar et al., 2017; Denton et al., 2019; Patel et al., 2019).

In a previous GEM challenge, the Metrics and Validation Focus Group compared ULF wave output of several global MHD simulation codes using idealized driving conditions, finding substantial differences. A few global MHD simulation studies have shown how, for example, grid resolution can profoundly affect wave properties using grid convergence tests and other calculations (e.g., Claudepierre et al., 2010; Hartinger et al., 2014). More model-model (different grid, different simulation code, different boundary condition) and model-data (event specific or idealized simulations compared to statistical results) comparisons are needed to improve the specification of ULF waves in global MHD simulations, and this approach needs to be extended beyond global MHD simulations. The earlier GEM ULF wave modeling challenge was continued by UMEA in order to better understand potential sources of model-model and model-data discrepancies—in particular, to discriminate between numerical effects and missing physics.

Over a series of sessions, the UMEA FG discussed data-model and model-model comparisons during idealized and realistic driving conditions. A project webpage describing this effort is at https://ccmc.gsfc.nasa.gov/challenges/ULF/, including a project summary, links to publications and simulation runs at the NASA GSFC Community Coordinated Modeling Center (CCMC).

8 SUMMARY

The 2016–2021 UMEA effort brought together researchers in different research areas that shared common interests related to ULF waves. This led to fruitful discussions that connected different research areas and GEM focus groups. Many of these discussions, such as the generation mechanisms of EMIC waves and the relative importance of radial transport and local acceleration, were motivated by the pioneering work of Richard Thorne and Peter Gary. Work related to these FG discussions has yielded new insights on the current state of the field and prospects for future research directions. A recurring theme across all 6 years of the FG: ULF waves are discussed in various contexts in virtually every area of geospace research (and every GEM FG) due to the wide variety of ways they can affect geospace system dynamics. In the future, continued coordination across research areas is needed to improve models of ULF waves and better capture their effect on solar wind-magnetosphere-ionosphere coupling and inner magnetosphere dynamics.

AUTHOR CONTRIBUTIONS

MH led the manuscript effort and provided text for **Sections 1**, **8**, and other sections. KT provided text for **Section 2**. MU provided text for **Section 3**, **4**. XS provided text for **Sections 4**, **6**. AD provided text for **Section 5**. BK provided text for **Section 7**.

FUNDING

MH was supported by NASA grants 80NSSC19K0127 and 80NSSC19K0907, and the International Space Sciences Institute (ISSI) international teams program (3D Alfvén resonances). XS was supported by NASA grants 80NSSC19K0907 and 80NSSC21K1677. KT was supported by NASA grants NNX17AD34G and 80NSSC19K0259. MU is thankful for support from the ISSI international teams program and NASA Award 80 NSSC19K0265.

ACKNOWLEDGMENTS

We thank all who participated in the UMEA focus group discussions from 2016 to 2021, but especially Seth Claudepierre and Scot Elkington who provided significant help in planning the UMEA effort and generated many of the ideas that led to the FG proposal.

REFERENCES

Abid, A. A., Lu, Q., Gao, X. L., Alotaibi, B. M., Ali, S., Qureshi, M. N. S., et al. (2021). Energization of Cold Ions by Electromagnetic Ion Cyclotron Waves: Magnetospheric Multiscale (MMS) Observations. *Phys. Plasmas* 28, 072901. doi:10.1063/5.0046764

Allen, R. C., Zhang, J.-C., Kistler, L. M., Spence, H. E., Lin, R.-L., Klecker, B., et al. (2016). A Statistical Study of EMIC Waves Observed by Cluster: 2. Associated Plasma Conditions. *J. Geophys. Res. Space Phys.* 121, 6458–6479. doi:10.1002/2016JA022541

Allison, H. J., Shprits, Y. Y., Zhelavskaya, I. S., Wang, D., and Smirnov, A. G. (2021). Gyroresonant Wave-Particle Interactions with Chorus Waves during Extreme Depletions of Plasma Density in the Van allen Radiation Belts. *Sci. Adv.* 7. doi:10.1126/sciadv.abc0380

Archer, M. O., Hartinger, M. D., Plaschke, F., Southwood, D. J., and Rastaetter, L. (2021). Magnetopause Ripples Going against the Flow Form Azimuthally Stationary Surface Waves. *Nat. Commun.* 12, 5697. doi:10.1038/s41467-021-25923-7

Archer, M. O., Hietala, H., Hartinger, M. D., Plaschke, F., and Angelopoulos, V. (2019). Direct Observations of a Surface Eigenmode of the Dayside Magnetopause. *Nat. Commun.* 10, 615. doi:10.1038/s41467-018-08134-5

Barani, M., Tu, W., Sarris, T., Pham, K., and Redmon, R. J. (2019). Estimating the Azimuthal Mode Structure of ULF Waves Based on Multiple GOES Satellite Observations. *J. Geophys. Res. Space Phys.* 124, 5009–5026. doi:10.1029/2019JA026927

Blum, L. W., and Breneman, A. W. (2020). "Observations of Radiation belt Losses Due to Cyclotron Wave-Particle Interactions," in *The Dynamic Loss of Earth's Radiation Belts*. Editors Jaynes, A. N., and Usanova, M. E. (Cambridge, MA: Elsevier), 49–98. doi:10.1016/B978-0-12-813371-2.00003-2

Blum, L. W., Halford, A., Millan, R., Bonnell, J. W., Goldstein, J., Usanova, M., et al. (2015). Observations of Coincident EMIC Wave Activity and Duskside Energetic Electron Precipitation on 18-19 January 2013. *Geophys. Res. Lett.* 42, 5727–5735. doi:10.1002/2015GL065245

Borovsky, J. E., and Valdivia, J. A. (2018). The Earth's Magnetosphere: A Systems Science Overview and Assessment. *Surv. Geophys.* 39, 817–859. doi:10.1007/s10712-018-9487-x

Brito, T., Hudson, M. K., Kress, B., Paral, J., Halford, A., Millan, R., et al. (2015). Simulation of ULF Wave-Modulated Radiation belt Electron Precipitation during the 17 March 2013 Storm. *J. Geophys. Res. Space Phys.* 120, 3444–3461. doi:10.1002/2014JA020838

Capannolo, L., Li, W., Ma, Q., Chen, L., Shen, X. C., Spence, H. E., et al. (2019). Direct Observation of Subrelativistic Electron Precipitation Potentially Driven by EMIC Waves. *Geophys. Res. Lett.* 46, 12711–12721. doi:10.1029/2019GL084202

Cervantes, S., Shprits, Y. Y., Aseev, N. A., and Allison, H. J. (2020). Quantifying the Effects of EMIC Wave Scattering and Magnetopause Shadowing in the Outer Electron Radiation Belt by Means of Data Assimilation. *J. Geophys. Res. Space Phys.* 125. doi:10.1029/2020JA028208

Chappell, C. R., Huddleston, M. M., Moore, T. E., Giles, B. L., and Delcourt, D. C. (2008). Observations of the Warm Plasma Cloak and an Explanation of its Formation in the Magnetosphere. *J. Geophys. Res.* 113, a–n. doi:10.1029/2007JA012945

Claudepierre, S. G., Elkington, S. R., and Wiltberger, M. (2008). Solar Wind Driving of Magnetospheric ULF Waves: Pulsations Driven by Velocity Shear at the Magnetopause. *J. Geophys. Res.* 113, a–n. doi:10.1029/2007JA012890

Claudepierre, S. G., Hudson, M. K., Lotko, W., Lyon, J. G., and Denton, R. E. (2010). Solar Wind Driving of Magnetospheric Ulf Waves: Field Line Resonances Driven by Dynamic Pressure Fluctuations. *J. Geophys. Res. Space Phys.* 115. doi:10.1029/2010ja015399

Claudepierre, S. G., Mann, I. R., Takahashi, K., Fennell, J. F., Hudson, M. K., Blake, J. B., et al. (2013). Van Allen Probes Observation of Localized Drift Resonance between Poloidal Mode Ultra-low Frequency Waves and 60 keV Electrons. *Geophys. Res. Lett.* 40, 4491–4497. doi:10.1002/grl.50901

Claudepierre, S. G., Toffoletto, F. R., and Wiltberger, M. (2016). Global Mhd Modeling of Resonant Ulf Waves: Simulations with and without a Plasmasphere. *J. Geophys. Res. Space Phys.* 121, 227–244. doi:10.1002/2015JA022048

Cornwall, J. M. (1965). Cyclotron Instabilities and Electromagnetic Emission in the Ultra Low Frequency and Very Low Frequency Ranges. *J. Geophys. Res.* 70, 61–69. doi:10.1029/JZ070i001p00061

Degeling, A. W., Rae, I. J., Watt, C. E. J., Shi, Q. Q., Rankin, R., and Zong, Q.-G. (2018). Control of Ulf Wave Accessibility to the Inner Magnetosphere by the Convection of Plasma Density. *J. Geophys. Res. Space Phys.* 123, 1086–1099. doi:10.1002/2017JA024874

Delzanno, G. L., Borovsky, J. E., Henderson, M. G., Resendiz Lira, P. A., Roytershteyn, V., and Welling, D. T. (2021). The Impact of Cold Electrons and Cold Ions in Magnetospheric Physics. *J. Atmos. Solar-Terrestrial Phys.* 220, 105599. doi:10.1016/j.jastp.2021.105599

Denton, R. E. (2018). Electromagnetic Ion Cyclotron Wavefields in a Realistic Dipole Field. *J. Geophys. Res. Space Phys.* 123, 1208–1223. doi:10.1002/2017JA024886

Denton, R. E., Jordanova, V. K., and Fraser, B. J. (2014). Effect of Spatial Density Variation and O+ Concentration on the Growth and Evolution of Electromagnetic Ion Cyclotron Waves. *J. Geophys. Res. Space Phys.* 119, 8372–8395. doi:10.1002/2014JA020384

Denton, R. E., Ofman, L., Shprits, Y. Y., Bortnik, J., Millan, R. M., Rodger, C. J., et al. (2019). Pitch Angle Scattering of Sub-MeV Relativistic Electrons by Electromagnetic Ion Cyclotron Waves. *J. Geophys. Res. Space Phys.* 124, 5610–5626. doi:10.1029/2018JA026384

Drozdov, A. Y., Allison, H. J., Shprits, Y. Y., Elkington, S. R., and Aseev, N. A. (2021). A Comparison of Radial Diffusion Coefficients in 1-D and 3-D Long-Term Radiation Belt Simulations. *JGR Space Physics]* 126. doi:10.1029/2020ja028707

Drozdov, A. Y., Shprits, Y. Y., Usanova, M. E., Aseev, N. A., Kellerman, A. C., and Zhu, H. (2017). EMIC Wave Parameterization in the Long-Term VERB Code Simulation. *J. Geophys. Res. Space Phys.* 122, 8488–8501. doi:10.1002/2017JA024389

Drozdov, A. Y., Usanova, M. E., Hudson, M. K., Allison, H. J., and Shprits, Y. Y. (2020). The Role of Hiss, Chorus, and EMIC Waves in the Modeling of the Dynamics of the Multi-MeV Radiation Belt Electrons. *J. Geophys. Res. Space Phys.* 125, 2628. doi:10.1029/2020JA028282

Elkington, S. R., Chan, A. A., and Wiltberger, M. (2012). *Global Structure of ULF Waves during the 24–26 September 1998 Geomagnetic Storm*. American Geophysical Union AGU, 127–138. doi:10.1029/2012GM001348

Elkington, S. R., Hudson, M. K., and Chan, A. A. (2003). Resonant Acceleration and Diffusion of Outer Zone Electrons in an Asymmetric Geomagnetic Field. *J. Geophys. Res.* 108. doi:10.1029/2001JA009202

Elsden, T., and Wright, A. (2020). Evolution of High- M Poloidal Alfvén Waves in a Dipole Magnetic Field. *J. Geophys. Res. Space Phys.* 125. doi:10.1029/2020JA028187

Elsden, T., Wright, A. N., and Hartinger, M. D. (2016). Deciphering Satellite Observations of Compressional Ulf Waveguide Modes. *J. Geophys. Res. Space Phys.* 121, 3381–3394. doi:10.1002/2016JA022351

Elsden, T., and Wright, A. N. (2018). The Broadband Excitation of 3-D Alfvén Resonances in a MHD Waveguide. *J. Geophys. Res. Space Phys.* 123, 530–547. doi:10.1002/2017JA025018

Elsden, T., and Wright, A. N. (2017). The Theoretical Foundation of 3-D Alfvén Resonances: Time-dependent Solutions. *J. Geophys. Res. Space Phys.* 122, 3247–3261. doi:10.1002/2016JA023811

Engebretson, M. J., Posch, J. L., Capman, N. S. S., Campuzano, N. G., Bělik, P., Allen, R. C., et al. (2018). MMS, Van Allen Probes, GOES 13, and Ground-Based Magnetometer Observations of EMIC Wave Events before, during, and after a Modest Interplanetary Shock. *J. Geophys. Res. Space Phys.* 123, 8331–8357. doi:10.1029/2018JA025984

Gamayunov, K. V., and Engebretson, M. J. (2021). Low Frequency ULF Waves in the Earth's Inner Magnetosphere: Statistics during Coronal Mass Ejections and Seeding of EMIC Waves. *JGR Space Phys.* 126. doi:10.1029/2021ja029247

Gary, S. P., Moldwin, M. B., Thomsen, M. F., Winske, D., and McComas, D. J. (1994). Hot Proton Anisotropies and Cool Proton Temperatures in the Outer Magnetosphere. *J. Geophys. Res.* 99, 23603–23616. doi:10.1029/94JA02069

Gary, S. P. (1992). The Mirror and Ion Cyclotron Anisotropy Instabilities. *J. Geophys. Res.* 97, 8519–8529. doi:10.1029/92JA00299

Gary, S. P., Thomsen, M. F., Yin, L., and Winske, D. (1995). Electromagnetic Proton Cyclotron Instability: Interactions with Magnetospheric Protons. *J. Geophys. Res.* 100, 21961–21972. doi:10.1029/95JA01403

Grison, B., Santolík, O., Lukačevič, J., and Usanova, M. E. (2021). Occurrence of EMIC Waves in the Magnetosphere According to Their Distance to the Magnetopause. *Geophys. Res. Lett.* 48. doi:10.1029/2020GL090921

Hao, Y. X., Zhao, X. X., Zong, Q. G., Zhou, X. Z., Rankin, R., Chen, X. R., et al. (2020). Simultaneous Observations of Localized and Global Drift Resonance. *Geophys. Res. Lett.* 47, e88019. doi:10.1029/2020GL088019

Hartinger, M. D., Angelopoulos, V., Moldwin, M. B., Takahashi, K., and Clausen, L. B. N. (2013). Statistical Study of Global Modes outside the Plasmasphere. *J. Geophys. Res. Space Phys.* 118, 804–822. doi:10.1002/jgra.50140

Hartinger, M. D., Shi, X., Lucas, G. M., Murphy, B. S., Kelbert, A., Baker, J. B. H., et al. (2020). Simultaneous Observations of Geoelectric and Geomagnetic fields Produced by Magnetospheric Ulf Waves. *Geophys. Res. Lett.* 47, e2020GL089441. doi:10.1029/2020GL089441

Hartinger, M. D., Welling, D., Viall, N. M., Moldwin, M. B., and Ridley, A. (2014). The Effect of Magnetopause Motion on Fast Mode Resonance. *J. Geophys. Res. Space Phys.* 119, 8212–8227. doi:10.1002/2014JA020401

Hartinger, M., Moldwin, M. B., Angelopoulos, V., Takahashi, K., Singer, H. J., Anderson, R. R., et al. (2010). Pc5 Wave Power in the Quiet-Time Plasmasphere and Trough: CRRES Observations. *Geophys. Res. Lett.* 37, a–n. doi:10.1029/2010GL042475

Heyns, M. J., Lotz, S. I., and Gaunt, C. T. (2021). Geomagnetic Pulsations Driving Geomagnetically Induced Currents. *Space Weather* 19, e2020SW002557. doi:10.1029/2020SW002557

Horne, R. B., and Thorne, R. M. (1993). On the Preferred Source Location for the Convective Amplification of Ion Cyclotron Waves. *J. Geophys. Res.* 98, 9233–9248. doi:10.1029/92JA02972

Jacobs, J. A., Kato, Y., Matsushita, S., and Troitskaya, V. A. (1964). Classification of Geomagnetic Micropulsations. *J. Geophys. Res.* 69, 180–181. doi:10.1029/JZ069i001p00180

Jaynes, A. N., Ali, A. F., Elkington, S. R., Malaspina, D. M., Baker, D. N., Li, X., et al. (2018). Fast Diffusion of Ultrarelativistic Electrons in the Outer Radiation belt: 17 March 2015 Storm Event. *Geophys. Res. Lett.* 45, 10874–10882. doi:10.1029/2018GL079786

Jaynes, A. N., Lessard, M. R., Takahashi, K., Ali, A. F., Malaspina, D. M., Michell, R. G., et al. (2015). Correlated Pc4-5 ULF Waves, Whistler-mode Chorus, and Pulsating aurora Observed by the Van Allen Probes and Ground-based Systems. *J. Geophys. Res. Space Phys.* 120, 8749–8761. doi:10.1002/2015JA021380

Jordanova, V. K., Welling, D. T., Zaharia, S. G., Chen, L., and Thorne, R. M. (2012). Modeling Ring Current Ion and Electron Dynamics and Plasma Instabilities during a High-Speed Stream Driven Storm. *J. Geophys. Res.* 117, a–n. doi:10.1029/2011JA017433

Jun, C. W., Miyoshi, Y., Kurita, S., Yue, C., Bortnik, J., Lyons, L., et al. (2021). The Characteristics of EMIC Waves in the Magnetosphere Based on the Van Allen Probes and Arase Observations. *J. Geophys. Res. Space Phys.* 126. doi:10.1029/2020JA029001

Jun, C. W., Yue, C., Bortnik, J., Lyons, L. R., Nishimura, Y., and Kletzing, C. (2019). EMIC Wave Properties Associated with and without Injections in the Inner Magnetosphere. *J. Geophys. Res. Space Phys.* 124, 2029–2045. doi:10.1029/2018JA026279

Kanekal, S. G., Baker, D. N., Fennell, J. F., Jones, A., Schiller, Q., Richardson, I. G., et al. (2016). Prompt Acceleration of Magnetospheric Electrons to Ultrarelativistic Energies by the 17 March 2015 Interplanetary Shock. *J. Geophys. Res. Space Phys.* 121, 7622–7635. doi:10.1002/2016JA022596

Keiling, A. (2009). Alfvén Waves and Their Roles in the Dynamics of the Earth's Magnetotail: A Review. *Space Sci. Rev.* 142, 73–156. doi:10.1007/s11214-008-9463-8

Keiling, A., and Takahashi, K. (2011). Review of Pi2 Models. *Space Sci. Rev.* 161, 63–148. doi:10.1007/s11214-011-9818-4

Kepko, L., and Kivelson, M. (1999). Generation of Pi2 Pulsations by Bursty Bulk Flows. *J. Geophys. Res.* 104, 25021–25034. doi:10.1029/1999JA900361

Kim, H., Schiller, Q., Engebretson, M. J., Noh, S., Kuzichev, I., Lanzerotti, L. J., et al. (2021). Observations of Particle Loss Due to Injection-Associated Electromagnetic Ion Cyclotron Waves. *J. Geophys. Res. Space Phys.* 126. doi:10.1029/2020JA028503

Kitamura, N., Kitahara, M., Shoji, M., Miyoshi, Y., Hasegawa, H., Nakamura, S., et al. (2018). Direct Measurements of Two-Way Wave-Particle Energy Transfer in a Collisionless Space Plasma. *Science* 361, 1000–1003. doi:10.1126/science.aap8730

Komar, C. M., Glocer, A., Hartinger, M. D., Murphy, K. R., Fok, M.-C., and Kang, S.-B. (2017). Electron Drift Resonance in the Mhd-Coupled Comprehensive Inner

Magnetosphere-Ionosphere Model. *J. Geophys. Res. Space Phys.* 122, 006–012. doi:10.1002/2017JA024163

Kozyra, J. U., Cravens, T. E., Nagy, A. F., Fontheim, E. G., and Ong, R. S. B. (1984). Effects of Energetic Heavy Ions on Electromagnetic Ion Cyclotron Wave Generation in the Plasmapause Region. *J. Geophys. Res.* 89, 2217–2234. doi:10.1029/JA089iA04p02217

Kress, B. T., Hudson, M. K., Ukhorskiy, A. Y., and Mueller, H.-R. (2013). *Nonlinear Radial Transport in the Earth's Radiation Belts*. (Washington, DC: American Geophysical Union AGU), 151–160. doi:10.1029/2012GM001333

Lee, D.-H., Hudson, M. K., Kim, K., Lysak, R. L., and Song, Y. (2002). Compressional MHD Wave Transport in the Magnetosphere 1. Reflection and Transmission across the Plasmapause. *J. Geophys. Res.* 107. doi:10.1029/2002JA009239

Lee, J. H., Turner, D. L., Toledo-Redondo, S., Vines, S. K., Allen, R. C., Fuselier, S. A., et al. (2019). MMS Measurements and Modeling of Peculiar Electromagnetic Ion Cyclotron Waves. *Geophys. Res. Lett.* 46, 11622–11631. doi:10.1029/2019GL085182

Lee, J. H., Turner, D. L., Vines, S. K., Allen, R. C., Toledo-Redondo, S., Bingham, S. T., et al. (2021). Application of Cold and Hot Plasma Composition Measurements to Investigate Impacts on Dusk-Side Electromagnetic Ion Cyclotron Waves. *J. Geophys. Res. Space Phys.* 126. doi:10.1029/2020JA028650

Lejosne, S., and Kollmann, P. (2020). Radiation Belt Radial Diffusion at Earth and Beyond. *Space Sci. Rev.* 216. doi:10.1007/s11214-020-0642-6

Li, W., Thorne, R. M., Bortnik, J., Nishimura, Y., and Angelopoulos, V. (2011). Modulation of Whistler Mode Chorus Waves: 1. Role of Compressional Pc4-5 Pulsations. *J. Geophys. Res.* 116, a–n. doi:10.1029/2010ja016312

Liang, J., Liu, W. W., Donovan, E. F., and Spanswick, E. (2009). In-situ Observation of ULF Wave Activities Associated with Substorm Expansion Phase Onset and Current Disruption. *Ann. Geophys.* 27, 2191–2204. doi:10.5194/angeo-27-2191-2009

Lin, D., Scales, W. A., and Sen, S. (2017). Flow Curvature Effects on the Kelvin-Helmholtz Instability: Hybrid Simulation. *Radiat. Effects Defects Sol.* 172, 750–753. doi:10.1080/10420150.2017.1398254

Lyons, L. R., and Thorne, R. M. (1972). Parasitic Pitch Angle Diffusion of Radiation belt Particles by Ion Cyclotron Waves. *J. Geophys. Res.* 77, 5608–5616. doi:10.1029/JA077i028p05608

Lysak, R. L., Song, Y., Sciffer, M. D., and Waters, C. L. (2015). Propagation of Pi2 Pulsations in a Dipole Model of the Magnetosphere. *J. Geophys. Res. Space Phys.* 120, 355–367. doi:10.1002/2014JA020625

Lysak, R. L., Song, Y., Waters, C. L., Sciffer, M. D., and Obana, Y. (2020). Numerical Investigations of Interhemispheric Asymmetry Due to Ionospheric Conductance. *J. Geophys. Res. Space Phys.* 125. doi:10.1029/2020JA027866

Ma, Q., Li, W., Thorne, R. M., Nishimura, Y., Zhang, X. J., Reeves, G. D., et al. (2016). Simulation of Energy-dependent Electron Diffusion Processes in the Earth's Outer Radiation belt. *J. Geophys. Res. Space Phys.* 121, 4217–4231. doi:10.1002/2016JA022507

Murphy, K. R., Mann, I. R., and Sibeck, D. G. (2015). On the Dependence of Storm Time ULF Wave Power on Magnetopause Location: Impacts for ULF Wave Radial Diffusion. *Geophys. Res. Lett.* 42, 9676–9684. doi:10.1002/2015GL066592

Nosé, M., Matsuoka, A., Kumamoto, A., Kasahara, Y., Teramoto, M., Kurita, S., et al. (2020). Oxygen Torus and its Coincidence with EMIC Wave in the Deep Inner Magnetosphere: Van Allen Probe B and Arase Observations. *Earth Planets Space* 72, 111. doi:10.1186/s40623-020-01235-w

Oimatsu, S., Nosé, M., Takahashi, K., Yamamoto, K., Keika, K., Kletzing, C. A., et al. (2018). Van allen Probes Observations of Drift-Bounce Resonance and Energy Transfer between Energetic Ring Current Protons and Poloidal Pc4 Wave. *J. Geophys. Res. Space Phys.* 123, 3421–3435. doi:10.1029/2017JA025087

Olifer, L., Mann, I. R., Ozeke, L. G., Claudepierre, S. G., Baker, D. N., and Spence, H. E. (2021). On the Similarity and Repeatability of Fast Radiation belt Loss: Role of the Last Closed Drift Shell. *JGR Space Phys.* 126. doi:10.1029/2021ja029957

Oliveira, D. M., Hartinger, M. D., Xu, Z., Zesta, E., Pilipenko, V. A., Giles, B. L., et al. (2020). Interplanetary Shock Impact Angles Control Magnetospheric ULF Wave Activity: Wave Amplitude, Frequency, and Power Spectra. *Geophys. Res. Lett.* 47. doi:10.1029/2020GL090857

Ozeke, L. G., Mann, I. R., Murphy, K. R., Jonathan Rae, I., and Milling, D. K. (2014). Analytic Expressions for ULF Wave Radiation belt Radial Diffusion Coefficients. *J. Geophys. Res. Space Phys.* 119, 1587–1605. doi:10.1002/2013JA019204

Patel, M., Li, Z., Hudson, M., Claudepierre, S., and Wygant, J. (2019). Simulation of Prompt Acceleration of Radiation belt Electrons during the 16 July 2017 Storm. *Geophys. Res. Lett.* 46, 7222–7229. doi:10.1029/2019GL083257

Pilipenko, V., Belakhovsky, V., Murr, D., Fedorov, E., and Engebretson, M. (2014). Modulation of Total Electron Content by Ulf Pc5 Waves. *J. Geophys. Res. Space Phys.* 119, 4358–4369. doi:10.1002/2013JA019594

Rankin, R., Wang, C. R., Wang, Y. F., Zong, Q., Zhou, X. Z., Degeling, A. W., et al. (2020). *Ultra-Low-Frequency Wave–Particle Interactions in Earth's Outer Radiation Belt*. (Hoboken, NJ: American Geophysical Union AGU), 189–205. chap. 11. doi:10.1002/9781119509592.ch11

Remya, B., Sibeck, D. G., Halford, A. J., Murphy, K. R., Reeves, G. D., Singer, H. J., et al. (2018). Ion Injection Triggered EMIC Waves in the Earth's Magnetosphere. *J. Geophys. Res. Space Phys.* 123, 4921–4938. doi:10.1029/2018JA025354

Ren, J., Zong, Q. G., Zhou, X. Z., Rankin, R., and Wang, Y. F. (2016). Interaction of Ulf Waves with Different Ion Species: Pitch Angle and Phase Space Density Implications. *J. Geophys. Res. Space Phys.* 121, 9459–9472. doi:10.1002/2016JA022995

Ren, J., Zong, Q. G., Zhou, X. Z., Spence, H. E., Funsten, H. O., Wygant, J. R., et al. (2019). Cold Plasmaspheric Electrons Affected by ULF Waves in the Inner Magnetosphere: A Van Allen Probes Statistical Study. *J. Geophys. Res. Space Phys.* 124, 7954–7965. doi:10.1029/2019JA027009

Sandhu, J. K., Rae, I. J., Staples, F. A., Hartley, D. P., Walach, M. T., Elsden, T., et al. (2021). The Roles of the Magnetopause and Plasmapause in Storm-Time ULF Wave Power Enhancements. *J. Geophys. Res. Space Phys.* 126. doi:10.1029/2021JA029337

Shang, X., Liu, S., Chen, L., Gao, Z., Wang, G., He, Q., et al. (2021). ULF-Modulation of Whistler-Mode Waves in the Inner Magnetosphere during Solar Wind Compression. *JGR Space Phys.* 126. doi:10.1029/2021ja029353

Shen, X.-C., Shi, Q., Wang, B., Zhang, H., Hudson, M. K., Nishimura, Y., et al. (2018). Dayside Magnetospheric and Ionospheric Responses to a Foreshock Transient on 25 June 2008: 1. FLR Observed by Satellite and Ground-Based Magnetometers. *J. Geophys. Res. Space Phys.* 123, 6335–6346. doi:10.1029/2018JA025349

Shi, X., Baker, J. B. H., Ruohoniemi, J. M., Hartinger, M. D., Murphy, K. R., Rodriguez, J. V., et al. (2018b). Long-Lasting Poloidal ULF Waves Observed by Multiple Satellites and High-Latitude SuperDARN Radars. *J. Geophys. Res. Space Phys.* 123, 8422–8438. doi:10.1029/2018JA026003

Shi, X., Ruohoniemi, J. M., Baker, J. B. H., Lin, D., Bland, E. C., Hartinger, M. D., et al. (2018a). Survey of Ionospheric Pc3-5 Ulf Wave Signatures in Superdarn High Time Resolution Data. *J. Geophys. Res. Space Phys.* 123, 4215–4231. doi:10.1029/2017JA025033

Shprits, Y. Y., Kellerman, A., Aseev, N., Drozdov, A. Y., and Michaelis, I. (2017). Multi-MeV Electron Loss in the Heart of the Radiation Belts. *Geophys. Res. Lett.* 44, 1204–1209. doi:10.1002/2016GL072258

Sigsbee, K., Kletzing, C. A., Faden, J. B., Jaynes, A. N., Reeves, G. D., and Jahn, J. M. (2020). Simultaneous Observations of Electromagnetic Ion Cyclotron (EMIC) Waves and Pitch Angle Scattering during a Van Allen Probes Conjunction. *J. Geophys. Res. Space Phys.* 125. doi:10.1029/2019JA027424

Sigsbee, K., Kletzing, C. A., Smith, C. W., MacDowall, R., Spence, H., Reeves, G., et al. (2016). Van Allen Probes, THEMIS, GOES, and Cluster Observations of EMIC Waves, ULF Pulsations, and an Electron Flux Dropout. *J. Geophys. Res. Space Phys.* 121, 1990–2008. doi:10.1002/2014JA020877

Søraas, F., Laundal, K. M., and Usanova, M. (2013). Coincident Particle and Optical Observations of Nightside Subauroral Proton Precipitation. *J. Geophys. Res. Space Phys.* 118, 1112–1122. doi:10.1002/jgra.50172

Soto-Chavez, A. R., Lanzerotti, L. J., Manweiler, J. W., Gerrard, A., Cohen, R., Xia, Z., et al. (2019). Observational Evidence of the Drift-Mirror Plasma Instability in Earth's Inner Magnetosphere. *Phys. Plasmas* 26, 042110. doi:10.1063/1.5083629

Takahashi, K., Hartinger, M. D., Angelopoulos, V., Glassmeier, K.-H., and Singer, H. J. (2013). Multispacecraft Observations of Fundamental Poloidal Waves without Ground Magnetic Signatures. *J. Geophys. Res. Space Phys.* 118, 4319–4334. doi:10.1002/jgra.50405

Thorne, R. M., and Horne, R. B. (1997). Modulation of Electromagnetic Ion Cyclotron Instability Due to Interaction with Ring Current O+during Magnetic Storms. *J. Geophys. Res.* 102, 14155–14163. doi:10.1029/96JA04019

Thorne, R. M., and Horne, R. B. (1992). The Contribution of Ion-Cyclotron Waves to Electron Heating and SAR-Arc Excitation Near the Storm-Time Plasmapause. *Geophys. Res. Lett.* 19, 417–420. doi:10.1029/92GL00089

Thorne, R. M., Li, W., Ni, B., Ma, Q., Bortnik, J., Chen, L., et al. (2013). Rapid Local Acceleration of Relativistic Radiation-belt Electrons by Magnetospheric Chorus. *Nature* 504, 411–414. doi:10.1038/nature12889

Thorne, R. M., Shprits, Y. Y., Meredith, N. P., Horne, R. B., Li, W., and Lyons, L. R. (2007). Refilling of the Slot Region between the Inner and Outer Electron Radiation Belts during Geomagnetic Storms. *J. Geophys. Res.* 112, a–n. doi:10.1029/2006JA012176

Trichtchenko, L. (2021). Frequency Considerations in Gic Applications. *Space Weather* 19, e2020SW002694. doi:10.1029/2020SW002694

Turner, D. L., Shprits, Y., Hartinger, M., and Angelopoulos, V. (2012). Explaining Sudden Losses of Outer Radiation belt Electrons during Geomagnetic Storms. *Nat. Phys* 8, 208–212. doi:10.1038/nphys2185

Usanova, M. E., Drozdov, A., Orlova, K., Mann, I. R., Shprits, Y., Robertson, M. T., et al. (2014). Effect of EMIC Waves on Relativistic and Ultrarelativistic Electron Populations: Ground-Based and Van allen Probes Observations. *Geophys. Res. Lett.* 41, 1375–1381. doi:10.1002/2013GL059024

Usanova, M. E. (2021). Energy Exchange between Electromagnetic Ion Cyclotron (EMIC) Waves and Thermal Plasma: From Theory to Observations. *Front. Astron. Space Sci.* 8. doi:10.3389/fspas.2021.744344

Usanova, M. E., Mann, I. R., and Darrouzet, F. (2016). EMIC Waves in the Inner Magnetosphere. *Wash. DC Am. Geophys. Union Geophys. Monogr. Ser.* 216, 65–78. doi:10.1002/9781119055006.ch5

Usanova, M. E., Mann, I. R., Kale, Z. C., Rae, I. J., Sydora, R. D., Sandanger, M., et al. (2010). Conjugate Ground and Multisatellite Observations of Compression-Related EMIC Pc1 Waves and Associated Proton Precipitation. *J. Geophys. Res.* 115, A07208. doi:10.1029/2009JA014935

Usanova, M., and Mann, I. (2016). "Waves, Particles, and Storms in Geospace," in *Waves, Particles and Storms in Geospace* (Hoboken, NJ: Oxford University Press). doi:10.1093/acprof:oso/9780198705246.001.0001

Verkhoglyadova, O. P., Meng, X., Mannucci, A. J., and McGranaghan, R. M. (2018). Semianalytical Estimation of Energy Deposition in the Ionosphere by Monochromatic Alfvén Waves. *J. Geophys. Res. Space Phys.* 123, 5210–5222. doi:10.1029/2017JA025097

Vines, S. K., Allen, R. C., Anderson, B. J., Engebretson, M. J., Fuselier, S. A., Russell, C. T., et al. (2019). EMIC Waves in the Outer Magnetosphere: Observations of an Off-Equator Source Region. *Geophys. Res. Lett.* 46, 5707–5716. doi:10.1029/2019GL082152

Vines, S. K., Anderson, B. J., Allen, R. C., Denton, R. E., Engebretson, M. J., Johnson, J. R., et al. (2021). Determining EMIC Wave Vector Properties through Multi-Point Measurements: The Wave Curl Analysis. *JGR Space Phys.* 126. doi:10.1029/2020JA028922

Wang, B., Liu, T., Nishimura, Y., Zhang, H., Hartinger, M., Shi, X., et al. (2020a). Global Propagation of Magnetospheric Pc5 ULF Waves Driven by Foreshock Transients. *J. Geophys. Res. Space Phys.* 125. doi:10.1029/2020JA028411

Wang, B., Nishimura, Y., Hartinger, M., Sivadas, N., Lyons, L. L., Varney, R. H., et al. (2020d). Ionospheric Modulation by Storm Time Pc5 ULF Pulsations and the Structure Detected by PFISR-THEMIS Conjunction. *Geophys. Res. Lett.* 47, e2020GL089060. doi:10.1029/2020GL089060

Wang, B., Nishimura, Y., Zhang, H., Shen, X. C., Lyons, L., Angelopoulos, V., et al. (2019). The 2-D Structure of Foreshock-Driven Field Line Resonances Observed by THEMIS Satellite and Ground-Based Imager Conjunctions. *J. Geophys. Res. Space Phys.* 124, 6792–6811. doi:10.1029/2019JA026668

Wang, C. P., Xing, X., Bortnik, J., and Chu, X. (2020b). Inward Propagation of Flow-Generated Pi2 Waves from the Plasma Sheet to the Inner Magnetosphere. *J. Geophys. Res. Space Phys.* 125, e27581. doi:10.1029/2019JA027581

Wang, D., Shprits, Y. Y., Zhelavskaya, I. S., Effenberger, F., Castillo, A. M., Drozdov, A. Y., et al. (2020c). The Effect of Plasma Boundaries on the Dynamic Evolution of Relativistic Radiation Belt Electrons. *J. Geophys. Res. Space Phys.* 125. doi:10.1029/2019JA027422

Wang, X. Y., Huang, S. Y., Allen, R. C., Fu, H. S., Deng, X. H., Zhou, M., et al. (2017). The Occurrence and Wave Properties of EMIC Waves Observed by the Magnetospheric Multiscale (MMS) mission. *J. Geophys. Res. Space Phys.* 122, 8228–8240. doi:10.1002/2017JA024237

Watson, C., Jayachandran, P. T., Singer, H. J., Redmon, R. J., and Danskin, D. (2016). Gps Tec Response to Pc4 "Giant Pulsations". *J. Geophys. Res. Space Phys.* 121, 1722–1735. doi:10.1002/2015JA022253

Watson, C., Jayachandran, P. T., Singer, H. J., Redmon, R. J., and Danskin, D. (2015). Large-amplitude GPS TEC Variations Associated with Pc5-6 Magnetic Field Variations Observed on the Ground and at Geosynchronous Orbit. *J. Geophys. Res. Space Phys.* 120, 7798–7821. doi:10.1002/2015JA021517

Wolf, R. A., Toffoletto, F. R., Schutza, A. M., and Yang, J. (2018). Buoyancy Waves in Earth's Magnetosphere: Calculations for a 2-D Wedge Magnetosphere. *J. Geophys. Res. Space Phys.* 123, 3548–3564. doi:10.1029/2017JA025006

Xia, Z., Chen, L., Zheng, L., and Chan, A. A. (2017). Eigenmode Analysis of Compressional Poloidal Modes in a Self-consistent Magnetic Field. *J. Geophys. Res. Space Phys.* 122, 10,369–10,381. doi:10.1002/2017JA024376

Yagova, N. V., Pilipenko, V. A., Sakharov, Y. A., and Selivanov, V. N. (2021). Spatial Scale of Geomagnetic Pc5/Pi3 Pulsations as a Factor of Their Efficiency in Generation of Geomagnetically Induced Currents. *Earth, Planets and Space* 73, 1–13. doi:10.1186/s40623-021-01407-2

Yahnin, A. G., Popova, T. A., Demekhov, A. G., Lubchich, A. A., Matsuoka, A., Asamura, K., et al. (2021). Evening Side EMIC Waves and Related Proton Precipitation Induced by a Substorm. *J. Geophys. Res. Space Phys.* 126, e29091. doi:10.1029/2020JA029091

Yamakawa, T., Seki, K., Amano, T., Takahashi, N., and Miyoshi, Y. (2020). Excitation of Internally Driven ULF Waves by the Drift-Bounce Resonance with Ring Current Ions Based on the Drift-Kinetic Simulation. *J. Geophys. Res. Space Phys.* 125, e2020JA028231. doi:10.1029/2020JA028231

Yamakawa, T., Seki, K., Amano, T., Takahashi, N., and Miyoshi, Y. (2019). Excitation of Storm Time Pc5 ULF Waves by Ring Current Ions Based on the Drift-Kinetic Simulation. *Geophys. Res. Lett.* 46, 1911–1918. doi:10.1029/2018GL081573

Yang, B., Zong, Q.-G., Wang, Y. F., Fu, S. Y., Song, P., Fu, H. S., et al. (2010). Cluster Observations of Simultaneous Resonant Interactions of Ulf Waves with Energetic Electrons and thermal Ion Species in the Inner Magnetosphere. *J. Geophys. Res.* 115, a–n. doi:10.1029/2009JA014542

Yue, C., Li, W., Nishimura, Y., Zong, Q., Ma, Q., Bortnik, J., et al. (2016). Rapid Enhancement of Low-energy (. *J. Geophys. Res. Space Phys.* 121, 6430–6443. doi:10.1002/2016JA022808

Zhai, C., Shi, X., Wang, W., Hartinger, M. D., Yao, Y., Peng, W., et al. (2021). Characterization of High-m ULF Wave Signatures in GPS TEC Data. *Geophys. Res. Lett.* 48. doi:10.1029/2021GL094282

Zhang, S., Tian, A., Degeling, A. W., Shi, Q., Wang, M., Hao, Y., et al. (2019a). Pc4-5 Poloidal ULF Wave Observed in the Dawnside Plasmaspheric Plume. *J. Geophys. Res. Space Phys.* 124, 9986–9998. doi:10.1029/2019JA027319

Zhang, X. J., Mourenas, D., Artemyev, A. V., Angelopoulos, V., and Sauvaud, J. A. (2019b). Precipitation of MeV and Sub-MeV Electrons Due to Combined Effects of EMIC and ULF Waves. *J. Geophys. Res. Space Phys.* 124, 7923–7935. doi:10.1029/2019JA026566

Zhao, X. X., Hao, Y. X., Zong, Q. G., Zhou, X. Z., Yue, C., Chen, X. R., et al. (2020). Origin of Electron Boomerang Stripes: Localized ULF Wave-Particle Interactions. *Geophys. Res. Lett.* 47, e87960. doi:10.1029/2020GL087960

Zong, Q.-G., Wang, Y. F., Zhang, H., Fu, S. Y., Zhang, H., Wang, C. R., et al. (2012). Fast Acceleration of Inner Magnetospheric Hydrogen and Oxygen Ions by Shock Induced ULF Waves. *J. Geophys. Res.* 117, a–n. doi:10.1029/2012JA018024

Zong, Q. (2021). Magnetospheric Response to Solar Wind Forcing: ULF Wave - Particle Interaction Perspective. *Ann. Geophysicae Discuss.* 2021, 1–68. doi:10.5194/angeo-2021-57

Zou, Z., Zuo, P., Ni, B., Gao, Z., Wang, G., Zhao, Z., et al. (2020). Two-step Dropouts of Radiation belt Electron Phase Space Density Induced by a Magnetic Cloud Event. *ApJ* 895, L24. doi:10.3847/2041-8213/ab9179

Conflict of Interest: The authors declare that the research was conducted in the absence of any commercial or financial relationships that could be construed as a potential conflict of interest.

frontiers | Frontiers in Physics

BRIEF RESEARCH REPORT
published: 11 May 2022
doi: 10.3389/fphy.2022.910193

The Role of Core and Strahlo Electrons Properties on the Whistler Heat-Flux Instability Thresholds in the Solar Wind

Bea Zenteno-Quinteros and Pablo S. Moya**

Departamento de Física, Facultad de Ciencias, Universidad de Chile, Santiago, Chile

There is wide observational evidence that electron velocity distribution functions (eVDF) observed in the solar wind generally present enhanced tails and field-aligned skewness. These properties may induce the excitation of electromagnetic perturbations through the whistler heat-flux instability (WHFI), that may contribute to a non-collisional regulation of the electron heat-flux values observed in the solar wind via wave-particle interactions. Recently, a new way to model the solar wind eVDF has been proposed: the core-strahlo model. This representation consist in a bi-Maxwellian core plus a Skew-Kappa distribution, representing the halo and strahl electrons as a single skewed distribution. The core-strahlo model is able to reproduce the main features of the eVDF in the solar wind (thermal core, enhanced tails, and skewness), with the advantage that the asymmetry is controlled by only one parameter. In this work we use linear kinetic theory to analyze the effect of solar wind electrons described by the core-strahlo model, over the excitation of the parallel propagating WHFI. We use parameters relevant to the solar wind and focus our attention on the effect on the linear stability introduced by different values of the core-to-strahlo density and temperature ratios, which are known to vary throughout the Heliosphere. We also obtain the stability threshold for this instability as a function of the electron beta and the skewness parameter, which is a better indicator of instability than the heat-flux macroscopic moment, and present a threshold conditions for the instability that can be compared with observational data.

Keywords: solar wind, heat-flux, electron instabilities, skew-kappa distributions, plasma waves

OPEN ACCESS

Edited by:
Misa Cowee,
Los Alamos National Laboratory (DOE), United States

Reviewed by:
Anton Artemyev,
Space Research Institute (RAS), Russia
Peter Haesung Yoon,
University of Maryland, College Park, United States

****Correspondence:***
Bea Zenteno-Quinteros
beatriz.zenteno@ug.uchile.cl
Pablo S. Moya
pablo.moya@uchile.cl

Specialty section:
This article was submitted to Space Physics, a section of the journal Frontiers in Physics

Received: *01 April 2022*
Accepted: *20 April 2022*
Published: *11 May 2022*

Citation:
Zenteno-Quinteros B and Moya PS (2022) The Role of Core and Strahlo Electrons Properties on the Whistler Heat-Flux Instability Thresholds in the Solar Wind. Front. Phys. 10:910193. doi: 10.3389/fphy.2022.910193

1 INTRODUCTION

Recent observations have shown that electron heat-flux measurements in the solar wind are not completely explained by the collisional transport model given by the Spitzer-Härm law [1]. The field aligned electron heat-flux at one AU from the Sun is consistent with this model only up to a Knudsen number $K_n \sim 0.3$, where K_n is the ratio between the mean free path and the temperature gradient scale. Beyond that, the observed heat-flux values are lower than those predicted by this law [2], which suggest that there exist non-collisional processes relevant to fully understand the electron thermal energy transport in the Heliosphere. Moreover, data also suggest that non-collisional mechanisms, e.g. electron micro-instabilities, may play an important role in the near-Sun environment as the heat-flux observations do not follow the Spitzer-Härm law for any range of the estimated K_n [3].

Electron heat-flux instabilities (HFI) in the solar wind are wave modes excited by the free energy provided by the skewness of the electron velocity distribution function (eVDF) along to the interplanetary magnetic field [4–6]. Among other non-thermal features of the eVDF, this field-

aligned skewness is clearly observed in solar wind's *in-situ* measurements [7–10]. Considering that the electron heat-flux is closely related to the eVDF skewness, the HFIs are the main candidates to be the non-collisional mechanism that self-regulate the heat-flux values in the solar wind, via wave-particle interactions. Therefore, they may explain the observed electron heat-flux profile in the solar wind [11–13]. Among these skewness-driven instabilities, the excitation of the whistler mode of the electron cyclotron branch, known as the whistler heat-flux instability (WHFI), has been often invoked as one of the most probable non collisional processes regulating the electron heat-flux [14–17]. However, the dominant wave mode is still under debate and recent works even suggest that it may not be possible to identify only one instability as the principal non-collisional mechanism [6]. Thus, studies regarding the electron heat-flux regulation in the solar wind should consider the interplay and/or succession of different instabilities [18].

Different theoretical and observational studies have tried to assess the importance of these HFI on the non-collisional regulation of the electron heat-flux in the solar wind. From the observational point of view, these studies focus on comparing measurements of the normalized electron heat-flux macroscopic moment in the solar wind with analytical expressions of marginal stability thresholds of electron HFI [2–4,19,20]. In Bale et al. [2] the authors contrast data obtained by the WIND spacecraft with theoretical thresholds values for the whistler and magnetosonic instabilities. They conclude that for the data set analyzed, the WHFI over constrain the observations, and the magnetosonic instability is more consistent in the collisionless regime when $K_n > 0.3$ and the plasma beta is large. In addition, in Halekas et al. [3] the authors used data provided by the Parker Solar Probe at heliocentric distances between 0.125 and 0.25 AU from the Sun, and concluded that the observed heat-flux dependence on plasma beta is consistent with theoretical thresholds associated with oblique whistler waves generated via the fan instability [21]. In contrast, in Cattell et al. [20], authors showed that whistlers waves are extremely rare inside ~0.13 AU and the heat-flux vs. beta relationship is not constrained by the heat-flux fan instability this close to the Sun.

Theoretical linear and quasilinear approximations, as well as particle simulations, have been used to address this issue. However, to develop these types of studies, it is necessary to model the eVDF. In the solar wind, the observed eVDF has been typically characterized in terms of three subpopulations: a quasithermal core at lower energies, which has most of the electron density; the suprathermal halo representing the enhanced high energy tails observed in the eVDF; and also the strahl, a suprathermal field-aligned beam which gives the eVDF its skewness. Under this context, different models have emerged to describe the plasma physics of solar wind electrons. Trying to mimic the observations, and to emulate the non-thermal characteristics of the electrons, most of the used models for the eVDF consists on the superposition of core, halo and/or strahl subpopulations. Among them, the most widely considered model consists on the superposition of two drifting bi-Maxwellian (typically core and strahl), which allows to have a skew distribution function [6,14–17]. More realistic models have also been used to describe the eVDF in the solar wind, where Kappa distribution functions are considered to reproduce the high energy tails (the halo) of the observed eVDF [12,22,23]. Furthermore, more exotic distributions have been also used to model the solar wind's suprathermal population, which by considering ad-hoc mathematical expressions are also able to address the electrons properties [21,24].

Under this context, a new way to describe the electron population in the solar wind has recently been proposed by Zenteno-Quinteros et al. [25] (from now on paper A). In this work, the authors propose the so called "core-strahlo model" as new way to describe the solar wind eVDF. This model consists on the sum of a drifting bi-Maxwellian (the core) and a Skew-Kappa function, representing halo and strahl in a single skew distribution. Therefore, using the superposition of only two functions, the model reproduces the three main kinetic features of the observed eVDF, namely: quasithermal core, enhanced tails and skewness. In paper A, the authors used the core-strahlo model and studied the effect of different plasma parameters on the excitation of the WHFI and its marginal stability thresholds. They showed that instead of the electron heat-flux moment q_e, which have been customarily used in to analyze the WHFI, the skewness parameter δ_s (i.e the parameter that controls the skewness of the core-strahlo distribution) is the most relevant when studying the WHFI. This is because high δ_s values rather than high q_e values are consistent with more unstable states to the WHFI when a more realistic representation is used to model the eVDF in the solar wind.

In paper A authors presented the core-strahlo model for the first time, and focused on the mathematical and technical details necessary to apply the model to the analysis of the whistler heat-flux instability (WHFI). They also compared the dispersion results with a two drifting Maxwellian model, and analyzed the instability as a function of the asymmetry parameter δ_s, the kappa parameter and also plasma beta. To do so they fixed the density of the strahlo and also the core-to-strahlo temperature ratio. Along the same lines, in this work we expand the analysis performed in paper A. Here we use the core-strahlo model to describe the electron population and examine how the WHFI behaves as the strahlo-to-core temperature ratio and the strahlo number density are modified. Thus, here we complement and complete the systematic analysis of the instability as a function of all relevant parameters that was started with paper A. Additionally, following Peter Gary's legacy, we obtain the marginal stability thresholds and analyze how they change as we modify these parameters. Indeed, *in situ* measurements show that these two parameters exhibit several values as a function of heliocentric distance and solar wind speed [26,27]. Thus, a systematic study on how the WHFI depends on density and temperature ratios of the solar subpopulations, becomes relevant for the understanding of the regulation of electron heat-flux in the solar wind. Accordingly, this article organized as follows: in **Section 2** we briefly describe the core-strahlo model and its properties, and performed the stability analysis of the parallel

propagating WHFI. In **Section 3** we obtain the marginal stability thresholds of the WHFI for different values of $T_{\parallel s}/T_{\parallel c}$ and n_s/n_e and present the best fit parameters for easier comparison with observational data. Finally, in **Section 4** we present the summary and conclusions of this work.

2 WHFI DISPERSION RELATION IN THE CONTEXT OF THE CORE-STRAHLO MODEL

To study the excitation of the parallel propagating whistler mode in a solar-wind-like plasma, we describe the electron population using the core-strahlo model. As already mentioned, this model was first proposed as a eVDF for the solar wind in paper A, where the authors showed that it is able to reproduce the quasi-thermal core, high energy tails, and field-aligned skewness observed in the eVDF. In this description, the electron distribution f_e is given by **Eq. 1** and consist on a superposition of a quasithermal core f_c, described by a drifting biMaxwellian; and a suprathermal strahlo f_s, described by a Skew-Kappa function.

$$f_e(v_\perp, v_\parallel) = f_c(v_\perp, v_\parallel) + f_s(v_\perp, v_\parallel), \tag{1}$$

where

$$f_c(v_\perp, v_\parallel) = \frac{n_c}{\pi^{3/2}\alpha_\perp^2\alpha_\parallel}\ \exp\left(-\frac{v_\perp^2}{\alpha_\perp^2} - \frac{(v_\parallel - U_c)^2}{\alpha_\parallel^2}\right), \tag{2}$$

and

$$f_s(v_\perp, v_\parallel) = n_s A_s\left[1 + \frac{1}{\kappa_s - \frac{3}{2}}\left(\frac{v_\perp^2}{\theta_\perp^2} + \frac{v_\parallel^2}{\theta_\parallel^2} + \delta_s\left(\frac{v_\parallel}{\theta_\parallel} - \frac{v_\parallel^3}{3\theta_\parallel^3}\right)\right)\right]^{-(\kappa_s+1)}. \tag{3}$$

In the above expressions the sub-indexes $\parallel$ and $\perp$ are with respect to the background magnetic field, n_c and n_s represent the core and strahlo number density, $\alpha_\parallel$ and $\alpha_\perp$ correspond to the thermal velocities of the core subpopulation, U_c is the core drift velocity, and $\theta_\parallel$ and $\theta_\perp$ are related to the thermal velocities of the strahlo. Additionally, the skewness parameter δ_s modifies the field-aligned skewness such that higher δ_s values indicate more skewed distributions. Furthermore, the kappa parameter κ_s controls the slope of the high energy tails such that as κ_s increases, the enhanced tails of distribution **Eq. 1** diminish (see Figure 3 in paper A). In paper A, the authors examined the behavior of the Skew-Kappa distribution **Eq. 3** in velocity space, which allowed them to establish a validity range for the core-strahlo model. Accordingly, we must impose small skweness i.e. $\delta_s^3 \ll 1$ for this description to be applicable as a distribution function for the solar wind's electrons. Moreover, the core-strahlo model must fulfill the quasi-neutrality condition:

$$n_c + n_s = n_e = n_p, \tag{4}$$

and also be current-free (see paper A for details).

$$U_c = \frac{n_s}{n_c}\frac{\delta_s}{4}\theta_\parallel. \tag{5}$$

As we previously pointed out, it has been reported in several works that the values of the relative density of the non-thermal electron population (the strahlo in this representation) and the temperature ratio between different subpopulations vary throughout the Heliosphere. Thus, it becomes relevant to understand how the total eVDF modifies with these parameters and the impact these changes have on the WHFI. In addition, $T_{\parallel s}/T_{\parallel c}$ and $\eta_s = n_s/n_e$ are the last two parameters that determine the shape of distribution **Eq. 1** that remains to be analyzed in the isotropic case ($\alpha_\perp = \alpha_\parallel$, and $\theta_\perp = \theta_\parallel$). Accordingly, **Figure 1** shows parallel cuts at $v_\perp = 0$ (left panels) and contour plots (right panels) of the core-strahlo distribution for: fixed $T_{\parallel s}/T_{\parallel c} = 7.0$ and different values the relative density of the strahlo subpopulation $\eta_s = 0.04, 0.08, 0.12$ (top panels); and fixed $\eta_s = 0.08$ with different values of the strahlo-to-core parallel temperature ratio $T_{\parallel s}/T_{\parallel c} = 5.0, 7.0, 9.0$ (bottom panels). To obtain all these plots, we consider isotropic core and strahlo distributions, with a skewness parameter $\delta_s = 0.2$, and a kappa parameter $\kappa_s = 3.0$. We can notice in this figure that the core-strahlo distribution display field-aligned skewness, enhanced tails and a narrower Maxwellian core, as was already established. From Panels 1A and 1B, we can see that the relative density of the strahlo subpopulation modifies the high energy tail of the distribution so that the tails of the distribution are enhanced, as the Skew-Kappa function describing the strahlo goes up, with increasing η_s. We can also notice that changes in η_s have a minor effect on the quasithermal core of the eVDF. Namely, as η_s increases the core has a slight decrease in amplitude.

Moreover, from panel 1A it seems that the slope of these energetic tails is not altered with η_s. The field-aligned skewness of the core-strahlo distribution appears to remain unchanged as well, which is more evident in the contour plot shown in panel 1B (compared with Figure 3B on paper A). We encounter a similar behavior when we modify the strahlo-to-core temperature ratio $T_{\parallel s}/T_{\parallel c}$, as we can see in panels 1C and 1D. It is clear that this parameter also modifies the high energy tails of the core-strahlo distribution, as the Skew-Kappa function describing the strahlo subpopulation widens with increasing $T_{\parallel s}/T_{\parallel c}$. We can also see that for higher values of $T_{\parallel s}/T_{\parallel c}$, the energetic tails are enhanced but, unlike the previous parameter, the Maxwellian core appears to remain the same. Moreover, it seems that the skewness of the core-strahlo distribution does not change when $T_{\parallel s}/T_{\parallel c}$ is modified, which is noticeable in the contour plot shown in panel 1D. Accordingly, both parameters, the strahlo-to-core temperature ratio and the density of the strahlo subpopulation, can alter the tails of distribution 1. The general behavior is that as $T_{\parallel s}/T_{\parallel c}$ and η_s decrease, the high energy tails diminish, while maintaining the skewness of the distribution unaltered. For both parameters we have use representative values that have been measured in the solar wind at different solar distances [27,28]. This dependence of the core-strahlo distribution on $T_{\parallel s}/T_{\parallel c}$ and η_s may influence the excitation of the WHFI, which we will study next. It is worth mentioning that it is the field-aligned skweness the non-thermal feature that provides the free energy for the excitation of the WHFI and, in this representation, it can be modified mostly through the skewness parameter δ_s. Nevertheless, as $T_{\parallel s}/T_{\parallel c}$ and η_s can also

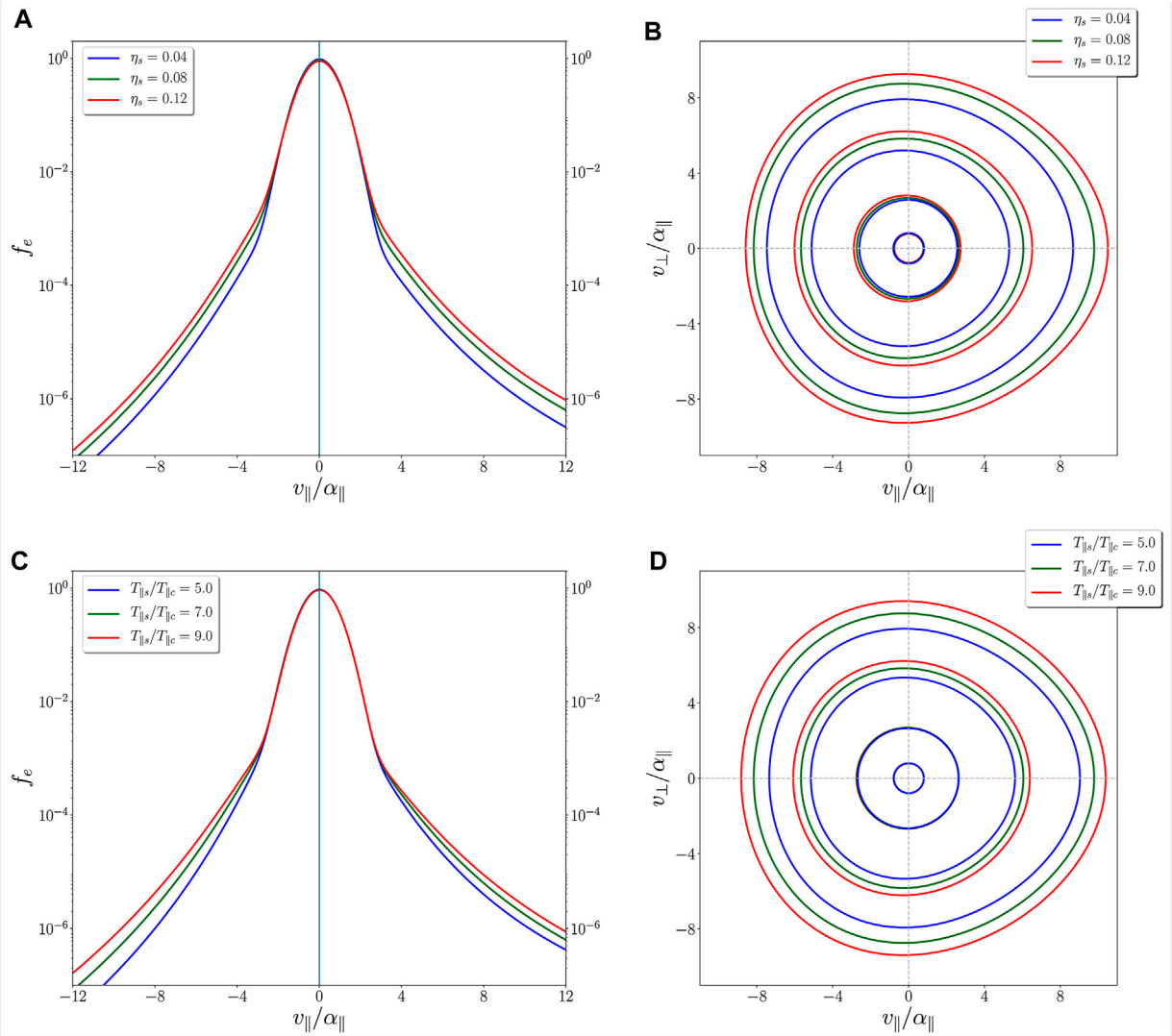

FIGURE 1 | Parallel cuts (left) and contour plots (right) of the core-strahlo distribution from **Eq. 1**. Panels A and B consider fixed $T_{\|s}/T_{\|c}$ =7.0, and different densities η_s =0.04 (blue), η_s =0.08 (green), and η_s =0.12 (red); Panels C and D consider fixed density (η_s =0.08), and different temperature ratios $T_{\|s}/T_{\|c}$ =5.0 (blue), $T_{\|s}/T_{\|c}$ =7.0 (green), and $T_{\|s}/T_{\|c}$ =7.0 (red). In all panels, we considered a skewness parameter δ_s =0.2, a kappa parameter κ_s =3.0 and set the anisotropy for the electron core and strahlo equal to one.

regulate the shape of the eVDF, and there is wide evidence that these parameters have several values throughout the Heliosphere, here we focus our analysis on the effect of them on the WHFI.

2.1 WHFI Dispersion Relation

Now we focus on the stability of the WHFI and study the effect $T_{\|s}/T_{\|c}$ and η_s have on the dispersion relation of the parallel propagating whistler mode. We model the solar wind populations using the core-strahlo distribution (**Eq.(1)**) for the electrons and a Maxwellian function for the protons. The procedure to obtain the dispersion relation for wave modes that propagate in this system parallel to the background magnetic field $\vec{B}_0 = B_0\hat{z}$ such that $\vec{k} = k\hat{z}$ was already discussed in detail in paper A, where an analytical expression for the dispersion tensor in the validity range of the model (i.e $\delta_s^3 \ll 1$) can be found (see Appendix B in paper A). The dispersion relation $\omega = \omega(k)$ between the wavenumber k and the complex wave frequency $\omega = \omega_r + i\gamma$ for the parallel propagating WHFI is obtained numerically in this analysis. We consider a proton population such that $\beta_{\|p} = 0.1$ where $\beta_{\|j}$ is the plasma beta of population j. For the eVDF we again set the kappa parameter to κ_s = 3.0, the skewness parameter to δ_s = 0.2 and work with isotropic subpopulations such that $T_{\perp c}/T_{\|c} = 1.0$ and $T_{\perp s}/T_{\|s} = 1.0$, We also fix the strength of the background magnetic field so that $\beta_{\|s} = 1.0$ and set the ratio between the electron plasma frequency (ω_{pe}) and electron gyrofrequency (Ω_e) to $\omega_{pe}/|\Omega_e| = 200$. Hence, with this selection of parameters, the only relevant non-thermal features in the study are the high energy tails and field-aligned skewness. Lastly, to analyze how the excitation of the whistler

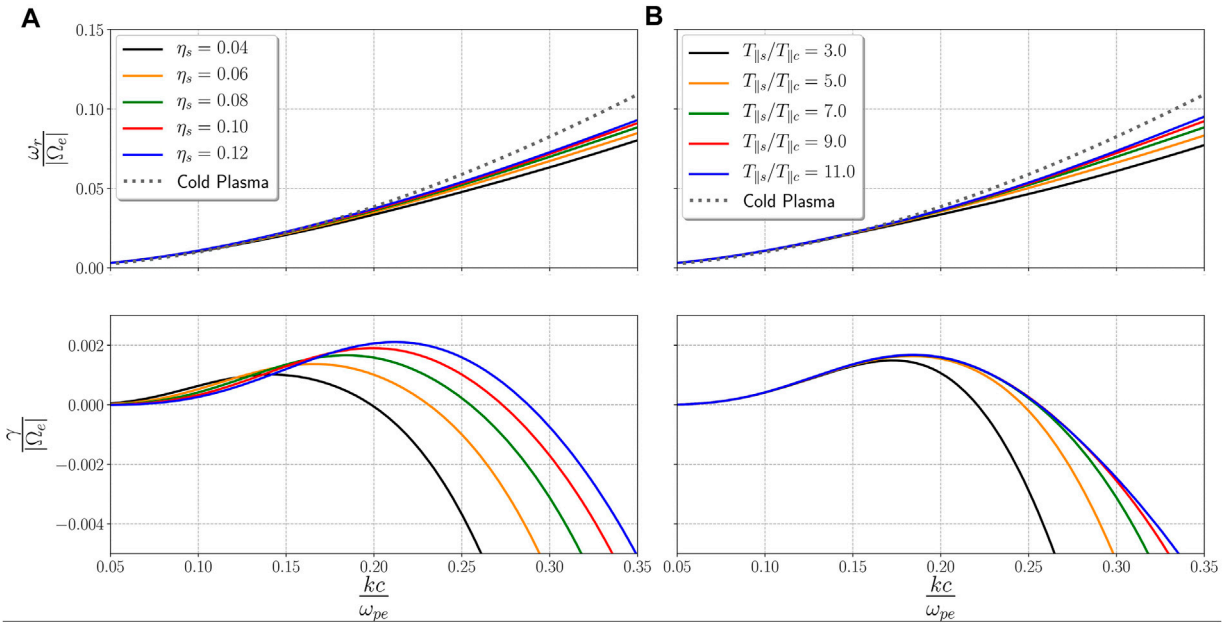

FIGURE 2 | Real (top) and imaginary (bottom) parts of the dispersion relation $\omega = \omega(k)$ for the whistler mode. Panel **(A)** consider $T_{\|s}/T_{\|c}$ =7.0 and different η_s. Panel **(B)** consider η_s =0.08 and different $T_{\|s}/T_{\|c}$ values. For these plots, we set $\beta_{\|s}$ =1.0 and all other parameters are the same as in **Figure 1**.

mode depends on η_s and $T_{\|s}/T_{\|c}$, we use values between $T_{\|s}/T_{\|c}$ = 3.0 and $T_{\|s}/T_{\|c}$ = 11.0 for the strahlo-to-core parallel temperature ratio and relative density for the strahlo up to 12% (i.e η_s = 0.12), all of which have been measured in the solar wind as reported by Lazar et al. [27].

Figure 2 shows the dispersion relation of the parallel-propagating whistler mode for: fixed $T_{\|s}/T_{\|c}$ = 7.0 and different values of η_s (left panel) and fixed η_s = 0.08 and different $T_{\|s}/T_{\|c}$ values (right panel). Top and bottom panels show, respectively, the real frequency ω_r and imaginary frequency γ, both expressed in units of $|\Omega_e|$ and as a function of the normalized wavenumber kc/ω_{pe}, where c/ω_{pe} is the electron inertial length. From Panel 2A we can see that, in the wavenumber range shown, the real part of the frequency has weak dependence on η_s such that ω_r slightly increases with this parameter. For comparison purposes we also include the cold plasma dispersion relation. We can see that for the case of the cold dispersion the frequency is larger, which is expected and consistent with previous studies (see e.g. [16]). From the imaginary part of the frequency, γ, we can see that the waves become more unstable as the strahlo relative density increases: the wavenumber range in which $\gamma > 0$ widens and the maximum growth rate value $\gamma_{\max}$ for this mode increases with η_s. Considering that the strahlo is the subpopulation that provides the free energy to radiate, it is expected the plasma to become more unstable with increasing η_s, as a higher value of this parameter represents a more important non-thermal subpopulation relative to the core, as shown in **Figure 1A**. This is consistent with similar already reported results but based on a model composed by two drifting Maxwellian VDFs (see for example Figure 3 in Gary [29]).

On the other hand, from panel 2B we can see that the real part of the frequency decreases when the strahlo-to-core temperature ratio decreases. The imaginary part γ, however, does not have such a straightforward behavior. For lower values of $T_{\|s}/T_{\|c}$, the wave mode becomes more unstable as this parameter increases, which is noticeable for the solutions with $T_{\|s}/T_{\|c}$ = 3.0 and $T_{\|s}/T_{\|c}$ = 5.0 (black and yellow curves, respectively). The wavenumber range in which the growth rates are positive widens and $\gamma_{\max}$ slightly increases with increasing $T_{\|s}/T_{\|c}$. From $T_{\|s}/T_{\|c}$ = 5.0 onward, however, the changes in γ with temperature ratio are barely noticeable and the curves remain almost the same. This behavior is maintained for even higher $T_{\|s}/T_{\|c}$ values than those shown in this plot. Therefore, a higher temperature (with respect to the core) of the subpopulation that provides the free energy (i.e the strahlo), does not further destabilize the plasma above the saturation point $T_{\|s}/T_{\|c} \approx 5.0$. A similar result can be seen in Figure 5b of paper A, where the growth rates also saturate at $T_{\|s}/T_{\|c} \approx 5.0$ for other plasma parameters. The complete characterization of the saturation point seems interesting, especially when considering that other models do not present this feature (see figure 4 in Gary [29], for example) but it requires a more in-depth analysis, beyond the scope of this study.

In summary, as we are using values relevant for the solar wind plasma, it is important to emphasize that the changes introduced by $T_{\|s}/T_{\|c}$ and η_s on the stability of the parallel propagating whistler mode, regardless how weak they seem), may have an impact on the thresholds we use to compare with observational data. This may be relevant to assess the importance of the WHFI, and the relative importance of its marginal stability thresholds, in the non-collisional regulation of the electron heat-flux in the solar wind.

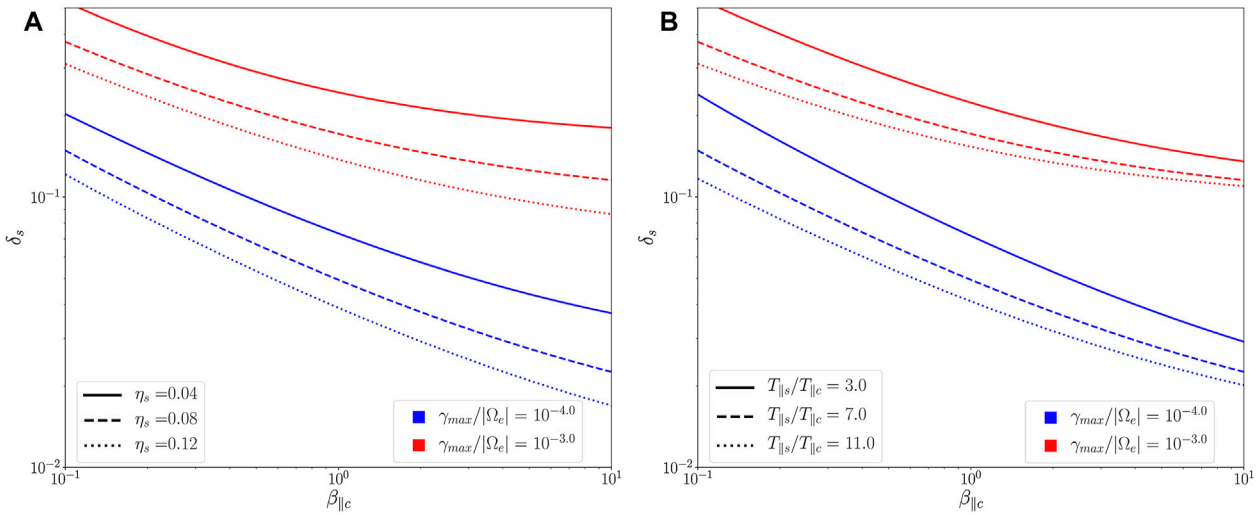

FIGURE 3 | Instability thresholds $\gamma_{max}/|\Omega_e|=10^{-3}$ (red lines) and $\gamma_{max}/|\Omega_e|=10^{-4}$ (blue lines) of the whistler heat-flux instability for **(A)** $T_{\parallel s}/T_{\parallel c}$ =7.0 and different η_s values **(B)** η_s =0.08 and different $T_{\parallel s}/T_{\parallel c}$ values. All calculations were performed using isotropic subpopulations and κ_s =3.0.

3 WHFI β AND δ THRESHOLDS

In this section, we systematize the linear analysis of the parallel propagating WHFI and present the marginal stability thresholds for this mode as function of δ_s and $\beta_{\parallel c}$. To obtain these thresholds, we describe the plasma populations as in the previous section. We use a Maxwellian distribution to model the protons and set $\beta_{\parallel p} = 0.1$. For the electrons we use the core-strahlo distribution with isotropic subpopulations and set $\kappa_s = 3.0$. Thus, with all these fixed parameters, we calculate the normalized maximum growth rate $\gamma_{\max}/|\Omega_e|$ of the parallel propagating whistler mode in the $\delta_s - \beta_{\parallel c}$ space. We repeat this procedure for different values of η_s and $T_{\parallel s}/T_{\parallel c}$ (as previously reported using solar wind electron measurements) to understand under which plasma conditions the whistler mode destabilize in the context of the core-strahlo model. Following the suggestion proposed in paper A, here we are presenting the stability thresholds as a function of the skewness parameter δ_s instead of the electron heat-flux macroscopic parameter $q_{\parallel e}$, which has been customarily used for this purpose in the past. As $q_{\parallel e}$ is a moment of the distribution function, its expression depends on all the parameters that determine its shape in velocity space. In our case, the analytical expression for the electron heat-flux in the validity range of the core-strahlo model, when considering isotropic subpopulations, is given by

$$\frac{q_{\parallel e}}{q_0} = \frac{\delta_s}{3}\frac{n_s}{n_e}\left(\frac{T_{\parallel s}}{T_{\parallel c}}\right)^{\frac{3}{2}}\left[\frac{7}{4\kappa_s - 10} + \frac{5}{4}\frac{T_{\parallel c}}{T_{\parallel s}} - \frac{3}{4}\right], \tag{6}$$

where q_0 is the free-streaming heat-flux (see paper A for details). As shown in **Eq. 6**, for fixed κ_s the heat-flux moment depends on all relevant parameters, and can have the same value for different combinations between them. Thus, to avoid this issue we solve the dispersion relation in the $\delta_s - \beta_{\parallel c}$ space. Nevertheless, using **Eq. 6** it is not difficult to find the same thresholds in terms of $q_{\parallel e}/q_0$ and $\beta_{\parallel c}$.

Figure 3 shows the contour levels $\gamma_{\max}/|\Omega_e| = 10^{-3}$ (red lines) and $\gamma_{\max}/|\Omega_e| = 10^{-4}$ (blue lines) of the normalized maximum growth rate for different values of η_s (left panel) and $T_{\parallel s}/T_{\parallel c}$ (right panel). Panel 3A shows these thresholds for a fixed value of $T_{\parallel s}/T_{\parallel c} = 7.0$, and $\eta_s = 0.04$, 0.08 and 0.12 (solid, dashed and pointed lines, respectively). We can see the thresholds move down and to the left as we increase the strahlo relative density. As expected, the plasma is more easily destabilize for higher values of η_s. In other words, as we increase η_s, lower values of δ_s or $\beta_{\parallel c}$ are needed to produce the same growth rate of the WHFI. On the other hand, Panel 3B shows the contours for $T_{\parallel s}/T_{\parallel c} = 3.0$, 7.0 and 11.0 (solid, dashed and pointed lines, respectively) and fixed $\eta_s = 0.08$. We can see the same trend as in the previous plot. The plasma becomes more unstable to the parallel propagating WHFI as $T_{\parallel s}/T_{\parallel c}$ increases, so that the thresholds move to the left and downward.

Finally, to facilitate the comparison between observational data and the linear prediction for the stability of the WHFI, we fit the contour lines $\gamma_{\max}/|\Omega_e| = 10^{-3}$ and 10^{-4} using a generalized Lorentzian function; namely

$$\delta_s = A + \frac{B}{\left(\beta_{\parallel c} - \epsilon_0^2\right)^{\alpha}}. \tag{7}$$

The best-fit value for parameters A, B, ϵ_0 and α of every threshold shown in **Figure 3** can be seen in **Table 1** for direct comparison with data in the beta range shown. With the results shown for η_s and $T_{\parallel s}/T_{\parallel c}$, we have established that each of them modify the stability of the whistler mode in a distinct way and with different strength. This reinforce the conclusion that it is not possible to assess if a plasma state is stable to the WHFI through

TABLE 1 | Best fit parameters for the $\gamma_{max}/|\Omega_e|=10^{-3}$ and 10^{-4} thresholds of the whistler heat-flux instability. The curve fitting for these thresholds was performed using the function shown in **Eq. 7**.

—	—	—	*A*	*B*	ϵ_0	α
$\gamma_{max} = 10^{-3}$	$\eta_s = 0.04$	$T_{\parallel s}/T_{\parallel c} = 7.0$	0.162	0.082	2.4×10^{-4}	0.648
		$T_{\parallel s}/T_{\parallel c} = 3.0$	0.102	0.122	4.9×10^{-6}	0.559
	$\eta_s = 0.08$	$T_{\parallel s}/T_{\parallel c} = 7.0$	0.094	0.077	4.8×10^{-6}	0.562
		$T_{\parallel s}/T_{\parallel c} = 11.0$	0.093	0.061	7.1×10^{-5}	0.557
	$\eta_s = 0.12$	$T_{\parallel s}/T_{\parallel c} = 7.0$	0.065	0.073	3.2×10^{-6}	0.530
$\gamma_{max} = 10^{-4}$	$\eta_s = 0.04$	$T_{\parallel s}/T_{\parallel c} = 7.0$	0.023	0.050	1.5×10^{-5}	0.554
		$T_{\parallel s}/T_{\parallel c} = 3.0$	0.013	0.059	0.117	0.553
	$\eta_s = 0.08$	$T_{\parallel s}/T_{\parallel c} = 7.0$	0.012	0.037	0.094	0.541
		$T_{\parallel s}/T_{\parallel c} = 11.0$	0.012	0.029	0.076	0.540
	$\eta_s = 0.12$	$T_{\parallel s}/T_{\parallel c} = 7.0$	0.008	0.031	0.107	0.538

$q_{\parallel e}$ without having additional information about the shape of the distribution and its dependence on all plasma parameters. Therefore, we believe that the role of WHFI in the relaxation process of plasma states should be studied in terms of microscopic parameters that determine the eVDF and not only macroscopic moments.

4 SUMMARY AND CONCLUSION

In this work we have used the core-strahlo model to describe the eVDF in the solar wind, and analyzed the stability of the parallel propagating whistler mode in a magnetized non collisional plasma. We have shown how the electron distribution modifies with the strahlo relative density and the strahlo-to-core temperature ratio density, and the impact these changes have on the excitation of the WHFI, as well as in the stability thresholds in delta-beta space. The general behavior is that as η_s and $T_{\parallel s}/T_{\parallel c}$ increase, the plasma becomes more unstable to the WHFI. However, the dependence on $T_{\parallel s}/T_{\parallel c}$ is much weaker, and above certain level ($T_{\parallel s}/T_{\parallel c} \sim 5$) the changes in growth rates are no longer noticeable. We have also shown the enhancing effect of η_s and $T_{\parallel s}/T_{\parallel c}$ on the stability thresholds in delta-beta space and provided the best-fit parameters for comparison with observations. With these results we have studied the dependence of the stability of the whistler mode on all the parameters that determine the shape of the eVDF in the isotropic case. Therefore, the usage of the core-strahlo model allowed us to study the WHFI in all the relevant parameter space in a manageable way, but considering a realistic representation of the solar wind electron population, including quasi-thermal core, high energy tails, and field-aligned skewness in the analysis all at once. It is important to mention that, besides the asymmetry represented by the heat-flux, temperature anisotropy should also play a role. However, as shown by several studies, among the anisotropic states, the isotropic state is also ubiquitous to the solar wind at different solar distances and solar wind speeds (see e.g. [27,30]), and here we have focused on the effect of asymmetry by itself. A systematic study on the combined effect of both free energy sources (asymmetry and anisotropy), and the subsequent interplay between the WHFI and electron-cyclotron or firehose instabilities should be also relevant but is beyond the scope of this study.

As mentioned, it has been reported in several works that the parameters here studied change with radial distance from the Sun [20,27,28]. For example, in Lazar et al. [27], the authors showed that the average temperature ratio between the halo and core subpopulations varies from $T_h/T_c \sim 8$ at one AU, to $T_h/T_c \sim 3$ at 0.3 AU. A variation with solar wind conditions (slow and fast wind) also exists, such that even at a given radial distance the measurements vary considerably, ranging between $T_h/T_c \sim 2$ and $T_h/T_c \sim 15$ at one AU for the temperature ratio, and between less that 1% up to 15% for the relative density of the halo (see Figures 2, 3 in Lazar et al. [27]). Accordingly, we believe that efforts should be made, to take into consideration the real impact that these parameters have on the stability of the WHFI. This should be particularly relevant when assessing the WHFI relevance on the non-collisional regulation of the heat-flux through comparison between theoretical prediction and data. We expect these predictions to be assessed and validated with electron measurements obtained with current and new solar wind missions. Systematic theoretical studies considering realistic solar wind conditions, and also comparisons between the results obtained with different kinetic model of the solar wind plasma, may be relevant in order to adequately understand the heat-flux transport through the Heliosphere.

DATA AVAILABILITY STATEMENT

The original contributions presented in the study are included in the article, further inquiries can be directed to the corresponding authors.

AUTHOR CONTRIBUTIONS

All authors listed have made a substantial, direct and intellectual contribution to the work, and approved it for publication. All authors contributed equally to this work.

FUNDING

This research was funded by ANID, Chile through the Doctoral National Scholarship N°21181965 (BZ-Q) and FONDECyT grant No. 1191351 (PM).

ACKNOWLEDGMENTS

We would like to thank Adolfo F. Viñas for useful discussion. We also gratefully acknowledge the support by ANID, Chile through a Doctoral Scholarship and a Fondecyt grant.

REFERENCES

1. Spitzer L, Jr, Härm R. Transport Phenomena in a Completely Ionized Gas. *Phys. Rev.* (1953) 89:977–81. doi:10.1103/physrev.89.977
2. Bale SD, Pulupa M, Salem C, Chen CHK, Quataert E. Electron Heat Conduction in the Solar Wind: Transition from Spitzer-Härm to the Collisionless Limit. *Astrophysical J* (2013) 769:L22. doi:10.1088/2041-8205/769/2/l22
3. Halekas JS, Whittlesey PL, Larson DE, McGinnis D, Bale SD, Berthomier M, et al. Electron Heat Flux in the Near-Sun Environment. *A&A* (2021) 650:A15. doi:10.1051/0004-6361/202039256
4. Gary SP, Skoug RM, Daughton W. Electron Heat Flux Constraints in the Solar Wind. *Phys Plasmas* (1999) 6:2607–12. doi:10.1063/1.873532
5. Shaaban SM, Lazar M, Yoon PH, Poedts S. Beaming Electromagnetic (Or Heat-Flux) Instabilities from the Interplay with the Electron Temperature Anisotropies. *Phys Plasmas* (2018) 25:082105. doi:10.1063/1.5042481
6. López RA, Lazar M, Shaaban SM, Poedts S, Moya PS. Alternative High-Plasma Beta Regimes of Electron Heat-Flux Instabilities in the Solar Wind. *Astrophysical J* (2020) 900:L25. doi:10.3847/2041-8213/abaf56
7. Feldman WC, Asbridge JR, Bame SJ, Montgomery MD, Gary SP. Solar Wind Electrons. *J. Geophys. Res.* (1975) 80:4181–96. doi:10.1029/ja080i031p04181
8. Pilipp WG, Miggenrieder H, Mühlhäuser K-H, Rosenbauer H, Schwenn R, Neubauer FM. Variations of Electron Distribution Functions in the Solar Wind. *J. Geophys. Res.* (1987) 92:1103–18. doi:10.1029/ja092ia02p01103
9. Nieves-Chinchilla T, Viñas AF. Solar Wind Electron Distribution Functions inside Magnetic Clouds. *J Geophys Res Space Phys* (2008) 113:12703. doi:10.1029/2007ja012703
10. Štverák Š, Maksimovic M, Trávníček PM, Marsch E, Fazakerley AN, Scime EE. Radial Evolution of Nonthermal Electron Populations in the Low-Latitude Solar Wind: Helios, Cluster, and Ulysses Observations. *J Geophys Res Space Phys* (2009) 114:A05104. doi:10.1029/2008JA013883
11. Gary SP, Feldman WC, Forslund DW, Montgomery MD. Heat Flux Instabilities in the Solar Wind. *J. Geophys. Res.* (1975) 80:4197–203. doi:10.1029/ja080i031p04197
12. Shaaban SM, Lazar M, Poedts S. Clarifying the Solar Wind Heat Flux Instabilities. *Mon Notices R Astronomical Soc* (2018) 480:310–9. doi:10.1093/mnras/sty1567
13. López RA, Shaaban SM, Lazar M, Poedts S, Yoon PH, Micera A, et al. Particle-in-cell Simulations of the Whistler Heat-Flux Instability in Solar Wind Conditions. *Astrophys J Lett* (2019) 882:L8. doi:10.3847/2041-8213/ab398b
14. Gary SP, Scime EE, Phillips JL, Feldman WC. The Whistler Heat Flux Instability: Threshold Conditions in the Solar Wind. *J. Geophys. Res.* (1994) 99:23391–9. doi:10.1029/94ja02067
15. Gary SP, Li H. Whistler Heat Flux Instability at High Beta. *Astrophysical J* (2000) 529:1131–5. doi:10.1086/308294
16. Kuzichev IV, Vasko IY, Soto-Chavez AR, Tong Y, Artemyev AV, Bale SD, et al. Nonlinear Evolution of the Whistler Heat Flux Instability. *Astrophysical J* (2019) 882:81. doi:10.3847/1538-4357/ab3290
17. Shaaban SM, Lazar M, Yoon PH, Poedts S, López RA. Quasi-linear Approach of the Whistler Heat-Flux Instability in the Solar Wind. *Mon Notices R Astronomical Soc* (2019) 486:4498–507. doi:10.1093/mnras/stz830
18. Shaaban SM, Lazar M, Yoon PH, Poedts S. The Interplay of the Solar Wind Core and Suprathermal Electrons: A Quasilinear Approach for Firehose Instability. *Astrophysical J* (2019) 871:237. doi:10.3847/1538-4357/aaf72d
19. Tong Y, Vasko IY, Artemyev AV, Bale SD, Mozer FS. Statistical study of whistler waves in the solar wind at 1 au. *Astrophysical J* (2019) 878:41. doi:10.3847/1538-4357/ab1f05
20. Cattell C, Breneman A, Dombeck J, Hanson E, Johnson M, Halekas J, et al. Parker Solar Probe Evidence for the Absence of Whistlers Close to the Sun to Scatter Strahl and to Regulate Heat Flux. *Astrophysical J Lett* (2022) 924:L33. doi:10.3847/2041-8213/ac4015
21. Vasko IY, Krasnoselskikh V, Tong Y, Bale SD, Bonnell JW, Mozer FS. Whistler Fan Instability Driven by Strahl Electrons in the Solar Wind. *Astrophysical J* (2019) 871:L29. doi:10.3847/2041-8213/ab01bd
22. Saeed S, Sarfraz M, Yoon PH, Lazar M, Qureshi MNS. Electron Heat Flux Instability. *Mon. Not. R. Astron. Soc.* (2016) 465:1672–81. doi:10.1093/mnras/stw2900
23. Lazar M, Shaaban SM, Fichtner H, Poedts S. Temperature Anisotropy Instabilities Stimulated by the Interplay of the Core and Halo Electrons in Space Plasmas. *Phys Plasmas* (2018) 25:022902. doi:10.1063/1.5016261
24. Horaites K, Boldyrev S, Medvedev MV. Electron Strahl and Halo Formation in the Solar Wind. *Mon Notices R Astronomical Soc* (2018) 484:2474–81. doi:10.1093/mnras/sty3504
25. Zenteno-Quinteros B, Viñas AF, Moya PS. Skew-kappa Distribution Functions and Whistler Heat Flux Instability in the Solar Wind: The Core-Strahlo Model. *Astrophysical J* (2021) 923:180. doi:10.3847/1538-4357/ac2f9c
26. Maksimovic M, Zouganelis I, Chaufray J-Y, Issautier K, Scime E, Littleton J, et al. Radial evolution of the electron distribution functions in the fast solar wind between 0.3 and 1.5 au. *J Geophys Res Space Phys* (2005) 110. doi:10.1029/2005ja011119
27. Lazar M, Pierrard V, Poedts S, Fichtner H. Characteristics of Solar Wind Suprathermal Halo Electrons. *A&A* (2020) 642:A130. doi:10.1051/0004-6361/202038830
28. Pierrard V, Lazar M, Poedts S, Štverák Š, Maksimovic M, Trávníček PM. The Electron Temperature and Anisotropy in the Solar Wind. Comparison of the Core and Halo Populations. *Sol Phys* (2016) 291:2165–79. doi:10.1007/s11207-016-0961-7
29. Gary SP. Electromagnetic Electron Beam Instabilities: Hot, Isotropic Beams. *J. Geophys. Res.* (1985) 90:10815–22. doi:10.1029/JA090iA11p10815
30. Adrian ML, Viñas AF, Moya PS, Wendel DE. Solar Wind Magnetic Fluctuations and Electron Non-thermal Temperature Anisotropy: Survey of Wind-Swe-Veis Observations. *Astrophys. J.* (2016) 833:10. doi:10.3847/1538-4357/833/1/49

Conflict of Interest: The authors declare that the research was conducted in the absence of any commercial or financial relationships that could be construed as a potential conflict of interest.

Publisher's Note: All claims expressed in this article are solely those of the authors and do not necessarily represent those of their affiliated organizations, or those of the publisher, the editors and the reviewers. Any product that may be evaluated in this article, or claim that may be made by its manufacturer, is not guaranteed or endorsed by the publisher.

frontiers | Frontiers in Astronomy and Space Sciences

ORIGINAL RESEARCH
published: 16 May 2022
doi: 10.3389/fspas.2022.899642

Linear Theory of Electromagnetic Ion Beam Instabilities in the Earth's Foreshock: Peter Gary's Contributions (1981–1991)

Dan Winske[1]* *and Lynn B. Wilson III*[2]

[1]Retired Laboratory Fellow, Los Alamos National Laboratory, Los Alamos, NM, United States, [2]Heliophysics Science Division, NASA Goddard Space Flight Center, Greenbelt, MD, United States

We discuss Peter Gary's contributions to the understanding of the origin and properties of ultra-low frequency (ULF) waves in the Earth's foreshock during the period when the International Sun Earth Explorer spacecraft (ISEE-1 and -2) provided unique data about the plasma and wave environment in this region. Peter's work concerning the linear theory of electromagnetic ion beam instabilities is contained in five journal articles and then summarized in a review article, all of which are discussed here. Brief summaries of observations and theory prior to ISEE as well as to later work are also included.

Keywords: earth foreshock, ULF waves, plasma theory, plasma instabilities, electromagnetic waves, ion beams in space

OPEN ACCESS

Edited by:
Joseph E. Borovsky, Space Science Institute, United States

Reviewed by:
Xochitl Blanco-Cano, National Autonomous University of Mexico, Mexico
Stephen A. Fuselier, Southwest Research Institute (SwRI), United States

***Correspondence:**
Dan Winske
winske@losalamos.com

Specialty section:
This article was submitted to Space Physics, a section of the journal Frontiers in Astronomy and Space Sciences

Received: *18 March 2022*
Accepted: *11 April 2022*
Published: *16 May 2022*

Citation:
Winske D and Wilson LB (2022) Linear Theory of Electromagnetic Ion Beam Instabilities in the Earth's Forshock: Peter Gary's Contributions (1981–1991). Front. Astron. Space Sci. 9:899642. doi: 10.3389/fspas.2022.899642

INTRODUCTION

As this collection of articles emphasizes, Peter Gary is best known for his work on linear Vlasov theory of plasma instabilities. In the early days of plasma physics (i.e., 1950s–1970s) plasma instabilities were often studied using a reduced fluid approach that yielded simplified equations that could be solved analytically. As plasma theory matured, a more complete, and complex theory developed based on the Vlasov equation that could be sometimes solved in reduced forms. Peter was one of the first to solve the complete Vlasov equation exactly using numerical methods and displaying the results with simple line plots. Nowadays, this is the common technique, and there are a number of widely available computer programs to do this with sophisticated graphical interfaces, e.g., WHAMP (Rönmark, 1982). But back in the 70s his method was a unique approach.

This article discusses Peter Gary's contributions to understanding the linear theory of ultra-low frequency (ULF) electromagnetic waves driven by ion beams in the Earth's foreshock. The foreshock is the broad region upstream of the bow shock where the solar wind interacts with electrons and ions flowing away from the shock and generating a wide spectrum of plasma waves. This work covers the period of time from the late 1970s to the late 1980s, when the three ISEE (International Sun Earth Explorer) spacecraft provided very significant and unique measurements in the foreshock as well as other regions both inside and outside of the magnetosphere. Much information about the observations in the foreshock has been published over the years and our goal here is only to emphasize a few key results, using appropriate references and reviews of this effort, to define the outstanding theoretical issues that Peter's work addressed and contributed to their understanding. So in this sense, this paper is a not a review article, but hopefully it summarizes a key feature of Peter's work, the legacy of which continues to the present. Peter and one of us (Dan) worked together during this time period on a number of these investigations. While he can report the results of these studies, they cannot convene the sense of excitement, wonder, and achievement that they shared as theory,

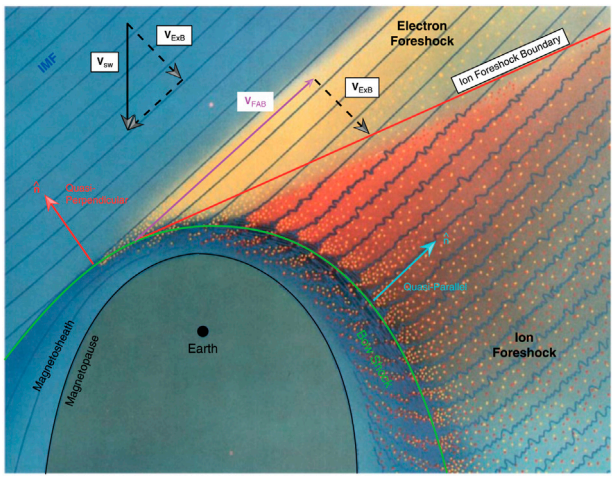

FIGURE 1 | Foreshock configuration showing incident solar wind magnetic field (blue lines), impinging on the bow shock (green curved line), producing backstreaming ions (yellow dots), leaked magnetosheath ions (red dots), and upstream waves (wavy blue lines). The ion foreshock boundary is shown as the red line. Figure is from Wilson, (2016), adapted from Tsurutani and Rodriguez (1981), and is reproduced with permission from The American Geophysical Union.

simulations and observations came together to produce new understanding. The other author here (Lynn) is much more familiar with work on more recent observations related to ion beams and low frequency waves in the foreshock from the Cluster and Magnetospheric Multiscale missions and how they relate to Peter's legacy.

We begin with a little background—a simplified version of the geometry of the foreshock, as shown in **Figure 1**. This figure is taken from Figure 16.1 of Wilson, (2016) and which in turn was adapted from Tsurutani and Rodriguez (Plate 1, 1981). The slanted straight lines are the magnetic field embedded in the solar wind that is flowing downward in the figure and encounters the curved bow shock (green curve). The angle between the magnetic field and the normal direction at the shock is denoted as θ_{Bn}. The portion of the bow shock where $\theta_{Bn} > 45^{\circ}$ (i.e., the region to the left of the Earth in the figure) is termed the "quasi-perpendicular shock", while the region to the right, $\theta_{Bn} < 45^{\circ}$, is the "quasi-parallel shock" that extends all the way down to $\theta_{Bn} \sim 0^{\circ}$—the "parallel shock". At the shock near $\theta_{Bn} \sim 90^{\circ}$, some of the incoming solar wind electrons, which have small gyroradii, are reflected and propagate back upstream creating the region known as the 'electron foreshock'. Some of the solar wind ions impinging on the bow shock near $\theta_{Bn} \sim 90^{\circ}$ are also reflected, but because they have larger gyroradii, quickly gyrate into the downstream. At somewhat smaller θ_{Bn}, but still associated with the quasi-perpendicular bow shock, a fraction of the solar wind ions are also reflected and travel back upstream along the magnetic field as well as being convected in the solar wind ($V_{E\times B}$ in the figure) to form the quasi-perpendicular portion of the ion foreshock. Farther to the right of the ion foreshock boundary shown in **Figure 1**, ions originating at the shock at even smaller θ_{Bn}, e.g., on the quasi-parallel portion of the shock, also propagate upstream (dots in the figure), generating larger amplitude waves in the magnetic field (blue wavy lines), to form the quasi-parallel portion of the ion foreshock. These backstreaming ions may have been from the solar wind and reflected at the shock or could have leaked out of the magnetosheath. This process extends deep in the foreshock to $\theta_{Bn} \sim 0^{\circ}$, where the shock normal is essentially parallel to the solar wind magnetic field.

In this article we discuss only electromagnetic instabilities that Peter studied during this time period that are driven by ion beams that are cold and fast, characteristically produced in the quasi-perpendicular portion of the foreshock. Electromagnetic ion beam instabilities with somewhat different properties are also found deeper in the foreshock on magnetic field lines that connect to the nearly parallel portion of the bow shock. Here the ion beams are slower and hotter and instead of being generated by reflection at the shock, are more likely to result from heating and scattering of the cold beam ions, processes related to the unsteady nature of the parallel shock, or from magnetosheath ions that leaked out into the foreshock. Other types of ion beam instabilities arise elsewhere in space, e.g., in the plasma sheet boundary layer upstream of slow-mode shocks in the magnetotail and in the vicinity of comets. Waves resulting from such instabilities were observed by ISEE-3 late in its mission. See, for example, articles by Smith et al. (1984) related to observations of slow-mode shocks in the magnetotail, by Tsurutani et al. (1985) concerning waves in the plasma sheet boundary layer, and by Smith et al. (1986) related to wave observations at Comet Giacobini-Zinner. As we discuss later, in his review article (Gary, 1991), Peter summarizes his contributions to relevant theory and simulations of all of these environments.

INTERNATIONAL SUN EARTH EXPLORER

In the decade before ISEE, numerous spacecraft observed ion beams streaming away from the Earth along the interplanetary magnetic field outward from the bow shock through the foreshock, e.g., measurements by the Vela satellites (Asbridge et al., 1968). In this region, low-frequency (0.01–0.05 Hz) transverse hydromagnetic waves were also observed (Greenstadt et al., 1968) and data from Explorer 34 led to the conclusion that these waves were indeed associated with the bow shock since they were seen only on field lines that intersect the shock (Fairfield, 1969). A direct correlation was subsequently established (Scarf et al., 1970) between the presence of the waves and a portion of the solar wind that was reflected at the bow shock by a process which had been demonstrated theoretically by Sonnerup (1969). While the early work suggested that the waves could be produced by an ion cyclotron resonance involving the beam ions, Barnes (1970) provided a detailed model for this wave generation process based on stochastic scattering and acceleration of the beam ions. Years later, Watanabe and Terasawa (1984) verified the correctness of the cyclotron resonance process using IMP-5 data from 1969.

During the late 60s and early 70s, Peter developed his linear theory of instabilities in magnetized plasmas, numerically solving the complete dispersion equation for both electrostatic and

electromagnetic waves, excited by various sorts of free energy: i.e., Beams of electrons or ions, temperature anisotropies in either the background or beam species, etc. Using Fried-Conte functions to characterize the various species as Maxwellians, he solved the resulting equation numerically without approximations. The full dispersion equation he used is found in the appendix of his review article (Gary, 1991). An early application of his methodology was to electromagnetic ion streaming instabilities in the solar wind (Montgomery et al., 1974). Both instabilities associated with magnetosonic and Alfvenic wave modes were investigated.

The early spacecraft observations in the foreshock helped motivate the International Space Earth Explorer (ISEE) mission which consisted of three spacecraft, ISEE-1 and ISEE-3 that were designed and built by the U.S., and ISEE-2 that was built and managed by the European Space Agency (ESA) (Ogilvie et al., 1977). It was realized from the earlier missions that with two spacecraft with similar instruments (ISEE-1 and -2), which when in essentially the same orbit but with variable spacing, would be able to measure the thickness of thin boundaries, such as the bow shock and the magnetopause that had been discovered earlier. And a third spacecraft (ISEE-3) could be positioned much far upstream to monitor the solar wind conditions. ISEE-1 and ISEE-2 were launched together in October 1977, in almost identical orbits around the earth with periods of approximately 57 h, and their separation in orbit could be altered by maneuvering ISEE-2. ISEE-3 was launched in August 1978, and inserted into orbit about the libation point situated ~240 Earth radii upstream of the Earth so that disturbances detected by ISEE-3 arrive at the Earth about 1 hour later. The satellites all carried a wide variety of instrumentation to measure not only the density and velocity distribution of the backstreaming ions and low frequency waves of interest to us here, but also to measure very energetic electrons and ions, ion composition, as well as a broad spectrum of both electrostatic and electromagnetic waves. All three spacecraft enjoyed long and successful lives. The ISEE-1 and ISEE-2 spacecraft reentered the Earth's atmosphere in September 1987 after more than 1,500 orbits of the Earth. ISEE-3 was taken out of its libation point orbit in the summer of 1983 and after a series of deep passes down the magnetotail, encountered Comet Giacobini-Zinner in September 1985.

In just its first few years, ISEE-1 and -2 greatly expanded on the earlier discoveries and understanding of backstreaming ions and low-frequency waves in the foreshock. The fast-plasma instruments on these satellites were able to show there are two main populations of backstreaming ions, termed "reflected" and "diffuse" (Gosling et al., 1978). The reflected ions have a sharply peaked energy spectrum and relatively collimated flow coming from the bow shock along the interplanetary magnetic field with number densities ~ 1.5% of the solar wind. In contrast, the diffuse ions have a much flatter energy spectrum and broad angular distributions, with lower density ~ 0.7% of the solar wind. These two populations occur in separate regions of the foreshock, with reflected ions in the quasi-perpendicular portion and the diffuse ions in the more nearly parallel portion of the foreshock, suggesting different mechanisms of origin and acceleration. Bonifazi and Moreno (1981) carried out a statistical analysis of these distributions, also showing that the reflected beams tended to be found in the quasi-perpendicular portion of the foreshock. In between the reflected and diffuse ion populations, were 'intermediate' ions that had a crescent shape in velocity space (Paschmann et al., 1981), the origin of which will be discussed later. Paschmann et al. also show examples of the velocity distributions of all three populations. The reflected ions were so named, because backstreaming beams of ions were observed traveling upstream in a direction determined by the interplanetary magnetic field and the convection velocity ($V_{E\times B}$), consistent with simple models of specular reflection at the bow shock (Sonnerup, 1969; Paschmann et al., 1980). Thomsen et al. (1983) examined the backstreaming ions to show that these simple models of reflection, along with the conservation of magnetic moment, could account for a number of the observations, although other observations indicated that backstreaming ions could instead arise from the leakage of shock-heated magnetosheath ions.

The ISEE spacecraft likewise produced new, detailed information about the low frequency waves associated with the backstreaming ions and the correlation between magnetic field and plasma density in wave events, expanding on the early work of Greenstadt et al. (1968). Paschmann et al. (1979) reported that there were usually weak waves occurring with reflected beam ions, while with diffuse ions large amplitude, compressive waves often occurred. Hoppe et al. (1981) and Hoppe and Russell (1983) further examined the waves associated with ion beam populations, measuring polarizations and frequencies. They observed magnetosonic waves that are right-hand polarized in the plasma rest frame but left-hand polarized in spacecraft frame and sometimes with large amplitudes. These waves have frequencies ~0.03 Hz and are often referred to as "30-s waves." Obliquely propagating waves were also observed, often in the form of steepened waves, termed shocklets. In addition, deeper in the foreshock Alfven waves were also generated in associated with the diffuse ions. Early theoretical analysis of the magnetosonic waves generated by the reflected ions was provided by Gary (1981), which will be discussed later in some detail. Sentman et al. (1981) also carried out linear analysis of both reflected and diffuse ion beams and examined both unstable magnetosonic and Alfvenic wave modes. And years later, Le and Russell (1992) determined the location in the foreshock where the low frequency waves begin to appear, the so-called ULF foreshock boundary, near the ion foreshock boundary.

A few years after the initial ISEE observations of backstreaming ions and associated waves in the foreshock, a closer examination of the intermediate ion distributions found that sometimes the backstreaming ions were gyrating in the magnetic field in the presence of large amplitude waves (Gurgiolo et al., 1981; Thomsen et al., 1985; Fuselier et al., 1986a). Fuselier et al. (1986b) carried out a large survey of intermediate ion observations and showed that roughly half involved ions gyrating in the magnetic field which could be due to how they interact with the bow shock, while other events, characterized by gyrophase-bunched beam ions that could be due to disruption of the beam later in time by the instability-generated waves. The issue of gyrophase-bunching will be discussed later in relation to Peter's theoretical work.

Further details and summaries of the many publications that came out of the ISEE mission concerning observations of foreshock ions and waves [including ions and waves produced deep in the foreshock near the quasi-parallel bow shock, termed "short large-amplitude magnetic structures" (SLAMS) by Schwartz et al. (1992), that we are not addressing here] were given by Tsurutani and Rodriguez (1981) discussing the early results, by Russell and Hoppe (1983) focusing on wave measurements, and Thomsen (1984) emphasizing the plasma measurements.

PETER GARY'S CONTRIBUTIONS

During the ISEE period, Peter made a number of significant contributions to the interpretation of the foreshock observations in terms of linear theory of electromagnetic ion beam instabilities, which were published in five journal articles and later summarized in a review article. We describe each of these publications in a short paragraph.

1. S. P. Gary, J. Geophys. Res. (1981): Microinstabilities Upstream of the Earth's Bow Shock: A Brief Review (Gary, 1981).

This first paper was part of a collection of papers summarizing the first several years of results from ISEE -1 and -2 observations in the Earth's foreshock (e.g., Tsurutani and Rodriguez, 1981). Part of Peter's paper is tutorial in nature, defining and contrasting terms such as: micro/macro plasma instabilities, linear/nonlinear fluctuations, weak/strong turbulence. He also describes his framework for studying instabilities: namely identifying the source of free energy, determining which instabilities can be excited from this energy source, understanding the properties of the instabilities as they grow and then saturate in such a way as to reduce the free energy. In the Earth's foreshock the free energy source is the ion beams streaming back from the bow shock along the magnetic field. As discussed earlier, the observations show two main classes of backstreaming ions, denoted as reflected and diffuse (e.g., Gosling et al., 1978) and that the reflected ions are energetically consistent with their being specularly reflected at the bow shock. Linear theory discussed in this paper shows the beam ions can excite unstable magnetosonic waves that are in cyclotron resonant with the beam ions. This instability is denoted as the "right-hand resonant electromagnetic ion beam instability" or simply as the "right-hand resonant instability". During the initial growth of the instability, the excited electromagnetic waves have group velocities close to the beam speed, so that the field energy propagates with the beam. The waves pitch-angle scatter the beam reducing the free energy. Based on this simplified picture, Peter suggested that this process could explain many of the general features of the observations: The magnetic field fluctuations observed in the foreshock, the deceleration and deflection of the solar wind, and the scattering of the beam to produce velocity distributions that were characteristic of intermediate and diffuse ions. However, his preliminary model assumed parallel propagating waves, which do not produce the observed large fluctuations in the solar wind density.

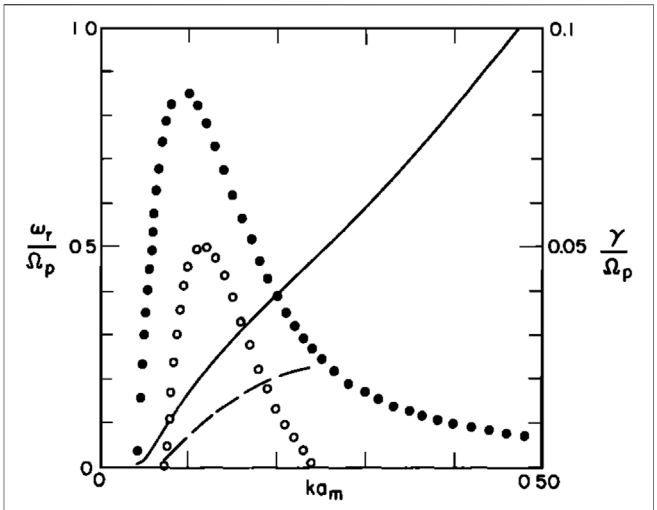

FIGURE 2 | Complex frequency ($\omega = \omega_r + i\gamma$) computed from linear theory for the right-hand resonant ion beam instability as a function of wavenumber (k). The beam density is 1% of the background ion density and beam speed is 10 v_A (v_A = Alfven speed). The frequencies are normalized by the background ion cyclotron frequency (Ω_i) and the wavenumbers to the background ion gyroradius (a_i). Two cases are shown: (*a*) parallel propagation ($\theta = 0°$) -- real frequencies are given by the solid line, growth rates by the solid circles; (*a*) oblique propagation ($\theta = 45°$) -- real frequencies are given by the dashed line, growth rates by the open circles. Figure is reproduced from Gary et al., 1981, with permission from The American Geophysical Union.

2. S. P. Gary, J. T. Gosling, and D. W. Forslund, J. Geophys. Res. (1981): The Electromagnetic Ion Beam Instability Upstream of the Earth's Bow Shock (Gary et al., 1981).

To address the question of the observed density fluctuations, in this paper the linear theory is extended to include oblique wave propagation. After summarizing the observations (e.g., Tsurutani and Rodriguez, 1981), the basic instability model is reviewed. Recalling that the basic physics of waves in cyclotron resonance with the beam that grow and scatter the beam (e.g., Barnes, 1970), the linear theory presented in Peter's previous paper provides a detailed description ion of wave properties (i.e., wavenumbers and real and imaginary frequencies of the unstable waves, that show how a weak (~1% density beam) initially produces a low level of waves and growth times > 25 s. Because the growth rate of the waves is small, the ion beam propagates a long distance upstream from the bow shock before the waves grow to large amplitude. But in the process of propagating upstream, the beam ions and the waves are convected deep into the quasi-parallel portion of the foreshock, where they are slowed. The beam ions loses parallel momentum as they are pitch-angle scattered by the waves, producing intermediate velocity distributions (kidney shaped). This loss of energy and momentum by the beam, and the waves, causes the solar wind to be deflected and slowed, as observed by Bame et al. (1980). An example of results of linear theory are shown in **Figure 2**. Taken from **Figure 1** in this paper, the real (ω_r) and imaginary (γ) frequencies of the unstable waves are plotted as a function of wavenumber (k), showing the instability is sharply peaked in wavenumber. In the vicinity of this peak the real frequency is

about a factor of two larger than the imaginary part and the dispersion of the wave is also modified in this region. The parameters of this calculation are given in the figure caption. The figure also shows the effect of extending the linear theory to include oblique wave propagation. Parallel ($\theta = 0^{\circ}$) and obliquely ($\theta \sim 45^{\circ}$) propagating unstable waves are compared, showing the maximum growth rate at large oblique angles is reduced by less than a factor of two and that maximum growth in both cases occurs essentially at the same wavenumber. But even at small oblique angles, $\sim 15^{\circ}$, the compressibility (i.e., the density fluctuations computed from linear theory) is significantly larger than for parallel propagation, so oblique waves can grow and produce density fluctuations in agreement with observations.

3. S. P. Gary, C. W. Smith, M. A. Lee, M. L. Goldstein and D. W. Forslund, Phys. Fluids (1984): Electromagnetic Ion Beam Instabilities (Gary et al., 1984).

In this paper Peter and his coauthors consider the linear properties four electromagnetic ion beam instabilities: the previously discussed right-hand resonant magnetosonic instability, the right-hand non-resonant Alfvenic instability that was studied by Sentman et al. (1981), a left-hand resonant Alfvenic hot beam instability, and a left-hand ion cyclotron anisotropy instability. To clarify these different modes, the concept of resonance and polarization are carefully defined. Numerical solutions of the linear dispersion relation are presented to show that for parallel propagation the righthand resonant instability has a lower instability threshold than the non-resonant instability unless the beam speed or beam density is sufficiently large. For hot ion beams a left-hand resonant instability is also excited, and if there is a large temperature anisotropy in the beam ($T_{b,\perp} >> T_{b,\|}$), a left-hand ion cyclotron instability is also possible. For parallel propagation, analytic solutions for the unstable modes are also presented. At oblique propagation and high beam speeds, it is demonstrated that an instability associated with the $m = 2$ cyclotron resonance is also excited for both the right-hand resonant and non-resonant instabilities.

4. S. P. Gary, M. F. Thomsen, and S. A. Fuselier, Phys. Fluids (1986): Electromagnetic Instabilities and Gyrophase-Bunched Particles (Gary et al., 1986a).

In this paper, linear theory of both the right-hand resonant and non-resonant instabilities driven by an energetic, cool ion beam is used to calculate the phase angle between the fluctuating velocity of the beam ions relative to the fluctuating magnetic field in order to determine whether gyrophase bunching of the beam ions is observable. As mentioned earlier, distinct gyrophase-bunched ions have been observed in the foreshock by ISEE (Gurgiolo et al., 1981; Thomsen et al., 1985; Fuslerier et al., 1986a). Hoshino and Terasawa (1985) investigated whether the right-hand resonant instability in the foreshock could lead to the observed gyrophase bunching. They demonstrated in their one-dimensional full particle simulations that during the growth of the instability the perpendicular component of the beam ions' velocity had a well-defined phase angle relationship relative to the growing waves. Peter's linear calculations showed that for the non-resonant mode, the phase angle is $\sim 0^{\circ}$, while for the resonant mode it is $\sim 90^{\circ}$ for the most unstable wavenumber. From these results it is concluded that the right-hand resonant instability will give rise to observable gyrophase bunching of the ion beam for foreshock conditions—consistent with the observations of Fuselier et al. (1986a) and the simulations of Hoshino and Terasawa (1985).

5. S. P. Gary, C. D. Madland, D. Schriver, and D. Winske, J. Geophys. Res. (1986): Computer Simulations of Electromagnetic Cool Ion Beam Instabilities (Gary et al., 1986b).

In this paper the authors discuss results of 1-D hybrid (particle ions, massless fluid electrons) simulations of the right-hand resonant and non-resonant electromagnetic ion beam instabilities. Unlike earlier simulations of these instabilities (Winske and Leroy, 1984), this study considers small-scale simulations, a system length of only one wavelength of the most unstable linear mode. In this way two issues can be addressed: 1) The properties of the instability at small relative drift of the beam ions relative to the background ions (V_b in terms of the Alfven speed v_A), and 2) gyrophase bunching of the beam ions. Three regimes common to the foreshock are considered: 1) low beam drift speed ($V_b = 3\ v_A$ and beam density $n_b = 0.05$), where the resonant instability dominates and the development of the system is quasilinear—the beam heats in the perpendicular direction, while the parallel velocity decreases (Gary and Tokar, 1985); 2) higher beam drift velocity ($n_b = 0.02$, $V_b = 10\ v_A$) with the resonant instability still dominating that shows gyrophase bunching of the beam at 90° with respect to the wave magnetic field is clearly visible; and 3) higher beam speeds or densities ($n_b = 0.10$, $V_b = 10\ v_A$) where the non-resonant instability dominates—here bunching still occurs, but is different as the phase angle is near 0°. The gyrophase bunching measured in the simulations is consistent with results from linear theory. In addition, a scaling for the magnetic fluctuation amplitudes at saturation of the instability is obtained from simulations that is valid in all three regimes: The energy in the perturbed magnetic fields is roughly half of the initial kinetic energy of the beam ions. The longer time behavior of the instability in each of the three cases is also discussed. While at later times, the resonant instability in the strong regime leads to a shift of the dominant unstable mode to shorter wavelengths, for both the resonant instability in the quasilinear regime and the non-resonant instability at higher beam energies, a shift to longer wavelengths after saturation is found.

6. S. P. Gary, Space Science Rev. (1991): Electromagnetic Ion/Ion Instabilities and Their Consequences in Space Plasmas: A Review (Gary, 1991).

This review article summarizes the work that Peter had done concerning low frequency (less than the ion cyclotron frequency) electromagnetic ion beam instabilities and their presence in various environments. While we have been dealing here only with Peter's work in the foreshock, Peter has also applied the same methodology to the solar wind, interplanetary shocks, the plasma sheet boundary layer, and near comets. These last two situations derived from observations from ISEE-3 after its position was moved from far upstream of the bow shock to the deep magnetotail, where it encountered ion beams upstream of slow mode shocks in the

plasma sheet boundary layer, and then later near Comet Giacobini-Zinner where heavy ions were emitted. Peter emphasizes throughout the review the characteristics of the various ion beam instabilities that can occur in space and compares their properties, such as growth rates, saturation levels, and the polarization/helicity of the unstable waves. His review gives appropriate and extensive references to observations as well as theory/simulation work that had been done in the last decade. He concentrates on cases where the background and beam ions are described as Maxwellians and focuses on parallel propagating modes, but does include some discussion of oblique modes as well. In addition, he treats cases that include anisotropic ($T_\perp > T_\parallel$) ions, ring-beams, and heavy ion beams. He gives a review of quasilinear theory as applied to these instabilities where appropriate and discusses results from hybrid computer simulations. Finally, in the appendix a very detailed discussion of the derivation and form of the linear dispersion equation used in all his studies is provided. This review also includes work on transport ratios, such as polarization, helicity, compressibility in stable plasmas (details in Gary, 1986) as well as unstable plasmas (in Gary, 1992). Finally, this article formed the basis of Peter's major opus, the monograph "Theory of Space Plasma Microinstabilities" published in the Cambridge Atmospheric and Space Science Series (Gary, 1993) that summarized his work on a large number of electromagnetic as well as electrostatic instabilities, with consistent methodology and notation throughout.

RECENT WORK

We conclude this article with some brief comments about more recent work, following the era of ISEE and Peter's publications concerning electromagnetic ion beam instabilities in the foreshock, which demonstrate Peter's continuing legacy. New insights have been gained from observations from of multi-spacecraft missions, such as Cluster, THEMIS, and the Magnetospheric Multi-Scale (MMS) missions. For example, the four Cluster spacecraft have observed field-aligned beams in the foreshock, but also gyrating ions that can be associated with the quasi-parallel bow shock (Meziane et al., 2004; Kis et al., 2007). Gyrophase-bunched ions have also been observed by Cluster in the foreshock (Mazelle et al., 2003). Cluster has also made interesting observations of ULF waves. The four spacecraft are able to more accurately show that most of the waves, consistent with earlier observations, are low frequency, left-hand polarized in the spacecraft frame, but right-hand polarized in the plasma frame (Eastwood, 2002, 2005a; Eastwood, 2005b; Hobara et al., 2007a; Hobara et al., 2007b). It has also been possible with the ARTEMIS spacecraft orbiting the moon to measure the growth rate of the waves as they propagate out farther in the foreshock (Dorfman et al., 2017) The observed waves are consistent with the linear theory of Gary et al. (1981), although reduced forms of the linear dispersion relation that ignore thermal effects need to be modified in cases of high-beta solar wind plasma beta to get better agreement (Hobara et al., 2007a; Hobara et al., 2007b). Wilson, (2016) has reached similar conclusions in his recent review of foreshock waves.

However, a major problem remains—the observed ULF waves are primarily propagating oblique to the magnetic field, contrary to linear theory that says the parallel mode has the largest growth rate and thus in time will grow to be the dominant mode. Measurements by the four Cluster spacecraft have been able to make this more quantitative, indicating that for some data-sets the mean angle of wave propagation is 21° (Eastwood et al., 2005b). One resolution of this issue was proposed some years ago by Hada et al. (1987). They suggested that the parallel propagating waves refract as they are carried by the solar wind deeper into the foreshock and become increasingly more oblique and compressive. This remains the most accepted explanation and is consistent with THEMIS observations of ULF waves in the foreshock (Hsieh and Shue, 2013). But multi-dimensional hybrid simulations have provided alternative explanations. Very early 2-D hybrid simulations by Winske and Quest (1986) show that the development of the instability in 2-D is not much different than in 1-D, but their rudimentary diagnostics of the spectrum of unstable waves, as well as the relatively small size of the simulations, limit the discussion on the development of oblique unstable modes. Hellinger and Mangeney (1999) observe in their simulations in a uniform background, but with slightly different beam parameters than are usually assumed, that oblique waves, even though their linear growth rates are smaller, grow to larger amplitudes. Blanco-Cano et al. (2006) include the bow shock in their calculations and show that parallel propagating ULF waves dominate far upstream from the bow shock, but oblique waves are excited relatively close to the shock. An even more interesting suggestion is given later by Strumik et al. (2015). In their foreshock simulations they assume that the solar wind is essentially radial so that the Hada et al. (1987) refraction mechanism is minimalized. They find that while parallel unstable modes dominate, oblique waves are also generated, and when properly averaged over phase space density, the "average" propagation direction is ~ 20°, consistent with Eastwood et al. (2005b). The bottom line from all this recent work is that the linear theory as worked out by Peter Gary and others years ago is sufficient to explain the origin of the ULF waves observed far upstream from the shock, but more realistic, probably 3-D, simulations in a foreshock geometry and maybe new observations will be needed to resolve this remaining issue of propagation direction. Perhaps other articles in this topical series will also shed new light on this problem.

DATA AVAILABILITY STATEMENT

The original contributions presented in the study are included in the article/Supplementary Material, further inquiries can be directed to the corresponding author.

AUTHOR CONTRIBUTIONS

DW wrote much of the text, provided Figure 2 and put the manuscript together. LWIII provided text, references, and Figure 1.

FUNDING

LBW was partially supported by Wind MO&DA funds

REFERENCES

Asbridge, J. R., Bame, S. J., and Strong, I. B. (1968). Outward Flow of Protons from the Earth's bow Shock. *J. Geophys. Res.* 73, 5777–5782. doi:10.1029/ja073i017p05777

Bame, S. J., Asbridge, J. R., Feldman, W. C., Gosling, J. T., Paschmann, G., and Sckopke, N. (1980). Deceleration of the Solar Wind Upstream from the Earth's bow Shock and the Origin of Diffuse Upstream Ions. *J. Geophys. Res.* 85, 2981–2990. doi:10.1029/ja085ia06p02981

Barnes, A. (1970). Theory of Generation of bow-shock-associated Hydromagnetic Waves in the Upstream Interplanetary Medium. *Cosmic Electrodyn* 1, 90–114.

Blanco-Cano, X., Omidi, N., and Russell, C. T. (2006). Macrostructure of Collisionless bow Shocks: 2. ULF Waves in the Foreshock and Magnetosheath. *J. Geophys. Res.* 111, A10205. doi:10.1029/2005ja011421

Bonifazi, C., and Moreno, G. (1981). Reflected and Diffuse Ions Backstreaming from the Earth's bow Shock 2. Origin. *J. Geophys. Res.* 86, 4405–4413. doi:10.1029/ja086ia06p04405

Dorfman, S., Hietala, H., Astfalk, P., and Angelopoulos, V. (2017). Growth Rate Measurement of ULF Waves in the Ion Foreshock. *Geophys. Res. Lett.* 44, 2120–2128. doi:10.1002/2017gl072692

Eastwood, J. P., Balogh, A., Dunlop, M. W., Horbury, T. S., and Dandouras, I. (2002). Cluster Observations of Fast Magnetosonic Waves in the Terrestrial Foreshock. *Geophys. Res. Lett.* 29, 2046. doi:10.1029/2002gl015582

Eastwood, J. P., Balogh, A., Lucek, E. A., Mazelle, C., and Dandouras, I. (2005a). Quasi-monochromatic ULF Foreshock Waves as Observed by the Four-Spacecraft Cluster mission: 1. Statistical Properties. *J. Geophys. Res.* 110, A11219. doi:10.1029/2004ja010617

Eastwood, J. P., Balogh, A., Lucek, E. A., Mazelle, C., and Dandouras, I. (2005b). Quasi-monochromatic ULF Foreshock Waves as Observed by the Four-Spacecraft Cluster mission: 2. Oblique Propagation. *J. Geophys. Res.* 110, A11220. doi:10.1029/2004ja010618

Fairfield, D. H. (1969). Bow Shock Associated Waves Observed in the Far Upstream Interplanetary Medium. *J. Geophys. Res.* 74, 3541–3553. doi:10.1029/ja074i014p03541

Fuselier, S. A., Thomsen, M. F., Gary, S. P., Bame, S. J., Russell, C. T., and Parks, G. K. (1986a). The Phase Relationship between Gyrophase-Bunched Ions and MHD-like Waves. *Geophys. Res. Lett.* 13, 60–63. doi:10.1029/gl013i001p00060

Fuselier, S. A., Thomsen, M. F., Gosling, J. T., Bame, S. J., and Russell, C. T. (1986b). Gyrating and Intermediate Ion Distributions Upstream from the Earth's bow Shock. *J. Geophys. Res.* 91, 91–99. doi:10.1029/ja091ia01p00091

Gary, S. P. (1991). Electromagnetic Ion/ion Instabilities and Their Consequences in Space Plasmas: A Review. *Space Sci. Rev* 56, 373–415. doi:10.1007/bf00196632

Gary, S. P., Gosling, J. T., and Forslund, D. W. (1981). The Electromagnetic Ion Beam Instability Upstream of the Earth's bow Shock. *J. Geophys. Res.* 86, 6691–6696. doi:10.1029/ja086ia08p06691

Gary, S. P. (1986). Low-frequency Waves in a High-Beta Collisionless Plasma: Polarization, Compressibility and Helicity. *J. Plasma Phys.* 35, 431–447. doi:10.1017/s0022377800011442

Gary, S. P., Madland, C. D., Schriver, D., and Winske, D. (1986b). Computer Simulations of Electromagnetic Cool Ion Beam Instabilities. *J. Geophys. Res.* 91, 4128–4200. doi:10.1029/ja091ia04p04188

Gary, S. P. (1981). Microinstabilities Upstream of the Earth's bow Shock: A Brief Review. *J. Geophys. Res.* 86, 4331–4336. doi:10.1029/ja086ia06p04331

Gary, S. P., Smith, C. W., Lee, M. A., Goldstein, M. L., and Forslund, D. W. (1984). Electromagnetic Ion Beam Instabilities. *Phys. Fluids* 27, 1852–1862. doi:10.1063/1.864797

Gary, S. P. (1993). *Theory of Space Plasma Microinstabilities*. New York: Cambridge University Press.

Gary, S. P., Thomsen, M. F., and Fuselier, S. A. (1986a). Electromagnetic Instabilities and Gyrophase-Bunched Particles. *Phys. Fluids* 29, 531–535. doi:10.1063/1.865441

Gary, S. P., and Tokar, R. L. (1985). The Second-Order Theory of Electromagnetic Hot Ion Beam Instabilities. *J. Geophys. Res.* 90, 65–72. doi:10.1029/ja090ia01p00065

Gary, S. P., and Winske, D. (1992). Correlation Function Ratios and the Identification of Space Plasma Instabilities. *J. Geophys. Res.* 97, 3103–3111. doi:10.1029/91ja02752

Gosling, J. T., Asbridge, J. R., Bame, S. J., Paschmann, G., and Sckopke, N. (1978). Observations of Two Distinct Populations of bow Shock Ions in the Upstream Solar Wind. *Geophys. Res. Lett.* 5, 957–960. doi:10.1029/gl005i011p00957

Greenstadt, E. W., Green, I. M., Inouye, G. T., Hundhausen, A. J., Bame, S. J., and Strong, I. B. (1968). Correlated Magnetic Field and Plasma Observations of the Earth's bow Shock. *J. Geophys. Res.* 73, 51–60. doi:10.1029/ja073i001p00051

Gurgiolo, C., Parks, G. K., Mauk, B. H., Lin, C. S., Anderson, K. A., Lin, R. P., et al. (1981). Non-E × Bordered Ion Beams Upstream of the Earth's bow Shock. *J. Geophys. Res.* 86, 4415–4424. doi:10.1029/ja086ia06p04415

Hada, T., Kennel, C. F., and Terasawa, T. (1987). Excitation of Compressional Waves and the Formation of Shocklets in the Earth's Foreshock. *J. Geophys. Res.* 92, 4423–4435. doi:10.1029/ja092ia05p04423

Hellinger, P., and Mangeney, A. (1999). Electromagnetic Ion Beam Instabilities: Oblique Pulsations. *J. Geophys. Res.* 104, 4669–4680. doi:10.1029/1998ja900157

Hobara, Y., Walker, S. N., Balikhin, M., Pokhotelov, O. A., Dunlop, M., Nilsson, H., et al. (2007a). Characteristics of Terrestrial Foreshock ULF Waves: Cluster Observations. *J. Geophys. Res.* 112, A07202. doi:10.1029/2006ja012142

Hobara, Y., Walker, S. N., Dunlop, M., Balikhin, M., Pokhotelov, O. A., Nilsson, H., et al. (2007b). Mode Identification of Terrestrial ULF Waves Observed by Cluster: A Case Study. *Planet. Space Sci.* 55, 2257–2260. doi:10.1016/j.pss.2007.05.020

Hoppe, M. M., Russell, C. T., Frank, L. A., Eastman, T. E., and Greenstadt, E. W. (1981). Upstream Hydromagnetic Waves and Their Association with Backstreaming Ion Populations: ISEE 1 and 2 Observations. *J. Geophys. Res.* 86, 4471–4492. doi:10.1029/ja086ia06p04471

Hoppe, M. M., and Russell, C. T. (1983). Plasma Rest Frame Frequencies and Polarizations of the Low-Frequency Upstream Waves: ISEE 1 and 2 Observations. *J. Geophys. Res.* 88, 2021–2028. doi:10.1029/ja088ia03p02021

Hoshino, M., and Terasawa, T. (1985). Numerical Study of the Upstream Wave Excitation Mechanism: 1. Nonlinear Phase Bunching of Beam Ions. *J. Geophys. Res.* 90, 57–64. doi:10.1029/ja090ia01p00057

Hsieh, W.-C., and Shue, J.-H. (2013). Dependence of the Oblique Propagation of ULF Foreshock Waves on Solar Wind Parameters. *J. Geophys. Res. Space Phys.* 118, 4151–4160. doi:10.1002/jgra.50225

Kis, A., Scholer, M., Klecker, B., Kucharek, H., Lucek, E. A., and Rème, H. (2007). Scattering of Field-Aligned Beam Ions Upstream of Earth's bow Shock. *Ann. Geophys.* 25, 785–799. doi:10.5194/angeo-25-785-2007

Le, G., and Russell, C. T. (1992). A Study of ULF Wave Foreshock Morphology-I: ULF Foreshock Boundary. *Planet. Space Sci.* 40, 1203–1213. doi:10.1016/0032-0633(92)90077-2

Mazelle, C., Meziane, K., LeQuéau, D., Wilber, M., Eastwood, J. P., Rème, H., et al. (2003). Production of Gyrating Ions from Nonlinear Wave-Particle Interaction Upstream from the Earth's bow Shock: A Case Study from Cluster-CIS. *Planet. Space Sci.* 51, 785–795. doi:10.1016/j.pss.2003.05.002

Meziane, K., Wilber, M., Mazelle, C., LeQueau, D., Kucharek, H., Lucek, E. A., et al. (2004). Simultaneous Observations of Field-Aligned Beams and Gyrating Ions in the Terrestrial Foreshock. *J. Geophys. Res.* 109, A05107. doi:10.1029/2003ja010374

Montgomery, M. D., Gary, S. P., Forslund, D. W., and Feldman, W. C. (1974). Electromagnetic Ion-Beam Instabilities in the Solar Wind. *Phys. Rev. Lett.* 35, 667–670. doi:10.1103/physrevlett.35.667

Ogilvie, K. W., von Rosenvinge, T., and Durney, A. C. (1977). International Sun-Earth Explorer: A Three-Spacecraft Program. *Science* 198, 131–138. doi:10.1126/science.198.4313.131

Paschmann, G., Sckopke, N., Asbridge, J. R., Bame, S. J., and Gosling, J. T. (1980). Energization of Solar Wind Ions by Reflection from the Earth's bow Shock. *J. Geophys. Res.* 85, 4689–4693. doi:10.1029/ja085ia09p04689

Paschmann, G., Sckopke, N., Bame, S. J., Asbridge, J. R., Gosling, J. T., Russell, C. T., et al. (1979). Association of Low-Frequency Waves with Suprathermal Ions in the Upstream Solar Wind. *Geophys. Res. Lett.* 6, 209–212. doi:10.1029/gl006i003p00209

Paschmann, G., Sckopke, N., Papamastorakis, I., Asbridge, J. R., Bame, S. J., and Gosling, J. T. (1981). Characteristics of Reflected and Diffuse Ions Upstream from the Earth's bow Shock. *J. Geophys. Res.* 86, 4355–4364. doi:10.1029/ja086ia06p04355

Rönmark, K. (1982). *Whamp-waves in Homogeneous, Anisotropic, Multicomponent Plasmas (Tech. Rep.)*. Sweden: Kiruna Geofysiska Inst.

Russell, C. T., and Hoppe, M. M. (1983). Upstream Waves and Particles. *Space Sci. Rev.* 34, 155–172. doi:10.1007/978-94-009-7096-0_12

Scarf, F. L., Fredricks, R. W., Frank, L. A., Russell, C. T., Coleman, P. J., and Neugebauer, M. (1970). Direct Correlations of Large-Amplitude Waves with Suprathermal Protons in the Upstream Solar Wind. *J. Geophys. Res.* 75, 7316–7322. doi:10.1029/ja075i034p07316

Schwartz, S. J., Burgess, D., Wilkinson, W. P., Kessel, R. L., Dunlop, M., and Lühr, H. (1992). Observations of Short Large-Amplitude Magnetic Structures at a Quasi-Parallel Shock. *J. Geophys. Res.* 97, 4209–4227. doi:10.1029/91ja02581

Sentman, D. D., Edmiston, J. P., and Frank, L. A. (1981). Instabilities of Low Frequency, Parallel Propagating Electromagnetic Waves in the Earth's Foreshock Region. *J. Geophys. Res.* 86, 7487–7497. doi:10.1029/ja086ia09p07487

Smith, E. J., Slavin, J. A., Tsurutani, B. T., Feldman, W. C., and Bame, S. J. (1984). Slow Mode Shocks in the Earth' Magnetotail: ISEE-3. *Geophys. Res. Lett.* 11, 1054–1057. doi:10.1029/gl011i010p01054

Smith, E. J., Tsurutani, B. T., Slavin, J. A., Jones, D. E., Siscoe, G. L., and Mendis, D. A. (1986). International Cometary Explorer Encounter with Giacobini-Zinner: Magnetic Field Observations. *Science* 232, 382–385. doi:10.1126/science.232.4748.382

Sonnerup, B. U. Ö. (1969). Acceleration of Particles Reflected at a Shock Front. *J. Geophys. Res.* 74, 1301–1304. doi:10.1029/ja074i005p01301

Strumik, M., Roytershteyn, V., Karimabadi, H., Stasiewicz, K., Grzesiak, M., and Przepiórka, D. (2015). Identification of the Dominant ULF Wave Mode and Generation Mechanism for Obliquely Propagating Waves in the Earth's Foreshock. *Geophys. Res. Lett.* 42, 5109–5116. doi:10.1002/2015gl064915

Thomsen, M. F. (1984). *Upstream Suprathermal Waves" in Collisionless Shocks in the Heliosphere: Reviews of Current Research, Geophys. Monogr. Ser.* Editors B. T. Tsurutani and R. Stone (Washington, DC: Amer. Geophys. Union), 35, 253–270.

Thomsen, M. F., Gosling, J. T., Bame, S. J., and Russell, C. T. (1985). Gyrating Ions and Large-Amplitude Monochromatic MHD Waves Upstream of the Earth's bow Shock. *J. Geophys. Res.* 90, 267–273. doi:10.1029/ja090ia01p00267

Thomsen, M. F., Schwartz, S. J., and Gosling, J. T. (1983). Observational Evidence on the Origin of Ions Upstream of the Earth's bow Shock. *J. Geophys. Res.* 88, 7843–7852. doi:10.1029/ja088ia10p07843

Tsurutani, B. T., Richardson, I. G., Thorne, R. M., Butler, W., Smith, E. J., Cowley, S. W. H., et al. (1985). Observations of the Right-Hand Resonant Ion Beam Instability in the Distant Plasma Sheet Boundary Layer. *J. Geophys. Res.* 90, 12159–12172. doi:10.1029/ja090ia12p12159

Tsurutani, B. T., and Rodriguez, P. (1981). Upstream Waves and Particles: An Overview of ISEE Results. *J. Geophys. Res.* 86, 4319–4324. doi:10.1029/ja086ia06p04317

Watanabe, Y., and Terasawa, T. (1984). On the Excitation Mechanism of the Low-Frequency Upstream Waves. *J. Geophys. Res.* 89, 6623–6630. doi:10.1029/ja089ia08p06623

Wilson, L. B., III (2016). "Low Frequency Waves at and Upstream of Collisionless Shocks," in *Low-frequency Waves at and Upstream of Collisionless Shocks" in Low-Frequency Waves in Space Plasmas, Geophys. Monogr. Ser.* Editors A. Keiling, D.-H. Lee, and V. Nakariakov (Washington, DC: Amer. Geophys. Union), 216, 269–291. doi:10.1002/9781119055006.ch16

Winske, D., and Leroy, M. M. (1984). Diffuse Ions Produced by Electromagnetic Ion Beam Instabilities. *J. Geophys. Res.* 89, 2673–2688. doi:10.1029/ja089ia05p02673

Winske, D., and Quest, K. B. (1986). Electromagnetic Ion Beam Instabilities: Comparison of One- and Two-Dimensional Simulations. *J. Geophys. Res.* 91, 8789–8997. doi:10.1029/ja091ia08p08789

Conflict of Interest: The authors declare that the research was conducted in the absence of any commercial or financial relationships that could be construed as a potential conflict of interest.

frontiers | Frontiers in Astronomy and Space Sciences

REVIEW
published: 13 June 2022
doi: 10.3389/fspas.2022.896245

Differentiating Between the Leading Processes for Electron Radiation Belt Acceleration

Solène Lejosne[1], Hayley J. Allison[2], Lauren W. Blum[3], Alexander Y. Drozdov[4], Michael D. Hartinger[5], Mary K. Hudson[6,7], Allison N. Jaynes[8], Louis Ozeke[9], Elias Roussos[10] and Hong Zhao[11]*

[1]Space Sciences Laboratory, University of California, Berkeley, Berkeley, CA, United States, [2]GFZ German Centre for Geosciences, Potsdam, Germany, [3]Laboratory for Atmospheric and Space Physics, University of Boulder, Boulder, CO, United States, [4]University of California, Los Angeles, Los Angeles, CA, United States, [5]Space Science Institute, Boulder, CO, United States, [6]Department of Physics and Astronomy, Dartmouth College, Hanover, NH, United States, [7]High Altitude Observatory, National Center for Atmospheric Research, Boulder, CO, United States, [8]Physics and Astronomy, University of Iowa, Iowa City, IA, United States, [9]Department of Physics, University of Alberta, Edmonton, AB, Canada, [10]Max Planck Institute for Solar System Research, Göttingen, Germany, [11]Department of Physics, Auburn University, Auburn, AL, United States

OPEN ACCESS

Edited by:
Misa Cowee, Los Alamos National Laboratory (DOE), United States

Reviewed by:
Philip J. Erickson, Massachusetts Institute of Technology, United States
Yoshiharu Omura, Kyoto University, Japan
Qiugang Zong, Peking University, China

***Correspondence:**
Solène Lejosne
solene@berkeley.edu

Specialty section:
This article was submitted to Space Physics, a section of the journal Frontiers in Astronomy and Space Sciences

Received: *14 March 2022*
Accepted: *18 May 2022*
Published: *13 June 2022*

Citation:
Lejosne S, Allison HJ, Blum LW, Drozdov AY, Hartinger MD, Hudson MK, Jaynes AN, Ozeke L, Roussos E and Zhao H (2022) Differentiating Between the Leading Processes for Electron Radiation Belt Acceleration. Front. Astron. Space Sci. 9:896245. doi: 10.3389/fspas.2022.896245

Many spacecraft fly within or through a natural and variable particle accelerator powered by the coupling between the magnetosphere and the solar wind: the Earth's radiation belts. Determining the dominant pathways to plasma energization is a central challenge for radiation belt science and space weather alike. Inward radial transport from an external source was originally thought to be the most important acceleration process occurring in the radiation belts. Yet, when modeling relied on a radial diffusion equation including electron lifetimes, notable discrepancies in model-observation comparisons highlighted a need for improvement. Works by Professor Richard M. Thorne and others showed that energetic (hundreds of keV) electrons interacting with whistler-mode chorus waves could be efficiently accelerated to very high energies. The same principles were soon transposed to understand radiation belt dynamics at Jupiter and Saturn. These results led to a paradigm shift in our understanding of radiation belt acceleration, supported by observations of a growing peak in the radial profile of the phase space density for the most energetic electrons of the Earth's outer belt. Yet, quantifying the importance of local acceleration at the gyroscale, versus large-scale acceleration associated with radial transport, remains controversial due to various sources of uncertainty. The objective of this review is to provide context to understand the variety of challenges associated with differentiating between the two main radiation belt acceleration processes: radial transport and local acceleration. Challenges range from electron flux measurement analysis to radiation belt modeling based on a three-dimensional Fokker-Planck equation. We also provide recommendations to inform future research on radiation belt radial transport and local acceleration.

Keywords: radiation belts, Earth, giant planets, local acceleration, radial acceleration, chorus waves, ULF waves, diffusion

1 INTRODUCTION

The outer radiation belt of the Earth's magnetosphere contains a complicated balance of acceleration and loss processes. Previous studies have found that while some geomagnetic storms acted as a significant driver of energetic electron enhancements, others did not (Summers et al., 2004; Hudson et al., 2008). Studies of flux changes following geomagnetic storms reveal that the system is highly non-linear, with a wide range of driving inputs resulting in either enhancement or depletion events (Reeves et al., 2003; Baker et al., 2004). Multiple results have shown the importance of southward interplanetary magnetic field, IMF B_z, for driving electron enhancements (Blake et al., 1997; Li X. et al., 2011), although high-speed solar wind also contributes to the effect (Paulikas and Blake, 1979; Baker et al., 1997; Kanekal et al., 1999). The need to forecast and predict these events has spurred increasing interest in the mechanisms by which acceleration takes place in the outer radiation belt. High energy electrons have deleterious effects on spacecraft systems as they can penetrate through satellite walls and cause deep-dielectric charging (e.g., Baker et al., 1987, 2018; Horne et al., 2013). Findings and models established in the case of the Earth's radiation belts have been transposed to the outer planets, and in particular the giant planets, Jupiter, and Saturn, with the shared objective of furthering our understanding of the physics of a magnetosphere.

Determining the dominant pathways to plasma energization in the radiation belts usually means focusing on either 1) relatively slow, large-scale acceleration processes associated with radial transport or 2) localized acceleration processes occurring on relatively smaller spatiotemporal scales, i.e., local acceleration. The objective of this review is to provide tools to approach this dichotomy. The review was motivated by a joint panel discussion on "Radial Transport vs. Local Acceleration" in the radiation belts, that took place during the Geospace Environment Modeling (GEM) Virtual Summer Workshop in July 2021 (Drozdov et al., 2022). It exemplifies the profound impact of Professor Richard M. Thorne on radiation belt science (e.g., Horne and Tsurutani, 2019; Li W. and Hudson, 2019). It provides the necessary context to navigate the (still) controversial topic of electron radiation belt acceleration. It is organized as follows:

Section 2 provides observational and theoretical background. Specifically, the characteristics of MeV electron flux enhancements are summarized (**Section 2.1**). The most commonly discussed mechanisms for electron radiation belt acceleration are introduced (**Section 2.2**), together with the modeling framework used to quantify their effects (**Section 2.3**). In **Section 3**, we show how the picture for radiation belt acceleration evolved over the years in response to measurements from new missions, from an initial emphasis on radial diffusion (**Section 3.1**) to an emphasis on local wave-particle interactions (**Section 3.2**). We also provide a summary of the current state of the art at the outer planets (**Section 3.3**). The topic is summarized and further discussed in **Section 4**. In particular, we provide a synthesis of the challenges associated with differentiating between the leading processes for electron radiation belt acceleration (**Section 4.1**) and we present a few suggestions for future research directions (**Section 4.2**).

2 OBSERVATIONAL AND THEORETICAL BACKGROUND

Electron flux enhancements at MeV energies are viewed as signatures of radiation belt acceleration. The main characteristics of these electron flux enhancements are provided in **Section 2.1**. The two main mechanisms thought to drive radiation belt acceleration are introduced in **Section 2.2**. These processes are included in a radiation belt model, detailed in **Section 2.3**, in order to quantify, compare and contrast the overall effects of these two acceleration mechanisms on radiation belt dynamics.

2.1 Observations Motivating the Research on Electron Radiation Belt Acceleration

A significant component of energetic (up to 10 MeV) electrons is rapidly produced at times in the Earth's outer radiation belt, within a couple of days or less (e.g., Baker et al., 1994; Foster et al., 2014). **Figure 1** (from Baker et al., 2019) displays six years (September 2012–2018) of >1 MeV electron fluxes measured by the Relativistic Electron-Proton Telescope (REPT, Baker et al., 2021) onboard the Van Allen Probes (Fox and Burch, 2014), together with information on solar wind properties. It reveals the highly variable and energy-dependent nature of MeV electron dynamics in the outer radiation belt. Despite radiation belts being one of the first discoveries of the space age, numerous questions remain regarding the nature of the processes that can accelerate radiation belt electrons and produce the dynamics observed in **Figure 1**.

2.1.1 Characteristics of Electron Flux Enhancements in the Earth's Outer Belt

Electron fluxes routinely increase by several orders of magnitude within days in the Earth's outer radiation belt (**Figure 1**, the article by Reeves et al., 2013). This flux increase may or may not be preceded by a brief, large decrease (e.g., Blake et al., 1997). Broadly speaking, the radiation belt electron flux enhancements are coherent: Increases occur on similar timescales across the radiation belt energy spectrum (50 keV–10 MeV) and across the outer zone (equatorial radial distance, L, between ~3 Re and 6.5 Re), regardless of altitude (e.g., Kanekal et al., 2001). Yet, the specific characteristics of these enhancements are variable. **Figure 1** shows that the magnitude of MeV electron flux usually peaks at a variable location within the outer region (i.e., below geostationary orbit). The rise time for electron flux enhancements increases with energy (e.g., Blake et al., 1997). In addition, the frequency and the L-coverage for electron flux enhancements generally decrease with energy (e.g., Reeves et al., 2013; Zhao et al., 2016).

2.1.2 Association With Solar Activity and Solar Wind Properties

An association between the state of the Earth's outer belt and the Sun was established in the early days of radiation belt science

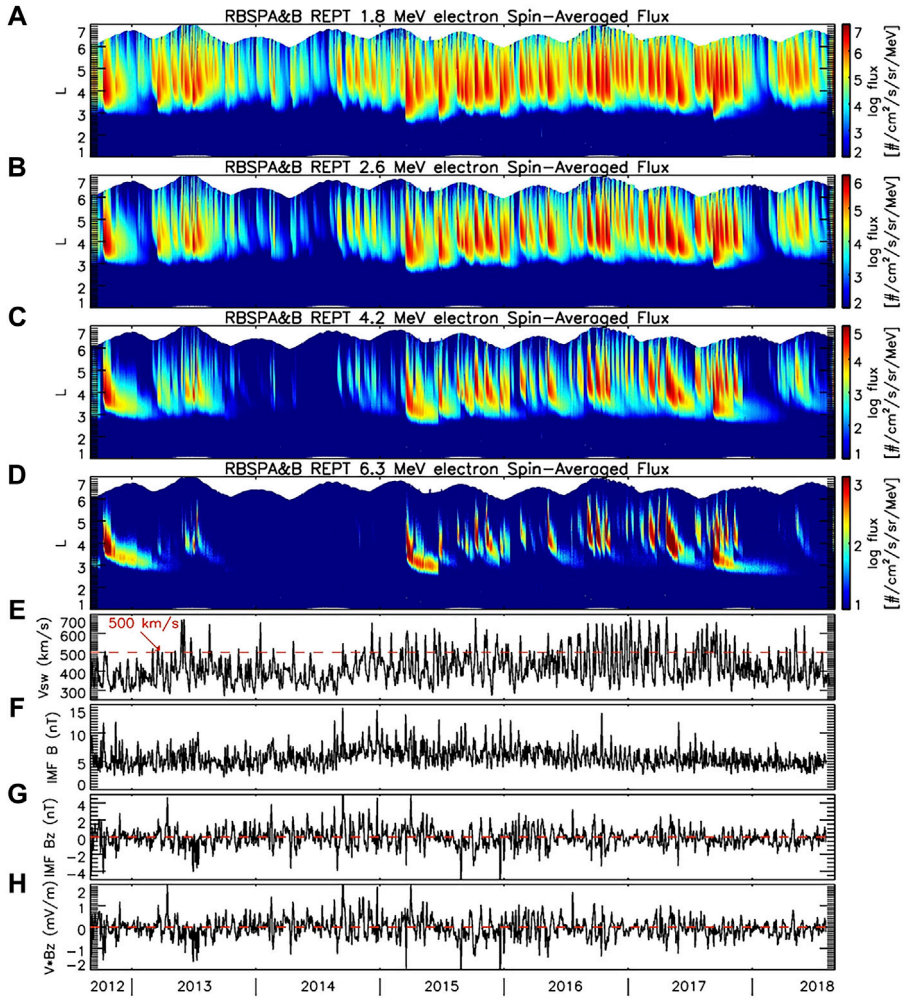

FIGURE 1 | Six years of MeV electron fluxes in the Earth's radiation belts, at **(A)** 1.8 MeV, **(B)** 2.6 MeV, **(C)** 4.2 MeV, and **(D)** 6.3 MeV, measured by both Van Allen Probes between 1 September 2012 and 1 September 2018, together with information on the solar wind properties, namely, the three-day running averages for **(E)** the solar wind speed, **(F)** the magnitude of the interplanetary magnetic field (IMF), **(G)** the north-south component of the IMF, Bz, and **(H)** the product of solar wind speed, V, and Bz (from Baker et al., 2019).

(Williams, 1966). It has remained a subject of research ever since (e.g., Hudson et al., 2008; Kellerman and Shprits, 2012; Kilpua et al., 2015; Zhao et al., 2019a; Ripoll et al., 2020). Connecting the Sun and solar wind properties with the state of the radiation belts is of prime importance for two main reasons. First, it provides observational constraints to radiation belt acceleration theories. Second, it constitutes the basis of radiation belt model developments, whether they are physics-based models (e.g., Xiang et al., 2021), empirical models such as AE9 and predecessors (Ginet et al., 2013), or machine learning models (e.g., Katsavrias et al., 2021a).

The most pronounced signature of the solar wind properties in the state of the Earth's outer radiation belt is the correlation between solar wind speed and MeV electron flux magnitude (Paulikas and Blake, 1979; Reeves et al., 2011; Wing et al., 2016). The sign of the north-south component of the interplanetary magnetic field (IMF), B_z, is also key (Blake et al., 1997). Most of the time, MeV electron flux enhancements occur when the speed of the solar wind is high ($\gtrsim$ 500 km/s) and the IMF B_z is southward, i.e., during conditions that are associated with geomagnetic storm times (e.g., Baker et al., 2019). While these solar wind conditions are the most common conditions for MeV electron flux enhancements, not all of them are necessary. Significant MeV electron flux enhancements have also been reported during non-storm times (e.g., Schiller et al., 2014) and without a high-speed solar wind (e.g., Li X. et al., 2011). A sustained southward IMF is the only necessary condition for MeV electron flux enhancements at geosynchronous orbit according to Li X. et al. (2011). Yet, this necessary condition is not a sufficient condition to guarantee radiation belt enhancements. Indeed, even though geomagnetic storms are associated with a strong and sustained southward IMF, not all geomagnetic storms result in electron flux enhancements (Reeves et al., 2003). The most significant relativistic electron flux enhancements occur outside the plasmapause, in association with periods of prolonged substorm

activity, as quantified by the AE index (Meredith et al., 2003). Moreover, MeV electron enhancements have been tied to High-Intensity Long-Duration Continuous AE Activity (HILDCAA) events (Tsurutani et al., 2006; Miyoshi and Kataoka, 2008; Hajra et al., 2015) and substorm clusters during geomagnetic disturbances (e.g., Rodger et al., 2022).

When electron flux enhancements occur during geomagnetic storms, the location of the peak in MeV electron flux enhancements during recovery phase is strongly correlated with the magnitude of the storm, as quantified by the Dst index (Tverskaya et al., 2003) or, equivalently, with the plasmapause location (O'Brien et al., 2003; Moya et al., 2017; Bruff et al., 2020). The equatorial pitch angle distribution of MeV electron flux enhancements at the center of the outer belt is most anisotropic (i.e., 90° peaked) within a day of the start of the recovery phase, and the degree of anisotropy increases with energy (e.g., Ozeke et al., 2022). The pitch-angle distribution of MeV electron flux becomes more isotropic in the week following the start of the recovery phase (Greeley et al., 2021).

One consequence of the relationship between the state of the Sun and the state of the Earth's outer radiation belt is that periodicities of the Sun, of the solar activity, and of the Sun-Earth connection lead to periodicities in the intensity of the outer belt occurring on a variety of timescales. For instance, the 27-day periodicity of the electron flux enhancements (Williams, 1966) is associated with the 27-day recurrence of geomagnetic activity. The latter comes from the fact that long-lived solar wind features, such as high-speed streams, recur at Earth after every Sun rotation period of ~27 days (e.g., Paulikas and Blake, 1979). The strong semiannual variations of MeV electron fluxes have been tied to the semiannual variation in the orientation between the Earth's magnetic dipole axis and the Sun vector, and more precisely, to the Russell-McPherron effect (McPherron et al., 2009; Katsavrias et al., 2021b). MeV electron fluxes are also more intense during the declining phase of the solar cycle than during the ascending phase. This is due to the fact that the declining phase of the solar cycle is dominated by recurrent high-speed solar wind streams while the ascending phase is dominated by more sporadic coronal mass ejection events (Kanekal, 2006; Reeves et al., 2011), and radiation belts respond differently to storms driven by coronal mass ejections (CMEs) and storms driven by corotating interaction regions (CIRs) (e.g., Turner et al., 2019).

2.2 Electron Radiation Belt Acceleration Mechanisms

Before relating observed electron flux enhancements (**Section 2.1**) to radiation belt energization (**Section 2.2.2**), we first provide a brief introduction to the theoretical framework associated with radiation belt dynamics (**Section 2.2.1**). While the concepts of adiabatic invariant theory are general, they are applied to the case of the Earth's radiation belts in the next paragraph.

2.2.1 Brief Introduction to Trapped Particles Dynamics and Adiabatic Invariant Theory

It takes a few hours down to a few minutes for the 50 keV to 5 MeV electrons of the outer belt to orbit around the Earth. During that time, these particles, trapped by the geomagnetic field, bounce 500 to 50,000 times from one hemisphere to the other while they gyrate 10^5 to 10^9 times around the magnetic field direction. In this context, it is convenient to describe the motion of radiation belt particles as the superposition of three quasi-periodic motions, each of them evolving on a very different timescale (e.g., Schulz and Lanzerotti, 1974):

1) A very fast motion of gyration around the magnetic field direction,
2) A slower bounce motion between the planet's hemispheres, and
3) A slow drift motion around the planet.

Each quasi-periodic motion is determined by the particle's characteristics (charge, mass, kinetic energy, pitch angle) as well as by the characteristics of the magnetic and electric fields (magnitude, direction, as well as spatial and temporal variability of the fields).

The magnitude of each quasi-periodic motion is quantified by an adiabatic coordinate, that is, by a quantity that is a constant of motion under certain spatial and temporal conditions. In particular, an adiabatic coordinate remains constant as long as the time variations for the fields are negligible on the timescale of the corresponding quasi-periodic motion (e.g., Northrop, 1963). That is why the reformulation of trapped particle dynamics in terms of adiabatic coordinates allows for a simplified description of radiation belt dynamics (e.g., Roederer, 2014).

In the absence of significant time variations in the fields, trapped radiation belt particles remain at about the same *average* equatorial radial distance from the center of the planet. They move along closed surfaces called *drift shells*. Their kinetic energy is conserved on average. In other words, in the steady state, there is neither net acceleration nor net deceleration occurring in the radiation belts. Energy variation for the trapped radiation belt particles requires time variations of the electric and/or magnetic fields. Since the magnetic force does no work, it is the electric field that exchanges energy with the trapped particles. This electric field may be induced by magnetic field time variations, or it may be due to variations in the electric potential. It is usually assumed that there is no component of the electric field parallel to the magnetic field direction, a good approximation in the inner magnetosphere on timescales longer than the gyro-period. In the DC realm, the electrical conductivity is orders of magnitude greater in the parallel direction of the magnetic field than in the perpendicular direction of the magnetic field so that the parallel conductivity is often approximated to be infinitely high (e.g., Stern, 1977).

2.2.2 Interpreting MeV Electron Flux Enhancements in Terms of Radiation Belt Acceleration

Electron flux enhancements are conventionally viewed as indicative of radiation belt acceleration because radiation belt spectra typically decrease with energy. Thus, the energization of a population of trapped particles is expected to manifest as a flux enhancement. The standard practice is to split the mechanisms driving radiation belt irreversible (i.e., non-adiabatic)

acceleration into two categories, depending on the source location of the population that is accelerated:

- The non-adiabatic acceleration is *local* when the energized population is already present within the drift shell.
- On the other hand, the non-adiabatic acceleration is *radial* (i.e., considered to be due to radial transport) when the energized population comes from another drift shell (i.e., roughly speaking, when the population was initially drifting at another average equatorial radial distance).

We focus below on the two most favored mechanisms for radiation belt energization, namely: 1) global acceleration *via* radial transport (**Section 2.2.2.1**) and 2) local acceleration *via* resonant interactions with chorus waves (**Section 2.2.2.2**). That said, many other mechanisms have been proposed over the years (see for instance the review by Friedel et al. (2002) for details).

2.2.2.1 Radial Acceleration and Radial Transport, Assuming Conservation of the First Two Adiabatic Anvariants

Acceleration by radial transport is usually associated with relatively slow field variations, occurring on a timescale longer than the bounce period. This includes ultra-low frequency (ULF) waves in the Pc4 and Pc5 ranges (2–22 mHz, (Jacobs, 1970)), which can be confined in magnetic local time (e.g., Li L. et al., 2017). One of the prevailing assumptions of radial transport mechanisms is that the first two adiabatic coordinates are conserved, as assumed below. That said, other types of radial transport processes have been proposed, and are expected to occur at times (e.g., Ukhorskiy et al., 2011; O'Brien, 2014).

In the following, we detail why acceleration is usually related to inward radial motion, and we illustrate the importance of analyzing radiation belt dynamics in terms of adiabatic coordinates.

2.2.2.1.1 Energization in a Dipole Field. In the special case of a dipole magnetic field, the association between inward radial transport and acceleration is straightforward. Drift shells are still in space, and they are conveniently labelled by their normalized equatorial radial distance, L (McIlwain, 1961). In that context, a particle transported from one drift shell to the other is displaced radially and its energy varies.

The relationship between radial transport and kinetic energy variation is straightforward when considering the conservation of the first two adiabatic invariants of the trapped particle. In the case of an equatorially trapped particle, we obtain that: $p^2/B = constant$, which is equivalent to: $p^2L^3 = constant$ in a dipole field, where $p = \sqrt{T\,(T + 2m_oc^2)}/c$ is the relativistic momentum, T is the kinetic energy, and B is the equatorial magnetic field strength. As a result, the amount of kinetic energy variation, dT, associated with the radial transport, dL, is defined as:

$$\frac{dT}{T} = -R\frac{(\gamma+1)}{\gamma}\frac{dL}{L} \tag{1}$$

where γ is the Lorentz factor and $R > 0$ is a function of pitch angle (e.g., Lejosne and Mozer, 2020, Eq. 9). The pitch-angle function is

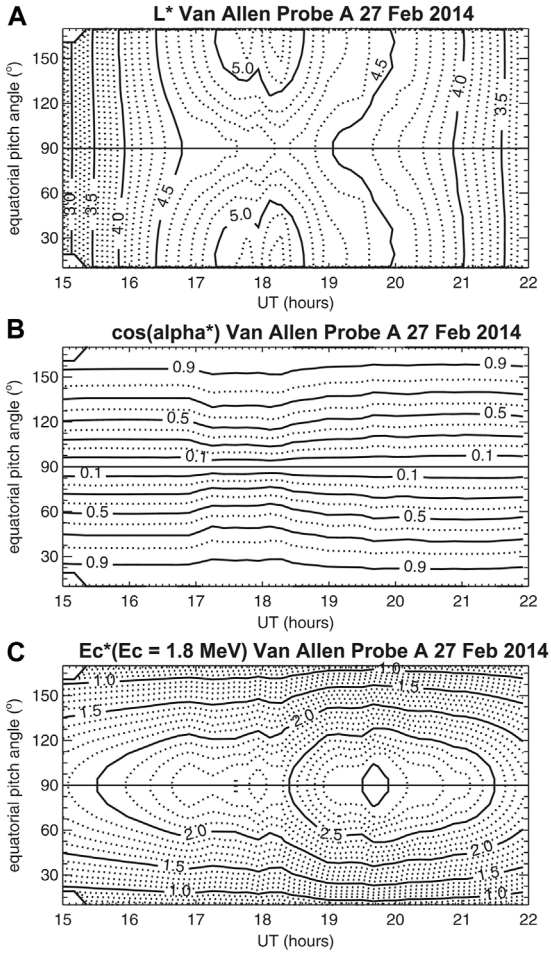

FIGURE 2 | The adiabatic coordinates $(L^*, \cos(\alpha^*), E_c^*)$ associated with a 1.8 MeV electron population measured by Van Allen probes A on the dayside during the 27 February 2014 event, as a function of the time of the measurement and for different equatorial pitch angles, α. From (Roederer and Lejosne, 2018).

such that $R = 3/2$ for equatorial particles. It decreases monotonically with decreasing pitch angle, until reaching a minimum value of $R = 1$ for field-aligned particles. This means that, for the same amount of radial transport, dL, equatorial particles experience the greatest amount of kinetic energy variation, dT. In all cases, **Eq. 1** details why inward radial transport ($dL < 0$) is usually associated with trapped particle energization ($dT > 0$). It also shows that radial transport is energy dependent: For the same amount of kinetic energy variation, dT, the amount of relative radial transport, dL/L, decreases with increasing kinetic energy, T.

2.2.2.1.2 Energization in a Distorted Field. At times, especially during active times in the Earth's outer belt, the magnetic field significantly departs from the dipole assumption. In that case, the relationship between inward radial transport and acceleration is more complex than **Eq. 1**. There is no longer a one-to-one correspondence between drift shell and normalized average

equatorial radial distance. The conservation of the first two adiabatic invariants only relates an amount of kinetic energy variation to an amount of magnetic field variation. Thus, an amount of kinetic energy variation does not inform about the amount of radial transport or change of drift shell for the trapped population. In the case of an equatorial particle, the relationship with kinetic energy variation, dT, and equatorial magnetic field variation, dB, is:

$$\frac{dT}{T} = \frac{1}{2}\frac{(\gamma+1)}{\gamma}\frac{dB}{B} \tag{2}$$

Trapped particles gain energy as they experience regions of higher magnetic field magnitude. Yet, this relationship does not tell us if particles travel from one drift shell to the other, or not. In other words, it does not inform us on the variation of the third adiabatic invariant. In fact, a population can gain kinetic energy and move radially in space while remaining on the same drift shell (i.e., while all three adiabatic invariants remain constant). Hence, "energization by radial motion" does not necessarily mean "violation of the third adiabatic invariant", because inward or outward radial motion can be fully adiabatic (see also, Lejosne and Kollmann, 2020). Such consideration demonstrates the importance of carefully defining the terms used to describe radiation belt acceleration.

To further illustrate this idea, **Figure 2** provides the (L^*, α^*, E_c^*) adiabatic coordinates associated with a population of 1.8 MeV electrons measured by Van Allen Probes A during the geomagnetic storm of 27 February 2014 (e.g., Xiang et al., 2017). The (L^*, α^*, E_c^*) coordinates were introduced by Roederer and Lejosne (2018) to provide a more intuitive quantification of the more commonly used adiabatic coordinates. They correspond to the equatorial radius of the drift shell (L^*), to the equatorial pitch angle (α^*), and to the kinetic energy (E_c^*) that the trapped 1.8 MeV electrons would have if the distorted magnetic field *slowly* turned into a dipole field (i.e., on a timescale that is slow enough to guarantee conservation of all three adiabatic coordinates). In the case of **Figure 2**, the quantities were computed assuming that the magnetic field is described by the model of Tsyganenko and Sitnov (2005). The spacecraft location and magnetic activity indices required by the magnetic field model were updated every 5 min. There is a small pocket of 1.8 MeV near-equatorial electrons with $E_c^* > 3$ MeV at $L^* \sim 4.4$ measured by Van Allen probes A around 19:40 UT, when the spacecraft is at $L = 5.5$. This means that, if no other processes occurred besides a *slow* magnetic field dipolarization (i.e., occurring on a timescale slower than their 10-min drift period), these trapped particles would be transported inward, from their current location in the compressed magnetic field, at $L = 5.5$, down to an equatorial altitude of 4.4 Earth radii, moving inward by 1.1 Earth radii while maintaining all three adiabatic coordinates constant (including $L^* = constant \sim 4.4$). They would become >3 MeV electrons: a >1.2 MeV energy gain that represents more than 65% of their initial kinetic energy. This amount of kinetic energy variation is altered by non-adiabatic effects that occur when field variations take place on a shorter timescale (<10 min). In short, it is important to take into account fully adiabatic processes when discussing trapped particle acceleration during active times in the Earth's outer belt (see also, Dessler and Karplus 1961; Kim and Chan 1997).

During data analysis, the component of radiation belt energization that is due to fully adiabatic processes (i.e., processes conserving all three adiabatic invariants) is the first component to be isolated by converting flux measurements into phase space density (PSD) parameterized in terms of adiabatic coordinates. The remaining dynamics result from processes that violate at least one adiabatic coordinate. **Figure 3**, from Jaynes et al. (2018), illustrates how mapping measured fluxes into adiabatic space provides a significantly different picture of radiation belt dynamics.

In this context, the correlation between the state of the Earth's outer belt and solar wind properties, as well as geomagnetic activity (**Section 2.1.2**) was revisited and quantified in terms of electron PSD and PSD dynamics (Zhao et al., 2017). In particular, electron PSD enhancements were shown to correlate well with the AL index, strengthening the role played by substorms in radiation belt acceleration.

2.2.2.1.3 Radial Transport, From One Drift Shell to Another. Defining radial transport as a motion from one drift shell to another, i.e., from one L^* coordinate to the other, allows us to disentangle adiabatic from non-adiabatic energization processes. The motion of a trapped particle from one drift shell to the other is associated with a violation (i.e., time variation) of its third adiabatic coordinate. The violation of a population's third adiabatic coordinate requires that 1) the time variations of the field occur on a timescale that is relatively short with respect to the drift period, and that 2) the time variations are asymmetric, i.e., that they vary with magnetic local time (e.g., Northrop, 1963). A detailed discussion of this process is provided in the review by Lejosne and Kollmann (2020), together with a derivation of the expression for the instantaneous rate of change of L^*.

When discussing radial transport from one drift shell to the other in the context of radiation belt acceleration, the focus is on two main regimes:

1) A coherent, sudden and significant variation of the third adiabatic coordinate, as in the case of a shock-induced acceleration associated with an injection or a drift resonant interaction, with an immediately significant effect on trapped particle dynamics (Li X. et al., 1993; Zong et al., 2009; Schiller et al., 2016; Hudson et al., 2017; Hao et al., 2019), or;
2) Many small uncorrelated variations in L^*, with a cumulative effect that becomes progressively significant for the trapped particle dynamics. This effect is conventionally assumed to be diffusive on sufficiently long timescales (e.g., Ukhorskiy and Sitnov, 2012). The magnitude of this radial diffusion process, i.e., the diffusion coefficient, D_{LL}, is defined as:

$$D_{LL} = \frac{\left[(\Delta L^*)^2\right]}{2\Delta t} \tag{3}$$

where the operator [ ] is the average over all magnetic local time sectors, and over many events (i.e., over many drift periods), and

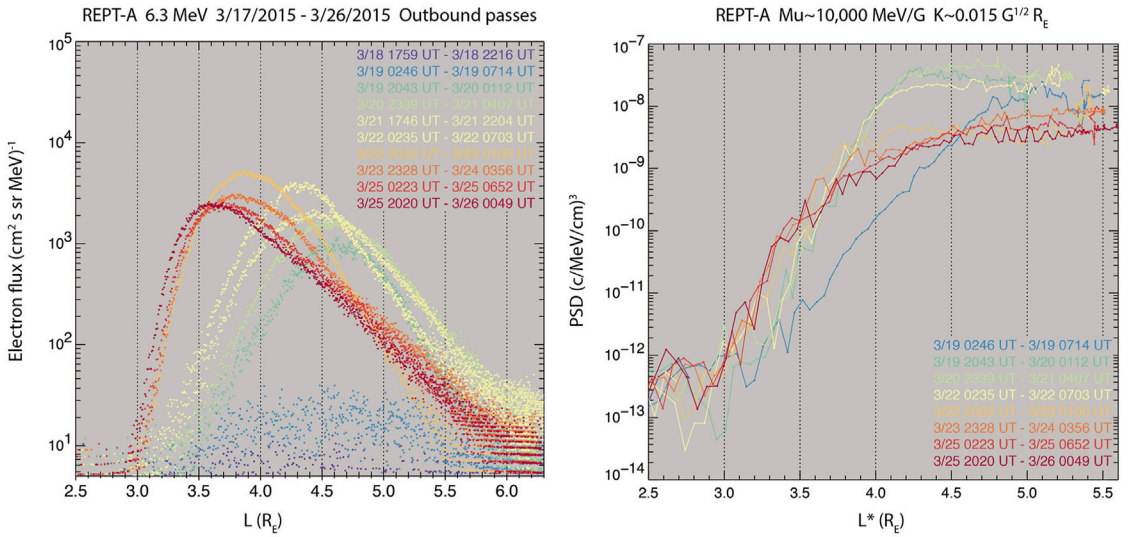

FIGURE 3 | (left) Time evolution of the 6.3 MeV electron flux as a function of the normalized equatorial radial distance, L, from 17 March 2015 to 26 March 2015; (right) Time evolution of the phase space density (PSD) of near equatorial electrons as a function of the L^* coordinate (for a first adiabatic invariant set to 10,000 MeV/G). From Jaynes et al. (2018).

ΔL^* corresponds to the total variation in L^* after a time interval, Δt. In theory, $[(\Delta L^*)^2]$ grows linearly with time once the time interval Δt is greater than the autocorrelation time for the variations of the field. As a result, D_{LL} is independent of the choice of Δt under this regime of normal diffusion.

These two regimes correspond to 1) non-linear and 2) quasi-linear descriptions of the large-scale wave-particle interactions.

Regardless of the type of radial transport process considered (fully adiabatic radial motion, rapid transport from one drift shell to the other, or slow diffusion from drift shell to drift shell), the amount of energy variation remains constrained by the conservation of at least the first two adiabatic coordinates. In the 1990s, it was suggested that fluxes of 20–200 keV electrons in the solar wind were insufficient to account for fluxes of MeV electrons measured in the Earth's outer belt, assuming that these electrons were simply transported radially inward (e.g., Li X. et al., 1997). While this finding was later questioned (e.g., Turner et al., 2021), it highlighted the need for an additional acceleration process at the time, and local acceleration by chorus waves was brought forward (e.g., Thorne, 2010).

2.2.2.2 Local Acceleration Associated With the Violation of the First Adiabatic Invariant

The other dominant mechanism for the acceleration of energetic (≳100 keV) electrons is resonant interactions with very low frequency (VLF) whistler-mode chorus waves outside the plasmasphere (e.g., Horne and Thorne, 1998; Summers et al., 1998; see also the reviews by: Bortnik et al., 2016; Koskinen and Kilpua, 2022). Chorus waves are naturally occurring electromagnetic emissions, commonly found in the Earth's radiation belt region. Plasma sheet electrons supplied to the inner magnetosphere during geomagnetically active times are unstable to the generation of whistler-mode chorus waves (e.g., Kennel and Thorne, 1967). The chorus emissions grow from thermal noise with a linear rate driven by the anisotropic distribution of these injected electrons, whose perpendicular temperature is greater than their parallel temperature (Kennel and Petschek, 1967). The path-integrated gain is sufficient to raise wave amplitudes to nonlinear levels (Li W. et al., 2007) where nonlinear trapping of electrons takes place (Nunn et al., 2003). Omura and Summers (2004) showed that chorus waves then ultimately grow non-linearly to a saturation level. As chorus waves propagate, they can interact resonantly with energetic electrons.

A resonance occurs when the Doppler-shifted wave frequency matches a multiple of the cyclotron frequency of an energetic electron moving through the wave packet, i.e., when:

$$\omega - k_{\parallel} v_{\parallel} = \frac{n\Omega_{ce}}{\gamma} \tag{4}$$

where ω is the frequency of a single wave, n is an integer ($n = 0, \pm 1, \pm 2, \ldots$), Ω_{ce}/γ is the magnitude of the electron gyrofrequency retaining the sign of the electron charge, k is the wave vector, and v is the electron velocity, where the parallel suffix indicates the direction parallel to the background magnetic field. The case of $n = 0$ corresponds to the Landau resonance where $\omega = k_{\parallel} v_{\parallel}$, and can arise when the chorus waves have an electric field component parallel to the background magnetic field, i.e., a non-zero wave normal angle. The cases $n = \pm 1, \pm 2, \ldots$ correspond to Doppler shifted cyclotron resonances. Here, in the frame of reference of the electron moving along the magnetic field, the wave frequency is Doppler shifted to the electron's cyclotron frequency and the electron experiences an electric field rotating at n times its rate of gyration. The electron is then accelerated or decelerated by this

electric field depending on the phase of the wave in relation to the electron's gyration phase. Whistler waves have frequencies below the electron cyclotron frequency, and so, in the case of a chorus wave propagating along the magnetic field, the frequency must be Doppler shifted up in order to achieve an $n = -1$ resonance with electrons. In the case of relativistic particles, where $\gamma > 1$, a smaller upwards Doppler shift is necessary for resonance than in the case of non-relativistic particles. The negative sign on the left-hand side of **Eq. 4** then needs to become positive, which can be achieved when $k_\parallel$ and $v_\parallel$ have different signs and, therefore, the waves resonate with electrons traveling in the opposite direction. Resonances where $|n| > 1$ take place for obliquely propagating waves as the wave field is then elliptically polarized, constructed from left- and right-handed wave components. In the non-relativistic case, $\gamma = 1$, and we can solve **Eq. 4** to obtain the parallel velocity of an electron in Doppler-shifted cyclotron resonance with the wave. As relativistic effects become important, the perpendicular component of the electron velocity, $v_\perp$, is introduced to the resonance condition *via* γ and a semi-ellipse in $v_\parallel$ and $v_\perp$ space defines the resonant velocities, constraining the resonant electron energies.

In case of resonance, the wave phase velocity, $\omega/k_\parallel$, and the components of the particle's velocity perpendicular and parallel to the ambient magnetic field, $v_\perp$ and $v_\parallel$, respectively, become linked. This relationship allows for efficient energy exchange between the wave and the electron. Gendrin (1981) showed that, for small amplitude waves, the kinetic energy of the electron is conserved in the reference frame of the wave. Transforming back to the lab reference frame in the non-relativistic case:

$$\left(\frac{\omega}{k_\parallel} - v_\parallel\right)^2 + v_\perp^2 = constant \tag{5}$$

and the electron can gain or lose energy to the monochromatic wave, potentially changing both the pitch angle and energy of the electron. For the interested reader, the relativistic case is shown by Summers et al. (1998). As $v_\parallel$ (and for the relativistic case $v_\perp$) changes, the phase velocity, and therefore the frequency of the wave that the electron resonantly interacts with, also changes in accordance with the resonance condition.

In practice, chorus waves are not monochromatic, i.e., they have a band width. For each wave frequency, **Eq. 5** defines a circle (or in the relativistic case, an ellipse) in $v_\parallel$ and $v_\perp$ space known as a *single wave characteristic*. The single wave characteristics cross the resonance condition in velocity space. Thus, a diffusion curve is defined in $v_\parallel$ and $v_\perp$, every point of which is tangential to some single wave characteristic, corresponding to a particular wave frequency. As mentioned above, electrons in Doppler-shifted cyclotron resonance can be accelerated or decelerated by the chorus wave according to the angle between the wave's magnetic field and the instantaneous perpendicular velocity of the electron. As such, electrons move randomly up or down single wave characteristics and the net behavior is in the direction of the decreasing particle distribution function along the single wave characteristic. A series of resonant interactions with chorus waves covering a range of frequencies then results in a net change of the particle's energy and pitch angle. The usual assumption is that each wave-particle interaction results in a small perturbation of the particles' characteristics. In that case, the cumulative effect of many interactions between chorus waves and radiation belt electrons is diffusive in energy and pitch angle.

When introducing more realistic conditions, including large amplitude waves, significant variations in energy and pitch angle can occur during a single interaction, and non-linear behaviors need to be considered (e.g., Bortnik et al., 2016). Theoretical analysis and test particle simulations have enabled detailed descriptions of the microphysics of chorus wave-particle interactions (e.g., Omura, 2021). They have shown how energetic electrons phase-trapped in coherent whistler waves can gain significant amount of energy over very short timescales (e.g. Albert, 2002). In particular, they have highlighted effective electron energization mechanisms, such as the relativistic turning acceleration of radiation belt electrons by chorus waves of sufficiently large amplitude (Omura et al., 2007), combined with ultra-relativistic acceleration interactions (Summers and Omura, 2007; Omura et al., 2015). Effective acceleration can occur through successive nonlinear trappings by consecutive multiple sub packets of a chorus wave element (Hiraga and Omura, 2020).

As a result, there is a dichotomy similar to what exists for radial transport modeling when it comes to describing local acceleration associated with the violation of the first adiabatic invariant in the radiation belts:

1) A non-linear framework, which can detail coherent, sudden and significant variations of the trapped electrons' energy and pitch angle *via* phase-trapping with realistic chorus wave models, and;
2) A quasi-linear model, where many small uncorrelated variations in pitch angle and energy have a cumulative effect that becomes progressively significant for the trapped particle dynamics, and that is assumed to be diffusive on sufficiently long timescales.

2.3 Modeling Framework to Quantify and Compare the Effects of Local and Radial Acceleration on Radiation Belt Dynamics

In order to quantify the effects of local and radial acceleration, and to put them into context, it is necessary to choose a global framework in which to model radiation belt dynamics. Here, it is important to realize that modeling implies trading off accuracy against practicality. A limit to the level of accuracy achievable by a radiation belt model is a potential limit to the level of accuracy with which the effects of local and radial acceleration can be quantified. Thus, it is important to keep in mind the set of assumptions underlying a radiation belt model and to remember the scope of the modeling framework. The formalism adopted by most radiation belt models (**Section 2.3.1**) as well as the limits to its accuracy (**Section 2.3.2**) are summarized below.

2.3.1 The Fokker-Planck Formalism, a Convenient Approximation for Radiation Belt Models

A detailed and accurate modeling of radiation belt particle dynamics is nothing short of impossible: It would require a

complete and highly accurate specification of the spatial and temporal variations of the electromagnetic fields on a multiplicity of spatio-temporal scales—from the drift-scale down to the gyro-scale. Particle-in-cell simulations allow for self-consistent interactions between particles and wave fields to be simulated, however computational requirements are high and only small spatial scales and time periods can be modelled this way (e.g., Camporeale, 2015; Allanson et al., 2019). Even when the fields are specified by numerical models (e.g., MHD fields), injecting test particles to simulate radiation belt dynamics remains cumbersome. This impossibility calls for necessary tradeoffs. A powerful way to reduce the number of variables to handle is the use of the adiabatic theory of magnetically trapped particles (**Section 2.2.1**). Adiabatic theory *"provides correct answers only as long as we don't look too close and are not expecting too detailed information"* (Roederer and Zhang, 2014). To account for uncertainties in electromagnetic field dynamics, we leverage probability theory, in particular the Fokker-Planck formalism. This formalism accounts for uncertainty by assuming random changes in the variables, relating average characteristics of the electromagnetic fields to average properties of the radiation belt dynamics. It is these tools (Fokker-Planck equation and adiabatic invariant theory) that have been successfully combined for more than 25 years (Beutier and Boscher, 1995) to facilitate operational radiation belt modeling. In particular, these simplifications allow for radiation belt simulations over long time intervals (months to years) (e.g., Glauert et al., 2018).

Specifically, most physics-based radiation belt models consist of solving a Fokker-Planck equation reduced to a diffusion equation, with the objective of providing an approximate description for the time evolution of the radiation belts:

$$\frac{\partial f}{\partial t} = \sum_{i,j} \frac{\partial}{\partial J_i}\left(D_{i,j} \frac{\partial f}{\partial J_j} \right) + Sources - Losses \qquad (6)$$

where $f(J_1, J_2, J_3)$ is the *drift-averaged* particle distribution function, J_i are the action variables, proportional to the adiabatic coordinates, and $D_{i,j}$ are the *drift-averaged* diffusion coefficients (e.g., Schulz and Lanzerotti, 1974). The "*Sources*" and "*Losses*" terms account for other non-diffusive processes affecting the distribution function. In practice, diffusion in terms of action variables is often reformulated in different coordinate systems. In particular, diffusion in terms of pitch angle, energy and L^* is often preferred. Thus, diverse reformulations of the same **Eq. 6** exist.

Defining realistic boundary conditions and performing model-observation comparisons require relating the variables of **Eq. 6** to measurable quantities. On one hand, it is straightforward to relate the trapped particle distribution in phase space (i.e., the phase space density, PSD) to experimental data: PSD is proportional to the directional differential flux, a measurable quantity (e.g., Roederer, 1970, p.93). On the other hand, defining the adiabatic coordinates cannot be done relying solely on experimental data. Indeed, since the adiabatic coordinates are:

1) $\mu = p_\perp^2 / 2 m_o B$, where m_o is the particle rest mass.

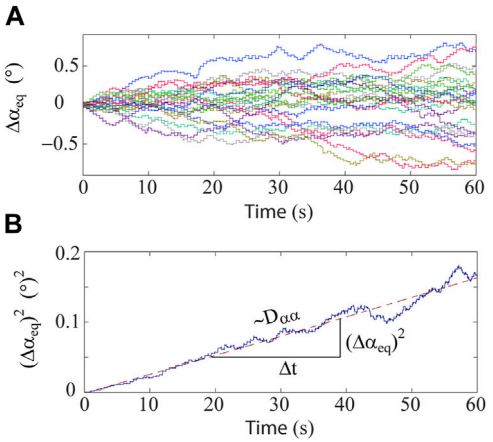

FIGURE 4 | A long-run simulation of 24 electrons experiencing cumulative linear scattering interactions, resulting in quasilinear diffusive behavior. **(A)** Change in equatorial pitch angle of all particles as a function of time. **(B)** The variance of all particles equatorial pitch angles increases linearly as a function of time, consistent with diffusive scattering. The rate of change of the variance yields the pitch angle diffusion coefficient, $D_{\alpha\alpha}$. Adapted from Bortnik et al. (2016).

2) $J = \oint p_\parallel ds$, where the integral goes over the full bounce motion along the magnetic field line, and
3) $\Phi = \oint_\Gamma \boldsymbol{A} \cdot \boldsymbol{dl} \propto 1/L^*$, where $\boldsymbol{A}$ is the magnetic potential vector and Γ is the instantaneous drift contour delimiting the drift shell,

Quantifying the adiabatic coordinates of MeV populations associated with a PSD sample requires information on the instantaneous magnetic field topology along the full drift contour. This means working with a magnetic field model. In addition, the adiabatic coordinates of a measurement can be undefined under certain conditions, as in the case in the presence of open drift shells—where particles are lost before completing a full drift around the Earth. This is a spatial limit to the scope of the model and outer boundary specification (e.g., Albert et al., 2018).

2.3.2 Limits to the Diffusion-Driven Radiation Belt Model

Diffusion-driven radiation belt models solving **Eq. 6** are thought to work best for very high energy particles (e.g., Fok, 2020). That said, they remain limited in several ways, as discussed below.

First, **Eq. 6** assumes that radiation belt dynamics are mainly due to physical processes whose overall effects can be encapsulated by diffusion coefficients. In other words, according to **Eq. 6**, radiation belt dynamics are primarily due to many very small, uncorrelated, time-stationary field fluctuations, resulting in many very small ($\Delta J_i / J_i \ll 1$), uncorrelated, perturbations of the trapped particle dynamics, akin to random walks in phase space at all scales—from the drift-scale down to the gyro-scale. In this diffusive picture, the scattering of a population of particles with the same initial characteristics increases linearly with time in phase space. This concept is illustrated in **Figure 4** in the case of pitch angle diffusion.

The postulate of a regime that is mainly diffusive also means that **Eq. 6** is ill-suited at times when particle dynamics are coherent, in particular at times when significant particle injections occur, and at times when large amplitude waves result in non-diffusive regimes (e.g., nonlinear phase bunching, phase trapping) (e.g., Riley and Wolf, 1992; Albert, 2002; Bortnik et al., 2008; Ukhorskiy et al., 2009; Omura et al., 2015).

Second, **Eq. 6** cannot resolve radiation belt dynamics on a timescale shorter than that of drift phase mixing. The dynamics of the PSD described by **Eq. 6** are drift-averaged. As a result, all equation variables are independent of magnetic local time by design. This means, for instance, that radiation belt drift echoes (e.g., Lanzerotti et al., 1967) cannot be reproduced using **Eq. 6**. That is also why this framework cannot reproduce shock-injections during sudden storm commencements for instance. In this case, the modelling efforts favor test particle simulations (e.g., Li X. et al., 1993; Hudson et al., 1997: Kress et al., 2007: Hudson et al., 2017).

3 ACCELERATION IN THE RADIATION BELTS: AN EVOLVING PICTURE

Keeping the observational (**Section 2.1**) and theoretical (**Sections 2.2**, **2.3**) context in mind, this section describes how the picture of radiation belt acceleration has evolved over the past 25 years, from an emphasis on radial diffusion (**Section 3.1.1**) to a paradigm shift underscoring the role of local acceleration in the radiation belts (**Section 3.1.2**). At the outer planets, a consensus is still pending, as detailed in **Section 3.2**. Unambiguously solving this puzzle remains a challenge, discussed in **Section 3.3**.

3.1 From the Importance of Radial Diffusion to the Importance of Local Wave Particle Interactions in the Earth's Radiation Belts

Radial diffusion from an external source towards the planet was originally thought to be the main mechanism for radiation belt acceleration (e.g., Fälthammar, 1965). When modeling relied on a radial diffusion equation including electron lifetimes, shortcomings in model-data comparisons highlighted a need for improvement. As a result, the role of local acceleration was brought forward (e.g., Horne and Thorne, 1998; Green and Kivelson, 2004; Horne et al., 2005; Koller et al., 2007; Reeves et al., 2013). This was supported in particular by observations of a growing peak in the radial PSD profile of the most energetic electrons of the Earth's outer belt, derived from measurements made during the recovery phase of geomagnetic storms (e.g., Brautigam and Albert, 2000; Iles et al., 2006). These points are detailed in this **Section 3.1**.

3.1.1 From Radiation Belt Modeling Based on the Normal Diffusion Equation

A first version of **Eq. 6** focuses on the effects of 1) radial diffusion and 2) losses due to pitch angle scattering into the loss cone, meaning finite electron lifetimes:

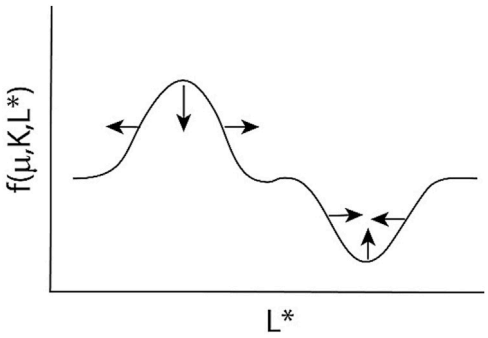

FIGURE 5 | Time evolution of a PSD described by a normal radial diffusion equation (from Green and Kivelson, 2004).

$$\frac{\partial f}{\partial t} = L^2 \frac{\partial}{\partial L}\left(\frac{D_{LL}}{L^2}\frac{\partial f}{\partial L}\right) - \frac{f}{\tau} \tag{7}$$

where L stands for L^*, inversely proportional to the third adiabatic coordinate, D_{LL} is the radial diffusion coefficient, and τ is the electron lifetime resulting from the combined effect of the pitch angle scattering induced by different waves.

The use of the master **Eq. 7** to describe radiation belt dynamics constrains the range of possible time variations for the modeled PSD. Indeed, following Fick's first law of diffusion, the net "current" of particles that flow through a unit area of drift shell per unit of time, i.e., the diffusion flux, is (e.g., Walt, 1994):

$$\text{"Current"} = -\frac{D_{LL}}{L^2}\frac{\partial f}{\partial L} \tag{8}$$

This means that radial diffusion acts to smooth the PSD radial profile. In other words, radial diffusion decreases peaks and increases valleys present in the PSD radial profile. An illustration is provided in **Figure 5**, in the case of a 1D diffusion equation in the absence of loss.

D_{LL} contains all the information on the physical processes that drive cross drift shell motion, i.e., it quantifies the *efficiency* of the radial diffusion process, and it directly relates to the field dynamics. Yet, the magnitude of D_{LL} alone is not enough to determine how much radial diffusion affects radiation belt dynamics. Indeed, it is the *"Current"* quantity, i.e., $-(D_{LL}/L^2)(\partial f/\partial L)$ (**Eq. 8**), that determines the *manifestation* of the diffusion process – that is, it is this quantity that drives the PSD time variations, $\partial f/\partial t$ (**Eq. 7**). Thus, if the PSD radial gradient, $\partial f/\partial L$, is significant, the effect of radial diffusion may appear significant, even if the magnitude of the radial diffusion coefficient D_{LL} is relatively small (as is the case at very low L shells in the Earth's inner radiation belt for instance). Conversely, if the PSD radial gradient is relatively small, radial diffusion may appear unimportant for the dynamics of this region of the belts, regardless of the magnitude of the radial diffusion coefficient. This reasoning applies to all diffusion modes. It demonstrates the importance of taking into account PSD gradients when comparing the effects of various diffusion processes (i.e., various waves) on the time

evolution of the PSD. This also highlights the difficulty of directly relating measured wave power to PSD and/or flux variations (e.g., Simms et al., 2021).

Solving **Eq. 7** for the PSD, f, requires characterizing the radial diffusion coefficient, D_{LL}, the electron lifetime, τ, and setting boundary conditions. Different studies choose different settings. The time-varying coefficients, D_{LL}, are often provided by an empirical law for electromagnetic radial diffusion, such as defined by Brautigam and Albert (2000) for example based on a combination of *in situ* and ground-based measurements of time-varying magnetic fields parametrized by a geomagnetic activity index (Kp). More recent data sets have used both ground-based and *in situ* magnetic and electric field measurements to infer D_{LL} (Ozeke et al., 2014a; Liu et al., 2016; Ali et al., 2016; Sandhu et al., 2021). Radial diffusion coefficients can also be determined from solar wind measurements (e.g., Li X. et al., 2001; Lejosne, 2020) or MHD test-particle simulations (Tu et al., 2012; Li Z. et al., 2017). The electron lifetime is usually parameterized based on plasmapause location and magnetic activity (e.g., Orlova et al., 2016). In all cases, the solution of the standard diffusion equation (**Eq. 7**) displays much of the variability of the Earth's outer belt on long timescales (months to years) (e.g., Li X. et al., 2001; Shprits et al., 2005; Chu et al., 2010; Ozeke et al., 2014b; Drozdov et al., 2015, 2017). In particular, it describes radiation belt dynamics well during geomagnetically quiet times (e.g., Selesnick et al., 1997; Su et al., 2015; Ripoll et al., 2019).

However, model-observation comparisons can also present notable discrepancies, in particular for MeV electron fluxes during the recovery phase of magnetic storms (e.g., Brautigam and Albert, 2000; Shprits et al., 2005; Shprits et al., 2007a; Ozeke et al., 2020). Specifically, the development of a peak in the PSD radial profile of the outer belt has been put forward as evidence of the effect of an additional local acceleration mechanism (e.g., Miyoshi et al., 2003; Chen et al., 2007; Reeves et al., 2013): It is contrary to what is expected from radiation belt dynamics driven primarily by radial diffusion (**Figure 5**). A growing local peak in the PSD radial profile appears to be a common feature of PSD enhancement events—at least for near-equatorial particles with a first adiabatic coordinate that corresponds to ~1 MeV at L = 5. Indeed, based on four years of flux measurements from Time History and Events of Macroscale Interactions during Substorms (THEMIS) and Van Allen Probes converted into PSD, 70 out of 80 observed enhancement events presented a growing peak (Boyd et al., 2018). The geomagnetic conditions for a growing peak are variable: 38 out of 70 occurred during moderate or strong storms, while 32 occurred during small storm or non-storm times (i.e., with a Dst index no less than −50 nT). In all cases, the location of the local peak in the PSD radial profile was shown to be outside of the plasmasphere, about 1.25 Earth radius away from the plasmapause location on average.

3.1.2 To the Current State of the Art

When the effect of chorus waves on radiation belt dynamics is included as an additional source term in the Fokker-Planck equation (e.g., Tu et al., 2009; Xiang et al., 2021), or, more commonly as additional diffusion terms (e.g., Varotsou et al., 2005; Glauert et al., 2018), the quality of radiation belt modeling improves: Simulations yield a peak in the PSD radial profile, in reasonable agreement with observations (e.g., Shprits et al., 2008; Subbotin et al., 2010; Thorne et al., 2013; Ma et al., 2018; Wang and Shprits, 2019).

This apparent improvement in radiation belt modeling leads to the "two-step" picture for the acceleration to relativistic and ultra-relativistic energies in the outer radiation belt, in which both local and radial processes contribute to MeV electron production. This mechanism is well supported by both case studies (e.g., Jaynes et al., 2015; Zhao et al., 2018) and statistical analysis (e.g., Zhao et al., 2019b). It works as follows: First, the injection of source (tens of keV) and seed (hundreds of keV) electrons during substorms lead to whistler mode chorus wave generation and subsequent acceleration of the seed population to relativistic, and potentially ultra-relativistic (Allison et al., 2021), energies *via* local wave-particle interactions (e.g., Meredith et al., 2002), on a relatively rapid timescale. An illustration of this concept is provided in **Figure 6** (Jaynes et al., 2015). Meanwhile, radial diffusion progressively redistributes the newly created MeV population, smoothing out the PSD radial profile and providing additional energy to the MeV particles transported inward.

In summary, the picture of electron radiation belt acceleration has evolved over time in response to measurements from new missions in the Earth's inner magnetosphere, most notably thanks to the NASA Combined Release and Radiation Effects Satellite (CRRES) in the 1990s and most recently, the NASA THEMIS and the Van Allen Probes. In comparison, the magnetospheres of the outer planets are lacking data to differentiate between the leading processes for electron radiation belt acceleration, as summarized below.

3.2 Differentiating Between the Leading Processes for Electron Radiation Belt Acceleration at the Outer Planets

The magnetospheres of the four strongly magnetized outer planets (Jupiter, Saturn, Uranus, and Neptune) are hosts to electron radiation belts that display considerable differences from those of the Earth, namely energetic electron distributions that permanently extend to energies in excess of 70 MeV at Jupiter or 20 MeV at Saturn (Bolton et al., 2002; Kollmann et al., 2011). In addition, there is a large diversity of acceleration modes not resolved in the terrestrial geospace, largely due to those planets' strong magnetic fields, fast rotation, and large amounts of neutral material within their volume (Roussos and Kollmann, 2021). A consensus on the role of adiabatic against local electron acceleration at the outer planets is thus still pending, especially since the challenges in measuring comprehensively these systems are even higher than at Earth (Roussos et al., 2018b).

Specifically, almost all *in-situ* energetic electron observations at the outer planet radiation belts are single point measurements. This means that crossings of the radiation belts occur typically between several days to few weeks after the seed electron population in the middle and outer magnetosphere and/or the

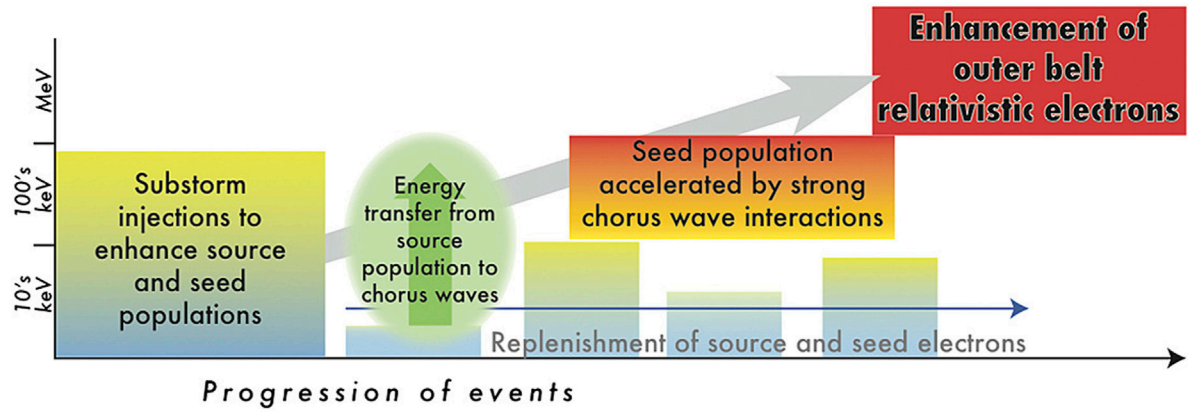

FIGURE 6 | Sequence for MeV acceleration by chorus waves in the Earth's outer radiation belt (from Jaynes et al., 2015).

solar wind has been sampled. Several methods that offer an indirect, quasi-regular monitoring of the seed regions (Tsuchiya et al., 2011; Murakami et al., 2016; Roussos et al., 2018a; Han et al., 2018; Bradley et al., 2020) reveal correlated appearances of MeV electron radiation belt transients at Jupiter and Saturn in response to episodic events in the outer magnetosphere, originating from internally-driven dynamics, or in the solar wind (Tsuchiya et al., 2011; Roussos et al., 2018b; Yuan et al., 2020). Such correlations alone, however, have proven insufficient to attribute the generation of transient populations to local or adiabatic acceleration. Another constraint derives from the difficulty to obtain energy-resolved measurements at all outer planets for electrons above ~1 MeV. As a consequence, available PSD electron profiles are largely limited to the sub-relativistic range (Kollmann et al., 2011; Ma et al., 2018), with only few exceptions where estimates of the macroscopic characteristics of electron spectra into the ultra-relativistic range (e.g., spectral slope) have been determined (e.g., Selesnick et al., 1997; Mihalov et al., 2000; Kollmann et al., 2018; Garrett and Jun 2021).

Despite the limitations, significant progress has been achieved in understanding electron acceleration at the outer planets, particularly at Jupiter and Saturn, thanks to extensive observations by the Galileo, Juno, and Cassini orbiters. Long-term imaging of the Jovian radiation belts in radio wavelengths also provides key evidence (de Pater and Goertz. 1990; Bolton et al., 2002). On average, adiabatic radial inward transport is important at the outer extension of both Jupiter's ($L > 10$) and Saturn's ($3.5 < L < 10$) electron belts (Kollmann et al., 2011, 2018; Roussos et al., 2018b; Ma et al., 2018; Sun et al., 2019, 2021; Paranicas et al., 2020; Yuan et al., 2021). This picture emerges either from mapping both the steady-state configuration of each electron belt, or by observing the temporal evolution of their perturbed states (e.g., Roussos et al., 2010). Radial transport can occur in various modes and be triggered by a variety of processes, such as ULF waves (Van Allen et al., 1980; Roussos et al., 2007), centrifugal interchange instability (Thorne et al., 1997; Mauk et al., 2005), transport by variable, large scale coherent plasma flows (Hao et al., 2020), or even solar wind transients.

The potential for local acceleration in the outer electron belt regions by whistler-mode chorus waves has been explored mostly through simulations (Shprits et al., 2012; Woodfield et al., 2014, 2019), but observationally, the case of important or even dominant contributions by local heating is even stronger for the innermost portion of the electron belts. The strong magnetic field and the low plasma densities in the inner jovian and saturnian magnetospheres generate an environment that is conducive to a continuous relativistic electron acceleration by Z-mode waves (Woodfield et al., 2018). Support for this case exists particularly for Saturn, in the form of butterfly pitch angle distributions (Yuan et al., 2021), and by simulations for Jupiter (Nénon et al., 2017). Even if local acceleration may be dominant at low L-shells, observations at both Jupiter and Saturn indicate that adiabatic transport is still a non-negligible regulator of the belts' state and dynamics. Episodes of strong electron enhancements in Jupiter's synchrotron belts have been attributed to periods of amplified radial diffusion rates (Miyoshi et al., 2000; Tsuchiya et al., 2011), triggered by periods of solar UV heating of the planet's thermosphere. These and many other observations (e.g., Louarn et al., 2014, 2016), indicate that the interplay between local and adiabatic heating at the outer planet electron belts likely changes with time and across a variety of temporal and spatial scales. Finally, local acceleration may also be important in generating the seed electron population of the radiation belts at Jupiter and Saturn. Impulsive injections of (ultra)relativistic electrons have been observed in the outer magnetospheres of both planets (Simpson et al., 1992; Mauk et al., 2005; Roussos et al., 2016; Palmaerts et al., 2016; Clark et al., 2017), but neither the acceleration process nor the fate of these electrons is yet fully resolved.

3.3 Solving the Radiation Belt dynamic Puzzle: A Multi-Faceted Challenge

While the role played by whistler-mode chorus waves in radiation belt acceleration is now well accepted at Earth, defining its relative importance remains controversial. In other words, we still do not know the percentage of radiation belt acceleration due to local acceleration *via* chorus wave-particle interactions. In the following, we highlight some of the major challenges to remove ambiguities and answer this question.

3.3.1 A Time-Varying Puzzle

First, the overall radiation belt dynamics result from concurrent processes that can influence each other and whose individual contributions are difficult to evaluate and time-varying (e.g., Tu et al., 2009; Xiang et al., 2021). Thus, any uncertainty in the magnitude of a source or loss process leads to other uncertainties in the magnitude of other processes.

In this context, it is also critical to quantify the losses that contribute to the "*Losses*" term in **Eq. 6** to fully understand acceleration events. Losses can be created internally *via* wave-particle pitch-angle scattering or ULF wave effects, resulting in atmospheric precipitation, or at the outer boundary of the magnetosphere, a process known as magnetopause shadowing (Turner et al., 2012), resulting in losses to the interplanetary medium. Radiation belt electrons are susceptible to pitch-angle scattering by three main wave modes: broadband VLF hiss, electromagnetic ion cyclotron (EMIC) waves, and coherent VLF chorus (Thorne et al., 2005). Hiss losses are most relevant within the dense plasmasphere region where hiss can persist (Thorne et al., 1979), although this loss mechanism becomes less important during active times when the plasmapause location can move inward on short timescales (Goldstein et al., 2005). When this happens, the particle distribution that was within the plasmasphere is suddenly outside and susceptible to other loss or acceleration processes. Electron lifetimes within the plasmasphere have been estimated using both theoretical and observational techniques (Jaynes et al., 2014; Orlova et al., 2014; Claudepierre et al., 2020). Hiss-driven loss is considered to be a slower, steady loss rather than an impulsive event. On the other hand, EMIC waves can cause intense, sudden scattering that manifests as localized depletions, and are thought to be a primary loss factor of relativistic and ultra-relativistic electrons in the heart of the outer radiation belts (Drozdov et al., 2021b). VLF chorus waves also scatter outer belt electrons efficiently, particularly in the ring current energy range (Shprits et al., 2007b). Microbursts, trains of which may be created by quasi-periodic chorus waves typically seen in the outer radiation belt, can cause relativistic losses in concert with lower energy loss due to wave propagation to higher latitudes (Miyoshi et al., 2020). Relativistic losses can also be contributed by the phenomenon referred to as dusk-side relativistic electron precipitation (Comess et al., 2013), which are driven by both microburst events and non-microburst events. Microburst trains may be long-lasting, as evidenced by their connection to pulsating aurora which can be long-duration and widespread (Jones et al., 2013), and therefore may be a significant loss process for relativistic outer belt electrons. Finally, ULF waves have been implicated in energetic electron losses through a mechanism by which the radial oscillatory motion causes a lowering of the mirror point in a modulated manner (Brito et al., 2012). Taken together, these effects contribute to a net loss term in the characterization of the outer radiation belt system, and must be accounted for in order to accurately quantify the acceleration terms.

In addition, an accurate determination of the location of the last closed drift shell is an important parameter to include in Earth's radiation belt modeling as it contributes to radiation belt losses during active times. Yet it requires assuming an instantaneous magnetic field topology, including the magnetopause location (e.g., Albert et al., 2018; Olifer et al., 2018; Staples et al., 2020), and the accuracy of such assumption is hard to quantify. In addition, diffusion coefficients require knowledge of instantaneous field variations and plasma conditions all along the trapped particles' drift shell, including plasmapause location (e.g., Malaspina et al., 2016, 2020; Wang et al., 2020). For the energy diffusion coefficient, this means knowing the chorus wave spectral intensity, amplitude, and plasma density at all magnetic local times over the drift shell in real time (Thorne et al., 2013; Allison et al., 2021). For the radial diffusion coefficient, this means knowing instantaneous electric and magnetic field variations all along the drift contour (e.g., Lejosne and Kollmann, 2020). Thus, assumptions need to be made, and averaged conditions are usually preferred. As a result, diffusion coefficients are often parameterized in terms of magnetic activity indices, smoothing out estimated errors as well as natural variability (e.g., Watt et al., 2017). Yet, the need for "event-specific" diffusion coefficients is now well recognized (e.g., Tu et al., 2009) and efforts have been made to provide such information (Tu et al., 2012; Li Z. et al., 2017; Lejosne, 2020; Ozeke et al., 2020).

That said, converting measurements into inputs to the 3D Fokker-Planck equation means complying with the presupposed diffusion framework (**Section 2.3**), an increasingly complicated task as data resolution improves.

3.3.2 Challenging the Applicability of Our Current Radiation Belt Master Equation: A Local Peak in the PSD Radial Profile is not Conclusive Evidence for Local Acceleration

Most counter-arguments to local acceleration as the prevailing radiation belt acceleration mechanism challenge the interpretation of experimental data resulting in a peak in the PSD radial profile. These counter-arguments boil down to two main reasons.

The first is technical: Mapping measurements into phase space requires assuming a magnetic field model, whose real-time accuracy is difficult to quantify (see also the review by Green (2006) for methods to obtain PSD estimates). Let us also mention that the DC and low frequency electric fields can affect the dynamics of source and seed particles (tens to hundreds of keV): They can distort trapped particle drift shells, thereby modifying their third adiabatic coordinate L^*.

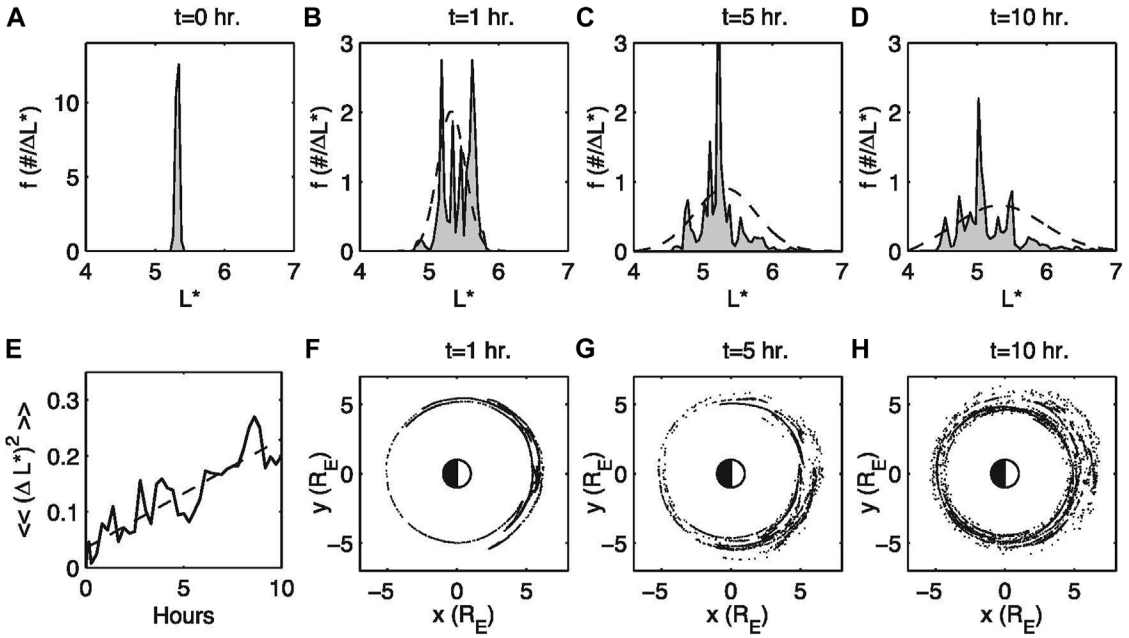

FIGURE 7 | Time evolution of a normalized distribution function, *f*, during a test particle simulation including 10,000 equatorial guiding centers injected in electric and magnetic fields provided by the Lyon-Fedder-Mobarry (LFM) global MHD simulation code (Lyon et al., 2004) during a 10 h time interval (3 January 2003) with "nothing unusual" (solar wind speed ~ 550 *km/s*, density ~ 10 cm^{-3} and IMF B_z fluctuating between ± 10 nT). The distribution is **(A)** initially radially localized at $L^* = 5.3$, and it spreads over time in L* **(B–D)**, to encapsulate the time evolution of the locations of the tracked test particles **(F–H)**. The time evolution of the distribution function representing the test particles is compared to the time evolution of the solution of the diffusion equation [dash lines in panels **(B–D)**], highlighting significant discrepancies, even after many drift periods (from Kress et al., 2012).

While this effect has been observed and studied for tens to hundreds of keV electrons in the Earth's inner belt (e.g., Selesnick et al., 2016; Lejosne et al., 2021), drift shell distortion by large-scale electric fields is reasonably omitted when it comes to defining the adiabatic coordinates of MeV particles in the Earth's outer radiation belt. Even when so, the conversion of experimental data into phase space density (PSD) parameterized by adiabatic coordinates remains a pitfall (e.g., Selesnick and Blake, 2000; Green and Kivelson, 2004). In particular, errors in magnetic field models can lead to the apparition of an artificial peak in the PSD radial profile, which vanishes when a realistic magnetic field model is used (e.g., Loridan et al., 2019). In addition, transient PSD peaks can also be spatio-temporal artifacts that disappear when leveraging multipoint measurements (e.g., Olifer et al., 2021). One way to test magnetic field model accuracy is to compare magnetic field model outputs and *in-situ* magnetic field measurements when available (e.g., Ozeke et al., 2019). In addition, the detection of a growing local peak requires observations during the acceleration process. Yet, the time resolution of *in-situ* measurements is constrained by spacecraft orbit period or revisit time.

The second reason is physical: Radial transport dynamics can also generate a local peak in the PSD radial profile (e.g., Ukhorskiy et al., 2006; Degeling et al., 2008), thereby further questioning the appropriateness of summarizing radial transport in terms of a diffusion process in the radiation belt master equation (**Eq. 7**) (e.g., Elkington et al., 1999; Kress et al., 2012, **Figure 7**).

In fact, a comparison between diffusion and particle drift descriptions of radial transport showed that the two modeling choices provide best agreement in the case of a series of sequential small storms and mediocre agreement during event analysis (Riley and Wolf, 1992). This is also why case events associated with fast radial transport (injection or drift resonance) are usually modeled by tracking test particles (i.e., guiding centers) drifting in analytical descriptions of the wave-associated electric field (e.g., Zong et al., 2017; Zong, 2022) or in MHD fields (e.g., Hudson et al., 2017). In contrast, summarizing local wave particle interactions in terms of diffusion in energy and pitch angle appears more reasonable (e.g., Tao et al., 2012), even though nonlinear effects occur in the presence of intense chorus waves, routinely measured *in-situ* (e.g., Zhang et al., 2019). In that context, alternative methods have been proposed to summarize the effect of chorus wave particle interactions on distribution functions (e.g., Furuya et al., 2008; Kubota and Omura, 2018; Artemyev et al., 2020).

While adjustments to the Fokker-Planck framework have been proposed to improve the description of trapped particle radial transport on timescales smaller than the drift period for the radiation belts (e.g., Bourdarie et al., 1997; Shprits et al., 2015) and for the ring current population (e.g., Fok et al., 2014; Jordanova

Table A: ***A Summary of the Approach***

Objective: Interpreting Measurements to Differentiate between Leading Acceleration Mechanisms	
Requirements	• ***Observations***: Energy and pitch angle resolved measurements over a time interval during which acceleration occurs • ***Discriminability for the acceleration processes***: Different acceleration mechanisms must have different signatures in measurements in order to be able to differentiate them
Applications	• ***Observations*****:** Flux, transformed into phase space density (PSD) • ***Interpretation, based on a 3D diffusion driven model*** **(Table C)**: A growing peak in the radial profile of the PSD is interpreted as a signature of local acceleration, while radial diffusion is expected to smooth out radial gradients
Drawbacks	• ***Observations***: Data resolution + data processing (***Table B2***) constrain the approach • ***Interpretation*****:** Based on a limited representation of radiation belt dynamics (***Table C***). Uncertainty as to where and when the leading acceleration processes results in different, identifiable signatures. This ambiguity results in controversies

Tables B: ***(B1) Observations Should be Converted into (B2) Adiabatic Space***

(B1) Observation: Electron Flux Enhancement	
Interpretation	• Radiation belt acceleration
Assumption	• More particles at lower energies. Thus, a greater flux indicates accelerated particles
Drawback	• Special circumstances under which the assumption is not valid (e.g. Bump-On-Tail distribution)

(B2) Data Product: Phase Space Density Mapped in Adiabatic Coordinates	
Requirements	• Choosing magnetic & electric field models • Specifying the adiabatic coordinates
Advantage	• Disentangling adiabatic from non-adiabatic effects
Drawbacks	• Inaccuracy associated with mapping into adiabatic space (model uncertainty) • Populations on open drift shells, open field lines, etc. excluded from the study (undefined adiabatic coordinates)

Table C: ***A Modeling Framework is Needed to Interpret Observations***

Model: 3D Fokker-Planck Equation in Adiabatic Space	
Requirements	• Specifying inputs (providing boundary conditions, including lower energy boundary, source, loss, diffusion coefficients) • Assuming diffusion (i.e., assuming that the overall effects of most processes modifying the population adiabatic coordinates can be encapsulated by diffusion coefficients)
Advantages	• Practical (modeling enabled and simplified) • Operational (dynamics over long time intervals can be reproduced, from months to years)
Drawbacks	• Uncertainty associated with input quantification • Cannot render non-diffusive effects (e.g., injections, non linear effects) • Coarse spatio-temporal resolution: Cannot model radiation belt dynamics on a timescale shorter than that of drift phase mixing. Cannot reproduce magnetic local time variations • No systematic knowledge of where and when the modeling assumptions are valid

FIGURE 8 | A summary chart on the challenges associated with differentiating between the leading processes for electron radiation belt acceleration.

et al., 2016), they also call for improved experimental knowledge of the electric and magnetic field variations driving radiation belt dynamics.

In summary, the appropriateness of our current master equation for modeling radiation belt dynamics has limitations, in particular when it comes to rendering the effects of radial transport on radiation belt dynamics on short time scales. In the absence of a modeling framework able to account for the effects of both diffusive and non-diffusive (i.e., coherent) radial transport, as well as for the effects of local acceleration (including non-linear regimes), it is not possible to quantify unequivocally the importance of local acceleration versus large-scale acceleration associated with radial transport. While the Fokker-Planck formalism has done well for long-term radiation belt modeling, it appears to be insufficient for definitive event analysis during active times. Thus, care must be taken when drawing conclusions on the physics at play solely based on PSD dynamics, and even more so on flux dynamics.

4 DISCUSSION

A summary of the challenges to address when interpreting measurements to differentiate between electron radiation belt leading acceleration mechanisms is provided in **Figure 8**. It is detailed and discussed below (**Section 4.1**). Suggestions for future research directions are provided in **Section 4.2**.

4.1 Topic Overview

The first challenge in discussing radiation belt electron acceleration is data procurement: Time series of flux measurements are needed to analyze radiation belt dynamics. It is indeed thanks to improved data sets from new missions that the picture of electron radiation belt acceleration in the Earth's magnetosphere has evolved over time. In contrast, the magnetospheres of the outer planets are still lacking key data to fully differentiate between the leading processes for electron radiation belt acceleration (**Section 3.2**). The measured electron flux time variations inform on the governing processes controlling radiation belt dynamics. That said, the experimental information is sparse as it mainly consists of samples along spacecraft trajectory. In addition, electron flux time variations only represent the *net result* of a variety of source and loss processes acting, and possibly interacting, concurrently. In that context, it is necessary to rely on a theoretical framework to determine how to identify and quantify the effect of each source and loss process.

Electron flux enhancements are readily associated with times during which acceleration processes dwarf losses. The equivalence between flux enhancement and trapped particle acceleration relies on the assumption that the accelerated particles correspond to a greater flux, i.e., that there are more particles at lower energies. While special cases such as bump-on-tail distributions challenge this assumption, they are unexpected. Bump-on-tail distributions for instance are usually observed in the plasmasphere at $L > 2.5$ during relatively quiet times (e.g., Zhao et al., 2019c) and are attributed to interactions with plasmaspheric hiss waves.

Times when radiation belt particles are accelerated are times during which the fields provide energy to the particles. Since the magnetic force does no work, it is the electric field that conveys energy. Because the electric field component parallel to the magnetic field direction is generally null, the focus is mainly on energization by perpendicular electric fields. That said, observations of large oblique chorus waves and time domain structures (TDS) in the outer belt indicate that transient parallel electric fields can also efficiently energize electrons, rapidly producing seed populations (e.g., Agapitov et al., 2015; Mozer et al., 2015, 2016). On the other hand, radiation belt acceleration produced by perpendicular electric fields occurs along the circle of gyration (gyro-betatron), and along the drift contour (drift betatron). It can be such that the adiabatic coordinates are conserved (e.g., **Figure 2**, see also Fillius and McIlwain, 1967) or violated.

Many candidate radiation belt acceleration mechanisms have been proposed over the years to account for the violation of one or several of the adiabatic coordinates parameterizing a trapped radiation belt electron population (see for instance the review by (Friedel et al., 2002), for details). Yet, the focus remains on 1) local acceleration by VLF whistler-mode chorus waves at the gyro-scale, and 2) global acceleration associated with radial transport by ULF waves at the drift-scale. Because these two mechanisms occur on two very different scales, their efficiency is usually quantified independently. On one hand, dividing radiation belt acceleration research between studies of local vs. global mechanisms is a convenient and efficient way to approach the problem, and adiabatic invariant theory provides an appropriate framework to do so. On the other hand, the divide is artificial, and it runs the risk of generating silos. Chorus and ULF waves can be concurrent (e.g., O'Brien et al., 2003) and possibly act in synergy (e.g., Simms et al., 2018, 2021). In addition, local processes can have global consequences as trapped particles continuously gyrate, bounce, and drift around the planet. For instance, pitch angle scattering of a trapped population in presence of drift shell splitting generates radial transport (e.g., Schulz, 1972). Yet, such effects—together with other "off-diagonal terms" of the diffusion tensor – are commonly omitted in radiation belt models, in part because of the numerical challenges that they pose (e.g., O'Brien, 2014; Zheng et al., 2016). It is also worth pointing out that interactions with VLF and ULF waves energize some part of the trapped population while de-energizing and/or contributing to the loss of another part of the population (e.g., Li W. et al., 2007; Shprits et al., 2006, 2008; Drozdov et al., 2020). Thereby, they act simultaneously as source and loss mechanisms for the trapped population. In this context, the efficiency of trapped particle interactions with VLF and ULF waves is usually encapsulated in the form of a few diffusion coefficients (and sometimes a lifetime coefficient), assuming a quasi-linear regime. These coefficients are then used as inputs for a physics-based radiation belt model that is diffusion-driven, and which consists of solving a 3D Fokker-Planck equation in adiabatic space.

Describing radiation belt dynamics by solving the 3D Fokker-Planck equation in adiabatic space remains the favored radiation

belt modeling approach because it is the most computationally efficient. It offers a relatively accessible way to render radiation belt dynamics while meeting the space weather needs for long term radiation belt modeling. In addition, it has proven to do well during geomagnetic quiet times. That said, it requires electron flux measurements to be converted into phase space density (PSD) mapped in adiabatic invariant space, to provide boundary conditions and to perform model-observation comparisons. This mapping inevitably adds uncertainty and limitation to the analysis (**Section 3.3.2**). In addition, the quasi-linear diffusive model does not necessarily provide a realistic picture of the physics of wave-particle interactions: Non-diffusive effects are left out from the analysis, by design (**Section 2.3.2**). This means for instance that the model is ill-suited to render times when particle dynamics are coherent (e.g., significant particle injections). The location of the outer boundary is also limited to the location of the last closed drift shell. Yet, modeling particle trapping beyond the outer boundary (i.e., dealing with populations with undefined adiabatic coordinates in the trapping region) is a requirement when the objective is to connect radiation belt populations to their outer source (e.g., energetic electrons in the magnetotail—Turner et al., 2021).

It is by relying on the interpretative framework provided by the solution of the 3D Fokker-Planck equation that measurements are analyzed to differentiate between leading acceleration mechanisms (**Figure 8A**). Observations of a growing peak in the radial profile of the PSD data product during enhancement events have been repeatedly interpreted as a telltale signature of local acceleration because radial diffusion can only smooth the PSD radial profile (e.g., Allison and Shprits, 2020). While a consensus appears to have emerged, ambiguities remain because of the set of limits associated with both data processing (**Figure 8B**) and theoretical framework (**Figure 8C**).

In particular, radial transport does not appear to be well described by a diffusive approximation during active times (**Section 3.3.2**). Drift echoes are experimental signatures of radial transport that can be observed when particles detectors have sufficiently high energy resolution (e.g., Hartinger et al., 2018; Hudson et al., 2020; Zhao et al., 2021). Yet they cannot be rendered by diffusion-driven radiation belt models. In the absence of a modeling framework able to account for 1) the effects of both diffusive and non-diffusive (i.e., rapid, significant and coherent) radial transport, as well as 2) the effects of local acceleration (including nonlinear effects), it is not possible to quantify the importance of local vs. radial acceleration unequivocally. Given current computational advances, time may have come to go beyond a purely diffusion-driven model, towards a more realistic modeling framework (e.g., Artemyev et al., 2021; Lukin et al., 2021; Allanson et al., 2022). That said, improved radiation belt modeling would also require improved knowledge of the characteristics of trapped particle interactions with VLF and ULF waves—*via* experimental determination of the correlation decay time for instance (e.g., Ukhorskiy and Sitnov, 2013). Currently, much work still remains to be done even when it comes to reducing uncertainty in the inputs for the 3D Fokker-Planck equation, including diffusion coefficients (e.g., Drozdov et al., 2021a). Thus, much remains to be done to quantify the importance of local vs. radial acceleration unambiguously.

4.2 Suggested Future Research Directions

Recent work discussed in **Section 3.3** suggests that many of the unresolved questions relating to the relative importance of radial transport and local acceleration could be addressed through expanded networks of multi-point observations. For example, Olifer et al. (2021) showed that when two Van Allen Probes spacecraft sample the same region of phase space in rapid succession, ambiguities concerning the origin of a local peak in radial PSD profile can be removed. Expanded constellations of satellites with similar orbits to the Van Allen Probes would further reduce ambiguities concerning the persistence of local PSD peaks and their origin; with each additional spacecraft added, processes that occur on shorter timescales and smaller spatial scales can be examined (e.g., Staples et al., 2022). Expanded networks of satellites with magnetic field, electric field, and energetic particle measurements would also provide 1) more robust constraints for magnetic field models used to obtain PSD, 2) more robust constraints for radiation belt models that require particle measurements for their boundary conditions, and 3) better information concerning global wave properties that are frequently used to both constrain radiation belt models and also provide diagnostics of the acceleration process. 1), 2), and 3) are all crucial for understanding dynamics during events with rapidly evolving features in radial PSD profiles. Even in the case of the Earth's radiation belts, there are still a few regions that are particularly undersampled, including Low Earth Orbit up to >1000 km ("High LEO"), and High-Inclination orbits where particle measurements could be used to distinguish between the dynamics of trapped, quasi-trapped, and precipitating particles. Finally, expanded networks of ground-based measurements could be used to remote sense global wave fields (e.g., magnetometers) and provide information about precipitating particles with different energies (e.g., riometers, incoherent scatter radars, all sky cameras), providing important constraints that supplement sparse satellite measurements, for example, networks of ground magnetometers have already proved essential in accurately capturing event-specific ULF wave power. To summarize, we already know from recent work that additional satellites and ground-based measurements can yield new insight into the relative importance of local acceleration and radial transport; we thus expect that future studies using expanding networks of multi-point observations would be able to probe dynamics on shorter timescales than were possible before (reduced satellite revisit time in radial PSD profile), more accurately than was possible before (better constraints on PSD and related magnetic field models), and with less uncertainty concerning the underlying processes causing acceleration (global, event-specific wave constraints).

AUTHOR CONTRIBUTIONS

The first author is the lead and corresponding author. All other authors are listed in alphabetical order. We describe

contributions to the paper using the CRediT (Contributor Roles Taxonomy) categories (Brand et al., 2015). Conceptualization: All authors. Writing—Original Draft: SL, HJA, MDH, ANJ, and ER. Writing—Review and Editing: All authors.

FUNDING

SL work was performed under NASA Grant 80NSSC18K1223. HA acknowledges support from the Alexander von Humboldt Foundation. LWB work was performed under NASA Grant 80NSSC21K1314. AYD contribution acknowledges NASA grant 80NSSC18K0663. MDH work was performed under NASA Grant 80NSSC19K0907. MKH contribution acknowledges NASA Grant 80NSSC17K0678. HZ was supported by the NSF Grant AGS 2140933 and NASA Grant 80NSSC22K0473.

ACKNOWLEDGMENTS

SL thanks Professor Jacob Bortnik for helping with **Figure 4**.

REFERENCES

Agapitov, O. V., Artemyev, A. V., Mourenas, D., Mozer, F. S., and Krasnoselskikh, V. (2015). Nonlinear Local Parallel Acceleration of Electrons through Landau Trapping by Oblique Whistler Mode Waves in the Outer Radiation Belt. *Geophys. Res. Lett.* 42 (10140–10), 149. doi:10.1002/2015GL066887

Albert, J. M. (2002). Nonlinear Interaction of Outer Zone Electrons with VLF Waves. *Geophys. Res. Lett.* 29 (8), 116–121. doi:10.1029/2001GL013941

Albert, J. M., Selesnick, R. S., Morley, S. K., Henderson, M. G., and Kellerman, A. C. (2018). Calculation of Last Closed Drift Shells for the 2013 GEM Radiation Belt Challenge Events. *J. Geophys. Res. Space Phys.* 123, 9597–9611. doi:10.1029/2018JA025991

Ali, A. F., Malaspina, D. M., Elkington, S. R., Jaynes, A. N., Chan, A. A., Wygant, J., et al. (2016). Electric and Magnetic Radial Diffusion Coefficients Using the Van Allen Probes Data. *J. Geophys. Res. Space Phys.* 121, 9586–9607. doi:10.1002/2016JA023002

Allanson, O., Elsden, T., Watt, C., and Neukirch, T. (2022). Weak Turbulence and Quasilinear Diffusion for Relativistic Wave-Particle Interactions via a Markov Approach. *Front. Astronomy Space Sci.* 8. doi:10.3389/fspas.2021.805699

Allanson, O., Watt, C. E. J., Ratcliffe, H., Meredith, N. P., Allison, H. J., Bentley, S. N., et al. (2019). Particle-in-cell Experiments Examine Electron Diffusion by Whistler-mode Waves: 1. Benchmarking with a Cold Plasma. *J. Geophys. Res. Space Phys.* 124, 8893–8912. doi:10.1029/2019ja027088

Allison, H. J., and Shprits, Y. Y. (2020). Local Heating of Radiation Belt Electrons to Ultra-relativistic Energies. *Nat. Commun.* 11, 4533. doi:10.1038/s41467-020-18053-z

Allison, H. J., Shprits, Y. Y., Zhelavskaya, I. S., Wang, D., and Smirnov, A. G. (2021). Gyroresonant Wave-Particle Interactions with Chorus Waves during Extreme Depletions of Plasma Density in the Van Allen Radiation Belts. *Sci. Adv.* 7 (5), eabc0380. doi:10.1126/sciadv.abc0380

Artemyev, A. V., Neishtadt, A. I., and Vasiliev, A. A. (2020). Mapping for Nonlinear Electron Interaction with Whistler-Mode Waves. *Phys. Plasmas* 27, 042902. doi:10.1063/1.5144477

Artemyev, A. V., Neishtadt, A. I., Vasiliev, A. A., Zhang, X.-J., Mourenas, D., and Vainchtein, D. (2021). Long-term Dynamics Driven by Resonant Wave-Particle Interactions: from Hamiltonian Resonance Theory to Phase Space Mapping. *J. Plasma Phys.* 87, 835870201. doi:10.1017/S0022377821000246

Baker, D. N., Belian, R. D., Higbie, P. R., Klebesadel, R. W., and Blake, J. B. (1987). Deep Dielectric Charging Effects Due to High-Energy Electrons in Earth's Outer Magnetosphere. *J. Electrost.* 20 (1). doi:10.1016/0304-3886(87)90082-9

Baker, D. N., Blake, J. B., Callis, L. B., Cummings, J. R., Hovestadt, D., Kanekal, S., et al. (1994). Relativistic Electron Acceleration and Decay Time Scales in the Inner and Outer Radiation Belts: SAMPEX. *Geophys. Res. Lett.* 21 (6), 409–412. doi:10.1029/93GL03532

Baker, D. N., Erickson, P. J., Fennell, J. F., Foster, J. C., Jaynes, A. N., and Verronen, P. T. (2018). Space Weather Effects in the Earth's Radiation Belts. *Space Sci. Rev.* 214. doi:10.1007/s11214-017-0452-7

Baker, D. N., Hoxie, V., Zhao, H., Jaynes, A. N., Kanekal, S., Li, X., et al. (2019). Multiyear Measurements of Radiation Belt Electrons: Acceleration, Transport, and Loss. *J. Geophys. Res. Space Phys.* 124, 2588–2602. doi:10.1029/2018JA026259

Baker, D. N., Kanekal, S. G., and Blake, J. B. (2004). Characterizing the Earth's Outer Van Allen Zone Using a Radiation Belt Content Index. *Space weather.* 2 (2). doi:10.1029/2003sw000026

Baker, D. N., Kanekal, S. G., Hoxie, V., Li, X., Jaynes, A. N., Zhao, H., et al. (2021). The Relativistic Electron-Proton Telescope (REPT) Investigation: Design, Operational Properties, and Science Highlights. *Space Sci. Rev.* 217, 68. doi:10.1007/s11214-021-00838-3

Baker, D. N., Li, X., Turner, N., Allen, J. H., Bargatze, L. F., Blake, J. B., Sheldon, R. B., Spence, H. E., Belian, R. D., Reeves, G. D., Kanekal, S. G., Klecker, B., Lepping, R. P., Ogilvie, K., Mewaldt, R. A., Onsager, T., Singer, H. J., and Rostoker, G. (1997). Recurrent Geomagnetic Storms and Relativistic Electron Enhancements in the Outer Magnetosphere: ISTP Coordinated Measurements. *J. Geophys. Res.* 102 (A7), 14141–14148. doi:10.1029/97ja00565

Beutier, T., and Boscher, D. (1995). A Three-Dimensional Analysis of the Electron Radiation Belt by the Salammbô Code. *J. Geophys. Res.* 100 (A8), 14853–14861. doi:10.1029/94JA03066

Blake, J. B., Baker, D. N., Turner, N., Ogilvie, K. W., and Lepping, R. P. (1997). Correlation of Changes in the Outer-Zone Relativistic-Electron Population with Upstream Solar Wind and Magnetic Field Measurements. *Geophys. Res. Lett.* 24 (NO.8), 927–929. doi:10.1029/97GL00859

Bolton, S. J., Janssen, M., Thorne, R., Levin, S., Klein, M., Gulkis, S., et al. (2002). Ultra-relativistic Electrons in Jupiter's Radiation Belts. *Nature* 415, 987–991. doi:10.1038/415987a

Bortnik, J., Thorne, R. M., and Inan, U. S. (2008). Nonlinear Interaction of Energetic Electrons with Large Amplitude Chorus. *Geophys. Res. Lett.* 35, L21102. doi:10.1029/2008GL035500

Bortnik, J., Thorne, R. M., Li, W., and Tao, X. (2016). "Chorus Waves in Geospace and Their Influence on Radiation Belt Dynamics," in *Waves, Particles, and Storms in Geospace: A Complex Interplay*, 192–216. doi:10.1093/acprof:oso/9780198705246.003.0009

Bourdarie, S., Boscher, D., Beutier, T., Sauvaud, J.-A., and Blanc, M. (1997). Electron and Proton Radiation Belt Dynamic Simulations during Storm Periods: A New Asymmetric Convection-Diffusion Model. *J. Geophys. Res.* 102 (A8), 17541–17552. doi:10.1029/97JA01305

Boyd, A. J., Turner, D. L., Reeves, G. D., Spence, H. E., Baker, D. N., and Blake, J. B. (2018). What Causes Radiation Belt Enhancements: A Survey of the Van Allen Probes Era. *Geophys. Res. Lett.* 45, 5253–5259. doi:10.1029/2018GL077699

Bradley, T. J., Cowley, S. W. H., Bunce, E. J., Melin, H., Provan, G., Nichols, J. D., et al. (2020). Saturn's Nightside Dynamics during Cassini's F Ring and Proximal Orbits: Response to Solar Wind and Planetary Period Oscillation Modulations. *J. Geophys. Res. Space Phys.* 125, e27907. doi:10.1029/2020JA027907

Brand, A., Allen, L., Altman, M., Hlava, M., and Scott, J. (2015). Beyond Authorship: Attribution, Contribution, Collaboration, and Credit. *Learn. Pub.* 28, 151–155. doi:10.1087/20150211

Brautigam, D. H., and Albert, J. M. (2000). Radial Diffusion Analysis of Outer Radiation Belt Electrons during the October 9, 1990, Magnetic Storm. *J. Geophys. Res.* 105 (A1), 291–309. doi:10.1029/1999JA900344

Brito, T., Woodger, L., Hudson, M., and Millan, R. (2012). Energetic Radiation Belt Electron Precipitation Showing ULF Modulation. *Geophys. Res. Lett.* 39 (22). doi:10.1029/2012gl053790

Bruff, M., Jaynes, A. N., Zhao, H., Goldstein, J., Malaspina, D. M., Baker, D. N., et al. (2020). The Role of the Dynamic Plasmapause in Outer Radiation Belt Electron

Flux Enhancementflux Enhancement. *Geophys. Res. Lett.* 47, e2020GL086991. doi:10.1029/2020GL086991

Camporeale, E. (2015). Resonant and Nonresonant Whistlers-Particle Interaction in the Radiation Belts. *Geophys. Res. Lett.* 42, 3114–3121. doi:10.1002/2015GL063874

Chen, Y., Reeves, G. D., and Friedel, R. H. W. (2007). The Energization of Relativistic Electrons in the Outer Van Allen Radiation Belt. *Nat. Phys.* 3, 614–617. doi:10.1038/nphys655

Chu, F., Hudson, M. K., Haines, P., and Shprits, Y. (2010). Dynamic Modeling of Radiation Belt Electrons by Radial Diffusion Simulation for a 2 Month Interval Following the 24 March 1991 Storm Injection. *J. Geophys. Res.* 115, a–n. doi:10.1029/2009JA014409

Claudepierre, S. G., Ma, Q., Bortnik, J., O'Brien, T. P., Fennell, J. F., and Blake, J. B. (2020). Empirically Estimated Electron Lifetimes in the Earth's Radiation Belts: Comparison with Theory. *Geophys Res. Lett.* 47 (3), e2019GL086056. doi:10.1029/2019GL086056

Comess, M. D., Smith, D. M., Selesnick, R. S., Millan, R. M., and Sample, J. G. (2013). Duskside Relativistic Electron Precipitation as Measured by SAMPEX: A Statistical Survey. *J. Geophys. Res. Space Phys.* 118 (8), 5050–5058. doi:10.1002/jgra.50481

de Pater, I., and Goertz, C. K. (1990). Radial Diffusion Models of Energetic Electrons and Jupiter's Synchrotron Radiation: 1. Steady State Solution. *J. Geophys. Res.* 95, 39. doi:10.1029/JA095iA01p00039

Degeling, A. W., Ozeke, L. G., Rankin, R., Mann, I. R., and Kabin, K. (2008). Drift Resonant Generation of Peaked Relativistic Electron Distributions by Pc 5 ULF Waves. *J. Geophys. Res.* 113, a–n. doi:10.1029/2007JA012411

Dessler, A. J., and Karplus, R. (1961). Some Effects of Diamagnetic Ring Currents on Van Allen Radiation. *J. Geophys. Res.* 66 (8), 2289–2295. doi:10.1029/JZ066i008p02289

Drozdov, A. Y., Allison, H. J., Shprits, Y. Y., Elkington, S. R., and Aseev, N. A. (2021a). A Comparison of Radial Diffusion Coefficients in 1-D and 3-D Long-Term Radiation Belt Simulations. *JGR Space Phys.* 126, e2020JA028707. doi:10.1029/2020JA028707

Drozdov, A. Y., Allison, H. J., Shprits, Y. Y., Usanova, M. E., Saikin, A. A., and Wang, D. (2021b). Depletions of Multi-MeV Electrons and Their Association to Minima in Phase Space Density. *Earth Space Sci. Open Archive* 19. doi:10.1002/essoar.10510085.1

Drozdov, A. Y., Blum, L. W., Hartinger, M., Zhao, H., Lejosne, S., Hudson, M. K., et al. (2022). Radial Transport versus Local Acceleration: The Long-Standing Debate. *Earth Space Sci.* 9, e2022EA002216. doi:10.1029/2022EA002216

Drozdov, A. Y., Shprits, Y. Y., Aseev, N. A., Kellerman, A. C., and Reeves, G. D. (2017). Dependence of Radiation Belt Simulations to Assumed Radial Diffusion Rates Tested for Two Empirical Models of Radial Transport. *Space weather.* 15, 150–162. doi:10.1002/2016SW001426

Drozdov, A. Y., Shprits, Y. Y., Orlova, K. G., Kellerman, A. C., Subbotin, D. A., Baker, D. N., et al. (2015). Energetic, Relativistic, and Ultrarelativistic Electrons: Comparison of Long-Term VERB Code Simulations with Van Allen Probes Measurements. *J. Geophys. Res. Space Phys.* 120, 3574–3587. doi:10.1002/2014JA020637

Drozdov, A. Y., Usanova, M. E., Hudson, M. K., Allison, H. J., and Shprits, Y. Y. (2020). The Role of Hiss, Chorus, and EMIC Waves in the Modeling of the Dynamics of the Multi-MeV Radiation Belt Electrons. *J. Geophys. Res. Space Phys.* 125 (9), 2628. doi:10.1029/2020JA028282

Elkington, S. R., Hudson, M. K., and Chan, A. A. (1999). Acceleration of Relativistic Electrons via Drift-Resonant Interaction with Toroidal-Mode Pc-5 ULF Oscillations. *Geophys. Res. Lett.* 26 (21), 3273–3276. doi:10.1029/1999GL003659

Fälthammar, C.-G. (1965). Effects of Time-dependent Electric Fields on Geomagnetically Trapped Radiation. *J. Geophys. Res.* 70 (11), 2503–2516. doi:10.1029/JZ070i011p02503

Fillius, R. W., and McIlwain, C. E. (1967). Adiabatic Betatron Acceleration by a Geomagnetic Storm. *J. Geophys. Res.* 72 (15), 4011–4015. doi:10.1029/JZ072i015p04011

Fok, M.-C., Buzulukova, N. Y., Chen, S.-H., Glocer, A., Nagai, T., Valek, P., et al. (2014). The Comprehensive Inner Magnetosphere-Ionosphere Model. *J. Geophys. Res. Space Phys.* 119, 7522–7540. doi:10.1002/2014JA020239

Fok, M. C. (2020). "Current Status of Inner Magnetosphere and Radiation Belt Modeling," in *Dayside Magnetosphere Interactions*. Editors Q. Zong, P. Escoubet, D. Sibeck, G. Le, and H. Zhang, 231–242. doi:10.1002/9781119509592.ch13

Foster, J. C., Erickson, P. J., Baker, D. N., Claudepierre, S. G., Kletzing, C. A., Kurth, W., et al. (2014). Prompt Energization of Relativistic and Highly Relativistic Electrons during a Substorm Interval: Van Allen Probes Observations. *Geophys. Res. Lett.* 41, 20–25. doi:10.1002/2013GL058438

Fox, N., and Burch, J. L. (2014). "The Van Allen Probes Mission," in *Physics and Astronomy* (Boston, MA: Springer). doi:10.1007/978-1-4899-7433-4

Friedel, R. H. W., Reeves, G. D., and Obara, T. (2002). Relativistic Electron Dynamics in the Inner Magnetosphere - a Review. *J. Atmos. Solar-Terrestrial Phys.* 64 (2), 265–282. doi:10.1016/S1364-6826(01)00088-8

Furuya, N., Omura, Y., and Summers, D. (2008). Relativistic Turning Acceleration of Radiation Belt Electrons by Whistler Mode Chorus. *J. Geophys. Res.* 113, a–n. doi:10.1029/2007JA012478

Garrett, H. B., and Jun, I. (2021). First Adiabatic Invariants and Phase Space Densities for the Jovian Electron and Proton Radiation Belts-Galileo and GIRE3 Estimates. *J. Geophys. Res. Space Phys.* 126, e28593. doi:10.1029/2020JA028593

Gendrin, R. (1981). General Relationships between Wave Amplification and Particle Diffusion in a Magnetoplasma. *Rev. Geophys.* 19, 171. doi:10.1029/rg019i001p00171

Ginet, G. P., O'Brien, T. P., Huston, S. L., Johnston, W. R., Guild, T. B., Friedel, R., et al. (2013). AE9, AP9 and SPM: New Models for Specifying the Trapped Energetic Particle and Space Plasma Environment. *Space Sci. Rev.* 179, 579–615. doi:10.1007/s11214-013-9964-y

Glauert, S. A., Horne, R. B., and Meredith, N. P. (2018). A 30-year Simulation of the Outer Electron Radiation Belt. *Space weather.* 16, 1498–1522. doi:10.1029/2018SW001981

Goldstein, J., Kanekal, S. G., Baker, D. N., and Sandel, B. R. (2005). Dynamic Relationship between the Outer Radiation Belt and the Plasmapause during March–May 2001. *Geophys. Res. Lett.* 32 (15). doi:10.1029/2005gl023431

Greeley, A. D., Kanekal, S. G., Sibeck, D. G., Schiller, Q., and Baker, D. N. (2021). Evolution of Pitch Angle Distributions of Relativistic Electrons during Geomagnetic Storms: Van Allen Probes Observations. *J. Geophys. Res. Space Phys.* 126, e2020JA028335. doi:10.1029/2020ja028335

Green, J. C., and Kivelson, M. G. (2004). Relativistic Electrons in the Outer Radiation Belt: Differentiating between Acceleration Mechanisms. *J. Geophys. Res.* 109, A03213. doi:10.1029/2003JA010153

Green, J. C. (2006). "Using Electron Phase Space Density Signatures to Identify the Electromagnetic Waves Responsible for Accelerating Relativistic Electrons in Earth's Magnetosphere," in *Magnetospheric ULF Waves: Synthesis and New Directions*. Editors K. Takahashi, P. J. Chi, R. E. Denton, and R. L. Lysak, 225–237. doi:10.1029/169GM15

Hajra, R., Tsurutani, B. T., Echer, E., Gonzalez, W. D., and Santolik, O. (2015). RELATIVISTIC (E> 0.6, > 2.0, AND > 4.0 MeV) ELECTRON ACCELERATION AT GEOSYNCHRONOUS ORBIT DURING HIGH-INTENSITY, LONG-DURATION, CONTINUOUS AE ACTIVITY (HILDCAA) EVENTS. *ApJ* 799, 39. doi:10.1088/0004-637X/799/1/39

Han, S., Murakami, G., Kita, H., Tsuchiya, F., Tao, C., Misawa, H., et al. (2018). Investigating Solar Wind-Driven Electric Field Influence on Long-Term Dynamics of Jovian Synchrotron Radiation. *J. Geophys. Res. Space Phys.* 123, 9508–9516. doi:10.1029/2018JA025849

Hao, Y.-X., Sun, Y.-X., Roussos, E., Liu, Y., Kollmann, P., Yuan, C.-J., et al. (2020). The Formation of Saturn's and Jupiter's Electron Radiation Belts by Magnetospheric Electric Fields. *ApJ* 905, L10. doi:10.3847/2041-8213/abca3f

Hao, Y. X., Zong, Q. G., Zhou, X. Z., Rankin, R., Chen, X. R., Liu, Y., et al. (2019). Global-Scale ULF Waves Associated with SSC Accelerate Magnetospheric Ultrarelativistic Electrons. *J. Geophys. Res. Space Phys.* 124, 1525–1538. doi:10.1029/2018JA026134

Hartinger, M. D., Claudepierre, S. G., Turner, D. L., Reeves, G. D., Breneman, A., Mann, I. R., et al. (2018). Diagnosis of ULF Wave-Particle Interactions with Megaelectron Volt Electrons: The Importance of Ultrahigh-Resolution Energy Channels. *Geophys. Res. Lett.* 45 (11), 883–11,892. doi:10.1029/2018GL080291

Hiraga, R., and Omura, Y. (2020). Acceleration Mechanism of Radiation Belt Electrons through Interaction with Multi-Subpacket Chorus Waves. *Earth Planets Space* 72, 21. doi:10.1186/s40623-020-1134-3

Horne, R. B., Glauert, S. A., Meredith, N. P., Boscher, D., Maget, V., Heynderickx, D., et al. (2013). Space Weather Impacts on Satellites and Forecasting the Earth's Electron Radiation Belts with SPACECAST. *Space weather.* 11, 169–186. doi:10.1002/swe.20023

Horne, R. B., and Thorne, R. M. (1998). Potential Waves for Relativistic Electron Scattering and Stochastic Acceleration during Magnetic Storms. *Geophys. Res. Lett.* 25 (15), 3011–3014. doi:10.1029/98GL01002

Horne, R. B., Thorne, R. M., Shprits, Y. Y., Meredith, N. P., Glauert, S. A., Smith, A. J., et al. (2005). Wave Acceleration of Electrons in the Van Allen Radiation Belts. *Nature* 437, 227–230. doi:10.1038/nature03939

Horne, R., and Tsurutani, B. (2019). Richard Mansergh Thorne (1942-2019). *Eos* 100. (Published on December 04, 2019). doi:10.1029/2019EO137322

Hudson, M., Jaynes, A., Kress, B., Li, Z., Patel, M., Shen, X. C., et al. (2017). Simulated Prompt Acceleration of Multi-MeV Electrons by the 17 March 2015 Interplanetary Shock. *J. Geophys. Res. Space Phys.* 122 (10), 10,036. doi:10.1002/2017JA024445

Hudson, M. K., Elkington, S. R., Li, Z., and Patel, M. (2020). Drift Echoes and Flux Oscillations: A Signature of Prompt and Diffusive Changes in the Radiation Belts. *J. Atmos. Solar-Terrestrial Phys.* 2072020 (105332), 105332–106826. doi:10.1016/j.jastp.2020.105332

Hudson, M. K., Elkington, S. R., Lyon, J. G., Marchenko, V. A., Roth, I., Temerin, M., et al. (1997). Simulations of Radiation Belt Formation during Storm Sudden Commencements. *J. Geophys. Res.* 102 (A7), 14087–14102. doi:10.1029/97JA03995

Hudson, M. K., Kress, B. T., Mueller, H.-R., Zastrow, J. A., and Bernard Blake, J. (2008). Relationship of the Van Allen Radiation Belts to Solar Wind Drivers. *J. Atmos. Solar-Terrestrial Phys.* 70 (5), 708–729. doi:10.1016/j.jastp.2007.11.003

Iles, R. H. A., Meredith, N. P., Fazakerley, A. N., and Horne, R. B. (2006). Phase Space Density Analysis of the Outer Radiation Belt Energetic Electron Dynamics. *J. Geophys. Res.* 111, A03204. doi:10.1029/2005JA011206

Jacobs, J. A. (1970). *Geomagnetic Micropulsations. Physics and Chemistry in Space*, Vol. 1. Berlin, Heidelberg: Springer, 15–63. doi:10.1007/978-3-642-86828-3_2The Morphology of Geomagnetic Micropulsations

Jaynes, A. N., Ali, A. F., Elkington, S. R., Malaspina, D. M., Baker, D. N., Li, X., et al. (2018). Fast Diffusion of Ultrarelativistic Electrons in the Outer Radiation Belt: 17 March 2015 Storm Event. *Geophys Res. Lett.* 45, 10,874–10882. doi:10.1029/2018GL079786

Jaynes, A. N., Baker, D. N., Singer, H. J., Rodriguez, J. V., Loto'aniu, T. M., Ali, A. F., et al. (2015). Source and Seed Populations for Relativistic Electrons: Their Roles in Radiation Belt Changes. *J. Geophys. Res. Space Phys.* 120, 7240–7254. doi:10.1002/2015JA021234

Jaynes, A. N., Li, X., Schiller, Q. G., Blum, L. W., Tu, W., Turner, D. L., Ni, B., Bortnik, J., Baker, D. N., Kanekal, S. G., Blake, J. B., and Wygant, J. (2014). Evolution of Relativistic Outer Belt Electrons during an Extended Quiescent Period. *J. Geophys. Res. Space Phys.* 119 (12), 9558–9566. doi:10.1002/2014ja020125

Jones, S. L., Lessard, M. R., Rychert, K., Spanswick, E., Donovan, E., and Jaynes, A. N. (2013). Persistent, Widespread Pulsating Aurora: A Case Study. *J. Geophys. Res. Space Phys.* 118 (6), 2998–3006. doi:10.1002/jgra.50301

Jordanova, V. K., Tu, W., Chen, Y., Morley, S. K., Panaitescu, A. D., Reeves, G. D., et al. (2016). RAM-SCB Simulations of Electron Transport and Plasma Wave Scattering during the October 2012 "double-dip" Storm. *J. Geophys. Res. Space Phys.* 121, 8712–8727. doi:10.1002/2016JA022470

Kanekal, S. G. (2006). "A Review of Recent Observations of Relativistic Electron Energization in the Earth's Outer Van Allen Radiation Belt (2006)," in *Proceedings of the ILWS Workshop*. Editors N. Gopalswamy and A. Bhattacharyya (Goa, India, 274. ISBN: 81-87099-40-2.

Kanekal, S. G., Baker, D. N., Blake, J. B., Klecker, B., Mewaldt, R. A., and Mason, G. M. (1999). Magnetospheric Response to Magnetic Cloud (Coronal Mass Ejection) Events: Relativistic Electron Observations from SAMPEX and Polar. *J. Geophys. Res.* 104 (A11), 24885–24894. doi:10.1029/1999ja900239

Kanekal, S. G., Baker, D. N., and Blake, J. B. (2001). Multisatellite Measurements of Relativistic Electrons: Global Coherence. *J. Geophys. Res.* 106 (A12), 29721–29732. doi:10.1029/2001JA000070

Katsavrias, C., Aminalragia-Giamini, S., Papadimitriou, C., Daglis, I. A., Sandberg, I., and Jiggens, P. (2022a). *Radiation Belt Model Including Semi-annual Variation and Solar Driving*, 20. Sentinel: Space Weather, e2021SW002936. doi:10.1029/2021SW002936

Katsavrias, C., Papadimitriou, C., Aminalragia-Giamini, S., Daglis, I. A., Sandberg, I., and Jiggens, P. (2021b). On the Semi-annual Variation of Relativistic Electrons in the Outer Radiation Belt. *Ann. Geophys.* 39, 413–425. doi:10.5194/angeo-39-413-2021

Kellerman, A. C., and Shprits, Y. Y. (2012). On the Influence of Solar Wind Conditions on the Outer-Electron Radiation Belt. *J. Geophys. Res.* 117, a–n. doi:10.1029/2011JA017253

Kennel, C. F., and Thorne, R. M. (1967). Unstable Growth of Unducted Whistlers Propagating at an Angle to the Geomagnetic Field. *J. Geophys. Res.* 72 (3), 871–878. doi:10.1029/JZ072i003p00871

Kilpua, E. K. J., Hietala, H., Turner, D. L., Koskinen, H. E. J., Pulkkinen, T. I., Rodriguez, J. V., et al. (2015). Unraveling the Drivers of the Storm Time Radiation Belt Response. *Geophys. Res. Lett.* 42, 3076–3084. doi:10.1002/2015GL063542

Kim, H.-J., and Chan, A. A. (1997). Fully Adiabatic Changes in Storm Time Relativistic Electron Fluxes. *J. Geophys. Res.* 102 (A10), 22107–22116. doi:10.1029/97JA01814

Koller, J., Chen, Y., Reeves, G. D., Friedel, R. H. W., Cayton, T. E., and Vrugt, J. A. (2007). Identifying the Radiation Belt Source Region by Data Assimilation. *J. Geophys. Res.* 112, a–n. doi:10.1029/2006JA012196

Kollmann, P., Roussos, E., Paranicas, C., Krupp, N., Jackman, C. M., Kirsch, E., et al. (2011). Energetic Particle Phase Space Densities at Saturn: Cassini Observations and Interpretations. *J. Geophys. Res.* 116, A05222. doi:10.1029/2010JA016221

Kollmann, P., Roussos, E., Paranicas, C., Woodfield, E. E., Mauk, B. H., Clark, G., et al. (2018). Electron Acceleration to MeV Energies at Jupiter and Saturn. *J. Geophys. Res. Space Phys.* 123, 9110–9129. doi:10.1029/2018JA025665

Koskinen, H. E. J., and Kilpua, E. K. J. (2022). *Physics of Earth's Radiation Belts, Theory and Observations*. Switzerland: Astronomy and Astrophysics Library, Springer. doi:10.1007/978-3-030-82167-8

Kress, B. T., Hudson, M. K., Looper, M. D., Albert, J., Lyon, J. G., and Goodrich, C. C. (2007). Global MHD Test Particle Simulations of >10 MeV Radiation Belt Electrons during Storm Sudden Commencement. *J. Geophys. Res.* 112, a–n. doi:10.1029/2006JA012218

Kress, B. T., Hudson, M. K., Ukhorskiy, A. Y., and Mueller, H.-R. (2012). "Nonlinear Radial Transport in the Earth's Radiation Belts," in *Dynamics of the Earth's Radiation Belts and Inner Magnetosphere, Geophys*. Editor D. Summers (Washington, D. C: Monogr. Ser), 199, 151–160. doi:10.1029/2012GM001333

Kubota, Y., and Omura, Y. (2018). Nonlinear Dynamics of Radiation Belt Electrons Interacting with Chorus Emissions Localized in Longitude. *J. Geophys. Res. Space Phys.* 123, 4835–4857. doi:10.1029/2017JA025050

Lanzerotti, L. J., Roberts, C. S., and Brown, W. L. (1967). Temporal Variations in the Electron Flux at Synchronous Altitudes. *J. Geophys. Res.* 72 (23), 5893–5902. doi:10.1029/JZ072i023p05893

Lejosne, S. (2020). Electromagnetic Radial Diffusion in the Earth's Radiation Belts as Determined by the Solar Wind Immediate Time History and a Toy Model for the Electromagnetic Fields. *JGR Space Phys.* 125, e2020JA027893. doi:10.1029/2020JA027893

Lejosne, S., Fedrizzi, M., Maruyama, N., and Selesnick, R. S. (2021). Thermospheric Neutral Winds as the Cause of Drift Shell Distortion in Earth's Inner Radiation Belt. *Front. Astron. Space Sci.* 8. doi:10.3389/fspas.2021.725800

Lejosne, S., and Kollmann, P. (2020). Radiation Belt Radial Diffusion at Earth and beyond. *Space Sci. Rev.* 216, 19. doi:10.1007/s11214-020-0642-6

Lejosne, S., and Mozer, F. S. (2020). Inversion of the Energetic Electron "Zebra Stripe" Pattern Present in the Earth's Inner Belt and Slot Region: First Observations and Interpretation. *Geophys. Res. Lett.* 47, e2020GL088564. doi:10.1029/2020GL088564

Li, L., Zhou, X. Z., Zong, Q. G., Rankin, R., Zou, H., Liu, Y., et al. (2017). Charged Particle Behavior in Localized Ultralow Frequency Waves: Theory and Observations. *Geophys. Res. Lett.* 44, 5900–5908. doi:10.1002/2017GL073392

Li, W., and Hudson, M. K. (2019). Earth's Van Allen Radiation Belts: From Discovery to the Van Allen Probes Era. *J. Geophys. Res. Space Phys.* 124, 8319–8351. doi:10.1029/2018JA025940

Li, W., Shprits, Y. Y., and Thorne, R. M. (2007). Dynamic Evolution of Energetic Outer Zone Electrons Due to Wave-Particle Interactions during Storms. *J. Geophys. Res.* 112 (A10), a–n. doi:10.1029/2007JA012368

Li, X., Baker, D. N., Temerin, M., Larson, D., Lin, R. P., Reeves, G. D., et al. (1997). Are Energetic Electrons in the Solar Wind the Source of the Outer Radiation Belt? *Geophys. Res. Lett.* 24 (8), 923–926. doi:10.1029/97GL00543

Li, X., Baker, D. N., Temerin, M., Reeves, G., Friedel, R., and Shen, C. (2005). Energetic Electrons, 50 keV to 6 MeV, at Geosynchronous Orbit: Their Responses to Solar Wind Variations. *Space weather.* 3, a–n. doi:10.1029/2004SW000105

Li, X., Roth, I., Temerin, M., Wygant, J. R., Hudson, M. K., and Blake, J. B. (1993). Simulation of the Prompt Energization and Transport of Radiation Belt Particles during the March 24, 1991 SSC. *Geophys. Res. Lett.* 20 (22), 2423–2426. doi:10.1029/93gl02701

Li, X., Temerin, M., Baker, D. N., and Reeves, G. D. (2011). Behavior of MeV Electrons at Geosynchronous Orbit during Last Two Solar Cycles. *J. Geophys. Res.* 116, a–n. doi:10.1029/2011JA016934

Li, X., Temerin, M., Baker, D. N., Reeves, G. D., and Larson, D. (2001). Quantitative Prediction of Radiation Belt Electrons at Geostationary Orbit Based on Solar Wind Measurements. *Geophys. Res. Lett.* 28 (9), 1887–1890. doi:10.1029/2000GL012681

Li, Z., Hudson, M., Patel, M., Wiltberger, M., Boyd, A., and Turner, D. (2017). ULF Wave Analysis and Radial Diffusion Calculation Using a Global MHD Model for the 17 March 2013 and 2015 Storms. *J. Geophys. Res. Space Phys.* 122, 7353–7363. doi:10.1002/2016JA023846

Liu, W., Tu, W., Li, X., Sarris, T., Khotyaintsev, Y., Fu, H., et al. (2016). On the Calculation of Electric Diffusion Coefficient of Radiation Belt Electrons with *In Situ* Electric Field Measurements by THEMIS. *Geophys. Res. Lett.* 43, 1023–1030. doi:10.1002/2015GL067398

Loridan, V., Ripoll, J.-F., Tu, W., and Cunningham, G. S. (2019). On the Use of Different Magnetic Field Models for Simulating the Dynamics of the Outer Radiation Belt Electrons During the October 1990 Storm. *J. Geophys. Res. Space Phys.* 124, 6453–6486. doi:10.1029/2018JA026392

Louarn, P., Kivelson, M. G., and Kurth, W. S. (2016). On the Links between the Radio Flux and Magnetodisk Distortions at Jupiter. *J. Geophys. Res. Space Phys.* 121, 9651–9670. doi:10.1002/2016JA023106

Louarn, P., Paranicas, C. P., and Kurth, W. S. (2014). Global Magnetodisk Disturbances and Energetic Particle Injections at Jupiter. *J. Geophys. Res. Space Phys.* 119, 4495–4511. doi:10.1002/2014JA019846

Lukin, A. S., Artemyev, A. V., and Petrukovich, A. A. (2021). On Application of Stochastic Differential Equations for Simulation of Nonlinear Wave-Particle Resonant Interactions. *Phys. Plasmas* 28, 092904. doi:10.1063/5.0058054

Lyon, J., Fedder, J., and Mobarry, C. (2004). The Lyon–Fedder–Mobarry (LFM) Global MHD Magnetospheric Simulation Code. *J. Atmos*.

Ma, Q., Li, W., Bortnik, J., Thorne, R. M., Chu, X., Ozeke, L. G., et al. (2018). Quantitative Evaluation of Radial Diffusion and Local Acceleration Processes during GEM Challenge Events. *J. Geophys. Res. Space Phys.* 123, 1938–1952. doi:10.1002/2017JA025114

Malaspina, D. M., Jaynes, A. N., Boulé, C., Bortnik, J., Thaller, S. A., Ergun, R. E., et al. (2016). The Distribution of Plasmaspheric Hiss Wave Power with Respect to Plasmapause Location. *Geophys. Res. Lett.* 43, 7878–7886. doi:10.1002/2016GL069982

Malaspina, D. M., Zhu, H., and Drozdov, A. Y. (2020). A Wave Model and Diffusion Coefficients for Plasmaspheric Hiss Parameterized by Plasmapause Location. *J. Geophys. Res. Space Phys.* 125, e2019JA027415. doi:10.1029/2019JA027415

Mauk, B. H., Saur, J., Mitchell, D. G., Roelof, E. C., Brandt, P. C., Armstrong, T. P., et al. (2005). Energetic Particle Injections in Saturn's Magnetosphere. *Geophys. Res. Lett.* 32, a–n. doi:10.1029/2005GL022485

McIlwain, C. E. (1961). Coordinates for Mapping the Distribution of Magnetically Trapped Particles. *J. Geophys. Res.* 66 (11), 3681–3691. doi:10.1029/JZ066i011p03681

McPherron, R. L., Baker, D. N., and Crooker, N. U. N. U. (2009). Role of the Russell-McPherron Effect in the Acceleration of Relativistic Electrons. *J. Atmos. Solar-Terrestrial Phys.* 71 (10–11), 1032–1044. doi:10.1016/j.jastp.2008.11.002

Meredith, N. P., Cain, M., Horne, R. B., Thorne, R. M., Summers, D., and Anderson, R. R. (2003). Evidence for Chorus-Driven Electron Acceleration to Relativistic Energies from a Survey of Geomagnetically Disturbed Periods. *J. Geophys. Res.* 108, 1248. doi:10.1029/2002JA009764

Meredith, N. P., Horne, R. B., Iles, R. H. A., Thorne, R. M., Heynderickx, D., and Anderson, R. R. (2002). Outer Zone Relativistic Electron Acceleration Associated with Substorm-Enhanced Whistler Mode Chorus. *J. Geophys. Res.* 107 (A7). doi:10.1029/2001JA900146

Mihalov, J. D., Fischer, H. M., Pehlke, E., and Lanzerotti, L. J. (2000). Energetic Trapped Electron Measurements from the Galileo Jupiter Probe. *Geophys. Res. Lett.* 27, 2445–2448. doi:10.1029/2000GL003812

Miyoshi, Y., and Kataoka, R. (2008). Flux Enhancement of the Outer Radiation Belt Electrons after the Arrival of Stream Interaction Regions. *J. Geophys. Res.* 113, a–n. doi:10.1029/2007JA012506

Miyoshi, Y., Misawa, H., Morioka, A., Kondo, T., Koyama, Y., and Nakajima, J. (1999). Observation of Short-Term Variation of Jupiter's Synchrotron Radiation. *Geophys. Res. Lett.* 26, 9–12. doi:10.1029/1998GL900244

Miyoshi, Y., Morioka, A., Obara, T., Misawa, H., Nagai, T., and Kasahara, Y. (2003). Rebuilding Process of the Outer Radiation Belt during the 3 November 1993 Magnetic Storm: NOAA and Exos-D Observations. *J. Geophys. Res.* 108 (A1), 1004. doi:10.1029/2001JA007542

Miyoshi, Y., Saito, S., Kurita, S., Asamura, K., Hosokawa, K., Sakanoi, T., and Blake, J. B. (2020). Relativistic Electron Microbursts as High-energy Tail of Pulsating Aurora Electrons. *Geophys. Res. Lett.* 47 (21), e2020GL090360. doi:10.1029/2020gl090360

Moya, P. S., Pinto, V. A., Sibeck, D. G., Kanekal, S. G., and Baker, D. N. (2017). On the Effect of Geomagnetic Storms on Relativistic Electrons in the Outer Radiation Belt: Van Allen Probes Observations. *J. Geophys. Res. Space Phys.* 122, 11,100–11,108. doi:10.1002/2017JA024735

Mozer, F. S., Agapitov, O. V., Artemyev, A., Drake, J. F., Krasnoselskikh, V., Lejosne, S., et al. (2015). Time Domain Structures: What and where They Are, what They Do, and How They Are Made. *Geophys. Res. Lett.* 42, 3627–3638. doi:10.1002/10.1002/2015gl063946

Mozer, F. S., Artemyev, A., Agapitov, O. V., Mourenas, D., and Vasko, I. (2016). Near-relativistic Electron Acceleration by Landau Trapping in Time Domain Structures. *Geophys. Res. Lett.* 43, 508–514. doi:10.1002/2015GL067316

Murakami, G., Yoshioka, K., Yamazaki, A., Tsuchiya, F., Kimura, T., Tao, C., et al. (2016). Response of Jupiter's Inner Magnetosphere to the Solar Wind Derived from Extreme Ultraviolet Monitoring of the Io Plasma Torus. *Geophys. Res. Lett.* 43 (12), 308. doi:10.1002/2016GL071675

Nénon, Q., Sicard, A., and Bourdarie, S. (2017). A New Physical Model of the Electron Radiation Belts of Jupiter inside Europa's Orbit. *J. Geophys. Res. Space Phys.* 122, 5148–5167. doi:10.1002/2017JA023893

Northrop, T. G. (1963). *The Adiabatic Motion of Charged Particles*. New York: Wiley-Interscience. 978-0470651391.

Nunn, D., Demekhov, A., Trakhtengerts, V., and Rycroft, M. J. (2003). VLF Emission Triggering by a Highly Anisotropic Energetic Electron Plasma. *Ann. Geophys.* 21, 481–492. doi:10.5194/angeo-21-481-2003

O'Brien, T. P. (2014). Breaking All the Invariants: Anomalous Electron Radiation Belt Diffusion by Pitch Angle Scattering in the Presence of Split Magnetic Drift Shells. *Geophys. Res. Lett.* 41, 216–222. doi:10.1002/2013GL058712

O'Brien, T. P., Lorentzen, K. R., Mann, I. R., Meredith, N. P., Blake, J. B., Fennell, J. F., et al. (2003). Energization of Relativistic Electrons in the Presence of ULF Power and MeV Microbursts: Evidence for Dual ULF and VLF Acceleration. *J. Geophys. Res.* 108, 1329. doi:10.1029/2002JA009784

Olifer, L., Mann, I. R., Morley, S. K., Ozeke, L. G., and Choi, D. (2018). On the Role of Last Closed Drift Shell Dynamics in Driving Fast Losses and Van Allen Radiation Belt Extinction. *J. Geophys. Res. Space Phys.* 123, 3692–3703. doi:10.1029/2018JA025190

Olifer, L., Mann, I. R., Ozeke, L. G., Morley, S. K., and Louis, H. L. (2021). On the Formation of Phantom Electron Phase Space Density Peaks in Single Spacecraft Radiation Belt Data. *Geophys. Res. Lett.* 48, e2020GL092351. doi:10.1029/2020GL092351

Omura, Y., Furuya, N., and Summers, D. (2007). Relativistic Turning Acceleration of Resonant Electrons by Coherent Whistler Mode Waves in a Dipole Magnetic Field. *J. Geophys. Res.* 112, a–n. doi:10.1029/2006JA012243

Omura, Y., Miyashita, Y., Yoshikawa, M., Summers, D., Hikishima, M., Ebihara, Y., et al. (2015). Formation Process of Relativistic Electron Flux through Interaction with Chorus Emissions in the Earth's Inner Magnetosphere. *J. Geophys. Res. Space Phys.* 120, 9545–9562. doi:10.1002/2015JA021563

Omura, Y. (2021). Nonlinear Wave Growth Theory of Whistler-Mode Chorus and Hiss Emissions in the Magnetosphere. *Earth Planets Space* 73, 95. doi:10.1186/s40623-021-01380-w

Omura, Y., and Summers, D. (2004). Computer Simulations of Relativistic Whistler-Mode Wave-Particle Interactions. *Phys. Plasmas* 11 (7), 3530–3534. doi:10.1063/1.1757457

Orlova, K., Shprits, Y., and Spasojevic, M. (2016). New Global Loss Model of Energetic and Relativistic Electrons Based on Van Allen Probes Measurements. *J. Geophys. Res. Space Phys.* 121, 1308–1314. doi:10.1002/2015JA021878

Orlova, K., Spasojevic, M., and Shprits, Y. (2014). Activity-dependent Global Model of Electron Loss inside the Plasmasphere. *Geophys. Res. Lett.* 41, 3744–3751. doi:10.1002/2014GL060100

Ozeke, L. G., Mann, I. R., Claudepierre, S. G., Henderson, M., Morley, S. K., and Murphy, K. R. (2019). The March 2015 Superstorm Revisited: Phase Space Density Profiles and Fast ULF Wave Diffusive Transport. *J. Geophys. Res. Space Phys.* 124, 1143–1156. doi:10.1029/2018JA026326

Ozeke, L. G., Mann, I. R., Dufresne, S. K. Y., Olifer, L., Morley, S. K., Claudepierre, S. G., et al. (2020). Rapid Outer Radiation Belt Flux Dropouts and Fast Acceleration during the March 2015 and 2013 Storms: The Role of ULF Wave Transport from a Dynamic Outer Boundary. *J. Geophys. Res. Space Phys.* 125, e2019JA027179. doi:10.1029/2019JA027179

Ozeke, L. G., Mann, I. R., Murphy, K. R., Jonathan Rae, I., and Milling, D. K. (2014a). Analytic Expressions for ULF Wave Radiation Belt Radial Diffusion Coefficients. *J. Geophys. Res. Space Phys.* 119, 1587–1605. doi:10.1002/2013JA019204

Ozeke, L. G., Mann, I. R., Olifer, L., Claudepierre, S. G., Spence, H. E., and Baker, D. N. (2022). Statistical Characteristics of Energetic Electron Pitch Angle Distributions in the Van Allen Probe Era: 1. Butterfly Distributions with Flux Peaks at Preferred Pitch Angles. *J. Geophys. Res. Space Phys.* 127, e2021JA029907. doi:10.1029/2021JA029907

Ozeke, L. G., Mann, I. R., Turner, D. L., Murphy, K. R., Degeling, A. W., Rae, I. J., et al. (2014b). Modeling Cross L Shell Impacts of Magnetopause Shadowing and ULF Wave Radial Diffusion in the Van Allen Belts. *Geophys. Res. Lett.* 41, 6556–6562. doi:10.1002/2014GL060787

Palmaerts, B., Roussos, E., Krupp, N., Kurth, W. S., Mitchell, D. G., and Yates, J. N. (2016). Statistical Analysis and Multi-Instrument Overview of the Quasi-Periodic 1-hour Pulsations in Saturn's Outer Magnetosphere. *Icarus* 271, 1. doi:10.1016/j.icarus.2016.01.025

Paranicas, C., Thomsen, M. F., Kollmann, P., Azari, A. R., Bader, A., Badman, S. V., et al. (2020). Inflow Speed Analysis of Interchange Injections in Saturn's Magnetosphere. *J. Geophys. Res. (Space Phys.* 125, e28299. doi:10.1029/2020JA028299

Paulikas, G. A., and Blake, J. B. (1979). "Effects of the Solar Wind on Magnetospheric Dynamics: Energetic Electrons at the Synchronous Orbit," in *Quantitative Modeling of Magnetospheric Processes*. Editor W. P. Olson (Washington, D. C: Geophys. Monogr. Ser.AGU), 21, 180–202.

Reeves, G. D., McAdams, K. L., Friedel, R. H. W., and O'Brien, T. P. (2003). Acceleration and Loss of Relativistic Electrons during Geomagnetic Storms. *Geophys. Res. Lett.* 30, 1529. doi:10.1029/2002GL016513

Reeves, G. D., Morley, S. K., Friedel, R. H. W., Henderson, M. G., Cayton, T. E., Cunningham, G., et al. (2011). On the Relationship between Relativistic Electron Flux and Solar Wind Velocity: Paulikas and Blake Revisited. *J. Geophys. Res.* 116, A02213. doi:10.1029/2010JA015735

Reeves, G. D., Spence, H. E., Henderson, M. G., Morley, S. K., Friedel, R. H. W., Funsten, H. O., et al. (2013). Electron Acceleration in the Heart of the Van Allen Radiation Belts. *Science* 341 (6149), 991–994. doi:10.1126/science.1237743

Riley, P., and Wolf, R. A. (1992). Comparison of Diffusion and Particle Drift Descriptions of Radial Transport in the Earth's Inner Magnetosphere. *J. Geophys. Res.* 97 (A11), 16865–16876. doi:10.1029/92JA01538

Ripoll, J-F. (2020). Particle Dynamics in the Earth's Radiation Belts: Review of Current Research and Open Questions. *J. Geophys. Res. Space Phys.* 125, 5e2019JA026735. doi:10.1029/2019ja026735

Ripoll, J.-F., Loridan, V., Denton, M. H., Cunningham, G., Reeves, G., Santolík, O., et al. (2019). Observations and Fokker-Planck Simulations of the L-Shell, Energy, and Pitch Angle Structure of Earth's Electron Radiation Belts during Quiet Times. *J. Geophys. Res. Space Phys.* 124, 1125–1142. doi:10.1029/2018JA026111

Rodger, C. J., Hendry, A. T., Clilverd, M. A., Forsyth, C., and Morley, S. K. (2022). Examination of Radiation Belt Dynamics during Substorm Clusters: Activity Drivers and Dependencies of Trapped Flux Enhancements. *J. Geophys. Res. Space Phys.* 127, e2021JA030003. doi:10.1029/2021JA030003

Roederer, J. G. (1970). *Dynamics of Geomagnetically Trapped Radiation*. New York: Springer. doi:10.1007/978-3-642-49300-3

Roederer, J. G., and Lejosne, S. (2018). Coordinates for Representing Radiation Belt Particle Flux. *J. Geophys. Res. Space Phys.* 123, 1381–1387. doi:10.1002/2017JA025053

Roederer, J. G., and Zhang, H. (2014). "Dynamics of Magnetically Trapped Particles," in *Foundations of the Physics of Radiation Belts and Space Plasmas. Astrophysics and Space Science Library* (Berlin: Springer), 403. doi:10.1007/978-3-642-41530-2

Roussos, E., Allanson, O., André, N., Bertucci, B., Branduardi-Raymont, G., Clark, G., et al. (2021). The Iin-Ssitu Exploration of Jupiter's Radiation Belts. *Exp. Astron.* doi:10.1007/s10686-021-09801-0

Roussos, E., Jackman, C. M., Thomsen, M. F., Kurth, W. S., Badman, S. V., Paranicas, C., et al. (2018b). Solar Energetic Particles (SEP) and Galactic Cosmic Rays (GCR) as Tracers of Solar Wind Conditions Near Saturn: Event Lists and Applications. *Icarus* 300, 47. doi:10.1016/j.icarus.2017.08.040

Roussos, E., Jones, G. H., Krupp, N., Paranicas, C., Mitchell, D. G., Lagg, A., et al. (2007). Electron Microdiffusion in the Saturnian Radiation Belts: Cassini MIMI/LEMMS Observations of Energetic Electron Absorption by the Icy Moons. *J. Geophys. Res. (Space Phys.* 112, A06214. doi:10.1029/2006JA012027

Roussos, E., Kollmann, P., Krupp, N., Paranicas, C., Dialynas, K., Sergis, N., et al. (2018a). Drift-resonant, Relativistic Electron Acceleration at the Outer Planets: Insights from the Response of Saturn's Radiation Belts to Magnetospheric Storms. *Icarus* 305, 160. doi:10.1016/j.icarus.2018.01.016

Roussos, E., and Kollmann, P. (2021). The Radiation Belts of Jupiter and Saturn. *Magnetos. Sol. Syst.* 2, 499. doi:10.1002/9781119815624.ch32

Roussos, E., Krupp, N., Mitchell, D. G., Paranicas, C., Krimigis, S. M., Andriopoulou, M., et al. (2016). Quasi-periodic Injections of Relativistic Electrons in Saturn's Outer Magnetosphere. *Icarus* 263, 101. doi:10.1016/j.icarus.2015.04.017

Roussos, E., Krupp, N., Paranicas, C. P., Mitchell, D. G., Müller, A. L., Kollmann, P., et al. (2010). Energetic Electron Microsignatures as Tracers of Radial Flows and Dynamics in Saturn's Innermost Magnetosphere. *J. Geophys. Res. (Space Phys.* 115, A03202. doi:10.1029/2009JA014808

Sandhu, J. K., Rae, I. J., Wygant, J. R., Breneman, A. W., Tian, S., Watt, C. E. J., et al. (2021). ULF Wave Driven Radial Diffusion during Geomagnetic Storms: A Statistical Analysis of Van Allen Probes Observations. *J. Geophys. Res. Space Phys.* 126, e2020JA029024. doi:10.1029/2020JA029024

Schiller, Q., Kanekal, S. G., Jian, L. K., Li, X., Jones, A., Baker, D. N., et al. (2016). *Prompt Injections of Highly Relativistic Electrons Induced by Interplanetary Shocks: A Statistical Study of Van Allen Probes Observations*.

Schiller, Q., Li, X., Blum, L., Tu, W., Turner, D. L., and Blake, J. B. (2014). A Nonstorm Time Enhancement of Relativistic Electrons in the Outer Radiation Belt. *Geophys. Res. Lett.* 41, 7–12. doi:10.1002/2013GL058485

Schulz, M. (1972). Drift-Shell Splitting at Arbitrary Pitch Angle. *J. Geophys. Res.* 77, 624–634. doi:10.1029/JA077i004p00624

Schulz, M., and Lanzerotti, L. J. (1974). *Particle Diffusion in the Radiation Belts*. Berlin: Springer. doi:10.1007/978-3-642-65675-0

Selesnick, R. S., Blake, J. B., Kolasinski, W. A., and Fritz, T. A. (1997). A Quiescent State of 3 to 8 MeV Radiation Belt Electrons. *Geophys. Res. Lett.* 24 (11), 1343–1346. doi:10.1029/97GL51407

Selesnick, R. S., and Blake, J. B. (2000). On the Source Location of Radiation Belt Relativistic Electrons. *J. Geophys. Res.* 105 (A2), 2607–2624. doi:10.1029/1999JA900445

Selesnick, R. S., and Stone, E. C. (1991). Energetic Electrons at Uranus: Bimodal Diffusion in a Satellite Limited Radiation Belt. *J. Geophys. Res.* 96, 5651. doi:10.1029/90JA02696

Selesnick, R. S., Su, Y.-J., and Blake, J. B. (2016). Control of the Innermost Electron Radiation Belt by Large-Scale Electric Fields. *J. Geophys. Res. Space Phys.* 121, 8417–8427. doi:10.1002/2016JA022973

Shprits, Y., Kondrashov, D., Chen, Y., Thorne, R., Ghil, M., Friedel, R., et al. (2007a). Reanalysis of Relativistic Radiation Belt Electron Fluxes Using CRRES Satellite Data, a Radial Diffusion Model, and a Kalman Filter. *J. Geophys. Res.* 112, A12216. doi:10.1029/2007JA012579

Shprits, Y. Y., Kellerman, A. C., Drozdov, A. Y., Spence, H. E., Reeves, G. D., and Baker, D. N. (2015). Combined Convective and Diffusive Simulations: VERB-4D Comparison with 17 March 2013 Van Allen Probes Observations. *Geophys. Res. Lett.* 42, 9600–9608. doi:10.1002/2015GL065230

Shprits, Y. Y., Menietti, J. D., Gu, X., Kim, K. C., and Horne, R. B. (2012). Gyroresonant Interactions between the Radiation Belt Electrons and Whistler Mode Chorus Waves in the Radiation Environments of Earth, Jupiter, and Saturn: A Comparative Study. *J. Geophys. Res. (Space Phys.* 117, A11216. doi:10.1029/2012JA018031

Shprits, Y. Y., Meredith, N. P., and Thorne, R. M. (2007b). Parameterization of Radiation Belt Electron Loss Timescales Due to Interactions with Chorus Waves. *Geophys. Res. Lett.* 34 (11). doi:10.1029/2006gl029050

Shprits, Y. Y., Subbotin, D. A., Meredith, N. P., and Elkington, S. R. (2008). Review of Modeling of Losses and Sources of Relativistic Electrons in the Outer Radiation Belt II: Local Acceleration and Loss. *J. Atmos. Solar-Terrestrial Phys.* 70 (14), 1694–1713. doi:10.1016/j.jastp.2008.06.014

Shprits, Y. Y., Thorne, R. M., Friedel, R., Reeves, G. D., Fennell, J., Baker, D. N., et al. (2006). Outward Radial Diffusion Driven by Losses at Magnetopause. *J. Geophys. Res.* 111, A11214. doi:10.1029/2006JA011657

Shprits, Y. Y., Thorne, R. M., Reeves, G. D., and Friedel, R. (2005). Radial Diffusion Modeling with Empirical Lifetimes: Comparison with CRRES Observations. *Ann. Geophys.* 23, 1467–1471. doi:10.5194/angeo-23-1467-2005

Shprits, Y. Y., and Thorne, R. M. (2004). Time Dependent Radial Diffusion Modeling of Relativistic Electrons with Realistic Loss Rates. *Geophys. Res. Lett.* 31, L08805. doi:10.1029/2004GL019591

Simms, L. E., Engebretson, M. J., Clilverd, M. A., Rodger, C. J., and Reeves, G. D. (2018). Nonlinear and Synergistic Effects of ULF Pc5, VLF Chorus, and EMIC Waves on Relativistic Electron Flux at Geosynchronous Orbit. *J. Geophys. Res. Space Phys.* 123, 4755–4766. doi:10.1029/2017JA025003

Simms, L. E., Engebretson, M. J., Rodger, C. J., Dimitrakoudis, S., Mann, I. R., and Chi, P. J. (2021). The Combined Influence of Lower Band Chorus and ULF Waves on Radiation Belt Electron Fluxes at Individual L-Shells. *J. Geophys. Res. Space Phys.* 126, e2020JA028755. doi:10.1029/2020JA028755

Staples, F. A., Kellerman, A., Murphy, K. R., Rae, I. J., Sandhu, J. K., and Forsyth, C. (2022). Resolving Magnetopause Shadowing Using Multimission Measurements of Phase Space Density. *J. Geophys. Res. Space Phys.* 127, e2021JA029298. doi:10.1029/2021JA029298

Staples, F. A., Rae, I. J., Forsyth, C., Smith, A. R. A., Murphy, K. R., Raymer, K. M., et al. (2020). Do statistical Models Capture the Dynamics of the Magnetopause during Sudden Magnetospheric Compressions? *J. Geophys. Res. Space Phys.* 125, e2019JA027289. doi:10.1029/2019ja027289

Stern, D. P. (1977). Large-scale Electric Fields in the Earth's Magnetosphere. *Rev. Geophys.* 15 (2), 156–194. doi:10.1029/RG015i002p00156

Su, Z., Zhu, H., Xiao, F., Zong, Q.-G., Zhou, X.-Z., Zhen, H., et al. (2015). Ultra-low-frequency Wave-Driven Diffusion of Radiation Belt Relativistic Electrons. *Nat. Commun.* 6, 10096. doi:10.1038/ncomms10096

Subbotin, D., Shprits, Y., and Ni, B. (2010). Three-dimensional VERB Radiation Belt Simulations Including Mixed Diffusion. *J. Geophys. Res. [Space Phys.* 115 (A3). doi:10.1029/2009JA015070

Summers, D., Ma, C., and Mukai, T. (2004). Competition between Acceleration and Loss Mechanisms of Relativistic Electrons during Geomagnetic Storms. *J. Geophys. Res. Space Phys.* 109 (A4). doi:10.1029/2004ja010437

Summers, D., and Omura, Y. (2007). Ultra-relativistic Acceleration of Electrons in Planetary Magnetospheres. *Geophys. Res. Lett.* 34, L24205. doi:10.1029/2007GL032226

Summers, D., Thorne, R. M., and Xiao, F. (1998). Relativistic Theory of Wave-Particle Resonant Diffusion with Application to Electron Acceleration in the Magnetosphere. *J. Geophys. Res.* 103 (A9), 20487–20500. doi:10.1029/98JA01740

Sun, Y. X., Roussos, E., Hao, Y. X., Zong, Q.-G., Liu, Y., Lejosne, S., et al. (2021). Saturn's Inner Magnetospheric Convection in the View of Zebra Stripe Patterns in Energetic Electron Spectra. *J. Geophys. Res. (Space Phys.* 126, e29600. doi:10.1029/2021JA029600

Sun, Y. X., Roussos, E., Krupp, N., Zong, Q. G., Kollmann, P., and Zhou, X. Z. (2019). Spectral Signatures of Adiabatic Electron Acceleration at Saturn through Corotation Drift Cancelation. *Geophys. Res. Lett.* 46 (10), 240. doi:10.1029/2019GL084113

Tao, X., Bortnik, J., Albert, J. M., and Thorne, R. M. (2012). Comparison of Bounce-Averaged Quasi-Linear Diffusion Coefficients for Parallel Propagating Whistler Mode Waves with Test Particle Simulations. *J. Geophys. Res.* 117, A10205. doi:10.1029/2012JA017931

Thorne, R., Li, W., Ni, B., Ma, Q., Bortnik, J., Chen, L., et al. (2013). Rapid Local Acceleration of Relativistic Radiation-Belt Electrons by Magnetospheric Chorus. *Nature* 504, 411–414. doi:10.1038/nature12889

Thorne, R. M., Armstrong, T. P., Stone, S., Williams, D. J., McEntire, R. W., Bolton, S. J., et al. (1997). Galileo Evidence for Rapid Interchange Transport in the Io Torus. *Geophys. Res. Lett.* 24, 2131. doi:10.1029/97GL01788

Thorne, R. M., Church, S. R., and Gorney, D. J. (1979). On the Origin of Plasmaspheric Hiss: The Importance of Wave Propagation and the Plasmapause. *J. Geophys. Res. Space Phys.* 84 (A9), 5241–5247. doi:10.1029/ja084ia09p05241

Thorne, R. M., Horne, R. B., Glauert, S., Meredith, N. P., Shprits, Y. Y., Summers, D., et al. (2005). The Influence of Wave-Particle Interactions on Relativistic Electron Dynamics during Storms. *Geophys. Monograph-American Geophys. Union* 159, 101. doi:10.1029/159gm07

Thorne, R. M. (2010). Radiation Belt Dynamics: The Importance of Wave-particle Interactions. *Geophys. Res. Lett.* 37, L22107. doi:10.1029/2010GL044990

Tsuchiya, F., Misawa, H., Imai, K., and Morioka, A. (2011). Short-term Changes in Jupiter's Synchrotron Radiation at 325 MHz: Enhanced Radial Diffusion in Jupiter's Radiation Belt Driven by Solar UV/EUV Heating. *J. Geophys. Res. (Space Phys.* 116, A09202. doi:10.1029/2010JA016303

Tsurutani, B. T., Gonzalez, W. D., Gonzalez, A. L. C., Guarnieri, F. L., Gopalswamy, N., Grande, M., et al. (2006). Corotating Solar Wind Streams and Recurrent Geomagnetic Activity: A Review. *J. Geophys. Res.* 111, A07S01. doi:10.1029/2005JA011273

Tu, W., Elkington, S. R., Li, X., Liu, W., and Bonnell, J. (2012). Quantifying Radial Diffusion Coefficients of Radiation Belt Electrons Based on Global MHD Simulation and Spacecraft Measurements. *J. Geophys. Res.* 117, A10210. doi:10.1029/2012JA017901

Tu, W., Li, X., Chen, Y., Reeves, G. D., and Temerin, M. (2009). Storm-dependent Radiation Belt Electron Dynamics. *J. Geophys. Res.* 114, A02217. doi:10.1029/2008JA013480

Turner, D. L., Cohen, I. J., Michael, A., Sorathia, K., Merkin, S., Mauk, B. H., et al. (2021). Can Earth's Magnetotail Plasma Sheet Produce a Source of Relativistic Electrons for the Radiation Belts? *Geophys. Res. Lett.* 48, e2021GL095495. doi:10.1029/2021GL095495

Turner, D. L., Kilpua, E. K. J., Hietala, H., Claudepierre, S. G., O'Brien, T. P., Fennell, J. F., et al. (2019). The Response of Earth's Electron Radiation Belts to Geomagnetic Storms: Statistics from the Van Allen Probes Era Including Effects from Different Storm Drivers. *J. Geophys. Res. Space Phys.* 124, 1013–1034. doi:10.1029/2018JA026066

Turner, D. L., Shprits, Y., Hartinger, M., and Angelopoulos, V. (2012). Explaining Sudden Losses of Outer Radiation Belt Electrons during Geomagnetic Storms. *Nat. Phys.* 8 (3), 208–212. doi:10.1038/nphys2185

Tverskaya, L. V., Pavlov, N. N., Blake, J. B., Selesnick, R. S., and Fennell, J. F. (2003). Predicting the L-Position of the Storm-Injected Relativistic Electron Belt. *Adv. Space Res.* 31 (4), 1039–1044. doi:10.1016/S0273-1177(02)00785-8

Ukhorskiy, A. Y., Anderson, B. J., Brandt, P. C., and Tsyganenko, N. A. (2006). Storm Time Evolution of the Outer Radiation Belt: Transport and Losses. *J. Geophys. Res.* 111, A11S03. doi:10.1029/2006JA011690

Ukhorskiy, A. Y., and Sitnov, M. I. (2012). "Dynamics of Radiation Belt Particles," in *The Van Allen Probes Mission*. Editors N. Fox and J. L. Burch (Boston, MA: Springer). doi:10.1007/978-1-4899-7433-4_17

Ukhorskiy, A. Y., and Sitnov, M. I. (2013). Dynamics of Radiation Belt Particles. *Space Sci. Rev.* 179, 545–578. doi:10.1007/s11214-012-9938-5

Ukhorskiy, A. Y., Sitnov, M. I., Millan, R. M., and Kress, B. T. (2011). The Role of Drift Orbit Bifurcations in Energization and Loss of Electrons in the Outer Radiation Belt. *J. Geophys. Res.* 116, A09208. doi:10.1029/2011JA016623

Ukhorskiy, A. Y., Sitnov, M. I., Takahashi, K., and Anderson, B. J. (2009). Radial Transport of Radiation Belt Electrons Due to Stormtime Pc5 Waves. *Ann. Geophys.* 27, 2173–2181. doi:10.5194/angeo-27-2173-2009

Van Allen, J. A., Thomsen, M. F., and Randall, B. A. (1980). The Energetic Charged Particle Absorption Signature of Mimas. *J. Geophys. Res.* 85, 5709. doi:10.1029/JA085iA11p05709

Varotsou, A., Boscher, D., Bourdarie, S., Horne, R. B., Glauert, S. A., and Meredith, N. P. (2005). Simulation of the Outer Radiation Belt Electrons Near Geosynchronous Orbit Including Both Radial Diffusion and Resonant Interaction with Whistler-Mode Chorus Waves. *Geophys. Res. Lett.* 32, L19106. doi:10.1029/2005GL023282

Walt, M. (1994). *Introduction to Geomagnetically Trapped Radiation*. Cambridge: Cambridge University Press. doi:10.1017/CBO9780511524981

Wang, D., and Shprits, Y. Y. (2019). On How High-Latitude Chorus Waves Tip the Balance between Acceleration and Loss of Relativistic Electrons. *Geophys. Res. Lett.* 46 (14), 7945–7954. doi:10.1029/2019GL082681

Wang, D., Shprits, Y. Y., Zhelavskaya, I. S., Effenberger, F., Castillo, A., Drozdov, A. Y., et al. (2020). The Effect of Plasma Boundaries on the Dynamic Evolution of Relativistic Radiation Belt Electrons. *J. Geophys. Res. Space Phys.* 125, e2019JA027422. doi:10.1029/2019JA027422

Watt, C. E. J., Rae, I. J., Murphy, K. R., Anekallu, C., Bentley, S. N., and Forsyth, C. (2017). The Parameterization of Wave-Particle Interactions in the Outer Radiation Belt. *J. Geophys. Res. Space Phys.* 122, 9545–9551. doi:10.1002/2017JA024339

Williams, D. J. (1966). A 27-day Periodicity in Outer Zone Trapped Electron Intensities. *J. Geophys. Res.* 71 (7), 1815–1826. doi:10.1029/JZ071i007p01815

Wing, S., Johnson, J. R., Camporeale, E., and Reeves, G. D. (2016). Information Theoretical Approach to Discovering Solar Wind Drivers of the Outer Radiation Belt. *J. Geophys. Res. Space Phys.* 121, 9378–9399. doi:10.1002/2016JA022711

Woodfield, E. E., Glauert, S. A., Menietti, J. D., Averkamp, T. F., Horne, R. B., and Shprits, Y. Y. (2019). Rapid Electron Acceleration in Low-Density Regions of Saturn's Radiation Belt by Whistler Mode Chorus Waves. *Geophys. Res. Lett.* 46, 7191. doi:10.1029/2019GL083071

Woodfield, E. E., Horne, R. B., Glauert, S. A., Menietti, J. D., Shprits, Y. Y., and Kurth, W. S. (2018). Formation of Electron Radiation Belts at Saturn by Z-Mode Wave Acceleration. *Nat. Commun.* 9, 5062. doi:10.1038/s41467-018-07549-4

Woodfield, E. E., Horne, R. B., Glauert, S. A., Menietti, J. D., and Shprits, Y. Y. (2014). The Origin of Jupiter's Outer Radiation Belt. *J. Geophys. Res. (Space Phys.* 119, 3490. doi:10.1002/2014JA019891

Xiang, Z., Li, X., Kapali, S., Gannon, J., Ni, B., Zhao, H., et al. (2021). Modeling the Dynamics of Radiation Belt Electrons with Source and Loss Driven by the Solar Wind. *J. Geophys. Res. Space Phys.* 126, e2020JA028988. doi:10.1029/2020JA028988

Xiang, Z., Tu, W., Li, X., Ni, B., Morley, S. K., and Baker, D. N. (2017). Understanding the Mechanisms of Radiation Belt Dropouts Observed by Van Allen Probes. *J. Geophys. Res. Space Phys.* 122, 9858–9879. doi:10.1002/2017JA024487

Yuan, C.-J., Roussos, E., Wei, Y., Krupp, N., Sun, Y. X., and Hao, Y. X. (2021). Cassini Observation of Relativistic Electron Butterfly Distributions in Saturn's Inner Radiation Belts: Evidence for Acceleration by Local Processes. *Geophys. Res. Lett.* 48, e92690. doi:10.1029/2021GL092690

Yuan, C.-J., Roussos, E., Wei, Y., and Krupp, N. (2020). Sustaining Saturn's Electron Radiation Belts through Episodic, Global-Scale Relativistic Electron Flux Enhancements. *J. Geophys. Res. (Space Phys.* 125, e27621. doi:10.1029/2019JA027621

Yuan, C., Zuo, Y., Roussos, E., Wei, Y., Hao, Y., Sun, Y., et al. (2021). Large-scale Episodic Enhancements of Relativistic Electron Intensities in Jupiter's Radiation Belt. *Earth Planet. Phys.* 5, 314. doi:10.26464/epp2021037

Zhang, X.-J., Mourenas, D., Artemyev, A. V., Angelopoulos, V., Bortnik, J., Thorne, R. M., et al. (2019). Nonlinear Electron Interactionwith Intense Chorus Waves: Statisticsof Occurrence Rates. *Geophys. Lett.* 46, 7182–7190. doi:10.1029/2019GL083833

Zhao, H., Baker, D. N., Jaynes, A. N., Li, X., Elkington, S. R., Kanekal, S. G., et al. (2017). On the Relation between Radiation Belt Electrons and Solar Wind Parameters/geomagnetic Indices: Dependence on the First Adiabatic Invariant and L. *J. Geophys. Res. Space Phys.* 122, 1624–1642. doi:10.1002/2016JA023658

Zhao, H., Baker, D. N., Li, X., Jaynes, A. N., and Kanekal, S. G. (2018). The Acceleration of Ultrarelativistic Electrons during a Small to Moderate Storm of 21 April 2017. *Geophys. Res. Lett.* 45. doi:10.1029/2018GL078582

Zhao, H., Baker, D. N., Li, X., Jaynes, A. N., and Kanekal, S. G. (2019a). The Effects of Geomagnetic Storms and Solar Wind Conditions on the Ultrarelativistic Electron Flux Enhancements. *J. Geophys. Res. Space Phys.* 124, 1948–1965. doi:10.1029/2018JA026257

Zhao, H., Baker, D. N., Li, X., Malaspina, D. M., Jaynes, A. N., and Kanekal, S. G. (2019b). On the Acceleration Mechanism of Ultrarelativistic Electrons in the Center of the Outer Radiation Belt: A Statistical Study. *J. Geophys. Res. Space Phys.* 124, 8590–8599. doi:10.1029/2019JA027111

Zhao, H., Johnston, W. R., Baker, D. N., Li, X., Ni, B., Jaynes, A. N., et al. (2019c). Characterization and Evolution of Radiation Belt Electron Energy Spectra Based on the Van Allen Probes Measurements. *J. Geophys. Res. Space Phys.* 124, 4217–4232. doi:10.1029/2019JA026697

Zhao, H., Li, X., Baker, D. N., Claudepierre, S. G., Fennell, J. F., Blake, J. B., et al. (2016). Ring Current Electron Dynamics during Geomagnetic Storms Based on the Van Allen Probes Measurements. *J. Geophys. Res. Space Phys.* 121, 3333–3346. doi:10.1002/2016JA022358

Zhao, H., Sarris, T. E., Li, X., Weiner, M., Huckabee, I. G., Baker, D. N., et al. (2021). Van Allen Probes Observations of Multi-MeV Electron Drift-Periodic Flux Oscillations in Earth's Outer Radiation Belt during the March 2017 Event. *J. Geophys. Res. Space Phys.* 126, e2021JA029284. doi:10.1029/2021JA029284

Zheng, L., Chan, A. A., O'Brien, T. P., Tu, W., Cunningham, G. S., Albert, J. M., et al. (2016). Effects of Magnetic Drift Shell Splitting on Electron Diffusion in the Radiation Belts. *J. Geophys. Res. Space Phys.* 121 (11), 985–12,000. doi:10.1002/2016JA023438

Zong, Q.-G., Zhou, X.-Z., Wang, Y. F., Li, X., Song, P., Baker, D. N., et al. (2009). Energetic Electron Response to ULF Waves Induced by Interplanetary Shocks in the Outer Radiation Belt. *J. Geophys. Res.* 114, A10204. doi:10.1029/2009JA014393

Zong, Q. (2022). Magnetospheric Response to Solar Wind Forcing: Ultra-low-frequency Wave–Particle Interaction Perspective. *Ann. Geophys.* 40, 121–150. doi:10.5194/angeo-40-121-2022

Zong, Q., Rankin, R., and Zhou, X. (2017). The Interaction of Ultra-low-frequency Pc3-5 Waves with Charged Particles in Earth's Magnetosphere. *Rev. Mod. Plasma Phys.* 1, 10. doi:10.1007/s41614-017-0011-4

Conflict of Interest: The authors declare that the research was conducted in the absence of any commercial or financial relationships that could be construed as a potential conflict of interest.

Publisher's Note: All claims expressed in this article are solely those of the authors and do not necessarily represent those of their affiliated organizations, or those of the publisher, the editors and the reviewers. Any product that may be evaluated in this article, or claim that may be made by its manufacturer, is not guaranteed or endorsed by the publisher.

frontiers | Frontiers in Astronomy and Space Sciences

ORIGINAL RESEARCH
published: 16 June 2022
doi: 10.3389/fspas.2022.910224

Equations of Motion Near Cyclotron Resonance

Jay M. Albert[1]*, *Anton Artemyev*[2], *Wen Li*[3], *Longzhi Gan*[3] and *Qianli Ma*[3,4]

[1]Air Force Research Laboratory, Kirtland AFB, NM, United States, [2]Department of Earth, Planetary, and Space Sciences, University of California, Los Angeles, Los Angeles, CA, United States, [3]Center for Space Physics, Boston University, Boston, MA, United States, [4]Department of Atmospheric and Oceanic Sciences, University of California, Los Angeles, Los Angeles, CA, United States

This work compares several versions of the equations of motion for a test particle encountering cyclotron resonance with a single, field-aligned whistler mode wave. The gyro-averaged Lorentz equation produces both widespread phase trapping (PT) and "positive phase bunching" of low pitch angle electrons by large amplitude waves. Approximations allow a Hamiltonian description to be reduced to a single pair of conjugate variables, which can account for PT as well as phase bunching at moderate pitch angle, and has recently been used to investigate this unexpected bahavior at low pitch angle. Here, numerical simulations using the Lorentz equation and several versions of Hamiltonian-based equations of motion are compared. Similar behavior at low pitch angle is found in each case.

Keywords: wave-particle interactions, radiation belts, nonlinear, Hamiltonian, test particle simulation

OPEN ACCESS

Edited by:
Yuri Y. Shprits,
GFZ German Research Centre for Geosciences, Germany

Reviewed by:
Peter Haesung Yoon,
University of Maryland, United States
Xin Tao,
University of Science and Technology of China, China

***Correspondence:**
Jay M. Albert
jay.albert@us.af.mil

Specialty section:
This article was submitted to Space Physics, a section of the journal Frontiers in Astronomy and Space Sciences

Received: *01 April 2022*
Accepted: *06 May 2022*
Published: *16 June 2022*

Citation:
Albert JM, Artemyev A, Li W, Gan L and Ma Q (2022) Equations of Motion Near Cyclotron Resonance. Front. Astron. Space Sci. 9:910224. doi: 10.3389/fspas.2022.910224

1 INTRODUCTION

Cyclotron-resonant wave-particle interactions are a crucial ingredient in magnetospheric dynamics, especially in the radiation belts, and there is a vast tradition of simulating the process as quasi-linear diffusion of phase space density by a broad-band spectrum of small, incoherent waves (Thorne, 2010; Thorne et al., 2013), following the pioneering work of Lyons et al. (1971) and Lyons et al. (1972). A complementary approach is that of test particle simulation, most often in the presence of a single, coherent wave whose amplitude need not be small. Inan et al. (1978) noted both quasi-linear and nonlinear behavior, including the "loss cone reflection effect" whereby low pitch angles increase rather than decrease below zero. In the quasi-linear regime, connections between the two perspectives have been provided by Lemons et al. (2009), Lemons (2012), Allanson et al. (2022), and a unified picture of quasi-linear and nonlinear behavior was obtained by Albert (2001), Albert (2010). These studies all used specified and idealized models of the waves, while Liu et al. (2010), Liu et al. (2012) examined test particles driven by waves from self-consistent particle-in-cell simulations.

This work compares several versions of the equations of motion for a test particle encountering cyclotron resonance with a single, field-aligned whistler mode plane wave. The Lorentz force law, resolved into components parallel and perpendicular to the background magnetic field and gyro-averaged, is commonly used for such simulations. Hamiltonian descriptions are in principle equivalent, and with several approximations they allow the reduction to a one-dimensional (1D) system (one action-angle pair, plus the independent variable playing the role of time). If the time dependence is slow enough, particle motion is nearly along instantaneously drawn contours, with invariant breaking at separatrix crossings. There is a rich literature of work based on these concepts, which has been exploited in this context to some degree. Among others, Shklyar (1986) Albert (1993), Albert (2000), Artemyev et al. (2018) further approximated the Hamiltonian as equivalent to

that of a time-dependent pendulum and obtained quantitative estimates of energy and pitch angle changes, which have proved useful and reliable.

Recently, using the gyro-averaged Lorentz equation, Kitahara and Katoh (2019), Gan et al. (2020) found both widespread (or "anomalous") phase trapping (APT) and "positive phase bunching (PPB)" of low pitch angle electrons by large amplitude waves. Both phenomena lead to pitch angle increase, in contrast to the phase bunching behavior that is the usual alternative to phase trapping, and are associated with low pitch angle, which violates a certain approximation made in obtaining the pendulum Hamiltonian. Albert et al. (2021), Artemyev et al. (2021) presented generalizations of the pendulum Hamiltonian which avoid that specific approximation, but still relied on several others. In particular, differences in the first-order (in wave amplitude) term of the phase evolution equation are present among several versions of the equations of motion. This work shows numerically that, despite these differences, the generalized 1D Hamiltonian reproduces the behavior at low pitch angle, and is therefore an appropriate framework for the future development of refined analytical estimates.

2 GYRO-AVERAGED EQUATIONS OF MOTION

Starting with the Lorentz equation for a charged particle in a background magnetic field and a single whistler-mode wave,

$$\frac{d\mathbf{p}}{dt} = q\left[\mathbf{E_w} + \frac{\mathbf{p}}{mc\gamma}\times(\mathbf{B}_0 + \mathbf{B_w})\right], \quad \frac{d\mathbf{x}}{dt} = \frac{\mathbf{p}}{m\gamma}, \tag{1}$$

where $\mathbf{p} = m\mathbf{v}\gamma$ is the mechanical momentum, γ is the relativistic factor, $\mathbf{B_0}$ is the local geomagnetic field strength with equatorial value B_{eq}, and $\mathbf{E_w}$ and $\mathbf{B_w}$ are the electric and magnetic fields of the wave. Gyro-averaged equations of motion valid near a single resonance have been obtained by many authors, including (Chang and Inan, 1983; Bell, 1984; Albert et al., 2012; Li et al., 2015; Kitahara and Katoh, 2019).

For primary resonance ($\ell = -1$) between an electron (charge $q = -e$) and a parallel-propagating whistler wave, equation 3 of Albert et al. (2012) simplifies to

$$\begin{aligned}
\frac{dp_\parallel}{dt} &= -\frac{p_\perp^2}{2m\gamma}\frac{d\Omega/dz}{\Omega} + \frac{eB_w}{mc}\frac{p_\perp}{\gamma}\cos\xi,\\
\frac{dp_\perp}{dt} &= \frac{p_\parallel p_\perp}{2m\gamma}\frac{d\Omega/dz}{\Omega} + \frac{eB_w}{mc}\frac{\Omega}{\omega\eta}\frac{mc}{\gamma}\cos\xi,\\
\frac{d\xi}{dt} &= \left[\frac{\Omega}{\gamma} - \omega + \frac{kp_\parallel}{m\gamma}\right] - \frac{eB_w}{mc}\frac{\Omega}{\omega\eta}\frac{mc}{p_\perp\gamma}\sin\xi,\\
\frac{dz}{dt} &= \frac{p_\parallel}{m\gamma}.
\end{aligned} \tag{2}$$

The angle ξ is a combination of wave phase and gyrophase, Ω is the local nonrelativistic electron gyrofrequency eB_0/mc, and η is the refractive index kc/ω. The standard resonance condition is just $d\xi/dt = 0$, neglecting the term proportional to B_w.

Equations 3–9 of Kitahara and Katoh (2019) are very similar after shifting ξ by $\pi/2$, using $\eta E_w = B_w$ (in Gaussian units), and accounting for the opposite sign convention in wave phase:

$$\begin{aligned}
\frac{dp_\parallel}{dt} &= -\frac{p_\perp^2}{2m\gamma}\frac{d\Omega/dz}{\Omega} + \frac{eB_w}{mc}\frac{p_\perp}{\gamma}\cos\xi,\\
\frac{dp_\perp}{dt} &= \frac{p_\parallel p_\perp}{2m\gamma}\frac{d\Omega/dz}{\Omega} + \frac{eB_w}{mc}\left(\frac{\gamma}{\eta} - \frac{p_\parallel}{mc}\right)\frac{mc}{\gamma}\cos\xi,\\
\frac{d\xi}{dt} &= \left[\frac{\Omega}{\gamma} - \omega + \frac{kp_\parallel}{m\gamma}\right] - \frac{eB_w}{mc}\left(\frac{\gamma}{\eta} - \frac{p_\parallel}{mc}\right)\frac{mc}{p_\perp\gamma}\sin\xi,\\
\frac{dz}{dt} &= \frac{p_\parallel}{m\gamma}.
\end{aligned} \tag{3}$$

These two versions are brought into agreement by invoking the lowest-order resonance condition, which consists of setting the bracketed expression in the equation for $d\xi/dt$ to zero.

3 TIME-DEPENDENT HAMILTONIAN EQUATIONS

Ginet and Heinemann (1990), Ginet and Albert (1991) used a Hamiltonian version of the equations of motion near resonance with a constant-frequency wave propagating obliquely to a constant background magnetic field $\mathbf{B_0}$, The Hamiltonan formulation uses canonical momentum $\mathbf{P} = \mathbf{p} + q\mathbf{A}/c$, where c is the speed of light, and $\mathbf{A}$ is the vector potential that describes both $\mathbf{B_0}$ and the wave electromagnetic field. A canonical transformation was made from (x, P_x, y, P_y, z, P_z) to variables $(I, \phi, X, P_X, z, P_z)$, with z the distance along $\mathbf{B_0}$ in slab geometry. I and ϕ correspond to standard first adiabatic invariant and gyrophase but have modifications proportional to the wave amplitude. After gyro-averaging, and specializing to the case of a parallel-propagating wave, the variables (ϕ, z, t) appeared only in the combination $\int kdz - \omega t - \phi$ (equation 19 of Ginet and Heinemann (1990) with $k_x = 0$ and $s\ell = 1$). Albert (1993) generalized the treatment to include slow dependence of Ω and η on z, obtaining the Hamiltonian

$$H(I, \phi, P_z, z, t) = \Upsilon + \frac{a_\ell}{2\Upsilon}\sin\xi \tag{4}$$

where

$$\Upsilon = \left(1 + 2\frac{\Omega}{\omega}I + P_z^2\right)^{1/2}, \quad a_\ell = -\sqrt{2\frac{\Omega}{\omega}I}\;\frac{1}{\eta}\frac{qB_w}{mc}, \tag{5}$$

and

$$\xi = \eta z - t + \phi, \tag{6}$$

using normalized variables $(\omega z/c, \omega t, \omega I/mc^2, P_z/mc)$ as in Albert (1993). Appropriate partial derivatives of H give equations of motion for (I, ϕ, P_z, z), e.g., $dI/dt = -\partial H/\partial\phi$ and $d\phi/dt = \partial H/\partial I$, from which

$$\frac{d\xi}{dt} = \eta\frac{P_z}{\Upsilon} - 1 + \frac{d\phi}{dt}. \tag{7}$$

It is also found that $dH/dt = \partial H/\partial t$ equals dI/dt, so that $I - H$ is a constant, denoted c_2:

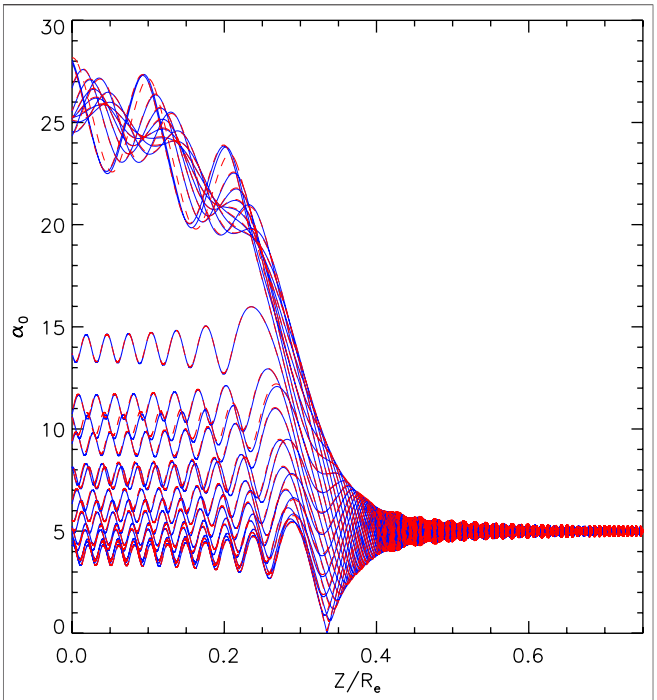

FIGURE 1 | Evolution of 24 electrons starting at $z/R_e = 1$ and interacting with a whistler mode wave, with particle and wave parameters as given in the text. Red curves show results for the equations of motion given in **Eq. 2**, and blue curves used **Eq. 3**.

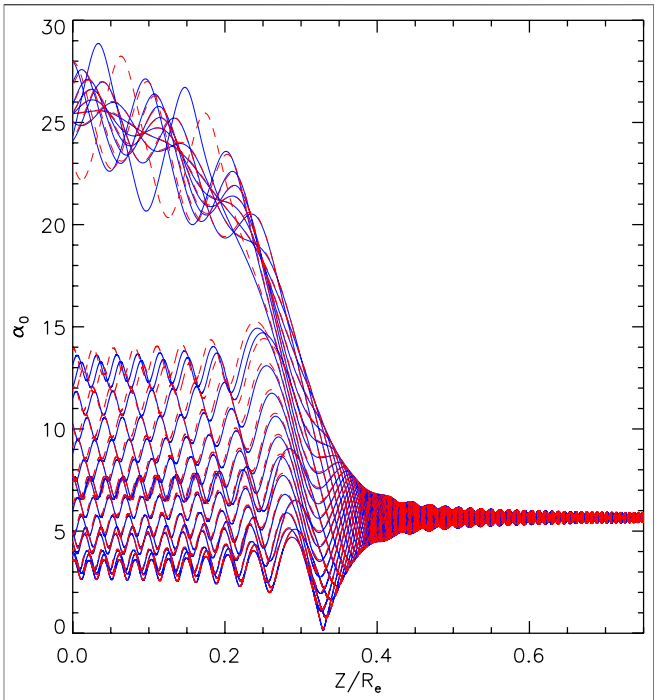

FIGURE 2 | Evolution of 24 electrons starting at $z/R_e = 1$ and interacting with a whistler mode wave, according to equations of motion based on $K(I, \xi, z, t)$. Blue curves show results for the equations of motion given in **Eq. 10**, and red curves used **Eq. 12**.

$$I - H = c_2. \tag{8}$$

Following Shklyar (1986), Albert (1993) solved this for P_z after approximating H by Υ, obtaining

$$\Upsilon \approx \Upsilon_0 \equiv I - c_2, \quad P_z^2 \approx P_0^2 \equiv (I - c_2)^2 - 1 - 2\frac{\Omega}{\omega} I. \tag{9}$$

These can be used to eliminate P_z in the equations of motion, giving

$$\begin{aligned} \frac{dI}{dt} &= -\frac{a_\ell}{2\Upsilon_0}\cos\xi, \\ \frac{d\xi}{dt} &= \left[-\eta\frac{P_0}{\Upsilon_0} + \frac{\Omega}{\omega\Upsilon_0} - 1\right] + a_\ell\frac{1+P_0^2}{4I\Upsilon_0^3}\sin\xi, \\ \frac{dz}{dt} &= -\frac{P_0}{\Upsilon_0}, \end{aligned} \tag{10}$$

as a closed set of equations in (I, ξ, z, t). Since P_0 is defined as always positive, explicit minus signs account for the motion of the particle toward the equator. The bracketed expression in the equation for $d\xi/dt$ gives the lowest order resonance condition.

Retaining the wave term in H to first order gives

$$\Upsilon \approx \Upsilon_0 - \frac{a_\ell}{2\Upsilon_0}\sin\xi, \quad P_z \approx -P_0 + \frac{a_\ell}{2P_0}\sin\xi, \tag{11}$$

again allowing P_z to be eliminated. The correction to P_z/Υ significantly affects **Eq. 7**, giving

$$\begin{aligned} \frac{dI}{dt} &= -\frac{a_\ell}{2\Upsilon_0}\cos\xi, \\ \frac{d\xi}{dt} &= \left[-\eta\frac{P_0}{\Upsilon_0} + \frac{\Omega}{\omega\Upsilon_0} - 1\right] + \frac{a_\ell}{4IP_0\Upsilon_0^3}\left[P_0\left(1+P_0^2\right)\right. \\ &\quad \left. +2\eta I\left(1+2\frac{\Omega}{\omega}I\right) + 2I\frac{\Omega}{\omega}P_0\right]\sin\xi, \\ \frac{dz}{dt} &= -\frac{P_0}{\Upsilon_0} + \frac{a_\ell}{2P_0\Upsilon_0^3}\left(1+2\frac{\Omega}{\omega}I\right)\sin\xi, \end{aligned} \tag{12}$$

which is also a closed set of equations in (I, ξ, z, t).

4 POSITION-DEPENDENT HAMILTONIAN EQUATIONS

Ginet and Heinemann (1990) and Ginet and Albert (1991) proceeded to transform to variables $(\xi, P_\xi, \mu, P_\mu, \tilde{\phi}, \tilde{I})$, with P_ξ canonically conjugate to ξ. However, doing so in an inhomogeneous setting reintroduces explicit time dependence in place of z dependence (see equation 68 of Ginet and Albert, 1991).

Instead, following Shklyar (1986), Albert (1993) divided the equations for dI/dt and $d\xi/dt$ by the equation for dz/dt and attempted to write the results in Hamiltonian form using z as the independent variable. With a Hamiltonian K of the form

$$K(I, \xi, z) = K_0(I, z) + K_1(I, z)\sin\xi, \tag{13}$$

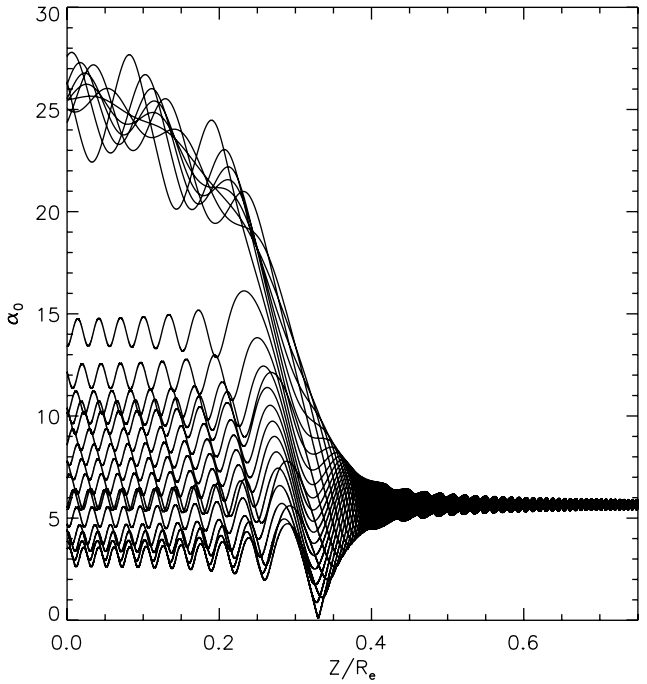

FIGURE 3 | Evolution of 24 electrons starting at $z/R_e = 1$ and interacting with a whistler mode wave, according to equations of motion based on $K(I, \xi, z)$, namely **Eqs 15**, **18**.

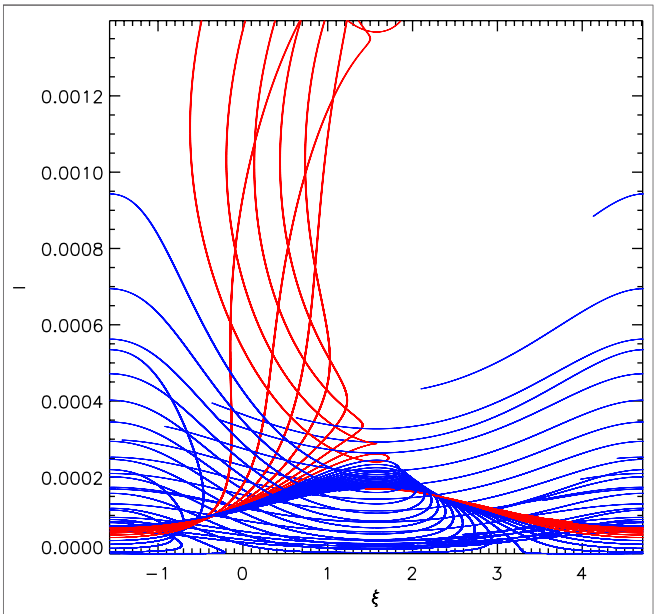

FIGURE 4 | Evolution of 24 electrons interacting with a whistler mode wave, according to equations of motion based on $K(I, \xi, z)$, shown in the (I, ξ) plane. Phase-trapped trajectories are shown for $0.4 > z/R_e > 0$, in red; other trajectories are shown in blue for $0.4 > z/R_e > 0.22$.

the choice

$$K_1 = -\frac{a_\ell}{2P_0} \tag{14}$$

gives

$$\frac{dI}{dz} = -K_1 \cos\xi, \tag{15}$$

which agrees with $(dI/dt)/(dz/dt)$ from **Eq. 10**. Using

$$K_0 = \eta(I - c_2) + P_0 \tag{16}$$

then gives

$$\frac{d\xi}{dz} = \frac{\eta P_0 + \Upsilon_0 - \Omega/\omega}{P_0} - a_\ell \frac{P_0^2 - 2I(\Upsilon_0 - \Omega/\omega)}{2IP_0^3} \sin\xi \tag{17}$$

or, once more using the lowest-order resonance condition,

$$\frac{d\xi}{dz} = \frac{\eta P_0 + \Upsilon_0 - \Omega/\omega}{P_0} - a_\ell \frac{P_0 + 2\eta I}{2IP_0^2} \sin\xi. \tag{18}$$

It is clear that the first-order term in $d\xi/dz$ obtained by this procedure, which enforces the form of **Eq. 13**, is not the same as that of $(d\xi/dt)/(dz/dt)$ from either **Eq. 10** or **Eq. 12**. The analogous disagreement is evident between equations 3.8 and 3.10 of Shklyar (1986), who treated the simpler case of an electrostatic wave and nonrelativistic protons. (Both equations give versions of $d\xi/ds$, the typesetting error in equation 3.8 notwithstanding.)

5 SIMULATIONS AND DISCUSSION

The consequences of the disagreement in the first-order terms of the various ξ evolution equations is studied here numerically. We choose wave and particle parameters following Kitahara and Katoh (2019); Gan et al. (2020). A Taylor expansion of the geodipole magnetic field about the equator gives the variation along a field line as $B/B_{eq} = 1 + 4.5z^2/(LR_e)^2$, with $L = 4$, where R_e is the radius of the Earth and LR_e is the field line equatorial crossing distance. The cold electron density is constant, and chosen to give the ratio of plasma frequency to gyrofrequency as $f_{pe}/f_{ce} = 4$ at the equator. The field-aligned whistler mode wave has frequency such that $\omega/\Omega_e = 0.3$ at the equator. We consider ensembles of 24 electrons, with energy 20 keV, uniformly distributed in initial gyrophase. We take equatorial pitch angle $\alpha_0 = 5^\circ$ and $B_w/B_{eq} = 3 \times 10^{-4}$ (with B_w fixed), since this case seems particularly complex, exhibiting a mixture of conventional phase trapping and "anomalous" phase trapping (as opposed to the oppositely directed change associated with phase bunching for larger pitch angles). The particles are launched towards the equator ($z = 0$) from a distance of 1 R$_e$, and the equations of motion are advanced with a standard Runge-Kutta integrator with variable step size.

Figure 1 shows results using **Eq. 2** (in red) and **Eq. 3** (in blue). The sets of trajectories are not expected to be identical because of accumulated phase differences far from resonance. Nevertheless the overall behavior is very similar, showing no significant change until reaching resonance around $z/R_e = 0.35$, after which the

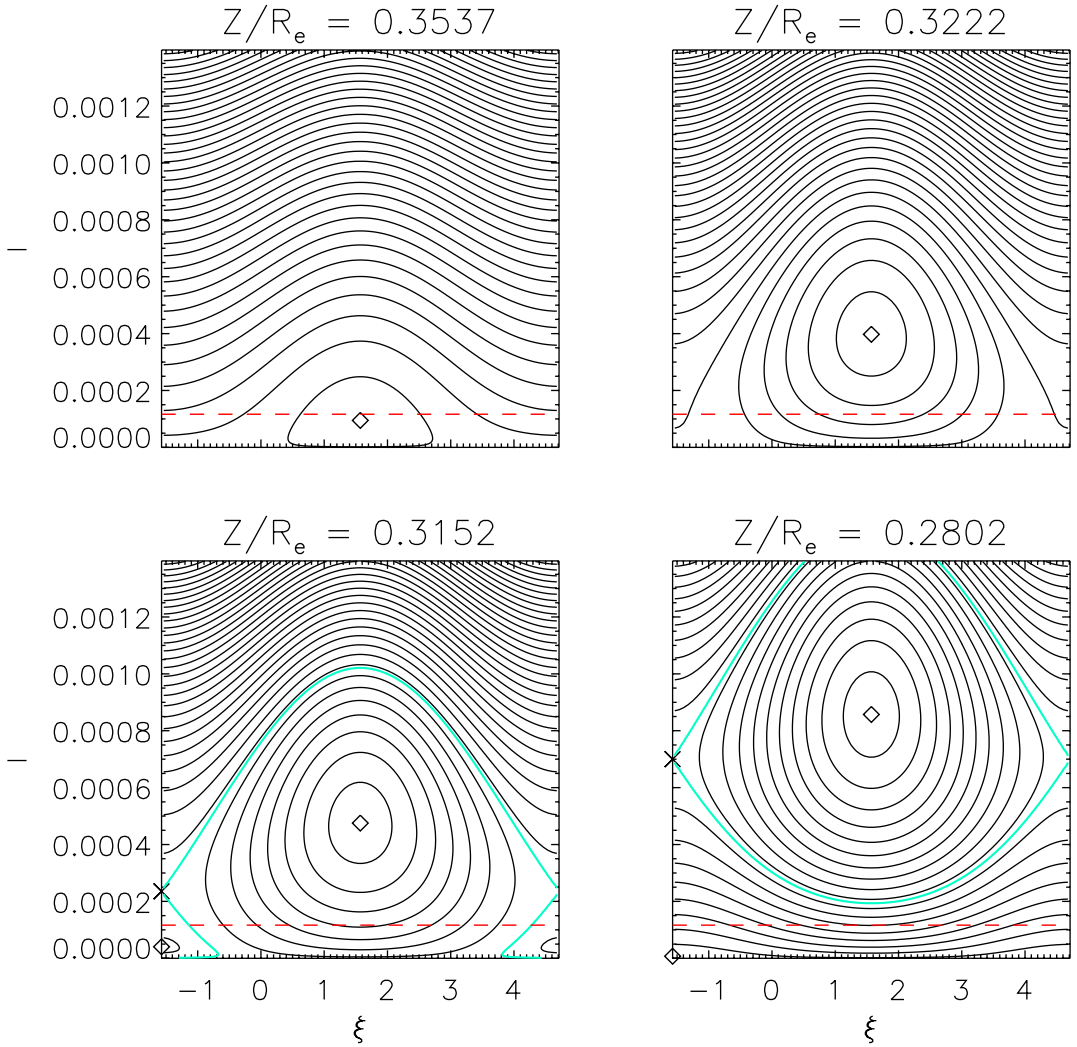

FIGURE 5 | Contours of $K(I, \xi, z)$, at several values of z shortly before and after resonance crossing, according to motion based on $K(I, \xi, z)$. O-points are shown as diamonds, and X-points (if present) are shown with an X symbol, with the contour through them is in cyan. The red, dashed curve shows the initial value of I.

equatorial pitch angle increases either over a sustained period (conventional phase trapping, PT) or transiently. The long-time behavior of the phase angle ξ is oscillatory for PT but monotonic otherwise. This corresponds to the NL1 regime of Gan et al. (2020), also referred to as positive phase bunching (PPB). Numerically, PT was identified by a change of sign in $d\xi/dt$ from one time step to the next after crossing below $z/R_e = 0.1$. Of 24 simulated particles, 10 became PT using either **Eq. 2** or **Eq. 3**.

Figure 2 shows results using **Eq. 10** (blue) or **Eq. 12** (red). The equatorial pitch angle α_0 obtained from the normalized variables (I, z) *via*

$$\frac{B}{B_{eq}}\sin^2\alpha_0 = \sin^2\alpha = \frac{p_\perp^2}{p^2} = \frac{2(\Omega/\omega)I}{(I-c_2)^2 - 1}. \tag{19}$$

The behavior turns out to be very similar to the previous run, with 9 instances of PT, leading to $\alpha_0 \approx 25^\circ$ at $z = 0$, with the rest of the particles ending up with α_0 spread between about 4° and 14°.

Finally, **Figure 3** shows results using **Eqs. 15**, **18**. Again the results are very similar in the final α_0 values reached by PT or PPB particles, and in the number of each. The number of PT particles in this run is 8, which does not deviate much from the previous values given the small number (24) of particles in each simulation.

We conclude that the reduced Hamiltonian $K(I, \xi, z)$ of **Eq. 13** captures the nature of the particle dynamics, including APT and PPB, with fidelity comparable to the other models. This is propitious because it allows access to a rich body of work on invariant breaking at separatrix crossings (e.g., Cary et al., 1986), enabling both qualitative understanding and quantitative analytical estimates.

Some steps have already been taken in that direction. **Figure 4** shows the results of **Figure 3** in the (I, ξ) plane, with PT trajectories (identified as above) over the interval $0.4 > z > 0$ shown in red, and become limited in ξ while reaching large values of I. The remaining paths, shown in blue (over the interval $0.4 > z > 0.22$, for clarity), do not reach such large values of I but are less

restricted in ξ. **Figure 5** shows contours of $K(I, \xi, z)$ at several fixed values of z chosen during the trapping process, based on **Figure 3**. They indicate that at early times (large values of z) there is only a single, O-type fixed point, while an X-point and separatrix, as well as another O-point, form around the time of the trapping process. Contours circling the O-point at $\xi = \pi/2$ correspond to the (red) PT trajectories of **Figure 4**, and PPB trajectories (in blue) are connected to the development of the O-point at low I and $\xi = -\pi/2$. Similar contours, developed from **Eq. 13** with further approximation, were obtained and studied by Albert et al. (2021), Artemyev et al. (2021). Quantitative analysis of separatrix formation and crossing, invariant breaking, and energy and pitch angle change will be the subject of future work.

DATA AVAILABILITY STATEMENT

The original contributions presented in the study are included in the article/supplementary material, further inquiries can be directed to the corresponding author.

AUTHOR CONTRIBUTIONS

JA conceived this work, and wrote and ran the simulations. AA helped analyze approaches to reducing the dimensionality of the system of equations. WL, QM, and LG consulted on the work and made several useful suggestions on the simulations and presentation.

FUNDING

JA was supported by NASA grant 80NSSC19K0845 and the Space Vehicles Directorate of the Air Force Research Laboratory. WL, LG, and QM also acknowledge the NASA grants 80NSSC20K1506 and 80NSSC20K0698, NSF grant AGS-1847818, and the Alfred P. Sloan Research Fellowship FG-2018-10936.

ACKNOWLEDGMENTS

The views expressed are those of the author and do not reflect the official guidance or position of the United States Government, the Department of Defense or of the United States Air Force. The appearance of external hyperlinks does not constitute endorsement by the United States Department of Defense (DoD) of the linked websites, or the information, products, or services contained therein. The DoD does not exercise any editorial, security, or other control over the information you may find at these locations.

REFERENCES

Albert, J. M., Artemyev, A. V., Li, W., Gan, L., and Ma, Q. (2021). Models of Resonant Wave-Particle Interactions. *J. Geophys. Res. Space Phys.* 126, e2021JA029216. doi:10.1029/2021JA029216

Albert, J. M. (2001). Comparison of Pitch Angle Diffusion by Turbulent and Monochromatic Whistler Waves. *J. Geophys. Res.* 106, 8477–8482. doi:10.1029/2000JA000304

Albert, J. M. (1993). Cyclotron Resonance in an Inhomogeneous Magnetic Field. *Phys. Fluids B Plasma Phys.* 5, 2744–2750. doi:10.1063/1.860715

Albert, J. M. (2010). Diffusion by One Wave and by Many Waves. *J. Geophys. Res.* 115, A00F05. doi:10.1029/2009JA014732

Albert, J. M. (2000). Gyroresonant Interactions of Radiation Belt Particles with a Monochromatic Electromagnetic Wave. *J. Geophys. Res.* 105, 21191–21209. doi:10.1029/2000JA000008

Albert, J. M., Tao, X., and Bortnik, J. (2012). "Aspects of Nonlinear Wave-Particle Interactions," in *Dynamics of the Earth's Radiation Belts and Inner Magnetosphere*. Editor D. Summers (Washington, DC: American Geophysical Union), 255–264. doi:10.1029/2012GM001324

Allanson, O., Elsden, T., Watt, C., and Neukirch, T. (2022). Weak Turbulence and Quasilinear Diffusion for Relativistic Wave-Particle Interactions via a Markov Approach. *Front. Astron. Space Sci.* 8, 805699. doi:10.3389/fspas.2021.805699

Artemyev, A. V., Neishtadt, A. I., Albert, J. M., Gan, L., Li, W., and Ma, Q. (2021). Theoretical Model of the Nonlinear Resonant Interaction of Whistler-Mode Waves and Field-Aligned Electrons. *Phys. Plasmas* 28, 052902. doi:10.1063/5.0046635

Artemyev, A. V., Neishtadt, A. I., Vainchtein, D. L., Vasiliev, A. A., Vasko, I. Y., and Zelenyi, L. M. (2018). Trapping (Capture) into Resonance and Scattering on Resonance: Summary of Results for Space Plasma Systems. *Commun. Nonlinear Sci. Numer. Simul.* 65, 111–160. doi:10.1016/j.cnsns.2018.05.004

Bell, T. F. (1984). The Nonlinear Gyroresonance Interaction between Energetic Electrons and Coherent VLF Waves Propagating at an Arbitrary Angle with Respect to the Earth's Magnetic Field. *J. Geophys. Res.* 89, 905–918. doi:10.1029/JA089iA02p00905

Cary, J. R., Escande, D. F., and Tennyson, J. L. (1986). Adiabatic-Invariant Change Due to Separatrix Crossing. *Phys. Rev. A* 34, 4256–4275. doi:10.1103/PhysRevA.34.4256

Chang, H. C., and Inan, U. S. (1983). Quasi-Relativistic Electron Precipitation Due to Interactions with Coherent VLF Waves in the Magnetosphere. *J. Geophys. Res.* 88, 318–328. doi:10.1029/ja083iA01p00318

Gan, L., Li, W., Ma, Q., Albert, J. M., Artemyev, A. V., and Bortnik, J. (2020). Nonlinear Interactions between Radiation Belt Electrons and Chorus Waves: Dependence on Wave Amplitude Modulation. *Geophys. Res. Lett.* 47, e2019GL085987. doi:10.1029/2019GL085987

Ginet, G. P., and Albert, J. M. (1991). Test Particle Motion in the Cyclotron Resonance Regime. *Phys. Fluids B* 3, 2994–3012. doi:10.1063/1.859778

Ginet, G. P., and Heinemann, M. A. (1990). Test Particle Acceleration by Small Amplitude Electromagnetic Waves in a Uniform Magnetic Field. *Phys. Fluids B* 2, 700–714. doi:10.1063/1.859307

Inan, U. S., Bell, T. F., and Helliwell, R. A. (1978). Nonlinear Pitch Angle Scattering of Energetic Electrons by Coherent VLF Waves in the Magnetosphere. *J. Geophys. Res.* 83, 3235–3253. doi:10.1029/ja083iA07p03235

Kitahara, M., and Katoh, Y. (2019). Anomalous Trapping of Low Pitch Angle Electrons by Coherent Whistler Mode Waves. *J. Geophys. Res. Space Phys.* 124, 5568–5583. doi:10.1029/2019JA026493

Lemons, D. S., Liu, K., Winske, D., and Gary, S. P. (2009). Stochastic Analysis of Pitch Angle Scattering of Charged Particles by Transverse Magnetic Waves. *Phys. Plasmas* 16, 112306. doi:10.1063/1.3264738

Lemons, D. S. (2012). Pitch Angle Scattering of Relativistic Electrons from Stationary Magnetic Waves: Continuous Markov Process and Quasilinear Theory. *Phys. Plasmas* 19, 012306. doi:10.1063/1.3676156

Li, J., Bortnik, J., Xie, L., Pu, Z., Chen, L., Ni, B., et al. (2015). Comparison of Formulas for Resonant Interactions between Energetic Electrons and Oblique Whistler-Mode Waves. *Phys. Plasmas* 22, 052902. doi:10.1063/1.4914852

Liu, K., Lemons, D. S., Winske, D., and Gary, S. P. (2010). Relativistic Electron Scattering by Electromagnetic Ion Cyclotron Fluctuations: Test Particle Simulations. *J. Geophys. Res.* 115, A04204. doi:10.1029/2009JA014807

Liu, K., Winske, D., Gary, S. P., and Reeves, G. D. (2012). Relativistic Electron Scattering by Large Amplitude Electromagnetic Ion Cyclotron Waves: The Role

of Phase Bunching and Trapping. *J. Geophys. Res.* 117, A06218. doi:10.1029/2011JA017476

Lyons, L. R., Thorne, R. M., and Kennel, C. F. (1971). Electron Pitch-Angle Diffusion Driven by Oblique Whistler-Mode Turbulence. *J. Plasma Phys.* 6, 589–606. doi:10.1017/S0022377800006310

Lyons, L. R., Thorne, R. M., and Kennel, C. F. (1972). Pitch-Angle Diffusion of Radiation Belt Electrons within the Plasmasphere. *J. Geophys. Res.* 77, 3455–3474. doi:10.1029/JA077i019p03455

Shklyar, D. R. (1986). Particle Interaction with an Electrostatic vlf Wave in the Magnetosphere with an Application to Proton Precipitation. *Planet. Space Sci.* 34, 1091–1099. doi:10.1016/0032-0633(86)90021-8

Thorne, R. M., Li, W., Ni, B., Ma, Q., Bortnik, J., Chen, L., et al. (2013). Rapid Local Acceleration of Relativistic Radiation-Belt Electrons by Magnetospheric Chorus. *Nature* 504, 411–414. doi:10.1038/nature12889

Thorne, R. M. (2010). Radiation Belt Dynamics: The Importance of Wave-Particle Interactions. *Geophys. Res. Lett.* 37, L22107. doi:10.1029/2010GL044990

Conflict of Interest: The authors declare that the research was conducted in the absence of any commercial or financial relationships that could be construed as a potential conflict of interest.

frontiers | Frontiers in Astronomy and Space Sciences

ORIGINAL RESEARCH
published: 23 June 2022
doi: 10.3389/fspas.2022.908730

Electron Anisotropies in Magnetotail Dipolarization Events

Joachim Birn[1,2]*, *Michael Hesse*[3] and *Andrei Runov*[4]

[1]Space Science Institute, Boulder, CO, United States, [2]Guest Scientist, Los Alamos National Laboratory, Los Alamos, NM, United States, [3]NASA Ames Research Center, Moffett Field, CA, United States, [4]Department of Earth, Planetary, and Space Sciences, University of California, Los Angeles, Los Angeles, CA, United States

Anisotropic electron distributions can be a major source of free energy for the generation of microinstabilities and waves. Here we investigate specifically anisotropies of the suprathermal electrons associated with dipolarization events in the geomagnetic tail. The investigation is based on an MHD simulation of magnetotail reconnection, flow bursts and dipolarization. This simulation is used to trace test particles in the electromagnetic fields of the MHD simulation and investigate their acceleration and contributions to flux increases. The simulated velocity distributions yield anisotropies which can be dominantly parallel ("cigar"-shaped), perpendicular ("pancake"-shaped) to the magnetic field, or a combination thereof (e.g., "rolling-pin"-shaped), depending on location, relative timing, and energy.

Keywords: electron anisotropies, particle acceleration, dipolarization events, magnetospheric substorms, particle sources

OPEN ACCESS

Edited by:
Charles William Smith, University of New Hampshire, United States

Reviewed by:
Thomas Earle Moore, Third Rock Research, United States
Agnit Mukhopadhyay, National Aeronautics and Space Administration, United States

***Correspondence:**
Joachim Birn
jbirn@spacescience.org

Specialty section:
This article was submitted to Space Physics, a section of the journal Frontiers in Astronomy and Space Sciences

Received: *30 March 2022*
Accepted: *30 May 2022*
Published: *23 June 2022*

Citation:
Birn J, Hesse M and Runov A (2022) Electron Anisotropies in Magnetotail Dipolarization Events. Front. Astron. Space Sci. 9:908730. doi: 10.3389/fspas.2022.908730

1 INTRODUCTION

Charged particle flux increases at suprathermal energies of tens to hundreds of keV are a typical signature of dipolarization events in the near magnetotail, associated with substorms and other activity (e.g., Lezniak et al., 1968; Parks and Winckler, 1968; Arnoldy and Chan, 1969; Baker et al., 1978; Belian et al., 1981; Nakamura et al., 2002; Runov et al., 2009; Sergeev et al., 2009; Deng et al., 2010; Fu et al., 2020). In the tail region beyond about 10 R_E distance, these events are commonly associated with earthward flow bursts, which are most likely caused by reconnection events farther tailward. They are characterized by a rapid increase of the normal magnetic field B_z (dipolarization front, "DF"), indicating a transient or permanent change from a stretched, tail-like, to a more dipolar magnetic field configuration. The region of enhanced B_z immediately after the DF has been named "dipolarizing flux bundle" (DFB) (Liu et al., 2013) or "flux pileup region" (FPR) (e.g., Khotyaintsev et al., 2011). A plausible interpretation identifies DFBs with entropy-depleted magnetic flux tubes (Sergeev et al., 1996; Wolf et al., 2009), originally proposed by Pontius and Wolf (1990) and also called "bubbles." They are likely caused by the severance, via reconnection, of parts of closed field lines, which are ejected tailward as "plasmoids" (e.g., Hones, 1979). The likely mechanism of the energetic particle flux increases is the acceleration of charged particles by the localized cross-tail electric field associated with a flow burst and dipolarization. This conclusion is supported particularly by particle tracing in analytic or numerically simulated electric field pulses associated with localized flow bursts (Zelenyi et al., 1990; Birn et al., 1997, 1998, 2004; Li et al., 1998; Zaharia et al., 2000; Ashour-Abdalla et al., 2011; Gabrielse et al., 2012; Pan et al., 2014; Artemyev et al., 2015; Gabrielse et al., 2016).

The major acceleration mechanisms affecting electrons are direct acceleration by the electric field in regions of low magnetic field strength, as well as betatron and Fermi acceleration, which affect

electrons more adiabatically. In the reconnection/dipolarization scenario, the direct acceleration is likely confined to the vicinity of the reconnection site, such that betatron and Fermi acceleration in the collapsing DFB are the most likely candidates (e.g., Fu et al., 2020, and references therein). Each mechanism may dominate at different times or in different regions, causing anisotropies of the distribution functions, which could provide free energy for microscopic waves and instabilities. The observed velocity distributions exhibit anisotropies that can be dominantly parallel ("cigar"-shaped), perpendicular ("pancake"-shaped) to the magnetic field, or a combination thereof (e.g., "rolling-pin"-shaped) (e.g., Liu et al., 2017, 2020).

Fu et al. (2011), using Cluster data in the region ~15 R_E downtail, found an association between pancake shaped distributions with "growing" FPRs, defined by increasing earthward flow velocity at the front and cigar-shaped distributions with "decaying" FPRs, defined by a peak of velocity coincident with the DF. On the basis of "Time History of Events and Macroscale Interactions during Substorms" (THEMIS) observations at distances of 11–14 R_E, Runov et al. (2013) found that suprathermal (< 30 keV) electron distributions at DFs were of pancake type near the neutral sheet ($|B_x| < 5$ nT) and mainly cigar type away from the neutral sheet at $|B_x| > 10$ nT. In theses cases, the plasma flow speed peaked just before or at the DF, thus satisfying the definition of a decaying FPR. Wu et al. (2013), using THEMIS electron data > 30keV between 10 and 25 R_E distance downtail, found a dominance of perpendicular anisotropy (indicating betatron acceleration) beyond 15 R_E, but dominance of parallel anisotropy (indicating Fermi acceleration), closer to Earth. Energetic electron distributions with triple peaks at 0, 90, and 180° pitch angles have been identified right after DFs by various observations and simulations (Runov et al., 2012; Wu et al., 2013; Birn et al., 2014; Liu et al., 2017). Liu et al. (2017) attributed the formation of such ("rolling pin") distributions to a mixture of Fermi acceleration in a field line collapsing earthward from the reconnection site, considered "global," and local betatron acceleration in the rapid field increase closer to Earth. They argued that this process should work only above 26 keV.

Such anisotropies may be the source of free energy driving microinstabilities and waves (Gary, 1993; Gary et al., 2014; Gary, 2015). Such waves, on one hand, would tend to reduce or limit the anisotropies (Khotyaintsev et al., 2011; Zhang et al., 2018) but, on the other, can also be a source of energy transport in the form of Poynting flux away from a DFB/FPR (Le Contel et al., 2009). Specifically, perpendicular electron anisotropies in the DFB region behind the front may be the source of whistler waves (Le Contel et al., 2009; Deng et al., 2010; Khotyaintsev et al., 2011; Viberg et al., 2014; Li et al., 2015; Breuillard et al., 2016; Le Contel et al., 2017) or electron-cyclotron waves (Zhou et al., 2009).

Using the three-dimensional time-dependent electric and magnetic field from MHD simulations of near-tail reconnection and flow bursts as basis for test particle studies, we have previously investigated electron acceleration associated with dipolarizations, identified acceleration mechanisms and source regions, and provided insights into spatial and temporal variations of electron and ion fluxes (Birn et al., 1997, 2004, 2013). These simulations also indicated energetic electron anisotropies with a dominance of perpendicular fluxes farther down the tail and closer to the equatorial plane, but an increasing importance of parallel anisotropy closer to Earth and at higher latitudes. In addition, a triple peak structure of flux increases near 0°, 90°, and 180° was found, which has been denoted a "rolling pin" distribution (Liu et al., 2017).

In the present paper we further investigate electron acceleration and flux properties, extending the results of Birn et al. (2013), and Birn et al. (2014) on the basis of the same MHD simulation (Birn et al., 2011). In **Section 2** we summarize major features of the MHD simulation and the test particle simulation approach. We focus on features in three different regions, the plasma sheet boundary layer, the inner flux pileup region earthward of an approaching and stopping bubble, and the stopping region of a DFB farther tailward that is reached by reconnected fields. **Section 3** demonstrates pitch angle variations and **Section 4** characteristic velocity distributions obtained from the test particle approach. **Section 5** then illustrates typical orbits and acceleration mechanisms affecting the distributions with a summary and discussion givrn in **Section 6**.

2 SIMULATION APPROACH

Our approach is based on a combination of a three-dimensional MHD simulation of near-tail reconnection and field collapse (Birn et al., 2011) with particle tracing in the fields of this simulation. Dimensionless units were used throughout. As in earlier papers, a realistic conversion to dimensional units may be based on a magnetic field unit (lobe field at the location of x-line formation) B_n = 12.6 nT, velocity (Alfvén speed) v_n = 1,000 km/s, and length unit of $L_n = 1.5R_E$, leading to a time unit ("Alfvén time") $t_n = L_n/v_n \approx 10$ s, and electric field $E_n = v_nB_n$ = 12.6 mV/m and an energy unit $W_n = \frac{1}{2}m_pv_n^2$ = 5.2keV, where m_p is the proton mass. The simulation covers the region $0 \geq x \geq -60$, $|y| \leq 40$, $|z| \leq 10$ with a 3D dipole located outside the box at $x = 5$, $y = z = 0$. The plasma pressure is normalized by $p_n = B_n^2/\mu_0$. Based on the chosen units, the inner boundary corresponds to $x_{GSM} = -7.5R_E$ and the outer boundary to $x_{GSM} = -97.5R_E$. However, for specific applications, other units may be more appropriate; therefore in the following we will mostly use dimensionless units.

The dynamic evolution was preceded by a period of external driving, which lasted until $t = 61$, leading to the formation of a thin embedded sheet of intensified current density in the near tail peaked around $x = -10$. In the following we will refer to the configuration at $t = 61$ as the "initial state." At this time a finite resistivity was imposed, localized in the region of enhanced current density, which was kept constant in time. (Birn et al., 2011). **Figure 1A** shows magnetic flux contours in the x, z plane at this time together with the initial pressure, which is used to categorize characteristic source regions, as indicated in **Figure 1B**: the inner central plasma sheet (CPS, red color), the outer CPS (orange), the plasma sheet boundary layers; ayer (PSBL, green) and the lobes (light blue). The dynamic evolution after $t = 61$ led to the formation of a neutral line ($B_z = 0$ line) at $t \approx 90$ and the initiation of slow reconnection. Faster reconnection and the generation of fast flows started at $t \approx 125$,

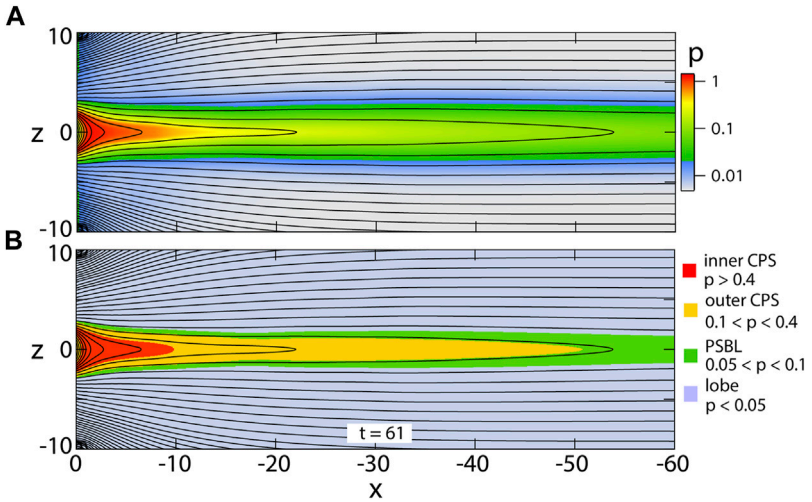

FIGURE 1 | Initial state after completion of the driving period, **(A)** magnetic flux contours and pressure (color) in the *x*, *z* plane at $t = 61$; **(B)** characteristic source regions defined by the initial pressure as indicated in the right margin: inner central plasma sheet (CPS), outer central plasma sheet, plasma sheet boundary layer (PSBL), and lobe.

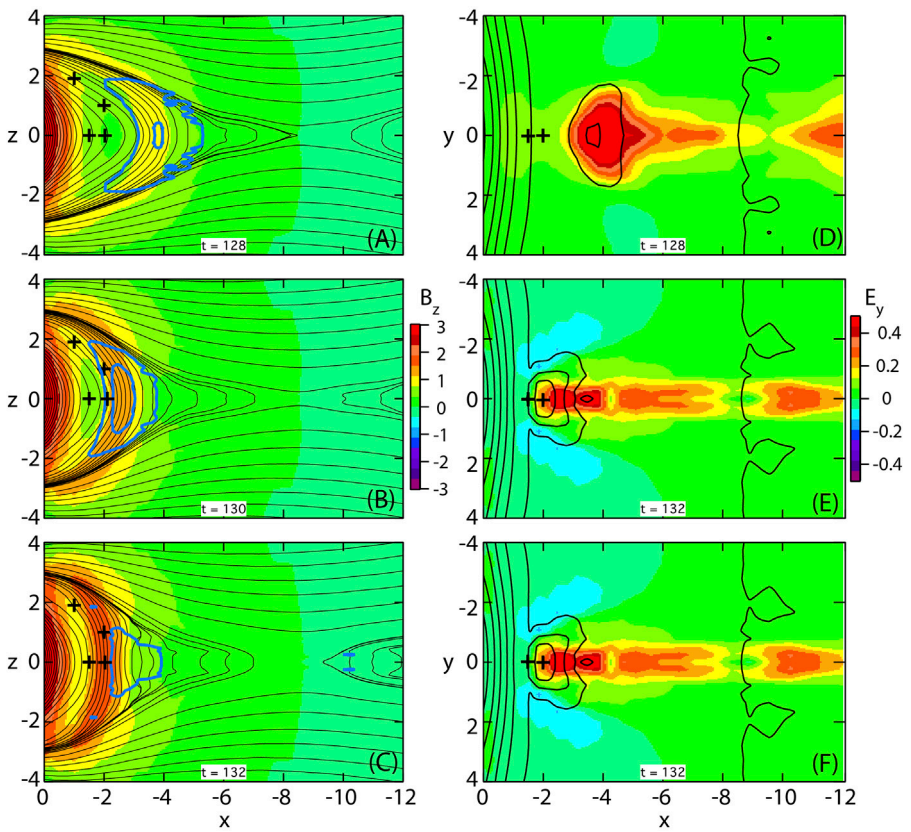

FIGURE 2 | Propagation of a DFB obtained form the MHD simulation. The left column **(A–C)** shows in color the magnetic field component B_z in the *x*, *z* plane together with magnetic flux contours (black lines). The heavy blue contours show the enhanced cross-tail electric field at intervals of 0.4 and the plus signs indicate locations where energetic electron fluxes are evaluated. The right column **(D–F)** shows in color the electric field component E_y in the *x*, *y* plane together with contours of B_z at intervals of 0.5.

when reconnection proceeded to the lobes, presumably due to a combination of reconnection with ballooning/interchange type modes, which were enabled by the reduced entropy of reconnected lobe magnetic flux tubes, which were shortened from plasmoid ejection (Birn et al., 2011, 2015).

Figure 2 illustrates the fast evolution, showing the propagation of a DFB. The color in the left column shows the magnetic field component B_z in the x, z plane together with magnetic flux contours (black lines). The heavy blue contours indicate the enhanced cross-tail electric field, and the plus signs indicate locations where energetic electron fluxes are evaluated. The color in the right column shows the electric field component E_y in the x, y plane together with contours of constant B_z; the contour near $x = -9$ is the $B_z = 0$ line, referred to as x-line. The DFB is indicated by the yellow and red color in **Figures 2A–C** and by a propagating contour in **Figures 2D–F**. It is limited in x and y to a few R_E, consistent with observations (e.g., Nakamura et al., 2004). It comes to rest and actually bounces back after about t = 132, also consistent with observations (Panov et al., 2010a; Panov et al., 2010b; Nakamura et al., 2012; Panov et al., 2013). It is characterized by a cross-tail electric field that far exceeds the reconnection electric field, which is of the order of 0.1, consistent with "fast reconnection" (e.g., Birn et al., 2001). (Our normalization is based on units near the location of the x-line.) The locations indicated by plus signs become enveloped by the DFB after $t \approx 132$. They are chosen to represent three characteristic regions: the location (−1,0,1.9) represents a PSBL location; the others correspond to central plasma sheet locations close to the stopping region, (−1.5,0) is just inward of the region reached by reconnected field lines, while (−2,0,0) and (−2,0,1) are reached even by reconnected lobe field lines, as concluded from the MHD simulation. The latter two locations are right at the equatorial plane and somewhat off the equator.

The orbit integration procedure was discussed in detail by Birn et al. (2004) and Birn et al. (2014). Here we repeat some major facts. The MHD results were saved at intervals of 1 Alfvén time (800 time steps, corresponding to ~ 10s for the chosen units). The orbits were integrated numerically, using linear interpolation between the stored time steps of the MHD fields. Electron orbits were integrated relativistically, using a combination of full orbits and gyro-drift orbits, based on conservation of the magnetic moment μ. The switch between the procedures was based on the magnitude of an adiabaticity parameter [ratio between field line curvature radius and gyoradius (Büchner and Zelenyi, 1989; Birn et al., 2004)]. We note that drift orbit continuity requires a cubic spline interpolation of the magnetic field in space, which could lead to artificial local maxima and minima. To avoid this, a monotonicity-conserving algorithm was employed (Hyman, 1983).

A backward tracing technique (Curran and Goertz, 1989) was used to integrate orbits from selected "final" times and locations backward in time until they reached the initial state (t = 61) or a boundary of the simulation box, using mirroring at the inner boundary x = 0. We then applied Liouville's theorem of the conservation of phase space density F along a phase space trajectory to calculate F values and differential energy fluxes at the final destination from the initial and boundary values at the "source" locations. A full distribution function at the chosen final location and time can then be obtained by varying the final energy and pitch angle. Time profiles of fluxes at selected locations, energies and pitch angles are obtained by varying the times from which particles are launched backwards.

The Validity of the backward tracing is based on the absence of collisions and becomes questionable when collisional regions are encountered. In our case one might consider the regions of low magnetic field, where orbits can undergo pitch angle scattering and our integrations change between drift orbits and full orbits as such regions. We found out, however, that this was not significant. Whereas pitch angles were conserved at these transitions, by accident we had initially set new phase angles to zero for continuing full orbits. Replacing that with random phase angles as intended did change some individual orbits significantly, but did not alter the characteristic pattern of the distributions.

Since the MHD simulation does not provide electron information (other than density, which should equal ion density), particular choices must be made in defining the initial and boundary electron distributions at the source locations. For the results reported here, we again imposed isotropic kappa-distributions (Vasyliunas, 1968; Christon et al., 1988; Christon et al., 1989)

$$F(W_0) \propto n_0 \left(1 + \frac{W_0}{(\kappa - 3/2)kT_e}\right)^{-\kappa-1} \tag{1}$$

with a κ value of 4.5 and chose a fixed initial and boundary temperature kT_e = 0.5 keV. Liouville's theorem of the conservation of F along a phase space trajectory implies that the final distribution is related to the source by

$$F(W) \propto n_0 \left(1 + \frac{W - \Delta W}{(\kappa - 3/2)kT_e}\right)^{-\kappa-1} \tag{2}$$

where ΔW is the energy gain (or loss) along the trajectory. Flux enhancements therefore are directly related to the energy gain and the density n_0 of the source plasma.

We note that the electron velocities were normalized by

$$v_{ne} = \left(m_p/m_e\right)^{1/2} v_n = 42,850\ \mathrm{km/s} \tag{3}$$

where m_p and m_e denote proton and electron mass, respectively. The (normalized) kinetic energy of an electron is then given, in the relativistic approach, by

$$W_k = \frac{1}{\epsilon}(\gamma - 1) \quad \text{with} \qquad \epsilon = W_n \Big/ \left(m_e c^2\right) \tag{4}$$

where

$$\gamma = \sqrt{1 + 2\epsilon u^2} \tag{5}$$

and u is the normalized electron velocity, given by

$$\begin{aligned} u^2 &= u_x^2 + u_y^2 + u_z^2 \qquad \text{(full orbit)} \\ u^2 &= u_\parallel^2 + u_\perp^2 \quad \text{with} \quad u_\perp^2 = \mu B \qquad \text{(drift orbit)} \end{aligned} \tag{6}$$

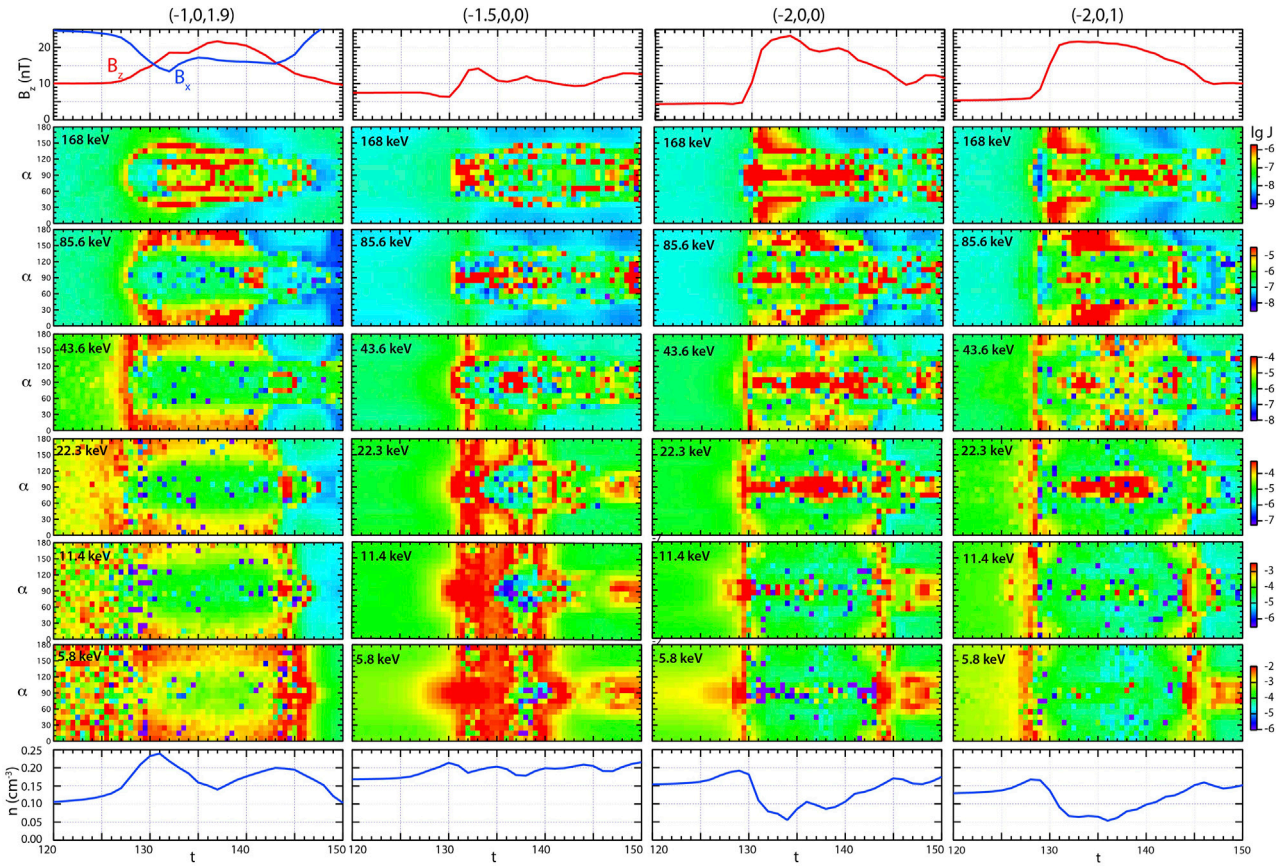

FIGURE 3 | Simulated electron fluxes as functions of time and pitch angle at four selected locations indicated on top. Different energies are indicated in the colored panels. The top and bottom panels show the magnetic field B_z (in red) and the plasma density n, respectively, at the three locations. For the PSBL location, (-1, 0, 1.9), the magnetic field component B_x is also added (blue curve, top left panel).

where μ is the normalized relativistic magnetic moment (Birn et al., 2004).

Our orbit integration includes several modifications from the approach described in Birn et al. (2004) and Birn et al. (2014):

1) The particle reflection at the inner boundary of the simulation box now takes into account a finite time of travel to the actual mirror point outside the box closer to Earth. This delay time was estimated by using a Tsyganenko model (Tsyganenko, 1987) to calculate this travel time based on the velocity and pitch angle at the inner boundary. This affected primarily particles at low pitch angles. As a consequence, they exhibit fewer bounces than if they are immediately reflected back into the box, reducing the number of neutral sheet crossing, which are the dominant source of Fermi acceleration type B (Northrop, 1963).
2) The linear interpolation of the electromagnetic fields between the finite grid points could lead to spurious parallel electric fields. This effect was eliminated by separating the electric field into a field-aligned and a perpendicular component, and interpolating the two individually. We found, however, that this affected only very few orbits and did not alter the distributions in a noticeable way.
3) We discovered that the fluxes and phase space densities shown in Birn et al. (2014) were inadvertently evaluated with $\kappa = 2.5$ rather than $\kappa = 4.5$ as stated in the paper. This has no effect on the particle orbits, however, nor on the qualitative features shown. The only effect is to raise the numerical values at high energies.

3 PITCH ANGLE DISTRIBUTIONS

The variations of electron fluxes at the four selected locations (indicated on top of the panels) are shown in **Figure 3** as functions of time and pitch angle for several energies, together with the variations of B_z (top, red curves) and plasma density (bottom) obtained from the MHD simulation. The energies are labeled based on our normalization factor W_n = 5.22 keV. (A different choice of v_n could reduce those energies, for instance v_n = 500 km/s, W_n = 1.30 keV, would reduce the energies by a factor 1/4.)

The MHD results (top and bottom) in **Figure 3** show characteristically different signatures at the selected locations. The B_z increase at the PSBL location (red curve, top left panel) is more gradual than at the equator; it goes together with an entry deeper into the plasma sheet, as shown by the decrease of B_x (blue

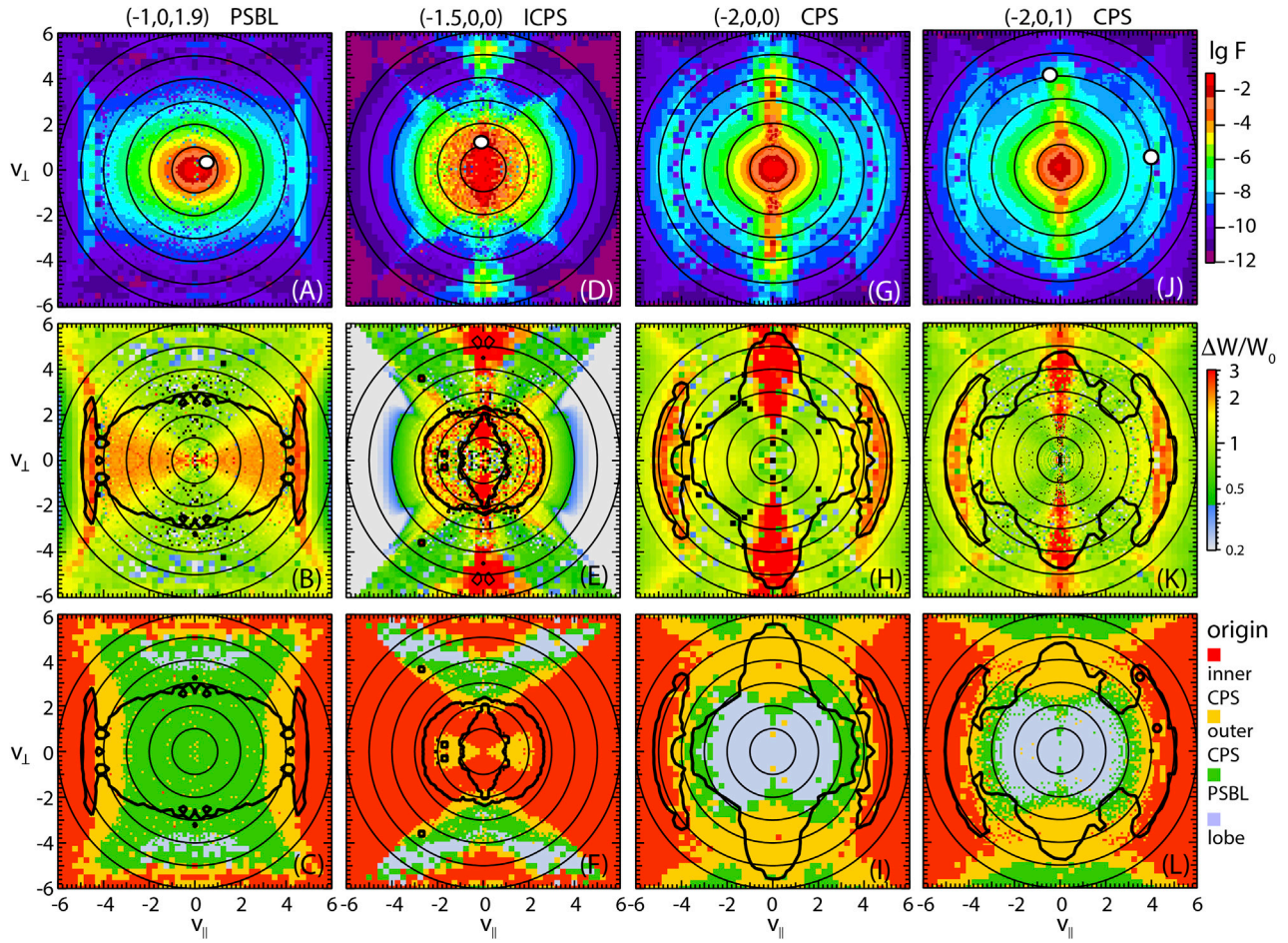

FIGURE 4 | Electron velocity distributions at chosen location for $t = 132$: **(top row, a, d, g, j)** phase space density, **(second row, b, e, h, k)** relative energy gain, and **(third row, c, f, i, l)** origin of particles contributing to the phase space density. For the chosen normalization, the velocity unit is given by **(3)** as 42,850 km/s. The heavy black contours indicate the regions of enhanced F (top row) and the white dots in the top panels show final velocities used to illustrate characteristic orbits in **Section 5**.

curve in the top left panel) and the density increase (bottom left panel). These features have been reported earlier in the context of energetic ion fluxes (Birn et al., 2017).

The inner CPS location (second column), which is not reached by reconnected, depleted flux tubes at the time of dipolarization, shows a more modest increase of B_z than the two locations farther tailward (third and fourth column). It also shows a slight increase in density (bottom panel), resulting from a compression of preexisting plasma sheet plasma, whereas the two locations farther out show a decrease, which is more typical (Runov et al., 2011) and consistent with the arrival of depleted reconnected PSBL and lobe flux tubes.

At low energies of a few keV the energetic electron fluxes reflect the behavior of the MHD plasma density at all locations, showing a drop when the plasma density is reduced and an increase at the innermost CPS location. At higher energies, the results are different. The PSBL location (left column) is characterized by a very brief increase, which tends to start near 90° but then rapidly spreads to all pitch angles. This is followed by a persistent increase around 0 and 180° at most energies. Only at the highest one of 168 keV the distribution becomes more complicated, with double peaks around 45 and 135°.

The inner CPS location (second column) up to ~23 keV is characterized by an enhancement of fluxes, which also starts around 90°. It is interrupted by a brief decrease around $t = 137$. A closer inspection (not shown here) indicates that this is due to the arrival of reconnected field lines, which carry plasma from the more distant tail and, at higher energies, PSBL and lobes. The highest energies show a more persistent enhancement around 90°.

The outer two CPS locations (third and fourth column) show very similar features. The third column corresponds to the results shown in the left column of Figure 4 in Birn et al. (2014) with the modifications discussed in **Section 2**. The qualitative features are not changed by those modifications. The major difference is a change of scales, which results from the steeper slope of the source energy distribution associated with the larger kappa value. Fluxes at 22.3 keV show a persistent perpendicular anisotropy (peak near 90°), after a very brief nearly isotropic enhancement. In contrast the higher energies show the triple peak (rolling pin)

structure at 0, 90, and 180°, discussed already by Birn et al. (2014). Interestingly, at the highest energy, the peaks at 0 and 180° tend to move away from the field-aligned direction toward 45 and 135° after the dipolarization.

4 VELOCITY DISTRIBUTIONS

Figure 4 shows velocity distributions at the chosen locations for t = 132, right after the dipolarization, which is the period most commonly investigated in observations. We note that each pixel again corresponds to a single trajectory mapping the source phase space density to the final location. This allows us to identify the relative energy gain $\Delta W/W_0$ (second row) as the main contribution to flux enhancements, where W_0 is the energy at the initial location, and the particle origins (bottom row), as defined in **Figure 1**. We note that both of these quantities do not depend on the assumed source distributions; they are simply a consequence of the orbits governed by the MHD electric and magnetic fields.

The distributions in **Figure 4** show characteristic differences, as well as some commonalities. The PSBL distribution (**Figure 4A**) shows the field-aligned anisotropy already demonstrated by **Figure 3** (left column). This extends also to two counter streaming beams, which, however, may not be distinct in observed distributions. They are slightly more enhanced relative to the lower energies because of their origin in the inner CPS, where the densities are higher (**Figure 4C**). Such beams are also present in the CPS distributions at x = −2 (**Figures 4G,J**) with similar origin in the inner CPS (**Figures 4I,L**). The distribution just earthward of the stopping (**Figure 4D**) does not show such beams. However, all CPS distributions show strong ring-like perpendicular anisotropies. For the outer locations, x = −2, the particles originate primarily from the outer CPS (orange color in **Figures 4I,L**, while hte contributions at the inner location x = −1.5 come predominantly from the inner CPS (red color in **Figure 4F**).

Overall, the contributions to the distribution at the inner location x = −1.5 come from the inner CPS, consistent with the conclusion from the MHD simulation that reconnected field lines do not reach this location. There is an inner region of the distribution just inside the almost circular contour in **Figure 4E** at $v \approx 2$ (corresponding to about 20 keV) that appears almost uniformly energized by factors $\Delta W/W_0 \approx 2$ enclosing the strongly anisotropic disk at lower energy. This appears to be region that is adiabatically compressed earthward of the DFB itself and roughly isotropically heated.

In the CPS distributions farther out there are similar regions of lobe origin (light blue color in (**Figures 4I,L**) that are also energized, but by smaller gains ($\Delta W/W_0 \approx 1$ corresponding to doubling the energy), representing the nearly isotropic cores of the distributions. Their origin is again consistent with a result from lobe field reconnection, inferred from the MHD simulation.

5 CHARACTERISTIC ORBITS

Figure 4 already provided some basic facts about the history and origin of the accelerated particles contributing to the enhanced energetic electron fluxes. However, it is instructive to illustrate these with specific orbits.

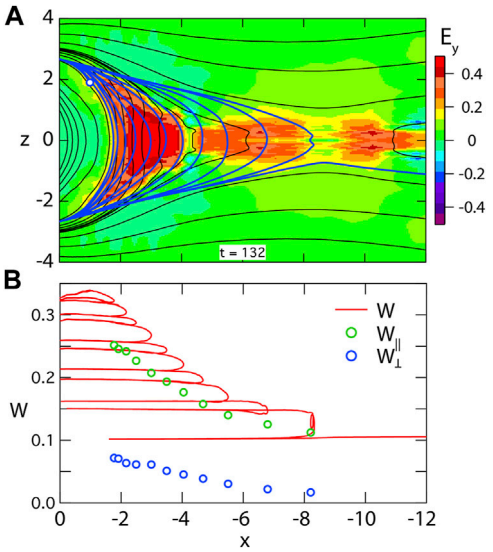

FIGURE 5 | Electron orbit contributing to the enhanced field-aligned fluxes at the PSBL location (−1, 0, 1.9), **(A)** projection of the orbit into the x, z plane superposed on the color-coded electric field at t = 132, **(B)** particle energy as function of x (red curve) together with the parallel (green circles) and perpendicular (blue circles) components at the equatorial crossings.

5.1 Field-Aligned Electrons in the PSBL

Details of the acceleration mechanism have been discussed previously by Birn et al. (2004, 2012). It is essentially the same at all energies. We therefore illustrate it in **Figure 5** for a particle at relatively low energy, close to the initial thermal energy of 0.1 (corresponding to ~0.52 keV for our chosen units). The particle originates from a closed field line extending into the more distant tail. It becomes trapped in the inner tail when the field line becomes reconnected and bounces several times while participating in the field collapse. **Figure 5B** demonstrates that the acceleration takes place at neutral sheet crossings, to be interpreted as first-order Fermi acceleration of type B (Northrop, 1963), akin to a slingshot effect in the curved earthward moving magnetic field. The parallel acceleration can equally well be interpreted as **E**×**B** drift in the direction of the magnetic field curvature vector or as curvature drift in the direction opposite to the cross-tail electric field E_y (Birn et al., 2013).

The particle illustrated in **Figure 5** also has a small perpendicular drift velocity component, which becomes enhanced at each neutral sheet crossing as well (Blue circles). This acceleration can be attributed to the betatron effect, which can also be interpreted in two ways (Birn et al., 2013): as **E** ×**B** drift in the direction of increasing magnetic field strength or as gradient B drift in the direction opposite to the cross-tail electric field.

5.2 Perpendicular Electrons in the Inner Pileup Region

Figure 6 illustrates the history of a particle contributing to the perpendicular anisotropy in the inner pileup region. This is a

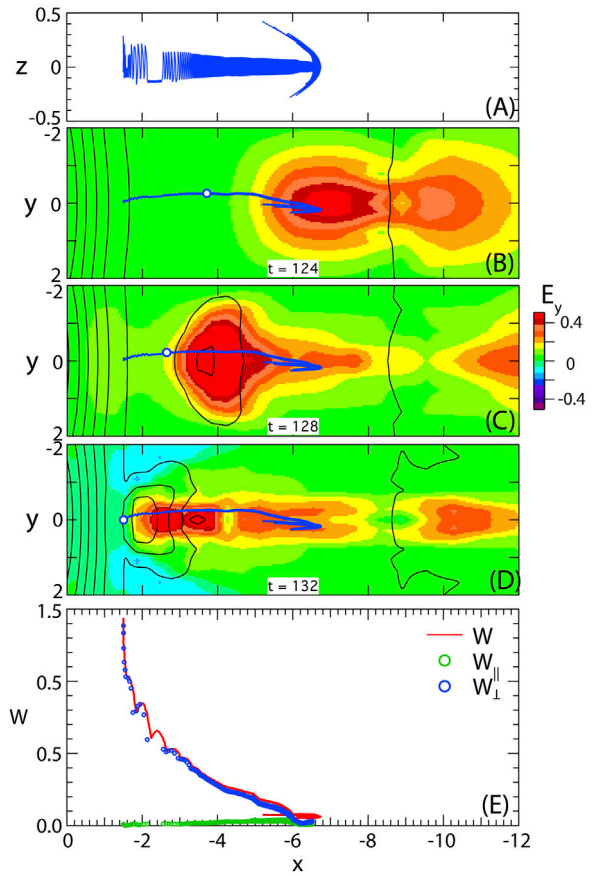

FIGURE 6 | Electron drift orbit contributing to the enhanced perpendicular fluxes at the inner location (−1.5, 0, 0), **(A)** projection of the orbit into the *x*, *z* plane, **(B–D)** orbit in the *x*, *y* plane, superposed on snapshots of the color-coded electric field and particle location (white dot) at *t* = 124, 128, 132, **(E)** particle energy as function of *x* (red curve) together with the parallel (green circles) and perpendicular (blue circles) components.

particle of initially thermal energy, less than 0.1, being almost at rest in the inner tail. It gets "scooped up" in front of the approaching DFB (**Figures 6B–D**) and experiences betatron acceleration from the magnetic field increase that also affects the field in front of the DFB flow bursts. As illustrated by **Figure 6A**, the particle initially exhibits a wider bounce near $x = -6$, before it its pitch angle gets scattered and it continues on a narrow bounce around $z = 0$ toward its final location at $x = -1.5$. For a brief period, near $x = -2.5$, it stays below the equatorial plane $z = 0$. This is due to the fact that the magnetic field at this time and location becomes indented (**Figure 2C**) such that the particle becomes trapped in a field minimum below $z = 0$.

5.3 DFB Orbits

Figure 7 contrasts the history of particles contributing to the high-energy field-aligned beams and the perpendicular fluxes in the CPS region of the DFB. These particles contribute to the peaks of the fluxes at 0, 90, and 180° described as rolling pin distributions (Liu et al., 2017). It is instructive to follow the two orbits backward in time from their final location at $t = 132$, focusing on the drift in the equatorial plane (**Figures 7B–D**). Note that the red/pink curves are close to the actual equatorial drift of the ~ 90° pitch angle particle, while the blue curves in **Figures 7B–D** represent only the equatorial crossing points of the multi-bounce orbit shown in **Figure 7A**. In either case the displacement in the *y* direction is related to their respective gradient or curvature drift, while the motion in the *x* direction is determined by the **E** ×**B** drift, which is similar in both cases but varies slightly according to the finite extent and variation in *y* of B_z and E_y, visible in **Figures 7B–D**.

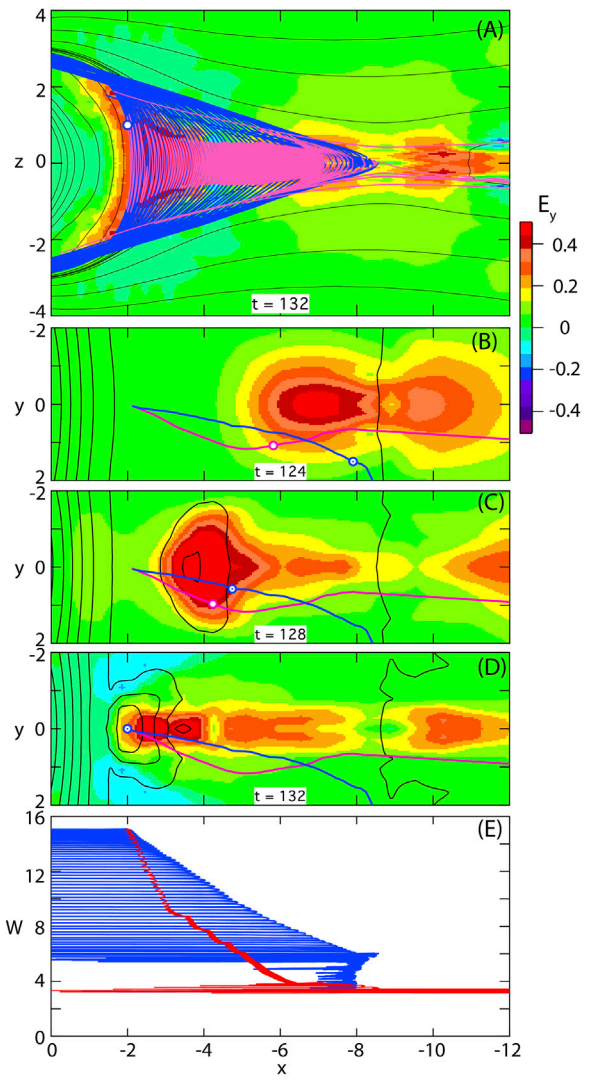

FIGURE 7 | Electron orbits contributing to the enhanced CPS fluxes at (−2, 0, 1). Blue curves represent an electron contributing to the field-aligned beam, red/pink curves correspond to a ~ 90° pitch angle orbit contributing to the enhanced perpendicular fluxes; **(A)** projection of the orbits into the *x*, *z* plane, **(B–D)** equatorial crossing points of the orbits in the *x*, *y* plane, superposed on snapshots of the color-coded electric field, with the particle locations at *t* = 124, 128, 132 shown as white dots; **(E)** particle energies as function of *x*.

The magnetic field gradient near the final, more dipolar, location is steep, while the curvature is weak. Therefore the gradient drift is stronger than the curvature drift and ~ 90° pitch angle particle (red curve) gets more displaced in the y direction than the ~ 0° pitch angle particle (blue curve). It also looses more energy (actually, gains in forward tracing) such that its energy is significantly lower at the entry into the acceleration region around t = 124 (**Figure 7B**). At this point the ~ 0° pitch angle particle still has a high energy of ~6, the magnetic field curvature is strong while the magnetic field gradient is weak. As a consequence the curvature drift now becomes dominant for the ~ 0° pitch angle particle, leading back to a source region on the duskside earthward of the neutral line, whereas the ~ 90° pitch angle particle can be traced back toward the neutral line, indicating its source in the closed field region extending farther tailward and its entry into the acceleration region via reconnection.

During the main acceleration, both particles satisfy the adiabaticity criterion. This breaks down in the low-field region in the vicinity of the x-line, such that both particles have undergone a number of pitch angle scatterings prior to the acceleration. Hence there is no correlation between the final pitch angle and the one in the source region. **Figure 7E** indicates that the particle with ~ 0° final pitch angle (blue curve) has changed from a nearly equatorial orbit prior to the entry into the main DFB; it has gained a small amount of energy by betatron acceleration drifting dawnward in the weaker electric field duskward of the region shown in **Figures 7B–D**. In this case both particles have started from similar initial energies, indicating similar final phase space densities. More typically, however, ~ 90° pitch angle particle that originate from the distant plasma sheet haves a lower source energy corresponding to a higher phase space density, when mapped along their trajectory to the final location than the ~ 0° pitch angle particles, which mainly originate on the dusk side. This explains the higher fluxes at ~ 90° pitch angle as compared to the field-aligned beams and thus a net perpendicular anisotropy.

6 SUMMARY AND DISCUSSION

Using a combined MHD/test particle approach, we have further investigated electron acceleration and energetic electron flux increases associated with dipolarization events in the region earthward of a near-tail reconnection site. In modification of earlier approaches we included a delay time from particle mirroring closer to Earth (outside the simulation box) and eliminated potential spurious parallel electric fields from an interpolation procedure. The latter, however, was found insignificant.

Our investigation focused on electron anisotropies, which can be the source of free energy driving microscopic waves and instabilities (e.g., Gary, 1993, 2015; Khotyaintsev et al., 2011), extending earlier results (Birn et al., 2014) particularly by deriving phase space distributions (PSDs) for the time right after dipolarization (that is, the increase of B_z) in three different regions, the plasma sheet boundary layer (PSBL), the inner flux pileup region (inner FPR) in the central plasma sheet (CPS), which is not reached (yet) by reconnected PSBL or lobe field lines, and the outer FPR, which is reached by such field lines. Selected orbits were shown to illustrate the findings in the velocity distributions.

We confirmed that betatron and first-order Fermi acceleration are the dominant acceleration mechanisms, operating in the regime of field collapse, consistent with earlier conclusions (e.g. Smets et al., 1999; Birn et al., 2004; Wu et al., 2006; Fu et al., 2011, 2020). This happened in the inner region where a drift orbit approximation was found to be valid, based on the conservation of the (relativistic) magnetic moment μ.

The Fermi acceleration, which dominates for small pitch angles, was found to happen at multiple neutral sheet crossings in the curved magnetic field of earthward moving field lines. This has been described as "type B" (Northrop, 1963) akin to a slingshot effect, associated with **E×B** drift in the direction of the field curvature vector. This, however, can equally well be described as curvature drift in the direction opposite to the cross-tail electric field (e.g., Birn et al., 2013). As the particle bounces happen on closed magnetic field lines that become shorter as the fields collapse toward Earth, this mechanism is also often described as Fermi acceleration of type A (Northrop, 1963), that is, multiple bounces between approaching mirrors. In that case the acceleration is commonly inferred from the conservation of the second adiabatic invariant. Here, we did not impose (or investigate) this conservation law, and it is an open question to what extent the two interpretations are equivalent quantitatively. The development of field-aligned anisotropy extends not only to high suprathermal energies but also to low sub-keV energies. This fact and the inferred acceleration in the collapsing field are consistent with observations at geosynchronous orbit (e.g., Moore and Arnoldy, 1982), providing a direct source of precipitating auroral electrons.

In addition, betatron acceleration was demonstrated, associated with the **E×B** drift in the direction of increasing magnetic field strength. This can also be described by (gradient) drift in the direction opposite to the (main) cross-tail electric field.

Our simulations yielded characteristic differences between the locations. The PSBL location was characterized by strong field-aligned anisotropy extending to high-energy beams. In contrast to the main population, these beams originated from the inner central plasma sheet, entering the acceleration by cross-tail drift, Their pitch angle was typically scattered several times during neutral sheet crossings prior to this entry. Similar beams with the same history were also found at the outer FPR locations in the CPS, however, together with strong enhancements around 90° pitch angles, causing net perpendicular anisotropies, consistent with observations by Runov et al. (2012).

At energies of a few tens of keV, the combination of the field-aligned beams with the perpendicular enhanced fluxes in the CPS resulted in the multi peak structure described as rolling pin distributions (Liu et al., 2017) and found earlier in observations (Runov et al., 2012; Wu et al., 2013) and simulations (Birn et al., 2014). Our results are consistent with conclusions by Liu et al. (2017) that these structures were restricted to energies just above 26 keV. However, Zhao et al. (2019) also observed such

distributions at energies above 1.7 keV. On the basis of our simulations, this difference could be understood by different scenarios with different background parameters. Our results depend on the chosen scaling. Reducing the characteristic velocity v_n by a factor λ would reduce the characteristic energy by λ^2. This could substantially lower the range where the rolling pin distributions are found.

Our simulations also enabled us to identify the source regions of particles contributing to the different final distributions. Particles in the PSBL distributions originated also from the PSBL (on either side). Particles in the inner flux pileup region originated from the inner CPS, were energized primarily through the betatron effect in the compressed plasma. The field-aligned beams were absent in that region.

The origin of the particles contributing to the distributions in the outer FPR/CPS was more complicated. The distributions consisted of an inner core of weakly, more isotropically, energized (i.e, heated) particles of lobe origin, surrounded by a population of outer CPS origin, which was energized by betatron acceleration. These distributions also contained field-aligned beams, which were of inner CPS origin with the same history as the high-energy beams in the PSBL.

Finally, some general comments: The distributions, particularly in the FPR region reached by reconnected lobe field lines, show high variability with time and energy. In evaluating the effects of different acceleration mechanisms it is important not only to consider the earthward transport of particles but also the finite extent and cross-tail variation of the acceleration region.

DATA AVAILABILITY STATEMENT

The datasets presented in this study can be found in online repositories. The names of the repository/repositories and accession number(s) can be found in the article/supplementary material.

AUTHOR CONTRIBUTIONS

JB performed the simulations and prepared the body of the text. MH and AR provided background and contributions to the text.

FUNDING

The simulation work was performed by JB at Los Alamos under the auspices of the US Department of Energy, supported by NASA grant 80NSSC18K0834 and NSF grant 1602655. AR acknowledges support from NASA contract NAS5-02099.

ACKNOWLEDGMENTS

This work is dedicated to the memory of Peter Gary, a close friend and valued advisor, who had a keen interest in the sources of electron anisotropy. The simulation work was performed by JB at Los Alamos under a guest scientist agreement.

REFERENCES

Arnoldy, R. L., and Chan, K. W. (1969). Particle Substorms Observed at the Geostationary Orbit. *J. Geophys. Res.* 74, 5019–5028. doi:10.1029/ja074i021p05019

Artemyev, A. V., Liu, J., Angelopoulos, V., and Runov, A. (2015). Acceleration of Ions by Electric Field Pulses in the Inner Magnetosphere. *J. Geophys. Res. Space Phys.* 120, 4628–4640. doi:10.1002/2015JA021160

Ashour-Abdalla, M., El-Alaoui, M., Goldstein, M. L., Zhou, M., Schriver, D., Richard, R., et al. (2011). Observations and Simulations of Non-local Acceleration of Electrons in Magnetotail Magnetic Reconnection Events. *Nat. Phys.* 7, 360–365. doi:10.1038/nphys1903

Baker, D. N., Higbie, P. R., Hones, E. W., Jr., and Belian, R. D. (1978). High-Resolution Energetic Particle Measurements at 6.6 RE, 3. Low-Energy Electron Anisotropies and Short-Term Substorm Predictions. *J. Geophys. Res.* 83, 4863–4868. doi:10.1029/ja083ia10p04863

Belian, R. D., Baker, D. N., Hones, E. W., Jr., Higbie, P. R., Bame, S. J., and Asbridge, J. R. (1981). Timing of Energetic Proton Enhancements Relative to Magnetospheric Substorm Activity and its Implication for Substorm Theories. *J. Geophys. Res.* 86, 1415. doi:10.1029/ja086ia03p01415

Birn, J., Artemyev, A. V., Baker, D. N., Echim, M., Hoshino, M., and Zelenyi, L. M. (2012). Particle Acceleration in the Magnetotail and Aurora. *Space Sci. Rev.* 173, 49–102. doi:10.1007/s11214-012-9874-4

Birn, J., Chandler, M., Moore, T., and Runov, A. (2017). Ion Velocity Distributions in Dipolarization Events: Beams in the Vicinity of the Plasma Sheet Boundary. *J. Geophys. Res. Space Phys.* 122, 8026–8036. doi:10.1002/2017JA024231

Birn, J., Drake, J. F., Shay, M. A., Rogers, B. N., Denton, R. E., Hesse, M., et al. (2001). Geospace Environmental Modeling (GEM) Magnetic Reconnection Challenge. *J. Geophys. Res.* 106, 3715–3719. doi:10.1029/1999ja900449

Birn, J., Hesse, M., Nakamura, R., and Zaharia, S. (2013). Particle Acceleration in Dipolarization Events. *J. Geophys. Res. Space Phys.* 118, 1960–1971. doi:10.1002/jgra.50132

Birn, J., Liu, Y.-H., Daughton, W., Hesse, M., and Schindler, K. (2015). Reconnection and Interchange Instability in the Near Magnetotail. *Earth Planet Sp.* 67, 110. doi:10.1186/s40623-015-0282-3

Birn, J., Nakamura, R., Panov, E. V., and Hesse, M. (2011). Bursty Bulk Flows and Dipolarization in MHD Simulations of Magnetotail Reconnection. *J. Geophys. Res.* 116, a–n. doi:10.1029/2010JA016083

Birn, J., Runov, A., and Hesse, M. (2014). Energetic Electrons in Dipolarization Events: Spatial Properties and Anisotropy. *J. Geophys. Res. Space Phys.* 119, 3604–3616. doi:10.1002/2013JA019738

Birn, J., Thomsen, M. F., Borovsky, J. E., Reeves, G. D., McComas, D. J., Belian, R. D., et al. (1998). Substorm Electron Injections: Geosynchronous Observations and Test Particle Simulations. *J. Geophys. Res.* 103, 9235–9248. doi:10.1029/97ja02635

Birn, J., Thomsen, M. F., Borovsky, J. E., Reeves, G. D., McComas, D. J., Belian, R. D., et al. (1997). Substorm Ion Injections: Geosynchronous Observations and Test Particle Orbits in Three-Dimensional Dynamic MHD Fields. *J. Geophys. Res.* 102, 2325–2341. doi:10.1029/96ja03032

Birn, J., Thomsen, M. F., and Hesse, M. (2004). Electron Acceleration in the Dynamic Magnetotail: Test Particle Orbits in Three-Dimensional Magnetohydrodynamic Simulation Fields. *Phys. Plasmas* 11, 1825–1833. doi:10.1063/1.1704641

Breuillard, H., Le Contel, O., Retino, A., Chasapis, A., Chust, T., Mirioni, L., et al. (2016). Multispacecraft Analysis of Dipolarization Fronts and Associated Whistler Wave Emissions Using MMS Data. *Geophys. Res. Lett.* 43, 7279–7286. doi:10.1002/2016GL069188

Büchner, J., and Zelenyi, L. M. (1989). Regular and Chaotic Charged Particle Motion in Magnetotaillike Field Reversals: 1. Basic Theory of Trapped Motion. *J. Geophys. Res.* 94, 11821–11842. doi:10.1029/JA094iA09p11821

Christon, S. P., Mitchell, D. G., Williams, D. J., Frank, L. A., Huang, C. Y., and Eastman, T. E. (1988). Energy Spectra of Plasma Sheet Ions and Electrons from ~50 eV/eto ~1 MeV during Plasma Temperature Transitions. *J. Geophys. Res.* 93, 2562. doi:10.1029/ja093ia04p02562

Christon, S. P., Williams, D. J., Mitchell, D. G., Frank, L. A., and Huang, C. Y. (1989). Spectral Characteristics of Plasma Sheet Ion and Electron Populations during Undisturbed Geomagnetic Conditions. *J. Geophys. Res.* 94, 13,409. doi:10.1029/ja094ia10p13409

Curran, D. B., and Goertz, C. K. (1989). Particle Distributions in a Two-Dimensional Reconnection Field Geometry. *J. Geophys. Res.* 94, 272. doi:10.1029/ja094ia01p00272

Deng, X., Ashour-Abdalla, M., Zhou, M., Walker, R., El-Alaoui, M., Angelopoulos, V., et al. (2010). Wave and Particle Characteristics of Earthward Electron Injections Associated with Dipolarization Fronts. *J. Geophys. Res.* 115, a–n. doi:10.1029/2009JA015107

Fu, H., Grigorenko, E. E., Gabrielse, C., Liu, C., Lu, S., Hwang, K. J., et al. (2020). Magnetotail Dipolarization Fronts and Particle Acceleration: A Review. *Sci. China Earth Sci.* 63, 235–256. doi:10.1007/s11430-019-9551-y

Fu, H. S., Khotyaintsev, Y. V., André, M., and Vaivads, A. (2011). Fermi and Betatron Acceleration of Suprathermal Electrons behind Dipolarization Fronts. *Geophys. Res. Lett.* 38, a–n. doi:10.1029/2011GL048528

Gabrielse, C., Angelopoulos, V., Runov, A., and Turner, D. L. (2012). The Effects of Transient, Localized Electric Fields on Equatorial Electron Acceleration and Transport toward the Inner Magnetosphere. *J. Geophys. Res.* 117, a–n. doi:10.1029/2012JA017873

Gabrielse, C., Harris, C., Angelopoulos, V., Artemyev, A., and Runov, A. (2016). The Role of Localized Inductive Electric Fields in Electron Injections Around Dipolarizing Flux Bundles. *J. Geophys. Res. Space Phys.* 121, 9560–9585. doi:10.1002/2016JA023061

Gary, S. P., Hughes, R. S., Wang, J., and Chang, O. (2014). Whistler Anisotropy Instability: Spectral Transfer in a Three-dimensional Particle-in-cell Simulation. *J. Geophys. Res. Space Phys.* 119, 1429–1434. doi:10.1002/2013JA019618

Gary, S. P. (2015). Short-wavelength Plasma Turbulence and Temperature Anisotropy Instabilities: Recent Computational Progress. *Phil. Trans. R. Soc. A* 373, 20140149. doi:10.1098/rsta.2014.0149

Gary, S. P. (1993). "Theory of Space Plasma Microinstabilities," in *Cambridge Atmospheric and Space Science Series* (Cambridge: Cambridge University Press). doi:10.1017/CBO9780511551512

Hones, E. W., Jr. (1979). Transient Phenomena in the Magnetotail and Their Relation to Substorms. *Space Sci. Rev.* 23, 393–410. doi:10.1007/bf00172247

Hyman, J. M. (1983). Accurate Monotonicity Preserving Cubic Interpolation. *SIAM J. Sci. Stat. Comput.* 4, 645–654. doi:10.1137/0904045

Khotyaintsev, Y. V., Cully, C. M., Vaivads, A., André, M., and Owen, C. J. (2011). Plasma Jet Braking: Energy Dissipation and Nonadiabatic Electrons. *Phys. Rev. Lett.* 106, 165001. doi:10.1103/PhysRevLett.106.165001

Le Contel, O., Nakamura, R., Breuillard, H., Argall, M. R., Graham, D. B., Fischer, D., et al. (2017). Lower Hybrid Drift Waves and Electromagnetic Electron Space-phase Holes Associated with Dipolarization Fronts and Field-Aligned Currents Observed by the Magnetospheric Multiscale Mission during a Substorm. *J. Geophys. Res. Space Phys.* 122, 236. doi:10.1002/2017JA024550

Le Contel, O., Roux, A., Jacquey, C., Robert, P., Berthomier, M., Chust, T., et al. (2009). Quasi-parallel Whistler Mode Waves Observed by THEMIS during Near-Earth Dipolarizations. *Ann. Geophys.* 27, 2259–2275. doi:10.5194/angeo-27-2259-2009

Lezniak, T. W., Arnoldy, R. L., Parks, G. K., and Winckler, J. R. (1968). Measurement and Intensity of Energetic Electrons at the Equator at 6.6Re. *Radio Sci.* 3, 710–714. doi:10.1002/rds196837710

Li, H., Zhou, M., Deng, X., Yuan, Z., Guo, L., Yu, X., et al. (2015). A Statistical Study on the Whistler Waves behind Dipolarization Fronts. *J. Geophys. Res. Space Phys.* 120, 1086–1095. doi:10.1002/2014JA020474

Li, X., Baker, D. N., Temerin, M., Reeves, G. D., and Belian, R. D. (1998). Simulation of Dispersionless Injections and Drift Echoes of Energetic Electrons Associated with Substorms. *Geophys. Res. Lett.* 25, 3763–3766. doi:10.1029/1998gl900001

Liu, C. M., Fu, H. S., Liu, Y. Y., Wang, Z., Chen, G., Xu, Y., et al. (2020). Electron Pitch-Angle Distribution in Earth's Magnetotail: Pancake, Cigar, Isotropy, Butterfly, and Rolling-Pin. *J. Geophys. Res. Space Phys.* 125, e2020JA027777. doi:10.1029/2020JA027777

Liu, C. M., Fu, H. S., Xu, Y., Cao, J. B., and Liu, W. L. (2017). Explaining the Rolling-Pin Distribution of Suprathermal Electrons behind Dipolarization Fronts. *Geophys. Res. Lett.* 44, 6492–6499. doi:10.1002/2017GL074029

Liu, J., Angelopoulos, V., Runov, A., and Zhou, X.-Z. (2013). On the Current Sheets Surrounding Dipolarizing Flux Bundles in the Magnetotail: The Case for Wedgelets. *J. Geophys. Res. Space Phys.* 118, 2000–2020. doi:10.1002/jgra.50092

Moore, T. E., and Arnoldy, R. L. (1982). Plasma Pitch Angle Distributions Near the Substorm Injection Front. *J. Geophys. Res.* 87, 265–270. doi:10.1029/JA087iA01p00265

Nakamura, R., Baumjohann, W., Klecker, B., Bogdanova, Y., Balogh, A., Réme, H., et al. (2002). Motion of the Dipolarization Front during a Flow Burst Event Observed by Cluster. *Geophys. Res. Lett.* 29, 1942. doi:10.1029/2002gl015763

Nakamura, R., Baumjohann, W., Mouikis, C., Kistler, L. M., Runov, A., Volwerk, M., et al. (2004). Spatial Scale of High-Speed Flows in the Plasma Sheet Observed by Cluster. *Geophys. Res. Lett.* 31, a–n. doi:10.1029/2004GL019558

Nakamura, R., Baumjohann, W., Panv, E., Volwerk, M., Birn, J., Artemyev, A., et al. (2012). Flow Bouncing and Electron Injection Observed by Cluster. *J. Geophys. Res.* 118, 2055. doi:10.1002/jgra.50134

Northrop, T. G. (1963). *The Adiabatic Motion of Charged Particles*. New York: Interscience.

Pan, Q., Ashour-Abdalla, M., Walker, R. J., and El-Alaoui, M. (2014). Electron Energization and Transport in the Magnetotail during Substorms. *J. Geophys. Res. Space Phys.* 119, 1060–1079. doi:10.1002/2013JA019508

Panov, E. V., Kubyshkina, M. V., Nakamura, R., Baumjohann, W., Angelopoulos, V., Sergeev, V. A., et al. (2013). Oscillatory Flow Braking in the Magnetotail: THEMIS Statistics. *Geophys. Res. Lett.* 40, 2505–2510. doi:10.1002/grl.50407

Panov, E. V., Nakamura, R., Baumjohann, W., Angelopoulos, V., Petrukovich, A. A., Retinò, A., et al. (2010a). Multiple Overshoot and Rebound of a Bursty Bulk Flow. *Geophys. Res. Lett.* 37, L8103. doi:10.1029/2009GL041971

Panov, E. V., Nakamura, R., Baumjohann, W., Sergeev, V. A., Petrukovich, A. A., Angelopoulos, V., et al. (2010b). Plasma Sheet Thickness during a Bursty Bulk Flow Reversal. *J. Geophys. Res.* 115, a–n. doi:10.1029/2009JA014743

Parks, G. K., and Winckler, J. R. (1968). Acceleration of Energetic Electrons Observed at the Synchronous Altitude during Magnetospheric Substorms. *J. Geophys. Res.* 73, 5786–5791. doi:10.1029/ja073i017p05786

Pontius, D. H., and Wolf, R. A. (1990). Transient Flux Tubes in the Terrestrial Magnetosphere. *Geophys. Res. Lett.* 17, 49–52. doi:10.1029/gl017i001p00049

Runov, A., Angelopoulos, V., Gabrielse, C., Zhou, X.-Z., Turner, D., and Plaschke, F. (2013). Electron Fluxes and Pitch-Angle Distributions at Dipolarization Fronts: THEMIS Multipoint Observations. *J. Geophys. Res. Space Phys.* 118, 744–755. doi:10.1002/jgra.50121

Runov, A., Angelopoulos, V., Sitnov, M. I., Sergeev, V. A., Bonnell, J., McFadden, J. P., et al. (2009). THEMIS Observations of an Earthward-Propagating Dipolarization Front. *Geophys. Res. Lett.* 36, L14106. doi:10.1029/2009GL038980

Runov, A., Angelopoulos, V., and Zhou, X.-Z. (2012). Multipoint Observations of Dipolarization Front Formation by Magnetotail Reconnection. *J. Geophys. Res.* 117, a–n. doi:10.1029/2011JA017361

Runov, A., Angelopoulos, V., Zhou, X.-Z., Zhang, X.-J., Li, S., Plaschke, F., et al. (2011). A THEMIS Multicase Study of Dipolarization Fronts in the Magnetotail Plasma Sheet. *J. Geophys. Res.* 116, A05216. doi:10.1029/2010JA016316

Sergeev, V. A., Angelopoulos, V., Apatenkov, S., Gosling, J. T., Cattell, C. A., and Russell, C. T. (1996). Detection of Localized, Plasma-Depleted Flux Tubes or Bubbles in the Midtail Plasma Sheet. *J. Geophys. Res.* 101, 10,817–10,826. doi:10.1029/96ja00460

Sergeev, V., Angelopoulos, V., Apatenkov, S., Bonnell, J., Ergun, R., Nakamura, R., et al. (2009). Kinetic Structure of the Sharp Injection/dipolarization Front in the Flow-Braking Region. *Geophys. Res. Lett.* 36, L21105. doi:10.1029/2009GL040658

Smets, R., Delcourt, D., Sauvaud, J. A., and Koperski, P. (1999). Electron Pitch Angle Distributions Following the Dipolarization Phase of a Substorm: Interball-Tail Observations and Modeling. *J. Geophys. Res.* 104, 14571–14581. doi:10.1029/1998JA900162

Tsyganenko, N. A. (1987). Global Quantitative Models of the Geomagnetic Field in the Cislunar Magnetosphere for Different Disturbance Levels. *Planet. Space Sci.* 35, 1347–1358. doi:10.1016/0032-0633(87)90046-8

Vasyliunas, V. M. (1968). A Survey of Low-Energy Electrons in the Evening Sector of the Magnetosphere with OGO 1 and OGO 3. *J. Geophys. Res.* 73, 2839–2884. doi:10.1029/ja073i009p02839

Viberg, H., Khotyaintsev, Y. V., Vaivads, A., André, M., Fu, H. S., and Cornilleau-Wehrlin, N. (2014). Whistler Mode Waves at Magnetotail Dipolarization Fronts. *J. Geophys. Res. Space Phys.* 119, 2605–2611. doi:10.1002/2014JA019892

Wolf, R. A., Wan, Y., Xing, X., Zhang, J.-C., and Sazykin, S. (2009). Entropy and Plasma Sheet Transport. *J. Geophys. Res.* 114, a–n. doi:10.1029/2009JA014044

Wu, M., Lu, Q., Volwerk, M., Vörös, Z., Zhang, T., Shan, L., et al. (2013). A Statistical Study of Electron Acceleration behind the Dipolarization Fronts in the Magnetotail. *J. Geophys. Res. Space Phys.* 118, 4804–4810. doi:10.1002/jgra.50456

Wu, P., Fritz, T. A., Larvaud, B., and Lucek, E. (2006). Substorm Associated Magnetotail Energetic Electrons Pitch Angle Evolutions and Flow Reversals: Cluster Observation. *Geophys. Res. Lett.* 33. doi:10.1029/2006GL026595

Zaharia, S., Cheng, C. Z., and Johnson, J. R. (2000). Particle Transport and Energization Associated with Substorms. *J. Geophys. Res.* 105, 18,741. doi:10.1029/1999ja000407

Zelenyi, L. M., Lominadze, J. G., and Taktakishvili, A. L. (1990). Generation of the Energetic Proton and Electron Bursts in Planetary Magnetotails. *J. Geophys. Res.* 95, 3883–3891. doi:10.1029/JA095iA04p03883

Zhang, X., Angelopoulos, V., Artemyev, A. V., and Liu, J. (2018). Whistler and Electron Firehose Instability Control of Electron Distributions in and Around Dipolarizing Flux Bundles. *Geophys. Res. Lett.* 45, 9380–9389. doi:10.1029/2018GL079613

Zhao, M. J., Fu, H. S., Liu, C. M., Chen, Z. Z., Xu, Y., Giles, B. L., et al. (2019). Energy Range of Electron Rolling Pin Distribution behind Dipolarization Front. *Geophys. Res. Lett.* 46, 2390–2398. doi:10.1029/2019GL082100

Zhou, M., Ashour-Abdalla, M., Deng, X., Schriver, D., El-Alaoui, M., and Pang, Y. (2009). THEMIS Observation of Multiple Dipolarization Fronts and Associated Wave Characteristics in the Near-Earth Magnetotail. *Geophys. Res. Lett.* 36, 20107. doi:10.1029/2009GL040663

Conflict of Interest: The authors declare that the research was conducted in the absence of any commercial or financial relationships that could be construed as a potential conflict of interest.

frontiers | Frontiers in Astronomy and Space Sciences

ORIGINAL RESEARCH
published: 29 June 2022
doi: 10.3389/fspas.2022.911002

Which Parameter Controls Ring Current Electron Dynamics

Bernhard Haas[1,2]*, *Yuri Y. Shprits*[1,2,3], *Hayley J. Allison*[1], *Michael Wutzig*[1] *and Dedong Wang*[1]

[1]GFZ German Research Centre for Geosciences, Potsdam, Germany, [2]Institute of Physics and Astronomy, University of Potsdam, Potsdam, Germany, [3]Department of Earth, Planetary, and Space Sciences, University of California, Los Angeles, Los Angeles, CA, United States

Predicting the electron population of Earth's ring current during geomagnetic storms still remains a challenging task. In this work, we investigate the sensitivity of 10 keV ring current electrons to different driving processes, parameterised by the Kp index, during several moderate and intense storms. Results are validated against measurements from the Van Allen Probes satellites. Perturbing the Kp index allows us to identify the most dominant processes for moderate and intense storms respectively. We find that during moderate storms (Kp < 6) the drift velocities mostly control the behaviour of low energy electrons, while loss from wave-particle interactions is the most critical parameter for quantifying the evolution of intense storms (Kp > 6). Perturbations of the Kp index used to drive the boundary conditions at GEO and set the plasmapause location only show a minimal effect on simulation results over a limited L range. It is further shown that the flux at L ~ 3 is more sensitive to changes in the Kp index compared to higher L shells, making it a good proxy for validating the source-loss balance of a ring current model.

Keywords: ring current, magnetosphere, electron lifetimes, electrons, van allen probes (RBSP), ring current model, verb

OPEN ACCESS

Edited by:
Richard Horne,
British Antarctic Survey (BAS),
United Kingdom

Reviewed by:
Victor Sergeev,
Saint Petersburg State University,
Russia
Amy Keesee,
University of New Hampshire,
United States

***Correspondence:**
Bernhard Haas
bhaas@gfz-potsdam.de

Specialty section:
This article was submitted to Space Physics, a section of the journal Frontiers in Astronomy and Space Sciences

Received: *01 April 2022*
Accepted: *06 June 2022*
Published: *29 June 2022*

Citation:
Haas B, Shprits YY, Allison HJ, Wutzig M and Wang D (2022) Which Parameter Controls Ring Current Electron Dynamics. Front. Astron. Space Sci. 9:911002. doi: 10.3389/fspas.2022.911002

1 INTRODUCTION

The Earth's ring current is a dynamic region and the enhancement of its electron and ion populations is one of the main characteristics during geomagnetic storms. While ions contribute most of the energy to the ring current (Williams, 1981; Zhao et al., 2016), low energy electrons (~ 1–100 keV) are also an important field of research, as the main source of spacecraft charging (Baker, 2000; Choi et al., 2011; Ganushkina et al., 2017). The focus of this study is the 10 keV electron flux, which constitutes a major portion of the population responsible for surface charging, and can additionally excite whistler-mode chorus waves (Hwang et al., 2007), which have a profound impact on radiation belt dynamics (see reviews by Millan and Thorne, 2007; Shprits et al., 2008a,b; Thorne, 2010, and references therein). Although there have been major advances in ring current modeling in recent years, accurately reproducing electron flux during storm times still remains a challenge.

The main source of ring current electrons is the plasma sheet population which gets transported towards Earth due to the convection electric field and substorm-associated impulsive electric fields (e.g. Zhao et al., 2016). Electrons are transported from the nightside to the dayside, due to the gradient-curvature (GC) drifts and the $\mathbf{E}\times\mathbf{B}$-drift (Roederer, 1970), and can complete drifts around Earth. Depending on the energy of the particles, either the GC drift or $\mathbf{E}\times\mathbf{B}$ drift dominates. For the electrons at approximately 10 keV considered in this study, the $\mathbf{E}\times\mathbf{B}$ drift dominates. During active periods, the strong convection electric field is capable of transporting these electrons down to L shells of 3 (Zhao et al., 2016), and they typically need about 8 h to complete a full drift around the Earth

(Schulz and Lanzerotti, 1974). This means that at the beginning of a geomagnetic storm, strong flux enhancements are apparent at low L shells first on the nightside and the ring current shows a great magnetic local time (MLT) asymmetry, until electrons have completed their first drift around the Earth.

The ring current source mechanisms are counteracted by different loss processes. First of all, electrons inside the bounce or drift loss-cone are lost to the Earth's atmosphere. Electrons are scattered into the loss-cone by wave-particle interactions leading to a diminution of electron flux. It has been shown that whistler-mode chorus waves are very effective in scattering low energy electrons (e.g. Millan and Thorne, 2007). Whistler mode chorus waves are observed in the low density plasmatrough and therefore the plasmapause location is an important parameter for the dynamics of the ring current. Inside the plasmasphere, hiss waves can lead to pitch-angle scattering of electrons, but several previous studies speculated, that these waves resonate more effectively with > 100 keV electrons and do not significantly scatter 10 keV electrons (e.g. Orlova et al., 2016). Electrons can also be lost, during their drift, when they encounter the magnetopause, which moves closer to Earth when the geomagnetic activity increases. Owing to the slow drift period of ring current electrons, encounters with the dayside magnetopause can introduce asymmetries in the distributions of the electron populations around Earth (Allison et al., 2017).

In the last decades, several ring current models have been developed, incorporating the processes mentioned above (e.g. Jordanova et al., 2006; Ganushkina et al., 2012; Fok et al., 2014; Aseev et al., 2019). The influence of different electric and magnetic field models on the ring current has been studied in detail (Jordanova et al., 2010; Yu et al., 2017; Aseev et al., 2019) and electron lifetime models due to whistler waves have been validated (Chen et al., 2015; Ferradas et al., 2019). Aseev et al. (2019) investigated the influence of the coupling of source and loss processes on the electron phase space density during the St. Patrick's Day 2013 geomagnetic storm. It was found that the electric field and electron lifetimes are likely to be the main cause of discrepancies between model results and observations at L < 4.5. However, it is difficult to determine the contribution of each process on the overall dynamics of the ring current as magnetospheric models are often driven by different input parameters. Hence, it is challenging to directly compare the sensitivity of different model parameters. This work circumvents this issue by using the Kp index as the only input to the model. Kp is a geomagnetic index with a 3 h cadence and monitors the subauroral geomagnetic disturbance globally in a semi-logarithmic manner. Despite the rather large time cadence, Kp has been shown to be a good proxy for various processes in the magnetosphere including the strength of the convection electric field (Thomsen, 2004), wave power of whistler-mode waves (e.g. Wang et al., 2019), and plasmapause location (Carpenter and Anderson, 1992), making it a widely used activity metric in radiation belt and ring current modelling.

In this work, we investigate which input parameters are most critical for the dynamics of the electron ring current under different levels of geomagnetic activity. To this end, we perform a sensitivity analysis of ring current processes in terms of Kp, for several intense storms and moderately disturbed periods. The results of one intense storm and one moderate event, both of which occurred in March 2013, are presented here, while four more events are displayed in the **Supplementary Material**.

2 METHODOLOGY

2.1 Geomagnetic Storms in March, 2013 and Electron Flux Observations

Two geomagnetic storms occurred in March 2013, both of which are analysed in this work. The first event is the St. Patrick's Day storm, with a Dst minimum of −132 nT (see **Figure 1A**). This intense storm has a Kp maximum of 7- by convenction and has been well studied previously (e.g. Boyd et al., 2014; Yu et al., 2015; Zhao et al., 2015; Ferradas et al., 2019). The second event is a moderately disturbed time with a Kp maximum of 5+ and a Dst minimum of −59 nT (see **Figure 1E**), which occurred at the end of March 2013 and has been also considered in several studies (e.g. Zhao et al., 2016; Ripoll et al., 2017; Reidy et al., 2021). Following Reeves et al. (2003), we characterize this event as a moderate storm. These two events are selected, since the Van Allen Probes twin satellites (RBSP-A and RBSP-B), providing us with *in situ* electron flux measurements for validation, have their apogee at ~ 00–01 MLT during March 2013 and therefore directly measure the incoming electrons from the plasmasheet, enabling us to better validate the source-loss balance on the nightside.

We use data from the Helium, Oxygen, Proton, and Electron (HOPE) instrument (Funsten et al., 2013), which is capable of measuring unidirectional electron flux from 1 eV to 50 keV. In this work, we compare against observations at 10 keV and local 54°pitch-angle. We are choosing this pitch-angle channel because missing data is rare for this channel and a pitch-angle in the middle of the distribution should reflect better the whole distribution compared to a pitch-angle at one of the edges. For each point in time, the local pitch-angle channel is mapped to the equatorial plane using the T89 magnetic field model (Tsyganenko, 1989), and we interpolate the simulation results in time, radial distance, MLT, energy and equatorial pitch-angle to those of the observations.

2.2 Quantification of Comparison

We quantify this validation by calculating three different metrics following the suggestions in Liemohn et al. (2021). The accuracy of the simulation is described by the root-mean-square error (RMSE), bias by the mean error (ME) and association by the Pearson correlation coefficient (CC). Additionally, we use the mean absolute error (MAE) to quantify the spread of simulation results in the sensitivity analysis. Since the electron flux can span over several magnitudes, these metrics are calculated on logarithmic flux. Hence, values lie within one order of magnitude, allowing us to use these simple metrics instead of more complicated ones, which are more difficult to interpret (Liemohn et al., 2021). Because of the nature of the satellite's orbit, it spends most of his time at large radial distances from Earth (L > 4.5). These would result in a strong bias in the calculated metrics towards errors at those distances. Therefore,

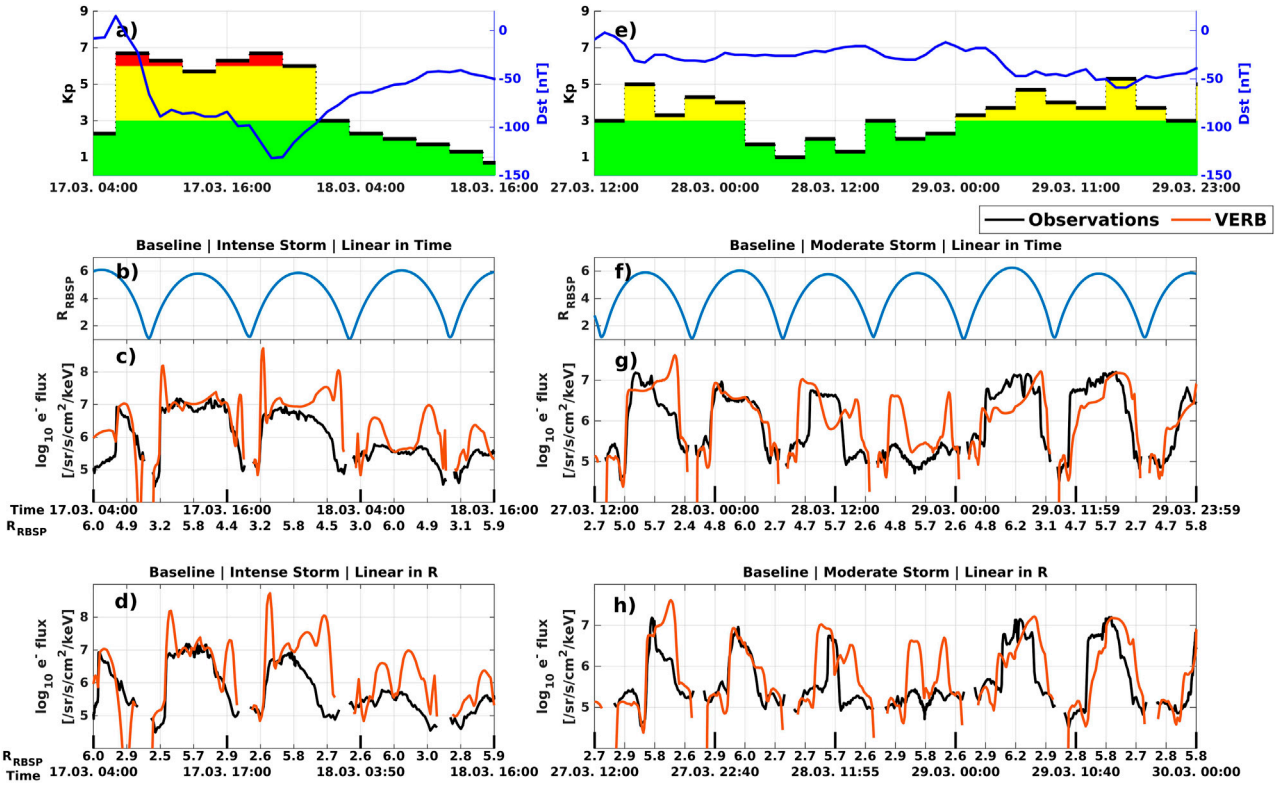

FIGURE 1 | Kp and Dst time series and results of the simulations in March 2013. **(A)** Kp (bars) and Dst (blue line) time series of the intense storm. **(B)** Radial distance of RBSP-B orbit mapped to the equatorial plane during the intense storm. **(C)** Comparison of RBSP-B (black) and baseline VERB-CS result (red) for 10 keV electron flux at 54°local pitch-angle at the spacecraft's location. **(D)** Same data as in **(C)** but linearized in radial distance. Panels **(E–H)** have the same format as **(A–D)** but for the moderate storm.

additionally to the uncorrected metrics, we provide bias-corrected metrics by weighting them inversely to the number of data points at a given radial distance:

$$\begin{aligned}
\text{wRMSE} &= \frac{\sqrt{\sum_i w_i (x_i - y_i)^2}}{\sqrt{\sum_i w_i}}, \qquad \text{wMAE} = \frac{\sum_i w_i |x_i - y_i|}{\sum_i w_i}, \\
\text{wME} &= \bar{x}_w - \bar{y}_w = \frac{\sum_i w_i x_i - \sum_i w_i y_i}{\sum_i w_i} \quad \text{and} \\
\text{wCC} &= \frac{\text{cov}(x, y, w)}{\sqrt{\text{cov}(x, x, w)\text{cov}(y, y, w)}}, \quad \text{with} \\
\text{cov}(x, y, w) &= \frac{\sum_i w_i (x_i - \bar{x}_w)(y_i - \bar{y}_w)}{\sum_i w_i}.
\end{aligned} \tag{1}$$

The weights w_i are calculated by counting the number of observations in the corresponding 0.25 L bin and reciprocate the result. Measurements below L = 2 are stripped since simulation results very close to Earth do not change much during the simulation and are only effected by the initial condition.

2.3 Reduced VERB-4D Model: VERB-CS

The four-dimensional Versatile Electron Radiation Belt code (VERB-4D) Shprits et al. (2015); Aseev et al. (2019) solves the modified Fokker-Planck equation in MLT, radial distance R and the two modified adiabatic invariants V and K Subbotin and Shprits (2012):

$$K = \frac{J}{\sqrt{8 m_0 \mu}} \quad \text{and} \quad V = \mu (K + 0.5)^2, \tag{2}$$

where μ and J are the first and second adiabatic invariants (Schulz and Lanzerotti, 1974) and m_0 is the electron rest mass. In this work, we are dealing with < 10 keV ring current electrons, which are dominated by convection rather than diffusion. Under weak pitch-angle diffusion, and for relatively monotonic diffusion coefficients in the pitch-angle dimension (Albert and Shprits, 2009), the pitch-angle distribution is expected to reach the lowest normal mode and decay with the same rate at all pitch-angles. This allows us to treat pitch-angle diffusion as an exponential loss process with electron lifetimes estimated as an inverse of the diffusion coefficient right at the edge of the loss cone (Shprits et al., 2006). Additionally, in this setup the loss in the loss cone does not need to be explicitly modeled, allowing us to simulate only a limited range of pitch-angles. Radial diffusion is also very

TABLE 1 | Metrics computed for the comparison of log10 (flux) of VERB results and RBSP-B observations for both events. For details, see **Section 2.2**.

Metric	Intense Storm	Moderate Storm
RMSE	0.81	0.67
ME	0.48	0.12
CC	0.65	0.64
wRMSE	0.96	0.65
wME	0.54	0.16
wCC	0.60	0.66

weak at low energies (Lyons and Schulz, 1989) and for energies < 300 keV chorus waves lead to a competition between acceleration and loss (Horne et al., 2005). Finally, we are only looking at events, where the magnetopause stays outside GEO for almost the full simulation duration, and is therefore unlikely to affect our results. We end up with the reduced modified Fokker-Planck equation solved in this work:

$$\frac{\partial f}{\partial t} = \langle v_\varphi \rangle \frac{\partial f}{\partial \varphi} + \langle v_R \rangle \frac{\partial f}{\partial R} - \frac{f}{\tau_{wave}} \tag{3}$$

that describes the time evolution of phase space density (PSD) f. The equation contains advection terms $\frac{\partial f}{\partial \varphi}$ and $\frac{\partial f}{\partial R}$ with respect to MLT, φ, and equatorial radial distance, R, and a loss term due to wave-particle interactions. This model has been previously used for data assimilative predictions of Earth's ring current (Aseev and Shprits, 2019) and is hereinafter referred to as VERB-CS (Convection Simplified).

The coefficients of these terms are bounce averaged drift velocities $\langle v_\varphi \rangle$ and $\langle v_R \rangle$, consisting of the $\mathbf{E} \times \mathbf{B}$ drift and the gradient and curvature drift. These drifts are calculated using the Kp-dependent T89 magnetic field model (Tsyganenko, 1989) and in the case of the $\mathbf{E} \times \mathbf{B}$ drift, the Volland-Stern (Volland, 1973; Stern, 1975) electric field model with the Maynard-Chen (Maynard and Chen, 1975) Kp-dependent parameterization is used.

The 4D numerical grid used in this work consists of 49 points in MLT and 29 points in R starting at 1 R_E and ending at 6.6 R_E. The logarithmic V and linear K grids consist of 31 and 11 points respectively and are set up in such a way that ensures that the desired energy of 10 keV for the equatorial pitch-angle range, which is defined by the equatorially mapped 54° local pitch-angle channel of RBSP-B, is covered over the whole spatial grid.

The initial condition for PSD is extracted from the last full trajectory of the RBSP-B satellite before the start of the simulation, assuming that the initial flux is symmetric in MLT. Periodic boundary conditions are used for MLT and the lower radial boundary condition at $R = 1$ is set to 0, while the upper boundary condition at geostationary orbit ($R = 6.6$) is provided by the Kp-dependent Denton model (Denton et al., 2015).

Electron lifetimes, τ_{wave}, due to wave-particle interactions correspond to either hiss or chorus associated lifetimes depending on whether a particle is inside the plasmasphere or outside. The plasmapause location is determined by the Kp-dependent C&A model (Carpenter and Anderson, 1992). Orlova and Shprits (2014) calculated and parameterised electron lifetimes associated with interactions with chorus waves, using wave properties derived from CRRES data (Spasojevic and Shprits, 2013). Similarly, Spasojevic et al. (2015) calculated wave properties of hiss waves from RBSP data, which was later translated into electron lifetimes (Orlova et al., 2016). Both the hiss and chorus lifetime models depend on radial distance, MLT, electron energy and Kp.

2.4 Setup of the Sensitivity Analysis

To find the dominant process or processes controlling the dynamics of the ring current electrons, we perform several sensitivity runs of VERB-CS with various perturbations of the Kp time series. In this work, the sensitivity analysis focuses on describing how uncertainty in the input variables affects the final output. Since all variability of the inputs of the VERB-CS model are driven by the Kp index, we can introduce variability by perturbing Kp and quantify the resulting uncertainty in flux. By doing a one-factor-at-a-time (OAT) analysis, we can see the effects of different processes in the model and quantify the effect of the variability of each input on the ring current simulation. To this end, the Kp input of a single part of the model is perturbed, while all other parts of the model are driven by the original Kp history. We perform two different experiments: one adding Gaussian noise with a variance of one to the original Kp time series; and another adding a uniform offset of ±1 to the original Kp history. Examples of such perturbed Kp time histories can be seen in **Figures 2A**, **3A**.

In the case of the Gaussian noise experiments, we are interested in the range of simulation results, defined as the 10th and 90th percentiles of electron flux along the RBSP-B trajectory for each point in time. We make this choice so that the impact of statistical outliers is reduced. We have tested how many simulations are necessary for convergence and found that 16 simulations are enough to see no significant change when adding additional simulations (see **Supplementary Figure S2**).

In the OAT sensitivity analysis we investigate the influence of changes in the plasmapause location; boundary conditions at GEO; drift velocities calculated from the electric and magnetic field; and electron lifetimes due to chorus and hiss scattering. We also present simulation results when the Kp input is perturbed for all processes combined.

3 BASELINE SIMULATION RESULTS

In **Figure 1** the VERB-CS results are displayed alongside RBSP-B observations and geomagnetic indices (Panel a and e) for the two considered events: a storm that occurred on 17 March 2013 and a period of disturbed activity from 27 until 29 March 2013. Panels b and f show the radial distance of the satellite mapped to the equatorial plane during the events. Panels c and g show observations and results along the satellite's orbit presented linearly in time, while the x-axis of Panels d and h is modified in a way such that the radial distance and not the time is presented linearly, ensuring that there is no bias towards certain radial distances in our plots. The exact setup is displayed in

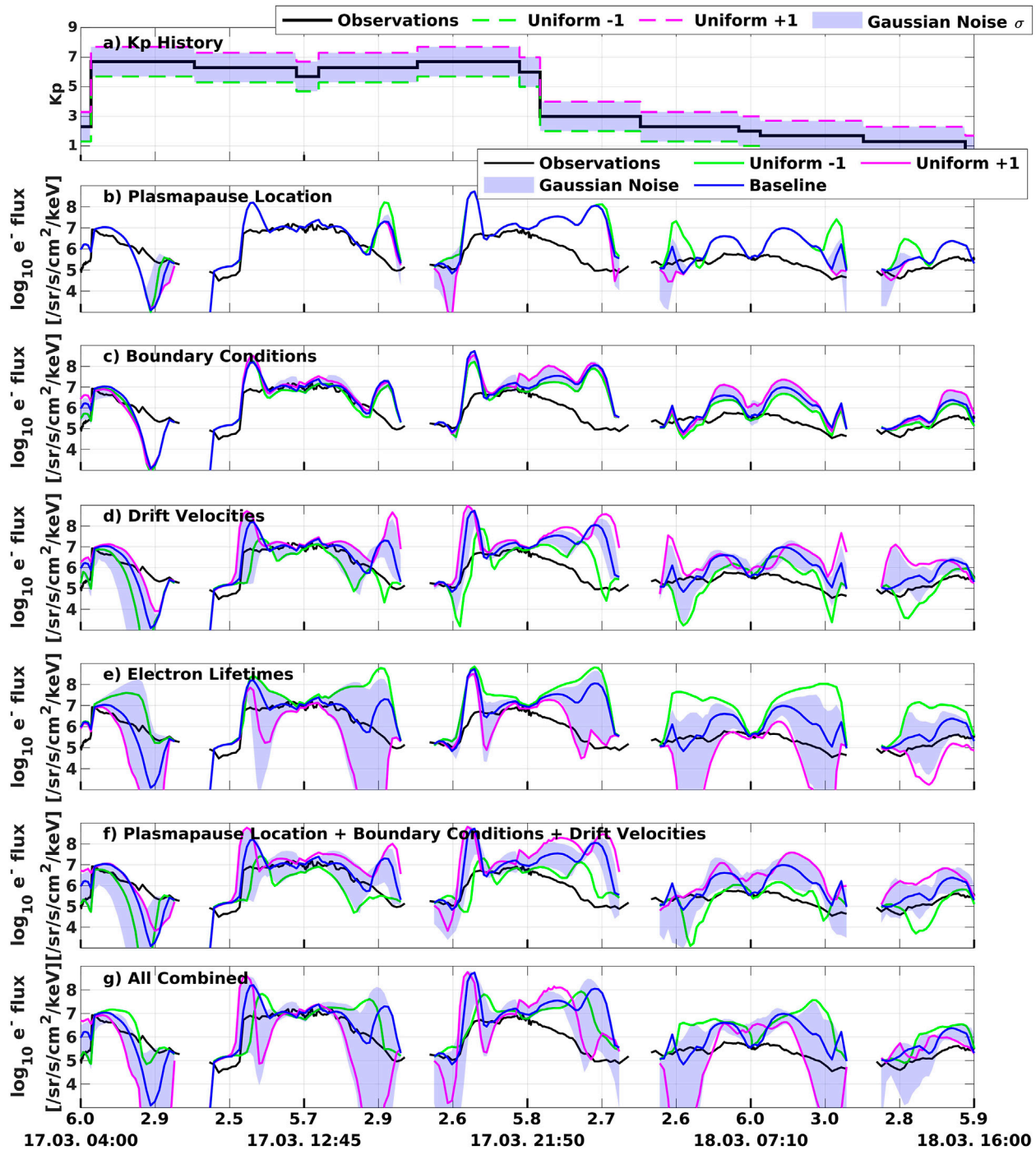

FIGURE 2 | Perturbation results of 10 keV electron flux and 54°local pitch-angle at the spacecraft's location for the intense event along the RBSP-B orbit. The blue areas show the range of simulation results, when Kp is perturbed using Gaussian noise. The black line in panels b–g shows the RBSP-B flux data. **(A)** Original Kp history and perturbed ones. **(B)** Perturbing plasmapause location model. **(C)** Perturbing boundary condition model. **(D)** Perturbing drift velocities. **(E)** Perturbing electron lifetime models. **(F)** Perturbing plasmapause location, boundary conditions and drift velocities combined. **(G)** Perturbing all processes combined.

Supplementary Figure S1. For this study, plotting with equidistant radial distance on the *x*-axis is preferred, since it is later shown that at middle radial distances (L ~ 3), we see the highest variance of model results.

Looking at VERB-CS results for the St. Patrick Day storm (left column), we can see that the VERB-CS model predicts an enhancement with the rise of Kp and agrees well for L > 5, although there is an overestimation at radial distances of three to

TABLE 2 | Metrics computed for the comparison between the simulation results using uniform offsets, and the results of the 10th and 90th percentile when adding Gaussian noise. For details, see **Section 2.2**.

Intense Storm	Uniform ± 1		Gaussian Noise Percentiles
	wMAE	wME	wMAE
Plasmapause location (PP)	0.28	–0.26	0.29
Boundary conditions (BC)	0.33	0.32	0.45
Drift velocities (DV)	1.08	1.02	1.07
Electron lifetimes	**2.01**	**–2.00**	1.92
PP + BC + DV	1.18	1.06	1.39
All combined	1.45	–0.95	**2.04**
Moderate Storm			
Plasmapause location	0.14	–0.14	0.09
Boundary conditions	0.26	0.59	0.31
Drift velocities	**1.33**	**1.30**	1.03
Electron lifetimes	0.55	–0.55	0.50
All combined	0.93	0.86	**1.07**

Bold values indicate the maximum absolute value of each metric for each event.

four Earth radii. This issue is discussed further in **Section 5** where the contributions of each parameter are investigated. The simulation results for the moderate geomagnetic activity (right column) show good agreement with observations and the enhancement of the 10 keV electron flux is correctly reproduced during this geomagnetically disturbed time.

Table 1 displays metrics quantifying the comparison between measurements and simulation results. It is apparent that the weighted metrics show worse performance of the model compared to the uncorrected metrics, which indicates that the model performs better at high L shells near GEO. All three weighted metrics indicate as well that the model gives worse results for the intense storm than the moderate storm. The model shows a positive bias in both events, although it is much higher for the intense storm as indicated by ME and wME. The correlation coefficient is comparable between both events, which is surprising because of the relatively good agreement for the second event. Small scale fluctuations in the flux measurements could be the cause for this, which are not resolved by our model. The simulation results shown in **Figure 1** are our baseline simulations for the following sensitivity analysis.

4 SENSITIVITY ANALYSIS RESULTS

The simulated electron flux when perturbing the processes in an OAT manner can be seen in **Figures 2B–E**. Comparing the range of simulated 10 keV electron flux when adding Gaussian noise (blue shaded regions) shows that perturbing the plasmapause location and boundary conditions does not have as large of an effect as compared to perturbing electron lifetimes, or drift velocities, through perturbations in the electric and magnetic field. The impact of the variance of the plasmapause location and boundary conditions is confined in a limited L range: plasmapause location only effecting low L shells; and boundary conditions effecting high L shells close to the boundary. Conversely, perturbing drift velocities and electron lifetimes results in a large variance across all L shells, with a maximum variability around L ~ 3. This is especially the case for electron lifetimes, where the perturbations show a substantial effect on the electron flux in this region.

Adding uniform offsets to the model's processes (green and magenta lines), leads to a larger change in the resulting electron flux in almost all cases as compared to using the Kp with added Gaussian noise.

As a final step, **Figure 2F** shows the variance, when perturbing plasmapause location, boundary conditions and drift velocities simultaneously, but leaving the lifetime as in the baseline simulation. It should be noted that this variance is not as large as when perturbing electron lifetimes alone. Interestingly enough, when we perturb all processes combined including electron lifetimes (Panel g), the uncertainty is again smaller compared to perturbing electron lifetimes alone (Panel e). Adding a positive uniform offset to all processes results in the simulated electron flux becoming smaller, as electron loss dominates over other processes, which is a very interesting and somewhat counter-intuitive result.

Table 2 reinforces these statements quantitatively, by displaying the wMAE and wME calculated by comparing the positive offset against the negative offset simulations, and the 10th and 90th percentiles of the Gaussian-noise-simulations. The metrics in this case do not describe the errors of simulations but rather the range of them. Looking at the uniform offset results, the wMAE describes the span between the simulation while the sign of the wME shows whether the positive (positive sign) or negative (negative sign) offset simulation leads to higher flux results. For the Gaussian-noise-experiments, the wMAE equals the wME, since the difference between the 90th to the 10th percentile is always positive by definition.

Figure 3 has the same format as **Figure 2**, showing the results for the moderate storm. As it has been seen for the intense storm, the perturbations of plasmapause location and boundary conditions result only in small variances over a limited L range. Panel e shows that electron lifetimes have less of an effect on the simulation results compared to the intense storm, while the most impactful parameter on the electron flux for the moderate storm are the drift velocities (Panel d). Perturbing drift velocities, through perturbations in electric and magnetic field, using the Gaussian noise method leads to a clear positive bias, due to the non-linearity of the electric and magnetic field models and the semi-logarithmic nature of the Kp index itself. The largest range of simulation results when perturbing electron lifetimes or drift velocities is apparent at L ~ 3, as it has been already observed for the intense storm. This region is very sensitive to perturbations of the source-loss balance of the model.

Adding a uniform offset of ±1 to the Kp input that drives various processes leads to large variability of simulation results, especially when perturbing drift velocities. This substantial effect is also apparent, when all processes combined are perturbed (Panel f), where adding a positive offset to Kp leads to higher electron flux, while adding a negative offset leads to smaller flux values.

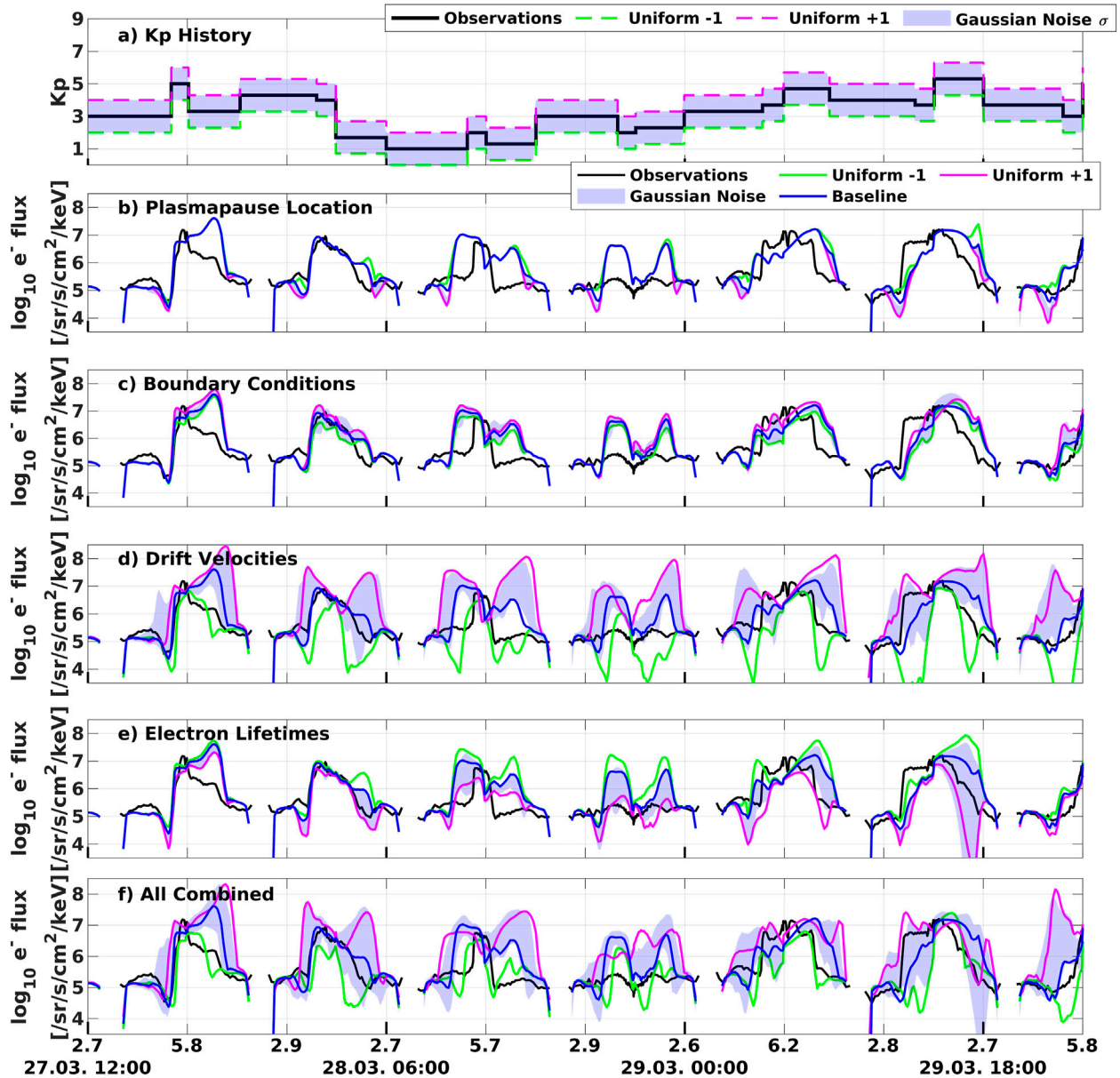

FIGURE 3 | Perturbation results of 10 keV electron flux and 54° local pitch-angle at the spacecraft's location for the moderate event along the RBSP-B orbit. The blue areas show the range of simulation results, when Kp is perturbed using Gaussian noise. The black line in panels b–g shows the RBSP-B flux data. **(A)** Original Kp history and perturbed ones. **(B)** Perturbing plasmapause location model. **(C)** Perturbing boundary condition model. **(D)** Perturbing drift velocities. **(E)** Perturbing electron lifetime models. **(F)** Perturbing all processes combined.

Comparing the calculated metrics for both events (**Table 2**), we can see that the maximum wMAE, observed for drift velocities for the moderate storm, is substantially lower than the maximum value observed for electron lifetimes in the case of the intense event. Generally speaking, the moderate storm shows a smaller range of perturbed simulation results. It is also interesting that the sign of the wME is different for both events, when the full simulation is perturbed. Contrary to the intense storm, it is not the loss processes controlling the dynamics of the ring current, but for moderate events, the drift velocities due to the changes of electric and magnetic field.

5 DISCUSSION

We have presented the results of a sensitivity analysis in terms of Kp for a moderate and an intense storm. Perturbing the Kp input for the calculation of the plasmapause location and the boundary condition model does not have a very significant influence on the resulting

electron flux in the case of either a strong or a moderate storm. The Denton et al. (2015) model provides the mean values of electron flux at GEO, which are used in this work, as well as statistical percentiles for each value of Kp. Aseev et al. (2019) investigated how this statistical variance influences the ring current and comparing with their results, the influence on electron flux due to this statistical spread is larger than the influence of a perturbation of the model's Kp input. It is well known that the plasmapause location influences magnetosphere dynamics (e.g. Wang et al., 2020), and it is therefore surprising, that perturbing this plasma boundary has only a small impact on simulation results. This effect may not be most accurately estimated due to uncertainties of the C&A model, which describes the plasmapause location in a very simple MLT-independent manner and therefore, does not represent the full dynamics of the plasmasphere during a geomagnetic storm.

The parameters with the largest impact, when perturbed through their Kp input, are drift velocities and electron lifetimes (see **Figures 2**, **3**). Drift velocities are strongly influenced through the change of the convection electric field during geomagnetically disturbed times. For intense storms, it has been shown that the convection electric field can saturate Liemohn et al. (2002); Califf et al. (2014), hence reducing the effect of the electric field during those times. This can also be seen in our results: for the moderate storm, the sensitivity due to the electric field still dominates over loss processes, while loss dominates over convection for the considered intense storm.

Whether loss or source processes dominate shows the largest effect at L ~ 3, which is consistent with the results presented in Aseev et al. (2019). While the electron flux at higher L near the GEO boundary responds quickly to changes in the convection field and boundary conditions, deeper L shells show slower dynamics. We conclude that the flux at L ~ 3 is a good proxy for validating the balance of source and loss processes during geomagnetic storms. For moderate storms (Kp < 6), this balance seems to be correctly modelled by VERB-CS for 10 keV electrons, while we see overestimation in the simulated flux blow L = 4 during intense storms. **Figures 3D,F** show that decreasing the Kp uniformly by one does not resolve the overestimation completely (third pass of the satellite). This shows that modeling errors of the electron flux supplied by the outer radial boundary are unlikely to be responsible for this source-loss imbalance alone.

To understand how our model behaves with a more complex electric field model, we run the same events using the model by Weimer (2005) and see almost the same overestimation of flux for the intense storm (see **Supplementary Figure S8**) and similar behaviour for the moderate event. It is concluded that VS. captures the general dynamics of the global convection field correctly compared to more complex models. Statistical studies have shown that strong large-scale electric fields are present at low L shells during intense storms. (Rowland and Wygant, 1998; Califf et al., 2014), which are not described by the simple Volland-Stern model. Fine electric field structures like these could alter the drift trajectories of electrons, and therefore also our simulation results, significantly. However, since we observe overestimation of flux for different events and MLT sectors (see **Supplementary Figures S3, S6, S7**), it seems unlikely that such a local phenomenon is the main issue of a global source-loss imbalance.

Another potential parameterization error is the magnetic field used for calculating drift velocities. The T89 model predicts compression and stretching of the magnetosphere during geomagnatically active times, but not to the same extend as newer models (e.g. Tsyganenko and Sitnov, 2005) explicitly designed for handling storm times (McCollough et al., 2008). On the dayside, compression of the magnetic field leads to more loss of particles to the magnetopause (Keika et al., 2005), while on the nightside the stretching results in a weaker magnetic fields. Since the strength of the $\mathbf{E} \times \mathbf{B}$-drift scales inversely with $|\mathbf{B}|$ and electrons at 10 keV are not affected much by the gradient-curvature-drift, this results in stronger convection and higher flux enhancements on the nightside during storms (Ganushkina et al., 2012). We conclude that newer magnetic field models would not help to reduce overestimation observed on the nightside, but should still be considered in future studies to represent a more accurate picture of the Earth's magnetic field.

These points make the investigation of the loss of electrons very important to better reproduce electron flux during intense storm events. Recent statistical wave studies have shown that chorus waves can be effective in scattering low energy electrons in the pre-midnight sector (Wang et al., 2019) and an event specific study has also shown stronger chorus wave activity in the pre-midnight sector as expected (Yu et al., 2022). This scattering process is currently not properly accounted for in the lifetimes used in our model and therefore this lack of loss may be responsible for the overestimation at $L \sim 3$.

For the moderate geomagnetically disturbed time, with a Kp maximum of 5+, electron flux observations are well reproduced by our model (see **Figure 1**) and all input models used in VERB-CS have been validated to at least Kp 6. The T89 models uses six bins between Kp = 0 and Kp = 5- for its parameterization, which could cause inaccuracies in the sensitivy analysis when combined with other models which use different parameterization boundaries. With the exception of T89, all the parameterized models used here are smooth functions of Kp, which reduces the effect of boundaries in the Kp parameterizations to a minimum. Therefore, we can conclude that for these Kp levels, our model is a realistic representation of Earth's ring current and the sensitivity analysis represents the sensitivity of the ring current itself. Regarding intense storm events, most of the empirical input models are not valid for such high Kp levels, hence it is difficult to estimate how well they will perform when extrapolated to very high activity levels. Despite these limitations, magnetospheric models often achieve convincing results using these parameterizations (e.g. Ganushkina et al., 2012; Aseev and Shprits, 2019; Ferradas et al., 2019) and also VERB-CS is capable of reproducing electron flux observations at a range of L shells for the St. Patrick's Day storm. Our results reveal the state as well as the limits of our current understanding of the electron dynamics of the ring current and allow prioritizing future efforts of improving predictive capabilities.

6 CONCLUSION

In this work we have investigated the sensitivity of the major driving processes on electron ring current dynamics. Although only two events were presented here, the same controlling processes were identified for comparable storm events (see

Supplementary Figures S4–S7). We showed that for moderate and intense storms, different processes dominate the behavior of the 10 keV electron population. Our conclusions are as following:

1. During intense storm events, perturbing electron lifetimes has the strongest effect on the evolution of the ring current electron flux within geosynchronous orbit. This result indicates the dominant role of wave-particle interactions and potentially other loss processes, that are currently not accounted for in VERB-CS, for the dynamics at these energies.
2. For moderate storms, the ring current is most strongly affected by changes of the drift velocities caused by the changes in the electric and magnetic fields.
3. High L shells near GEO are not strongly affected by perturbations of Kp, while the electron flux at L ~ 3 is very sensitive to the assumed parameters and shows under- and overestimation. The validation of the ring current codes at tens of keV should include the low L-shell region at L ~ 3 where the simulations are most sensitive to the assumptions about loss and transport mechanisms.

DATA AVAILABILITY STATEMENT

Publicly available datasets were analyzed in this study. This data can be found here: https://omniweb.gsfc.nasa.gov/form/dx1.html http://rbsp.space.umn.edu/data/rbsp/ect/rbspa/hope/level3/PA/.

AUTHOR CONTRIBUTIONS

BH and YS conceived the idea of the study. BH performed the analysis with input from YS, HA, MW, and DW. BH wrote the first draft of the manuscript; YS, HA, MW, and, DW contributed to structuring and editing the manuscript, and approved of the submitted version.

FUNDING

This project has received funding from the European Union's Horizon 2020 research and innovation programme under grant agreement No. 870452 (PAGER). HA was supported by the Alexander von Humboldt foundation.

ACKNOWLEDGMENTS

The authors acknowledge the NASA OMNI database (https://omniweb.gsfc.nasa.gov/form/dx1.html) and thank the developers of the IRBEM library (https://github.com/PRBEM/IRBEM), which was used for magnetic field calculations. The authors are grateful to the RBSP-ECT team for the provision of Van Allen Probes observations. All RBSP-ECT data are publicly available at the web site http://rbsp.space.umn.edu/data/rbsp/ect/rbspa/hope/level3/PA/.

SUPPLEMENTARY MATERIAL

The Supplementary Material for this article can be found online at: https://www.frontiersin.org/articles/10.3389/fspas.2022.911002/full#supplementary-material

REFERENCES

Albert, J. M., and Shprits, Y. Y. (2009). Estimates of Lifetimes against Pitch Angle Diffusion. *J. Atmos. Solar-Terrestrial Phys.* 71, 1647–1652. doi:10.1016/J.JASTP.2008.07.004

Allison, H. J., Horne, R. B., Glauert, S. A., and Zanna, G. D. (2017). The Magnetic Local Time Distribution of Energetic Electrons in the Radiation Belt Region. *J. Geophys. Res. Space Phys.* 122, 8108–8123. doi:10.1002/2017JA024084

Aseev, N. A., and Shprits, Y. Y. (2019). Reanalysis of Ring Current Electron Phase Space Densities Using Van Allen Probe Observations, Convection Model, and Log-Normal Kalman Filter. *Space weather.* 17, 619–638. doi:10.1029/2018SW002110

Aseev, N. A., Shprits, Y. Y., Wang, D., Wygant, J., Drozdov, A. Y., Kellerman, A. C., et al. (2019). Transport and Loss of Ring Current Electrons inside Geosynchronous Orbit during the 17 March 2013 Storm. *JGR Space Phys.* 124, 915–933. doi:10.1029/2018JA026031

Baker, D. N. (2000). The Occurrence of Operational Anomalies in Spacecraft and Their Relationship to Space Weather. *IEEE Trans. Plasma Sci.* 28, 2007–2016. doi:10.1109/27.902228

Boyd, A. J., Spence, H. E., Claudepierre, S. G., Fennell, J. F., Blake, J. B., Baker, D. N., et al. (2014). Quantifying the Radiation Belt Seed Population in the 17 March 2013 Electron Acceleration Event. *Geophys. Res. Lett.* 41, 2275–2281. doi:10.1002/2014GL059626

Califf, S., Li, X., Blum, L., Jaynes, A., Schiller, Q., Zhao, H., et al. (2014). THEMIS Measurements of Quasi-static Electric Fields in the Inner Magnetosphere. *J. Geophys. Res. Space Phys.* 119, 9939–9951. doi:10.1002/2014JA020360

Carpenter, D. L., and Anderson, R. R. (1992). An Isee/whistler Model of Equatorial Electron Density in the Magnetosphere. *J. Geophys. Res.* 97, 1097. doi:10.1029/91JA01548

Chen, M. W., Lemon, C. L., Orlova, K., Shprits, Y., Hecht, J., and Walterscheid, R. L. (2015). Comparison of Simulated and Observed Trapped and Precipitating Electron Fluxes during a Magnetic Storm. *Geophys. Res. Lett.* 42, 8302–8311. doi:10.1002/2015GL065737

Choi, H.-S., Lee, J., Cho, K.-S., Kwak, Y.-S., Cho, I.-H., Park, Y.-D., et al. (2011). Analysis of GEO Spacecraft Anomalies: Space Weather Relationships. *Space weather.* 9, a–n. doi:10.1029/2010SW000597

Denton, M. H., Thomsen, M. F., Jordanova, V. K., Henderson, M. G., Borovsky, J. E., Denton, J. S., et al. (2015). An Empirical Model of Electron and Ion Fluxes Derived from Observations at Geosynchronous Orbit. *Space weather.* 13, 233–249. doi:10.1002/2015SW001168

Ferradas, C. P., Jordanova, V. K., Reeves, G. D., and Larsen, B. A. (2019). Comparison of Electron Loss Models in the Inner Magnetosphere during the 2013 St. Patrick's Day Geomagnetic Storm. *J. Geophys. Res. Space Phys.* 124, 7872–7888. doi:10.1029/2019JA026649

Fok, M.-C., Buzulukova, N. Y., Chen, S.-H., Glocer, A., Nagai, T., Valek, P., et al. (2014). The Comprehensive Inner Magnetosphere-Ionosphere Model. *J. Geophys. Res. Space Phys.* 119, 7522–7540. doi:10.1002/2014JA020239

Funsten, H. O., Skoug, R. M., Guthrie, A. A., Macdonald, E. A., Baldonado, J. R., Harper, R. W., et al. (2013). Helium, Oxygen, Proton, and Electron (Hope) Mass Spectrometer for the Radiation Belt Storm Probes Mission. *Space Sci. Rev.* 179, 423–484. doi:10.1007/s11214-013-9968-7

Ganushkina, N., Jaynes, A., and Liemohn, M. (2017). Space Weather Effects Produced by the Ring Current Particles. *Space Sci. Rev.* 212, 1315–1344. doi:10.1007/s11214-017-0412-2

Ganushkina, N. Y., Liemohn, M. W., and Pulkkinen, T. I. (2012). Storm-time Ring Current: Model-dependent Results. *Ann. Geophys.* 30, 177–202. doi:10.5194/ANGEO-30-177-2012

Horne, R. B., Thorne, R. M., Glauert, S. A., Albert, J. M., Meredith, N. P., and Anderson, R. R. (2005). Timescale for Radiation Belt Electron Acceleration by Whistler Mode Chorus Waves. *J. Geophys. Res.* 110. doi:10.1029/2004JA010811

Hwang, J. A., Lee, D.-Y., Lyons, L. R., Smith, A. J., Zou, S., Min, K. W., et al. (2007). Statistical Significance of Association between Whistler-Mode Chorus Enhancements and Enhanced Convection Periods during High-Speed Streams. *J. Geophys. Res.* 112, a–n. doi:10.1029/2007JA012388

Jordanova, V. K., Miyoshi, Y. S., Zaharia, S., Thomsen, M. F., Reeves, G. D., Evans, D. S., et al. (2006). Kinetic Simulations of Ring Current Evolution during the Geospace Environment Modeling Challenge Events. *J. Geophys. Res.* 111, 1–16. doi:10.1029/2006JA011644

Jordanova, V. K., Zaharia, S., and Welling, D. T. (2010). Comparative Study of Ring Current Development Using Empirical, Dipolar, and Self-Consistent Magnetic Field Simulations. *J. Geophys. Res.* 115, a–n. doi:10.1029/2010JA015671

Keika, K., Nosé, M., Ohtani, S., Takahashi, K., Christon, S. P., and McEntire, R. W. (2005). Outflow of Energetic Ions from the Magnetosphere and its Contribution to the Decay of the Storm Time Ring Current. *J. Geophys. Res.* 110. doi:10.1029/2004JA010970

Liemohn, M. W., Kozyra, J. U., Hairston, M. R., Weimer, D. R., Lu, G., Ridley, A. J., et al. (2002). Consequences of a Saturated Convection Electric Field on the Ring Current. *Geophys. Res. Lett.* 29, 62-1–62-4. doi:10.1029/2001gl014270

Liemohn, M. W., Shane, A. D., Azari, A. R., Petersen, A. K., Swiger, B. M., and Mukhopadhyay, A. (2021). RMSE Is Not Enough: Guidelines to Robust Data-Model Comparisons for Magnetospheric Physics. *J. Atmos. Solar-Terrestrial Phys.* 218. doi:10.1016/j.jastp.2021.105624

Lyons, L. R., and Schulz, M. (1989). Access of Energetic Particles to Storm Time Ring Current through Enhanced Radial "Diffusion". *J. Geophys. Res.* 94, 5491. doi:10.1029/ja094ia05p05491

Maynard, N. C., and Chen, A. J. (1975). Isolated Cold Plasma Regions: Observations and Their Relation to Possible Production Mechanisms. *J. Geophys. Res.* 80, 1009–1013. doi:10.1029/JA080I007P01009

McCollough, J. P., Gannon, J. L., Baker, D. N., and Gehmeyr, M. (2008). A Statistical Comparison of Commonly Used External Magnetic Field Models. *Space weather.* 6, a–n. doi:10.1029/2008SW000391

Millan, R. M., and Thorne, R. M. (2007). Review of Radiation Belt Relativistic Electron Losses. *J. Atmos. Solar-Terrestrial Phys.* 69, 362–377. doi:10.1016/J.JASTP.2006.06.019

Orlova, K., and Shprits, Y. (2014). Model of Lifetimes of the Outer Radiation Belt Electrons in a Realistic Magnetic Field Using Realistic Chorus Wave Parameters. *J. Geophys. Res. Space Phys.* 119, 770–780. doi:10.1002/2013JA019596

Orlova, K., Shprits, Y., and Spasojevic, M. (2016). New Global Loss Model of Energetic and Relativistic Electrons Based on Van Allen Probes Measurements. *J. Geophys. Res. Space Phys.* 121, 1308–1314. doi:10.1002/2015JA021878

Reeves, G. D., McAdams, K. L., Friedel, R. H. W., and O'Brien, T. P. (2003). Acceleration and Loss of Relativistic Electrons during Geomagnetic Storms. *Geophys. Res. Lett.* 30, a–n. doi:10.1029/2002GL016513

Reidy, J. A., Horne, R. B., Glauert, S. A., Clilverd, M. A., Meredith, N. P., Woodfield, E. E., et al. (2021). Comparing Electron Precipitation Fluxes Calculated from Pitch Angle Diffusion Coefficients to LEO Satellite Observations. *JGR Space Phys.* 126, e2020JA028410. doi:10.1029/2020JA028410

Ripoll, J. F., Santolík, O., Reeves, G. D., Kurth, W. S., Denton, M. H., Loridan, V., et al. (2017). Effects of Whistler Mode Hiss Waves in March 2013. *J. Geophys. Res. Space Phys.* 122, 7433–7462. doi:10.1002/2017JA024139

Roederer, J. G. (1970). *Dynamics of Geomagnetically Trapped Radiation*. Springer-Verlag Berlin.

Rowland, D. E., and Wygant, J. R. (1998). Dependence of the Large-Scale, Inner Magnetospheric Electric Field on Geomagnetic Activity. *J. Geophys. Res.* 103, 14959–14964. doi:10.1029/97JA03524

Schulz, M., and Lanzerotti, L. J. (1974). *Particle Diffusion in the Radiation Belts, Vol. 7*. Springer Science & Business Media.

Shprits, Y. Y., Elkington, S. R., Meredith, N. P., and Subbotin, D. A. (2008a). Review of Modeling of Losses and Sources of Relativistic Electrons in the Outer Radiation Belt I: Radial Transport. *J. Atmos. Solar-Terrestrial Phys.* 70, 1679–1693. doi:10.1016/J.JASTP.2008.06.008

Shprits, Y. Y., Kellerman, A. C., Drozdov, A. Y., Spence, H. E., Reeves, G. D., and Baker, D. N. (2015). Combined Convective and Diffusive Simulations: Verb-4d Comparison with 17 March 2013 Van Allen Probes Observations. *Geophys. Res. Lett.* 42, 9600–9608. doi:10.1002/2015GL065230

Shprits, Y. Y., Li, W., and Thorne, R. M. (2006). Controlling Effect of the Pitch Angle Scattering Rates Near the Edge of the Loss Cone on Electron Lifetimes. *J. Geophys. Res.* 111, 12206. doi:10.1029/2006JA011758

Shprits, Y. Y., Subbotin, D. A., Meredith, N. P., and Elkington, S. R. (2008b). Review of Modeling of Losses and Sources of Relativistic Electrons in the Outer Radiation Belt Ii: Local Acceleration and Loss. *J. Atmos. Solar-Terrestrial Phys.* 70, 1694–1713. doi:10.1016/J.JASTP.2008.06.014

Spasojevic, M., and Shprits, Y. Y. (2013). Chorus Functional Dependencies Derived from Crres Data. *Geophys. Res. Lett.* 40, 3793–3797. doi:10.1002/GRL.50755

Spasojevic, M., Shprits, Y. Y., and Orlova, K. (2015). Global Empirical Models of Plasmaspheric Hiss Using Van Allen Probes. *J. Geophys. Res. Space Phys.* 120, 10370–10383. doi:10.1002/2015JA021803/FORMAT/PDF

Stern, D. P. (1975). The Motion of a Proton in the Equatorial Magnetosphere. *J. Geophys. Res.* 80, 595–599. doi:10.1029/JA080I004P00595

Subbotin, D. A., and Shprits, Y. Y. (2012). Three-dimensional Radiation Belt Simulations in Terms of Adiabatic Invariants Using a Single Numerical Grid. *J. Geophys. Res. Space Phys.* 117. doi:10.1029/2011JA017467/FORMAT/PDF

Thomsen, M. F. (2004). WhyKpis Such a Good Measure of Magnetospheric Convection. *Space weather.* 2, a–n. doi:10.1029/2004SW000089

Thorne, R. M. (2010). Radiation Belt Dynamics: The Importance of Wave-Particle Interactions. *Geophys. Res. Lett.* 37. doi:10.1029/2010GL044990

Tsyganenko, N. A. (1989). A Magnetospheric Magnetic Field Model with a Warped Tail Current Sheet. *Planet. Space Sci.* 37, 5–20. doi:10.1016/0032-0633(89)90066-4

Tsyganenko, N. A., and Sitnov, M. I. (2005). Modeling the Dynamics of the Inner Magnetosphere during Strong Geomagnetic Storms. *J. Geophys. Res.* 110. doi:10.1029/2004JA010798

Volland, H. (1973). A Semiempirical Model of Large-Scale Magnetospheric Electric Fields. *J. Geophys. Res.* 78, 171–180. doi:10.1029/JA078I001P00171

Wang, D., Shprits, Y. Y., Zhelavskaya, I. S., Agapitov, O. V., Drozdov, A. Y., and Aseev, N. A. (2019). Analytical Chorus Wave Model Derived from Van Allen Probe Observations. *JGR Space Phys.* 124, 1063–1084. doi:10.1029/2018JA026183

Wang, D., Shprits, Y. Y., Zhelavskaya, I. S., Effenberger, F., Castillo, A. M., Drozdov, A. Y., et al. (2020). The Effect of Plasma Boundaries on the Dynamic Evolution of Relativistic Radiation Belt Electrons. *J. Geophys. Res. Space Phys.* 125. doi:10.1029/2019JA027422

Weimer, D. R. (2005). Improved Ionospheric Electrodynamic Models and Application to Calculating Joule Heating Rates. *J. Geophys. Res.* 110, 1–21. doi:10.1029/2004JA010884

Williams, D. J. (1981). Ring Current Composition and Sources: An Update. *Planet. Space Sci.* 29, 1195–1203. doi:10.1016/0032-0633(81)90124-0

Yu, Y., Hosokawa, K., Ni, B., Jordanova, V. K., Miyoshi, Y., Cao, J., et al. (2022). On the Importance of Using Event-Specific Wave Diffusion Rates in Modeling Diffuse Electron Precipitation. *JGR Space Phys.* 127. doi:10.1029/2021JA029918

Yu, Y., Jordanova, V. K., Ridley, A. J., Toth, G., and Heelis, R. (2017). Effects of Electric Field Methods on Modeling the Midlatitude Ionospheric Electrodynamics and Inner Magnetosphere Dynamics. *J. Geophys. Res. Space Phys.* 122, 5321–5338. doi:10.1002/2016JA023850

Yu, Y., Jordanova, V., Zou, S., Heelis, R., Ruohoniemi, M., and Wygant, J. (2015). Modeling Subauroral Polarization Streams during the 17 March 2013 Storm. *J. Geophys. Res. Space Phys.* 120, 1738–1750. doi:10.1002/2014JA020371

Zhao, H., Li, X., Baker, D. N., Claudepierre, S. G., Fennell, J. F., Blake, J. B., et al. (2016). Ring Current Electron Dynamics during Geomagnetic Storms Based on

the Van Allen Probes Measurements. *J. Geophys. Res. Space Phys.* 121, 3333–3346. doi:10.1002/2016JA022358

Zhao, L., Yu, Y., Delzanno, G. L., and Jordanova, V. K. (2015). Bounce- and MLT-averaged Diffusion Coefficients in a Physics-based Magnetic Field Geometry Obtained from RAM-SCB for the 17 March 2013 Storm. *J. Geophys. Res. Space Phys.* 120, 2616–2630. doi:10.1002/2014JA020858/FORMAT/PDF

Conflict of Interest: The authors declare that the research was conducted in the absence of any commercial or financial relationships that could be construed as a potential conflict of interest.

The handling editor RH is currently organizing a Research Topic with the author(s) YS.

Publisher's Note: All claims expressed in this article are solely those of the authors and do not necessarily represent those of their affiliated organizations, or those of the publisher, the editors and the reviewers. Any product that may be evaluated in this article, or claim that may be made by its manufacturer, is not guaranteed or endorsed by the publisher.

frontiers | Frontiers in Astronomy and Space Sciences

REVIEW
published: 03 August 2022
doi: 10.3389/fspas.2022.951628

Electron-Driven Instabilities in the Solar Wind

Daniel Verscharen[1], B. D. G. Chandran[2,3], E. Boella[4,5], J. Halekas[6], M. E. Innocenti[7], V. K. Jagarlamudi[8,9], A. Micera[10], V. Pierrard[10,11], Š. Štverák[12,13], I. Y. Vasko[14,15], M. Velli[16] and P. L. Whittlesey[14]*

[1]Mullard Space Science Laboratory, University College London, Dorking, United Kingdom, [2]Space Science Center, University of New Hampshire, Durham, NH, United States, [3]Department of Physics and Astronomy, University of New Hampshire, Durham, NH, United States, [4]Physics Department, Lancaster University, Lancaster, United Kingdom, [5]Cockroft Institute, Daresbury Laboratory, Warrington, United Kingdom, [6]Department of Physics and Astronomy, University of Iowa, Iowa, IA, United States, [7]Institut für Theoretische Physik, Ruhr-Universität Bochum, Bochum, Germany, [8]Applied Physics Laboratory, Johns Hopkins University, Laurel, MD, United States, [9]National Institute for Astrophysics—Institute for Space Astrophysics and Planetology, Rome, Italy, [10]Solar-Terrestrial Centre of Excellence, Royal Observatory of Belgium, Brussels, Belgium, [11]Center for Space Radiations (CSR) and Georges Lemaître Centre for Earth and Climate Research (TECLIM), Earth and Life Institute (ELI), Université Catholique de Louvain (UCLouvain), Louvain-La-Neuve, Belgium, [12]Institute of Atmospheric Physics of the Czech Academy of Sciences, Prague, Czech Republic, [13]Astronomical Institute of the Czech Academy of Sciences, Prague, Czech Republic, [14]Space Sciences Laboratory, University of California, Berkeley, Berkeley, CA, United States, [15]Space Research Institute, Russian Academy of Sciences, Moscow, Russia, [16]Department of Earth, Planetary, and Space Sciences, University of California, Los Angeles, Los Angeles, CA, United States

OPEN ACCESS

Edited by:
Misa Cowee, Los Alamos National Laboratory (DOE), United States

Reviewed by:
Dan Winske, Los Alamos National Laboratory (DOE), United States
Laxman Adhikari, University of Alabama in Huntsville, United States

***Correspondence:**
Daniel Verscharen
d.verscharen@ucl.ac.uk

Specialty section:
This article was submitted to Space Physics, a section of the journal Frontiers in Astronomy and Space Sciences

Received: *24 May 2022*
Accepted: *21 June 2022*
Published: *03 August 2022*

Citation:
Verscharen D, Chandran BDG, Boella E, Halekas J, Innocenti ME, Jagarlamudi VK, Micera A, Pierrard V, Štverák Š, Vasko IY, Velli M and Whittlesey PL (2022) Electron-Driven Instabilities in the Solar Wind. Front. Astron. Space Sci. 9:951628. doi: 10.3389/fspas.2022.951628

The electrons are an essential particle species in the solar wind. They often exhibit non-equilibrium features in their velocity distribution function. These include temperature anisotropies, tails (kurtosis), and reflectional asymmetries (skewness), which contribute a significant heat flux to the solar wind. If these non-equilibrium features are sufficiently strong, they drive kinetic micro-instabilities. We develop a semi-graphical framework based on the equations of quasi-linear theory to describe electron-driven instabilities in the solar wind. We apply our framework to resonant instabilities driven by temperature anisotropies. These include the electron whistler anisotropy instability and the propagating electron firehose instability. We then describe resonant instabilities driven by reflectional asymmetries in the electron distribution function. These include the electron/ion-acoustic, kinetic Alfvén heat-flux, Langmuir, electron-beam, electron/ion-cyclotron, electron/electron-acoustic, whistler heat-flux, oblique fast-magnetosonic/whistler, lower-hybrid fan, and electron-deficit whistler instability. We briefly comment on non-resonant instabilities driven by electron temperature anisotropies such as the mirror-mode and the non-propagating firehose instability. We conclude our review with a list of open research topics in the field of electron-driven instabilities in the solar wind.

Keywords: solar wind, plasma, instabilities, electrons, temperature anisotropy, heat flux, quasi-linear theory

1 INTRODUCTION

The solar wind is a fully ionised and quasi-neutral plasma flow (for a recent review about the solar wind, see Verscharen et al., 2019b). Plasma flows with these properties consist of free negatively charged electrons and free positively charged ions. The majority of the ions in the solar wind are protons with an addition of 2–5% of α-particles and a minority contribution of heavier ions. Quasi-neutrality requires that electrons and ions are spatially distributed so that the total charge density of

the plasma is approximately zero on scales much greater than the Debye length. In order to fulfill quasi-neutrality, electrons must be, on average, the particle species with the greatest number density in fully ionised and quasi-neutral plasmas like the solar wind.

The mass of an electron is by a factor of 1836 times smaller than the mass of a proton. Therefore, the direct contributions of electrons to the solar-wind mass, momentum, angular-momentum, and kinetic-energy fluxes are negligible compared to the proton contributions. However, electrons contribute significantly to the overall momentum balance of the solar wind through their thermal pressure gradient (Parker, 1958; Landi and Pantellini, 2003) and to the overall energy balance of the solar wind through their heat flux (Hollweg, 1974; Scime et al., 1994; Scime et al., 1999; Pagel et al., 2005; Bale et al., 2013; Borovsky and Gary, 2014; Cranmer and Schiff, 2021). This is true both for fast solar-wind streams, whose sources are open coronal field regions such as polar coronal holes, as well as for the wind originating from the more complex coronal regions associated with helmet streamers and pseudo-streamers. In the simplest models of coronal acceleration, the fluid electron pressure gradient reflects the effects of the interplanetary electric field set up by the much greater scale height of electrons compared to protons of similar temperatures (Parker, 2010). The subsequent (Jeans-theorem) evolution of the wind, taking into account charge conservation (the outflow must be globally neutral) as well as local charge neutrality, together with magnetic-moment conservation for particles of each species, leads to distribution functions in the supersonic wind that are strongly out of equilibrium. These distributions become unstable to plasma and electromagnetic field oscillations that most likely play a major role in shaping the observed distributions as we discuss in this article.

Electron-kinetic processes such as resonant damping and instabilities modify the overall energy budget of the electromagnetic plasma fluctuations, which has an impact on the overall evolution of the solar wind (Gary et al., 1975b; Feldman et al., 1976a; Ramani and Laval, 1978; Gary et al., 1999b; Alexandrova et al., 2009; Schekochihin et al., 2009; Štverák et al., 2015). Estimates of the empirical proton-to-total heating ratio based on observed temperature profiles in the inner heliosphere suggest that a significant fraction (~ 40%) of the turbulent energy is dissipated by electrons (Cranmer et al., 2009). Therefore, electrons and electron-driven processes are considered essential for our understanding of the global evolution of the solar wind (and for other astrophysical plasmas, see Verscharen et al., 2021a,b).

In-situ solar-wind measurements show that the electrons, like the ions, often exhibit deviations from thermodynamic equilibrium (Feldman et al., 1975; Rosenbauer et al., 1977; Pilipp et al., 1987; Maksimovic et al., 1997). These deviations become apparent in the electrons' velocity distribution function f_e that often differs from the Maxwellian equilibrium distribution. We define f_e so that $f_e(\boldsymbol{x}, \boldsymbol{v}, t)\, \mathrm{d}^3x\, \mathrm{d}^3v$ describes the total number of electrons in the phase-space volume $\mathrm{d}^3x\, \mathrm{d}^3v$ centred around the coordinates $(\boldsymbol{x}, \boldsymbol{v})$ at time t. If binary Coulomb collisions between the plasma particles were the dominant process that determined f_e, the observed deviations from the Maxwellian equilibrium would not persist, at least not over long timescales when compared to the Coulomb collision time. We, therefore, refer to the solar wind often as a *collisionless plasma* (Marsch, 2006). Given the steep energy dependence of the Coulomb-collision cross section, this applies especially to the suprathermal electrons; however, for the thermal electrons, collisions remain important (Scudder and Olbert, 1979; Landi et al., 2012).

Temperature anisotropy is a typical non-thermal feature associated with f_e in the solar wind (Phillips et al., 1989; Salem et al., 2003; Štverák et al., 2008). Temperature anisotropy is characterised by different temperatures in the directions perpendicular and parallel to the local magnetic field. In this context, we understand temperature as the *kinetic temperature* based on the diagonal elements of the electron pressure tensor (i.e., the second velocity moment of f_e). We define the temperature of a plasma species j in the direction perpendicular to the magnetic field as $T_{\perp j}$ and its temperature in the direction parallel to the magnetic field as $T_{\parallel j}$.

Another important non-thermal feature of the solar-wind electron distribution function is its ternary structure consisting of a thermal core, a suprathermal halo (Feldman et al., 1975; Pilipp et al., 1987; Lie-Svendsen et al., 1997; Maksimovic et al., 1997), and a field-aligned beam (Pilipp et al., 1987; Lin, 1998).

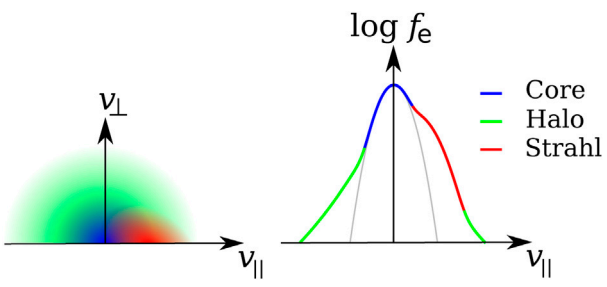

FIGURE 1 | Schematic of a typical electron distribution function in the solar wind. Left: two-dimensional distribution function in ($v_\perp$, $v_\parallel$) space. Right: cut of the distribution function along the $v_\parallel$-axis. The blue colour indicates the electron core, the green colour represents the halo, and the red colour represents the strahl.

Figure 1 illustrates the three populations of the electron distribution function in velocity space and the formation of the overall electron distribution in the solar wind.

The thermal core consists of about 95% of the electrons (blue colour in **Figure 1**). It has a shape close to a Maxwellian distribution and temperatures comparable to the proton temperatures in the solar wind. The Maxwellian shape of the core is often attributed to the lower mean free path for Coulomb collisions at low speeds in the distribution (Phillips and Gosling, 1990).

The suprathermal halo is a quasi-isotropic tail of electrons represented by an enhancement of f_e above the Maxwellian distribution. It is primarily observed at energies above a breakpoint of about 50 eV at 1 au (green colour in **Figure 1**; McComas et al., 1992; Lie-Svendsen et al., 1997). The location of this breakpoint and the relative density of the halo population vary with distance from the Sun and show correlations with solar-wind parameters such as speed and temperature (Maksimovic et al., 2000, 2005; Pierrard et al., 2016, 2020; Bakrania et al., 2020). The halo population is often successfully modelled with a κ-distribution (using the Greek letter "kappa"; for detailed information about κ-distributions, see the recent textbooks by Livadiotis, 2017 and Lazar and Fichtner, 2021).

The field-aligned beam population is called the electron strahl (red colour in **Figure 1**). This population appears as a "shoulder" on the electron distribution at small pitch-angles around the directions parallel or anti-parallel to the magnetic field and typically in the anti-sunward direction (Hammond et al., 1996; Fitzenreiter et al., 1998). As in the case of the halo, the breakpoint energy between the core and the strahl populations and the relative density of the strahl vary with distance from the Sun and exhibit correlations with the solar-wind speed and temperature (Maksimovic et al., 2005; Pagel et al., 2007; Štverák et al., 2009; Graham et al., 2017; Abraham et al., 2022). The bulk velocities of the core, halo, and strahl often exhibit non-zero differences in their components parallel to the magnetic field. Given the requirement for global quasi-neutrality imposed by Poisson's equation, these field-aligned relative drifts must be such that the total electron charge flux is equal to the total ion charge flux. Given the outward drift of the strahl, this typically leads to a sunward drift of the core distribution. The relative drifts, particularly those of the suprathermal components, are responsible for the majority of the heat flux in the electron distribution.

If the deviations from thermodynamic equilibrium are large and certain criteria, which we discuss in this review, are fulfilled, the kinetic configuration of f_e drives kinetic micro-instabilities. These instabilities lead to the exponential growth of fluctuations in the electromagnetic or electrostatic fields over time at the expense of the integrated particle kinetic energy. During the growth of these instabilities, particles interact with the growing fluctuations, leading to a change of f_e that reduces the non-thermal drivers of the instability, until f_e achieves a marginally stable state. In the case of instabilities driven by temperature anisotropy, this process leads to a reduction of the anisotropy. In the case of instabilities driven by heat flux, this process leads to a reduction of the heat flux (López et al., 2020). The efficiency of the heat-flux reduction by different instabilities is a matter of ongoing research. The ability of electron-driven instabilities to regulate electron temperatures, temperature anisotropies, and potentially heat flux makes them important for the overall evolution of the solar wind. We often characterise these instabilities in terms of instability thresholds that depend on plasma bulk parameters, such as the densities, bulk speeds, and temperatures of the involved plasma populations.

The launch of *Parker Solar Probe* in 2018 and the launch of *Solar Orbiter* in 2020 have started a new era of electron observations in the solar wind (Fox et al., 2016; Müller et al., 2020; Owen et al., 2020; Whittlesey et al., 2020). These spacecraft measure the three-dimensional solar-wind electron distribution function over a wide range of heliocentric distances and with unprecedented accuracy and cadence. Electrons are particularly difficult to measure due to their small mass and due to the small kinetic energies of a large number of electrons in the distribution (Wüest et al., 2007). These energies are often comparable to the energy associated with the spacecraft electrostatic potential at the measurement point. Nevertheless, these modern observations confirm earlier suggestions that the electron distribution evolves with distance from the Sun and that non-thermal features are essential for a complete description of the evolution of the solar wind, especially near the Sun (Halekas et al., 2020; Berčič et al., 2021b; Halekas et al., 2021b; Abraham et al., 2022; Jeong et al., 2022b). These results and extrapolations based on previous measurements also suggest that electron-driven instabilities play an important role in the shaping of the electron distribution (Berčič et al., 2019), although many questions about electron kinetics and its impact on the evolution of the solar wind remain open.

With this review, we pay tribute to the many theoretical and numerical discoveries made by Peter Gary in the field of electron-driven instabilities in the solar wind. Through his application of linear Vlasov–Maxwell theory, Peter made crucial contributions to the understanding of the energetics of the solar wind. In **Section 2**, we present a basic summary of linear Vlasov–Maxwell theory and our quasi-linear framework to visualise the impact of electron-driven instabilities. In **Section 3**, we discuss instabilities driven by temperature anisotropies in the solar-wind electron populations. In **Section 4**, we explore instabilities driven by reflectional asymmetries in the electron distribution function, including instabilities driven by electron heat flux. **Section 5** gives a short summary of non-resonant electron-driven instabilities. Finally, **Section 6** presents the conclusions of our work as well as an outlook on open questions and future observations of electron-driven instabilities.

2 THEORETICAL FRAMEWORK FOR THE DESCRIPTION OF RESONANT MICRO-INSTABILITIES

In this section, we summarise linear Vlasov–Maxwell theory for the calculation of the hot-plasma dispersion relation of plasma waves and instabilities. We then introduce a quasi-linear

framework for the description of the evolution of the electron distribution function under the action of electron-driven instabilities. The framework described in this section applies both to electrons and to ions in collisionless plasmas. This prepares us for the discussion in the subsequent sections of specific electron-driven instabilities in the solar wind.

2.1 Linear Vlasov–Maxwell Theory

Linear Vlasov–Maxwell theory is a framework for the description of small-amplitude plasma waves in kinetic plasmas. The starting point for the derivation of the hot-plasma dispersion relation in linear Vlasov–Maxwell theory is the Vlasov equation,

$$\frac{\partial f_j}{\partial t} + \boldsymbol{v}\cdot\frac{\partial f_j}{\partial \boldsymbol{x}} + \frac{q_j}{m_j}\left(\boldsymbol{E} + \frac{1}{c}\boldsymbol{v}\times\boldsymbol{B}\right)\cdot\frac{\partial f_j}{\partial \boldsymbol{v}} = 0, \tag{1}$$

combined with Maxwell's equations,

$$\nabla\cdot\boldsymbol{E} = 4\pi\varrho, \tag{2}$$

$$\nabla\cdot\boldsymbol{B} = 0, \tag{3}$$

$$\nabla\times\boldsymbol{E} = -\frac{1}{c}\frac{\partial \boldsymbol{B}}{\partial t}, \tag{4}$$

and

$$\nabla\times\boldsymbol{B} = \frac{4\pi}{c}\boldsymbol{j} + \frac{1}{c}\frac{\partial \boldsymbol{E}}{\partial t}. \tag{5}$$

In this coupled set of equations, f_j ($\boldsymbol{x}$, $\boldsymbol{v}$, t) is the velocity distribution function of species j, $\boldsymbol{E}$ is the electric field, $\boldsymbol{B}$ is the magnetic field, q_j and m_j are the charge and the mass of a particle of species j, ϱ is the charge density, $\boldsymbol{j}$ is the current density, and c is the speed of light. Self-consistency demands that

$$\varrho = \sum_j q_j \int f_j \,\mathrm{d}^3 v \tag{6}$$

and

$$\boldsymbol{j} = \sum_j q_j \int \boldsymbol{v} f_j \,\mathrm{d}^3 v, \tag{7}$$

showing that **Eqs. 1–5** represent a complicated, coupled set of integro-differential equations in six-dimensional phase space and time. Linear Vlasov–Maxwell theory simplifies this set of equations by linearisation so that

$$f_j(\boldsymbol{x},\boldsymbol{v},t) = f_{0j}(\boldsymbol{v}) + \delta f_j(\boldsymbol{x},\boldsymbol{v},t), \tag{8}$$

$\boldsymbol{E}(\boldsymbol{x},t) = \delta\boldsymbol{E}(\boldsymbol{x},t)$, and $\boldsymbol{B}(\boldsymbol{x},t) = \boldsymbol{B}_0 + \delta\boldsymbol{B}(\boldsymbol{x},t)$, where the subscript 0 indicates a *background* quantity and δ indicates a *fluctuating* quantity that averages to zero over time and space. Moreover, we make the assumption that all fluctuating quantities behave like plane waves, $\propto e^{i\boldsymbol{k}\cdot\boldsymbol{x}-i\omega t}$, where $\boldsymbol{k}$ is the wave vector and ω is the wave frequency. As described in the literature (e.g., Stix, 1992), the application of these assumptions and Landau's procedure for the analytic continuation around poles in the complex plane lead to the dispersion relation in the form

$$\det\mathcal{D} = 0, \tag{9}$$

where

$$\mathcal{D} = \begin{pmatrix} \epsilon_{xx} - n_z^2 & \epsilon_{xy} & \epsilon_{xz} + n_x n_z \\ \epsilon_{yx} & \epsilon_{yy} - n_x^2 - n_z^2 & \epsilon_{yz} \\ \epsilon_{zx} + n_z n_x & \epsilon_{zy} & \epsilon_{zz} - n_x^2 \end{pmatrix}, \tag{10}$$

is the dispersion tensor, $\boldsymbol{\epsilon}$ is the plasma susceptibility tensor, and $\boldsymbol{n} = \boldsymbol{k}c/\omega$. In this convention, the reference frame is chosen so that $k_y = 0$. The entries of the $\mathbf{3}\times\mathbf{3}$ matrix $\mathcal{D}$ depend on the plasma background properties (q_j, m_j, $f_{\{0j\}}$, and B_0) and of the wave properties ($\boldsymbol{k}$ and ω). Numerous numerical tools exist that solve **Eq. 9**, often assuming closed expressions for f_{0j} such as Maxwellian or bi-Maxwellian distributions (Roennmark, 1982; Klein et al., 2012; Verscharen and Chandran, 2018).

The standard approach for finding the dispersion relation (corresponding to an initial-value problem) involves the determination of a complex ω that solves **Eq. 9** for given plasma background properties at fixed $\boldsymbol{k}$. In general, these solutions are complex-valued. We define the complex ω that solves **Eq. 9** for given background parameters and $\boldsymbol{k}$ as

$$\omega_k = \omega_{kr} + i\gamma_k, \tag{11}$$

where $\omega_{kr} = \mathrm{Re}(\omega_k)$ is the real wave frequency and $\gamma_k = \mathrm{Im}(\omega_k)$ is the growth/damping rate at wave vector $\boldsymbol{k}$. The fluctuation amplitudes of solutions with $\gamma_k < 0$ exponentially decrease with time, while the fluctuation amplitudes of solutions with $\gamma_k > 0$ exponentially increase with time. Therefore, we refer to solutions with $\gamma_k < 0$ as *damped waves* and to solutions with $\gamma_k > 0$ as *instabilities*. In linear theory, the damping rate γ_k is generally a function of $\boldsymbol{k}$ that possesses a global maximum at fixed plasma background properties. We refer to the maximum growth rate γ_m as the maximum γ_k over all $\boldsymbol{k}$ for a given instability and given plasma background properties.

Due to the kinetic (microphysical) nature of these instabilities, we also find the term *micro-instabilities* for these solutions in the literature. Peter Gary pioneered the application of linear Vlasov–Maxwell theory to the study of micro-instabilities in space plasmas.

2.2 Quasi-Linear Evolution of Micro-Instabilities

If $\gamma_k \neq 0$, the energy density of the electromagnetic fluctuations changes over time. This process exchanges energy between the electromagnetic field and the plasma particles, either in the form of a particle energy loss ($\gamma_k > 0$) or gain ($\gamma_k < 0$) in order to conserve the total energy. This fundamental concept helps us understand the evolution of the velocity distribution function under the action of micro-instabilities.

Resonant micro-instabilities are a family of micro-instabilities in which the energy exchange occurs via resonant wave–particle interactions between the unstable waves and the plasma particles.

Quasi-linear theory is a mathematical framework to describe the evolution of f_{0j} (Vedenov et al., 1961; Drummond and Pines, 1964; Kennel and Engelmann, 1966; Rowlands et al., 1966). It requires that the amplitude of the resonant waves and their damping rates are small ($|\delta f_j| \ll f_{0j}$ in **Eq. 8**, and $|\gamma_m| \ll |\omega_{kr}|$ in **Eq. 11** at the unstable $\boldsymbol{k}$), so that the timescale of the evolution of f_{0j} is much greater than the period of the resonant wave $1/\omega_{kr}$.

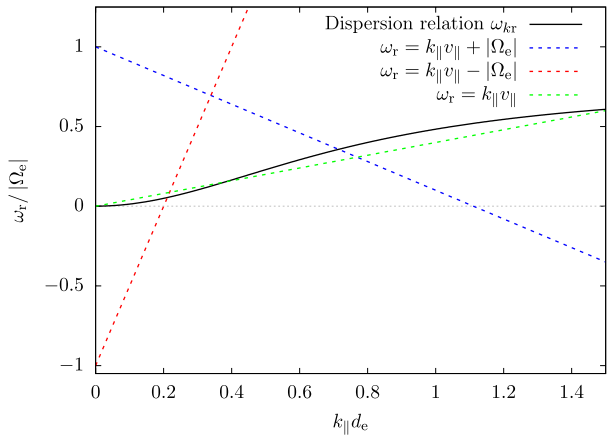

FIGURE 2 | Dispersion relation and resonance conditions. The black curve shows a solution to **Eq. 9** for the fast-magnetosonic/whistler wave. We assume an angle of 40° between $\boldsymbol{k}$ and $\boldsymbol{B}_0$ and a very cold plasma ($\beta_j = 10^{-8}$) consisting of Maxwellian protons and electrons. For our definition of β_j, see **Eq. 22**. The dashed lines represent electron resonance conditions according to **Eq. 16** for different n and $v_\parallel$. The wavenumber is normalised by the inverse of the electron inertial length d_e

Under the assumptions of quasi-linear theory, the background distribution is gyrotropic; i.e., cylindrically symmetric around $\boldsymbol{B}_0$. Therefore, it is helpful to work in cylindrical coordinates in velocity space, so that $\boldsymbol{v}$ is represented by the velocity component $v_\perp$ perpendicular to $\boldsymbol{B}_0$, the velocity component $v_\parallel$ parallel to $\boldsymbol{B}_0$, and the azimuthal angle ϕ_v. Likewise, we express $\boldsymbol{k}$ with its cylindrical coordinates $k_\perp$, $k_\parallel$, and ϕ_k.

The slow, quasi-linear evolution of f_{0j} over time due to resonant wave–particle interactions is given by the equation (Stix, 1992)

$$\frac{\partial f_{0j}}{\partial t} = \lim_{V\to\infty} \sum_{n=-\infty}^{+\infty} \frac{q_j^2}{8\pi^2 m_j^2} \int \frac{1}{v_\perp V} \hat{G} v_\perp \delta\left(\omega_{kr} - k_\parallel v_\parallel - n\Omega_j\right) \left|\psi_k^{j,n}\right|^2 \hat{G} f_{0j}\, \mathrm{d}^3 k, \tag{12}$$

where

$$\hat{G} \equiv \left(1 - \frac{k_\parallel v_\parallel}{\omega_{kr}}\right) \frac{\partial}{\partial v_\perp} + \frac{k_\parallel v_\perp}{\omega_{kr}} \frac{\partial}{\partial v_\parallel}, \tag{13}$$

$$\psi_k^{j,n} \equiv \frac{1}{\sqrt{2}} \left[E_{k,r} e^{i\phi_k} J_{n+1}\left(\xi_j\right) + E_{k,l} e^{-i\phi_k} J_{n-1}\left(\xi_j\right)\right] + \frac{v_\parallel}{v_\perp} E_{kz} J_n\left(\xi_j\right), \tag{14}$$

$\Omega_j \equiv q_j B_0/m_j c$ is the cyclotron frequency[1], $\xi_j = k_\perp v_\perp/\Omega_j$ is the argument of the Bessel function J_m of order m, and n is an integer that marks the order of the resonance. We refer to the resonance with $n = 0$ as the *Landau resonance* and to all other resonances with $n \neq 0$ as *cyclotron resonances*. The left and right circularly polarised components of the electric field are given by $E_{k,l} \equiv (E_{kx} + iE_{ky})/\sqrt{2}$ and $E_{k,r} \equiv (E_{kx} - iE_{ky})/\sqrt{2}$, where we use the Fourier transformation of the electric field in the convention

$$\boldsymbol{E}_k(\boldsymbol{k}, t) = \int_V \delta\boldsymbol{E}(\boldsymbol{x}, t) e^{-i\boldsymbol{k}\cdot\boldsymbol{x}}\, \mathrm{d}^3 x \tag{15}$$

over the spatial volume V. We define the sense of the polarisation of a given wave mode in terms of $E_{k,l}$, $E_{k,r}$, and E_{kz}.

Due to the δ-function in **Eq. 12**, only particles fulfilling the resonance condition

$$\omega_{kr} = k_\parallel v_\parallel + n\Omega_j \tag{16}$$

participate in the resonant wave–particle interactions associated with a given n. In the case of Landau-resonant interactions, a resonant particle travels along $\boldsymbol{B}_0$ with the parallel phase speed of the resonant wave, $v_\parallel = \omega_{kr}/k_\parallel$. This resonant particle experiences a constant parallel wave electric field $E_\parallel \equiv \delta\boldsymbol{E} \cdot \boldsymbol{B}_0/B_0$. In the case of cyclotron-resonant interactions, a resonant particle travels along $\boldsymbol{B}_0$ at a speed such that the Doppler-shifted wave frequency in the particle's frame of reference is an integer multiple of the particle's cyclotron frequency. Such a particle experiences a perpendicular wave electric field $\boldsymbol{E}_\perp \equiv \delta\boldsymbol{E} - E_\parallel \boldsymbol{B}_0/B_0$ that does not average to zero over multiple cyclotron periods of the particle. This description captures the fundamental nature of resonant wave–particle interactions. We note, however, that **Eq. 12** includes more subtleties such as higher-order and anomalous cyclotron resonances as well as transit-time damping, which lie outside the scope of this review.

Figure 2 illustrates an example for a solution to the linear Vlasov–Maxwell dispersion relation from **Eq. 9** and the resonance conditions from quasi-linear theory in **Eq. 16**. The black curve shows a solution of the Vlasov–Maxwell dispersion relation from **Eq. 9** in terms of ω_{kr} for the fast-magnetosonic/whistler wave as a function of $k_\parallel$. The dashed lines describe the resonance conditions from **Eq. 16** for $n = -1$ (blue), $n = +1$ (red), and $n = 0$ (green). Their slopes correspond to different values of $v_\parallel$. At any intersection between a line representing a resonance condition and the plot of the dispersion relation, **Eq. 16** is fulfilled.

Eq. 12 represents a diffusion equation in velocity space. The operator $\hat{G}$ dictates the direction of the diffusive flux when the resonance condition is fulfilled and $\psi_k^{j,n} \neq 0$. The diffusive flux of resonant particles through velocity space is locally tangent to semicircles in velocity space of the form

$$\left(v_\parallel - v_{ph}\right)^2 + v_\perp^2 = \text{constant}, \tag{17}$$

where $v_{ph} \equiv \omega_{kr}/k_\parallel$ is the field-parallel phase speed of the resonant waves. According to **Eq. 17**, quasi-linear diffusion conserves particle kinetic energy in the reference frame that moves with the velocity $v_{ph}\boldsymbol{B}_0/B_0$. The description of **Eq. 17** leaves us with an ambiguity in the direction of the diffusive flux of resonant particles (clockwise or counter-clockwise in velocity space). This ambiguity is resolved by the requirement that **Eq. 12** demands, like other diffusion processes, a diffusive flux from larger values of f_{0j} to smaller values of f_{0j}.

[1]In our convention, Ω_j has the same sign as q_j. This means particularly with regard to electrons that $\Omega_e < 0$.

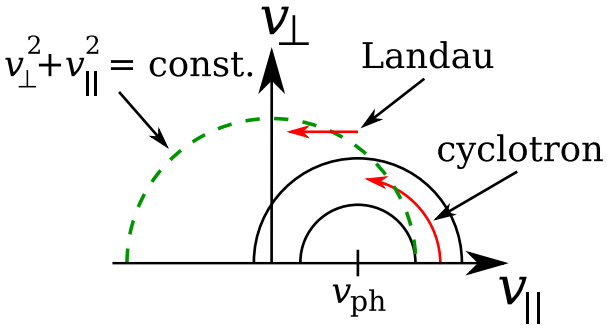

FIGURE 3 | Schematic illustration of quasi-linear diffusion in velocity space. The black semi-circles represent **Eq. 17** for a given parallel phase speed v_{ph}. The diffusive flux of resonant particles is locally tangent to these semi-circles (marked by the red arrows). The green-dashed semi-circle indicates $v_\perp^2 + v_\parallel^2$ = constant. If the diffusive flux crosses the green-dashed semi-circle from larger to smaller values of $(v_\perp^2 + v_\parallel^2)$, the resonant wave–particle interaction contributes to the growth of the resonant waves with parallel phase speed v_{ph}. Examples for Landau-resonant and cyclotron-resonant interactions are indicated.

Our cylindrical coordinate system is aligned with $\boldsymbol{B}_0$, so that waves with $v_{ph} > 0$ propagate in the direction of $\boldsymbol{B}_0$. The direction of propagation of wave solutions with respect to $\boldsymbol{B}_0$ can be reversed mathematically in two ways: either by changing the sign of ω_{kr} or by changing the sign of $k_\parallel$. Although this choice does not affect the physics described by the wave theory, it has an impact on the polarisation and thus the applicable resonance condition. We implicitly assume that $\omega_{kr} \geq 0$ throughout this work, so that a reversal of the direction of propagation corresponds to changing the sign of $k_\parallel$ in our convention[2].

Figure 3 illustrates the quasi-linear diffusion in velocity space. The black semi-circles represent **Eq. 17**. Particles at $v_\parallel = v_{ph}$ fulfill the Landau-resonance condition with $n = 0$ according to **Eq. 16**. If $\hat{G} f_{0j} > 0$ at $v_\parallel = v_{ph}$, the direction of the diffusive flux of Landau-resonant particles is as indicated by the red arrow marked "Landau". For Landau-resonant particles, $\hat{G} f_{0j} = (v_\perp / v_{ph})(\partial f_{0j}/\partial v_\parallel)$.

Assuming that particles with $v_\parallel = v_{res} > v_{ph}$ fulfill a cyclotron resonance condition according to **Eq. 16** in this example, the diffusive flux of these cyclotron-resonant particles is as indicated by the red arrow marked "cyclotron" as long as $\hat{G} f_{0j} > 0$ at $v_\parallel = v_{res}$.

As the resonant particles diffuse through velocity space, their $v_\parallel$ changes. If the particles interact with waves with $k_\perp = 0$ on only a single branch of the dispersion relation, then at each value of $v_\parallel$ the particles typically resonate with waves at a single value of $k_\parallel$. This resonant value of $k_\parallel$, which can be regarded as a function of $v_\parallel$, corresponds to a unique parallel phase velocity v_{ph}, and over time the particles trace out a one-dimensional diffusion contour in velocity space that is locally tangent to the semicircles defined by **Eq. 17**. For dispersive waves, v_{ph} varies with $k_\parallel$, and hence with $v_\parallel$ of the resonant particles, and thus the full diffusion contour is not semi-circular, because the centre of the locally tangent semi-circle evolves during the diffusion process.

The quasi-linear evolution according to the concepts outlined so far generally leads to a change of the integrated particle kinetic energy of f_{0j} (i.e., the second velocity moment of f_{0j}). If the average kinetic energy $m_j (v_\perp^2 + v_\parallel^2)/2$ of the resonant particles decreases in the quasi-linear diffusion process, this energy is transferred into the resonant waves, leading to growth of the wave amplitude and thus instability. If the average energy of the resonant particles increases, this energy is taken from the resonant waves, corresponding to wave damping. Our graphical representation in **Figure 3** allows us to evaluate the energy behaviour by comparing the direction of the diffusive flux of resonant particles with semi-circles around the origin (green-dashed in **Figure 3**). These semi-circles represent isocontours of constant $(v_\perp^2 + v_\parallel^2)$. If the direction of the diffusive flux locally crosses these semi-circles from larger to smaller $(v_\perp^2 + v_\parallel^2)$, the process corresponds to an instability. If it crosses these semi-circles in the other direction, the process corresponds to damping. In the specific example shown in **Figure 3**, both the marked Landau-resonant and the marked cyclotron-resonant particles contribute to an instability of the resonant wave at phase speed v_{ph}. The question of damping/instability thus ultimately simplifies to an investigation of the relative alignments between the semi-circles in velocity space defined by **Eq. 17**, the isocontours of f_{0j}, and the isocontours of $(v_\perp^2 + v_\parallel^2)$ at the speed that fulfills **Eq. 16** for resonant wave–particle interactions.

The propagation direction and the polarisation of the waves under consideration have a strong impact on the quasi-linear diffusion process. If the waves are purely parallel-propagating (i.e., $k_\perp = 0$), then $\xi_j = k_\perp v_\perp / \Omega_j = 0$ in **Eq. 14**. The Bessel functions have the property

$$J_m(0) = \begin{cases} 1 & \text{if } m = 0, \\ 0 & \text{otherwise.} \end{cases} \tag{18}$$

This property simplifies **Eq. 12** considerably for parallel-propagating waves. According to **Eq. 14**, parallel-propagating waves only have $\psi_k^{j,n} \neq 0$ if $n = +1$, $n = -1$, or $n = 0$. If a parallel-

[2]In this convention, $E_{k,l}$ corresponds to left-hand polarisation and $E_{k,r}$ corresponds to right-hand polarisation. The meaning of $E_{k,l}$ and $E_{k,r}$ for the characterisation of the sense of polarisation as left-circular and right-circular swaps when $\omega_{kr} < 0$. In a plasma with symmetric distribution functions around $v_\parallel = 0$, a forward-propagating wave solution with $\omega_{kr} > 0$ and $k_\parallel > 0$ has the same sense of polarisation in terms of $E_{k,l}$ and $E_{k,r}$ as the corresponding backward-propagating solution with $\omega_{kr} > 0$ and $k_\parallel < 0$.

propagating wave is purely left-circularly polarised (i.e., if $E_{k,\mathrm{r}} = E_{kz} = 0$), only the cyclotron resonance with $n = +1$ contributes to the sum in **Eq. 12**. If a parallel-propagating wave is purely right-circularly polarised (i.e., if $E_{k,\mathrm{l}} = E_{kz} = 0$), only the cyclotron resonance with $n = -1$ contributes to the sum in **Eq. 12**. Lastly, if a parallel-propagating wave is purely longitudinal (i.e., if $E_{k,\mathrm{r}} = E_{k,\mathrm{l}} = 0$), only the Landau resonance with $n = 0$ contributes to the sum in **Eq. 12**. This simplification of the quasi-linear diffusion equations is particularly useful since many instabilities have maximum growth for $k_\perp = 0$, in which case they exhibit these pure polarisation properties according to linear Vlasov–Maxwell theory. For example, the parallel-propagating fast-magnetosonic/whistler wave is purely right-circularly polarised. The parallel-propagating Alfvén/ion-cyclotron wave is purely left-circularly polarised, and the parallel-propagating Langmuir wave is purely longitudinal. We note that these definitions only apply when $\omega_{kr} > 0$ according to our convention. For waves with oblique wave vectors, in general, all n must be considered and the polarisation is typically "mixed" with contributions from non-zero $E_{k,\mathrm{r}}$, $E_{k,\mathrm{l}}$, and E_{kz}. Nevertheless, it is often useful to consider that the Bessel-function contributions $J_m(\xi_j)$ in **Eq. 12** are greater for $m = 0$ than for other m when ξ_j is moderately small, which is often the case for the majority of the resonant particles.

In addition to its mathematical rigour, the quasi-linear-diffusion framework provides us with a visual aid to understand the physics of resonant micro-instabilities. It can be shown that the description of wave damping and instability in terms of quasi-linear diffusion is consistent with its description in terms of γ_k from solutions of linear Vlasov–Maxwell theory as far as the assumptions of both frameworks are fulfilled (Kennel and Engelmann, 1966; Kennel and Wong, 1967; see also Chandran et al., 2010).

The instabilities discussed in this review occur on a variety of length scales, which are often related to the characteristic plasma scales of the system (Verscharen et al., 2019b). We define the inertial length of species j as

$$d_j \equiv \frac{c}{\omega_{\mathrm{p}j}} = \frac{v_{\mathrm{A}j}}{|\Omega_j|} = \sqrt{\frac{m_j c^2}{4\pi n_j q_j^2}}, \tag{19}$$

where $\omega_{\mathrm{p}j} \equiv \sqrt{4\pi n_j q_j^2/m_j}$ is the plasma frequency of species j, $v_{\mathrm{A}j} \equiv B_0/\sqrt{4\pi n_j m_j}$ is the Alfvén speed of species j and n_j is the background number density of species j. We define the gyro-radius of species j as

$$\rho_j \equiv \frac{w_{\perp j}}{|\Omega_j|} = \sqrt{\frac{2k_{\mathrm{B}}T_{\perp j} m_j c^2}{q_j^2 B_0^2}}, \tag{20}$$

where $w_{\perp j} \equiv \sqrt{2k_{\mathrm{B}}T_{\perp j}/m_j}$ is the perpendicular thermal speed of species j and k_{B} is the Boltzmann constant. For electrostatic instabilities, the Debye length

$$\lambda_j \equiv \sqrt{\frac{k_{\mathrm{B}}T_{\parallel j}}{4\pi n_j q_j^2}} \tag{21}$$

of species j defines an important spatial reference scale. Lastly, we define the following dimensionless ratios of kinetic to magnetic pressure:

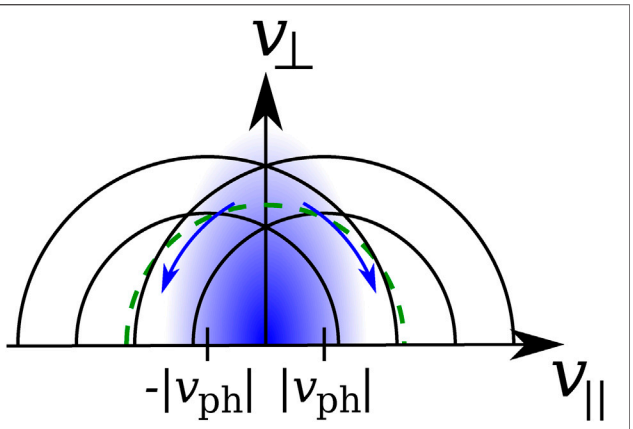

FIGURE 4 | Schematic illustration of the quasi-linear diffusion in the electron whistler anisotropy instability. The blue shaded area represents the anisotropic electron population with $T_{\perp\mathrm{e}} > T_{\parallel\mathrm{e}}$. The black semi-circles represent **Eq. 17** for fast-magnetosonic/whistler waves with parallel phase speed $|v_{\mathrm{ph}}|$ (propagating in the direction parallel to $\boldsymbol{B}_0$) and $-|v_{\mathrm{ph}}|$ (propagating in the direction anti-parallel to $\boldsymbol{B}_0$). The diffusive flux of cyclotron-resonant particles is shown by the blue arrows. The green-dashed semi-circle indicates $v_\perp^2 + v_\parallel^2 =$ constant.

$$\beta_j \equiv \frac{8\pi n_j k_{\mathrm{B}} T_j}{B_0^2}, \qquad \beta_{\perp j} \equiv \frac{8\pi n_j k_{\mathrm{B}} T_{\perp j}}{B_0^2}, \qquad \text{and} \qquad \beta_{\parallel j} \equiv \frac{8\pi n_j k_{\mathrm{B}} T_{\parallel j}}{B_0^2}, \tag{22}$$

where T_j is the scalar temperature of species j, which we use in the case of isotropic plasmas when $T_j = T_{\perp j} = T_{\parallel j}$.

3 RESONANT INSTABILITIES DRIVEN BY TEMPERATURE ANISOTROPIES

We discuss two types of resonant instabilities driven by electron temperature anisotropy: the electron whistler anisotropy instabilty and the propagating electron firehose instability. Both instabilities are associated with electromagnetic normal modes of the plasma. Under typical solar-wind conditions, non-resonant anisotropy-driven instabilities often have lower thresholds than the resonant instabilities. The non-resonant instabilities are discussed in **Section 5**. In plasmas with $\omega_{\mathrm{pe}} < |\Omega_{\mathrm{e}}|$, electrostatic instabilities exist that are driven by electron anisotropy (Gary and Cairns, 1999). However, since this condition is not fulfilled in the solar wind, we do not discuss these instabilities further.

3.1 Electron Whistler Anisotropy Instability

The electron whistler anisotropy instability is driven when $T_{\perp\mathrm{e}} > T_{\parallel\mathrm{e}}$ (Kennel and Petschek, 1966; Scharer and Trivelpiece, 1967; Gary and Karimabadi, 2006; Lazar et al., 2022). It is an instability of the fast-magnetosonic/whistler wave with $\Omega_{\mathrm{p}} \ll \omega_{kr} < |\Omega_{\mathrm{e}}|$ and $k \lesssim 1/d_{\mathrm{e}}$ at maximum growth. The instability has maximum growth when $k_\perp = 0$.

Figure 4 describes the quasi-linear evolution of $f_{0\mathrm{e}}$ under the action of the electron whistler anisotropy instability. The initial

electron distribution is elongated (i.e., anisotropic) in the direction perpendicular to the background magnetic field. Electrons with $v_\parallel > 0$ resonate with fast-magnetosonic/whistler waves at parallel phase speed $-|v_{\rm ph}|$ (i.e., propagating oppositely to the direction of $\boldsymbol{B}_0$) through the $n = +1$ cyclotron resonance according to **Eq. 16**. Electrons with $v_\parallel < 0$ resonate with waves at parallel phase speed $+|v_{\rm ph}|$ through the $n = -1$ cyclotron resonance according to **Eq. 16**.

The relative alignment between the isocontours of f_{0e} at the value of $v_\parallel$ that fulfills **Eq. 16** and the black semi-circles around $\pm|v_{\rm ph}|$ in **Figure 4** guarantees that the quasi-linear diffusion is locally directed tangent to the blue arrows. Therefore, $v_\perp$ of the resonant electrons decreases while their $|v_\parallel|$ increases. Overall, this process leads to a reduction of $(v_\perp^2 + v_\parallel^2)$ and thus of the energy of the resonant electrons. This energy is transferred into the resonant fast-magnetosonic/whistler waves in both directions of propagation. As in the case of the propagating electron firehose instability presented in **Section 3.2**, the overall temperature anisotropy of the distribution decreases in this process until the distribution function relaxes to a quasi-linear plateau in the part of velocity space occupied by resonant electrons. If f_{0e} is asymmetric around $v_\parallel = 0$, the energy in the unstable counter-propagating waves can be imbalanced.

Kennel and Petschek (1966) give a necessary condition for instability of the electron whistler anisotropy instability as

$$\frac{T_{\perp e}}{T_{\parallel e}} - 1 > \frac{1}{\frac{|\Omega_e|}{\omega_{kr}} - 1}. \tag{23}$$

The unstable mode follows the approximate dispersion relation (Gary, 1993)

$$\frac{\omega_{kr}}{\Omega_p} \simeq k_\parallel^2 d_p^2 \left[1 + \left(\frac{T_{\perp e}}{T_{\parallel e}} - 1\right)\frac{\beta_{\parallel e}}{2}\right]. \tag{24}$$

When $T_{\parallel e} \sim T_{\parallel p}$ and $\beta_{\parallel e} \sim 1$ as in the solar wind, protons are unlikely to undergo a significant resonant interaction with parallel-propagating fast-magnetosonic/whistler waves. Therefore, this instability does not compete with proton-resonant damping.

The necessary relative alignment between the isocontours of f_{0e} at the value of $v_\parallel$ that fulfills **Eq. 16** and the semi-circles around $\pm|v_{\rm ph}|$ as shown in **Figure 4** can also be fulfilled in bi-κ electron distributions (Lazar et al., 2011, 2013; Shaaban et al., 2021). Likewise, the instability criteria can also be fulfilled in plasmas consisting of anisotropic core and halo populations (Gary et al., 2012; Lazar et al., 2018a). In these cases, anisotropic halo electrons resonate with parallel-propagating fast-magnetosonic/whistler waves through the same mechanism as the electron core (Lazar et al., 2015). If the core is isotropic, the halo driving competes with cyclotron-resonant core damping.

The electron whistler anisotropy instability is believed to be responsible for the sporadic generation of parallel-propagating fast-magnetosonic/whistler waves that are intermittently observed in the solar wind (Tong et al., 2019a; Jagarlamudi et al., 2020; Vasko et al., 2020). Observations show that the solar wind very rarely exhibits plasma conditions above the instability threshold though (Štverák et al., 2008).

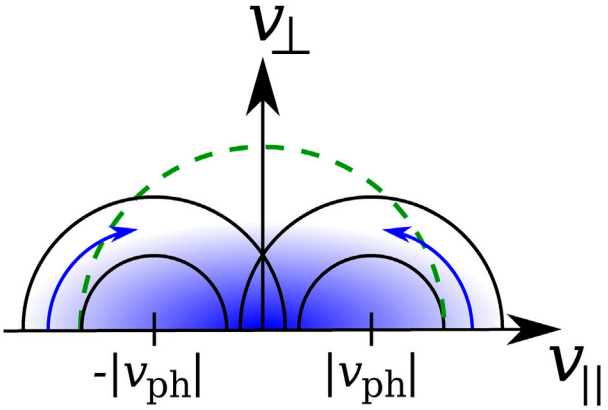

FIGURE 5 | Schematic illustration of the quasi-linear diffusion in the propagating electron firehose instability. The blue shaded area represents the anisotropic electron population with $T_{\parallel e} > T_{\perp e}$. The black semi-circles represent **Eq. 17** for modified fast-magnetosonic/whistler waves with parallel phase speed $|v_{\rm ph}|$ (propagating in the direction parallel to $\boldsymbol{B}_0$) and $-|v_{\rm ph}|$ (propagating in the direction anti-parallel to $\boldsymbol{B}_0$). The diffusive flux of cyclotron-resonant particles is shown by the blue arrows. The green-dashed semi-circle indicates $v_\perp^2 + v_\parallel^2 =$ constant.

A review of early simulation work of the electron whistler anisotropy instability with quasi-linear context is given by Cuperman (1981). Particle-in-cell simulations reveal that this instability changes its properties in the low-$\beta_{\parallel e}$ regime, in which the wave at maximum growth is predominantly oblique and electrostatic, so that Landau-resonant processes become important (Gary et al., 2011). Kinetic simulations of the electron whistler anisotropy instability agree reasonably well with quasi-linear predictions in terms of the behaviour of the instability at saturation (Kim et al., 2017). In particular, these simulations indicate the occurrence of weakly resonant wave–particle interactions. While these numerical simulations start with bi-Maxwellian electron distributions, more recently, the impact of more realistic electron distribution functions has been explored. For instance, Lazar et al. (2022) perform particle-in-cell simulations with bi-κ electron distributions with different $\beta_{\parallel e}$. In the explored cases, the presence of suprathermal electrons leads to higher growth rates and oscillation amplitudes than in the bi-Maxwellian case.

3.2 Propagating Electron Firehose Instability

The propagating electron firehose instability is driven when $T_{\parallel e} > T_{\perp e}$ (Hollweg and Völk, 1970; Pilipp and Völk, 1971; Li and Habbal, 2000). It corresponds to an instability of left-hand polarised fast-magnetosonic/whistler modes that undergo a significant change in their dispersion relation under the relevant unstable plasma conditions. In the following discussion, we focus on the parallel-propagating case, in which $k_\perp = 0$.

When $T_{\perp e} = T_{\parallel e}$, the fast-magnetosonic/whistler branch of the dispersion relation is right-circularly polarised. However, when $T_{\perp e}/T_{\parallel e}$ is sufficiently small, the fast-magnetosonic/

whistler wave becomes left-circularly polarised as $|k_\parallel|$ increases from small to large values. These left-circularly polarised fast-magnetosonic/whistler waves can interact with electrons when **Eq. 16** is satisfied for the $n = +1$ resonance, and such interactions can drive the wave unstable. When unstable, this mode satisfies $\Omega_p < \omega_{kr} \ll |\Omega_e|$ and $1/d_p < k_\parallel < 1/d_e$ (Micera et al., 2020a).

Figure 5 describes the quasi-linear evolution of f_{0e} under the action of the propagating electron firehose instability. The initial electron distribution is elongated (i.e., anisotropic) in the direction parallel to the background magnetic field. Electrons with $v_\parallel > |v_{ph}|$ resonate with waves at $+|v_{ph}|$ through the $n = +1$ cyclotron resonance according to **Eq. 16**. Electrons with $v_\parallel < -|v_{ph}|$ resonate with waves propagating in the anti-parallel direction to $\boldsymbol{B}_0$ (i.e., with a phase speed $-|v_{ph}|$) through the $n = -1$ cyclotron resonance according to **Eq. 16**.

The relative alignment between the isocontours of f_{0e} at the value of $v_\parallel$ that fulfills **Eq. 16** and the black semi-circles around $\pm|v_{ph}|$ in **Figure 5** guarantees that the quasi-linear diffusion is locally directed tangent to the blue arrows. Therefore, $v_\perp$ of the resonant electrons increases while their $|v_\parallel|$ decreases. Overall, this process leads to a reduction of $(v_\perp^2 + v_\parallel^2)$ and thus of the kinetic energy of the resonant electrons. This energy is transferred into the resonant fast-magnetosonic/whistler waves in both directions of propagation. As in the case of the electron whistler anisotropy instability discussed in **Section 3.1**, the overall temperature anisotropy of the distribution decreases in this process until the distribution function relaxes to a quasi-linear plateau in the part of velocity space occupied by resonant electrons. If f_{0e} is asymmetric around $v_\parallel = 0$, the energy in the unstable counter-propagating waves can be imbalanced.

In addition to anisotropic core electrons, also suprathermal electron populations such as an anisotropic halo with a bi-κ distribution can drive the propagating electron firehose instability (Lazar et al., 2017; Shaaban et al., 2021).

Since this instability is left-hand polarised, cyclotron-resonant proton damping counteracts the driving by cyclotron-resonant electrons. Due to its high frequency compared to Ω_p, the instability's growth rate depends only weakly on $T_{\parallel e}/T_{\parallel p}$ and $T_{\perp p}/T_{\parallel p}$ (Hollweg and Völk, 1970; Gary and Madland, 1985). The non-propagating firehose instability discussed in **Section 5.2** often has a lower threshold than the propagating firehose instability under most solar-wind conditions (Paesold and Benz, 1999; Li and Habbal, 2000; Gary and Nishimura, 2003).

One-dimensional, relativistic particle-in-cell simulations of the propagating electron firehose instability underline its possible role as a temperature-isotropisation mechanism in solar-flare plasmas (Paesold and Benz, 1999; Messmer, 2002). Simulations with both anisotropic protons and electrons reveal that the concurrent presence of a proton and electron temperature anisotropy can increase the growth rate of the propagating *proton* firehose instability compared to plasmas with isotropic electrons (Micera et al., 2020a). Quasi-parallel and exactly parallel electron firehose modes become dominant after the saturation of oblique modes with higher growth rates (see also **Section 5.2**; Camporeale and Burgess, 2008; Innocenti et al., 2019a, the latter study is conducted within an expanding-box framework).

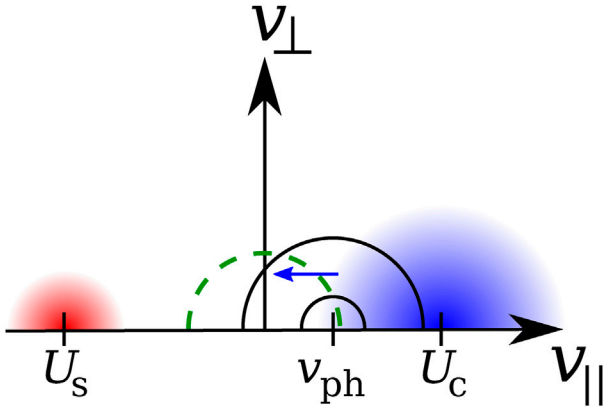

FIGURE 6 | Schematic illustration of the quasi-linear diffusion in the electron/ion-acoustic instability and in the kinetic Alfvén heat-flux instability. The blue shaded area represents the core electron population with bulk velocity U_c, and the red shaded area represents the strahl population with bulk velocity U_s. The black semi-circles represent **Eq. 17** for either wave type with parallel phase speed v_{ph}. The diffusive flux of Landau-resonant particles is shown by the blue arrow. The green-dashed semi-circle indicates $v_\perp^2 + v_\parallel^2$ = constant. In our geometrical convention with $v_{ph} > 0$, $U_s < 0$ here, which indicates that the diffusive flux points in the $-\boldsymbol{B}_0$ direction. We note that $U_s < 0$ still corresponds to the anti-sunward direction if $\boldsymbol{B}_0$ points towards the Sun.

4 RESONANT INSTABILITIES DRIVEN BY REFLECTIONAL ASYMMETRIES IN THE DISTRIBUTION FUNCTION

In this section, we discuss instabilities driven by asymmetries in the electron distribution function around $v_\parallel = 0$. These asymmetries can be represented by beams, multi-beam structures, or skewness in the electron distribution (Forslund, 1970). We distinguish between electrostatic and electromagnetic instabilities driven by reflectional asymmetries in the distribution function. The electrostatic approximation is valid in plasmas with $\beta_j \ll 1$ for all j. In this case, $\boldsymbol{E} \approx -\nabla\phi$, where ϕ is the electrostatic potential, and $\boldsymbol{B} \approx \boldsymbol{B}_0$. With increasing β_j, however, the coupling between electric and magnetic fluctuations increases, and the fluctuations become increasingly electromagnetic. Nevertheless, some electrostatic modes also exist in plasmas with moderate to high β_j, especially when they propagate along $\boldsymbol{B}_0$. Electromagnetic beam instabilities compete with their electrostatic counterparts in the presence of hot electron beams and reasonably large β_j, which is often (but not always) the case in the solar wind. Unless stated otherwise, we work in the reference frame in which the background bulk speed of the protons is zero.

4.1 Electron/Ion-Acoustic Instability

The electron/ion-acoustic instability is an example of an electrostatic instability driven by an asymmetry in the electron distribution function. It is driven by the Landau-resonance of

electrons with the ion-acoustic mode (Fried and Gould, 1961). In a magnetised plasma, it has maximum growth when $k_\perp = 0$.

The electron/ion-acoustic instability can be driven if there is a non-zero current parallel to $\boldsymbol{B}_0$ in a plasma with a single proton and a single electron component. While the ion-acoustic wave is strongly Landau-damped in plasmas with $T_e \approx T_p$, a sufficiently large relative drift between the protons and the electrons leads to an instability. The dispersion relation of the ion-acoustic wave is given by (Gary, 1993; Verscharen et al., 2017)

$$\omega_{kr} \approx k_\parallel c_s = k_\parallel \sqrt{\frac{3k_B T_{\parallel p} + k_B T_{\parallel e}}{m_p}}, \tag{25}$$

where c_s is the ion-acoustic speed. The protons provide the wave inertia, while the proton and electron pressures provide the restoring force. In their wave evolution, protons behave like a one-dimensional adiabatic fluid, while the electrons are isothermal according to **Eq. 25**. When the instability is only weakly unstable (i.e., small $\gamma_m > 0$), it is a long-wavelength electrostatic instability with $k \ll 1/\lambda_p$. With increasing γ_m, the unstable wave-vector space increases to $0 < k \lesssim 1/\lambda_p$ (Gary, 1993).

The quasi-linear evolution of f_{0e} under the action of the electron/ion-acoustic instability corresponds to the case shown in **Figure 6**. If it is driven by the current between a single proton and a single electron component, the red strahl population in **Figure 6** can be ignored. Due to the relative drift between the core population and the protons, Landau-resonant electrons diffuse towards smaller $v_\parallel$, leading to a reduction in the kinetic energy of the resonant electrons. This process drives the resonant ion-acoustic waves unstable at the expense of the relative drift between protons and electrons.

For the case of a single drifting electron component, Gary (1993) gives an expression for the growth rate of the electron/ion-acoustic instability in a plasma with Maxwellian distribution functions under the assumption that $T_e \gg T_p$:

$$\gamma_k = \frac{\sqrt{\pi}\omega_{kr}^3}{2|k_\parallel|^3}\left(\frac{m_p}{k_B T_e}\right)\frac{k_\parallel U_c - \omega_{kr}}{w_e}\exp\left(-\frac{\left(\omega_{kr}/k_\parallel - U_c\right)^2}{w_e^2}\right), \tag{26}$$

where U_c is the bulk velocity of the single electron component in the proton reference frame. Combining **Eqs 25** and **26** shows that $\gamma_k > 0$ if $U_c > v_{ph}$, where $v_{ph} \approx c_s$. As shown in **Figure 6**, the transition from $U_c < v_{ph}$ to $U_c > v_{ph}$ marks the transition from a diffusion that raises $v_\parallel$ (the blue arrow would be pointing to the right in this case) of the Landau-resonant electrons to a diffusion that lowers their $v_\parallel$ (blue arrow pointing to the left as shown). The growth rate according to **Eq. 26** has a strong dependence on the electron temperature.

If the electron beam is very fast or the electrons are cold (i.e., $U_c \gtrsim w_e$), the dispersion relation of this unstable mode changes significantly from **Eq. 25**. In this cold-plasma regime, the instability transitions into the classic Buneman electron/ion two-stream instability (Buneman, 1959). It corresponds to the $P = 0$ mode in cold-plasma theory (Stix, 1992) with $\omega_{kr} \sim \omega_{pe}$ and maximum growth at $k_\parallel \simeq \omega_{pe}/U_c$ when $U_c \gg w_e$.

In the solar wind, the persistent occurrence of sufficiently strong field-aligned currents to drive the electron/ion-acoustic instability via this mechanism is unlikely. For reference, the most intense current densities in the solar wind at 1 au are typically $\sim 5\,\mathrm{nA/m^2}$ (Podesta and Roytershteyn, 2017), and the corresponding net drift between ions and electrons is very small (Vasko et al., 2022). However, a two-component electron configuration as shown in **Figure 6** consisting of a core and strahl population enables the same instability mechanism. In an electron–proton plasma with core and strahl populations, the system is free from parallel currents if

$$n_s U_s + n_c U_c = n_p U_p, \tag{27}$$

which is typically the case in the solar wind (Feldman et al., 1975; Salem et al., 2021). In this configuration, the Landau-resonant interaction between unstable core electrons and ion-acoustic waves leads to a reduction of $v_\parallel$ of the resonant electrons. As this corresponds to a reduction in U_c, the current-balance requirement from quasi-neutrality then also leads to a reduction in $|U_s|$ (see also Schroeder et al., 2021). Therefore, the electron/ion-acoustic instability is a candidate for the (indirect) regulation of the strahl heat flux in the solar wind (Gary, 1978). As shown in **Figure 6**, this instability does not scatter strahl electrons into the halo, although such a behaviour is found in the solar wind (Štverák et al., 2009).

Ion-acoustic waves have been observed in the solar wind (Gurnett and Anderson, 1977; Kurth et al., 1979; Gurnett, 1991; Píša et al., 2021). They often occur in sporadic bursts and at times when $T_{\parallel e} > T_{\parallel p}$ (Mozer et al., 2021b). Near the Sun, the condition that $T_{\parallel e} \gg T_{\parallel p}$ can be satisfied in low-speed solar wind. At small heliocentric distances, the proton temperature remains correlated with the wind speed, but the electron temperature is anti-correlated with the wind speed, most likely due to the initial conditions in the corona (Halekas et al., 2020; Maksimovic et al., 2020). The resulting conditions in slow-speed near-Sun solar wind thus favour the growth of the ion-acoustic wave. Indeed, Parker Solar Probe observes ion-acoustic waves under these conditions (Mozer et al., 2022). The loose correlation between ion-acoustic waves with periods of enhanced electron temperatures suggests that these waves may heat the core electrons. However, since high electron temperature itself favours the growth of the waves, the causality remains unclear.

Near 1 au, other instabilities often have lower thresholds than the electron/ion-acoustic instability though (Gary, 1978; Lemons et al., 1979). A direct stability analysis of measured electron distributions from Helios identifies a case that is unstable against the electron/ion-acoustic instability (Dum et al., 1980). Strong ion-acoustic wave bursts are also found near magnetic switchbacks (Mozer et al., 2021a). The exact generation mechanism of these waves is unclear, as an ion/ion-acoustic instability is also a possible candidate for the generation of these waves (Mozer et al., 2020; Graham et al., 2021).

The current-driven electron/ion-acoustic instability is studied numerically in the context of laser-heated laboratory plasmas (Detering et al., 2005).

4.2 Kinetic Alfvén Heat-Flux Instability

The kinetic Alfvén heat-flux instability is driven by the same instability mechanism as the electron/ion-acoustic instability shown in **Figure 6**. Also in this instability, Landau-resonant core electrons diffuse towards smaller $v_\parallel$. The unstable wave mode in this case is the highly-oblique kinetic Alfvén wave, which is an electromagnetic plasma mode. It corresponds to the small-wavelength extension of the Alfvén wave in highly oblique propagation (i.e., $k_\perp \rho_\mathrm{p} \gtrsim 1$ and $k_\perp \gg k_\parallel$). Its dispersion relation is given by (Howes et al., 2006)

$$\omega_{kr} \approx \frac{k_\parallel v_\mathrm{A} k_\perp \rho_\mathrm{p}}{\sqrt{\beta_\mathrm{p} + \frac{2}{1+T_\mathrm{e}/T_\mathrm{p}}}}. \tag{28}$$

In a Maxwellian electron–proton plasma, kinetic Alfvén waves undergo electron-Landau damping. With the introduction of a core–strahl configuration with sufficiently large $U_\mathrm{c} > 0$, the plasma can achieve $\partial f_{0\mathrm{e}}/\partial v_\parallel > 0$ at $v_\parallel = v_\mathrm{ph}$, in which case the kinetic Alfvén wave is driven unstable. The quasi-neutrality condition in **Eq. 27** enforces a simultaneous reduction of $|U_\mathrm{s}|$ when the instability reduces U_c like in the case of the electron/ion-acoustic instability. The kinetic Alfvén heat-flux instability has maximum growth at $k_\perp \lesssim 1/\rho_\mathrm{p}$ (Gary et al., 1975b).

Under typical solar-wind conditions with $\beta_j \sim 1$, the kinetic Alfvén heat-flux instability has a significantly greater threshold than the parallel whistler heat-flux instability (**Section 4.6**; Gary et al., 1975a; Gary et al., 1975b). In addition, this instability does not explain the observed scattering of strahl electrons into the halo population (Štverák et al., 2009) since only core electrons diffuse in velocity space towards smaller $v_\parallel$ (Verscharen et al., 2019a).

Kinetic Alfvén waves are often observed in the solar wind (Leamon et al., 1998; Bale et al., 2005; Chen et al., 2010; Salem et al., 2012; Šafránková et al., 2019; Roberts et al., 2020). However, their presence is generally neither attributed to ion-driven nor to electron-driven instabilities. Instead, they are interpreted as the small-wavelength extension of the Alfvénic cascade of solar-wind turbulence (Howes et al., 2006; Schekochihin et al., 2009).

The kinetic Alfvén heat-flux instability has not been investigated extensively via numerical simulations. In contrast, kinetic Alfvén waves more generally have been the subject of intense study. For example, Gary and Nishimura (2004) compare linear theory and particle-in-cell simulations (albeit employing a low proton-to-electron mass ratio) of kinetic Alfvén waves to quantify the associated electron heating. Particle-in-cell and gyrokinetic simulations of kinetic Alfvén turbulence in the solar wind are used to investigate ion and electron heating (Howes et al., 2008, 2011; Parashar et al., 2015; Hughes et al., 2017; Grošelj et al., 2018; Cerri et al., 2019). Furthermore, kinetic Alfvén waves are routinely generated in particle-in-cell simulations of magnetic reconnection in conjunction with Hall physics in the diffusion region (Rogers et al., 2001; Shay et al., 2011).

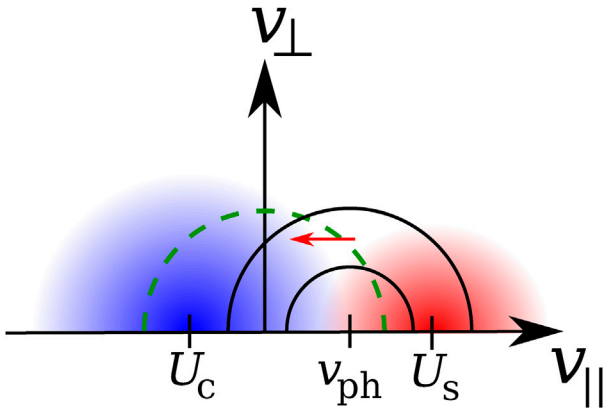

FIGURE 7 | Schematic illustration of the quasi-linear diffusion in the Langmuir instability and the electron-beam instability. The blue shaded area represents the core electron population with bulk velocity U_c, and the red shaded area represents the strahl population with bulk velocity U_s. The black semi-circles represent **Eq. 17** for either wave type with parallel phase speed v_ph. The diffusive flux of Landau-resonant particles is shown by the red arrow. The green-dashed semi-circle indicates $v_\perp^2 + v_\parallel^2 =$ constant.

4.3 Langmuir Instability and Electron-Beam Instability

The Langmuir instability and the electron-beam instability are two examples of beam-driven electrostatic instabilities (also called "high-frequency electron/electron instabilities"; Gary, 1985b). They are both driven by Landau-resonant electrons, which requires that $\partial f_{0\mathrm{e}}/\partial v_\parallel > 0$ at $v_\parallel = v_\mathrm{ph}$ when $v_\mathrm{ph} > 0$. This configuration corresponds to a bump-on-tail distribution. Both instabilities have maximum growth when $k_\perp = 0$.

In the relevant high-frequency range and assuming only a small modification to the real-part of the dispersion relation from any electron beam components, there are two solutions to the dispersion relation that become unstable. The Langmuir wave follows the dispersion relation

$$\omega_{kr} \approx \sqrt{\omega_\mathrm{pe}^2 + \frac{3}{2} k_\parallel^2 w_\mathrm{c}^2}. \tag{29}$$

If an electron-beam (strahl) component with bulk velocity U_s is present, the plasma also supports an electron-beam mode with (Gary, 1978)

$$\omega_{kr} \approx k_\parallel U_\mathrm{s}. \tag{30}$$

The criterion for distinguishing which of the two modes becomes unstable when $\partial f_{0\mathrm{e}}/\partial v_\parallel > 0$ at $v_\parallel = v_\mathrm{ph}$ depends on the speed, temperature, and relative density of the beam (O'Neil and Malmberg, 1968). Under unstable conditions, the Langmuir wave is the relevant mode if (Gary, 1993)

$$\left(\frac{\sqrt{2}\,U_\mathrm{s}}{w_\mathrm{s}}\right)^3 \left(\frac{n_\mathrm{s}}{n_\mathrm{c}}\right) < 1, \tag{31}$$

and the electron-beam mode is the relevant mode if

$$\left(\frac{\sqrt{2}U_s}{w_s}\right)^3\left(\frac{n_s}{n_c}\right)\gtrsim 1. \quad (32)$$

Both the Langmuir and the electron-beam instability have high frequencies (compared to Ω_p) and wave numbers $k_\parallel \ll 1/\lambda_e$, often even $k_\parallel \lesssim 1/\lambda_p$, at maximum growth (Gary, 1993).

The quasi-linear evolution of f_{0e} under the action of the Langmuir instability or of the electron-beam instability is shown in **Figure 7**. Landau-resonant strahl electrons diffuse towards smaller $v_\parallel$ in this configuration, while the core bulk velocity increases in order to guarantee current balance according to **Eq. 27**. This process leads to a flattening of the distribution function around $v_\parallel = v_{ph}$. If the dispersion relation in **Eq. 30** were fulfilled exactly and the strahl distribution were symmetric around $v_\parallel = U_s$, then $\partial f_{0e}/\partial v_\parallel = 0$ for Landau-resonant electrons at $v_\parallel = v_{ph}$. In this case, the instability would not act. This illustrates the importance of subtle modifications to the dispersion relation due to the beam component itself so that U_s is slightly greater than v_{ph} in order to create an unstable configuration.

Under certain parameter combinations, especially at large beam speeds, the Langmuir mode and the electron-beam mode couple in their dispersion relation (Gary, 1993). Since the electron-beam mode's phase speed is approximately equal to the parallel speed of the resonant electrons, it typically grows over a wide range of frequencies, which is important in the Earth's foreshock, where bump-on-tail configurations occur frequently (Fuselier et al., 1985). However, this behaviour changes when the modes couple because then the dispersion relation becomes more complex.

In the cold-plasma limit (i.e., for very fast and cold beams with $U_s \gg w_s$ and $U_s \gg w_c$), the electron-beam instability corresponds to the classical electron two-stream instability. In this limit, the instability has $\omega_{kr} \simeq \omega_{pe}$ and a maximum growth rate of (Gary, 1993)

$$\gamma_m \simeq \frac{\sqrt{3}}{2}\left(\frac{n_s}{2n_c}\right)^{1/3}\omega_{pc}. \quad (33)$$

In low-β_c conditions, the Langmuir and electron-beam instabilities can have lower thresholds than other beam-driven instabilities. However, they both require a bump-on-tail configuration in order to be driven. The electron strahl does not generally generate such a non-monotonic $v_\parallel$-dependence of f_{0e}. However, observations in the Earth's foreshock find evidence for the Langmuir instability when tenuous and fast electron beams are present, and for the electron-beam instability when denser and slower electron beams are present (Etcheto and Faucheux, 1984; Lacombe et al., 1985; Onsager and Holzworth, 1990).

Langmuir waves are often observed in the solar wind at different heliospheric distances (Kennel et al., 1980). They frequently occur at the same time as narrow-band electromagnetic waves identified as whistler waves, potentially suggesting a common origin (Jagarlamudi et al., 2021).

Two-dimensional, electromagnetic particle-in-cell simulations of a core-strahl electron configuration reveal that the electrostatic electron-beam instability also develops fluctuations in the perpendicular electric-field component, which scatter strahl electrons towards greater $v_\perp$ (Gary and Saito, 2007). A Fokker–Planck model of wave–particle interactions between an electron beam and the Langmuir instability suggests a similar process (Pavan et al., 2013).

4.4 Electron/Ion-Cyclotron Instability

In low-β_j plasmas, highly oblique electrostatic ion-cyclotron waves exist (D'Angelo and Motley, 1962; Stix, 1992). These modes occur in bands between the harmonics of the proton gyrofrequency (Gary, 1993):

$$m\Omega_p < \omega_{kr} < (m+1)\Omega_p, \quad (34)$$

where $m \geq 1$ is the integer harmonic order of the electrostatic ion-cyclotron wave.

In a plasma consisting of a single electron and a single proton population, electrostatic ion-cyclotron waves can become unstable if there is a sufficiently large current given by a difference in the bulk speeds of the electrons and the protons parallel to $\boldsymbol{B}_0$ (Drummond and Rosenbluth, 1962; Kindel and Kennel, 1971). Strong Landau-resonant interactions between the electrons and the harmonics of the ion-cyclotron wave are responsible for the driving of this instability. The wave number at maximum growth typically fulfills $k_\perp \sim 1/\rho_p$.

The quasi-linear evolution of f_{0e} is similar to the process described in **Figure 7**, but where the strahl population is the only electron population. Since electrostatic ion-cyclotron waves are highly dispersive, v_{ph} depends strongly on $v_\parallel$ of the resonant electrons.

The ion-cyclotron wave with $m = 1$ has the lowest threshold. With increasing U_c, harmonics with higher m become unstable as well. Cyclotron-resonant interactions with protons compete with the Landau-resonant electron driving. Therefore, the instability threshold depends strongly on T_p (Gary, 1993). For $T_e/T_p \lesssim 10$, the electron/ion-cyclotron instability has a lower threshold than the current-driven electron/ion-acoustic instability. At $T_e/T_p \gtrsim 50$, the unstable ion-cyclotron branch of the dispersion relation merges with the unstable ion-acoustic branch, so that this instability loses its identity.

As in the case of other current-driven instabilities, we expect that the introduction of a core-strahl configuration can also create the conditions necessary for the electron/ion-cyclotron instability in a plasma fulfilling **Eq. 27**. In this case, the instability mechanism requires $\partial f_{0e}/\partial v_\parallel > 0$ at $v_\parallel = v_{ph}$ and would be the same as shown in **Figure 7**. However, we are not aware of detailed studies of the conditions necessary for a core-strahl electron system to drive electrostatic ion-cyclotron waves unstable.

In order to overcome cyclotron-resonant proton damping, this instability is only relevant in plasma environments with $\beta_{\parallel p} \ll 1$. Therefore, the electron/ion-cyclotron instability is mostly thought to occur within low-β_j environments such as the auroral ionosphere (Ashour-Abdalla and Thorne, 1978; Bergmann, 1984). Driven by electrons and damped by protons, the unstable ion-cyclotron waves lead to efficient proton heating in this environment (Okuda and Ashour-Abdalla, 1983; Ashour-Abdalla and Okuda, 1984).

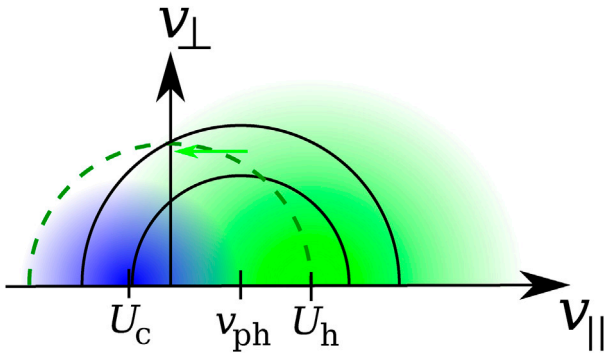

FIGURE 8 | Schematic illustration of the quasi-linear diffusion in the electron/electron-acoustic instability. The blue shaded area represents the core electron population with bulk velocity U_c, and the green shaded area represents the halo population with bulk velocity U_h. The electron/electron-acoustic instability requires $T_h \gg T_c$. The black semi-circles represent **Eq. 17** for electron-acoustic waves with parallel phase speed v_{ph}. The diffusive flux of Landau-resonant particles is shown by the green arrow. The green-dashed semi-circle indicates $v_\perp^2 + v_\parallel^2 =$ constant.

A Fokker–Planck model of the current-driven electron/ion-cyclotron instability shows the presence of quasi-linear cyclotron-resonant diffusion effects on the proton distribution function, leading to its flattening in the resonance region (Harvey, 1975). These simulation results also confirm that the conditions for this instability to be excited are not commonly satisfied in typical solar-wind conditions.

4.5 Electron/Electron-Acoustic Instability

In a plasma consisting of protons and two electron populations, an additional electrostatic mode with properties similar to the ion-acoustic wave from **Section 4.1** emerges (Watanabe and Taniuti, 1977). This mode is called the electron-acoustic wave. In order for this mode to have a small damping rate, it is required that the two electron components have comparable densities but that one of the electron components is much hotter than the other (Gary, 1987). We identify the hotter component with a possible halo population in the solar wind.

If $n_h \sim n_c$, $T_h \gg T_c$, and $U_h = U_c = 0$, the electron-acoustic wave has the dispersion relation (Watanabe and Taniuti, 1977; Gary, 1987)

$$\omega_{kr} \approx \omega_{pc} \sqrt{\frac{1 + 3k_\parallel^2 \lambda_c^2}{1 + 1/k_\parallel^2 \lambda_h^2}}. \tag{35}$$

The cold electron component provides the wave inertia, while the high mobility of the hot electrons provides the restoring force of the electron-acoustic wave. At long wavelengths, v_{ph} is approximately proportional to $\sqrt{T_h}$.

With the introduction of a sufficient relative drift speed between the core and halo populations, the electron-acoustic mode becomes unstable through the Landau-resonant interaction between halo electrons and the electron-acoustic mode. In this case, the mode still fulfills **Eq. 35**, but in the frame of the core electrons, which provide the wave inertia. The wave number of the electron/electron-acoustic instability at maximum growth typically fulfills $1/\lambda_h < k_\parallel < 1/\lambda_c$. It has maximum growth when $k_\perp = 0$.

If the electron-acoustic mode is moderately unstable (i.e., $|\gamma_m| \ll \omega_{kr}$), its growth rate is given by (Gary, 1993)

$$\gamma_k \simeq \frac{\omega_{pc}}{2|k_\parallel|^3 \lambda_h^2} \sqrt{\pi} \left(\frac{k_\parallel U_h' - \omega_{kr}'}{w_h} \right) \exp\left(- \frac{\left(U_h' - \omega_{kr}'/k_\parallel \right)^2}{w_h^2} \right) \tag{36}$$

where U_h' and ω_{kr}' are the bulk velocity of the halo population and the wave frequency in the reference frame of the core population: $U_h' = U_h - U_c$ and $\omega_{kr}' = \omega_{kr} - k_\parallel U_c$. **Eq. 36** shows that, as for all Landau-resonant instabilities, the electron/electron-acoustic instability requires $U_h > v_{ph}$ when $v_{ph} > 0$ so that $\partial f_{0e}/\partial v_\parallel > 0$ at the value of $v_\parallel$ of the resonant electrons.

The quasi-linear evolution of f_{0e} under the action of the electron/electron-acoustic instability is shown in **Figure 8**. Landau-resonant halo electrons diffuse towards smaller $v_\parallel$ in this configuration.

The electron/ion-acoustic instability from **Section 4.1** has a lower threshold than the electron/electron-acoustic instability unless $T_h \gg T_c$ (Gary, 1987). In addition, a substantial $n_h \sim n_c$ is required. Both conditions are not generally fulfilled in the solar wind. However, cusp hiss fluctuations in the magnetospheric context are attributed to electron-acoustic fluctuations (Thomsen et al., 1983; Marsch, 1985). Electron-acoustic waves, typically with nonlinearly steepened wave forms, are reported in the Earth's inner magnetosphere, where the density of hot electrons can be greater than the density of cold electrons during hot plasma injections from the magnetotail (Vasko et al., 2017; Dillard et al., 2018). In the near-Sun environment, the electron/electron-acoustic instability may be relevant for the regulation of the solar-wind heat flux (Sun et al., 2021).

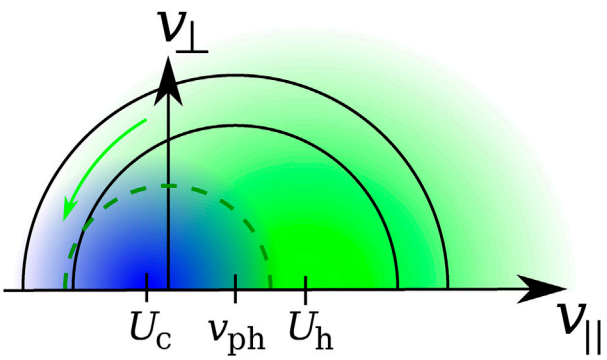

FIGURE 9 | Schematic illustration of the quasi-linear diffusion in the whistler heat-flux instability. The blue shaded area represents the core electron population with bulk velocity U_c, and the green shaded area represents the halo population with bulk velocity U_h. The black semi-circles represent **Eq. 17** for parallel-propagating fast-magnetosonic/whistler waves with parallel phase speed v_{ph}. The diffusive flux of cyclotron-resonant particles is shown by the green arrow. The green-dashed semi-circle indicates $v_\perp^2 + v_\parallel^2 =$ constant.

Fully electromagnetic particle-in-cell simulations of the electron/electron-acoustic instability show that heating of the cold core component quenches the instability due to a breakdown of its requirement that $T_h \gg T_c$ (Lin et al., 1985). This appears to be the dominant nonlinear saturation mechanism for the electron/electron-acoustic instability (Gary, 1993).

4.6 Whistler Heat-Flux Instability

The whistler heat-flux instability is a cyclotron-resonant instability of the electromagnetic fast-magnetosonic/whistler wave (Gary et al., 1975a, Gary et al., 1975b; Schwartz, 1980). It has maximum growth at $k_\perp = 0$. Quasi-parallel fast-magnetosonic/whistler waves follow the approximate cold-plasma dispersion relation (Verscharen et al., 2019b)

$$\frac{\omega_{kr}}{\Omega_p} \approx \frac{k_\parallel^2 d_p^2}{2}\left(\sqrt{1+\frac{4k_\parallel^2}{d_p^2}}+1\right), \tag{37}$$

when $\omega_{kr} \ll |\Omega_e|$. The cyclotron-resonant electrons interact with the right-hand circularly polarised electric field of the fast-magnetosonic/whistler wave through the $n = -1$ resonance. According to **Eq. 16**, only electrons with $v_\parallel < 0$ can fulfill the resonance condition when $v_{ph} > 0$. In a plasma consisting of protons and two isotropic electron populations, the driving electron population must have a bulk velocity greater than v_{ph}. Therefore, this instability is typically driven by a hot beam population like the halo. At maximum growth, $\Omega_p \ll \omega_{kr} \ll |\Omega_e|$ and $1/d_p \ll k_\parallel \lesssim 1/d_e$.

Figure 9 shows the quasi-linear evolution of f_{0e} in the whistler heat-flux instability. In this case, $0 < v_{ph} < U_h$, and halo electrons with $v_\parallel < 0$ resonate with the whistler wave. This setup guarantees that the flux of diffusing electrons in velocity space is directed as shown by the green arrow in **Figure 9** as particles diffuse towards smaller values of f_{0e} (see also Shaaban et al., 2019c). The resonant electrons diffuse towards smaller $v_\perp$ but larger $|v_\parallel|$, while their $(v_\perp^2 + v_\parallel^2)$ decreases. This decreasing kinetic energy is transferred into the resonant fast-magnetosonic/whistler waves. Increasing the halo density and temperature brings a larger number of electrons into resonance with the wave and thus leads to an increase in the growth rate. This instability is not a good candidate to explain the regulation of the strahl heat flux since the strahl does not provide a sufficient number of electrons at $v_\parallel < 0$ when $U_s > 0$ (Verscharen et al., 2019a).

With increasing halo speed, ω_{kr} decreases compared to the traditional dispersion relation in **Eq. 37**. Figure 7 of Gary (1985a) compares the thresholds of the whistler heat-flux instability with the thresholds of the electron/ion-acoustic instability (see **Section 4.1**) and the electron-beam instability (see **Section 4.3**). Under typical solar-wind conditions, the whistler heat-flux instability has the lowest threshold of these instabilities. Only at large n_h/n_c, large T_h/T_c, and small β_j, the other instabilities can compete with the whistler heat-flux instability.

The instability mechanism of the whistler heat-flux instability is similar to the instability mechanism of the electron whistler anisotropy instability presented in **Section 3.1**. The introduction of a halo anisotropy modifies the shape of f_{0e} in the velocity space occupied by resonant electrons. Consequently, the threshold of the whistler heat-flux instability decreases with increasing halo anisotropy $T_{\perp h}/T_{\parallel h} > 0$ (in general, the instability is sensitive to the shape of the halo distribution; see Abraham-Shrauner and Feldman, 1977; Dum et al., 1980).

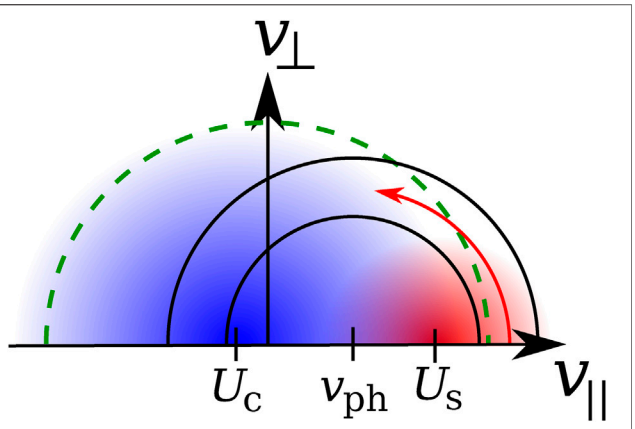

FIGURE 10 | Schematic illustration of the quasi-linear diffusion in the oblique fast-magnetosonic/whistler instability and in the lower-hybrid fan instability. The blue shaded area represents the core electron population with bulk velocity U_c, and the red shaded area represents the strahl population with bulk velocity U_s. The black semi-circles represent **Eq. 17** for oblique fast-magnetosonic/whistler waves or lower-hybrid waves with parallel phase speed v_{ph}. The diffusive flux of cyclotron-resonant particles is shown by the red arrow. The green-dashed semi-circle indicates $v_\perp^2 + v_\parallel^2 =$ constant.

The cyclotron-resonant halo driving competes with the cyclotron-resonant core damping of the fast-magnetosonic/whistler wave in this instability. Introducing a core anisotropy with $T_{\perp c}/T_{\parallel c} > 0$ lowers the cyclotron-resonant core damping though and thus raises the growth rate. Treatments of the whistler heat-flux instability in bi-Maxwellian and κ-distributed plasmas confirm this picture (Shaaban et al., 2018; Sarfraz and Yoon, 2020). Quasi-linear models of the whistler heat-flux and electron whistler anisotropy instability driven by a combination of heat flux and anisotropy are also available (Shaaban et al., 2019b; Vasko et al., 2020).

The thresholds of the whistler heat-flux instability have often been compared with the observed heat flux in the solar wind (Gary and Feldman, 1977; Gary et al., 1999a; Tong et al., 2019b). This instability is likely to operate near 1 au (Tong et al., 2019b), but it appears unlikely to prove important near the Sun, where the halo is an almost negligible component of the distribution (Halekas et al., 2020, 2021b; Abraham et al., 2022). Conditions relevant for the driving of this instability also occur near interplanetary shocks and in the Earth's foreshock (Wilson et al., 2009, 2013; Page et al., 2021). Quasi-parallel whistler waves are observed in solar-wind intervals with strong heat flux, supporting the links between core-halo heat flux and the whistler heat-flux instability (Lacombe et al., 2014; Stansby et al., 2016; Tong et al., 2019a; Jagarlamudi et al., 2020). The contributions of core and halo anisotropies to the growth of the instability are confirmed observationally through the presence of a clear positive correlation between the occurrence of whistler waves and core/halo anisotropies (Jagarlamudi et al.,

2020). Like the relative halo density, the core and halo anisotropies decrease with decreasing heliocentric distance, which is consistent with the observed lack of whistler waves at heliocentric distances $\lesssim$ 0.13 au (Cattell et al., 2022).

Particle-in-cell simulations of the whistler heat-flux instability reveal that beam scattering and core heating occur simultaneously due to cyclotron-resonant wave–particle interactions (López et al., 2019b). The quasi-linear pitch-angle diffusion of the resonant electrons as shown in **Figure 9** saturates quickly so that a significant heat-flux regulation is not expected. Numerical simulations confirm this expectation under typical solar-wind conditions (Kuzichev et al., 2019). Therefore, despite a significant amount of research into the action of the whistler heat-flux instability, its contribution to the observed heat-flux regulation in the solar wind is still not fully understood (for observational constraints, see Feldman et al., 1976a,b).

4.7 Oblique Fast-Magnetosonic/Whistler Instability

When the fast-magnetosonic/whistler wave is not exactly parallel in propagation, it develops a non-zero left-circularly polarised component in its electric-field fluctuations. Unlike in the case of the whistler heat-flux instability presented in **Section 4.6**, this allows electrons with $v_\parallel > 0$ to resonate according to **Eq. 16** with fast-magnetosonic/whistler waves with $v_{\rm ph} > 0$ via the $n = +1$ cyclotron resonance (Verscharen et al., 2019a), provided $v_\parallel$ is sufficiently large. This enables strahl electrons with $v_\parallel > 0$ to drive the oblique whistler wave unstable (Vasko et al., 2019). At maximum growth, $\Omega_{\rm p} \ll \omega_{kr} \lesssim |\Omega_{\rm e}|$ and $1/d_{\rm p} \ll k_\parallel \lesssim 1/d_{\rm e}$.

The quasi-linear evolution of $f_{0\rm e}$ in the oblique fast-magnetosonic/whistler instability is shown in **Figure 10**. If the strahl distribution is isotropic, the resonant electrons diffuse towards larger $v_\perp$ and smaller $v_\parallel$ given that $0 < v_{\rm ph} < U_{\rm s}$. In this case, $(v_\perp^2 + v_\parallel^2)$ of the resonant strahl electrons decreases, corresponding to a loss of kinetic energy and thus a transfer of energy into the growing fast-magnetosonic/whistler waves.

Due to its obliqueness, the fast-magnetosonic/whistler wave also possesses fluctuations in the electric-field component $E_\parallel$ parallel to $\boldsymbol{B}_0$. Therefore, the cyclotron-resonant driving by resonant strahl electrons competes not just with cyclotron-resonant damping by core electrons via $n = -1$ but also with Landau-resonant damping by core electrons via $n = 0$. These competitions between driving and damping define two regimes of the oblique fast-magnetosonic/whistler instability: a high-$\beta_{\parallel \rm c}$ regime and a low-$\beta_{\parallel \rm c}$ regime.

In the high-$\beta_{\parallel \rm c}$ regime (i.e., when $w_{\parallel \rm c} \gtrsim v_{\rm Ae}/2$), the competition between cyclotron-resonant strahl driving and Landau-resonant core damping determines the instability threshold. The oblique fast-magnetosonic/whistler wave is unstable in this case if (Verscharen et al., 2019a)

$$U_{\rm s} \gtrsim \left[2\frac{n_{\rm c}}{n_{\rm s}}\sqrt{\frac{T_{\parallel \rm s}}{T_{\parallel \rm c}}}v_{\rm Ae}^2 w_{\parallel \rm c}^2 \frac{(1+\cos\theta)}{(1-\cos\theta)\cos\theta}\right]^{1/4}, \tag{38}$$

where θ is the angle between the wave vector and the background magnetic field.

In the low-$\beta_{\parallel \rm c}$ regime (i.e., when $w_{\parallel \rm c} \lesssim v_{\rm Ae}/2$), the competition between cyclotron-resonant strahl driving, cyclotron-resonant core damping, and Landau-resonant core damping determines the instability threshold. The oblique fast-magnetosonic/whistler wave is unstable in this case if

$$U_{\rm s} \gtrsim 3w_{\parallel \rm c}. \tag{39}$$

In the low-$\beta_{\parallel \rm c}$ regime, $\omega_{kr} \approx |\Omega_{\rm e}|/2$, $k_\parallel \approx |\Omega_{\rm e}|/2w_{\parallel \rm c}$, and $\theta = 60^\circ$ at maximum growth.

Eqs 38 and **39** have been tested successfully against numerical solutions to the linear Vlasov–Maxwell dispersion relation for typical solar-wind parameters (Verscharen et al., 2019a).

Statistical comparisons of instability thresholds with electron measurements in the solar wind from Wind (Verscharen et al., 2019a) and from Parker Solar Probe (Halekas et al., 2021b) show that the strahl parameters are limited by **Eq. 38** to the stable parameter space. However, a recent analysis of Parker Solar Probe and Helios data suggests that the strahl very rarely reaches the threshold in the inner heliosphere, so that the importance of this instability is now put into question (Jeong et al., 2022a). This finding is consistent with the observed lack of fast-magnetosonic/whistler waves in Parker Solar Probe data at heliocentric distances $\lesssim$ 0.13 au (Cattell et al., 2022). Moreover, the majority of the fast-magnetosonic/whistler waves observed farther away from the Sun have a quasi-parallel direction of propagation with respect to the magnetic field (Kretzschmar et al., 2021). Therefore, other mechanisms than the self-induced scattering of strahl electrons by the oblique fast-magnetosonic/whistler instability may thus be needed to explain the observed scattering of strahl electrons into the halo population (e.g., the interaction with pre-existing fast-magnetosonic/whistler waves; Vocks et al., 2005; Vocks and Mann, 2009; Pierrard et al., 2011; Jagarlamudi et al., 2021; Cattell and Vo, 2021; Cattell et al., 2021). Moreover, Bernstein and ion-acoustic waves become more dominant than fast-magnetosonic/whistler waves in the very inner heliosphere, suggesting a transition into an electrostatic regime which could affect the electron distributions near the Sun (Mozer et al., 2021b; Malaspina et al., 2021). The observed Bernstein and ion-acoustic waves occur in very specific types of solar wind: Bernstein waves occur predominantly in quiet wind with magnetic field close to the ideal Parker spiral, while ion-acoustic waves occur predominantly in slow solar wind. This correlation underlines the importance of the careful investigation of the electron distribution's evolution as a function of wind parameters.

Numerical evaluations of the quasi-linear diffusion equation confirm that the oblique fast-magnetosonic/whistler instability scatters resonant strahl electrons as shown in **Figure 10** (Jeong et al., 2020; Sun et al., 2021). Numerical particle-in-cell simulations also confirm this evolution under conditions consistent with observed solar-wind parameters (Micera et al., 2020b).

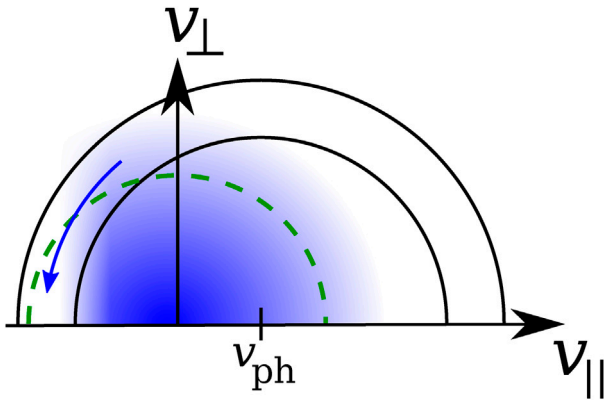

FIGURE 11 | Schematic illustration of the quasi-linear diffusion in the electron-deficit whistler instability. The blue shaded area represents the electron population with a deficit at $v_\parallel < 0$. The black semi-circles represent **Eq. 17** for parallel-propagating fast-magnetosonic/whistler waves with parallel phase speed v_{ph}. The diffusive flux of cyclotron-resonant particles is shown by the blue arrow. The green-dashed semi-circle indicates $v_\perp^2 + v_\parallel^2 =$ constant.

4.8 Lower-Hybrid Fan Instability

At very large angles of propagation ($k_\parallel^2/k^2 < m_e/m_p$), the fast-magnetosonic/whistler wave solution of the Vlasov–Maxwell dispersion relation is also known as the lower-hybrid mode. Its wave frequency asymptotes to the lower-hybrid frequency (Verdon et al., 2009)

$$\omega_{kr} \approx \omega_{LH} \equiv \frac{\omega_{pp}}{\sqrt{1+\frac{\omega_{pe}^2}{\Omega_e^2}}} \tag{40}$$

in the low-β_j limit. Landau-resonant core damping strongly suppresses the lower-hybrid mode (Lakhina, 1979), so that it becomes most relevant when $\beta_c \ll 1$, in which case the mode becomes largely electrostatic (Marsch and Chang, 1983).

In this low-β_c case, the lower-hybrid wave can be driven unstable by strahl electrons via the $n = +1$ cyclotron resonance like the oblique fast-magnetosonic/whistler instability (see **Section 4.7**; Omelchenko et al., 1994; Krafft and Volokitin, 2003; Shevchenko and Galinsky, 2010). At maximum growth, the lower-hybrid fan instability has $\omega_{kr} \approx \omega_{LH}$ and $k_\parallel \approx (\omega_{LH} + |\Omega_e|)/U_s$.

The instability mechanism for the lower-hybrid fan instability is the same as the mechanism driving the oblique fast-magnetosonic/whistler instability shown in **Figure 10**. Since the cyclotron-resonant diffusion leads to a fan-like widening of the strahl component in the perpendicular direction, this instability received the name lower-hybrid fan instability.

Numerical Hamiltonian simulations of the lower-hybrid fan instability confirm the importance of both cyclotron-resonant and Landau-resonant interactions between electrons and waves (Krafft et al., 2005; Krafft and Volokitin, 2006). In its nonlinear stage, the lower-hybrid fan instability is prone to strong wave trapping that is not captured by quasi-linear theory.

4.9 Electron-Deficit Whistler Instability

Up until this point, we have discussed the canonical examples of electron instabilities driven by anisotropy, drifts, or beams in the electron distribution function. However, other deviations from thermodynamic equilibrium are also able to drive instabilities if the deformation of the distribution is sufficiently strong in the range of resonant velocities (Dum et al., 1980).

One example of such a deformation of f_{0e} is the sunward deficit in the electron distribution (Halekas et al., 2020; Abraham et al., 2022). As expected in exospheric models of the solar wind (Lemaire and Scherer, 1971; Pierrard and Lemaire, 1996; Maksimovic et al., 2001), the interplanetary potential reflects electrons that leave the Sun with a kinetic energy below a cut-off value that depends on the potential. These reflected electrons return towards the Sun and form part of the sunward half of the electron distribution in the inner heliosphere. Electrons above the cut-off energy do not return. If collisions and other scattering mechanisms are neglected, a sharp cut-off is thus expected on the sunward side of the electron distribution, marking the separation between the reflected and the (missing) electrons that have escaped the potential. This cut-off has been observed in the form of a sunward deficit in the electron distribution function in data from Parker Solar Probe (Berčič et al., 2021a; Halekas et al., 2021a).

The sunward deficit can create conditions in which electrons near the cut-off resonantly interact with parallel fast-magnetosonic/whistler waves such that they lose their kinetic energy and drive the wave unstable (Berčič et al., 2021b). This interaction leads to the electron-deficit whistler instability. The instability at maximum growth has $\Omega_p \ll \omega_{kr} \ll |\Omega_e|$ and $k_\perp = 0$. The wave number at maximum growth depends on the parallel velocity of the deficit in velocity space according to **Eq. 16**. The properties of this instability are still under study, but Berčič et al. (2021b) suggest that the wave number at maximum growth is typically $\sim 1/d_e$.

The quasi-linear evolution of f_{0e} in the electron-deficit whistler instability is shown in **Figure 11**. The deficit is located at $v_\parallel < 0$, where it modifies the relative alignment between the pitch-angle gradients of f_{0e} and the direction of the diffusive flux of resonant electrons (locally tangent to the black semi-circles). Resonant electrons diffuse towards smaller $v_\perp$ and larger $|v_\parallel|$. The parallel fast-magnetosonic/whistler wave with phase speed v_{ph} grows at the expense of the energy of the diffusing electrons. This quasi-linear process fills up the electron deficit.

High-cadence and high-resolution measurements of the electron distribution function from Solar Orbiter show pronounced deficits at times when pronounced amplitudes of quasi-parallel fast-magnetosonic/whistler waves are seen (Berčič et al., 2021b). This observation suggests the sporadic occurrence of the electron-deficit whistler instability in the solar wind. Since the sunward electron deficit is more pronounced near the Sun, a systematic study of the this instability would be worthwhile in data from Parker Solar Probe and Solar Orbiter at small heliocentric distances.

The observed deficit, rather than forming a sharp cutoff at a specific $v_\parallel$ as shown in **Figure 11**, also extends to larger pitch angles, encompassing locally mirroring electrons with largely perpendicular velocities. This observation could indicate that

the operation of the instability has already resulted in diffusion from perpendicular to parallel velocities, or it could indicate that those regions of phase space are also unpopulated as suggested by Halekas et al. (2021a).

Simulations of the electron-deficit whistler instability are not available yet.

4.10 The Impact of Ion Beams on Electron-Driven Instabilities

If the plasma consists of one electron population and multiple ion populations, relative drifts between the electrons and the ion populations can drive instabilities. The current balance in a system consisting of an electron component and two proton components demands

$$n_e U_e = n_{pc} U_{pc} + n_{pb} U_{pb}, \tag{41}$$

where the subscript e refers to the single electron species, pc to the proton core, and pb to the proton beam. If such a proton beam–core configuration with $U_{pc} \neq U_{pb}$ exists, then $U_e \neq U_{pc}$; i.e., there is a non-zero drift between the proton core and the electrons. If the proton beam is sufficiently dense and fast in the proton-core frame, the fast-magnetosonic/whistler wave can be driven through cyclotron-resonant wave–particle interactions with the electrons (Akimoto et al., 1987). The mechanism is similar to the one shown in **Figure 9** for the whistler heat-flux instability, where the population marked as the halo now corresponds to the only electron population. For isotropic electrons, this instability still requires that $U_e > v_{ph}$. The separation between U_e and v_{ph} depends on the proton-beam and proton-core properties. The same mechanism is also potentially able to drive other instabilities presented in **Section 4**.

5 NON-RESONANT INSTABILITIES

The instabilities discussed thus far are characterised by resonant wave–particle interactions that lead to quasi-linear diffusion of resonant electrons in velocity space. Another family of instabilities is characterised by non-resonant plasma processes. These non-resonant instabilities often also exist in fluid plasma models (Verscharen et al., 2019b). Our quasi-linear model does not apply to this family of instabilities. Therefore, we give a brief summary of two important examples only: the electron mirror-mode instability and the non-propagating firehose instability.

5.1 Electron Mirror-Mode Instability

The mirror-mode instability is an example for a non-resonant, anisotropy-driven instability. It corresponds to the oblique non-propagating slow mode with $\omega_{kr} = 0$ (Chandrasekhar et al., 1958; Barnes, 1966; Basu and Coppi, 1984; Verscharen et al., 2017). Due to the polarisation of the non-propagating slow mode, the mirror-mode instability exhibits a significant component of magnetic-field fluctuations $\delta B_\parallel \equiv \delta \boldsymbol{B} \cdot \boldsymbol{B}_0 / B_0$ parallel to $\boldsymbol{B}_0$. The fluctuations in $\delta B_\parallel$ are anti-correlated with the fluctuations in δn_e. Trapping of slow ($v_\parallel \approx 0$) particles through the mirror force plays an important role in the nonlinear evolution of the mirror-mode instability (Southwood and Kivelson, 1993). However, particle trapping is not captured by our quasi-linear framework, and our requirement that $\omega_{kr} \gg \gamma_K$ is violated in the mirror-mode instability.

Unlike the resonant instabilities discussed in **Sections 3** and **4**, the mirror-mode instability is less sensitive to the shape of the distribution function in a defined narrow part of velocity space. Instead, its stability depends on the total pressure anisotropy of the system. This point is also illustrated by the analytical threshold for the mirror-mode instability which depends on the pressure contributions of both species in an electron–proton plasma: the mirror mode is unstable if (for a gyrokinetic derivation, see Verscharen et al., 2019a)

$$\beta_{\perp p}\left(\frac{T_{\perp p}}{T_{\parallel p}} - 1\right) + \beta_{\perp e}\left(\frac{T_{\perp e}}{T_{\parallel e}} - 1\right) > 1. \tag{42}$$

This type of analysis has also been extended to the case in which there are more than two particle species present (Hall, 1979; Hellinger, 2007; Chen et al., 2016).

Eq. 42 illustrates that the mirror-mode instability can be driven unstable by both ions and electrons (see also Migliuolo, 1986). The wave number at maximum growth shows an interesting transition between ion scales ($k \lesssim 1/d_p$) and electron scales ($k \lesssim 1/d_e$) depending on the species with the dominant anisotropy (Hellinger and Štverák, 2018). The saturation of the mirror-mode instability happens via a fluid-level rearrangement of the plasma that reduces the overall pressure anisotropy (Kivelson and Southwood, 1996; Rincon et al., 2015; Riquelme et al., 2015).

Linear theory predicts that, for the same $\beta_{\parallel e}$ and $T_{\perp e}/T_{\parallel e}$ in a bi-Maxwellian plasma, the electron whistler anisotropy instability discussed in **Section 3.1** generally has higher growth rates and lower thresholds than the oblique electron mirror-mode instability (Gary and Karimabadi, 2006). However, two-dimensional particle-in-cell simulations show that both instabilities compete, and the oblique electron mirror-mode instability often becomes dominant in the nonlinear phase after the parallel electron whistler anisotropy instability saturates (Hellinger and Štverák, 2018). Hellinger and Štverák (2018) also note that the importance of the mirror-mode instability potentially increases in more realistic three-dimensional simulations due to the higher degrees of freedom in such a system[3].

5.2 Non-Propagating Electron Firehose Instability

The non-propagating electron firehose instability is another non-resonant instability driven by anisotropy. It corresponds to a non-propagating (i.e., $\omega_{kr} = 0$) solution of the oblique Alfvén-wave

[3]Surprisingly, Sarfraz et al. (2021) perform two-dimensional simulations with the same physical parameters used by Hellinger and Štverák (2018) and do not observe any oblique modes. However, their simulation box is much smaller than that employed by Hellinger and Štverák (2018) and, as a consequence, the growth of the mirror instability may have been inhibited.

branch (Li and Habbal, 2000). If the plasma pressure anisotropy with $p_\parallel > p_\perp$ is sufficiently large, the magnetic tension is unable to provide a sufficient restoring force for the propagation of the Alfvén wave anymore, and the mode becomes aperiodic (Squire et al., 2016). In this context, we define the total pressures $p_\perp \equiv \sum_j n_j k_B T_{\perp j}$ and $p_\parallel \equiv \sum_j n_j k_B T_{\parallel j}$. Like in the case of the mirror-mode instability, the instability threshold of the non-propagating firehose instability depends on both electron and proton pressure contributions. In an electron–proton plasma, the non-propagating firehose mode is unstable if (for a gyrokinetic derivation, see Verscharen et al., 2019a)

$$\beta_{\parallel p} - \beta_{\perp p} + \beta_{\parallel e} - \beta_{\perp e} > 2. \tag{43}$$

If multiple species are present, this condition can be extended to (Kunz et al., 2015; Chen et al., 2016)

$$\sum_j \left(\beta_{\parallel j} - \beta_{\perp j} + \frac{8\pi m_j n_j U_j^2}{B_0^2} \right) > 2, \tag{44}$$

which also accounts for the contributions of relative drifts to the total parallel pressure (Gary et al., 1975b). Therefore, the non-propagating firehose instability can also be driven unstable in the presence of isotropic or anisotropic beam populations. At maximum growth, the non-propagating electron firehose instability has $k \sim 1/d_e$.

The non-propagating electron firehose has a significantly lower threshold than the propagating electron firehose instability under typical solar-wind conditions (Gary and Nishimura, 2003; Lazar et al., 2022). The presence of suprathermal electron populations with properties consistent with observed solar-wind conditions lowers the threshold of the non-propagating firehose instability even further (Shaaban et al., 2019a). In the expanding solar wind, conservation of the first adiabatic invariant (magnetic moment) in a decreasing magnetic field naturally increases $T_{\parallel e}/T_{\perp e}$ and drives the distribution toward the firehose instability thresholds (Innocenti et al., 2020). If this process happens faster than Coulomb collisions can moderate the anisotropy, then the non-propagating firehose instability can be triggered.

The non-propagating electron firehose instability thresholds constrain slow wind (but not fast wind) core electrons to the stable parameter space in electron measurements from Helios, Cluster, and Ulysses (Štverák et al., 2008). Electrons measured by Parker Solar Probe during encounters 1 to 9 are stable and far from the thresholds of the non-propagating electron firehose instability (Cattell et al., 2022).

Particle-in-cell simulations of the non-propagating electron firehose instability show that nonlinear wave–wave interactions play an important role during the nonlinear stage of the instability (Camporeale and Burgess, 2008; Hellinger et al., 2014). Highly oblique fluctuations grow initially, which then couple to modes with less oblique wave vectors. The interplay of the various modes leads to a situation in which the plasma "bounces" around the marginal stability threshold in parameter space. An anisotropy in suprathermal electron populations relaxes more quickly than an anisotropy in thermal electron populations during the instability's nonlinear evolution (López et al., 2019a), which is also consistent with the observation of lower halo anisotropies (Štverák et al., 2008). Fully kinetic, expanding-box simulations demonstrate that the non-propagating electron firehose instability arises self-consistently in the expanding solar wind due to the conservation of the magnetic moment (Innocenti et al., 2019a). After onset, the firehose instability and its nonlinear evolution compete against the ongoing expansion to drive the system between stability and instability: also in expanding-box simulations, the electrons bounce around the marginal stability threshold in parameter space.

6 CONCLUSIONS AND OPEN QUESTIONS

We develop a semi-graphical framework for the analysis of resonant micro-instabilities based on the equations of quasi-linear theory. We apply this framework to electron-driven instabilities with relevance to the solar wind. With the help of this description, we discuss instabilities driven by temperature anisotropy and reflectional asymmetry in the electron distribution function.

Electrons make an important contribution to the overall dynamics and energetics of the solar wind through their pressure gradient and through their heat flux. Micro-instabilities modify the kinetic properties of the electron distribution function locally and thus have a local impact on the electron contributions to the global dynamics and energetics of the solar wind. Once triggered, they regulate the temperatures, temperature anisotropies, field-parallel currents, or heat flux. Throughout his career, Peter Gary has made groundbreaking contributions to the study of electron-driven instabilities in the solar wind, especially from the perspective of linear Vlasov–Maxwell theory and nonlinear plasma simulations.

Measurements with modern space missions have revealed a number of open questions regarding the action and role of electron-driven instabilities in the solar wind. Here, we list a selection of these topics that we consider important for future research:

1. While most linear-theory calculations assume a homogeneous and steady-state background plasma, the solar wind is far from homogeneity and a steady state. The plasma exhibits variations and inhomogeneities on a broad range of scales (Verscharen et al., 2019b). The action of micro-instabilities in such a turbulent and variable plasma is not understood. Most relevant electron-driven instabilities act on small electron scales ($\sim d_e$ or $\sim \rho_e$) at which the amplitude of the ubiquitous turbulent fluctuations in the solar wind is small. Therefore, they are likely to experience a less variable background on the relevant scales than ion-driven instabilities. Moreover, interactions between electrons and turbulent fluctuations also modify the electron distribution, so that a separation between the effects of micro-instabilities and the effects of turbulent dissipation is complex.
2. The solar wind is an expanding plasma flow. Therefore, the background parameters of the system change as a parcel of solar-wind plasma travels through the heliosphere with its local bulk velocity. This global large-scale evolution modifies the kinetic structure of the particle distributions. Through

numerical models such as expanding-box simulations (Innocenti et al., 2019b, 2020; Micera et al., 2021) or semi-analytical kinetic approaches (Sun et al., 2021; Jeong et al., 2022b), a simultaneous treatment of instabilities and expansion effects has become possible. In this context, the implementation of the regulating impact of electron-driven instabilities in global solar-wind models is an important goal for our understanding of the solar wind (e.g., Chandran et al., 2011). Despite progress in our numerical capabilities, a fully self-consistent treatment of the large-scale expansion and electron-driven instabilities still lies far in the future.

3. Electron-driven instabilities are often treated in isolation. In reality, however, it is likely that electron-driven and ion-driven instabilities co-exist, depending on the mechanisms that create the driving deviations of the particle distributions from thermodynamic equilibrium. Numerical simulations that resolve both ion and electron processes and scales are a crucial tool for the understanding of the nonlinear stages of these combined instabilities (Schriver and Ashour-Abdalla, 1990; Riquelme et al., 2018, 2022). For example, shearing particle-in-cell simulations show that unstable electron-scale fluctuations can grow inside the unstable ion-scale fluctuations in systems with driven anisotropy (Riquelme et al., 2016). Fully kinetic particle-in-cell simulations show that the electron firehose instabilities develop concurrently with the ion firehose instabilities (López et al., 2022), which is a likely scenario since both species develop a temperature anisotropy due to solar-wind expansion. This effect increases the growth rate of the firehose instabilities compared to the linear prediction for the ion-driven firehose instabilities alone. We require such a combined description of electron-driven and ion-driven instabilities under realistic solar-wind conditions.
4. Although some of the instabilities discussed in this review are able to regulate the heat flux of the electron distribution, recent research suggests that the solar-wind plasma rarely exceeds the linear instability thresholds for heat-flux driven instabilities (Horaites et al., 2018; Schroeder et al., 2021; Jeong et al., 2022a). These findings highlight the uncertainty in our understanding of the *importance* of electron-driven instabilities in the solar wind. For all instabilities, it is crucial to investigate (a) how often they occur in the solar wind and (b) how strong their impact is on the evolution of the global system. These questions can only be answered by combining theory, simulations, and spacecraft observations. A quantification of the different contributions of instabilities would be worthwhile, as recently provided by Zhao et al. (2022) for Alfvén waves in collisionless plasmas.
5. As we show through our quasi-linear model, resonant instabilities strongly depend on the exact shape of the distribution function near the parallel speed that fulfills **Eq. 16** via $\hat{G}f_{0j}$. While temperature anisotropies and reflectional asymmetries in the distribution function each represent non-equilibrium features, natural plasmas are likely to exhibit a combination of both. Some recent studies combine these drivers in their analyses of electron-driven instabilities (Lazar et al., 2018b; Shaaban and Lazar, 2020; Vasko et al., 2020). While most theoretical descriptions characterise the instability-driving non-equilibrium features with prescribed distributions (e.g., with drifting bi-Maxwellian or bi-κ-distributions), it is more reliable (and potentially necessary) to evaluate the stability of the actual distribution functions without relying on distribution models (Dum et al., 1980). Modern numerical tools such as LEOPARD (Astfalk and Jenko, 2017) and ALPS (Verscharen et al., 2018) exist that are capable of this evaluation; however, a systematic application to measured electron distributions is still outstanding (for notable exceptions, see Husidic et al., 2020; Page et al., 2021; Schroeder et al., 2021).
6. Parker Solar Probe will continue to measure electron distribution functions in close proximity to the Sun. Solar Orbiter will measure electron distribution functions outside the ecliptic plane. With its modern sets of instrumentation, both missions will generate unprecedented amounts of solar-wind electron data in combination with measurements of fluctuations in the magnetic and electric fields. These data will resolve some of the listed science challenges here but also pose new questions about the action and role of electron-driven instabilities in the solar wind. Moreover, the space-plasma community is planning future missions, like the mission proposal Debye, dedicated to electron-scale kinetics and its impact on the global plasma system (Wicks et al., 2019; Verscharen et al., 2021a).

AUTHOR CONTRIBUTIONS

DV took the lead role of the coordination and writing of the article. JH, VJ, SS, and PW contributed to the writing of the paper, focusing on the comparison to observations. EB, MI, and AM contributed to the writing of the paper, focusing on the numerical simulations of electron-driven instabilities. BC, VP, IV, and MV contributed to the writing of the paper, the broader context, and by completing the list of references.

FUNDING

DV is supported by the UK Science and Technology Facilities Council (STFC) Ernest Rutherford Fellowship ST/P003826/1, and STFC Consolidated Grants ST/S000240/1 and ST/W001004/1. BC acknowledges support from NASA grant 80NSSC19K0829 and from the Parker Solar Probe FIELDS Experiment through NASA grant NNN06AA01C. JH is supported by the Parker Solar Probe mission through the SWEAP contract NNN06AA01C. MI acknowledges support from the German Science Foundation DFG within the Collaborative Research Center SFB1491.

ACKNOWLEDGMENTS

DV is very grateful for many discussions with Peter Gary at various occasions about linear Vlasov–Maxwell theory, plasma instabilities, and turbulence in the solar wind. In particular,

conversations with Peter about the oblique fast-magnetosonic/whistler instability at the 2014 SHINE Workshop in Telluride CO and more broadly about electron kinetics at the 2015 SHINE Workshop in Stowe VT sparked DV's interest in electron-driven instabilities in the solar wind. DV also appreciates discussions about the theory of the oblique fast-magnetosonic/whistler instability with Stuart Bale, Eliot Quataert, and Chadi Salem at the 2013 HTP team meeting in Berkeley CA. The authors acknowledge insightful discussions within the International Team "Heliospheric Energy Budget: From Kinetic Scales to Global Solar Wind Dynamics" at the International Space Science Institute (ISSI) in Bern led by ME. Innocenti and A. Tenerani. This work was discussed at the "Joint Electron Project" at MSSL.

REFERENCES

Abraham, J. B., Owen, C. J., Verscharen, D., Bakrania, M., Stansby, D., Wicks, R. T., et al. (2022). Radial Evolution of Thermal and Suprathermal Electron Populations in the Slow Solar Wind from 0.13 to 0.5 au: Parker Solar Probe Observations. *Astrophysical J.* 931, 118. doi:10.3847/1538-4357/ac6605

Abraham-Shrauner, B., and Feldman, W. C. (1977). Whistler Heat Flux Instability in the Solar Wind with Bi-lorentzian Velocity Distribution Functions. *J. Geophys. Res.* 82, 1889–1892. doi:10.1029/JA082i013p01889

Akimoto, K., Gary, S. P., and Omidi, N. (1987). Electron/ion Whistler Instabilities and Magnetic Noise Bursts. *J. Geophys. Res.* 92, 11209–11214. doi:10.1029/ja092ia10p11209

Alexandrova, O., Saur, J., Lacombe, C., Mangeney, A., Mitchell, J., Schwartz, S. J., et al. (2009). Universality of Solar-Wind Turbulent Spectrum from MHD to Electron Scales. *Phys. Rev. Lett.* 103, 165003. doi:10.1103/physrevlett.103.165003

Ashour-Abdalla, M., and Okuda, H. (1984). Turbulent Heating of Heavy Ions on Auroral Field Lines. *J. Geophys. Res.* 89, 2235–2250. doi:10.1029/JA089iA04p02235

Ashour-Abdalla, M., and Thorne, R. M. (1978). Toward a Unified View of Diffuse Auroral Precipitation. *J. Geophys. Res.* 83, 4755–4766. doi:10.1029/JA083iA10p04755

Astfalk, P., and Jenko, F. (2017). LEOPARD: A Grid-based Dispersion Relation Solver for Arbitrary Gyrotropic Distributions. *J. Geophys. Res. Space Phys.* 122, 89–101. doi:10.1002/2016JA023522

Bakrania, M. R., Rae, I. J., Walsh, A. P., Verscharen, D., Smith, A. W., Bloch, T., et al. (2020). Statistics of Solar Wind Electron Breakpoint Energies Using Machine Learning Techniques. *Astronomy Astrophysics* 639, A46. doi:10.1051/0004-6361/202037840

Bale, S. D., Kellogg, P. J., Mozer, F. S., Horbury, T. S., and Reme, H. (2005). Measurement of the Electric Fluctuation Spectrum of Magnetohydrodynamic Turbulence. *Phys. Rev. Lett.* 94, 215002. doi:10.1103/physrevlett.94.215002

Bale, S. D., Pulupa, M., Salem, C., Chen, C. H. K., and Quataert, E. (2013). Electron Heat Conduction in the Solar Wind: Transition from Spitzer-Härm to the Collisionless Limit. *Astrophysical J.* 769, L22. doi:10.1088/2041-8205/769/2/l22

Barnes, A. (1966). Collisionless Damping of Hydromagnetic Waves. *Phys. Fluids* 9, 1483–1495. doi:10.1063/1.1761882

Basu, B., and Coppi, B. (1984). Theory of Field-Swelling Instability in Anisotropic Plasmas. *Phys. Fluids* 27, 1187–1193. doi:10.1063/1.864725

Berčič, L., Maksimović, M., Halekas, J. S., Landi, S., Owen, C. J., Verscharen, D., et al. (2021a). Ambipolar Electric Field and Potential in the Solar Wind Estimated from Electron Velocity Distribution Functions. *Astrophysical J.* 921, 83. doi:10.3847/1538-4357/ac1f1c

Berčič, L., Maksimović, M., Landi, S., and Matteini, L. (2019). Scattering of strahl electrons in the solar wind between 0.3 and 1 au: Helios observations. *Mon. Not. R. Astron. Soc.* 486, 3404–3414. doi:10.1093/mnras/stz1007

Berčič, L., Verscharen, D., Owen, C. J., Colomban, L., Kretzschmar, M., Chust, T., et al. (2021b). Whistler Instability Driven by the Sunward Electron Deficit in the Solar Wind. High-Cadence Solar Orbiter Observations. *Astron. Astrophys.* 656, A31. doi:10.1051/0004-6361/202140970

Bergmann, R. (1984). Electrostatic Ion (Hydrogen) Cyclotron and Ion Acoustic Wave Instabilities in Regions of Upward Field-Aligned Current and Upward Ion Beams. *J. Geophys. Res.* 89, 953–968. doi:10.1029/ja089ia02p00953

Borovsky, J. E., and Gary, S. P. (2014). How Important Are the Alpha-Proton Relative Drift and the Electron Heat Flux for the Proton Heating of the Solar Wind in the Inner Heliosphere? *J. Geophys. Res. Space Phys.* 119, 5210–5219. doi:10.1002/2014JA019758

Buneman, O. (1959). Dissipation of Currents in Ionized Media. *Phys. Rev.* 115, 503–517. doi:10.1103/physrev.115.503

Camporeale, E., and Burgess, D. (2008). Electron Firehose Instability: Kinetic Linear Theory and Two-Dimensional Particle-In-Cell Simulations. *J. Geophys. Res.* 113, a–n. doi:10.1029/2008JA013043

Cattell, C., Breneman, A., Dombeck, J., Hanson, E., Johnson, M., Halekas, J., et al. (2022). Parker Solar Probe Evidence for the Absence of Whistlers Close to the Sun to Scatter Strahl and to Regulate Heat Flux. *Astrophysical J. Lett.* 924, L33. doi:10.3847/2041-8213/ac4015

Cattell, C., Breneman, A., Dombeck, J., Short, B., Wygant, J., Halekas, J., et al. (2021). Parker Solar Probe Evidence for Scattering of Electrons in the Young Solar Wind by Narrowband Whistler-Mode Waves. *Astrophysical J. Lett.* 911, L29. doi:10.3847/2041-8213/abefdd

Cattell, C., and Vo, T. (2021). Modeling Interactions of Narrowband Large Amplitude Whistler-mode Waves with Electrons in the Solar Wind inside ~0.3 au and at 1 au Using a Particle Tracing Code. *Astrophysical J. Lett.* 914, L33. doi:10.3847/2041-8213/ac08a1

Cerri, S. S., Grošelj, D., and Franci, L. (2019). Kinetic Plasma Turbulence: Recent Insights and Open Questions from 3D3V Simulations. *Front. Astron. Space Sci.* 6, 64. doi:10.3389/fspas.2019.00064

Chandran, B. D. G., Dennis, T. J., Quataert, E., and Bale, S. D. (2011). Incorporating Kinetic Physics into a Two-Fluid Solar-Wind Model with Temperature Anisotropy and Low-Frequency Alfvén-Wave Turbulence. *Astrophysical J.* 743, 197. doi:10.1088/0004-637X/743/2/197

Chandran, B. D. G., Pongkitiwanichakul, P., Isenberg, P. A., Lee, M. A., Markovskii, S. A., Hollweg, J. V., et al. (2010). Resonant Interactions between Protons and Oblique Alfvén/ion-Cyclotron Waves in the Solar Corona and Solar Flares. *Astrophysical J.* 722, 710–720. doi:10.1088/0004-637x/722/1/710

Chandrasekhar, S., Kaufman, A. N., and Watson, K. M. (1958). The Stability of the Pinch. *Proc. R. Soc. Lond. Ser. A* 245, 435–455. doi:10.1098/rspa.1958.0094

Chen, C. H. K., Horbury, T. S., Schekochihin, A. A., Wicks, R. T., Alexandrova, O., and Mitchell, J. (2010). Anisotropy of Solar Wind Turbulence between Ion and Electron Scales. *Phys. Rev. Lett.* 104, 255002. doi:10.1103/physrevlett.104.255002

Chen, C. H. K., Matteini, L., Schekochihin, A. A., Stevens, M. L., Salem, C. S., Maruca, B. A., et al. (2016). Multi-species Measurements of the Firehose and Mirror Instability Thresholds in the Solar Wind. *Astrophysical J.* 825, L26. doi:10.3847/2041-8205/825/2/L26

Cranmer, S. R., Matthaeus, W. H., Breech, B. A., and Kasper, J. C. (2009). Empirical Constraints on Proton and Electron Heating in the Fast Solar Wind. *Astrophysical J.* 702, 1604–1614. doi:10.1088/0004-637X/702/2/1604

Cranmer, S. R., and Schiff, A. J. (2021). Electron Heat Flux in the Solar Wind: Generalized Approaches to Fluid Transport with a Variety of Skewed Velocity Distributions. *JGR Space Phys.* 126, e29666. doi:10.1029/2021JA029666

Cuperman, S. (1981). Electromagnetic Kinetic Instabilities in Multicomponent Space Plasmas: Theoretical Predictions and Computer Simulation Experiments. *Rev. Geophys.* 19, 307–343. doi:10.1029/RG019i002p00307

[Dataset] Roennmark, K. (1982). *Waves in Homogeneous, Anisotropic Multicomponent Plasmas (WHAMP).*

D'Angelo, N., and Motley, R. W. (1962). Electrostatic Oscillations Near the Ion Cyclotron Frequency. *Phys. Fluids* 5, 633–634. doi:10.1063/1.1706672

Detering, F., Rozmus, W., Brantov, A., Bychenkov, V. Y., Capjack, C. E., and Sydora, R. (2005). Particle-in-cell Simulations of Heat Flux Driven Ion Acoustic Instability. *Phys. Plasmas* 12, 012321. doi:10.1063/1.1835344

Dillard, C. S., Vasko, I. Y., Mozer, F. S., Agapitov, O. V., and Bonnell, J. W. (2018). Electron-acoustic Solitary Waves in the Earth's Inner Magnetosphere. *Phys. Plasmas* 25, 022905. doi:10.1063/1.5007907

Drummond, W. E., and Pines, D. (1964). Nonlinear Plasma Oscillations. *Ann. Phys.* 28, 478–499. doi:10.1016/0003-4916(64)90205-2

Drummond, W. E., and Rosenbluth, M. N. (1962). Anomalous Diffusion Arising from Microinstabilities in a Plasma. *Phys. Fluids* 5, 1507–1513. doi:10.1063/1.1706559

Dum, C. T., Marsch, E., and Pilipp, W. (1980). Determination of Wave Growth from Measured Distribution Functions and Transport Theory. *J. Plasma Phys.* 23, 91–113. doi:10.1017/S0022377800022170

Elena Innocenti, M., Tenerani, A., and Velli, M. (2019b). A Semi-implicit Particle-In-Cell Expanding Box Model Code for Fully Kinetic Simulations of the Expanding Solar Wind Plasma. *Astrophysical J.* 870, 66. doi:10.3847/1538-4357/aaf1be

Etcheto, J., and Faucheux, M. (1984). Detailed Study of Electron Plasma Waves Upstream of the Earth's Bow Shock. *J. Geophys. Res.* 89, 6631–6653. doi:10.1029/ja089ia08p06631

Feldman, W. C., Asbridge, J. R., Bame, S. J., Gary, S. P., and Montgomery, M. D. (1976a). Electron Parameter Correlations in High-Speed Streams and Heat Flux Instabilities. *J. Geophys. Res.* 81, 2377–2382. doi:10.1029/JA081i013p02377

Feldman, W. C., Asbridge, J. R., Bame, S. J., Gary, S. P., Montgomery, M. D., and Zink, S. M. (1976b). Evidence for the Regulation of Solar Wind Heat Flux at 1 AU. *J. Geophys. Res.* 81, 5207–5211. doi:10.1029/ja081i028p05207

Feldman, W. C., Asbridge, J. R., Bame, S. J., Montgomery, M. D., and Gary, S. P. (1975). Solar Wind Electrons. *J. Geophys. Res.* 80, 4181–4196. doi:10.1029/JA080i031p04181

Fitzenreiter, R. J., Ogilvie, K. W., Chornay, D. J., and Keller, J. (1998). Observations of Electron Velocity Distribution Functions in the Solar Wind by the WIND Spacecraft: High Angular Resolution Strahl Measurements. *Geophys. Res. Lett.* 25, 249–252. doi:10.1029/97GL03703

Forslund, D. W. (1970). Instabilities Associated with Heat Conduction in the Solar Wind and Their Consequences. *J. Geophys. Res.* 75, 17–28. doi:10.1029/JA075i001p00017

Fox, N. J., Velli, M. C., Bale, S. D., Decker, R., Driesman, A., Howard, R. A., et al. (2016). The Solar Probe Plus Mission: Humanity's First Visit to Our Star. *Space Sci. Rev.* 204, 7–48. doi:10.1007/s11214-015-0211-6

Fried, B. D., and Gould, R. W. (1961). Longitudinal Ion Oscillations in a Hot Plasma. *Phys. Fluids* 4, 139–147. doi:10.1063/1.1706174

Fuselier, S. A., Gurnett, D. A., and Fitzenreiter, R. J. (1985). The Downshift of Electron Plasma Oscillations in the Electron Foreshock Region. *J. Geophys. Res.* 90, 3935–3946. doi:10.1029/JA090iA05p03935

Gary, S. P., and Cairns, I. H. (1999). Electron Temperature Anisotropy Instabilities: Whistler, Electrostatic and Z Mode. *J. Geophys. Res.* 104, 19835–19842. doi:10.1029/1999ja900296

Gary, S. P. (1985a). Electromagnetic Electron Beam Instabilities: Hot, Isotropic Beams. *J. Geophys. Res.* 90, 10815–10823. doi:10.1029/JA090iA11p10815

Gary, S. P., Feldman, W. C., Forslund, D. W., and Montgomery, M. D. (1975a). Electron Heat Flux Instabilities in the Solar Wind. *Geophys. Res. Lett.* 2, 79–82. doi:10.1029/gl002i003p00079

Gary, S. P., Feldman, W. C., Forslund, D. W., and Montgomery, M. D. (1975b). Heat Flux Instabilities in the Solar Wind. *J. Geophys. Res.* 80, 4197–4203. doi:10.1029/ja080i031p04197

Gary, S. P., and Feldman, W. C. (1977). Solar Wind Heat Flux Regulation by the Whistler Instability. *J. Geophys. Res.* 82, 1087–1094. doi:10.1029/JA082i007p01087

Gary, S. P. (1978). Ion-acoustic-like Instabilities in the Solar Wind. *J. Geophys. Res.* 83, 2504–2510. doi:10.1029/ja083ia06p02504

Gary, S. P., and Karimabadi, H. (2006). Linear Theory of Electron Temperature Anisotropy Instabilities: Whistler, Mirror, and Weibel. *J. Geophys. Res.* 111, A11224. doi:10.1029/2006JA011764

Gary, S. P., Liu, K., Denton, R. E., and Wu, S. (2012). Whistler Anisotropy Instability with a Cold Electron Component: Linear Theory. *J. Geophys. Res.* 117, a–n. doi:10.1029/2012JA017631

Gary, S. P., Liu, K., and Winske, D. (2011). Whistler Anisotropy Instability at Low Electron β: Particle-In-Cell Simulations. *Phys. Plasmas* 18, 082902. doi:10.1063/1.3610378

Gary, S. P., and Madland, C. D. (1985). Electromagnetic Electron Temperature Anisotropy Instabilities. *J. Geophys. Res.* 90, 7607–7610. doi:10.1029/JA090iA08p07607

Gary, S. P., Neagu, E., Skoug, R. M., and Goldstein, B. E. (1999a). Solar Wind Electrons: Parametric Constraints. *J. Geophys. Res.* 104, 19843–19849. doi:10.1029/1999JA900244

Gary, S. P., and Nishimura, K. (2004). Kinetic Alfvén Waves: Linear Theory and a Particle-In-Cell Simulation. *J. Geophys. Res. (Space Phys.* 109, A02109. doi:10.1029/2003ja010239

Gary, S. P., and Nishimura, K. (2003). Resonant Electron Firehose Instability: Particle-In-Cell Simulations. *Phys. Plasmas* 10, 3571–3576. doi:10.1063/1.1590982

Gary, S. P., and Saito, S. (2007). Broadening of Solar Wind Strahl Pitch-Angles by the Electron/electron Instability: Particle-In-Cell Simulations. *Geophys. Res. Lett.* 34, L14111. doi:10.1029/2007GL030039

Gary, S. P., Skoug, R. M., and Daughton, W. (1999b). Electron Heat Flux Constraints in the Solar Wind. *Phys. Plasmas* 6, 2607–2612. doi:10.1063/1.873532

Gary, S. P. (1987). The Electron/electron Acoustic Instability. *Phys. Fluids* 30, 2745–2749. doi:10.1063/1.866040

Gary, S. P. (1993). *Theory of Space Plasma Microinstabilities*. Cambridge: Cambridge University Press.

Graham, D. B., Khotyaintsev, Y. V., Vaivads, A., Edberg, N. J. T., Eriksson, A. I., Johansson, E. P. G., et al. (2021). Kinetic Electrostatic Waves and Their Association with Current Structures in the Solar Wind. *Astronomy Astrophysics* 656, A23. doi:10.1051/0004-6361/202140943

Graham, G. A., Rae, I. J., Owen, C. J., Walsh, A. P., Arridge, C. S., Gilbert, L., et al. (2017). The Evolution of Solar Wind Strahl with Heliospheric Distance. *J. Geophys. Res. Space Phys.* 122, 3858–3874. doi:10.1002/2016JA023656

Grošelj, D., Mallet, A., Loureiro, N. F., and Jenko, F. (2018). Fully Kinetic Simulation of 3D Kinetic Alfvén Turbulence. *Phys. Rev. Lett.* 120, 105101. doi:10.1103/PhysRevLett.120.105101

Gurnett, D. A., and Anderson, R. R. (1977). Plasma Wave Electric Fields in the Solar Wind: Initial Results from Helios 1. *J. Geophys. Res.* 82, 632–650. doi:10.1029/JA082i004p00632

Gurnett, D. A. (1991). "Waves and Instabilities," in *Physics of the Inner Heliosphere II. Particles, Waves and Turbulence. Series: Physics and Chemistry in Space*. Editors R. Schwenn, and E. Marsch (Berlin, Heidelberg: Springer), 152. doi:10.1007/978-3-642-75364-0_4

Halekas, J. S., Berčič, L., Whittlesey, P., Larson, D. E., Livi, R., Berthomier, M., et al. (2021a). The Sunward Electron Deficit: A Telltale Sign of the Sun's Electric Potential. *Astrophysical J.* 916, 16. doi:10.3847/1538-4357/ac096e

Halekas, J. S., Whittlesey, P., Larson, D. E., McGinnis, D., Maksimovic, M., Berthomier, M., et al. (2020). Electrons in the Young Solar Wind: First Results from the Parker Solar Probe. *Astrophysical J. Suppl. Ser.* 246, 22. doi:10.3847/1538-4365/ab4cec

Halekas, J. S., Whittlesey, P. L., Larson, D. E., McGinnis, D., Bale, S. D., Berthomier, M., et al. (2021b). Electron Heat Flux in the Near-Sun Environment. *Astronomy Astrophysics* 650, A15. doi:10.1051/0004-6361/202039256

Hall, A. N. (1979). Finite Ion Larmor Radius Modifications to the Firehose and Mirror Instabilities. *J. Plasma Phys.* 21, 431–443. doi:10.1017/S0022377800022005

Hammond, C. M., Feldman, W. C., McComas, D. J., Phillips, J. L., and Forsyth, R. J. (1996). Variation of Electron-Strahl Width in the High-Speed Solar Wind: ULYSSES Observations. *Astron. Astrophys.* 316, 350–354.

Harvey, R. W. (1975). Quasi-linear Spectrum of Current Driven Ion Cyclotron Waves. *Phys. Fluids* 18, 1790–1799. doi:10.1063/1.861060

Hellinger, P. (2007). Comment on the Linear Mirror Instability Near the Threshold. *Phys. Plasmas* 14, 082105. doi:10.1063/1.2768318

Hellinger, P., and Štverák, Š. (2018). Electron Mirror Instability: Particle-In-Cell Simulations. *J. Plasma Phys.* 84, 905840402. doi:10.1017/S0022377818000703

Hellinger, P., Trávníček, P. M., Decyk, V. K., and Schriver, D. (2014). Oblique Electron Fire Hose Instability: Particle-In-Cell Simulations. *J. Geophys. Res. Space Phys.* 119, 59–68. doi:10.1002/2013JA019227

Hollweg, J. V. (1974). On Electron Heat Conduction in the Solar Wind. *J. Geophys. Res.* 79, 3845–3850. doi:10.1029/ja079i025p03845

Hollweg, J. V., and Völk, H. J. (1970). New Plasma Instabilities in the Solar Wind. *J. Geophys. Res.* 75, 5297–5309. doi:10.1029/JA075i028p05297

Horaites, K., Astfalk, P., Boldyrev, S., and Jenko, F. (2018). Stability Analysis of Core-Strahl Electron Distributions in the Solar Wind. *Mon. Not. R. Astron. Soc.* 480, 1499–1506. doi:10.1093/mnras/sty1808

Howes, G. G., Tenbarge, J. M., Dorland, W., Quataert, E., Schekochihin, A. A., Numata, R., et al. (2011). Gyrokinetic Simulations of Solar Wind Turbulence from Ion to Electron Scales. *Phys. Rev. Lett.* 107, 035004. doi:10.1103/PhysRevLett.107.035004

Howes, G. G., Cowley, S. C., Dorland, W., Hammett, G. W., Quataert, E., and Schekochihin, A. A. (2006). Astrophysical Gyrokinetics: Basic Equations and Linear Theory. *Astrophysical J.* 651, 590–614. doi:10.1086/506172

Howes, G. G., Dorland, W., Cowley, S. C., Hammett, G. W., Quataert, E., Schekochihin, A. A., et al. (2008). Kinetic Simulations of Magnetized Turbulence in Astrophysical Plasmas. *Phys. Rev. Lett.* 100, 065004. doi:10.1103/PhysRevLett.100.065004

Hughes, R. S., Gary, S. P., Wang, J., and Parashar, T. N. (2017). Kinetic Alfvén Turbulence: Electron and Ion Heating by Particle-In-Cell Simulations. *Astrophysical J.* 847, L14. doi:10.3847/2041-8213/aa8b13

Husidic, E., Lazar, M., Fichtner, H., Scherer, K., and Astfalk, P. (2020). Linear Dispersion Theory of Parallel Electromagnetic Modes for Regularized Kappa-Distributions. *Phys. Plasmas* 27, 042110. doi:10.1063/1.5145181

Innocenti, M. E., Boella, E., Tenerani, A., and Velli, M. (2020). Collisionless Heat Flux Regulation via the Electron Firehose Instability in the Presence of a Core and Suprathermal Population in the Expanding Solar Wind. *Astrophysical J.* 898, L41. doi:10.3847/2041-8213/aba591

Innocenti, M. E., Tenerani, A., Boella, E., and Velli, M. (2019a). Onset and Evolution of the Oblique, Resonant Electron Firehose Instability in the Expanding Solar Wind Plasma. *Astrophysical J.* 883, 146. doi:10.3847/1538-4357/ab3e40

Jagarlamudi, V. K., Alexandrova, O., Berčič, L., de Wit, T. D., Krasnoselskikh, V., Maksimovic, M., et al. (2020). Whistler Waves and Electron Properties in the Inner Heliosphere: Helios Observations. *Astrophysical J.* 897, 118. doi:10.3847/1538-4357/ab94a1

Jagarlamudi, V. K., Dudok de Wit, T., Froment, C., Krasnoselskikh, V., Larosa, A., Bercic, L., et al. (2021). Whistler Wave Occurrence and the Interaction with Strahl Electrons during the First Encounter of Parker Solar Probe. *Astronomy Astrophysics* 650, A9. doi:10.1051/0004-6361/202039808

Jeong, S.-Y., Abraham, J. B., Verscharen, D., Berčič, L., Stansby, D., Nicolaou, G., et al. (2022a). The Stability of the Electron Strahl against the Oblique Fast-magnetosonic/Whistler Instability in the Inner Heliosphere. *Astrophysical J. Lett.* 926, L26. doi:10.3847/2041-8213/ac4dff

Jeong, S.-Y., Verscharen, D., Vocks, C., Abraham, J. B., Owen, C. J., Wicks, R. T., et al. (2022b). The Kinetic Expansion of Solar-Wind Electrons: Transport Theory and Predictions for the Very Inner Heliosphere. *Astrophysical J.* 927, 162. doi:10.3847/1538-4357/ac4805

Jeong, S.-Y., Verscharen, D., Wicks, R. T., and Fazakerley, A. N. (2020). A Quasi-Linear Diffusion Model for Resonant Wave-Particle Instability in Homogeneous Plasma. *Astrophysical J.* 902, 128. doi:10.3847/1538-4357/abb099

Kennel, C. F., and Engelmann, F. (1966). Velocity Space Diffusion from Weak Plasma Turbulence in a Magnetic Field. *Phys. Fluids* 9, 2377–2388. doi:10.1063/1.1761629

Kennel, C. F., and Petschek, H. E. (1966). Limit on Stably Trapped Particle Fluxes. *J. Geophys. Res.* 71, 1–28. doi:10.1029/jz071i001p00001

Kennel, C. F., Scarf, F. L., Coroniti, F. V., Fredricks, R. W., Gurnett, D. A., and Smith, E. J. (1980). Correlated Whistler and Electron Plasma Oscillation Bursts Detected on ISEE-3. *Geophys. Res. Lett.* 7, 129–132. doi:10.1029/gl007i002p00129

Kennel, C. F., and Wong, H. V. (1967). Resonant Particle Instabilities in a Uniform Magnetic Field. *J. Plasma Phys.* 1, 75–80. doi:10.1017/S002237780000310X

Kim, H. P., Hwang, J., Seough, J. J., and Yoon, P. H. (2017). Electron Temperature Anisotropy Regulation by Whistler Instability. *J. Geophys. Res. Space Phys.* 122, 4410–4419. doi:10.1002/2016JA023558

Kindel, J. M., and Kennel, C. F. (1971). Topside Current Instabilities. *J. Geophys. Res.* 76, 3055–3078. doi:10.1029/ja076i013p03055

Kivelson, M. G., and Southwood, D. J. (1996). Mirror Instability II: The Mechanism of Nonlinear Saturation. *J. Geophys. Res.* 101, 17365–17371. doi:10.1029/96JA01407

Klein, K. G., Howes, G. G., TenBarge, J. M., Bale, S. D., Chen, C. H. K., and Salem, C. S. (2012). Using Synthetic Spacecraft Data to Interpret Compressible Fluctuations in Solar Wind Turbulence. *Astrophysical J.* 755, 159. doi:10.1088/0004-637x/755/2/159

Krafft, C., and Volokitin, A. (2003). Interaction of Suprathermal Solar Wind Electron Fluxes with Sheared Whistler Waves: Fan Instability. *Ann. Geophys.* 21, 1393–1403. doi:10.5194/angeo-21-1393-2003

Krafft, C., and Volokitin, A. (2006). Stabilization of the Fan Instability: Electron Flux Relaxation. *Phys. Plasmas* 13, 122301. doi:10.1063/1.2372464

Krafft, C., Volokitin, A., and Zaslavsky, A. (2005). Saturation of the Fan Instability: Nonlinear Merging of Resonances. *Phys. Plasmas* 12, 112309. doi:10.1063/1.2118727

Kretzschmar, M., Chust, T., Krasnoselskikh, V., Graham, D., Colomban, L., Maksimovic, M., et al. (2021). Whistler Waves Observed by Solar Orbiter/RPW between 0.5 AU and 1 AU. *Astronomy Astrophysics* 656, A24. doi:10.1051/0004-6361/202140945

Kunz, M. W., Schekochihin, A. A., Chen, C. H. K., Abel, I. G., and Cowley, S. C. (2015). Inertial-range Kinetic Turbulence in Pressure-Anisotropic Astrophysical Plasmas. *J. Plasma Phys.* 81, 325810501. doi:10.1017/s0022377815000811

Kurth, W. S., Gurnett, D. A., and Scarf, F. L. (1979). High-resolution Spectrograms of Ion Acoustic Waves in the Solar Wind. *J. Geophys. Res.* 84, 3413. doi:10.1029/ja084ia07p03413

Kuzichev, I. V., Vasko, I. Y., Soto-Chavez, A. R., Tong, Y., Artemyev, A. V., Bale, S. D., et al. (2019). Nonlinear Evolution of the Whistler Heat Flux Instability. *Astrophysical J.* 882, 81. doi:10.3847/1538-4357/ab3290

Lacombe, C., Alexandrova, O., Matteini, L., Santolík, O., Cornilleau-Wehrlin, N., Mangeney, A., et al. (2014). Whistler Mode Waves and the Electron Heat Flux in the Solar Wind: Cluster Observations. *Astrophysical J.* 796, 5. doi:10.1088/0004-637X/796/1/5

Lacombe, C., Mangeney, A., Harvey, C. C., and Scudder, J. D. (1985). Electron Plasma Waves Upstream of the Earth's Bow Shock. *J. Geophys. Res.* 90, 73–94. doi:10.1029/ja090ia01p00073

Lakhina, G. S. (1979). Electromagnetic Lower Hybrid Instability Driven by Solar Wind Heat Flux. *Astrophys. Space Sci.* 63, 511–516. doi:10.1007/BF00638919

Landi, S., Matteini, L., and Pantellini, F. (2012). On the Competition between Radial Expansion and Coulomb Collisions in Shaping the Electron Velocity Distribution Function: Kinetic Simulations. *Astrophysical J.* 760, 143. doi:10.1088/0004-637X/760/2/143

Landi, S., and Pantellini, F. (2003). Kinetic Simulations of the Solar Wind from the Subsonic to the Supersonic Regime. *Astronomy Astrophysics* 400, 769–778. doi:10.1051/0004-6361:20021822

Lazar, M., and Fichtner, H. (2021). "Kappa Distributions," in *Springer Nature Switzerland AG* (Berlin, Germany: Springer). doi:10.1007/978-3-030-82623-9

Lazar, M., López, R. A., Shaaban, S. M., Poedts, S., Yoon, P. H., and Fichtner, H. (2022). Temperature Anisotropy Instabilities Stimulated by the Solar Wind Suprathermal Populations. *Front. Astron. Space Sci.* 8, 249. doi:10.3389/fspas.2021.777559

Lazar, M., Poedts, S., and Michno, M. J. (2013). Electromagnetic Electron Whistler-Cyclotron Instability in Bi-kappa Distributed Plasmas. *Astronomy Astrophysics* 554, A64. doi:10.1051/0004-6361/201220550

Lazar, M., Poedts, S., Schlickeiser, R., and Dumitrache, C. (2015). Towards Realistic Parametrization of the Kinetic Anisotropy and the Resulting Instabilities in Space Plasmas. Electromagnetic Electron-Cyclotron Instability in the Solar Wind. *Mon. Not. R. Astron. Soc.* 446, 3022–3033. doi:10.1093/mnras/stu2312

Lazar, M., Poedts, S., and Schlickeiser, R. (2011). Instability of the Parallel Electromagnetic Modes in Kappa Distributed Plasmas - I. Electron Whistler-Cyclotron Modes. *Mon. Not. R. Astron. Soc.* 410, 663–670. doi:10.1111/j.1365-2966.2010.17472.x

Lazar, M., Shaaban, S. M., Fichtner, H., and Poedts, S. (2018a). Temperature Anisotropy Instabilities Stimulated by the Interplay of the Core and Halo Electrons in Space Plasmas. *Phys. Plasmas* 25, 022902. doi:10.1063/1.5016261

Lazar, M., Shaaban, S. M., Poedts, S., and Štverák, Š. (2017). Firehose Constraints of the Bi-kappa-distributed Electrons: a Zero-Order Approach for the Suprathermal Electrons in the Solar Wind. *Mon. Not. R. Astron. Soc.* 464, 564–571. doi:10.1093/mnras/stw2336

Lazar, M., Yoon, P. H., López, R. A., and Moya, P. S. (2018b). Electromagnetic Electron Cyclotron Instability in the Solar Wind. *JGR Space Phys.* 123, 6–19. doi:10.1002/2017JA024759

Leamon, R. J., Smith, C. W., Ness, N. F., Matthaeus, W. H., and Wong, H. K. (1998). Observational Constraints on the Dynamics of the Interplanetary Magnetic Field Dissipation Range. *J. Geophys. Res.* 103, 4775–4787. doi:10.1029/97ja03394

Lemaire, J., and Scherer, M. (1971). Kinetic Models of the Solar Wind. *J. Geophys. Res.* 76, 7479–7490. doi:10.1029/ja076i031p07479

Lemons, D. S., Asbridge, J. R., Bame, S. J., Feldman, W. C., Gary, S. P., and Gosling, J. T. (1979). The Source of Electrostatic Fluctuations in the Solar Wind. *J. Geophys. Res.* 84, 2135–2138. doi:10.1029/JA084iA05p02135

Li, X., and Habbal, S. R. (2000). Electron Kinetic Firehose Instability. *J. Geophys. Res.* 105, 27377–27385. doi:10.1029/2000ja000063

Lie-Svendsen, Ø., Hansteen, V. H., and Leer, E. (1997). Kinetic Electrons in High-Speed Solar Wind Streams: Formation of High-Energy Tails. *J. Geophys. Res.* 102, 4701–4718. doi:10.1029/96JA03632

Lin, C. S., Winske, D., and Tokar, R. L. (1985). Simulation of the Electron Acoustic Instability in the Polar Cusp. *J. Geophys. Res.* 90, 8269–8280. doi:10.1029/ja090ia09p08269

Lin, R. P. (1998). WIND Observations of Suprathermal Electrons in the Interplanetary Medium. *Space Sci. Rev.* 86, 61–78. doi:10.1007/978-94-011-4762-0_4

Livadiotis, G. (2017). *Kappa Distributions – Theory and Applications in Plasmas*. Amsterdam, Netherlands: Elsevier.

López, R. A., Lazar, M., Shaaban, S. M., Poedts, S., and Moya, P. S. (2020). Alternative High-Plasma Beta Regimes of Electron Heat-Flux Instabilities in the Solar Wind. *Astrophysical J.* 900, L25. doi:10.3847/2041-8213/abaf56

López, R. A., Lazar, M., Shaaban, S. M., Poedts, S., Yoon, P. H., Viñas, A. F., et al. (2019a). Particle-in-cell Simulations of Firehose Instability Driven by Bi-kappa Electrons. *Astrophysical J.* 873, L20. doi:10.3847/2041-8213/ab0c95

López, R. A., Micera, A., Lazar, M., Poedts, S., Lapenta, G., Zhukov, A. N., et al. (2022). Mixing the Solar Wind Proton and Electron Scales. Theory and 2D-PIC Simulations of Firehose Instability. *arXiv e-prints*. arXiv:2205.02338. doi:10.3847/1538-4357/ac66e4

López, R. A., Shaaban, S. M., Lazar, M., Poedts, S., Yoon, P. H., Micera, A., et al. (2019b). Particle-in-cell Simulations of the Whistler Heat-Flux Instability in Solar Wind Conditions. *Astrophysical J.* 882, L8. doi:10.3847/2041-8213/ab398b

Maksimovic, M., Bale, S. D., Berčič, L., Bonnell, J. W., Case, A. W., Wit, T. D. d., et al. (2020). Anticorrelation between the Bulk Speed and the Electron Temperature in the Pristine Solar Wind: First Results from the Parker Solar Probe and Comparison with Helios. *Astrophysical J. Suppl. Ser.* 246, 62. doi:10.3847/1538-4365/ab61fc

Maksimovic, M., Gary, S. P., and Skoug, R. M. (2000). Solar Wind Electron Suprathermal Strength and Temperature Gradients: Ulysses Observations. *J. Geophys. Res.* 105, 18337–18350. doi:10.1029/2000JA900039

Maksimovic, M., Pierrard, V., and Lemaire, J. (2001). On the Exospheric Approach for the Solar Wind Acceleration. *Astrophys. Space Sci.* 277, 181–187. doi:10.1007/978-94-010-0904-1_23

Maksimovic, M., Pierrard, V., and Riley, P. (1997). Ulysses Electron Distributions Fitted with Kappa Functions. *Geophys. Res. Lett.* 24, 1151–1154. doi:10.1029/97GL00992

Maksimovic, M., Zouganelis, I., Chaufray, J. Y., Issautier, K., Scime, E. E., Littleton, J. E., et al. (2005). Radial Evolution of the Electron Distribution Functions in the Fast Solar Wind between 0.3 and 1.5 AU. *J. Geophys. Res. (Space Phys.* 110, A09104. doi:10.1029/2005ja011119

Malaspina, D. M., Wilson, L. B., III, Bale, S. D., Bonnell, J. W., Goodrich, K., Goetz, K., et al. (2021). Electron Bernstein Waves and Narrowband Plasma Waves Near the Electron Cyclotron Frequency in the Near-Sun Solar Wind. *Astronomy Astrophysics* 650, A97. doi:10.1051/0004-6361/202140449

Marsch, E. (1985). Beam-driven Electron Acoustic Waves Upstream of the Earth's Bow Shock. *J. Geophys. Res.* 90, 6327–6336. doi:10.1029/JA090iA07p06327

Marsch, E., and Chang, T. (1983). Electromagnetic Lower Hybrid Waves in the Solar Wind. *J. Geophys. Res.* 88, 6869–6880. doi:10.1029/JA088iA09p06869

Marsch, E. (2006). Kinetic Physics of the Solar Corona and Solar Wind. *Living Rev. Sol. Phys.* 3, 1. doi:10.12942/lrsp-2006-1

McComas, D. J., Bame, S. J., Feldman, W. C., Gosling, J. T., and Phillips, J. L. (1992). Solar Wind Halo Electrons from 1-4 AU. *Geophys. Res. Lett.* 19, 1291–1294. doi:10.1029/92gl00631

Messmer, P. (2002). Temperature Isotropization in Solar Flare Plasmas Due to the Electron Firehose Instability. *Astronomy Astrophysics* 382, 301–311. doi:10.1051/0004-6361:20011583

Micera, A., Boella, E., Zhukov, A. N., Shaaban, S. M., López, R. A., Lazar, M., et al. (2020a). Particle-in-cell Simulations of the Parallel Proton Firehose Instability Influenced by the Electron Temperature Anisotropy in Solar Wind Conditions. *Astrophysical J.* 893, 130. doi:10.3847/1538-4357/ab7faa

Micera, A., Zhukov, A. N., López, R. A., Boella, E., Tenerani, A., Velli, M., et al. (2021). On the Role of Solar Wind Expansion as a Source of Whistler Waves: Scattering of Suprathermal Electrons and Heat Flux Regulation in the Inner Heliosphere. *Astrophysical J.* 919, 42. doi:10.3847/1538-4357/ac1067

Micera, A., Zhukov, A. N., López, R. A., Innocenti, M. E., Lazar, M., Boella, E., et al. (2020b). Particle-in-cell Simulation of Whistler Heat-Flux Instabilities in the Solar Wind: Heat-Flux Regulation and Electron Halo Formation. *Astrophysical J. Lett.* 903, L23. doi:10.3847/2041-8213/abc0e8

Migliuolo, S. (1986). The Field Swelling and Mirror Modes: Connection of the Two Instabilities. *J. Geophys. Res.* 91, 7981–7988. doi:10.1029/JA091iA07p07981

Mozer, F. S., Bonnell, J. W., Bowen, T. A., Schumm, G., and Vasko, I. Y. (2020). Large-amplitude, Wideband, Doppler-Shifted, Ion Acoustic Waves Observed on the Parker Solar Probe. *Astrophysical J.* 901, 107. doi:10.3847/1538-4357/abafb4

Mozer, F. S., Bale, S. D., Cattell, C. A., Halekas, J., Vasko, I. Y., Verniero, J. L., et al. (2022). Core Electron Heating by Triggered Ion Acoustic Waves in the Solar Wind. *Astrophysical J. Lett.* 927, L15. doi:10.3847/2041-8213/ac5520

Mozer, F. S., Bonnell, J. W., Hanson, E. L. M., Gasque, L. C., and Vasko, I. Y. (2021a). Nonlinear Ion-Acoustic Waves, Ion Holes, and Electron Holes in the Near-Sun Solar Wind. *Astrophysical J.* 911, 89. doi:10.3847/1538-4357/abed52

Mozer, F. S., Vasko, I. Y., and Verniero, J. L. (2021b). Triggered Ion-Acoustic Waves in the Solar Wind. *Astrophysical J. Lett.* 919, L2. doi:10.3847/2041-8213/ac2259

Müller, D., St. Cyr, O. C., Zouganelis, I., Gilbert, H. R., Marsden, R., Nieves-Chinchilla, T., et al. (2020). The Solar Orbiter Mission. *Astronomy AstrophysicsAstron. Astrophys.* 642, A1. doi:10.1051/0004-6361/202038467

Okuda, H., and Ashour-Abdalla, M. (1983). Acceleration of Hydrogen Ions and Conic Formation along Auroral Field Lines. *J. Geophys. Res.* 88, 899–915. doi:10.1029/ja088ia02p00899

Omelchenko, Y. A., Shapiro, V. D., Shevchenko, V. I., Ashour-Abdalla, M., and Schriver, D. (1994). Modified Lower Hybrid Fan Instability Excited by Precipitating Auroral Electrons. *J. Geophys. Res.* 99, 5965–5976. doi:10.1029/93ja01323

O'Neil, T. M., and Malmberg, J. H. (1968). Transition of the Dispersion Roots from Beam-type to Landau-type Solutions. *Phys. Fluids* 11, 1754–1760. doi:10.1063/1.1692190

Onsager, T. G., and Holzworth, R. H. (1990). Measurement of the Electron Beam Mode in Earth's Foreshock. *J. Geophys. Res.* 95, 4175–4186. doi:10.1029/JA095iA04p04175

Owen, C. J., Bruno, R., Livi, S., Louarn, P., Al Janabi, K., Allegrini, F., et al. (2020). The Solar Orbiter Solar Wind Analyser (SWA) Suite. *Astron. Astrophys.* 642, A16. doi:10.1051/0004-6361/201937259

Paesold, G., and Benz, A. O. (1999). Electron Firehose Instability and Acceleration of Electrons in Solar Flares. *Astron. Astrophys.* 351, 741–746.

Page, B., Vasko, I. Y., Artemyev, A. V., and Bale, S. D. (2021). Generation of High-Frequency Whistler Waves in the Earth's Quasi-Perpendicular Bow Shock. *Astrophysical J. Lett.* 919, L17. doi:10.3847/2041-8213/ac2748

Pagel, C., Crooker, N. U., Larson, D. E., Kahler, S. W., and Owens, M. J. (2005). Understanding Electron Heat Flux Signatures in the Solar Wind. *J. Geophys. Res.* 110, A01103. doi:10.1029/2004JA010767

Pagel, C., Gary, S. P., de Koning, C. A., Skoug, R. M., and Steinberg, J. T. (2007). Scattering of Suprathermal Electrons in the Solar Wind: ACE Observations. *J. Geophys. Res. (Space Phys.* 112, A04103. doi:10.1029/2006ja011967

Parashar, T. N., Salem, C., Wicks, R. T., Karimabadi, H., Gary, S. P., and Matthaeus, W. H. (2015). Turbulent Dissipation Challenge: a Community-Driven Effort. *J. Plasma Phys.* 81, 905810513. doi:10.1017/s0022377815000860

Parker, E. N. (1958). Dynamics of the Interplanetary Gas and Magnetic Fields. *Astrophysical J.* 128, 664. doi:10.1086/146579

Parker, E. N., Maksimovic, M., Issautier, K., Meyer-Vernet, N., Moncuquet, M., and Pantellini, F. (2010). "Kinetic and Hydrodynamic Representations of

Coronal Expansion and the Solar Wind," in *Twelfth International Solar Wind Conference. Vol. 1216 of American Institute of Physics Conference Series*. Editors M. Maksimovic, K. Issautier, N. Meyer-Vernet, M. Moncuquet, and F. Pantellini, 3–7. doi:10.1063/1.3395887

Pavan, J., Viñas, A. F., Yoon, P. H., Ziebell, L. F., and Gaelzer, R. (2013). Solar Wind Strahl Broadening by Self-Generated Plasma Waves. *Astrophysical J.* 769, L30. doi:10.1088/2041-8205/769/2/L30

Peter Gary, S. (1985b). Electrostatic Instabilities in Plasmas with Two Electron Components. *J. Geophys. Res.* 90, 8213–8222. doi:10.1029/JA090iA09p08213

Phillips, J. L., Gosling, J. T., McComas, D. J., Bame, S. J., Gary, S. P., and Smith, E. J. (1989). Anisotropic Thermal Electron Distributions in the Solar Wind. *J. Geophys. Res.* 94, 6563–6579. doi:10.1029/JA094iA06p06563

Phillips, J. L., and Gosling, J. T. (1990). Radial Evolution of Solar Wind Thermal Electron Distributions Due to Expansion and Collisions. *J. Geophys. Res.* 95, 4217–4228. doi:10.1029/ja095ia04p04217

Pierrard, V., Lazar, M., Poedts, S., Štverák, Š., Maksimovic, M., and Trávníček, P. M. (2016). The Electron Temperature and Anisotropy in the Solar Wind. Comparison of the Core and Halo Populations. *Sol. Phys.* 291, 2165–2179. doi:10.1007/s11207-016-0961-7

Pierrard, V., Lazar, M., and Schlickeiser, R. (2011). Evolution of the Electron Distribution Function in the Whistler Wave Turbulence of the Solar Wind. *Sol. Phys.* 269, 421–438. doi:10.1007/s11207-010-9700-7

Pierrard, V., Lazar, M., and Štverák, S. (2020). Solar Wind Plasma Particles Organized by the Flow Speed. *Sol. Phys.* 295, 1–14. doi:10.1007/s11207-020-01730-z

Pierrard, V., and Lemaire, J. (1996). Lorentzian Ion Exosphere Model. *J. Geophys. Res.* 101, 7923–7934. doi:10.1029/95ja03802

Pilipp, W. G., Miggenrieder, H., Montgomery, M. D., Mühlhäuser, K.-H., Rosenbauer, H., and Schwenn, R. (1987). Characteristics of Electron Velocity Distribution Functions in the Solar Wind Derived from the Helios Plasma Experiment. *J. Geophys. Res.* 92, 1075–1092. doi:10.1029/ja092ia02p01075

Pilipp, W., and Völk, H. J. (1971). Analysis of Electromagnetic Instabilities Parallel to the Magnetic Field. *J. Plasma Phys.* 6, 1–17. doi:10.1017/s0022377800025654

Píša, D., Souček, J., Santolík, O., Hanzelka, M., Nicolaou, G., Maksimovic, M., et al. (2021). First-year Ion-Acoustic Wave Observations in the Solar Wind by the RPW/TDS Instrument on Board Solar Orbiter. *Astron. Astrophys.* 656, A14. doi:10.1051/0004-6361/202140928

Podesta, J. J., and Roytershteyn, V. (2017). The Most Intense Electrical Currents in the Solar Wind: Comparisons between Single-spacecraft Measurements and Plasma Turbulence Simulations. *J. Geophys. Res. Space Phys.* 122, 6991–7004. doi:10.1002/2017JA024074

Ramani, A., and Laval, G. (1978). Heat Flux Reduction by Electromagnetic Instabilities. *Phys. Fluids* 21, 980–991. doi:10.1063/1.862342

Rincon, F., Schekochihin, A. A., and Cowley, S. C. (2015). Non-linear Mirror Instability. *Mon. Not. R. Astron. Soc.* 447, L45–L49. doi:10.1093/mnrasl/slu179

Riquelme, M. A., Quataert, E., and Verscharen, D. (2015). Particle-in-cell Simulations of Continuously Driven Mirror and Ion Cyclotron Instabilities in High Beta Astrophysical and Heliospheric Plasmas. *Astrophysical J.* 800, 27. doi:10.1088/0004-637x/800/1/27

Riquelme, M. A., Quataert, E., and Verscharen, D. (2016). PIC Simulations of the Effect of Velocity Space Instabilities on Electron Viscosity and Thermal Conduction. *Astrophysical J.* 824, 123. doi:10.3847/0004-637X/824/2/123

Riquelme, M., Osorio, A., Verscharen, D., and Sironi, L. (2022). Stochastic Electron Acceleration by Temperature Anisotropy Instabilities under Solar Flare Plasma Conditions. *Astrophysical J.* 924, 52. doi:10.3847/1538-4357/ac3e67

Riquelme, M., Quataert, E., and Verscharen, D. (2018). PIC Simulations of Velocity-Space Instabilities in a Decreasing Magnetic Field: Viscosity and Thermal Conduction. *Astrophysical J.* 854, 132. doi:10.3847/1538-4357/aaa6d1

Roberts, O. W., Verscharen, D., Narita, Y., Nakamura, R., Vörös, Z., and Plaschke, F. (2020). Possible Coexistence of Kinetic Alfvén and Ion Bernstein Modes in Sub-ion Scale Compressive Turbulence in the Solar Wind. *Phys. Rev. Res.* 2, 043253. doi:10.1103/PhysRevResearch.2.043253

Rogers, B. N., Denton, R. E., Drake, J. F., and Shay, M. A. (2001). Role of Dispersive Waves in Collisionless Magnetic Reconnection. *Phys. Rev. Lett.* 87, 195004. doi:10.1103/physrevlett.87.195004

Rosenbauer, H., Schwenn, R., Marsch, E., Meyer, B., Miggenrieder, H., Montgomery, M. D., et al. (1977). A Survey on Initial Results of the HELIOS Plasma Experiment. *J. Geophys. Zeitschrift Geophys.* 42, 561–580.

Rowlands, J., Shapiro, V. D., and Shevchenko, V. I. (1966). Quasilinear Theory of Plasma Cyclotron Instability. *Soviet J. Exp. Theor. Phys.* 23, 651.

Šafránková, J., Němeček, Z., Němec, F., Verscharen, D., Chen, C. H. K., Ďurovcová, T., et al. (2019). Scale-dependent Polarization of Solar Wind Velocity Fluctuations at the Inertial and Kinetic Scales. *Astrophysical J.* 870, 40. doi:10.3847/1538-4357/aaf239

Salem, C., Hubert, D., Lacombe, C., Bale, S. D., Mangeney, A., Larson, D. E., et al. (2003). Electron Properties and Coulomb Collisions in the Solar Wind at 1 AU:WindObservations. *Astrophysical J.* 585, 1147–1157. doi:10.1086/346185

Salem, C. S., Howes, G. G., Sundkvist, D., Bale, S. D., Chaston, C. C., Chen, C. H. K., et al. (2012). Identification of Kinetic Alfvén Wave Turbulence in the Solar Wind. *Astrophysical J.* 745, L9. doi:10.1088/2041-8205/745/1/l9

Salem, C. S., Pulupa, M., Bale, S. D., and Verscharen, D. (2021). Precision Electron Measurements in the Solar Wind at 1 au from NASA's Wind Spacecraft. *arXiv e-prints*. arXiv:2107.08125.

Sarfraz, M., Abbas, G., Farooq, H., and Zeba, I. (2021). Impact of Non-thermal Electrons on Spatial Damping: a Kinetic Model for the Parallel Propagating Modes. *Z. Naturforsch. Teil A* 76, 661–669. doi:10.1515/zna-2020-0352

Sarfraz, M., and Yoon, P. H. (2020). Combined Whistler Heat Flux and Anisotropy Instabilities in Solar Wind. *J. Geophys. Res. (Space Phys.* 125, e27380. doi:10.1029/2019ja027380

Scharer, J. E., and Trivelpiece, A. W. (1967). Cyclotron Wave Instabilities in a Plasma. *Phys. Fluids* 10, 591–595. doi:10.1063/1.1762153

Schekochihin, A. A., Cowley, S. C., Dorland, W., Hammett, G. W., Howes, G. G., Quataert, E., et al. (2009). Astrophysical Gyrokinetics: Kinetic and Fluid Turbulent Cascades in Magnetized Weakly Collisional Plasmas. *Astrophysical J. Suppl. Ser.* 182, 310–377. doi:10.1088/0067-0049/182/1/310

Schriver, D., and Ashour-Abdalla, M. (1990). Cold Plasma Heating in the Plasma Sheet Boundary Layer: Theory and Simulations. *J. Geophys. Res.* 95, 3987–4005. doi:10.1029/ja095ia04p03987

Schroeder, J. M., Boldyrev, S., and Astfalk, P. (2021). Stability of Superthermal Strahl Electrons in the Solar Wind. *Mon. Not. R. Astron. Soc.* 507, 1329–1336. doi:10.1093/mnras/stab2228

Schwartz, S. J. (1980). Plasma Instabilities in the Solar Wind: a Theoretical Review. *Rev. Geophys.* 18, 313–336. doi:10.1029/RG018i001p00313

Scime, E. E., Badeau, A. E., Littleton, J. E., and Littleton, J. E. (1999). The Electron Heat Flux in the Polar Solar Wind: Ulysses Observations. *Geophys. Res. Lett.* 26, 2129–2132. doi:10.1029/1999GL900503

Scime, E. E., Bame, S. J., Feldman, W. C., Gary, S. P., Phillips, J. L., and Balogh, A. (1994). Regulation of the Solar Wind Electron Heat Flux from 1 to 5 AU: Ulysses Observations. *J. Geophys. Res.* 99, 23401–23410. doi:10.1029/94JA02068

Scudder, J. D., and Olbert, S. (1979). A Theory of Local and Global Processes Which Affect Solar Wind Electrons, 1. The Origin of Typical 1 AU Velocity Distribution Functions-Steady State Theory. *J. Geophys. Res.* 84, 2755–2772. doi:10.1029/ja084ia06p02755

Shaaban, S. M., Lazar, M., López, R. A., Fichtner, H., and Poedts, S. (2019a). Firehose Instabilities Triggered by the Solar Wind Suprathermal Electrons. *Mon. Not. R. Astron. Soc.* 483, 5642–5648. doi:10.1093/mnras/sty3377

Shaaban, S. M., Lazar, M., López, R. A., Yoon, P. H., and Poedts, S. (2021). "Advanced Interpretation of Waves and Instabilities in Space Plasmas," in *Kappa Distributions; from Observational Evidences via Controversial Predictions to a Consistent Theory of Nonequilibrium Plasmas. Vol. 464 of Astrophysics and Space Science Library*. Editors M. Lazar, and H. Fichtner, 185–218. doi:10.1007/978-3-030-82623-9_10

Shaaban, S. M., Lazar, M., and Poedts, S. (2018). Clarifying the Solar Wind Heat Flux Instabilities. *Mon. Not. R. Astron. Soc.* 480, 310–319. doi:10.1093/mnras/sty1567

Shaaban, S. M., and Lazar, M. (2020). Whistler Instabilities from the Interplay of Electron Anisotropies in Space Plasmas: a Quasi-Linear Approach. *Mon. Not. R. Astron. Soc.* 492, 3529–3539. doi:10.1093/mnras/stz3569

Shaaban, S. M., Lazar, M., Yoon, P. H., Poedts, S., and López, R. A. (2019c). Quasi-linear Approach of the Whistler Heat-Flux Instability in the Solar Wind. *Mon. Not. R. Astron. Soc.* 486, 4498–4507. doi:10.1093/mnras/stz830

Shaaban, S. M., Lazar, M., Yoon, P. H., and Poedts, S. (2019b). Quasilinear Approach of the Cumulative Whistler Instability in Fast Solar Wind:

Constraints of Electron Temperature Anisotropy. *Astronomy Astrophysics* 627, A76. doi:10.1051/0004-6361/201935515

Shay, M. A., Drake, J. F., Eastwood, J. P., and Phan, T. D. (2011). Super-Alfvénic Propagation of Substorm Reconnection Signatures and Poynting Flux. *Phys. Rev. Lett.* 107, 065001. doi:10.1103/PhysRevLett.107.065001

Shevchenko, V. I., and Galinsky, V. L. (2010). Stability of the Strahl Electron Distribution Function and its Dynamics. *Nonlin. Process. Geophys.* 17, 593–597. doi:10.5194/npg-17-593-2010

Southwood, D. J., and Kivelson, M. G. (1993). Mirror Instability: 1. Physical Mechanism of Linear Instability. *J. Geophys. Res.* 98, 9181–9187. doi:10.1029/92JA02837

Squire, J., Quataert, E., and Schekochihin, A. A. (2016). A Stringent Limit on the Amplitude of Alfvénic Perturbations in High-Beta Low-Collisionality Plasmas. *Astrophysical J.* 830, L25. doi:10.3847/2041-8205/830/2/L25

Stansby, D., Horbury, T. S., Chen, C. H. K., and Matteini, L. (2016). Experimental Determination of Whistler Wave Dispersion Relation in the Solar Wind. *Astrophysical J.* 829, L16. doi:10.3847/2041-8205/829/1/L16

Stix, T. H. (1992). *Waves in Plasmas*. College Park, Maryland, USA: American Institute of Physics.

Štverák, Š., Maksimovic, M., Trávníček, P. M., Marsch, E., Fazakerley, A. N., and Scime, E. E. (2009). Radial Evolution of Nonthermal Electron Populations in the Low-Latitude Solar Wind: Helios, Cluster, and Ulysses Observations. *J. Geophys. Res.* 114, a–n. doi:10.1029/2008JA013883

Štverák, Š., Trávníček, P. M., and Hellinger, P. (2015). Electron Energetics in the Expanding Solar Wind via Helios Observations. *J. Geophys. Res. Space Phys.* 120, 8177–8193. doi:10.1002/2015JA021368

Štverák, Š., Trávníček, P., Maksimovic, M., Marsch, E., Fazakerley, A. N., and Scime, E. E. (2008). Electron Temperature Anisotropy Constraints in the Solar Wind. *J. Geophys. Res.* 113, a–n. doi:10.1029/2007JA012733

Sun, H., Zhao, J., Liu, W., Voitenko, Y., Pierrard, V., Shi, C., et al. (2021). Electron Heat Flux Instabilities in the Inner Heliosphere: Radial Distribution and Implication on the Evolution of the Electron Velocity Distribution Function. *Astrophysical J. Lett.* 916, L4. doi:10.3847/2041-8213/ac0f02

Thomsen, M. F., Barr, H. C., Gary, S. P., Feldman, W. C., and Cole, T. E. (1983). Stability of Electron Distributions within the Earth's Bow Shock. *J. Geophys. Res.* 88, 3035–3045. doi:10.1029/JA088iA04p03035

Tong, Y., Vasko, I. Y., Artemyev, A. V., Bale, S. D., and Mozer, F. S. (2019a). Statistical Study of Whistler Waves in the Solar Wind at 1 au. *Astrophysical J.* 878, 41. doi:10.3847/1538-4357/ab1f05

Tong, Y., Vasko, I. Y., Pulupa, M., Mozer, F. S., Bale, S. D., Artemyev, A. V., et al. (2019b). Whistler Wave Generation by Halo Electrons in the Solar Wind. *Astrophysical J.* 870, L6. doi:10.3847/2041-8213/aaf734

Vasko, I. Y., Agapitov, O. V., Mozer, F. S., Bonnell, J. W., Artemyev, A. V., Krasnoselskikh, V. V., et al. (2017). Electron-acoustic Solitons and Double Layers in the Inner Magnetosphere. *Geophys. Res. Lett.* 44, 4575–4583. doi:10.1002/2017gl074026

Vasko, I. Y., Alimov, K., Phan, T., Bale, S. D., Mozer, F. S., and Artemyev, A. V. (2022). Kinetic-scale Current Sheets in the Solar Wind at 1 au: Scale-dependent Properties and Critical Current Density. *Astrophysical J. Lett.* 926, L19. doi:10.3847/2041-8213/ac4fc4

Vasko, I. Y., Krasnoselskikh, V., Tong, Y., Bale, S. D., Bonnell, J. W., and Mozer, F. S. (2019). Whistler Fan Instability Driven by Strahl Electrons in the Solar Wind. *Astrophysical J.* 871, L29. doi:10.3847/2041-8213/ab01bd

Vasko, I. Y., Kuzichev, I. V., Artemyev, A. V., Bale, S. D., Bonnell, J. W., and Mozer, F. S. (2020). On Quasi-Parallel Whistler Waves in the Solar Wind. *Phys. Plasmas* 27, 082902. doi:10.1063/5.0003401

Vedenov, A. A., Velikhov, E. P., and Sagdeev, R. d. Z. (1961). Stability of Plasma. *Sov. Phys. Usp.* 4, 332–369. doi:10.1070/PU1961v004n02ABEH003341

Verdon, A. L., Cairns, I. H., Melrose, D. B., and Robinson, P. A. (2009). Warm Electromagnetic Lower Hybrid Wave Dispersion Relation. *Phys. Plasmas* 16, 052105. doi:10.1063/1.3132628

Verscharen, D., Chandran, B. D. G., Jeong, S.-Y., Salem, C. S., Pulupa, M. P., and Bale, S. D. (2019a). Self-induced Scattering of Strahl Electrons in the Solar Wind. *Astrophysical J.* 886, 136. doi:10.3847/1538-4357/ab4c30

Verscharen, D., and Chandran, B. D. G. (2018). NHDS: The New Hampshire Dispersion Relation Solver. *Res. Notes AAS* 2, 13. doi:10.3847/2515-5172/aabfe3

Verscharen, D., Chen, C. H. K., and Wicks, R. T. (2017). On Kinetic Slow Modes, Fluid Slow Modes, and Pressure-Balanced Structures in the Solar Wind. *Astrophysical J.* 840, 106. doi:10.3847/1538-4357/aa6a56

Verscharen, D., Klein, K. G., Chandran, B. D. G., Stevens, M. L., Salem, C. S., and Bale, S. D. (2018). ALPS: the Arbitrary Linear Plasma Solver. *J. Plasma Phys.* 84, 905840403. doi:10.1017/S0022377818000739

Verscharen, D., Klein, K. G., and Maruca, B. A. (2019b). The Multi-Scale Nature of the Solar Wind. *Living Rev. Sol. Phys.* 16, 5. doi:10.1007/s41116-019-0021-0

Verscharen, D., Wicks, R. T., Alexandrova, O., Bruno, R., Burgess, D., Chen, C. H. K., et al. (2021a). A Case for Electron-Astrophysics. *Exp. Astron*. doi:10.1007/s10686-021-09761-5

Verscharen, D., Wicks, R. T., Branduardi-Raymont, G., Erdélyi, R., Frontera, F., Götz, C., et al. (2021b). The Plasma Universe: A Coherent Science Theme for Voyage 2050. *Front. Astron. Space Sci.* 8, 30. doi:10.3389/fspas.2021.651070

Vocks, C., and Mann, G. (2009). Scattering of Solar Energetic Electrons in Interplanetary Space. *Astronomy Astrophysics* 502, 325–332. doi:10.1051/0004-6361/200911738

Vocks, C., Salem, C., Lin, R. P., and Mann, G. (2005). Electron Halo and Strahl Formation in the Solar Wind by Resonant Interaction with Whistler Waves. *Astrophysical J.* 627, 540–549. doi:10.1086/430119

Watanabe, K., and Taniuti, T. (1977). Electron-acoustic Mode in a Plasma of Two-Temperature Electrons. *J. Phys. Soc. Jpn.* 43, 1819–1820. doi:10.1143/jpsj.43.1819

Whittlesey, P. L., Larson, D. E., Kasper, J. C., Halekas, J., Abatcha, M., Abiad, R., et al. (2020). The Solar Probe ANalyzers-Electrons on the Parker Solar Probe. *Astrophysical J. Suppl. Ser.* 246, 74. doi:10.3847/1538-4365/ab7370

Wicks, R. T., and Verscharen, D.the Debye Team (2019). Debye: Proposal for a Fast Mission to Study Electron-Astrophysics. *Mission Propos. Eur. Space Agency*.

Wilson, L. B., Cattell, C. A., Kellogg, P. J., Goetz, K., Kersten, K., Kasper, J. C., et al. (2009). Low-frequency Whistler Waves and Shocklets Observed at Quasi-Perpendicular Interplanetary Shocks. *J. Geophys. Res.* 114, A10106. doi:10.1029/2009JA014376

Wilson, L. B., Koval, A., Sibeck, D. G., Szabo, A., Cattell, C. A., Kasper, J. C., et al. (2013). Shocklets, SLAMS, and Field-Aligned Ion Beams in the Terrestrial Foreshock. *J. Geophys. Res. Space Phys.* 118, 957–966. doi:10.1029/2012ja018186

Wüest, M., Evans, D. S., and von Steiger, R. (2007). *Calibration of Particle Instruments in Space Physics*. Noordwijk, Netherlands: Published for the International Space Science Institute by ESA Communications.

Zhao, J., Lee, L., Xie, H., Yao, Y., Wu, D., Voitenko, Y., et al. (2022). Quantifying Wave–Particle Interactions in Collisionless Plasmas: Theory and its Application to the Alfvén-Mode Wave. *Astrophys. J.* 930. doi:10.3847/1538-4357/ac59b7

Conflict of Interest: The authors declare that the research was conducted in the absence of any commercial or financial relationships that could be construed as a potential conflict of interest.

Publisher's Note: All claims expressed in this article are solely those of the authors and do not necessarily represent those of their affiliated organizations, or those of the publisher, the editors and the reviewers. Any product that may be evaluated in this article, or claim that may be made by its manufacturer, is not guaranteed or endorsed by the publisher.

frontiers | Frontiers in Physics

PERSPECTIVE
published: 04 August 2022
doi: 10.3389/fphy.2022.942167

The Gary Picture of Short-Wavelength Plasma Turbulence—The Legacy of Peter Gary

Y. Narita[1]*, *T.N. Parashar*[2] *and J. Wang*[3]

[1]Space Research Institute, Austrian Academy of Sciences, Graz, Austria, [2]Victoria University of Wellington, Wellington, New Zealand, [3]Department of Astronautical Engineering, University of Southern California, Los Angeles, CA, United States

Collisionless plasmas in space often evolve into turbulence by exciting an ensemble of broadband electromagnetic and plasma fluctuations. Such dynamics are observed to operate in various space plasmas such as in the solar corona, the solar wind, as well as in the Earth and planetary magnetospheres. Though nonlinear in nature, turbulent fluctuations in the kinetic range (small wavelengths of the order of the ion inertial length or smaller) are believed to retain some properties reminiscent of linear-mode waves. In this paper we discuss what we understand, to the best of our ability, was Peter Gary's view of kinetic-range turbulence. We call it the Gary picture for brevity. The Gary picture postulates that kinetic-range turbulence exhibits two different channels of energy cascade: one developing from Alfvén waves at longer wavelengths into kinetic Alfvén turbulence at shorter wavelengths, and the other developing from magnetosonic waves into whistler turbulence. Particle-in-cell simulations confirm that the Gary picture is a useful guide to reveal various properties of kinetic-range turbulence such as the wavevector anisotropy, various heating mechanisms, and control parameters that influence the evolution of turbulence in the kinetic range.

Keywords: plasma turbulence, kinetic range, particle-in-cell simulations, whistler waves, Kinetic Alfvén waves

OPEN ACCESS

Edited by:
Joseph E Borovsky,
Space Science Institute, United States

Reviewed by:
Kristopher G Klein,
University of Arizona, United States

***Correspondence:**
Y. Narita
yasuhito.narita@oeaw.ac.at

Specialty section:
This article was submitted to Space Physics, a section of the journal Frontiers in Physics

Received: *12 May 2022*
Accepted: *20 June 2022*
Published: *04 August 2022*

Citation:
Narita Y, Parashar TN and Wang J (2022) The Gary Picture of Short-Wavelength Plasma Turbulence—The Legacy of Peter Gary. Front. Phys. 10:942167. doi: 10.3389/fphy.2022.942167

1 INTRODUCTION

Understanding solar wind dynamics requires the ability to model not only the plasma flows and the evolution of turbulent electromagnetic field fluctuations, but also the exchange of energy between the plasma and the turbulent fluctuations. This exchange between fields and plasma can be thought of as operating in two regimes: the relatively long wavelengths of the inertial range (where the fluid description of plasma is valid) and the relatively shorter wavelengths of the kinetic range (where the kinetic behavior of plasma plays an important role).

The kinetic-range turbulence makes a marked difference from fluid turbulence. Due to the collisionless nature of space plasma, the velocity distribution can take any non-Maxwellian form allowed by the Vlasov equation. The non-Maxwellian features could include, for example, a beam component or temperature anisotropy as internal degree of freedom [1,2]. The non-Maxwellian features necessitate a kinetic treatment where the particle motions play an important role. Many collective effects such as wave-particle resonances (e.g. Landau and cyclotron resonances) [3,4] and kinetic instabilities [5,6] come into play, enriching the kinetic range dynamics significantly.

In both the fluid and kinetic regimes the fluctuation energy undergoes a forward energy cascade from longer to shorter wavelengths. In incompressible MHD (magnetohydrodynamics) the energy supplied by the largest scales is distributed across scales in the inertial range by a conservative cascade

down to the dissipative scales [7–9]. The MHD cascade also develops strong anisotropy in the wavenumber space, with excess energy in perpendicular wavevector components $k_\perp > k_\parallel$ [8,10], where $k_\perp$ and $k_\parallel$ denote the wavevector components perpendicular and parallel to the mean magnetic field $\boldsymbol{B}_0$, respectively. This picture modifies when compressive effects are included. At some scale in the inertial range, the compressive and incompressible cascades decouple and progress independently [11,12]. The nature of the cascade changes even more drastically near the kinetic scales. Accurate modeling of short-wavelength turbulence requires using the fully kinetic framework of Vlasov-Maxwell equations (1), (2), (13)–(16). The equations are typically studied under various limits: linear, quasi-linear, and nonlinear. The tools used vary from linear dispersion solvers to fully nonlinear kinetic simulations or a combination thereof [17–21].

In the spirit of celebrating the achievements and legacy of Stephen Peter Gary (1939–2021) and of extending his review [22], here we discuss the detailed profile of short-wavelength turbulence such as the energy cascade and wavevector anisotropy, heating rates, potential controlling parameters, competition between linear instabilities and nonlinearities. This is not going to be a comprehensive description of kinetic-range turbulence, but a summary of what we believe Peter Gary's view of kinetic-range turbulence was, which we call *the Gary picture of kinetic-range turbulence*.

Peter Gary was a pioneer of using the kinetic theory and numerical simulations, and tackled many different problems in space plasma physics. He discovered, for example, in his seminal work in Gary [23] the reversal of field rotation sense as the ion cyclotron wave (left-hand polarized wave) turns into the kinetic Alfvén wave (right-hand polarized) at highly oblique propagation. The mechanism remained a mystery for a long time, and was finally understood as the transition from the Hall current into the diamagnetic current in the wave dynamics [24]. Peter Gary used analytic and numerical methods to understand the properties of linear-mode waves and microinstabilities in the kinetic plasma theory with applications to the wave activity in space plasmas such as the solar corona, the solar wind, the shock-upstream and shock-downstream regions, the magnetosphere, and the planetary and cometary environments [5]. Peter Gary also developed and ran simulations to reveal the nonlinear processes in turbulent plasmas beyond the limit of linear kinetic theory.

A huge amount of literature has been devoted to the nature of kinetic-range turbulence (see e.g., [22,25–29], and many references therein). There is an ongoing discussion in the solar wind turbulence community as to the character of the constituent fluctuations of the kinetic range; the majority of observations indicate that kinetic Alfvén modes are dominant at proton scales, while a minority of measurements implies that significant amplitudes of magnetosonic/whistler (MSW) mode are present as well [30–32]. The Gary picture is based on the notion that both types of fluctuations are present with an emphasis that the relative importance of these modes is given as functions of the plasma and turbulence parameters. The Gary picture has widely been tested against both two- and three-dimensional PIC (particle-in-cell) simulations (see, e.g. [33], about the concept and algorithm). The interpretation of the simulation results by Gary and his collaborators was accompanied by linear Vlasov theory and spacecraft observations in the solar wind.

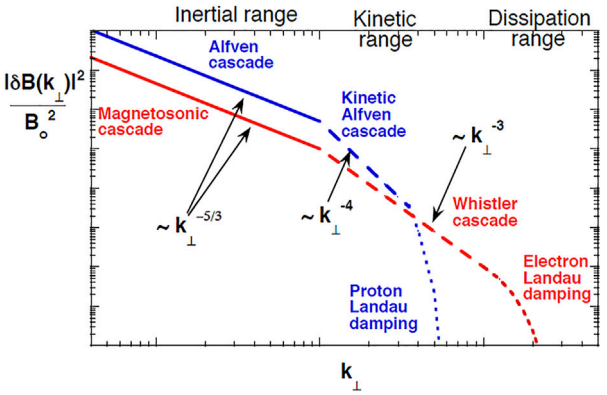

FIGURE 1 | Schematic energy spectra suggesting the co-existence and competition between kinetic Alfvén turbulence (Alfvén channel) and whistler turbulence (magnetosonic channel) in the short-wavelength range. Each type of turbulence may have a non-trivial domain over which it dominates the magnetic fluctuation spectra. Picture drawn by Peter Gary.

2 TWO COMPETING CHANNELS OF ENERGY CASCADE

One may define plasma turbulence as an ensemble of broadband, relatively large amplitude, stochastic incoherent fluctuations in an ionized gas. Plasma turbulence is observed in many astrophysical systems [34,35], in the solar corona [36], in the solar wind [37,38], as well as in terrestrial and planetary magnetospheres [28]. The energy in turbulent magnetic fields is a likely source of accelerating or thermalizing electrons and ions in many space and astrophysical plasmas, although the scientific understanding of these energy transfer processes is yet incomplete and is the subject of substantial current research [39–41].

Given the highly nonlinear nature of turbulent processes, a common strategy is to perform simulations that run on massively parallel computers. Depending on the regime of interest single/multi fluid MHD simulations or kinetic simulations with varied levels of physics are used to study plasma turbulence [20,21,42–49]. In the kinetic range fully kinetic simulations that treat both ions and electrons as kinetic species are desirable. Of these, the most common simulation method is particle-in-cell [20,21]. Nonlinear computations usually lead to complex results which are not subject to simple interpretations such as scalings predicted by linear theory. Yet, the quasi-linear theory offers a hope that, perhaps under some conditions, some aspects of plasma turbulence can be represented in terms of relatively simple scaling relations.

The adjectives whistler and kinetic Alfvén are widely used to describe components of short-wavelength turbulence in space. The Gary picture describes whistler turbulence and kinetic Alfvén

turbulence as co-existing, competing channels of energy cascade as follows:

1. Wavevectors develop nearly perpendicular to the local mean magnetic field (as a consequence of magnetohydrodynamic turbulence).
2. Whistler and kinetic Alfvén waves (or whistler and kinetic Alfvén turbulence, respectively1) are dominant at shorter wavelengths (in the sense that the energy exceeds that of other components such as sideband waves, pumped waves by wave-wave couplings, and short-living coherent or solitary waves).
3. Both of whistler and kinetic Alfvén channels forms an inertial-range spectrum with a power law.
4. Ions (protons) are primarily heated by the interaction with the kinetic Alfvén waves; Electrons are primarily heated by the interaction with the whistler waves.

The evidence is far from conclusive that only one kind of fluctuation mode is dominant in energetics throughout the inertial as well as the kinetic ranges. **Figure 1** illustrates how both kinetic Alfvén and magnetosonic/whistler fluctuations contribute to kinetic-range turbulence. Although the overall energy density of magnetosonic/whistler turbulence may be small compared to that of Alfvén turbulence, it is possible that the former type may dominate fluctuation amplitudes and electron dissipation at sufficiently short wavelengths.

From a theoretical perspective, Howes et al. [50] argued using gyrokinetic linear theory that the solar wind like parameters are a sweet spot for kinetic Alfvén waves to have very low damping rates and hence argued that kinetic Alfvén waves can cascade down to electron scales. Podesta et al. [51] however argued that the damping rates of kinetic Alfvén waves become significant before electron scales are approached. Howes et al. [52] used data from WIND spacecraft to argue that the fast mode fluctuations in the inertial range have much less power compared to the Alfvén fluctuations. They further argued that this implied negligible power in the fast magnetosonic/whistler branch in the kinetic scales. However theoretical considerations from compressible MHD turbulence suggest that Alfvén-Alfvén-fast triadic interactions, that are missing in incompressible MHD turbulence such as that by Goldreich and Sridhar [53], can pump power into higher wavenumber fast mode fluctuations [54]. There is evidence that in compressible MHD, there is a parallel cascade of the compressive fluctuations [55]. The compressive cascade decouples from the incompressible cascade at some scale in the inertial range and proceeds independently in a conservative fashion [12]. Such a decoupling could provide conditions for the cascade of compressive fluctuations to potentially transfer energy down to electron scales.

Another important fluctuation type is the left-hand polarized ion-cyclotron waves (or Alfvén-cyclotron waves) at relatively high frequencies in space plasmas. Parallel propagating cyclotron waves are likely to be local sources of turbulent energy in the solar wind. Indeed, the ion-cyclotron waves are observed by the Wind spacecraft in the solar wind, and the wave events are reported and analyzed by Peter Gary himself [56], indicating the excitation of ion-cyclotron waves (ICWs) by proton temperature anisotropy (with an excess of perpendicular temperature) and the excitation of whistler-type right-hand polarized magnetosonic waves by the ion component relative flows. The spacecraft observations of magnetic helicity by Podesta and Gary. [57], He et al. [58] support the presence of both kinetic Alfvén waves and parallel propagating ion-cyclotron waves or whistler waves in the turbulent solar wind. It was hypothesized by Klein et al. [59] that the ICWs and whistler waves are produced by kinetic instabilities and are not part of the turbulent cascade. Recent hybrid kinetic simulations of imbalanced turbulence, relevant to inner heliospheric conditions, also show evidence for possible localized generation of ICWs [60]. These ICWs were suggested to not have a significant energy budget but have enough energy perpendicularly heat of ions.

3 LESSONS FROM THEORETICAL AND NUMERICAL STUDIES

Peter Gary and his collaborators have done extensive PIC simulations and other theoretical analyses to test the Gary picture. The PIC simulations are typically initialized with a narrow-band spectrum of relatively gyrotropic, relatively long wavelength normal modes which satisfy the properties of kinetic Alfvén waves and/or whistler waves derived from the linear Vlasov theory. It is possible to visualize the turbulence energy in the four-dimensional spectral domain (spanning the frequencies and the three components of wavevectors), and the spectra from the PIC simulations can nowadays be compared to that from the multi-spacecraft data [61]. The nonlinear temporal evolution of the system leads to a forward energy cascade that develops a broadband, anisotropic spectrum of turbulence. Both electrons and ions gain energy as well as show increased species entropies. The simulations were performed using two different codes: 1) the P3D code with MHD-like initial conditions under both 2.5D and 3D configurations [62], [63] and 2) the 3D-EMPIC code [64] in which initial spectra of relatively long-wavelength fluctuations were imposed. Both P3D and 3D-EMPIC are fully three-dimensional (3D) codes. The simulations represent magnetized collisionless plasmas and a broad range of kinetic waves (such as kinetic Alfvén and whistler waves) are set.

3.1 Energy Cascade and Wavevector Anisotropy

Cascade Mechanism

The fundamental processes of energy cascade are formulated by nonlinear interactions that transfer energy across scales. The most likely process (in terms of probability or cross section) is the triadic interaction which models two waves interacting with each other to generate a different wave. These triadic interactions are constrained to the conservation of frequencies and wavenumbers in the form of.

$$\omega_1 + \omega_2 = \omega_3 \quad (1)$$

$$\boldsymbol{k}_1 + \boldsymbol{k}_2 = \boldsymbol{k}_3. \quad (2)$$

These couplings hold regardless of whether the fluctuations are linear wave like or nonlinear. Peter Gary liked to think of these interactions in the sense of two waves interacting to produce a third wave [7,53]. Any combination of the frequencies between ω_1 and ω_2 is possible although the most efficient couplings in hydrodynamics are $k_1 \sim k_2$ and $\omega_1 \sim \omega_2$. If the generated wave ω_3 falls onto the solution of linear Vlasov dispersion equation, the wave ω_3 may have a longer lifetime as the fluctuation is supported by the background plasma condition. In general, the generated wave ω_3 does not fall onto the linear-mode dispersion relation and appears as a pumped or forced wave. The frequency and wavevector matching conditions (**Eqs. 1** and **2**) are a useful tool to test for the hypothesis that the forward cascade leads to wavevector anisotropies in a homogeneous, collisionless, magnetized plasma.

Gary [65] revisited the linear Vlasov theory and evaluated the matching conditions for three linear-mode modes: 1) Alfvén-cyclotron waves (at longer wavelengths), 2) magnetosonic waves (at longer wavelengths), and 3) whistler waves (at intermediate wavelengths). The test successfully explains that Alfvén waves and magnetosonic-whistler waves develop into forward cascade and wavevector anisotropy in favor of generating higher wavenumbers perpendicular to the mean magnetic field (energy spectrum extending perpendicular to the mean field). An exceptional case is that when the ion beta is close to unity, the cascade of long wavelength magnetosonic waves is favored by $k_\perp \sim k_\parallel$. The forward cascade of whistler turbulence shows a consistent development to wavevector directions predominantly quasi-perpendicular to the mean magnetic field in the PIC simulations [66–68] and in the Cluster and MMS observations in the solar wind [32,69–71].

Kinetic extension is needed to account for the energy transfer from the waves into the particles in the quasi-linear fashion. The wave-particle interactions occur efficiently when either the Landau resonance condition

$$\omega - k_\parallel v_\parallel = 0 \quad (3)$$

or the cyclotron resonance condition

$$\omega - k_\parallel v_\parallel = \pm\, \Omega_j \quad (4)$$

is satisfied. Here, $v_\parallel$ is the parallel velocity of particle of jth species, and Ω_j is the cyclotron frequency of jth species. The wave-particle interactions involving wave-wave couplings are, for example, represented by the condition

$$\omega_1 - \omega_2 = \left(k_{\parallel,1} - k_{\parallel,2}\right) v_\parallel. \quad (5)$$

for the Landau resonance [22].

The dispersion relation was used by Narita and Gary [72] and Saito et al. [73] to derive scaling laws for self-interacting whistler waves at highly oblique propagation with respect to the mean magnetic field. In the fashion of a phenomenological model, the inertial-range spectrum was constructed for homogeneous, highly-oblique whistler turbulence as a generalization of the Iroshnikov-Kraichnan model for magnetohydrodynamic turbulence [7,74]. The modeled whistler turbulence is characterized by an energy spectrum with a spectral index of −5/2 as a function of the perpendicular components of the wavevectors.

Wavevector Anisotropy

The simulations by Chang et al. [45,66,67,75], Gary et al. [68], and Hughes et al. [46,76] used a realistic ion-to-electron mass ratio of 1836, and focused on understanding the relationships between field fluctuations and both the electron and ion dynamics. These computations followed the time evolution of whistler fluctuations as they decay via forward cascade into a broadband, anisotropic, turbulent spectrum at shorter wavelengths (**Figure 2**). This cascade leads to a spectrum of fluctuations that are consistent with the linear dispersion solution for whistler modes especially in the low electron-beta case $\beta_e \ll 1$ (**Figure 3**).

The consequent reduced magnetic fluctuation spectra show clear breaks as functions of $k_\perp$ corresponding to transitions from relatively steep slopes at long wavelengths to even steeper slopes at shorter wavelengths, similar to electron-scale spectral break measured near 50 Hz in Cluster spacecraft measurements of solar wind turbulence [30,77,78].

Defining the wavevector anisotropy factor A as the spectral moment (see, e.g. [79])

$$A = \frac{\sum_k k_\perp^2 |\delta \boldsymbol{B}(\boldsymbol{k})|^2}{\sum_k k_\parallel^2 |\delta \boldsymbol{B}(\boldsymbol{k})|^2}, \quad (6)$$

the forward cascade of whistler turbulence in the 3D PIC simulations consistently leads to wavevector anisotropy extending perpendicular to the mean magnetic field characterized by $A \gg 1$, consistent with analytic and numerical calculations for electron magnetohydrodynamic (EMHD) [80,81] as well as two-dimensional PIC simulations [82]. As the plasma beta increases, whistler turbulence becomes less anisotropic and evolves towards nearly isotropic spectra. This has been shown to be true in both PIC simulations [67] as well as the solar wind observations [83].

3.2 Heating Profile

Using 3D PIC simulations, a number of papers by Peter Gary and collaborators also elaborated on the issue of electron and ion heating rates by whistler turbulence [46,47,56,76]. The heating rate of jth species is evaluated by

$$Q_j = \frac{1}{T_{j,\mathrm{ini}}} \frac{\mathrm{d}T_j}{\mathrm{d}t}, \quad (7)$$

where T_j is the temperature of jth species (in units of energy, including the Boltzmann constant), $T_{j,\mathrm{ini}}$ is the initial temperature, and t the elapsed time normalized to the electron plasma frequency. The temperature is estimated from the pressure p_j (the trace of pressure tensor) and the number density n_j as $T_j = \frac{p_j}{n_j}$. We call T_j the total temperature of the jth species even though the corresponding distributions are not necessarily Maxwellians for two reasons: 1) it is the definition of temperature for collisional fluids with Maxwellian distributions,

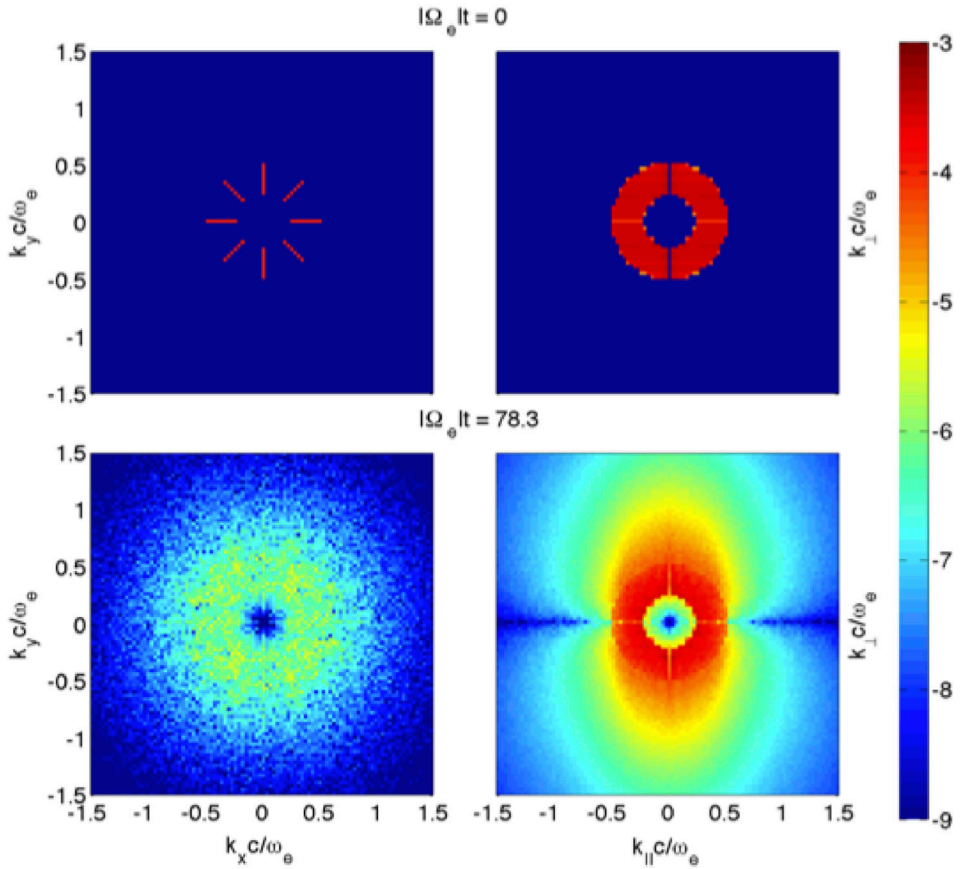

FIGURE 2 | 3D PIC simulations of whistler turbulence cascade. Simulation domain: 2048^3 cells. Macro-particles: 2.75×10^{11}/species. The plot shows magnetic energy wavevector spectra at two times: $t = 0$ (top) and $t\,\Omega_e = 78.3$ (bottom). Left column: $k_x - k_y$ spectra cut at $k_\parallel = 0$. Right column: $k_\parallel - k_\perp$ spectra reduced over the azimuthal angle of the perpendicular wavevectors [45].

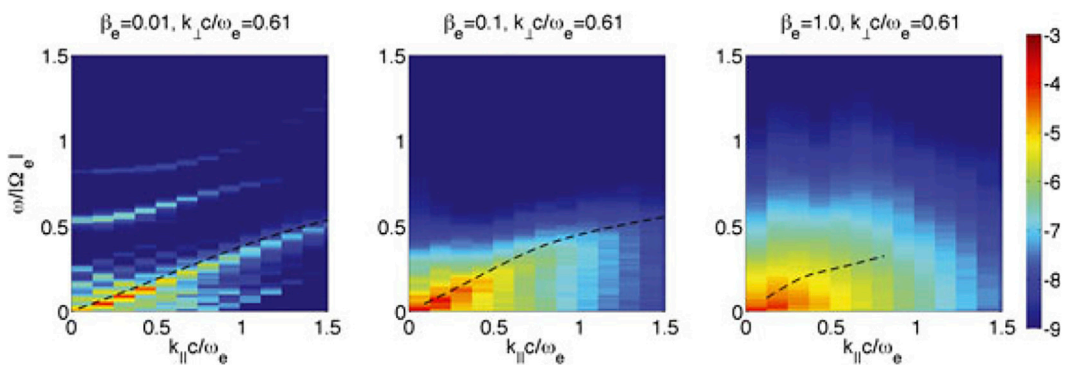

FIGURE 3 | Energy spectrum in the domain of frequency and parallel wavenumber to the mean magnetic field computed over the full time evolution of PIC simulation using three different values electron beta: 0.01 (left), 0.1 (middle), and 1 (right). From Chang et al. [67].

and 2) it is the quantity that is typically computed from spacecraft observations of distribution functions.

Considering the maximum values of the heating rates Q_i (for ions) and Q_e (for electrons) across each simulation, an approximately linear relationship was found between the heating rate ratio Q_i/Q_e and the mass ratio m_i/m_e, suggesting that an artificially reduced mass ratio may not change the fundamental physics of whistler turbulence dissipation. Hughes et al. [76] showed that, although whistler turbulence heats electrons more rapidly than ions, ion heating does play a

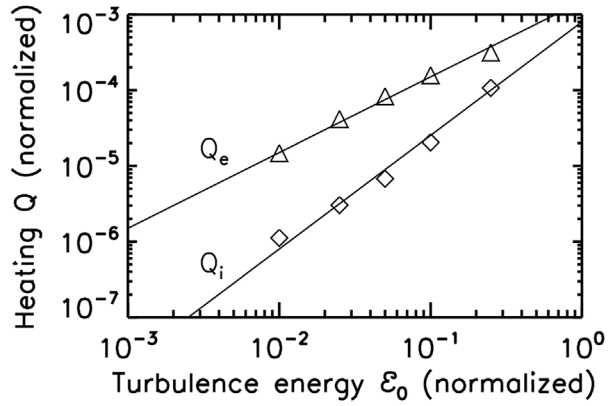

FIGURE 4 | Heating rate Q for electrons and ions as a function of the magnetic fluctuation energy $\mathcal{E}_0$ at the initial time obtained from the 3D PIC simulations by Gary et al. [56]. The power-law fitting yields empirical scaling of $Q_e = 0.0015\mathcal{E}_0$ for the electrons and $Q_i = 0.0008\mathcal{E}_0^{3/2}$ for the ions.

role in whistler turbulence dissipation. In particular, the ions experience the majority of their energy gain in directions perpendicular to the mean magnetic field, consistent with the temperature anisotropy observed in the solar wind [1,2,84,85]. Moreover, successively larger simulation domains corresponding to successively longer wavelengths of whistler turbulence yield weaker electron heating and stronger ion heating. This is consistent with the findings of Saito and Nariyuki [86] who used 2.5D PIC simulations of whistler turbulence leading to perpendicular proton heating. This is also qualitatively consistent with the findings of Wu et al. [87] and Matthaeus et al. [88]. In particular, Matthaeus et al. [88] suggested that the ratio of ion cyclotron time to nonlinear time computed at the proton scales is an important factor in determining the relative heating of ions and electrons. The ratio is directly proportional to a positive power of the system size ($\lambda^{2/3}$). See **Eq. 3** in Matthaeus et al. [88].

Gary et al. [56] used 3D PIC simulations to study ion and electron heating due to whistler turbulence as functions of the fluctuation energy $\mathcal{E}_0$ (at the initial time)

$$\mathcal{E}_0 = \frac{\sum_k |\delta \boldsymbol{B}_k|^2}{B_0^2}. \tag{8}$$

They found that the maximum rate of electron heating scales approximately linearly with the fluctuation energy, suggesting a quasi-linear type heating due to electron Landau damping. The maximum ion heating on the other hand scales with the fluctuation energy roughly by a power of 3/2,

$$Q_e \propto \mathcal{E}_0; \quad Q_i \propto \mathcal{E}_0^{3/2}, \tag{9}$$

suggesting a nonlinear mechanism acting to heat the relatively unmagnetized ions (**Figure 4**). The scalings (**Eq. 9**) are consistent with the non-resonant "stochastic heating" discussed by Chandran et al. [89], and is also close to the scaling $Q_i \propto \mathcal{E}_0^{1.6}$ obtained from the 3D hybrid PIC simulations of Alfvén turbulence by Vasquez et al. [90]. This scaling is also consistent with the findings of Matthaeus et al. [88]. They also found that (see their **Eq. 3**) $Q_i/Q_e \propto \tau_{ci}/\tau_{nl} = \delta B/B_0 = \mathcal{E}_0^{0.5}$ where τ_{ci} is the cyclotron time and τ_{nl} is the nonlinear time computed from fluctuations at the system size. Hughes et al. [46] studied whistler turbulence dissipation via ion and electron heating as functions of electron beta β_e, and found that at $\mathcal{E}_0 = 0.10$ (10% fluctuation energy relative to that of the large-scale magnetic field) the maximum values of both Q_e and Q_i scale as β_e^{-1}. It is worth noting that while there are similarities between the scaling laws derived by Gary et al. [56] and other works, more studies are needed to quantitatively differentiate or compare these theories further.

Hughes et al. [46] used 3D PIC simulations to study electron and ion heating due to kinetic Alfvén turbulence. Similar to the 3D PIC simulations of whistler turbulence, the computations represent the forward cascade of freely-decaying turbulence carried out as an initial-value problem on a collisionless, homogeneous, magnetized plasma. In common with the whistler turbulence simulations, electron heating by kinetic Alfvén turbulence is preferentially in directions parallel/anti-parallel to the mean magnetic field (Landau damping) and the maximum electron heating rate linearly scales with the initial fluctuation energy, $Q_e \propto \mathcal{E}_0$. In contrast to the whistler turbulence case, however, the kinetic Alfvén turbulence simulations yield ion velocity distributions that remain relatively isotropic. The maximum heating rate is higher for the ions than for the electrons, $Q_i > Q_e$. An important difference between the whistler and kinetic Alfvén simulations was that the mass ratio used in the latter was $m_i/m_e = 100$. One of the side effects of lower mass ratio, in the linear limit, is that the kinetic Alfvén waves can reach beyond electron scales for smaller mass ratio, but damp critically well before electron scales are reached for realistic mass ratios [91].

Based on the considerations above, a desirable set of simulations would cover not only a large inertial range above ion scales, but also have a realistic mass ratio. This is still computationally challenging by the present standards.

3.3 Search for Control Parameters and Scaling Relations

In the physical sense, dynamics and dissipation mechanism of kinetic-range turbulence are expected to depend on control parameters such as the fluctuation energy $\mathcal{E}_0$ and beta values (β_e and β_i) to be consistent with those observed in the solar wind. However, the large computational resources needed for the PIC simulations of plasma turbulence require that unphysical values have to be introduced to secure three-dimensional, long-time simulations such as the mass ratio m_i/m_e and the electron thermal speed or Alfvén speed relative to the speed of light ($v\mathrm{th}_{,e}/c$, v_A/c). Another free parameter is the system size which, as discussed above, can have a significant effect on the cascade of energy and hence the relative heating of ions and electrons.

These parameters are varied over a broad range of values. For example, in the linear theory calculations, Verscharen et al. [91] studied $1 < m_i/m_e < 1836$ and $10^{-4} < v_A/c < 1/3$. In nonlinear PIC simulations Gary et al. [56] studied $25 < m_i/m_e < 1836$ and Hughes et al. [93] studied $0.025 < v\mathrm{th}_{,e}/c < 0.10$. Verscharen et al. [91] showed that mass ratio had a drastic effect on quasi-parallel magnetosonic/whistler branch, and quasi-perpendicular kinetic

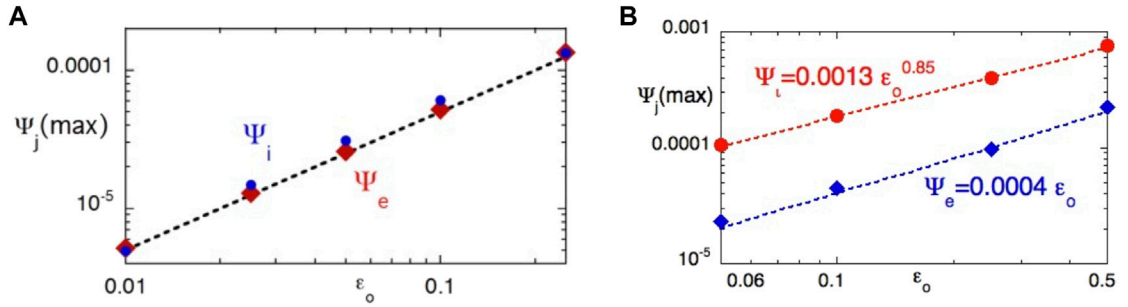

FIGURE 5 | Simple scaling relations derived from PIC simulations [92]. **(A)** The maximum values of the dimensionless time rates of change of the electron (blue dots) and ion (red diamonds) entropies derived from the whistler turbulence PIC simulations of [56]. The scaling relations derived for whistler turbulence are: the maximum entropy increase for electron: $\Psi_e \simeq 0.0005\mathcal{E}_0$; the maximum entropy increase for ion: $\Psi_i \simeq 0.0005\mathcal{E}_0$ **(B)** The maximum positive values of the dimensionless time rates of change of the electron (blue boxes) and the ion (red dots) entropies of the kinetic Alfvén PIC simulations of [47]. The scaling relations derived for kinetic Alfven turbulence are: the maximum entropy increase for electron: $\Psi_e \simeq 0.0004\mathcal{E}_0$; the maximum entropy increase for ion: $\Psi_i \simeq 0.0013\mathcal{E}_0^{0.85}$.

Alfvén branch. The kinetic Aflvén waves get critically damped for realistic mass ratio but can reach electron scales for artificially large electron mass. v_A/c was not shown to have significant effect on the wave properties in the non-relativistic case. The simulations give us a sense of how the unphysical values affect the simulation results so that, even if we do not have the resources to run simulations with fully physical values, we can expect that whistler turbulence dissipation is likely to scale as the mass ratio m_e/m_i. In another study Parashar and Gary [63] studied the effect of variations in relative ion/electron temperatures. They found that $Q_i/Q_e \approx (T_e/T_i)^2$. These results have qualitative similarities with the scalings found by Kawazura et al. [94], Schekochihin et al. [95], but are slightly different from the scaling found by Zhdankin et al. [96]. The difference in physical model, system size, inclusion of relativistic effects, and system size etc. can all contribute to the different findings. See Parashar and Gary [63] for a detail discussion of these issues.

There is ample evidence that the dissipation of kinetic-range turbulence happens in an intermittent way similar to magnetohydrodynamic turbulence [4,97–99]. Statistical tools such as probability density functions of increments, or scale dependent kurtosis are useful tools to quantify this intermittency. Using PIC simulations Chang et al. [75] showed that intermittency level increases with the fluctuation energy $\mathcal{E}_0$ and the electron beta β_e and that the nonlinear dissipation processes are primarily associated with the localized current structures.

Within the theme of identifying scaling relations, Peter Gary also studied how the species entropies change with turbulence amplitude. For instance, Gary et al. [92] showed that the electron and ion heating rate (**Figure 5A**) and electron and ion entropies (**Figure 5B**) can be summarized as simple power law relations as a function of the dimensionless fluctuating magnetic field energy $\mathcal{E}_0$ for both whistler and the kinetic Alfvén turbulence.

3.4 Linear Instabilities Versus Nonlinear Effects

An important dichotomy that arises in kinetic theory is the interplay of linear waves and instabilities with nonlinear turbulence. Solar wind and magnetosheath data organize themselves in the $\beta_\parallel$—R_p plane, where $\beta_\parallel$ is the parallel proton beta and R_p is the anisotropy of protons, in such a way that linear instability thresholds appear to constrain the data [6,100]. Based on these observations, it has been suggested that the microinstabilities play an important role in regulating the solar wind evolution. It has also been suggested that "majority of solar wind intervals support ion-driven instabilities" [101]. This raises a natural question: What is the relative importance of linear time scales (wave frequencies and instability growth rates) compared to nonlinear time scales? Peter Gary and collborators have addressed this question in many papers [102–105].

Matthaeus et al. [102] showed that the kinetic scale nonlinear times in the solar wind are comparable to or smaller than the linear timescales of waves and instabilities. Qudsi et al. [103] analyzed data from the MMS spacecraft as well as fully kinetic 2.5D simulations of turbulence with mean magnetic field out of the plane of simulation. The instability growth rates were computed based on the local $\beta_\parallel$ and proton anisotropies R_p. They showed that the instabilities thresholds are large in intermittent locations near intense current sheets. It has been shown that a lot of kinetic activity happens near strong current sheets [106–108]. Intense distortions of the distribution function can happen near such current sheets and can render the distribution function unstable. Qudsi et al. [103] showed this proximity of instability growth rates and intermittent structures in both PIC simulations and MMS data.

As discussed earlier, the computational expense of fully kinetic simulations forces one to run them with artificial parameters and in reduced dimensionality. A good understanding of dissipative processes in kinetic plasmas requires comparative studies of various models and geometries. In the spirit of Turbulent Dissipation Challenge [98], Gary et al. [104] compared simulations in three different geometries to study the relative importance of instability time scales and nonlinear times. **Figure 6** shows two dimensional probability distribution functions (PDFs) of kinetic instability rates and nonlinear rates computed at the scale of maximum instability growth rate at each point for 1) 2.5D perpendicular turbulence with

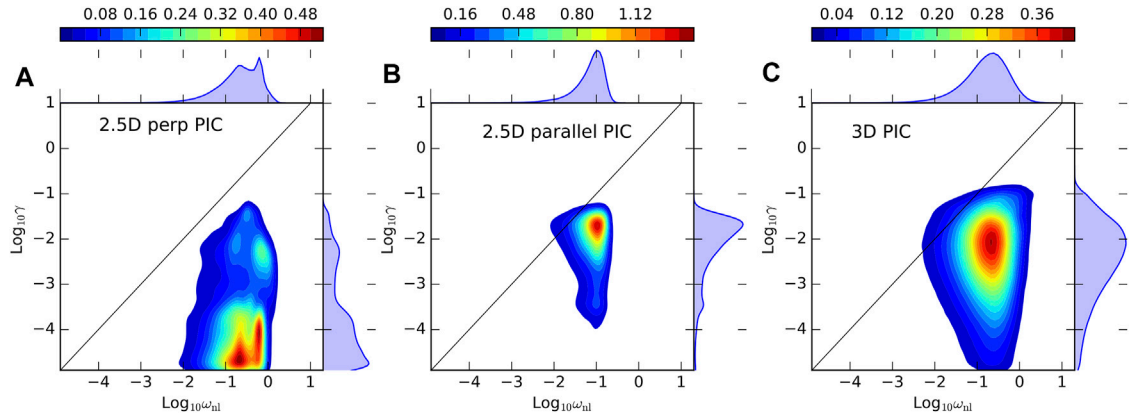

FIGURE 6 | Probability distribution functions (PDFs) of t_{nl} vs $t_{inst.}$ for three fully kinetic simulations [104]. **(A)** 2.5D perpendicular PIC with mean field out of the plane of simulation, **(B)** 2.5D parallel PIC with mean field in the plane of simulation, and **(C)** 3D PIC. The 2.5D perp PIC simulation shows a dominance of nonlinear time scales. The 2.5D parallel PIC simulation shows a distribution where nonlinear timescale dominates still. However, the distribution lies close to unity. 3D PIC shows a distribution that is similar to observations in the magnetosheath [105].

mean magnetic field out of the plane of simulation, 2) 2.5D parallel turbulence with mean magnetic field in the plane of the simulation, and 3) a fully 3D turbulence simulation. It is evident from all three panels that the nonlinear rates are almost always larger than the instability growth rates. Only a small fraction of population lies in the regime where the instability growth rate is larger than the nonlinear rate. 2.5D perpendicular-plane simulation shows a complete dominance of nonlinear rates. Although the 2.5D parallel simulation shows a dominance of nonlinear rates, the ratio of the two rates is closer to unity compared to the perpendicular simulation. 3D simulation shows a wide spread in the rates while retaining the dominance of nonlinear rates. The PDFs in the 3D simulation show many qualitative and quantitative similarities to the magnetosheath dara from the MMS spacecraft and the solar wind data from the Wind spacecraft [105].

Peter Gary studied instabilities extensively starting in the 1990s, e.g. Gary et al. [109]. While the linear instabilities were often studied under the simplified assumption of a single anisotropic distribution, the presence of secondary populations, either as proton beams or alpha particles, can significantly impact the stability and thus the predicted growth rates.

The streaming speed of alpha particles relative to the protons (which is about the local Alfvén speed in the solar wind) can cause alpha/proton magnetosonic and Alfvén instabilities [110]. The relative flow difference between the alpha particles and the protons changes the occurrence of maximum growth rate for the temperature anisotropy instability of protons (exciting the ion cyclotron waves) into the direction of flow difference [111].

Linear instability analysis using the Helios data shows that the alpha particles in the solar wind play a more important role at larger distances from the Sun [112]. The growth rate under the presence of alph particles becomes non-negligible when compared with the turbulent cascade rate. Hence, the alpha particles can potentially impact the turbulent cascade through this channel.

4 CONCLUSIONS AND OUTLOOK

Observations of solar wind turbulence near proton scales, the beginning of kinetic range, show that kinetic Alfvén turbulence dominates magnetosonic-whistler turbulence at those scales. However, at shorter wavelengths of the order of the electron inertial lengths neither observations nor fully kinetic simulations have yielded definitive results. The studies carried out by Peter Gary and collaborators addressed several specific questions across the kinetic range to construct a more complete picture of plasma turbulence:

1. *How do the spectra for kinetic Alfvén and whistler turbulence compare and scale with the plasma parameters beta and the fluctuation amplitudes?*
2. *What are the dissipation mechanisms for kinetic Alfvén and whistler turbulence, and if there is a cross-over from the former to the latter, what are its scaling properties?*
3. *Sample computations show that electrons are preferentially heated in directions parallel/anti-parallel to the large-scale magnetic field in both kinetic Alfvén and whistler turbulence, while the solar wind observations indicate that both an excess of parallel temperature and that of perpendicular temperare are possible. How can we systematically understand the electron temperature evolution in the frame of kinetic-range turbulence?*
4. *What are the parametric dependencies for electron and ion heating by kinetic Alfvén and whistler turbulence scenarios?*
5. *Can kinetic-range fluctuations be represented by dispersion relations derived from linear Vlasov theory while at the same time the fluctuations participate in the strongly nonlinear interactions characteristic of intermittent turbulence?*

The central thesis of the Gary picture is that the kinetic Alfvén cascade dominates at the proton scales but critically damps before reaching electron scales. Near the electron scales, whistler

turbulence starts dominating and plays an important role in electron dynamics. The kinetic-range turbulence depends on many variables, physical as well as numerical. Physical variables include the temperatures of ions and electrons (T_e, T_i), their anisotropy ($T_{j,\perp}/T_{j\parallel}$), their plasma betas ($\beta_e$, β_i), the amplitude of turbulent fluctuations at the largest scales ($\mathcal{E}_0$), and the energy containing scale (Λ). The physical but typically inexact parameters include the mass ratio of ions to electrons (m_i/m_e) and the ratio of thermal (or Alfvén) speed to the speed of light ($v\mathrm{th}_{,e}/c$, v_A/c). The parameter space to explore is extremely large and a successful exploration of it will keep many research groups busy for a long time to come. The solar wind plasma exhibits electron temperature with an excess of parallel temperature in the high-speed streasm and that with an excess of perpendicular temperature in the low-speed and high-density conditions [113]. Perhaps there are different scenarios of kinetic-range turbulence evolution.

Peter Gary through his numerous collaborations addressed various aspects of kinetic-range turbulence that support the Gary picture. Many papers have studied these parameter variations in the kinetic range using linear Vlasov theory, fully kinetic simulations in varied geometries, as well as spacecraft data from the solar wind and magnetosheath. Their results show that whistler and kinetic Alfvén turbulence can generate or sustain anisotropic power spectra, predict heating rates from whistler and kinetic Alfvén turbulence under varied conditions, explore effects of parameter variations on such heating profiles, and identify potential channels for the interplay between linear instabilities and intermittent structures. The work done by Peter Gary and collaborators contributing to the Gary picture of turbulence raises further questions that should be addressed by future studies.

6. *What are the important parameters that determine the nature of kinetic range cascade and dissipation?*

The large parameter space that needs to be explored implies that many linear theory studies and nonlinear kinetic studies are needed to identify how the variations of temperatures, betas, fluctuation amplitudes, and system size affect the kinetic-range turbulence. For example, careful and detailed maps of damping rates as a function of various physical and numerical parameters are still lacking. A catalogue of such maps can prove valuable to guide parameter searches for much more expensive nonlinear numerical simulations. Another interesting direction to explore within this theme is a comprehensive study to identify the nature of fluctuations near electron scales from large fully kinetic simulations. These simulations will need to span a large range of scales from the inertial range down to sub-electron scales. Parameter variations such as large-scale turbulence amplitude, plasma beta, and anisotropies etc. will need to be varied to get more details.

7. *How do kinetic instabilities interplay with turbulence driven by large scales into the kinetic range?*

Many papers have started to appear under this theme recently but much needs to be explored. How much power can such instabilities pump into the kinetic range? How frequent are such instabilities? Do they happen only near intermittent structures or can they be pumped by large scale conditions as well?

8. *How critical are the approximations of the model used to describe kinetic-range turbulence?*

Many models such as gyrokinetic, ten-moment two fluid, hybrid kinetic, Vlasov-Maxwell etc. are used to study kinetic-range turbulence. The gyrokinetic model, for example, does not include whistler physics and hence cannot address the issues regarding the competition between kinetic Alfvén and whistler cascades. The hybrid kinetic model does not include electron kinetic physics and hence is also unable to describe the electron scale kinetic physics. Ten-moment models, successfully applied to the global simulations of Earth's magnetosphere and the plasma environment around Ganymede and Mercury, do not contain a time-evolution equation for the heat flux although the models include the evaluation of third-order moments in the anisotropy and non-gyrotropy of the pressure tensor [114]. Fully kinetic models are extremely expensive. Hence, comparative studies of these models are critical to identify the right tools and physics. On the numerical front, PIC has traditionally been the popular model for its relatively less computational expense. However, the noise stemming from finite number of particles can affect the electron scale dynamics significantly. On the other hand, the Eulerian Vlasov models have been computationally much more expensive. Newer finite element [48] and Hermite spectral methods [115] are being developed as well. With increasing computing power and improved numerical schemes, such models may become more desirable than PIC.

9. *What are desirable analyses to identify and differentiate between whistler and kinetic Alfvén fluctuations and their role in plasma heating?*

Commonly employed analyses include power spectra, heating rates, and intermittency analyses. Other potential analysis to perform could be to theoretically identify and analyse various dissipation measures such as Pi-D [99], stochastic heating [89], and field particle correlator [116]. Can four-dimensional Fourier spectra of kinetic-range turbulence simulations yield some interesting differentiating conclusions?

This is just a sampling of questions that directly follow up on Peter Gary's contributions. The Gary picture addresses a relatively less explored part of the kinetic range, i.e., between proton and electron scales. Hence, the Gary picture has the potential, when properly validated and revised, to not only strengthen our understanding of turbulence in the near-Earth solar wind but will also lay the groundwork for interpretation of data collected by the on-going missions in the inner heliosphere by Parker Solar Probe, Solar Orbiter, and BepiColombo, and the upcoming HelioSwarm mission.

DATA AVAILABILITY STATEMENT

The original contributions presented in the study are included in the article/supplementary material, further inquiries can be directed to the corresponding author.

AUTHOR CONTRIBUTIONS

All authors listed have made a substantial, direct, and intellectual contribution to the work and approved it for publication.

ACKNOWLEDEMENT AND DEDICATION

The authors are highly indebted to S. Peter Gary for his mentorship over the years and have written this paper as their tribute to him. Through his exceptional career spanning many decades, he not only made major contributions to the field of space plasma physics but also served as a mentor to countless number of young scientists. That includes the authors of this paper. A curious, passionate, and humble man, he treated beginning students as his peers and supported many young PhDs in finding their own place in field. Many like us, who were fortunate enough to interact with Peter for a long time, will keep getting inspired over the coming decades, fondly remembering our interactions with him. Though Peter is no longer with us, his legacy will continue to inspire young minds for the decades to come.

Dedication by TNP: I have very clear and inspirational memories of my first encounter with Peter. I was a first year graduate student when I met him on my poster in the 2007 AGU Fall Meeting. I was scared to get one of the great scientists of my field on my first ever poster. When Peter started discussing, I didn't feel like a student for a moment. He treated me as a peer, asked me questions as if he would ask a seasoned scientist. His curiosity, passion, and humility left a lifelong impression on me. Peter guided me to get my first ever proposal funded. He was actively mentoring a lot of my peers in a way similar to how he mentored me. The animated, highly educational, and all the time inspiring arguments with Peter on various topics have shaped my thought process significantly.

Dedication by JW: I first met Peter in 1992 via emails on research questions and discussions at the AGU Fall meeting. That encounter quickly turned into a mentorship and friendship from Peter lasting for almost 30 years. I am indebted to Peter not only for his guidance in our research collaboration but also for sharing his advice and wisdom on life. I would also like to thank Peter on behalf of my students, O. Chang, S. Hughes, and C. Cui, for helping to guide their Ph.D dissertations. A true scientist to the end, Peter was as passionate and sharp as ever debating the possible sources of kinetic-range turbulence at our last research zoom meeting just a few days before his passing.

Dedication by YN: I first met Peter at the IAGA conference in Toulouse, France, in July 2005. We chatted about some physics, and I confessed to him that I was a fan of Peter's paper series. Peter answered, “Thank you, but don't trust all of my papers. You are working in the observations. You should visit Los Alamos!” Peter really invited me to Los Alamos in December 2006. Peter showed me the laboratory, introduced me to his friends and colleagues, and took me to hiking and swimming (he was my swimming teacher, too). I really enjoyed working with Peter on the observational data and theoretical modeling of turbulence, and also thank him for hosting not only my visit but also the visit of my student (C. Perschke) to Los Alamos.

REFERENCES

1. Marsch E. Kinetic Physics of the Solar corona and Solar Wind. *Living Rev Solar Phys* (2006) 3. doi:10.12942/lrsp-2006-1
2. Marsch E. Solar Wind and Kinetic Heliophysics. *Ann Geophys* (2018) 36: 1607–30. doi:10.5194/angeo-36-1607-2018
3. Hollweg JV, Isenberg PA. Generation of the Fast Solar Wind: A Review with Emphasis on the Resonant Cyclotron Interaction. *J Geophys Res* (2002) 107: SSH-12. doi:10.1029/2001JA000270
4. TenBarge JM, Howes GG, Dorland W. Collisionless Damping at Electron Scales in Solar Wind Turbulence. *Astrophysical J* (2013) 774:139. doi:10.1088/0004-637X/774/2/139
5. Gary SP. *Theory of Space Plasma Microinstabilities*. Cambridge: Cambridge University Press (1993). doi:10.1017/CBO9780511551512
6. Bale SD, Kasper JC, Howes GG, Quataert E, Salem C, Sundkvist D. Magnetic Fluctuation Power Near Proton Temperature Anisotropy Instability Thresholds in the Solar Wind. *Phys Rev Lett* (2009) 103:211101. doi:10.1103/PhysRevLett.103.211101
7. Kraichnan RH. Inertial-range Spectrum of Hydromagnetic Turbulence. *Phys Fluids* (1965) 8:1385–7. doi:10.1063/1.1761412
8. Goldreich P, Sridhar S. Magnetohydrodynamic Turbulence Revisited. *Astrophysical J* (1997) 485:680–8. doi:10.1086/304442
9. Biskamp D. *Magnetohydrodynamic Turbulence*. Cambridge: Cambridge University Press (2003).
10. Shebalin JV, Matthaeus WH, Montgomery D. Anisotropy in MHD Turbulence Due to a Mean Magnetic Field. *J Plasma Phys* (1983) 29: 525–47. doi:10.1017/S0022377800000933
11. Aluie H. Compressible Turbulence: the cascade and its Locality. *Phys Rev Lett* (2011) 106:174502. doi:10.1103/PhysRevLett.106.174502
12. Bian X, Aluie H. Decoupled Cascades of Kinetic and Magnetic Energy in Magnetohydrodynamic Turbulence. *Phys Rev Lett* (2019) 122:135101. doi:10.1103/PhysRevLett.122.135101
13. Schekochihin AA, Cowley SC, Dorland W, Hammett GW, Howes GG, Quataert E, et al. Astrophysical Gyrokinetics: Kinetic and Fluid Turbulent Cascades in Magnetized Weakly Collisional Plasmas. *The Astrophysical JournalS* (2009) 182:310–77. doi:10.1088/0067-0049/182/1/310
14. Boldyrev S, Horaites K, Xia Q, Perez JC. Toward a Theory of Astrophysical Plasma Turbulence at Subproton Scales. *Astrophysical J* (2013) 777:41. doi:10.1088/0004-637X/777/1/41
15. Eyink GL. Cascades and Dissipative Anomalies in Nearly Collisionless Plasma Turbulence. *Phys Rev X* (2018) 8:041020. doi:10.1103/PhysRevX.8.041020
16. Matthaeus WH, Yang Y, Wan M, Parashar TN, Bandyopadhyay R, Chasapis A, et al. Pathways to Dissipation in Weakly Collisional Plasmas. *Astrophysical J* (2020) 891:101. doi:10.3847/1538-4357/ab6d6a
17. Bowers KJ, Albright BJ, Yin L, Bergen B, Kwan TJT. Ultrahigh Performance Three-Dimensional Electromagnetic Relativistic Kinetic Plasma Simulation. *Phys Plasmas* (2008) 15:055703. doi:10.1063/1.2840133
18. Klein KG, Howes GG, TenBarge JM, Bale SD, Chen CHK, Salem CS. Using Synthetic Spacecraft Data to Interpret Compressible Fluctuations in Solar Wind Turbulence. *Astrophysical J* (2012) 755:159. doi:10.1088/0004-637X/755/2/159
19. Verscharen D, Chandran BDG. NHDS: the new hampshire Dispersion Relation Solver. *Res Notes AAS* (2018) 2:13. doi:10.3847/2515-5172/aabfe3
20. Derouillat J, Beck A, P,érez F, Vinci T, Chiaramello M, Grassi A, et al. Smilei : A Collaborative, Open-Source, Multi-Purpose Particle-In-Cell Code for

Plasma Simulation. *Comput Phys Commun* (2018) 222:351–73. doi:10.1016/j.cpc.2017.09.024
21. Bird R, Tan N, Luedtke SV, Harrell SL, Taufer M, Albright B. VPIC 2.0: Next Generation Particle-In-Cell Simulations. *IEEE Trans Parallel Distrib Syst* (2022) 33:952–63. doi:10.1109/TPDS.2021.3084795
22. Gary SP. Short-wavelength Plasma Turbulence and Temperature Anisotropy Instabilities: Recent Computational Progress. *Phil Trans R Soc A* (2015) 373: 20140149. doi:10.1098/rsta.2014.0149
23. Gary SP. Low-frequency Waves in a High-Beta Collisionless Plasma: Polarization, Compressibility and Helicity. *J Plasma Phys* (1986) 35: 431–47. doi:10.1017/S0022377800011442
24. Narita Y, Roberts OW, Vörös Z, Hoshino M. Transport Ratios of the Kinetic Alfvén Mode in Space Plasmas. *Front Phys* (2020) 8:166. doi:10.3389/fphy.2020.00166
25. Servidio S, Valentini F, Perrone D, Greco A, Califano F, Matthaeus WH, et al. A Kinetic Model of Plasma Turbulence. *J Plasma Phys* (2015) 81:325810107. doi:10.1017/S0022377814000841
26. Chen CHK. Recent Progress in Astrophysical Plasma Turbulence from Solar Wind Observations. *J Plasma Phys* (2016) 82:535820602. doi:10.1017/S0022377816001124
27. Verscharen D, Klein KG, Maruca BA. The Multi-Scale Nature of the Solar Wind. *Living Rev Sol Phys* (2019) 16:5. doi:10.1007/s41116-019-0021-0
28. Sahraoui F, Hadid L, Huang S. Magnetohydrodynamic and Kinetic Scale Turbulence in the Near-Earth Space Plasmas: A (Short) Biased Review. *Rev Mod Plasma Phys* (2020) 4:1–33. doi:10.1007/s41614-020-0040-2
29. Matthaeus WH. Turbulence in Space Plasmas: Who Needs it? *Phys Plasmas* (2021) 28:032306. doi:10.1063/5.0041540
30. Sahraoui F, Goldstein ML, Belmont G, Canu P, Rezeau L. Three Dimensional AnisotropickSpectra of Turbulence at Subproton Scales in the Solar Wind. *Phys Rev Lett* (2010) 105:131101. doi:10.1103/PhysRevLett.105.131101
31. Salem CS, Howes GG, Sundkvist D, Bale SD, Chaston CC, Chen CHK, et al. Identification of Kinetic Alfvén Wave Turbulence in the Solar Wind. *Astrophysical J* (2012) 745:L9. doi:10.1088/2041-8205/745/1/L9
32. Narita Y, Gary SP, Saito S, Glassmeier K-H, Motschmann U. Dispersion Relation Analysis of Solar Wind Turbulence. *Geophys Res Lett* (2011) 38:a–n. doi:10.1029/2010GL046588
33. Birdsall CK, Langdon AB. *Plasma Physics via Computer Simulation*. New York: McGraw-Hill Book Company (1985).
34. Schuecker P, Finoguenov A, Miniati F, Böhringer H, Briel UG. Probing Turbulence in the Coma Galaxy Cluster. *A&A* (2004) 426:387–97. doi:10.1051/0004-6361:20041039
35. Churazov E, Vikhlinin A, Zhuravleva I, Schekochihin A, Parrish I, Sunyaev R, et al. X-ray Surface Brightness and Gas Density Fluctuations in the Coma Cluster. *Mon Not R Astron. Soc.* (2012) 421:1123–35. doi:10.1111/j.1365-2966.2011.20372.x
36. Kasper JC, Klein KG, Lichko E, Huang J, Chen CHK, Badman ST, et al. Parker Solar Probe Enters the Magnetically Dominated Solar corona. *Phys Rev Lett* (2021) 127:255101. doi:10.1103/PhysRevLett.127.255101
37. Tu C-Y, Marsch E. MHD Structures, Waves and Turbulence in the Solar Wind: Observations and Theories. *Space Sci Rev* (1995) 73:1–210. doi:10.1007/BF00748891
38. Bruno R, Carbone V. The Solar Wind as a Turbulence Laboratory. *Living Rev Solar Phys* (2013) 10:2. doi:10.12942/lrsp-2013-2
39. Caprioli D, Brunetti G, Jones TW, Kang H, Kunz M, Oh SP, et al. Plasma 2020 – Intracluster Medium Plasmas. *arXiv:1903.08751* (2019). doi:10.48550/arXiv.1903.08751
40. Shalchi A. Perpendicular Transport of Energetic Particles in Magnetic Turbulence. *Space Sci Rev* (2020) 216:1–134. doi:10.1007/s11214-020-0644-4
41. Oughton S, Engelbrecht NE. Solar Wind Turbulence: Connections with Energetic Particles. *New Astron* (2021) 83:101507. doi:10.1016/j.newast.2020.101507
42. Jardin S. *Computational Methods in Plasma Physics*. Boca Raton, FL, USA: CRC Press (2010).
43. Lipatov AS. *The Hybrid Multiscale Simulation Technology: An Introduction with Application to Astrophysical and Laboratory Plasmas*. Berlin, Germany: Springer-Verlag (2002).
44. Valentini F, Trávníček P, Califano F, Hellinger P, Mangeney A. A Hybrid-Vlasov Model Based on the Current advance Method for the Simulation of Collisionless Magnetized Plasma. *J Comput Phys* (2007) 225:753–70. doi:10.1016/j.jcp.2007.01.001
45. Chang O, Gary SP, Wang J. Whistler Turbulence Forward cascade versus Inverse cascade: Three-Dimensional Particle-In-Cell Simulations. *Astrophysical J* (2015) 800:87. doi:10.1088/0004-637X/800/2/87
46. Hughes RS, Gary SP, Wang J. Particle-in-cell Simulations of Electron and Ion Dissipation by Whistler Turbulence: Variations with Electron β. *Astrophysical J* (2017) 835:L15. doi:10.3847/2041-8213/835/1/L15
47. Hughes RS, Gary SP, Wang J, Parashar TN. Kinetic Alfvén Turbulence: Electron and Ion Heating by Particle-In-Cell Simulations. *Astrophysical J* (2017) 847:L14. doi:10.3847/2041-8213/aa8b13
48. Juno J, Hakim A, TenBarge J, Shi E, Dorland W. Discontinuous Galerkin Algorithms for Fully Kinetic Plasmas. *J Comput Phys* (2018) 353:110–47. doi:10.1016/j.jcp.2017.10.009
49. Koshkarov O, Manzini G, Delzanno GL, Pagliantini C, Roytershteyn V. The Multi-Dimensional Hermite-Discontinuous Galerkin Method for the Vlasov-Maxwell Equations. *Comput Phys Commun* (2021) 264:107866. doi:10.1016/j.cpc.2021.107866
50. Howes GG, Cowley SC, Dorland W, Hammett GW, Quataert E, Schekochihin AA. A Model of Turbulence in Magnetized Plasmas: Implications for the Dissipation Range in the Solar Wind. *J Geophys Res* (2008) 113:a–n. doi:10.1029/2007JA012665
51. Podesta JJ, Borovsky JE, Gary SP. A Kinetic Alfvén Wave Cascade Subject to Collisionless Damping Cannot Reach Electron Scales in the Solar Wind at 1 Au. *Astrophysical J* (2010) 712:685–91. doi:10.1088/0004-637X/712/1/685
52. Howes GG, Bale SD, Klein KG, Chen CHK, Salem CS, TenBarge JM. The Slow-Mode Nature of Compressible Wave Power in Solar Wind Turbulence. *Astrophysical J* (2012) 753:L19. doi:10.1088/2041-8205/753/1/L19
53. Goldreich P, Sridhar S. Toward a Theory of Interstellar Turbulence. 2: Strong Alfvenic Turbulence. *Astrophysical J* (1995) 438:763–75. doi:10.1086/175121
54. Chandran BDG. Weak Compressible Magnetohydrodynamic Turbulence in the Solar Corona. *Phys Rev Lett* (2005) 95(26):265004. doi:10.1103/physrevlett.95.265004
55. Yang Y, Shi Y, Wan M, Matthaeus WH, Chen S. Energy cascade and its Locality in Compressible Magnetohydrodynamic Turbulence. *Phys Rev E* (2016) 93:061102. doi:10.1103/PhysRevE.93.061102
56. Gary SP, Hughes RS, Wang J. Whistler Turbulence Heating of Electrons and Ions: Three-Dimensional Particle-In-Cell Simulations. *Astrophysical J* (2016) 816:102. doi:10.3847/0004-637X/816/2/102
57. Podesta JJ, Gary SP. Magnetic Helicity Spectrum of Solar Wind Fluctuations as a Function of the Angle with Respect to the Local Mean Magnetic Field. *Astrophysical J* (2011) 734:15. doi:10.1088/0004-637X/734/1/15
58. He J, Marsch E, Tu C, Yao S, Tian H. Possible Evidence of Alfvén-Cyclotron Waves in the Angle Distribution of Magnetic Helicity of Solar Wind Turbulence. *Astrophysical J* (2011) 731(2):85. doi:10.1088/0004-637x/731/2/85
59. Klein KG, HowesTen Barge GG, Ten Barge JM, Podesta JJ. Physical Interpretation of the Angle-dependent Magnetic Helicity Spectrum in the Solar Wind: the Nature of Turbulent Fluctuations Near the Proton Gyroradius Scale. *Astrophysical J* (2014) 785(2):138. doi:10.1088/0004-637x/785/2/138
60. Squire J, Meyrand R, Kunz MW, Lev A, Schekochihin AA, Quataert E. High-frequency Heating of the Solar Wind Triggered by Low-Frequency Turbulence. *Nat Astron* (2022) 2022:1–9. doi:10.1038/s41550-022-01624-z
61. Narita Y. Space-time Structure and Wavevector Anisotropy in Space Plasma Turbulence. *Living Rev Sol Phys* (2018) 15:2. doi:10.1007/s41116-017-0010-0
62. Zeiler A, Biskamp D, Drake JF, Rogers BN, Shay MA, Scholer M. Three-dimensional Particle Simulations of Collisionless Magnetic Reconnection. *J Geophys Res* (2002) 107:1230. doi:10.1029/2001JA000287
63. Parashar TN, Gary SP. Dissipation of Kinetic Alfvénic Turbulence as a Function of Ion and Electron Temperature Ratios. *Astrophysical J* (2019) 882: 29. doi:10.3847/1538-4357/ab2fc8
64. Wang J, Liewer P, Decyk V. 3D Electromagnetic Plasma Particle Simulations on a MIMD Parallel Computer. *Comput Phys Commun* (1995) 87:35–53. doi:10.1016/0010-4655(94)00167-Z
65. Gary SP. Test for Wavevector Anisotropies in Plasma Turbulence Cascades. *Astrophysical J* (2013) 769:36. doi:10.1088/0004-637X/769/1/36

66. Chang O, Peter Gary S, Wang J. Whistler Turbulence Forward cascade: Three-Dimensional Particle-In-Cell Simulations. *Geophys Res Lett* (2011) 38: a–n. doi:10.1029/2011GL049827
67. Chang O, Gary SP, Wang J. Whistler Turbulence at Variable Electron Beta: Three-dimensional Particle-in-cell Simulations. *J Geophys Res Space Phys* (2013) 118:2824–33. doi:10.1002/jgra.50365
68. Gary SP, Chang O, Wang J. Forward cascade of Whistler Turbulence: Three-Dimensional Particle-In-Cell Simulations. *Astrophysical J* (2012) 755:142. doi:10.1088/0004-637X/755/2/142
69. Narita Y, Nakamura R, Baumjohann W, Glassmeier K-H, Motschmann U, Giles B, et al. On Electron-Scale Whistler Turbulence in the Solar Wind. *Astrophysical J* (2016) 827:L8. doi:10.3847/2041-8205/827/1/L8
70. Perschke C, Narita Y, Gary SP, Motschmann U, Glassmeier K-H. Dispersion Relation Analysis of Turbulent Magnetic Field Fluctuations in Fast Solar Wind. *Ann Geophys* (2013) 31:1949–55. doi:10.5194/angeo-31-1949-2013
71. Roberts OW, Alexandrova O, Kajdič P, Turc L, Perrone D, Escoubet CP, et al. Variability of the Magnetic Field Power Spectrum in the Solar Wind at Electron Scales. *Astrophysical J* (2017) 850:120. doi:10.3847/1538-4357/aa93e5
72. Narita Y, Gary SP. Inertial-range Spectrum of Whistler Turbulence. *Ann Geophys* (2010) 28:597–601. doi:10.5194/angeo-28-597-2010
73. Saito S, Gary SP, Narita Y. Wavenumber Spectrum of Whistler Turbulence: Particle-In-Cell Simulation. *Phys Plasmas* (2010) 17:122316. doi:10.1063/1.3526602
74. Iroshnikov PS. Turbulence of a Conducting Fluid in a strong Magnetic Field. *Sov Astron* (1964) 7:566–71. Available at: https://ui.adsabs.harvard.edu/abs/1964SvA.....7..566I/ (Accessed June 30, 2022).
75. Chang O, Peter Gary S, Wang J. Energy Dissipation by Whistler Turbulence: Three-Dimensional Particle-In-Cell Simulations. *Phys Plasmas* (2014) 21: 052305. doi:10.1063/1.4875728
76. Hughes RS, Gary SP, Wang J. Electron and Ion Heating by Whistler Turbulence: Three-Dimensional Particle-In-Cell Simulations. *Geophys Res Lett* (2014) 41:8681–7. doi:10.1002/2014GL062070
77. Alexandrova O, Saur J, Lacombe C, Mangeney A, Mitchell J, Schwartz SJ, et al. Universality of Solar-Wind Turbulent Spectrum from MHD to Electron Scales. *Phys Rev Lett* (2009) 103:165003. doi:10.1103/PhysRevLett.103.165003
78. Sahraoui F, Goldstein ML, Robert P, Khotyaintsev YV. Evidence of a cascade and Dissipation of Solar-Wind Turbulence at the Electron Gyroscale. *Phys Rev Lett* (2009) 102:231102. doi:10.1103/PhysRevLett.102.231102
79. Narita Y. Spectral Moments for the Analysis of Frequency Shift, Broadening, and Wavevector Anisotropy in a Turbulent Flow. *Earth Planets Space* (2017) 69:73. doi:10.1186/s40623-017-0658-7
80. Galtier S, Bhattacharjee A. Anisotropic Weak Whistler Wave Turbulence in Electron Magnetohydrodynamics. *Phys Plasmas* (2003) 10:3065–76. doi:10.1063/1.1584433
81. Cho J, Lazarian A. The Anisotropy of Electron Magnetohydrodynamic Turbulence. *Astrophysical J* (2004) 615:L41–L44. doi:10.1086/425215
82. Saito S, Gary SP, Li H, Narita Y. Whistler Turbulence: Particle-In-Cell Simulations. *Phys Plasmas* (2008) 15:102305. doi:10.1063/1.2997339
83. Narita Y, ComiÅŸel H, Motschmann U. Spatial Structure of Ion-Scale Plasma Turbulence. *Front Phys* (2014) 2:13. doi:10.3389/fphy.2014.001310.3389/fphy.2014.00013
84. Hellinger P, Matteini L, Štverák Š, Trávníček PM, Marsch E. Heating and Cooling of Protons in the Fast Solar Wind between 0.3 and 1 AU: Helios Revisited. *J Geophys Res* (2011) 116:a–n. doi:10.1029/2011JA016674
85. Hellinger P, Trávníček PM, Štverák Š, Matteini L, Velli M. Proton thermal Energetics in the Solar Wind: Helios Reloaded. *J Geophys Res Space Phys* (2013) 118:1351–65. doi:10.1002/jgra.50107
86. Saito S, Nariyuki Y. Perpendicular Ion Acceleration in Whistler Turbulence. *Phys Plasmas* (2014) 21:042303. doi:10.1063/1.4870757
87. Wu P, Wan M, Matthaeus WH, Shay MA, Swisdak M. von Kármán Energy Decay and Heating of Protons and Electrons in a Kinetic Turbulent Plasma. *Phys Rev Lett* (2013) 111:121105. doi:10.1103/PhysRevLett.111.121105
88. Matthaeus WH, Parashar TN, Wan M, Wu P. Turbulence and Proton-Electron Heating in Kinetic Plasma. *Astrophysical J* (2016) 827:L7. doi:10.3847/2041-8205/827/1/L7
89. Chandran BDG, Li B, Rogers BN, Quataert E, Germaschewski K. Perpendicular Ion Heating by Low-Frequency Alfvén-Wave Turbulence in the Solar Wind. *Astrophysical J* (2010) 720:503–15. doi:10.1088/0004-637X/720/1/503
90. Vasquez BJ, Markovskii SA, Chandran BDG. Three-dimensional Hybrid Simulation Study of Anisotropic Turbulence in the Proton Kinetic Regime. *Astrophysical J* (2014) 788:178. doi:10.1088/0004-637X/788/2/178
91. Verscharen D, Parashar TN, Gary SP, Klein KG. Dependence of Kinetic Plasma Waves on Ion-To-Electron Mass Ratio and Light-To-Alfvén Speed Ratio. *Mon Not R Astron. Soc.* (2020) 494:2905–11. doi:10.1093/mnras/staa977
92. Gary SP, Zhao Y, Hughes RS, Wang J, Parashar TN. Species Entropies in the Kinetic Range of Collisionless Plasma Turbulence: Particle-In-Cell Simulations. *Astrophysical J* (2018) 859:110. doi:10.3847/1538-4357/aac022
93. Hughes RS, Wang J, Decyk VK, Gary SP. Effects of Variations in Electron thermal Velocity on the Whistler Anisotropy Instability: Particle-In-Cell Simulations. *Phys Plasmas* (2016) 23:042106. doi:10.1063/1.4945748
94. Kawazura Y, Barnes M, Schekochihin AA. Thermal Disequilibration of Ions and Electrons by Collisionless Plasma Turbulence. *Proc Natl Acad Sci U.S.A* (2019) 116:771–6. doi:10.1073/pnas.1812491116
95. Schekochihin AA, Kawazura Y, Barnes MA. Constraints on Ion versus Electron Heating by Plasma Turbulence at Low Beta. *J Plasma Phys* (2019) 85:905850303. doi:10.1017/S0022377819000345
96. Zhdankin V, Uzdensky DA, Werner GR, Begelman MC. Electron and Ion Energization in Relativistic Plasma Turbulence. *Phys Rev Lett* (2019) 122: 055101. doi:10.1103/PhysRevLett.122.055101
97. Parashar TN, Servidio S, Shay MA, Breech B, Matthaeus WH. Effect of Driving Frequency on Excitation of Turbulence in a Kinetic Plasma. *Phys Plasmas* (2011) 18:092302. doi:10.1063/1.3630926
98. Parashar TN, Salem C, Wicks RT, Karimabadi H, Gary SP, Matthaeus WH. Turbulent Dissipation challenge: A Community-Driven Effort. *J Plasma Phys* (2015) 81:10. doi:10.1017/S0022377815000860
99. Yang Y, Matthaeus WH, Parashar TN, Wu P, Wan M, Shi Y, et al. Energy Transfer Channels and Turbulence cascade in Vlasov-Maxwell Turbulence. *Phys Rev E* (2017) 95:061201. doi:10.1103/PhysRevE.95.061201
100. Maruca BA, Chasapis A, Gary SP, Bandyopadhyay R, Chhiber R, Parashar TN, et al. MMS Observations of Beta-dependent Constraints on Ion Temperature Anisotropy in Earth's Magnetosheath. *Astrophysical J* (2018) 866:25. doi:10.3847/1538-4357/aaddfb
101. Klein KG, Alterman BL, Stevens ML, Vech D, Kasper JC. Majority of Solar Wind Intervals Support Ion-Driven Instabilities. *Phys Rev Lett* (2018) 120: 205102. doi:10.1103/PhysRevLett.120.205102
102. Matthaeus WH, Oughton S, Osman KT, Servidio S, Wan M, Gary SP, et al. Nonlinear and Linear Timescales Near Kinetic Scales in Solar Wind Turbulence. *Astrophysical J* (2014) 790:155. doi:10.1088/0004-637X/790/2/155
103. Qudsi RA, Bandyopadhyay R, Maruca BA, Parashar TN, Matthaeus WH, Chasapis A, et al. Intermittency and Ion Temperature-Anisotropy Instabilities: Simulation and Magnetosheath Observation. *Astrophysical J* (2020) 895:83. doi:10.3847/1538-4357/ab89ad
104. Gary SP, Bandyopadhyay R, Qudsi RA, Matthaeus WH, Maruca BA, Parashar TN, et al. Particle-in-cell Simulations of Decaying Plasma Turbulence: Linear Instabilities versus Nonlinear Processes in 3D and 2.5D Approximations. *Astrophysical J* (2020) 901:160. doi:10.3847/1538-4357/abb2ac
105. Bandyopadhyay R, Ramiz AQ, Matthaeus WH, Parashar TN, Maruca BA, Gary SP, et al. Interplay of Turbulence and Proton-Microinstability Growth in Space Plasmas. *arXiv:2006.10316* (2020). doi:10.48550/arXiv.2006.10316
106. Servidio S, Valentini F, Califano F, Veltri P. Local Kinetic Effects in Two-Dimensional Plasma Turbulence. *Phys Rev Lett* (2012) 108:045001. doi:10.1103/PhysRevLett.108.045001
107. Greco A, Valentini F, Servidio S, Matthaeus WH. Inhomogeneous Kinetic Effects Related to Intermittent Magnetic Discontinuities. *Phys Rev E* (2012) 86:066405. doi:10.1103/PhysRevE.86.066405
108. Parashar TN, Matthaeus WH. Propinquity of Current and Vortex Structures: Effects on Collisionless Plasma Heating. *Astrophysical J* (2016) 832:57. doi:10.3847/0004-637X/832/1/57

109. Gary SP, Yin L, Winske D. Electromagnetic Proton Cyclotron Anisotropy Instability: Wave-Particle Scattering Rate. *Geophys Res Lett* (2000) 27:2457–9. doi:10.1029/2000GL000055
110. Gary SP, Yin L, Winske D, Reisenfeld DB. Electromagnetic Alpha/proton Instabilities in the Solar Wind. *Geophys Res Lett* (2000) 27:1355–8. doi:10.1029/2000GL000019
111. Podesta JJ, Gary SP. Effect of Differential Flow of Alpha Particles on Proton Pressure Anisotropy Instabilities in the Solar Wind. *Astrophysical J* (2011) 742:41. doi:10.1088/0004-637X/742/1/41
112. Klein KG, Martinović M, Stansby D, Horbury TS. Linear Stability in the Inner Heliosphere: Helios Re-evaluated. *Astrophysical J* (2019) 887:234. doi:10.3847/1538-4357/ab5802
113. Pierrard V, Lazar M, Poedts S, Štverák Š, Maksimovic M, Trávníček PM. The Electron Temperature and Anisotropy in the Solar Wind. Comparison of the Core and Halo Populations. *Sol Phys* (2016) 291:2165–79. doi:10.1007/s11207-016-0961-7
114. Ng J, Hakim A, Wang L, Bhattacharjee A. An Improved Ten-Moment Closure for Reconnection and Instabilities. *Phys Plasmas* (2020) 27:082106. doi:10.1063/5.0012067
115. Roytershteyn V, Delzanno GL. Spectral Approach to Plasma Kinetic Simulations Based on Hermite Decomposition in the Velocity Space. *Front Astron Space Sci* (2018) 5:27. doi:10.3389/fspas.2018.00027
116. Howes GG, Klein KG, Li TC. Diagnosing Collisionless Energy Transfer Using Field-Particle Correlations: Vlasov-Poisson Plasmas. *J Plasma Phys* (2017) 83:705830102. doi:10.1017/S0022377816001197
117. Cerri SS, Arzamasskiy L, Kunz MW. On Stochastic Heating and its Phase-Space Signatures in Low-Beta Kinetic Turbulence. *Astrophysical J* (2021) 916(2):120. doi:10.3847/1538-4357/abfbde
118. Gary SP, Jian LK, Broiles TW, Stevens ML, Podesta JJ, Kasper JC. Ion-driven Instabilities in the Solar Wind: Wind Observations of 19 March 2005. *J Geophys Res Space Phys* (2016) 121:30–41. doi:10.1002/2015JA021935
119. Gary SP, Cui C, Wang J. Plasma Turbulence from the Alfvén-Cyclotron Instability: Particle-In-Cell Simulations, SH016-0002. In: American Geophysical Union Fall Meeting (Virtual); December 1–17, 2020 (2020).
120. Howes GG. The Inherently Three-Dimensional Nature of Magnetized Plasma Turbulence. *J Plasma Phys* (2015) 81:325810203. doi:10.1017/S0022377814001056
121. Karimabadi H, Roytershteyn V, Wan M, Matthaeus WH, Daughton W, Wu P, et al. Coherent Structures, Intermittent Turbulence, and Dissipation in High-Temperature Plasmas. *Phys Plasmas* (2013) 20:012303. doi:10.1063/1.4773205
122. Parashar TN, Matthaeus WH, Shay MA, Wan M. Transition from Kinetic to MHD Behavior in a Collisionless Plasma. *Astrophysical J* (2015) 811:112. doi:10.1088/0004-637X/811/2/112
123. Parashar TN, Matthaeus WH, Shay MA. Dependence of Kinetic Plasma Turbulence on Plasma β. *Astrophysical J* (2018) 864:L21. doi:10.3847/2041-8213/aadb8b
124. Wan M, Matthaeus WH, Roytershteyn V, Karimabadi H, Parashar T, Wu P, et al. Intermittent Dissipation and Heating in 3D Kinetic Plasma Turbulence. *Phys Rev Lett* (2015) 114:175002. doi:10.1103/PhysRevLett.114.175002

Conflict of Interest: The authors declare that the research was conducted in the absence of any commercial or financial relationships that could be construed as a potential conflict of interest.

Publisher's Note: All claims expressed in this article are solely those of the authors and do not necessarily represent those of their affiliated organizations, or those of the publisher, the editors and the reviewers. Any product that may be evaluated in this article, or claim that may be made by its manufacturer, is not guaranteed or endorsed by the publisher.

frontiers | Frontiers in Astronomy and Space Sciences

TYPE Original Research
PUBLISHED 19 August 2022
DOI 10.3389/fspas.2022.941241

OPEN ACCESS

EDITED BY
Misa Cowee,
Los Alamos National Laboratory (DOE),
United States

REVIEWED BY
Yasuhito Narita,
Austrian Academy of Sciences (OeAW),
Austria
Muhammad Fraz Bashir,
University of California, Los Angeles,
United States

*CORRESPONDENCE
Joseph Wang,
josephjw@usc.edu

SPECIALTY SECTION
This article was submitted to Space Physics,
a section of the journal
Frontiers in Astronomy and Space Sciences

RECEIVED 11 May 2022
ACCEPTED 25 July 2022
PUBLISHED 19 August 2022

CITATION
Cui C, Gary SP and Wang J (2022), Whistler turbulence vs. whistler anisotropy instability: Particle-in-cell simulation and statistical analysis. *Front. Astron. Space Sci.* 9:941241. doi: 10.3389/fspas.2022.941241

Whistler turbulence vs. whistler anisotropy instability: Particle-in-cell simulation and statistical analysis

Chen Cui [1], S. Peter Gary [2] and Joseph Wang [1]*

[1]Department of Astronautical Engineering, University of Southern California, Los Angeles, CA, United States, [2]Space Science Institute, Boulder, CO, United States

Particle-in-Cell simulations and statistical analysis are carried out to study the dynamic evolution of a collisionless, magnetized plasma with co-existing whistler turbulence and electron temperature anisotropy as the initial condition, and the competing consequences of whistler turbulence cascade and whistler anisotropy instability growth. The results show that the operation of the whistler instability within whistler turbulence has almost no effects on the fluctuating magnetic field energy and intermittency generated by turbulence. However, it leads to a small reduction of the magnetic field wavevector anisotropy and a major reduction of the intermittency of electron temperature anisotropy. Hence, while the overall effect from whistler instability is minor as compared to that of whistler turbulence due to its much smaller field energy, the whistler instability may act as a regulation mechanism for kinetic-range turbulence through wave-particle interactions.

KEYWORDS

whistler anisotropy instability, whistler turbulence, space plasma, 3D fully kinetic EMPIC simulation, statistical analysis

1 Introduction

High-frequency short-wavelength whistler turbulences are often observed in space plasma (Beinroth and Neubauer, 1981; Lengyel-Frey et al., 1996; Narita et al., 2011, 2016). We define whistler turbulence as a broadband ensemble of incoherent field fluctuations in a magnetized plasma at frequencies between the lower hybrid and electron cyclotron frequencies and at wavelengths much shorter than the ion inertial length. There have been significant debates about the possible sources of whistler turbulence in recent years. One possible scenario is the cascade of fluctuations from the longer wavelength inertial range. Kinetic Alfvén waves and higher frequency magnetosonic-whistler fluctuations have been considered as the two candidates (Gary and Smith, 2009). Recent solar wind observations (Leamon et al., 1998; Sahraoui et al., 2009, 2010; Kiyani et al., 2012; Salem et al., 2012) and numerical simulations (Howes et al., 2008; TenBarge et al., 2013) have identified the existence of the kinetic Alfvén fluctuations with a wavelength around the ion inertial length or ion thermal gyro-radius. However, the mechanism on how such modes

cascade fluctuation energy down to electron scale remains unclear. For instance, as the inertial range cascade preferentially transfers fluctuation energy to propagation directions relatively perpendicular to background magnetic field, where whistler fluctuations can be damped (Mithaiwala et al., 2012; Cerri et al., 2016), the cascade processes may not be able to provide a sufficiently large amplitude to feed to whistler turbulence.

Another possible scenario is kinetic whistler instabilities. A specific growing mode which can be a source for whistler turbulence at relatively long electron-scale wavelengths is the whistler anisotropy instability. We use subscripts "$\perp$" and "$\parallel$" to denote the directions perpendicular and parallel to the background magnetic field $\boldsymbol{B}_0$, respectively, subscripts e and i to denote electrons and ions, respectively, and $\vec{k}$ to denote the wave-vector. This instability is driven by electron temperature anisotropy $T_{\perp e}/T_{\parallel e} > 1$ and propagates at $\vec{k} \times \boldsymbol{B}_0 = 0$ in a homogeneous plasma. Observations have indicated that this instability is operating in the terrestrial magnetosheath (Gary et al., 2005). In the solar wind, while adiabatic expansion of the solar wind would typically lead to $T_{\parallel e} > T_{\perp e}$ which can excite the firehose instability, there is evidence that local compressions and turbulence in the solar wind may also create $T_{\perp e} > T_{\parallel e}$ (Gary and Madland, 1985; Gary, 1993; Karimabadi et al., 2013), which can excite the whistler instability. Particle-in-Cell (PIC) simulations (Gary and Wang, 1996; Gary et al., 2000, 2014; Saito et al., 2008) have demonstrated that this mode can generate enhanced whistler fluctuations and spectral transfer (Gary and Wang, 1996; Gary et al., 2000, 2014; Saito et al., 2008; Chang et al., 2014, 2015).

To further investigate the aforementioned scenarios, one must first understand the competing effects from whistler turbulence and whistler anisotropy instability. For instance, one of the primary consequences of plasma turbulence is to produce sharp spatial gradients in the plasma which can produce enhanced anisotropies locally and forward cascade to dissipate the energy from long wavelength to short wavelength (Osman et al., 2010; Greco et al., 2012; Parashar and Matthaeus, 2016). On the other hand, simulations of whistler anisotropy instabilities driven by a bi-Maxwellian velocity distribution for electrons in a homogeneous plasma showed that the instability imposes an upper bound or constraint on that anisotropy uniformly across the plasma (Gary and Wang, 1996; Gary et al., 2000, 2014; Hughes et al., 2016). The electron anisotropy upper bound derived by Gary and Wang (1996) was verified by observations in the solar wind and magnetosphere (Gary et al., 2005; MacDonald et al., 2008; Štverák et al., 2008; An et al., 2017). However, past studies have mostly addressed the effects from whistler turbulence and whistler anisotropy instability separately.

Gary et al. (2008, 2010), Saito et al. (2008, 2010), and Saito and Gary (2012) presented the first 2-dimensional (2D) PIC simulations of whistler turbulence, and Gary et al. (2012, 2014) and Chang et al. (2011, 2013, 2014, 2015) presented the first 3-dimensional (3D) PIC simulations of whistler turbulence. These simulations considered a homogeneous, magnetized, collisionless plasma upon which an initial spectrum of relatively long wavelength whistler fluctuations is imposed. The results showed that the forward cascade leads to fluctuations which are consistent with the linear dispersion solution for whistler fluctuations. Electron temperature anisotropy were also found to form during forward cascade. Hughes et al. (2014, 2017) and Gary et al. (2016) further investigated electron/ion heating due to whistler turbulence as a function of the initial fluctuating magnetic field energy density, and found the maximum electron heat rate scales approximately linearly with the fluctuating field energy density. This suggests a quasi-linear type heating due to electron Landau damping (Gary et al., 2016).

In this paper, we consider a collisionless, magnetized plasma with co-existing whistler turbulence and the electron temperature anisotropy as the initial condition, and investigate the consequences of both microinstability growth and turbulent cascade using 3D fully kinetic PIC simulations. Qudsi et al. (2020) and Bandyopadhyay et al. (2020) carried out 2D PIC simulations of the Alfvénic turbulence, where ion temperature anisotropy is generated by the development of the turbulence. The results showed that microinstabilities can develop locally in response to ion temperature anisotropies generated by turbulence and may affect the plasma globally, and that there is an apparent correlation between linear instability theory and strongly intermittent turbulence. It was also speculated that a similar process might also occur on electron scale. In this paper, in order to evaluate the effect from whistler instability at a given temperature anisotropy, we prescribe electron temperature anisotropy as the initial condition to drive the instability.

We carry out four different ensembles of PIC simulations: 1) an initially quiet, anisotropic plasma with prescribed initial electron temperature anisotropy; 2) an isotropic plasma with prescribed initial whistler fluctuations; 3) an anisotropic plasma with initial whistler fluctuations (varying initial electron temperature anisotropy and fixed initial fluctuation field energy); and 4) an anisotropic plasma with initial whistler fluctuations (fixed initial electron temperature anisotropy and varying initial fluctuation field energy). Results from PIC simulation are linked with a statistical analysis to understand whether there is any interplay between whistler turbulence and whistler instability, and what are the competing effects from these two processes.

2 Simulation model and setup

We consider a collisionless electron-ion plasma with a uniform background magnetic field $\boldsymbol{B}_0 = B_0\hat{z}$. For the jth (j =

e, i) species, we denote the plasma frequency as $\omega_{pj} = \sqrt{4\pi n_j e^2/m_j}$, the cyclotron frequency as $\Omega_j = eB_0/m_j c$, the thermal speed as $v_{tj} = \sqrt{T_{\|j}/m_j}$, and $\beta_j = 8\pi n_j T_{\|j}/B_0^2$. We denote the angle of mode propagation θ by $\boldsymbol{k} \cdot \boldsymbol{B}_0 = kB_0 \cos(\theta)$.

The physical and numerical parameters are chosen to assure that the consequences of both microinstability growth and turbulent cascade can be accurately resolved in the simulation. In this paper, the initial electron plasma beta is taken to be of a typical value for the solar wind plasma, $\beta_e = 0.1$. To study the effects of whistler anisotropy instability, we consider a range of initial $T_{\perp e}/T_{\|e}$ values that are below and above the instability threshold in the simulation. Through a sequence of test runs with varying initial $T_{\perp e}/T_{\|e}$ values, we find the threshold to excite whistler anisotropy instability for the parameters considered is $T_{\perp e}/T_{\|e} \simeq 2.3$, close to the calculation using the linear theory from (Gary, 1993). In this paper, we present simulations with initial temperature anisotropy of $T_{\perp e}/T_{\|e} = 1, 2, 3, 5, 7, 9$. To study the effects of whistler turbulence, an ensemble of whistler fluctuations are imposed at $t = 0$. The initially loaded whistler fluctuations are set to be relatively long-wavelength with approximately isotropic wavevectors. The spectrum is the same as that used in our previous simulation studies on whistler turbulence (Chang et al., 2011; Gary et al., 2012; Chang et al., 2013; Hughes et al., 2014; Chang et al., 2015). The initial whistler modes include $n = 0, \pm1, \pm2$, and ±3 of the fundamental wavenumber in the perpendicular direction, and $n = \pm1, \pm2$, and ±3 of the fundamental wavenumber in the parallel direction, where the fundamental wavenumber corresponds to the maximum wavelength that can be contained in the domain. This leads to a total of $N = 150$ normal modes with random phases (Chang et al., 2013). The simulations will consider initial total fluctuating magnetic field energy density.

$$\epsilon = \sum_{n=1}^{N} |\delta \boldsymbol{B}_n (t = 0)|^2 \Big/ B_0^2 \tag{1}$$

at $\epsilon = 0, 0.05, 0.25$, and 0.5.

We apply a three-dimensional (3D) full particle electromagnetic particle-in-cell code, 3D-EMPIC by Wang et al. (1995), to simulate the evolution of plasma under four different sets of initial conditions. In Simulation Group A, the ions are set to follow an isotropic velocity distribution while the electrons follow an anisotropic bi-Maxwellian velocity distribution function with different initial values of $T_{\perp e}/T_{\|e}$, at $T_{\perp e}/T_{\|e} = 2, 3, 5, 7$, and 9. The plasma has no initial field fluctuations, $\epsilon = 0$. Simulation Group A is a typical setup for simulations of whistler anisotropy instability (Gary and Wang, 1996). In Simulation Group B, both the ions and electrons are set to have an isotropic velocity distribution. An ensemble of whistler fluctuations are imposed at $t = 0$, with the initial total fluctuating magnetic field energy density at $\epsilon = 0, 0.05, 0.25$, and 0.5. The initial condition in Simulation Groups C and D is a combination of that of Groups A and B, where the electrons follow an anisotropic bi-Maxwellian velocity distribution function and the plasma is initially loaded with an ensemble of whistler fluctuations. In Group C, we take the initial field fluctuation at $\epsilon = 0.25$ and change the initial temperature anisotropy at $T_{\perp e}/T_{\|e} = 2, 3, 5, 7, 9$. In Group D, we take the initial temperature anisotropy at $T_{\perp e}/T_{\|e} = 3$ and change the initial field fluctuation field density at $\epsilon = 0, 0.05, 0.25, 0.50$. The simulation groups are summarized in Table 1.

All the simulations are run using an artificial ion to electron mass ratio of $m_i/m_e = 400$. The ion initial temperature is set to be $T_i = T_{\|e}$. The ratio of the electron gyro-frequency to plasma frequency is $\Omega_e/\omega_{pe} \simeq 0.447$. The simulation box is a cube with a size in each direction at $51.2d_e$, where $d_e = c/\omega_e$ is the electron inertial length. The grid spacing is set to be $\Delta = 0.10d_e$, and hence the mesh size is $512 \times 512 \times 512$. The time step is set to be $\Delta t\omega_{pe} = 0.05$. All the simulations are run for $t\omega_{pe} > 1000$ ($t\Omega_{pe} > 447.20$), i.e. more than 20,000 steps. The macro-particles used is 48 ions and 48 electrons per cell or about 3.1×10^{11} total macro-particles.

We use the Probability Density Function (PDF) in statistical analysis of magnetic fluctuations. The PDF of a random field $B(x)$ may be defined as (Matthaeus et al., 2015)

$$\text{PDF}(\mathbf{B})d\mathbf{B} = \text{probability that the random value lies between } \mathbf{B} \text{ and } \mathbf{B} + d\mathbf{B} \tag{2}$$

Then the increments of the field components are

$$\delta \mathbf{B}(\mathbf{x}) = \mathbf{e}_r \cdot [\mathbf{B}(\mathbf{x} + \mathbf{r}) - \mathbf{B}(\mathbf{x})] \tag{3}$$

where $\mathbf{r}$ is the spatial separation length vector along the direction of any unit vector $\mathbf{e}_r$. By summing over all the cells of a PIC simulation, one may construct a PDF for each component of the fluctuating fields as a function of the spatial separation r. If the random variable r is subject to a central limit theorem, the distribution is expected to be a Gaussian, whereas any departure from a Gaussian corresponds to a more strongly intermittent ensemble of fluctuations. An important advantage of the PDF analyses is that, by statistically averaging over a large body of observational and/or computational data, one may draw general conclusions which are less readily available via other means of data analysis. For example, the statistical analysis of solar wind magnetic fluctuations measured from the Cluster and ACE spacecraft by Kiyani et al. (2012) shows that the PDFs of both $\delta B_\|$ and $\delta B_\perp$ exhibit the same functional form in the kinetic range but not in the inertial range. The PDF analysis of the solar wind data from the Helios spacecraft (He et al., 2013) shows that, as the heliospheric distance of the spacecraft increases, the distribution of the local mean magnetic field vectors gradually broadens in the radial direction and becomes more scattered. The PDF analysis of 3D PIC simulations of whistler turbulence

TABLE 1 Summary of simulation cases. In all cases, β_e = 0.1 and v_{te}/c = 0.1.

Group	Initial Condition	Run No.	$T_{\perp e}/T_{\parallel e}$	ϵ
A	Quiet, Anistrophic electrons	1,2,3,4,5	2,3,5,7,9	0.00
B	Isotropic electrons with whistler fluctuations	1,2,3,4	1,1,1,1	0.00, 0.05, 0.25, 0.50
C	Anisotropic electrons with whistler fluctuations	1,2,3,4,5	2,3,5,7,9	0.25
D	Anisotropic electrons with whistler fluctuations	1,2,3,4	3,3,3,3	0.00, 0.05, 0.25, 0.50

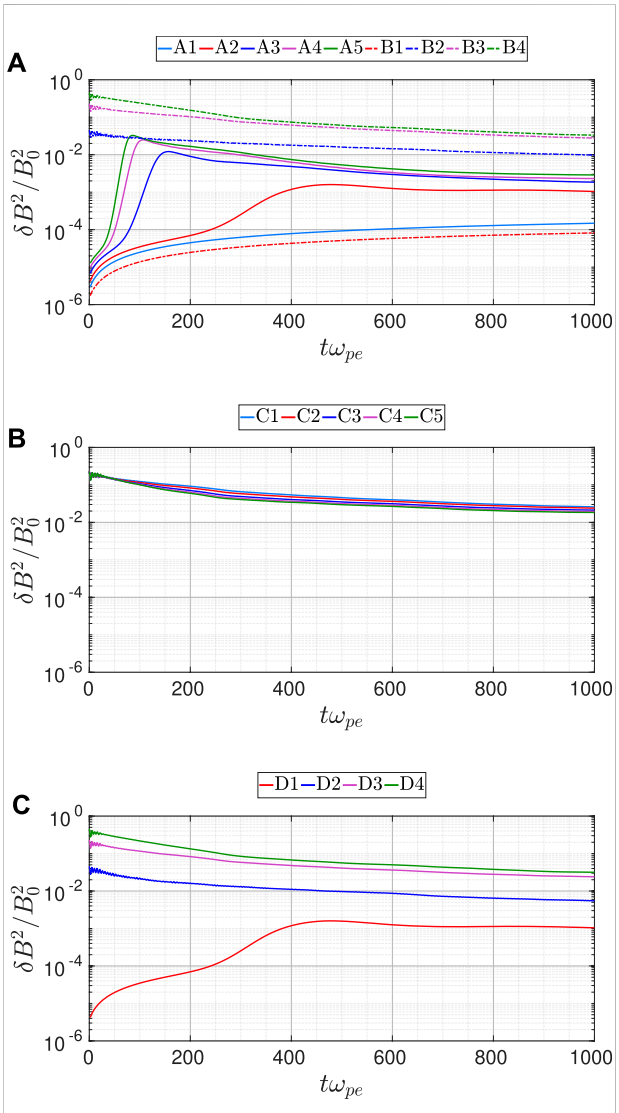

FIGURE 1
Time history of $\delta B(t)^2/B_0^2$ for all simulation cases. **(A)** Simulation Groups A and B **(B)** Simulation Group C **(C)** Simulation Group D

(Chang et al., 2014) shows distinct non-Gaussian "tails" in both the $\delta B_\parallel$ and $\delta B_\perp$ distributions as well as distinctly different functional forms between the two magnetic polarizations.

3 Results and discussions

3.1 Fluctuating magnetic fields

Figure 1 shows the normalized fluctuating magnetic field energy density averaged over all mesh points, $|\delta B(t)|^2/B_0^2$, as a function of time for all the simulation runs. The results from Group A show that the fluctuating magnetic fields in Run A2 through A5 ($T_{\perp e}/T_{\parallel e} \geq 3$) grow rapidly to saturation, with the growth rate in the linear phase matching the value calculated from the linear theory (Gary, 1993). This is similar to that in previous simulations of whistler anisotropy instability (Gary and Wang, 1996), where it showed pitch-angle scattering of the electrons by fluctuating magnetic fields reduces $T_{\perp e}$ and increases $T_{\parallel e}$, and thus the temperature anisotropy. In Run A1 ($T_{\perp e}/T_{\parallel e}$ = 2), the fluctuating magnetic field stays relatively unchanged because the initial anisotropy is below the instability excitation threshold and thus the instability is not excited. The results from Group B show that the fluctuating magnetic field energy decreases with time. This is similar to that in previous simulations of whistler turbulence (Gary et al., 2012), where it showed that the decrease of fluctuating magnetic field corresponds to an increase in the electron thermal energy with the parallel electron temperatures gaining more energy than the perpendicular electron temperatures. Gary et al. (2012) showed that such energy dissipation is primarily through wave-particle interactions via linear Landau damping at relatively small initial fluctuating field energy ($0.02 \leq \epsilon \leq 0.2$) and fully nonlinear processes at large initial fluctuating field energy ($\epsilon > 0.2$). Recent studies have suggested that both nonlinear Landau damping (Ganguli et al., 2010; Chang et al., 2013; Li et al., 2016) and current structure dissipation (Wan et al., 2012, 2015; Karimabadi et al., 2013) contribute to the nonlinear dissipation processes. Chang et al. (2014) suggested current structure dissipation as the dominant nonlinear dissipation process in whistler turbulence.

The results from Group C show that, for a plasma with co-existing whistler fluctuations and electron temperature anisotropy as the initial condition, the time history of $|\delta B(t)|^2/B_0^2$ is almost identical to that from Run B3 (ϵ = 0.25, $T_{\perp e}/T_{\parallel e}$ = 1). The initial temperature anisotropy, whether below the instability threshold (Run C1) or above the instability threshold (Run C2 through C5), has little effect on

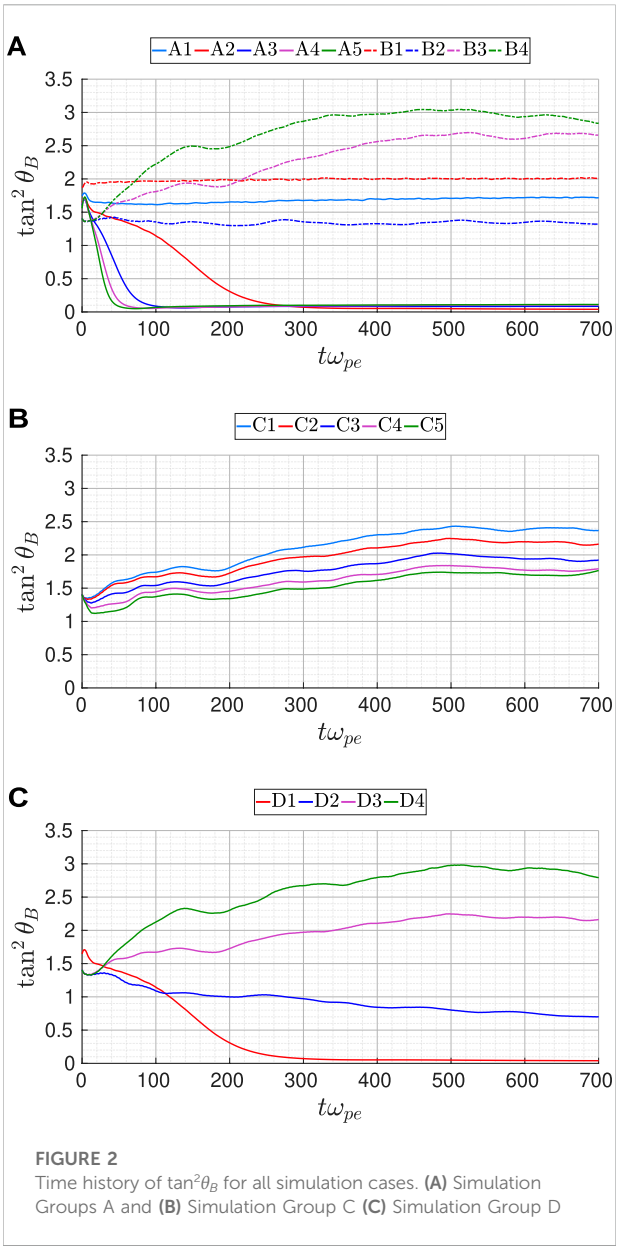

FIGURE 2
Time history of $\tan^2\theta_B$ for all simulation cases. **(A)** Simulation Groups A and **(B)** Simulation Group C **(C)** Simulation Group D

$|\delta B(t)^2|/B_0^2$. Comparing the results from Group D with that from Group B further shows that the time history of $|\delta B(t)|^2/B_0^2$ is influenced only by the initial fluctuating field energy density ϵ. The whistler anisotropy instability has almost no effect on the evolution of the overall magnitude of the fluctuating magnetic fields.Figure 2 shows the magnetic fluctuation wavevector anisotropy averaged over all mesh points

$$\tan^2\theta_B = \frac{\sum_{\boldsymbol{k}} k_\perp^2 |\delta \boldsymbol{B}(\boldsymbol{k})^2|}{\sum_{\boldsymbol{k}} k_\parallel^2 |\delta \boldsymbol{B}(\boldsymbol{k})^2|} \quad (4)$$

as a function of time for all the simulation runs. The $\tan^2\theta_B$ history in Run A1 is nearly constant as no whistler anisotropy instability is excited. The results from Run A2 through A5 follow the predictions of the linear theory (Gary, 1993): the maximum growth rate happens in the direction of $\boldsymbol{k}\times\boldsymbol{B} = 0$; the energy in the perpendicular direction is quickly damped due to resonance scattering of pitch angle, and thus the energy perturbation is mostly along $\boldsymbol{B}_0$. The results from Group B shows that the wavevector anisotropy increases rapidly. Larger initial fluctuating magnetic field energy density leads to a more rapid increase in wavevector anisotropy. This reflects the effect of forward cascade of whistler turbulence, which transfers the energy preferentially for $k_\perp \gg k_\parallel$, thus leading to the expansion of wavevector in the perpendicular direction. The forward cascade of whistler turbulence was discussed in detail in Gary et al. (2012) and Chang et al. (2011, 2013, 2014).

The $\tan^2\theta_B$ history from Group C qualitatively follows that of Run B3 ($\epsilon = 0.25$, $T_{\perp e}/T_{\parallel e} = 1$). However, the initial temperature anisotropy also has a limited effect, showing that an increase of $T_{\perp e}/T_{\parallel e}$ reduces the growth rate of $\tan^2\theta_B$. This may be explained as a result of the action by the whistler anisotropy instability. A larger initial temperature anisotropy leads to a larger growth rate of whistler anisotropy instability, which in turn leads to stronger scattering of pitch angle, and thus faster damping of the energy in the perpendicular direction. Comparing the results from Group D with that from Group B, we find that, at a given initial temperature anisotropy, the effect of the whistler instability diminishes as the initial fluctuating field energy increases. This suggests that forward cascade from whistler turbulence has a far more dominating effect over pitch angle scattering from whistler instability on wavevector anisotropy.

To further investigate the effects of the whistler anisotropy instability on the intermittency generated by whistler turbulence, we calculate the probability density function (PDF) of the local fluctuating magnetic $\delta\boldsymbol{B}$ (i, j, k) for each cell. Figure 3 shows the PDF along the y direction. For Groups A and C, the PDFs from Run A1 and C1 are not shown because the whistler anisotropy instability is not excited in these two cases. Figure 3E (Run B1) shows the result for a quiet isotropic plasma. Figures 3A–D (Run A2-A5 from Group A) show the result for a quiet anisotropic plasma. The initial temperature anisotropy excites whistler anisotropy instability. As there is little change in the tail region, the whistler anisotropy instability did not generate enhanced whistler fluctuations for the simulation parameters considered. Figures 3E–H (Group B) show the result for an isotropic plasma with whistler fluctuations. Similar to previous simulations of whistler turbulence (Chang et al., 2014), an increase in ϵ leads to an enhanced tail region and the increased deviation from the Gaussian distribution. Figures 3I-L (Group C) show the PDFs for Group C are qualitatively similar to that in Group B, indicating that increasing the initial electron temperature anisotropy has very little effect on the fluctuating magnetic fields. Figures 3M–P (Group D) further show that the PDFs are only influenced by the initial fluctuating field energy.

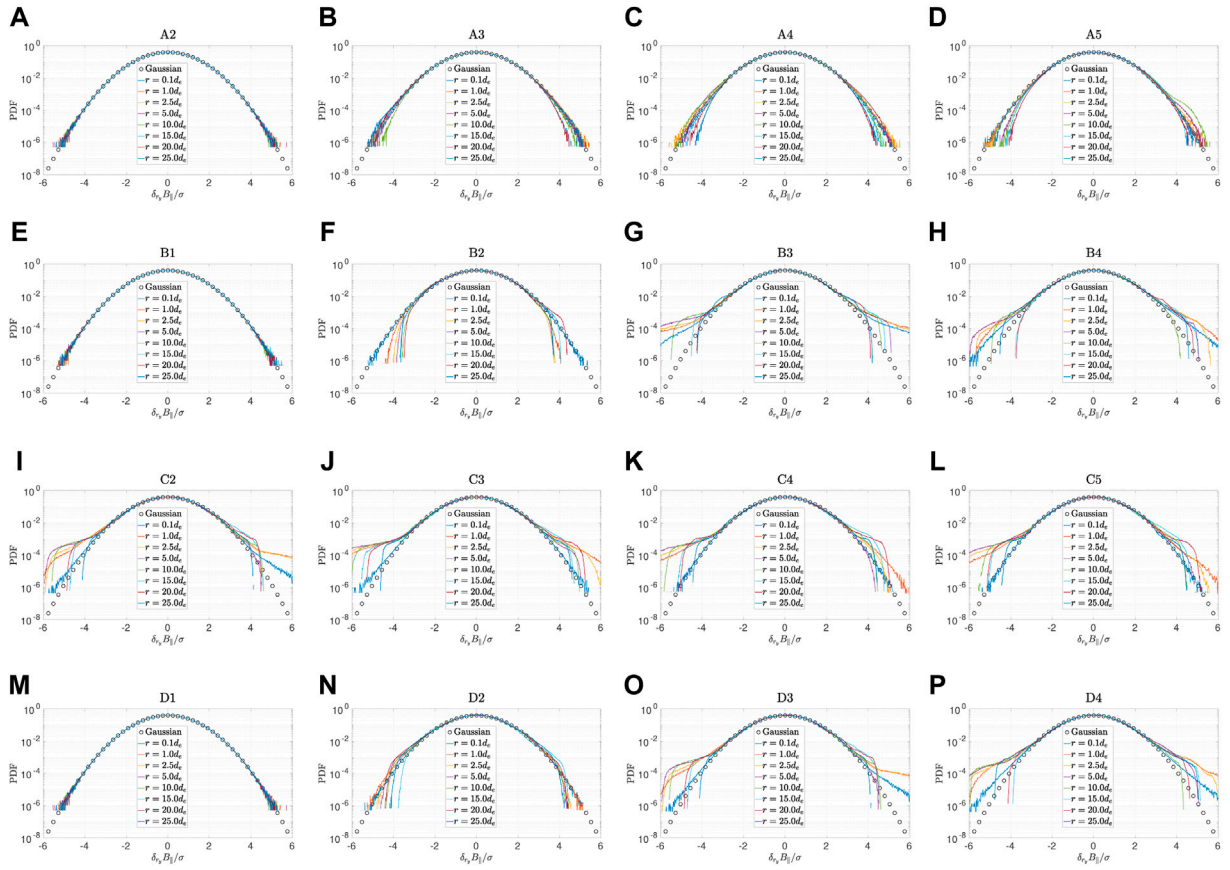

FIGURE 3
Comparison of the probability distribution function of $\delta B_\parallel$ along Y axis at $\Omega_e t \approx 111.80$. **(A)**–**(D)**: Run A2 to A5. **(E)**–**(H)**: Run B1 to B4. **(I)**–**(L)**: Run C2 to C5 **(M)**–**(P)**: Run D1 to D4.

The results from Figures 1–3 are not surprising. As the magnetic field energy from the broad band whistler turbulence dominates over that from the narrow band, the operation of whistler anisotropy instability will have a very minor effect on the evolution of the fluctuating magnetic field.

3.2 Electron temperature anisotropy

We next compare the effects of whistler turbulence and whistler instability on electron temperature anisotropy. We calculate both the local temperature anisotropy $R_e\ (i,\ j,\ k) = T_{\perp e}\ (i,\ j,\ k)/T_{\parallel e}\ (i,\ j,\ k)$ from macro-particles in each cell and the average temperature anisotropy over all the cells of the simulation domain

$$R_e = \frac{1}{N_x N_y N_z} R_e(i,j,k) = \frac{1}{N_x N_y N_z} \sum_{i,j,k} \frac{T_{\perp e}(i,j,k)}{T_{\parallel e}(i,j,k)} \quad (5)$$

where N_x, N_y, N_z are the total mesh points each direction, and subscripts i, j, k denote the cell number. Figure 4 compares R_e vs. β_e for Groups A and C at $\omega_{pe}t = 1000$ ($\Omega_e t \simeq 447.2$), when both the whistler turbulence and the whistler instability are developed (see Figure 1).

Gary and Wang (1996) showed that the wave-particle scattering from whistler instability imposes an upper bound on $T_{\perp e}/T_{\parallel e}$ commensurate with that predicted by linear theory:

$$R_e - 1 = \frac{S_e}{\beta_{e\parallel}^{\alpha_e}} \quad (6)$$

where S_e is the dimensionless scalar conductivity of electrons (Gary, 1993; Gary and Wang, 1996). The anisotropy upper bound in the form of Eq. 6 was numerically fitted in Gary and Wang (1996) for parameters similar to that used here, and is shown as the dotted line in Figure 4. The results show that the average temperature anisotropy R_e at the end of the simulations from Run A2 through A5 lay under the upper bound of Eq. 6. The R_e from Run A1 is almost unchanged, as expected, as the whistler instability is not excited in this case. It is interesting to observe that the R_e points from Group C are

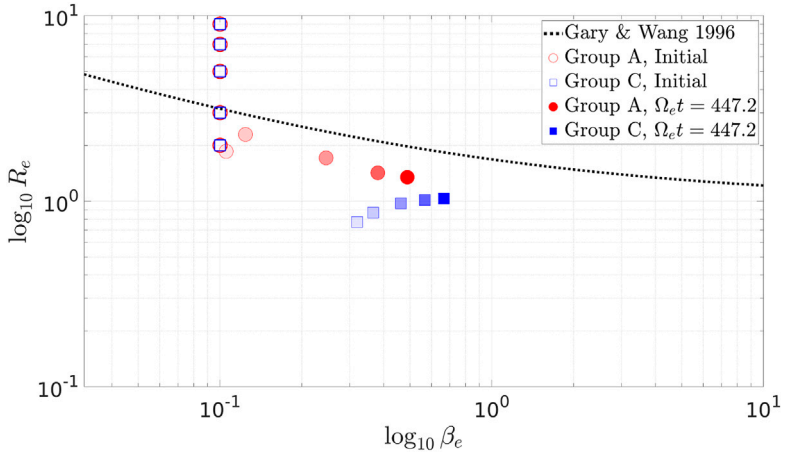

FIGURE 4
Average electron temperature anisotropy R_e v. s. β_e at $\Omega_e t = 0$ and at $\Omega_e t \approx 447.2$ for Group A and Group C. The initial anisotropies are shown as transparent circle for Group A and transparent square for Group C, respectively. The final anisotropies for Run A1 through A5 are color circles with increasingly dark shades, and that for Run C1 through C5 are color squares with increasingly dark shades. The upper bound predicted by Eq. 6 is shown as the dotted line.

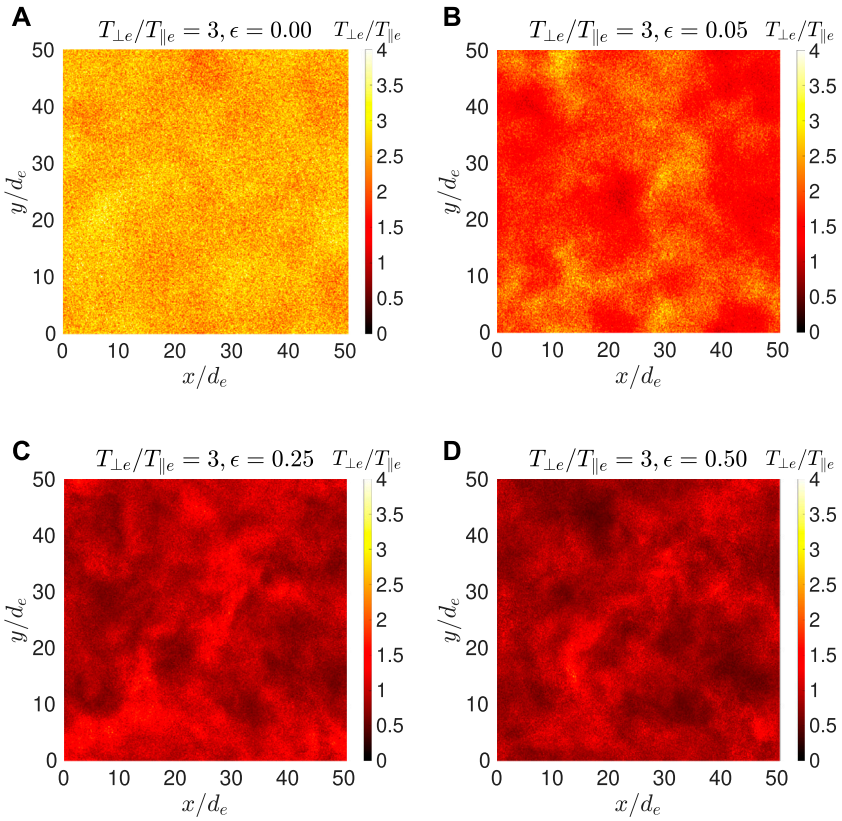

FIGURE 5
Contours of R_e (i, j, k) on an x-y plane in the middle of the simulation box at time $\Omega_e t \approx 223.60$ for Run D1 **(A)**, D2 **(B)**, D3 **(C)**, and D4 **(D)**.

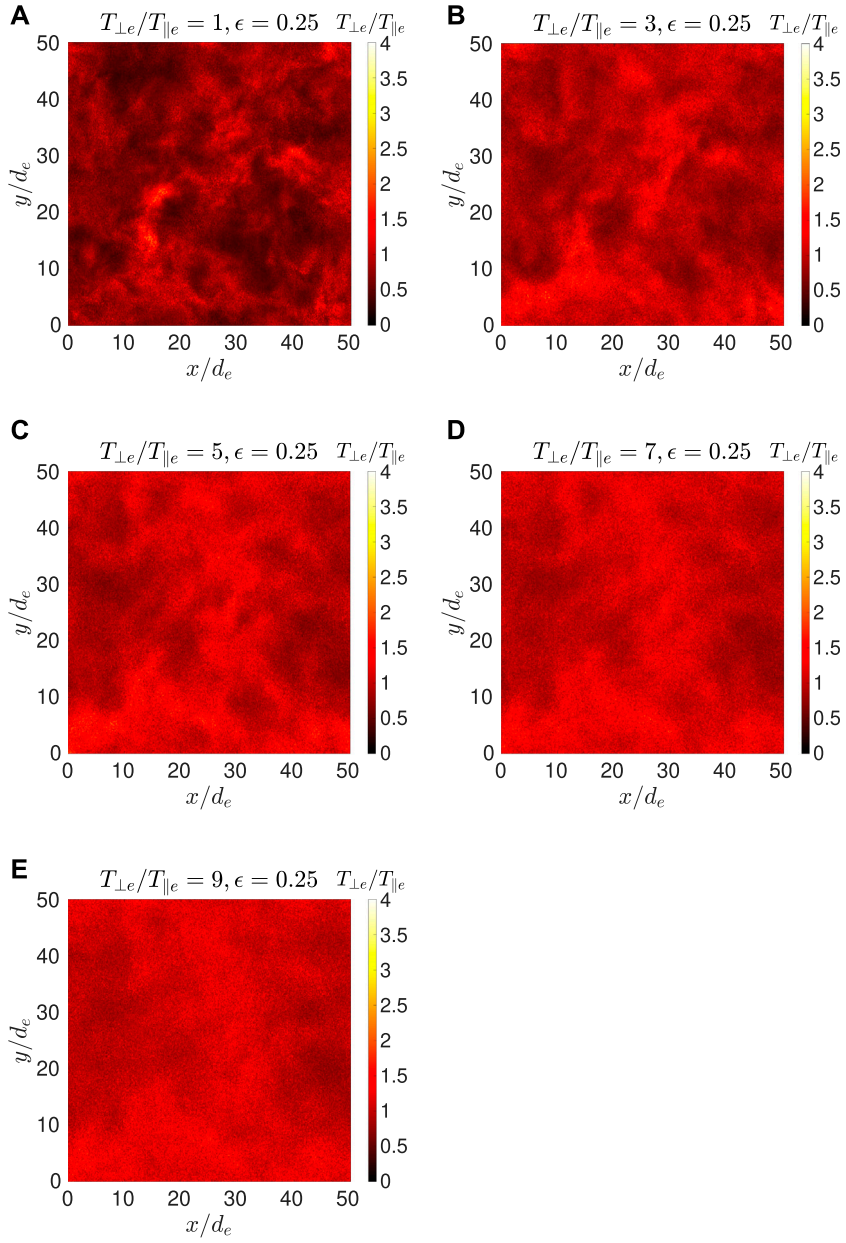

FIGURE 6
Contours of R_e (*i*, *j*, *k*) on an x-y plane in the middle of the simulation box at time $\Omega_e t \approx 223.60$ for Run B3 **(A)**, C2 **(B)**, C3 **(C)**, C4 **(D)**, and C5 **(E)**.

further below the upper bound from the linear theory prediction.

As turbulence produces strong inhomogeneity in plasma, we next examine the contours of local electron temperature anisotropy, R_e (*i*, *j*, *k*). Figures 5, 6 show the contours of R_e (*i*, *j*, *k*), on an x-y plane in the middle of the simulation domain, where we compare R_e (*i*, *j*, *k*) for increasing initial fluctuating field energy (from left to right) for a fixed initial temperature anisotropy ($T_{\perp e}/T_{\|e}$ = 3). In Figure 6, we compare R_e (*i*, *j*. *k*) for increasing initial $T_{\perp e}/T_{\|e}$ (from left to right) for a fixed initial fluctuating field energy (ϵ = 0.25). Both Figures 5, 6 are plotted for $\omega_{pe}t$ = 500 ($\Omega_e t \simeq 223.6$), when all the cases are starting to approach an asymptote.

Figure 5A (Run D1) has no initial whistler fluctuation and thus the temperature anisotropy distribution is homogenous. As the initial spectrum strength ϵ increases, Figure 5 shows increasing intermittent fluctuations in temperature anisotropy due to turbulence. Figure 6A (Run B3) shows that turbulence

TABLE 2 R_e (i, j, k) value range of Figure 6.

Sub Figure No.	$T_{\perp e}/T_{\parallel e}$	min (R_e (i, j, k))	max (R_e (i, j, k))
A	1	0.1738	4.8790
B	3	0.2415	4.8039
C	5	0.2975	3.8607
D	7	0.3531	3.0551
E	9	0.3942	2.8061

produces strong anisotropies in an initially isotropic plasma. All of these results are to be expected. However, in Figure 6, as the initial anisotropy increases, we find that the intermittent fluctuations in the R_e (i, j, k) contours start to diminish. The range of R_e (i, j, k) in Figure 6 (from left to right) is summarized in Table 2, showing the temperature becomes more homogenous as the initial $T_{\perp e}/T_{\parallel e}$ increases.

Figures 5, 6 show that, in contrast to the minor effects on the fluctuating magnetic field, the whistler anisotropy instability has a major effect on the intermittency of temperature anisotropy generated by turbulence. The whistler anisotropy instability acts to reduce electron temperature anisotropy through wave-particle scattering. Wave-particle scattering is a microscopic process. Wave-particle scattering of electrons are affected more efficiently by local field fluctuations and are less dependent on the overall field energy. The results suggest that the fluctuation from the growth of a single mode of whistler anisotropy instability is more efficient in wave-particle scattering of the electrons than that of a spectrum of whistler modes. A stronger initial temperature anisotropy leads to a larger whistler instability growth rate, and stronger wave-particle scattering effect, and thus reducing the intermittency in temperature anisotropy generated by turbulence.

4 Summary and conclusion

3D PIC simulations are carried out to study the dynamic evolution of a collisionless, magnetized plasma with co-existing whistler turbulence and electron temperature anisotropy as the initial condition, and the competing consequences of whistler turbulence cascade and whistler anisotropy instability growth. The results show that the operation of the whistler instability within whistler turbulence has no obvious effects on the fluctuating magnetic field. We find the overall fluctuating magnetic field energy and intermittency generated by turbulence are not influenced by the inclusion of an initial electron temperature anisotropy, while wavevector anisotropy is reduced somewhat by increased electron temperature anisotropy. In contrast, the results show that whistler instability has a major effect on electron temperature anisotropy. While whistler turbulence produces sharp gradients and enhanced electron temperature anisotropies locally, we find that increasing the initial electron temperature anisotropy actually leads to a reduction of the intermittency in the electron temperature anisotropy generated by turbulence, and the reduction of the average electron temperature anisotropy further below the upper bound as predicted by the linear theory for a homogeneous anisotropic plasma. The results suggest the small reduction of wavevector anisotropy and major reduction of electron temperature anisotropy are apparently due to whistler instability growth. Comparing to an isotropic plasma with whistler turbulence, an increase in the initial electron temperature anisotropy leads to a larger growth rate of the whistler anisotropy instability, resulting in faster damping of the energy in this perpendicular direction, and thus a small reduction of the growth rate of the wavevector anisotropy $\tan^2\theta_B$. While turbulence produce sharp gradients and local enhanced anisotropies, the whistler anisotropy instability acts to reduce electron temperature anisotropy through wave-particle scattering. The results suggest that the fluctuation from the growth of a single mode of whistler anisotropy instability is more efficient in wave-particle scattering of the electrons than that of a spectrum of whistler modes. Thus, a larger initial global electron temperature anisotropy, when combined with enhanced local electron temperature anistropy, would lead to even stronger wave-particle scattering effects locally, thus leading to local temperature anisotropy reduction and a more homogeneous electron temperature landscape.

In conclusion, we find that the overall effect of whistler anisotropy instability on a plasma with co-existing whistler turbulence and global electron temperature anisotropy is minor comparing to that of whistler turbulence. This is because the fluctuating energy associated with the narrowband whistler instability is dominated by that from the broadband whistler turbulence. However, as field fluctuations from the growth of a single instability mode may be more efficient in the wave-particle scattering process than that from a spectrum of whistler modes, the whistler instability can significantly reduces the intermittency of electron temperature anisotropy generated by turbulence. This suggests that microinstability may act as a regulation mechanism on turbulence development. In this study, the whistler instability is generated by imposing a bi-Maxwellian electron velocity distribution as the initial condition. The competing consequences of whistler turbulence cascade and whistler anisotropy instability growth will need to be further evaluated in a more realistic setup where the instability develops naturally from turbulence in future study.

Data availability statement

The raw data supporting the conclusions of this article will be made available by the authors, without undue reservation.

Author contributions

The authors contributed equally to this research.

Funding

SPG acknowledges support from NASA grant NNX16AM98G (80NSSC19K0652) and NSF Award 2031024. CC and JW acknowledge support from NSF Award 2031024 through a sub-award from Space Science Institute to USC.

Acknowledgments

CC and JW acknowledge helpful discussions with Vadim Roytershtey and the computational resources provided by the Cheyenne cluster (Computational And Information Systems Laboratory, 2017) at the National Center for Atmospheric Research (NCAR) and the computational resources provided by the Center for Advanced Research Computing at the University of Southern California (USC CARC).

Conflict of interest

The authors declare that the research was conducted in the absence of any commercial or financial relationships that could be construed as a potential conflict of interest.

Publisher's note

All claims expressed in this article are solely those of the authors and do not necessarily represent those of their affiliated organizations, or those of the publisher, the editors and the reviewers. Any product that may be evaluated in this article, or claim that may be made by its manufacturer, is not guaranteed or endorsed by the publisher.

References

An, X., Yue, C., Bortnik, J., Decyk, V., Li, W., and Thorne, R. M. (2017). On the parameter dependence of the whistler anisotropy instability. *JGR. Space Phys.* 122, 2001–2009. doi:10.1002/2017ja023895

Bandyopadhyay, R., Qudsi, R. A., Matthaeus, W. H., Parashar, T. N., Maruca, B. A., Gary, S. P., et al. (2020). *Interplay of turbulence and proton-microinstability growth in space plasmas. arXiv preprint arXiv:2006.10316.*

Beinroth, H., and Neubauer, F. (1981). Properties of whistler mode waves between 0.3 and 1.0 au from helios observations. *J. Geophys. Res.* 86, 7755–7760. doi:10.1029/ja086ia09p07755

Cerri, S. S., Califano, F., Jenko, F., Told, D., and Rincon, F. (2016). Subproton-scale cascades in solar wind turbulence: Driven hybrid-kinetic simulations. *Astrophys. J.* 822, L12. doi:10.3847/2041-8205/822/1/l12

Chang, O., Gary, S. P., and Wang, J. (2013). Whistler turbulence at variable electron beta: Three-dimensional particle-in-cell simulations. *J. Geophys. Res. Space Phys.* 118, 2824–2833. doi:10.1002/jgra.50365

Chang, O., Gary, S. P., and Wang, J. (2015). Whistler turbulence forward cascade versus inverse cascade: Three-dimensional particle-in-cell simulations. *Astrophys. J.* 800, 87. doi:10.1088/0004-637x/800/2/87

Chang, O., Peter Gary, S., and Wang, J. (2014). Energy dissipation by whistler turbulence: Three-dimensional particle-in-cell simulations. *Phys. Plasmas* 21, 052305. doi:10.1063/1.4875728

Chang, O., Peter Gary, S., and Wang, J. (2011). Whistler turbulence forward cascade: Three-dimensional particle-in-cell simulations. *Geophys. Res. Lett.* 38. doi:10.1029/2011gl049827

Computational And Information Systems Laboratory (2017). *Cheyenne: SGI ICE XA cluster*. doi:10.5065/D6RX99HX

Ganguli, G., Rudakov, L., Scales, W., Wang, J., and Mithaiwala, M. (2010). Three dimensional character of whistler turbulence. *Phys. Plasmas* 17, 052310. doi:10.1063/1.3420245

Gary, S. P., Chang, O., and Wang, J. (2012). Forward cascade of whistler turbulence: Three-dimensional particle-in-cell simulations. *Astrophys. J.* 755, 142. doi:10.1088/0004-637x/755/2/142

Gary, S. P., Hughes, R. S., Wang, J., and Chang, O. (2014). Whistler anisotropy instability: Spectral transfer in a three-dimensional particle-in-cell simulation. *J. Geophys. Res. Space Phys.* 119, 1429–1434. doi:10.1002/2013ja019618

Gary, S. P., Hughes, R. S., and Wang, J. (2016). Whistler turbulence heating of electrons and ions: Three-dimensional particle-in-cell simulations. *Astrophys. J.* 816, 102. doi:10.3847/0004-637x/816/2/102

Gary, S. P., Lavraud, B., Thomsen, M. F., Lefebvre, B., and Schwartz, S. J. (2005). Electron anisotropy constraint in the magnetosheath: Cluster observations. *Geophys. Res. Lett.* 32, L13109. doi:10.1029/2005gl023234

Gary, S. P., and Madland, C. D. (1985). Electromagnetic electron temperature anisotropy instabilities. *J. Geophys. Res.* 90, 7607–7610. doi:10.1029/ja090ia08p07607

Gary, S. P., Saito, S., and Li, H. (2008). Cascade of whistler turbulence: Particle-in-cell simulations. *Geophys. Res. Lett.* 35, L02104. doi:10.1029/2007gl032327

Gary, S. P., Saito, S., and Narita, Y. (2010). Whistler turbulence wavevector anisotropies: Particle-in-cell simulations. *Astrophys. J.* 716, 1332–1335. doi:10.1088/0004-637x/716/2/1332

Gary, S. P., and Smith, C. W. (2009). Short-wavelength turbulence in the solar wind: Linear theory of whistler and kinetic alfvén fluctuations. *J. Geophys. Res.* 114. doi:10.1029/2009ja014525

Gary, S. P. (1993). *Theory of space plasma microinstabilities. Cambridge atmospheric and space science series*. Cambridge University Press. doi:10.1017/CBO9780511551512

Gary, S. P., and Wang, J. (1996). Whistler instability: Electron anisotropy upper bound. *J. Geophys. Res.* 101, 10749–10754. doi:10.1029/96ja00323

Gary, S. P., Winske, D., and Hesse, M. (2000). Electron temperature anisotropy instabilities: Computer simulations. *J. Geophys. Res.* 105, 10751–10759. doi:10.1029/1999ja000322

Greco, A., Valentini, F., Servidio, S., and Matthaeus, W. H. (2012). Inhomogeneous kinetic effects related to intermittent magnetic discontinuities. *Phys. Rev. E* 86, 066405. doi:10.1103/PhysRevE.86.066405

He, J., Tu, C., Marsch, E., Bourouaine, S., and Pei, Z. (2013). Radial evolution of the wavevector anisotropy of solar wind turbulence between 0.3 and 1 au. *Astrophys. J.* 773, 72. doi:10.1088/0004-637x/773/1/72

Howes, G., Dorland, W., Cowley, S., Hammett, G., Quataert, E., Schekochihin, A., et al. (2008). Kinetic simulations of magnetized turbulence in astrophysical plasmas. *Phys. Rev. Lett.* 100, 065004. doi:10.1103/physrevlett.100.065004

Hughes, R. S., Gary, S. P., and Wang, J. (2014). Electron and ion heating by whistler turbulence: Three-dimensional particle-in-cell simulations. *Geophys. Res. Lett.* 41, 8681–8687. doi:10.1002/2014gl062070

Hughes, R. S., Gary, S. P., and Wang, J. (2017). Particle-in-cell simulations of electron and ion dissipation by whistler turbulence: Variations with electron β. *Astrophys. J.* 835, L15. doi:10.3847/2041-8213/835/1/l15

Hughes, R. S., Wang, J., Decyk, V. K., and Gary, S. P. (2016). Effects of variations in electron thermal velocity on the whistler anisotropy instability: Particle-in-cell simulations. *Phys. Plasmas* 23, 042106. doi:10.1063/1.4945748

Karimabadi, H., Roytershteyn, V., Wan, M., Matthaeus, W., Daughton, W., Wu, P., et al. (2013). Coherent structures, intermittent turbulence, and dissipation in high-temperature plasmas. *Phys. Plasmas* 20, 012303. doi:10.1063/1.4773205

Kiyani, K. H., Chapman, S. C., Sahraoui, F., Hnat, B., Fauvarque, O., and Khotyaintsev, Y. V. (2012). Enhanced magnetic compressibility and isotropic scale invariance at sub-ion larmor scales in solar wind turbulence. *Astrophys. J.* 763, 10. doi:10.1088/0004-637x/763/1/10

Leamon, R. J., Smith, C. W., Ness, N. F., Matthaeus, W. H., and Wong, H. K. (1998). Observational constraints on the dynamics of the interplanetary magnetic field dissipation range. *J. Geophys. Res.* 103, 4775–4787. doi:10.1029/97ja03394

Lengyel-Frey, D., Hess, R., MacDowall, R., Stone, R., Lin, N., Balogh, A., et al. (1996). Ulysses observations of whistler waves at interplanetary shocks and in the solar wind. *J. Geophys. Res.* 101, 27555–27564. doi:10.1029/96ja00548

Li, T. C., Howes, G. G., Klein, K. G., and TenBarge, J. M. (2016). Energy dissipation and landau damping in two-and three-dimensional plasma turbulence. *Astrophys. J.* 832, L24. doi:10.3847/2041-8205/832/2/l24

MacDonald, E., Denton, M., Thomsen, M., and Gary, S. (2008). Superposed epoch analysis of a whistler instability criterion at geosynchronous orbit during geomagnetic storms. *J. Atmos. solar-terrestrial Phys.* 70, 1789–1796. doi:10.1016/j.jastp.2008.03.021

Matthaeus, W. H., Wan, M., Servidio, S., Greco, A., Osman, K. T., Oughton, S., et al. (2015). Intermittency, nonlinear dynamics and dissipation in the solar wind and astrophysical plasmas. *Phil. Trans. R. Soc. A* 373, 20140154. doi:10.1098/rsta.2014.0154

Mithaiwala, M., Rudakov, L., Crabtree, C., and Ganguli, G. (2012). Co-existence of whistler waves with kinetic alfven wave turbulence for the high-beta solar wind plasma. *Phys. Plasmas* 19, 102902. doi:10.1063/1.4757638

Narita, Y., Gary, S., Saito, S., Glassmeier, K.-H., and Motschmann, U. (2011). Dispersion relation analysis of solar wind turbulence. *Geophys. Res. Lett.* 38. doi:10.1029/2010gl046588

Narita, Y., Nakamura, R., Baumjohann, W., Glassmeier, K.-H., Motschmann, U., Giles, B., et al. (2016). On electron-scale whistler turbulence in the solar wind. *Astrophys. J.* 827, L8. doi:10.3847/2041-8205/827/1/l8

Osman, K., Matthaeus, W., Greco, A., and Servidio, S. (2010). Evidence for inhomogeneous heating in the solar wind. *Astrophys. J.* 727, L11. doi:10.1088/2041-8205/727/1/l11

Parashar, T. N., and Matthaeus, W. H. (2016). Propinquity of current and vortex structures: Effects on collisionless plasma heating. *Astrophys. J.* 832, 57. doi:10.3847/0004-637x/832/1/57

Qudsi, R. A., Bandyopadhyay, R., Maruca, B. A., Parashar, T. N., Matthaeus, W. H., Chasapis, A., et al. (2020). Intermittency and ion temperature–anisotropy instabilities: Simulation and magnetosheath observation. *Astrophys. J.* 895, 83. doi:10.3847/1538-4357/ab89ad

Sahraoui, F., Goldstein, M. L., Belmont, G., Canu, P., and Rezeau, L. (2010). Three dimensional AnisotropickSpectra of turbulence at subproton scales in the solar wind. *Phys. Rev. Lett.* 105, 131101. doi:10.1103/physrevlett.105.131101

Sahraoui, F., Goldstein, M., Robert, P., and Khotyaintsev, Y. V. (2009). Evidence of a cascade and dissipation of solar-wind turbulence at the electron gyroscale. *Phys. Rev. Lett.* 102, 231102. doi:10.1103/physrevlett.102.231102

Saito, S., and Gary, S. (2012). Beta dependence of electron heating in decaying whistler turbulence: Particle-in-cell simulations. *Phys. Plasmas* 19, 012312. doi:10.1063/1.3676155

Saito, S., Gary, S. P., Li, H., and Narita, Y. (2008). Whistler turbulence: Particle-in-cell simulations. *Phys. Plasmas* 15, 102305. doi:10.1063/1.2997339

Saito, S., Gary, S. P., and Narita, Y. (2010). Wavenumber spectrum of whistler turbulence: Particle-in-cell simulation. *Phys. Plasmas* 17, 122316. doi:10.1063/1.3526602

Salem, C. S., Howes, G., Sundkvist, D., Bale, S., Chaston, C., Chen, C., et al. (2012). Identification of kinetic alfvén wave turbulence in the solar wind. *Astrophys. J.* 745, L9. doi:10.1088/2041-8205/745/1/l9

Štverák, Š., Trávníček, P., Maksimovic, M., Marsch, E., Fazakerley, A. N., and Scime, E. E. (2008). Electron temperature anisotropy constraints in the solar wind. *J. Geophys. Res.* 113. doi:10.1029/2007ja012733

TenBarge, J., Howes, G., and Dorland, W. (2013). Collisionless damping at electron scales in solar wind turbulence. *Astrophys. J.* 774, 139. doi:10.1088/0004-637x/774/2/139

Wan, M., Matthaeus, W., Karimabadi, H., Roytershteyn, V., Shay, M., Wu, P., et al. (2012). Intermittent dissipation at kinetic scales in collisionless plasma turbulence. *Phys. Rev. Lett.* 109, 195001. doi:10.1103/physrevlett.109.195001

Wan, M., Matthaeus, W., Roytershteyn, V., Karimabadi, H., Parashar, T., Wu, P., et al. (2015). Intermittent dissipation and heating in 3d kinetic plasma turbulence. *Phys. Rev. Lett.* 114, 175002. doi:10.1103/physrevlett.114.175002r

Wang, J., Liewer, P., and Decyk, V. (1995). 3d electromagnetic plasma particle simulations on a mimd parallel computer. *Comput. Phys. Commun.* 87, 35–53. doi:10.1016/0010-4655(94)00167-z

frontiers | Frontiers in Astronomy and Space Sciences

TYPE Original Research
PUBLISHED 10 January 2023
DOI 10.3389/fspas.2022.1100472

OPEN ACCESS

EDITED BY
Charles William Smith,
University of New Hampshire, United States

REVIEWED BY
Daniel Verscharen,
University College London, United Kingdom
Mourad Djebli,
USTHB, Algeria

*CORRESPONDENCE
Ari Le,
arile@lanl.gov

SPECIALTY SECTION
This article was submitted to Space Physics, a section of the journal Frontiers in Astronomy and Space Sciences

RECEIVED 16 November 2022
ACCEPTED 21 December 2022
PUBLISHED 10 January 2023

CITATION
Le A, Chen L-J, Wetherton B, Keenan B and Stanier A (2023), Oblique propagation and temperature effects on the resonant right-hand ion beam instability.
Front. Astron. Space Sci. 9:1100472.
doi: 10.3389/fspas.2022.1100472

Oblique propagation and temperature effects on the resonant right-hand ion beam instability

Ari Le[1]*, Li-Jen Chen[2], Blake Wetherton[1], Brett Keenan[1] and Adam Stanier[1]

[1]Los Alamos National Laboratory, Los Alamos, NM, United States, [2]Goddard Space Flight Center, National Aeronautics and Space Administration, Greenbelt, MD, United States

The resonant right-hand instability (RHI) is often the dominant mode driven by reflected ions upstream of Earth's quasi-parallel bow shock. In the tradition of Peter Gary, this paper further explores the right-hand instability using numerical solutions of the plasma dispersion relation and non-linear kinetic simulations, with parameters inspired by observations from NASA's Magnetospheric Multiscale (MMS) mission. Agreement is found between the ion distributions in the particle-in-cell simulations and Magnetospheric Multiscale spacecraft data, which show the gyrophase bunching characteristic of the instability. The non-linear structures created by right-hand instability tend to be stronger when the plasma beta is lower. These structures have sizes of around 100 to 200 ion inertial lengths perpendicular to the magnetic field, presenting planet-sized disturbances to the magnetosphere. 2d and 3D hybrid particle-in-cell simulations show that modes with a range of propagation angles oblique to the magnetic field are excited, providing a ground to understand previous statistical studies of observed foreshock waves.

KEYWORDS

foreshock, instability, oblique, electromagnetic, ions, bow shock

1 Introduction

At Earth's bow shock, like at other collisionless shocks, ions reflected back upstream may form a beam population in velocity space. The free energy of this backstreaming ion beam drives a range of kinetic instabilities in the foreshock. For relatively tenuous and fast (compared to the background Alfven speed) ion beams traveling parallel to the magnetic field, the fastest growing linear instability is the resonant right-hand instability (RHI) (Gary, 1991). For low beam densities, this mode is a low-frequency wave carried by the background and excited by a cyclotron resonance with the beam ions. As described in another article in this collection (Winske and Wilson, 2022), Peter Gary was a pioneer in the Vlasov theory of electromagnetic ion beam instabilities in space plasmas (Gary et al., 1984; Gary et al., 1985; Gary, 1991). Gary's work is an important piece of a large body of research on the theory and observation of RHI waves in the foreshock. Here,

we re-examine properties and dynamics of the RHI using a modern hybrid particle-in-cell (PIC) code and example data from NASA's Magnetospheric Multiscale (MMS) mission. The hybrid PIC simulations show that a finite temperature of the background decreases the amplitude of non-linear structures that develop and that a relatively broadband spectrum of modes may be excited with a range of propagation angles oblique to the local magnetic field.

Many early studies of RHI were inspired by data from the International Sun-Earth Explorer (ISEE) spacecraft. The data showed abundant wave activity in the foreshock, and it was recognized that RHI and other low-freqency modes were associated with backstreaming ions (Hoppe et al., 1981). Some effects of these waves include modifying the transport and heating of ions in the upstream plasma (Lee, 1982). The RHI in particular may also drive ultra-low frequency (ULF) waves in the 30-s period range (Watanabe and Terasawa, 1984; Greenstadt et al., 1995), which couple to particles trapped in Earth's radiation belts. The non-linear evolution of RHI was found to be a possible driver of large-amplitude magnetic pulsations observed in the forshock (Akimoto et al., 1993). More recent simulation studies of RHI have focused on the global context of (ULF) waves and their transport into the magnetosphere (Blanco-Cano et al., 2009; Palmroth et al., 2015; Kajdič et al., 2021; Turc et al., 2022). In addition, very high-resolution field and particle data are now available from NASA's MMS mission (Burch et al., 2016). Meanwhile, laser-driven laboratory experiments have offered a means of taking detailed measurements of ion beam instabilities in a reproducible environment (Heuer et al., 2020).

Here, we revisit RHI with a hybrid PIC code to further explore the waves and non-linear structures associated with the instability. Because earlier work focused on moderately cool beams with $v_{thb} \lesssim v_A$ (Hoshino and Terasawa, 1985; Winske and Gary, 1986; Akimoto et al., 1993) we also consider the effects of warmer beam and background ion populations. The finite temperatures moderately reduce the RHI growth rate, and they tend to reduce the amplitude of non-linear structures. We also explore the spectrum of oblique waves excited by a parallel ion beam. A statistical analysis of Cluster spacecraft data uptream of the quasi-parallel bow shock showed that the beam-driven waves have a power spectrum peaked at oblique propagation angles (Eastwood et al., 2005). This is at first glance at odds with the fact that the fastest growing mode for the beam and plasma conditions is the purely parallel propagating RHI. We find a range of oblique modes are excited in 2D and 3D simulations, consistent with solutions of the hot plasma dispersion relation. The simulations predict a typical perpendicular scale length of the non-linear RHI structures to be ~100 to 200d_i, indicating that the structures are planet-sized and may significantly impact the magnetosphere.

2 Review of the resonant ion beam instability

In this section, we include a brief review of the resonant right-hand instability (RHI) and define the conventions we use in our analysis. The RHI is a solution of the dispersion relation for magnetized plasmas with a beam ion population traveling along the magnetic field. For the cases of interest here, the fastest growing mode is purely parallel propagating. For purely parallel modes, the relevant dispersion relation for a plasma where each species j has an isotropic Maxwellian velocity distribution is (Gary et al., 1984):

$$1 - \frac{k^2c^2}{\omega^2} + \sum_j \frac{w_{pj}^2}{\omega^2}\zeta_j Z\left(\zeta_j^+\right) = 0 \tag{1}$$

$$\zeta_j = \left(\omega - ku_j\right)/kv_{thj} \tag{2}$$

$$\zeta_j^+ = \left(\omega - ku_j + \omega_{cj}\right)/kv_{thj} \tag{3}$$

where k is the parallel wavenumber, $\omega_{pj}^2 = n_j Z_j^2 e^2/\epsilon_0 m_j$, $v_{thj} = \sqrt{2T_j/m_j}$, u_j is the bulk fluid drift velocity, and $Z(x)$ is the plasma dispersion function. In the quasi-neutral cold plasma limit, this results in a polynomial relation $D(\omega, k) = 0$ that yields four distinct unstable modes (Weidl et al., 2019) including the RHI.

To study the linear growth rates of the RHI for oblique propagation including finite beam and background ion temperatures, we consider numerical solutions (Montgomery et al., 1975) of the full hot plasma dispersion relation assuming drifting Maxwellian ion distributions (see, for example the appendix of Gary, 1991). We use the open-source New Hampshire Dispersion Solver (NHDS) (Verscharen and Chandran, 2018). We work in the rest frame of the background plasma, where the background ions have no net drift. The background plasma is taken to be uniform and consisting of ions of mass m_i and unit charge. We denote the background density n_0 and the temperature T_0. The background magnetic field is also uniform, in the positive x direction, and of strength B_0. A drifting Maxwellian ion beam population is included with a density n_b, temperature T_b, and a drift speed u_b in the positive x direction. The Alfven Mach number of the beam is $M_A = u_b/v_A$, were we normalize the drift speed to the background Alfven speed $v_A = B_0/\sqrt{\mu_0 n_0 m_i}$. For simplicity, we take beam ions to be the same species as the background ions. The electron population is charge- and current-neutralizing.

At Earth's bow shock, the reflected ion population is characteristically low-density (with relative beam fractions less than a few percent) and fast (with Alfven Mach numbers $M_A > 2$). Under these conditions, the low-frequency wave

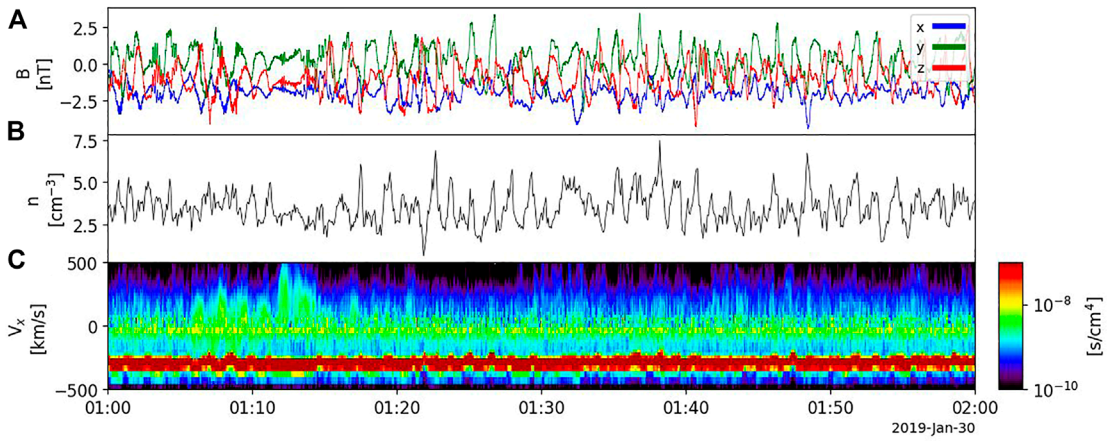

FIGURE 1
Example of RHI waves typical of the quasi-parallel foreshock as observed by the MMS2 spacecraft. The magnetic field in **(A)** is primarily in the x direction with large-amplitude waves in B_y and B_z. The total ion density it plotted in **(B)**. The reduced ion velocity distribution in terms of v_x is plotted in **(C)**. In the spacecraft frame, the background moves in the $-v_x$ direction while the beam population is centered near $v_x = 0$. The reflected beam ions have a relatively broad velocity spread compared to the colder solar wind population.

spectrum is dominated by the RHI. **Figure 3** shows the maximum growth rate of the RHI over a range of propagation angles for a beam of density $n_b/n_0 = .015$ and an Alfven Mach number of $M_A = 10$, similar to typical parameters at Earth's foreshock. The three curves show the growth rates for three different beam temperatures. The uppermost curve is a relatively cold beam, and the peak growth rate for parallel propagation agrees with the large M_A approximation for cold plasmas (Gary, 1978; Weidl et al., 2019), $\gamma/\Omega_{ci} \sim (n_b/2n_0)^{1/3}$. When finite temperature effects are included, the growth rate decreases as the beam temperature increases. This is because a smaller fraction of the beam is gyroresonant with the mode. The background temperature has a very minor effect on the growth rates as long as the background thermal speed is relatively low ($v_{th0} \ll u_b$) as is typically observed at Earth's foreshock. We note that while additional beam-driven modes, including oblique Alfven modes Daughton and Gary. (1998) and the non-resonant mode (e.g., Gary. (1991), Chen et al. (2022), exist over this range, the RHI is dominant for the relatively fast ($M_A > 2$) and tenuous beams that we consider here. In **Section 3**, we explore the non-linear development of the purely parallel-propagating RHI using a hybrid PIC code.

3 1D hybrid simulation and example event

We begin this section with an example of foreshock waves driven by reflected ions observed by NASA's MMS mission (Burch et al., 2016). The MMS data are plotted in **Figure 1**, showing a fairly typical foreshock crossing in an interval upstream of the quasi-parallel bow shock on 30 January 2019. The magnetic field components in **Figure 1A** show a background field dominated by the radial B_x component along with large-amplitude wave fields (mainly B_y and B_z). The wave power is peaked near the local ion cyclotron frequency ($\sim$0.01 Hz). In the spacecraft frame, the bulk solar wind velocity is $u_x \sim -300\ km/s \sim -10 v_A$, and the reflected ions appear as a more diffuse population centered near $v_x \sim 0$ (see **Figure 1C**). The approximate relative density of the reflected population is $n_b/n_0 \lesssim .05$, and the relative parallel drift of the beam gives an Alven Mach number of $M_A \sim 10$. These rough parameters, which are fairly typical of Earth's foreshock, serve as the basis for the numerical simulations below.

Because the electrons are far from resonance with the RHI and the mode frequencies are well below the electron plasma and cyclotron frequencies, hybrid numerical codes (Lipatov, 2002; Winske et al., 2003) that treat the ions as a kinetic species and the electrons as a massless neutralizing background are suitable for studying the linear and non-linear evolution of the RHI. Here, we use a hybrid version of the particle-in-cell (PIC) code VPIC (Bowers et al., 2008; Le et al., 2021; Keenan et al., 2022) to model the RHI. Numerous earlier studies of ion streaming instabilities have used similar electromagnetic hybrid PIC codes (e.g., Winske and Quest., 1986; Hada et al., 1987; Gary and Winske, 1990; Winske and Omidi, 1992; Akimoto et al., 1993; Dubouloz and Scholer, 1995; Hellinger and Mangeney, 1999; Wang and Lin, 2003; Heuer et al., 2018; Weidl et al., 2019; Holcomb and Spitkovsky, 2019). Because the simulations in this section are 1D in the x direction, they only allow the growth of the purely

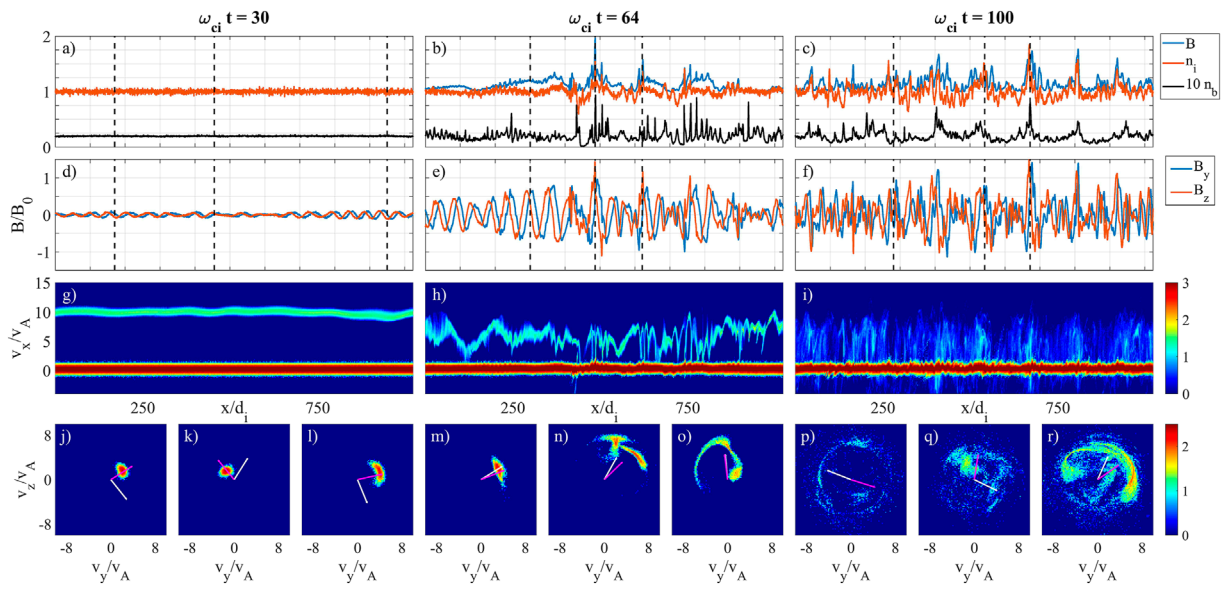

FIGURE 2
Results from 1D hybrid simulations of the resonant right-hand instability (RHI) with cold ($v_{thi} = v_{thb} = 0.1v_A$) ion populations. The left panels are at early time $t\omega_{ci} = 30$, middle panels are at $t\omega_{ci} = 64$, and right panels are at $t\omega_{ci} = 100$. **(A–C)** Background (red) and beam (black) ion density profiles and magnetic field strength (blue). **(D–F)** Wave magnetic field components B_y and B_z. **(G–I)** Parallel $x - v_x$ phase space distribution of the ions, showing the dense background at v_x~0 and the beam with an Alfven Mach number of $M_A = 10$. **(J–R)** Beam ion distributions in the perpendicular $v_y - v_z$ plane at the points marked by the vertical dashed lines in **(A–C)**. The white lines show the direction of the perpendicular wave magnetic fields B_y and B_z, and the magenta lines show the direction of the bulk beam perpendicular velocity.

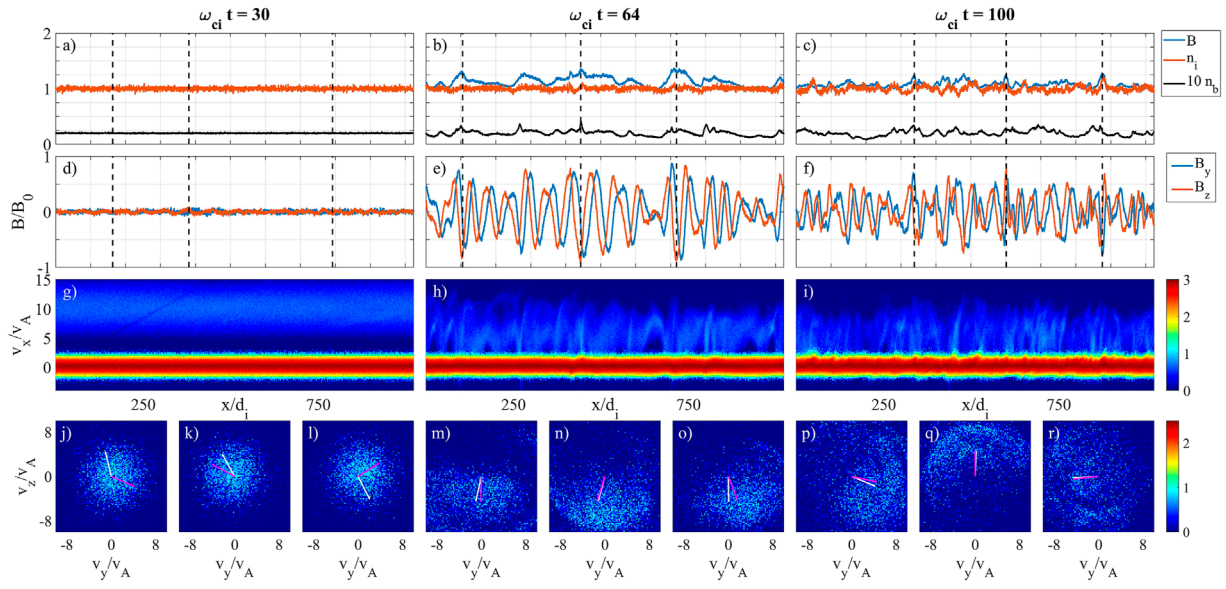

FIGURE 3
Similar plots as in **Figure 2**, but with warm background ($v_{thi} = \sqrt{2T_i/m_i} = v_A$ or $\beta_i = 1$) and beam ($v_{thb} = 3v_A$) ion populations. Again, the left panels are at early time $t\omega_{ci} = 30$, middle panels are at $t\omega_{ci} = 64$, and right panels are at $t\omega_{ci} = 100$. **(A–C)** Background (red) and beam (black) ion density profiles and magnetic field strength (blue). **(D–F)** Wave magnetic field components B_y and B_z. **(G–I)** Parallel $x - v_x$ phase space distribution of the ions, showing the dense background at v_x~0 and the beam with an Alfven Mach number of $M_A = 10$. **(J–R)** Beam ion distributions in the perpendicular $v_y - v_z$ plane at the points marked by the vertical dashed lines in **(A–C)**. The white lines show the direction of the perpendicular wave magnetic fields B_y and B_z, and the magenta lines show the direction of the bulk beam perpendicular velocity.

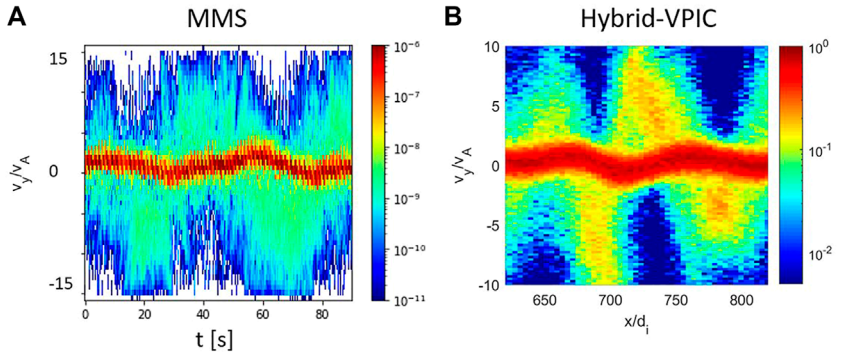

FIGURE 4
Ion velocity distributions in v_y from **(A)** the MMS event displayed in **Figure 1** in an interval starting near time 01:05 and **(B)** from the hybrid PIC simulation with warm beam ($v_{thb} = 3v_A$) and background ($v_{th0} = v_A$)) ions of **Figure 3** at $t = 40/\omega_{ci}$. In **(A)**, the time t may be considered a proxy for the position x in **(B)** as the solar wind passes the spacecraft at the solar wind drift speed of 300 $km/s \sim 10v_A$. The correspondence is 50 $s \sim 100d_i$.

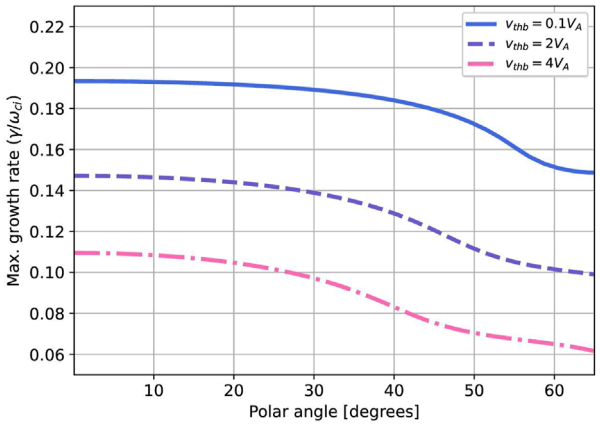

FIGURE 5
Growth rate of the RHI for oblique propagation as a function of the angle between the wave vector k and the background magnetic field for $n_b/n_0 = .015$ and $M_A = 10$. Note that the growth rate is very similar for angles $\lesssim 35°$. The three curves show the growth rate for different beam temperatures with thermal speeds indicated in the legend.

parallel propagating modes, which are the fastest growing modes for the parameters we use. Note that for 2D or 3D systems with oblique modes, damping on the electrons can become more important. While this effect is included in the linear dispersion solver, it is not captured by the fluid model of the hybrid code.

As in other hybrid PIC codes, the electron model in Hybrid-VPIC takes the form of an Ohm's law for the electric field:

$$\mathbf{E} = -\mathbf{u_i} \times \mathbf{B} - \frac{1}{ne}\nabla p_e + \frac{1}{ne}\mathbf{J} \times \mathbf{B} + \eta \mathbf{J} - \eta_H \nabla^2 \mathbf{J} \qquad (4)$$

where quasi-neutrality imposes $n = n_e = \sum_s Z_s n_s$ (including a sum over species s of ions), the velocity u_i is the charge-weighted ion flow $\mathrm{u_i} = \sum_s Z_s n_s \mathbf{u_s}/n_e$, and the current density is taken in the low-frequency approximation as $\mu_0 \mathbf{J} = \nabla \times \mathbf{B}$. We use a system of units based on the background magnetic field B_0 and ion density n_0, with times normalized by the cyclotron frequency $\omega_{ci} = eB_0/m_i$ and lengths given in terms of the ion inertial length $d_i = (\epsilon_0 m_i c^2/e^2 n_0)^{1/2}$. Because we use particle shapes that are sums of quadratics in each direction, we choose grid resolutions with Δx ranging from .25 to 1 d_i to avoid an unphysical numerical dispersion that occurs when low spatial resolution and high-order particle shapes are used in hybrid PIC codes (Stanier et al., 2020). For these 1D simulations, we include 2000 particles per cell for each ion population. The normalized resistivity $\eta/(B_0/n_0)$ and hyper-resistivity $\eta_H/(B_0/n_0 e d_i^2)$ are set to small values in the range of 1×10^{-4} to 5×10^{-3}. For the simulations here, the electron pressure follows a simple isothermal closure, such that the electron pressure is given by $p_e = n_e T_e$, with T_e a constant (Le et al., 2016). Test simulations with an adiabatic electron closure showed no discernible differences.

As described in **Section 2**, our 1D simulations contain a uniform background plasma of density n_0 and temperature T_0 (we set $T_i = T_e = T_0$) and magnetic field B_0 in the x direction. To this is added a streaming population of beam ions of density n_b (recall an equal number density of electrons is implicit in the quasi-neutral assumption of the hybrid code), drift velocity in the positive x direction u_b, and temperature T_b. **Figure 2** shows typical results from an RHI simulation with relatively cold background and beam populations. The three sets of panels in **Figure 2** are at three different times over the course of simulation.

The leftmost panels are at time $t^*\omega_{ci} = 30$ when the RHI is nearing the end of a phase growth consistent with the linear instability. The background and beam density profiles as well as the total magnetic field magnitude in **Figure 2A**

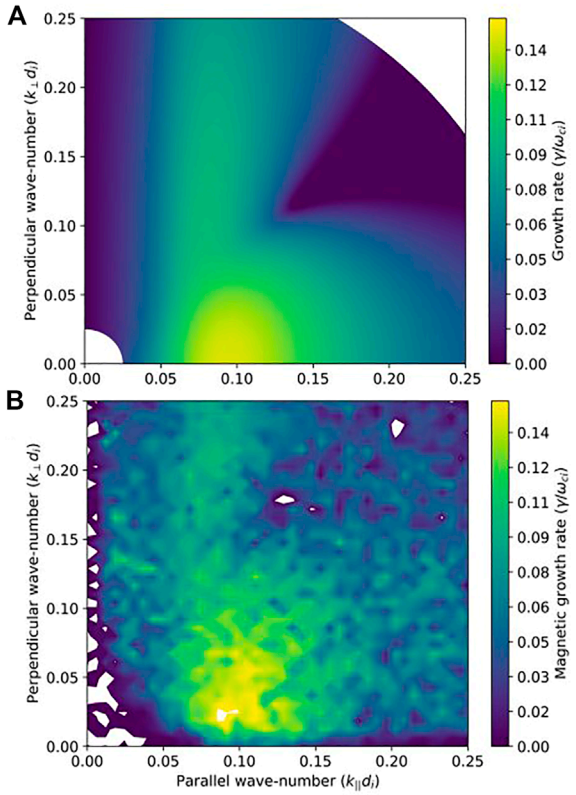

FIGURE 6
(A) Growth rate computed using the NHDS Verscharen and Chandran, (2018) as a function of parallel ($k_\parallel d_i$) and perpendicular ($k_\perp d_i$) normalized wave numbers for a beam of density $n_b/n_0 = .02$, Alfven Mach number $M_A = 10$, and beam thermal speed of $v_{thb} = 3v_A$. **(B)** Growth rate extracted from a 2D hybrid simulation with the same parameters as above measured by taking a time derivative of the magnetic field fluctuations.

are relatively unperturbed. The ion phase space distribution in $x - v_x$ space in **Figure 2** shows a weak modulation of the beam ions (the population centered at $v_x \sim 10v_A$). Nevertheless, the RHI is here already strong enough to modulate the beam ions in perpendicular velocity space. The three panels of **Figures 2J–L** show the perpendicular velocity distribution of the beam ions in $v_y - v_z$ space at the three locations marked by vertical dashed lines in **Figure 2A**. These distributions exhibit gyrophase bunching, with the beam ions undergoing motion in the plane perpendicular to the magnetic field. As in previous simulations and observations (Hoshino and Terasawa, 1985; Thomsen et al., 1985; Fuselier et al., 1986; Gary et al., 1986), the gyrophase bunched ions are out of phase with the wave magnetic field. In **Figures 2J–L**, the white line gives the direction of the wave magnetic field (B_y and B_z), while the black line shows the direction of the local bulk beam velocity in the $y - z$ plane. The field and beam velocity are roughly 90° out of phase.

At later time, the RHI waves steepen into non-linear features. Non-linear structures have been observed with beam populations upstream of the bow shock, and they have been identified as shocklets (Hoppe et al., 1981; Hada et al., 1987) or magnetic pulsations (Akimoto et al., 1993). As in the earlier simulations of Akimoto et al., 1993, the non-linear pulsations driven by the RHI are characterized by correlated magnetic field strength $|B|$ perturbations (see the blue curve in **Figure 2B**) that are correlated with the density n perturbations (red curve).

Thermal velocity spreads of the background and beam ions that are not large compared to the relative drift speed do not qualitatively affect the linear properties of the RHI, though the finite temperatures moderately reduce the growth rates. The non-linear features that develop, however, are weaker in amplitude in our simulations with higher beam and background temperatures. We show example data from a simulation with a beam thermal spread $v_{thb} = 3v_A$ and background thermal speed of $v_{th0} = v_A$ in **Figure 3**. For cold beams ions as in **Figure 2**, practically all of the beam ions can become bunched where the RHI waves steepen. In addition to bunching in gyrophase angle, these resonant beam ions can be dramatically slowed down in the parallel direction, even locally coming to a stop in the background frame (see **Figure 2H**). For hot beams that are more diffuse in velocity space, on the other hand, a relatively smaller fraction of the beams ions are near exact resonance with the RHI mode. As a result, a smaller fraction of the beam ions in **Figure 3H** are slowed by the wave fields. This results in a much less spiky beam ion density profile in **Figure 3B** than for the cold ions case. Furthermore, because the RHI couples to compressional modes, the higher background pressure weakens the amplitude of the non-linear features. For even higher background temperatures with $v_{th0} = 4v_A$ (not plotted), there are no discernible pulsations or spikes in the density or magnetic field profiles.

The beam ions do display strong gyrophase bunching in perpendicular velocity space, although the non-linear structures that develop are relatively weak for the warmer beam and background temperatures (see **Figure 3**). We display side-by-side in **Figure 4** ion v_y velocity distributions from the MMS event and from the Hybrid-VPIC simulation of **Figure 3**. The MMS data in **Figure 4A** show the v_y distribution of ions over time, which may be taken as a proxy for distance x because the waves rapidly cross the spacecraft. A distribution in $x - v_y$ phase space from the hybrid PIC model is displayed in **Figure 3B** covering a range with a similar wave phase and amplitude as the MMS data. Note that ~90° phase shift characteristic of the RHI between the wave fluctuations (carried by the background ions) and the gyro-bunched beam ions is visible in both the MMS data and the hybrid PIC simulation data.

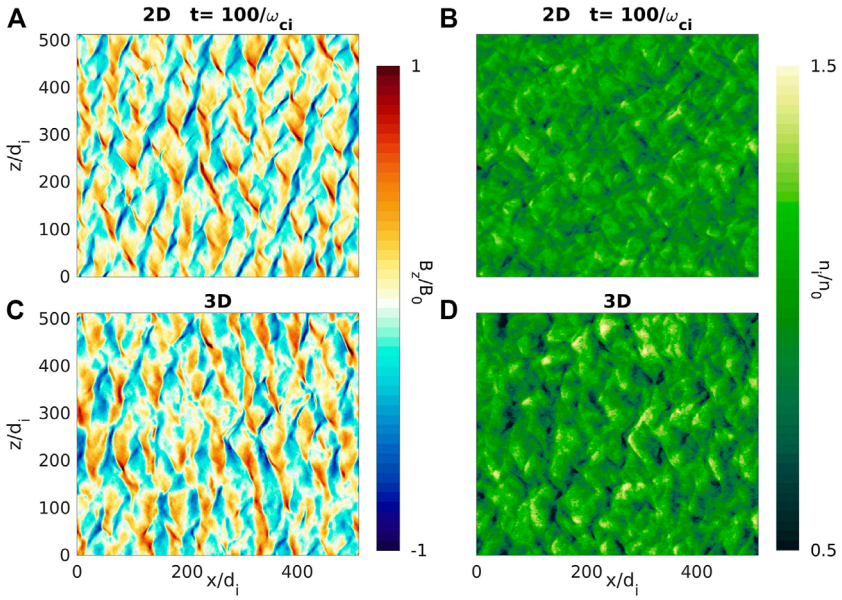

FIGURE 7
Comparison between **(A, B)** 2D and **(C, D)** 3D simulations. Left panels show B_z magnetic field component and right panels show density fluctuations in two runs with identical parameters ($n_b/n_0 = .02$, $M_A = 10$, $\beta_i = 1$, $\beta_b = 4.5$) at a late phase after the resonant mode has saturated.

4 2D and 3D hybrid simulations

In this section, we consider 2D and 3D hybrid simulations to study the evolution of the RHI in multiple spatial dimensions. The 2D or 3D geometry allows the development of a spectrum of modes with k vectors oblique to the magnetic field. As visible in **Figure 5**, the RHI growth rate is relatively insensitive to the propagation angle out to ∼35°. Interestingly, a statistical survey of 30-s waves observed in the Earth's foreshock found that the distribution of wave propagation angles was typically peaked at an oblique angle of ∼20° to the magnetic field (Eastwood et al., 2005). Previous hybrid simulations suggested that refraction of steepening waves driven by the fastest growing parallel propagating modes could explain the presence of oblique modes in observations (Dubouloz and Scholer, 1995). On the other hand, (Strumik et al. 2015) studied the development of ULF waves in the foreshock of a 2D hybrid global magnetosphere model with a quasi-radial IMF and quasi-parallel bow shock. They found that averaging over the spectrum of excited RHI modes at different propagation angles gave a spectrum similar to the observations. We consider this possibility in our simplified uniform beam simulations below.

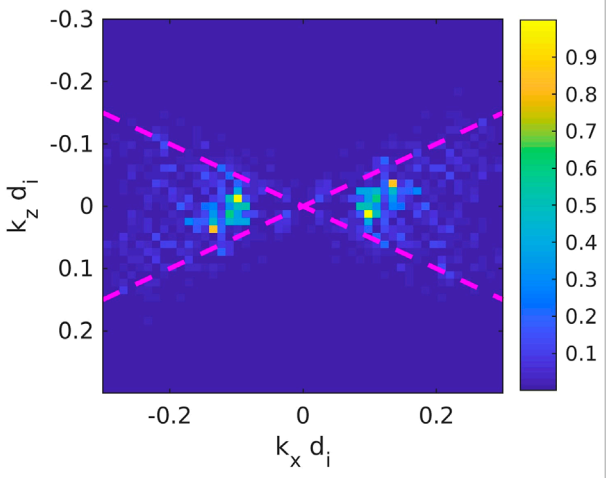

FIGURE 8
Power spectrum $|B_z(k_x,k_z)|^2$ of the magnetic field plotted in **Figure 7A**. The dashed magenta lines indicate where the propagation angle is 30° with respect to the background field B_x.

To examine the spectrum of oblique modes, we consider a 2D simulation in the $x-z$ plane of a uniform beam, building on early hybrid simulation work on 2D ion-ion beam instability growth (Winske and Quest, 1986). The simulation domain is of size $L_x \times L_z = 1024d_i \times 1024d_i = 2048 \times 2048$ cells, the background ($v_{th0} = v_A$) and beam ($n_b/n_0 = .02, M_A = 10, v_{thb} = 4.3v_A$) ion populations are each sampled by 400 particles per cell, and the time step is $\delta t = .01/\Omega_{ci}$. In **Figure 6**, we compare the growth rates predicted by numerical solution of the hot plasma dispersion relation in (a) to the growth rates extracted directly from the hybrid PIC simulation in (b). The growth rate in each case is plotted in terms of the parallel ($k_\parallel$ and perpendicular

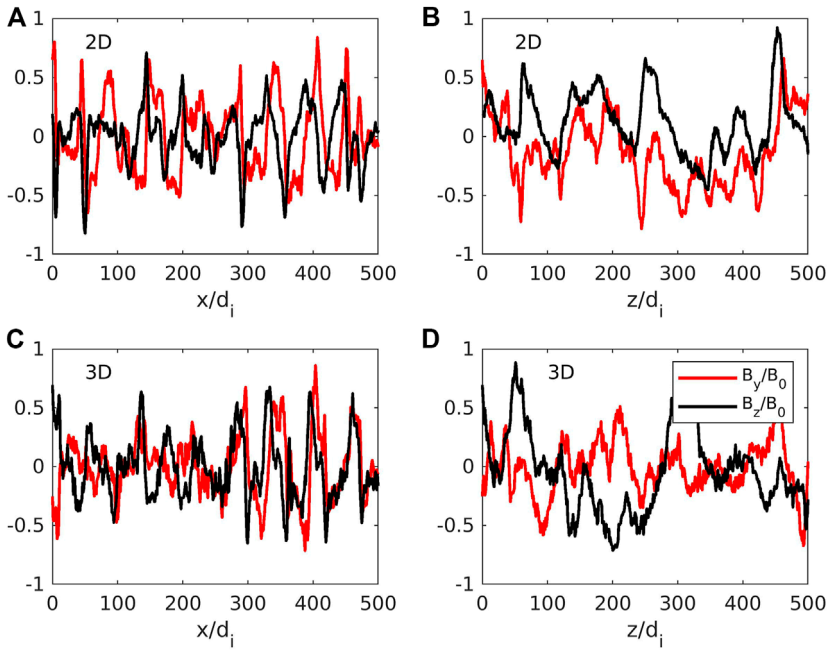

FIGURE 9
Comparison between **(A, B)** 2D and **(C, D)** 3D simulations. Left panels show B_z magnetic field component and right panels show density fluctuations in runs with identical parameters ($n_b/n_0 = .02$, $M_A = 10$, $\beta_i = 1$, $\beta_b = 4.5$) at a late phase after the resonant mode has saturated. The 2D and 3D simulations have similar characteristic parallel and perpendicular length scales.

$k_\perp$ wave numbers. The peak growth rate occurs for parallel propagation and corresponds to the usual RHI. Consistent with **Figure 5**, there is a relatively broad range of oblique wave vectors with growth rates very close to the maximum. Because of this, a wide spectrum of waves with varying propagation angles is excited. The modes plotted are all almost exactly right circularly polarized. The real frequency increases by a factor of few beyond propagation angles of 40°, and those more perpendicular modes may connect to a different wave branch.

The magnetic field and density structures that develop after the RHI saturates are very similar in 2D and 3D. **Figure 7** shows comparisons of (a, c) the magnetic field component B_z and the (b, d) the plasma density between a 2D and a corresponding 3D hybrid simulation. These simulations are similar to the above simulation, but with a domain of size of $L = 512d_i = 512$ cells in each spatial dimension. The wide spectrum of unstable oblique modes produces magnetic fluctuations with oblique phase fronts. To quantify this effect, we show in **Figure 8** a Fourier power spectrum of the wave magnetic field component B_z plotted in **Figure 7A**. The symmetry of the spectrum for $\mathbf{k}$ going to $-\mathbf{k}$ is simply a result of the Fourier transform of the real function B_z. The peak in the power spectrum is at $k_x d_i \sim .1$, corresponding to a characteristic wavelength of $\sim 60d_i$. As noted by (Strumik et al., 2015), the fluctuation power density is spread over a range of different $\mathbf{k}$ vectors centered at $k_z = 0$. Averaging over this spectrum can explain the statistics of oblique ULF waves observed by (Eastwood et al., 2005) in Earth's foreshock.

As another way of displaying the parallel and perpendicular structure of the saturated magnetic field fluctuations, we plot cuts of the magnetic field components in **Figure 9** along the (a, c) parallel or x direction and the (b, d) perpendicular or z direction. Again, the characteristic parallel wavelengths here are $\sim 60d_i$. While the parallel mode ($k_z = 0$) is fastest growing, the cuts in z show large variations in the perpendicular direction. The typical perpendicular length scales are ~ 100 to $200d_i$ and are associated with the excitation of a wide spectrum of oblique wave vectors in the original linear modes. Although not studied here, this spectrum of non-linear fluctuations in 3D can contribute to cross-field diffusion of ions (Kucharek et al., 2000).

5 Summary discussion

Using a modern hybrid PIC code, we revisited the resonant right-hand instability (RHI), which is the dominant electromagnetic ion beam instability for parallel-propagating ion beams that are relatively fast and tenuous. The parameters for the simulations were inspired by MMS observations of typical quasi-parallel foreshock fluctuations. RHI is prevalent upstream of the quasi-parallel region of Earth's bow shock and has been the subject of a large number of previous observational and

theoretical studies, including important early works by Peter Gary (Gary et al., 1984; Gary et al., 1985; Gary et al., 1986; Gary and Winske, 1990; Gary, 1991). Here, we focused on properties of the RHI related to finite temperature effects and oblique propagation. The hybrid simulations show that warm ($\beta > 1$) background and beam ion populations produce less steep non-linear features than the cold populations assumed in many previous studies. Note the RHI itself scatters reflected beam ions effectively, and it is possible that the RHI scatters an initially cooler beam into the more diffuse beam with a larger velocity spread observed by MMS. In any case, a high-beta background plasma requires additional energy to be compressed, which explains the weaker non-linear compressional features observed in simulations with high plasma beta (particularly $\beta \gg 1$, which is not typical of the solar wind at Earth's foreshock).

Multi-dimensional (2D and 3D) hybrid simulations demonstrated that a wide spectrum of oblique modes is excited, in agreement with growth rates predicted by numerical solution of the hot plasma dispersion relation. The RHI instability growth rate is a fairly flat function of propagation angle out to ∼35°. The theoretical growth rates for the RHI agreed with the range of modes excited in the hybrid simulations, and the non-linear stage contained fluctuations with characteristic perpendicular length scales 2–3 times longer than the typical parallel wavelength. At Earth's bow shock, typical parallel length scales would be $60d_i$, which corresponds to .5 to $1.5R_E$ (Earth radii) for typical solar wind densities. The corresponding perpendicular lengths scales are $2–3R_E$. These non-linear structures are therefore planet-sized, and they may impact the planetary magnetopshere.

Data availability statement

The simulation data for this study can be reproduced by running the open-source Hybrid-VPIC code branch found at https://github.com/lanl/vpic-kokkos/tree/hybridVPIC. MMS datasets are retained and available through https://lasp.colorado.edu/mms/sdc/public/.

Author contributions

AL conceived the paper idea and formulated the investigation with L-JC. AL ran simulations, analyzed data, and prepared the manuscript. L-JC prepared figures of MMS data. BW ran simulations and prepared figures. BK analyzed simulation data, ran the NHDS code, and prepared figures. All authors discussed the results and reviewed the manuscript.

Funding

This work was supported by the Los Alamos LDRD program and by NASA's Magnetospheric Multiscale Mission. Simulations used LANL Institutional Computing resources.

Conflict of interest

The authors declare that the research was conducted in the absence of any commercial or financial relationships that could be construed as a potential conflict of interest.

Publisher's note

References

Akimoto, K., Winske, D., Gary, S., and Thomsen, M. (1993). Nonlinear evolution of electromagnetic ion beam instabilities. *J. Geophys. Res. Space Phys.* 98, 1419–1433. doi:10.1029/92ja02345

Blanco-Cano, X., Omidi, N., and Russell, C. (2009). Global hybrid simulations: Foreshock waves and cavitons under radial interplanetary magnetic field geometry. *J. Geophys. Res. Space Phys.* 114, 13406. doi:10.1029/2008ja013406

Bowers, K. J., Albright, B., Yin, L., Bergen, B., and Kwan, T. (2008). Ultrahigh performance three-dimensional electromagnetic relativistic kinetic plasma simulation. *Phys. Plasmas* 15, 055703. doi:10.1063/1.2840133

Burch, J., Torbert, R., Phan, T., Chen, L. J., Moore, T., Ergun, R., et al. (2016). Electron-scale measurements of magnetic reconnection in space. *Science* 352, aaf2939. doi:10.1126/science.aaf2939

Chen, L. J., Halekas, J., Wang, S., DiBraccio, G. A., Romanelli, N., Ng, J., et al. (2022). Solitary magnetic structures developed from gyro-resonance with solar wind ions at Mars and Earth. *Geophys. Res. Lett.* 49, e2021GL097600. doi:10.1029/2021gl097600

Daughton, W., and Gary, S. P. (1998). Electromagnetic proton/proton instabilities in the solar wind. *J. Geophys. Res. Space Phys.* 103, 20613–20620. doi:10.1029/98ja01385

Dubouloz, N., and Scholer, M. (1995). Two-dimensional simulations of magnetic pulsations upstream of the Earth's bow shock. *J. Geophys. Res. Space Phys.* 100, 9461–9474. doi:10.1029/94ja03239

Eastwood, J., Balogh, A., Lucek, E., Mazelle, C., and Dandouras, I. (2005). Quasi-monochromatic ulf foreshock waves as observed by the four-spacecraft cluster mission: 2. Oblique propagation. *J. Geophys. Res. Space Phys.* 110, A11220. doi:10.1029/2004ja010618

Fuselier, S., Thomsen, M., Gary, S., Bame, S., Russell, C., and Parks, G. (1986). The phase relationship between gyrophase-bunched ions and mhd-like waves. *Geophys. Res. Lett.* 13, 60–63. doi:10.1029/gl013i001p00060

Gary, S. P. (1991). Electromagnetic ion/ion instabilities and their consequences in space plasmas: A review. *Space Sci. Rev.* 56, 373–415. doi:10.1007/bf00196632

Gary, S. P., Madland, C. D., and Tsurutani, B. T. (1985). Electromagnetic ion beam instabilities: Ii. *Phys. fluids* 28, 3691–3695. doi:10.1063/1.865101

Gary, S. P., Smith, C. W., Lee, M. A., Goldstein, M. L., and Forslund, D. W. (1984). Electromagnetic ion beam instabilities. *Phys. fluids* 27, 1852–1862. doi:10.1063/1.864797

Gary, S. P. (1978). The electromagnetic ion beam instability and energy loss of fast alpha particles. *Nucl. fusion* 18, 327–334. doi:10.1088/0029-5515/18/3/003

Gary, S. P., Thomsen, M. F., and Fuselier, S. A. (1986). Electromagnetic instabilities and gyrophase-bunched particles. *Phys. fluids* 29, 531–535. doi:10.1063/1.865441

Gary, S. P., and Winske, D. (1990). Computer simulations of electromagnetic instabilities in the plasma sheet boundary layer. *J. Geophys. Res. Space Phys.* 95, 8085–8094. doi:10.1029/ja095ia06p08085

Greenstadt, E., Le, G., and Strangeway, R. (1995). Ulf waves in the foreshock. *Adv. Space Res.* 15, 71–84. doi:10.1016/0273-1177(94)00087-h

Hada, T., Kennel, C., and Terasawa, T. (1987). Excitation of compressional waves and the formation of shocklets in the Earth's foreshock. *J. Geophys. Res. Space Phys.* 92, 4423–4435. doi:10.1029/ja092ia05p04423

Hellinger, P., and Mangeney, A. (1999). Electromagnetic ion beam instabilities: Oblique pulsations. *J. Geophys. Res. Space Phys.* 104, 4669–4680. doi:10.1029/1998ja900157

Heuer, P. V., Weidl, M. S., Dorst, R. S., Schaeffer, D. B., Tripathi, S. K., Vincena, S., et al. (2020). Laboratory observations of ultra-low-frequency analog waves driven by the right-hand resonant ion beam instability. *Astrophysical J. Lett.* 891, L11. doi:10.3847/2041-8213/ab75f4

Heuer, P., Weidl, M., Dorst, R., Schaeffer, D., Bondarenko, A., Tripathi, S., et al. (2018). Observations of a field-aligned ion/ion-beam instability in a magnetized laboratory plasma. *Phys. Plasmas* 25, 032104. doi:10.1063/1.5017637

Holcomb, C., and Spitkovsky, A. (2019). On the growth and saturation of the gyroresonant streaming instabilities. *Astrophysical J.* 882, 3. doi:10.3847/1538-4357/ab328a

Hoppe, M., Russell, C., Frank, L., Eastman, T., and Greenstadt, E. (1981). Upstream hydromagnetic waves and their association with backstreaming ion populations: Isee 1 and 2 observations. *J. Geophys. Res. Space Phys.* 86, 4471–4492. doi:10.1029/ja086ia06p04471

Hoshino, M., and Terasawa, T. (1985). Numerical study of the upstream wave excitation mechanism: 1. Nonlinear phase bunching of beam ions. *J. Geophys. Res. Space Phys.* 90, 57–64. doi:10.1029/ja090ia01p00057

Kajdič, P., Pfau-Kempf, Y., Turc, L., Dimmock, A. P., Palmroth, M., Takahashi, K., et al. (2021). Ulf wave transmission across collisionless shocks: 2.5 d local hybrid simulations. *J. Geophys. Res. Space Phys.* 126, e2021JA029283. doi:10.1029/2021ja029283

Keenan, B. D., Le, A., Winske, D., Stanier, A., Wetherton, B., Cowee, M., et al. (2022). Hybrid particle-in-cell simulations of electromagnetic coupling and waves from streaming burst debris. *Phys. Plasmas* 29, 012107. doi:10.1063/5.0075482

Kucharek, H., Scholder, M., and Matthews, A. (2000). Three-dimensional simulation of the electromagnetic ion/ion beam instability: Cross field diffusion. *Nonlinear Process. Geophys.* 7, 167–172. doi:10.5194/npg-7-167-2000

Le, A., Daughton, W., Karimabadi, H., and Egedal, J. (2016). Hybrid simulations of magnetic reconnection with kinetic ions and fluid electron pressure anisotropy. *Phys. Plasmas* 23, 032114. doi:10.1063/1.4943893

Le, A., Winske, D., Stanier, A., Daughton, W., Cowee, M., Wetherton, B., et al. (2021). Astrophysical explosions revisited: Collisionless coupling of debris to magnetized plasma. *J. Geophys. Res. Space Phys.* 126, e2021JA029125. doi:10.1029/2021ja029125

Lee, M. A. (1982). Coupled hydromagnetic wave excitation and ion acceleration upstream of the Earth's bow shock. *J. Geophys. Res. Space Phys.* 87, 5063–5080. doi:10.1029/ja087ia07p05063

Lipatov, A. S. (2002). *The hybrid multiscale simulation technology: An introduction with application to astrophysical and laboratory plasmas*. Berlin, Germany: Springer Science & Business Media.

Montgomery, M. D., Gary, S. P., Forslund, D., and Feldman, W. (1975). Electromagnetic ion-beam instabilities in the solar wind. *Phys. Rev. Lett.* 35, 890. doi:10.1103/physrevlett.35.890.3

Palmroth, M., Archer, M., Vainio, R., Hietala, H., Pfau-Kempf, Y., Hoilijoki, S., et al. (2015). Ulf foreshock under radial imf: Themis observations and global kinetic simulation vlasiator results compared. *J. Geophys. Res. Space Phys.* 120, 8782–8798. doi:10.1002/2015ja021526

Stanier, A., Chacon, L., and Le, A. (2020). A cancellation problem in hybrid particle-in-cell schemes due to finite particle size. *J. Comput. Phys.* 420, 109705. doi:10.1016/j.jcp.2020.109705

Strumik, M., Roytershteyn, V., Karimabadi, H., Stasiewicz, K., Grzesiak, M., and Przepiórka, D. (2015). Identification of the dominant ulf wave mode and generation mechanism for obliquely propagating waves in the Earth's foreshock. *Geophys. Res. Lett.* 42, 5109–5116. doi:10.1002/2015gl064915

Thomsen, M., Gosling, J., Bame, S., and Russell, C. (1985). Gyrating ions and large-amplitude monochromatic mhd waves upstream of the Earth's bow shock. *J. Geophys. Res. Space Phys.* 90, 267–273. doi:10.1029/ja090ia01p00267

Turc, L., Zhou, H., Tarvus, V., Ala-Lahti, M., Battarbee, M., Pfau-Kempf, Y., et al. (2022). A global view of pc3 wave activity in near-Earth space: Results from hybrid-vlasov simulations. *Front. Astronomy Space Sci.* 9, 989369. doi:10.3389/fspas.2022.989369

Verscharen, D., and Chandran, B. (2018). Nhds: The New Hampshire dispersion relation solver. *Res. Notes AAS* 2, 13. doi:10.3847/2515-5172/aabfe3

Wang, X., and Lin, Y. (2003). Generation of nonlinear alfvén and magnetosonic waves by beam–plasma interaction. *Phys. Plasmas* 10, 3528–3538. doi:10.1063/1.1599359

Watanabe, Y., and Terasawa, T. (1984). On the excitation mechanism of the low-frequency upstream waves. *J. Geophys. Res. Space Phys.* 89, 6623–6630. doi:10.1029/ja089ia08p06623

Weidl, M. S., Winske, D., and Niemann, C. (2019). Three regimes and four modes for the resonant saturation of parallel ion-beam instabilities. *Astrophysical J.* 873, 57. doi:10.3847/1538-4357/ab0462

Winske, D., and Gary, S. (1986). Electromagnetic instabilities driven by cool heavy ion beams. *J. Geophys. Res. Space Phys.* 91, 6825–6832. doi:10.1029/ja091ia06p06825

Winske, D., and Omidi, N. (1992). Electromagnetic ion/ion cyclotron instability: Theory and simulations. *J. Geophys. Res. Space Phys.* 97, 14779–14799. doi:10.1029/92ja00902

Winske, D., and Quest, K. (1986). Electromagnetic ion beam instabilities: Comparison of one-and two-dimensional simulations. *J. Geophys. Res. Space Phys.* 91, 8789–8797. doi:10.1029/ja091ia08p08789

Winske, D., and Wilson, L. B. (2022). Linear theory of electromagnetic ion beam instabilities in the Earth's forshock: Peter gary's contributions (1981–1991). *Front. Astronomy Space Sci.* 9, 899642. doi:10.3389/fspas.2022.899642

Winske, D., Yin, L., Omidi, N., Karimabadi, H., and Quest, K. (2003). "Hybrid simulation codes: Past, present and future—A tutorial," in *Space plasma simulation* (Springer, Berlin, Heidelberg: Spinger), 136–165. doi:10.1007/3-540-36530-3_8

Frontiers in
Astronomy and Space Sciences

Explores planetary science and extragalactic astronomy in all wavelengths

Advances the understanding of our universe - from planetary science to extragalactic astronomy, to high-energy and astroparticle physics.

Discover the latest Research Topics

See more →

Frontiers

Avenue du Tribunal-Fédéral 34
1005 Lausanne, Switzerland
frontiersin.org

Contact us

+41 (0)21 510 17 00
frontiersin.org/about/contact